

**Institute of Low Temperature and Structure Research  
Polish Academy of Sciences**



## **DOCTORAL DISSERTATION**

**mgr Maja Szymczak**

***The investigations of the influence of the applied pressure  
on the luminescence properties of the Cr<sup>3+</sup>-doped inorganic materials  
for luminescence manometry applications***

in the form of a thematically coherent series of articles published in scientific journals

**Supervisor: prof. dr hab. Łukasz Marciniak**

**Wrocław 2025**



*I would like to express my deepest and most heartfelt gratitude **to my supervisor, Professor Łukasz Marciniak**, who has been the best mentor I could have ever hoped for on my scientific path. Thank you for creating an environment in which I felt truly supported, respected, and genuinely encouraged - an environment that allowed me to discover my own potential and grow into the scientist I aspired to become. You have shown me, day by day, what it means to be a great scientist - not just through your knowledge, patience, and unwavering dedication. I carry your example with me, and I hope that one day I can inspire someone the way you have inspired me.*

***To my Mom** - for everything that cannot be measured in words. For your calm presence during moments of doubt, and for celebrating even the smallest successes as if they were your own. You were always there as a reminder that I am stronger than I think and I learned what true strength means by watching you.*

***To my Dear Friends** - thank you for being there in ways I didn't always know I needed. For reminding me to eat and to sleep. Thank you for not letting me disappear completely into work - for pulling me back into life when I needed it most.*





This doctoral dissertation was supported by the **National Science Center (NCN) Poland** under project number 2020/37/B/ST5/00164 “*Nanocrystalline luminescent manometers based on transition metal ions emission*”.



Maja Szymczak also gratefully acknowledges the support received from **Foundation L’Oréal, UNESCO and the Ministry of Science and Higher Education of the Republic of Poland**, as well as **the Foundation for Polish Science (FNP)** under the **START** programme.



Ministry of Science and Higher Education  
Republic of Poland

---



Foundation for  
Polish Science



## TABLE OF CONTENT

---

ABSTRACT.....	10
STRESZCZENIE.....	11
SCIENTIFIC INFORMATIONS ABOUT THE AUTHOR.....	12
BRIEF BACKGROUND & MOTIVATION FOR THE RESEARCH.....	21
DISSERTATION OBJECTIVES.....	24
ABBREVIATIONS.....	25
DESCRIPTIVE PART.....	26
1. Luminescent materials doped with transition metal ions.....	26
1.1. Introduction to spectroscopic properties of Cr <sup>3+</sup> ions.....	27
1.1.1. Pressure - dependent Cr <sup>3+</sup> luminescence.....	30
1.2. Potential applications of Cr <sup>3+</sup> - doped phosphors.....	33
1.2.1. Luminescence-based sensors.....	34
2. Luminescence manometry.....	35
2.1. Manometric parameters.....	35
2.2. Brief overview of phosphors and sensing approaches exploited in luminescence manometry.....	36
2.3. Advantages and disadvantages of the materials and approaches used in luminescence manometry.....	40
3. High-pressure luminescence measurements in diamond anvil cell - construction and experimental methodology.....	43
3.1. Diamonds.....	44
3.2. Gasket.....	45
3.3. Pressure Indicator.....	46
3.4. Pressure-Transmitting Medium.....	47
EXPERIMENTAL PART.....	49
4. Experimental methods.....	49
4.1. Syntheses.....	49
4.2. Measurement methods and apparatus.....	51
5. Results and discussion.....	54
5.1. Development of a pioneering ratiometric LIR-based luminescent manometer based on the <sup>4</sup> T <sub>2g</sub> → <sup>4</sup> A <sub>2g</sub> electronic transition of Cr <sup>3+</sup> in doped Li <sub>2</sub> Mg <sub>3</sub> TiO <sub>6</sub> .....	54
5.2. Validation of two LIR-based ratiometric approaches utilizing emission from <sup>2</sup> E <sub>g</sub> and <sup>4</sup> T <sub>2g</sub> excited states of Cr <sup>3+</sup> - studies of MgO and CaMgSi <sub>2</sub> O <sub>6</sub> doped with Cr <sup>3+</sup> .....	57
5.3. Confirmation of manometric potential of matrices providing weak crystal field for Cr <sup>3+</sup> ions: multimodal luminescent manometer based on LiScGeO <sub>4</sub> :Cr <sup>3+</sup> and Li <sub>3</sub> Sc <sub>2</sub> (PO <sub>4</sub> ) <sub>3</sub> :Cr <sup>3+</sup> as	

an optical pressure sensor operating on three spectroscopic parameters.....	63
5.4. Studies of the potential of $\text{Cr}^{3+}\text{-Cr}^{3+}$ pairs emission in doped $\text{CaAl}_{12}\text{O}_{19}$ - development of a luminescent bifunctional pressure-temperature sensor.....	70
5.5. Comparative analysis of ratiometric LIR-based strategies for phosphors with two distinct crystallographic positions for $\text{Cr}^{3+}$ ions - studies of $\text{MgGeO}_3\text{:Cr}^{3+}$ .....	73
SUMMARY.....	77
Conclusions.....	77
Further research directions.....	82
COPY OF PUBLICATIONS INCLUDED IN THE DOCTORAL DISSERTATION.....	84
COPIES OF THE CO-AUTHORS' STATEMENTS.....	239
REFERENCES.....	259



---

## ABSTRACT

---

Precise control of pressure remains a fundamental requirement in high-pressure research and technology. Consequently, the development of more accurate and reliable pressure monitoring techniques and devices continues to be a central focus of experimental advancement. Among the most promising approaches are luminescent manometers - optical sensors capable of remote, non-invasive, real-time pressure readout by utilizing pressure-induced changes in the luminescent properties of phosphor materials.

The most prevalent strategy in luminescence manometry involves monitoring the pressure-induced spectral shift of a narrow emission line. Since its introduction in the mid-20th century, ruby has served as a robust and highly accurate pressure sensor in diamond anvil cell experiments under high pressure. However, despite its widespread adoption, ruby exhibits inherent limitations, including relatively low pressure sensitivity and considerable susceptibility to temperature fluctuations. These temperature-dependent effects can compromise measurement accuracy, particularly in experimental conditions where pressure and temperature change simultaneously. Such limitations highlight the critical demand for advanced sensing approaches and materials that combine high sensitivity to pressure changes, resistance to thermal perturbations, and outstanding measurement precision - key attributes required for the successful implementation of luminescence manometry in industrial applications.

In response to these requirements and the underlying challenges associated with proposed luminescent pressure-sensing approaches, the overarching objective of this doctoral dissertation was to conduct a systematic investigation of the pressure-dependent spectroscopic behavior of  $\text{Cr}^{3+}$  ions, with the aim of assessing their potential for application in luminescence manometry. The outcome of this research is the development and advancement of a novel class of luminescent pressure sensors that leverage the pressure-sensitive  ${}^4\text{T}_{2g} \rightarrow {}^4\text{A}_{2g}$  electronic transition of  $\text{Cr}^{3+}$  - marking a significant leap forward in the development of high-performance optical manometers. The findings, as presented in the series of peer-reviewed publications constituting this dissertation, demonstrate that the proposed  $\text{Cr}^{3+}$ -based luminescent manometers exhibit high readout precision, outstanding sensitivity to pressure variations, and remarkable independence from temperature of the system. These attributes collectively define a new generation of luminescent pressure sensors with exceptional application potential, advancing the field toward practical deployment in complex, real-world environments beyond the constraints of the laboratory.

---

## STRESZCZENIE

---

Precyzyjna kontrola ciśnienia niezmiennie stanowi podstawowe wymaganie w badaniach naukowych i technologiach wykorzystujących warunki wysokiego ciśnienia. W konsekwencji, rozwój coraz dokładniejszych i bardziej niezawodnych metod oraz urządzeń do monitorowania ciśnienia pozostaje jednym z kluczowych kierunków postępu eksperymentalnego. Wśród najbardziej obiecujących podejść znajdują się manometry luminescencyjne - optyczne czujniki umożliwiające zdalny, nieinwazyjny odczyt ciśnienia w czasie rzeczywistym, oparty na wykorzystaniu zmian właściwości luminescencyjnych materiału wywołanych działaniem ciśnienia.

Najczęściej stosowaną strategią w manometrii luminescencyjnej jest monitorowanie przesunięcia spektralnego wąskiej linii emisyjnej wywołanego przez zmiany ciśnienia. Od połowy XX wieku, rubin pełni rolę wysoce precyzyjnego indykatora ciśnienia w wysokociśnieniowych eksperymentach z użyciem komór diamentowych. Jednak pomimo szerokiego zastosowania, rubin posiada istotne ograniczenia, w tym stosunkowo niską czułość na zmiany ciśnienia oraz znaczną podatność pozycji spektralnej pasma na wahania temperatury. Czułość ta może znacząco obniżać dokładność odczytów, szczególnie w warunkach, w których ciśnienie i temperatura zmieniają się jednocześnie. Ograniczenia te wyraźnie wskazują na potrzebę opracowania zaawansowanych metod detekcji i materiałów, które będą charakteryzować się jednocześnie wysoką czułością na zmiany ciśnienia, odpornością na wpływ temperatury oraz wysoką precyzją pomiaru - cechy kluczowe dla wdrożenia manometrii luminescencyjnej w zastosowaniach przemysłowych.

W odpowiedzi na wspomniane wymagania oraz wyzwania związane z dotychczasowymi metodami luminescencyjnego pomiaru ciśnienia, nadrzędnym celem niniejszej rozprawy doktorskiej było przeprowadzenie systematycznych badań ciśnieniowych właściwości luminescencyjnych jonów  $\text{Cr}^{3+}$ , w celu oceny ich potencjału do zastosowania w manometrii luminescencyjnej. Rezultatem tych badań było opracowanie i rozwój czujników ciśnienia, wykorzystujących wrażliwe na zmiany ciśnienia przejście elektronowe  ${}^4\text{T}_{2g} \rightarrow {}^4\text{A}_{2g}$  jonów  $\text{Cr}^{3+}$  - co stanowi istotny krok naprzód w rozwoju wysokowydajnych manometrów luminescencyjnych. Wyniki, przedstawione w serii recenzowanych publikacji składających się na niniejszą dysertację, dowodzą, że zaproponowane manometry luminescencyjne oparte na jonach  $\text{Cr}^{3+}$  cechują się wysoką precyzją odczytu, wyjątkową czułością na zmiany ciśnienia oraz niewrażliwością na zmiany temperatury układu. Zestaw tych cech definiuje nową generację luminescencyjnych czujników ciśnienia o wyjątkowym potencjale aplikacyjnym, znacząco przybliżając tę technologię do praktycznego zastosowania w złożonych, rzeczywistych warunkach operacyjnych, wykraczających poza kontrolowane środowiska laboratoryjne

---

## SCIENTIFIC INFORMATION ABOUT THE AUTHOR

---

**M. Sc. Maja Szymczak**

**SCIENTIFIC IMPACT INDICATORS** (according to **Scopus/Google Scholar**, 26.05.2025):

---

Total citations: **269/300**

h-index: **9/10**

---

## EDUCATION

---

10/2021 - present **PhD Studies**, Institute of Low Temperature and Structure Research, Polish Academy Of Sciences

- Discipline: Chemical sciences
- Supervisor: Prof. dr hab. Lukasz Marciniak

07/2021 **Master of Science in Chemistry**

- Master's thesis "*Hydrophilic Ag<sub>2</sub>S quantum dots*"
- Supervisor: dr Jakub Cichos

2019 - 2021 **Master's studies**, Faculty of Chemistry, University of Wroclaw, Poland

- Chemistry, specialization: Instrumental Analytical Chemistry

2019 **Bachelor of Medical Chemistry**

- Bachelor's thesis "*Stabilization of semiquinone radicals through their interaction with cations*"
- Supervisor: dr hab. Maciej Witwicki

2016 - 2019 **Bachelor's studies**, Faculty of Chemistry, University of Wroclaw, Poland

- Medical Chemistry

---

## PARTICIPATION IN RESEARCH PROJECTS

---

- **Principal Investigator** - NCN PRELUDIUM 2023/49/N/ST5/01020 "*Synthesis and investigation of spectroscopic properties of  $XGa_2O_4:Ni^{2+}$  ( $X = Zn, Mg, Ca$ ) for luminescence manometry applications*" (01/2024 - present)
- **Investigator** - Polish-Taiwanese Joint Mobility Project between the Polish Academy of Sciences (PAS) and Academia Sinica (Taiwan) "*High Pressure Studies of Doped Perovskites Doped with Lanthanide Ions*" (05/2025-present)



- **Investigator** - NCN OPUS 2023/49/B/ST5/03384 “Multiparametric phosphors database on  $Mn^{4+}$  ions for knowledgeable development of the lifetime-based luminescence thermometry: synergetic combination of experiment and machine learning driven theory” (01/2024 - present)
- **Investigator** - NCN WEAVE-UNISONO 2023/05/Y/ST5/00013 „Novel materials based on lignin from biomass with enhanced luminescent activity” (09/2024 - present)
- **Investigator** - NCN OPUS 2022/45/B/ST5/01629 “Luminescence thermometry based on first-order structural phase transition” (01/2024 - present)
- **Investigator** - Polish-Vietnamese Joint Mobility Project between Polish Academy of Sciences (PAS) and Vietnam Academy of Science and Technology (VAST) “Luminescent thermometers and manometers based on Gd-MOF:Eu<sup>3+</sup>, Tb<sup>3+</sup> metal-organic framework” (2024)
- **Investigator** (PhD scholarship) - NCN OPUS 2020/37/B/ST5/00164 “Nanocrystalline luminescent manometers based on transition metal ion emission” (10/2021 - present)

#### PUBLICATIONS INCLUDED IN THE DOCTORAL DISSERTATION

---

- P1. **M. Szymczak**, P. Wozny, M. Runowski, M. Pieprz, V. Lavín, L. Marciniak, *Temperature invariant ratiometric luminescence manometer based on Cr<sup>3+</sup> ions emission*, Chemical Engineering Journal, 2023, 453, 139632, (IF = 13.4, MNiSW Points: 200)
- P2. **M. Szymczak**, M. Runowski, V. Lavín, L. Marciniak, *Highly Pressure-Sensitive, Temperature Independent Luminescence Ratiometric Manometer Based on MgO:Cr<sup>3+</sup> Nanoparticles*, Laser & Photonics Reviews, 2023, 17, 2200801, (IF = 9.8, MNiSW Points: 200)
- P3. **M. Szymczak**, K. Su, L. Mei, M. Runowski, P. Woźny, Q. Guo, L. Liao, L. Marciniak, *Investigating the Potential of Cr<sup>3+</sup>-Doped Pyroxene for Highly Sensitive Optical Pressure Sensing*, ACS Applied Materials & Interfaces 2024, 16, 44, 60491-60500, (IF = 8.5, MNiSW Points: 200)
- P4. **M. Szymczak**, M. Runowski, M.G. Brik, L. Marciniak, *Multimodal, super-sensitive luminescent manometer based on giant pressure-induced spectral shift of Cr<sup>3+</sup> in the NIR range*, Chemical Engineering Journal, 2023, 466, 143130, (IF = 13.4, MNiSW Points: 200)
- P5. **M. Szymczak**, J. Jaśkielewicz, M. Runowski, J. Xue, S. Mahlik, L. Marciniak, *Highly-Sensitive, Tri-Modal Luminescent Manometer Utilizing Band-Shift, Ratiometric and Lifetime-Based Sensing Parameters*, Advanced Functional Materials, 2024, 34, 22, 2314068, (IF = 18.5, MNiSW Points: 200)
- P6. **M. Szymczak**, A. Antuzevics, P. Rodionovs, M. Runowski, U.R. Rodríguez-Mendoza, D. Szymanski, V. Kinzhybalo, L. Marciniak, *Bifunctional Luminescent Thermometer-*

*Manometer Based on Cr<sup>3+</sup>-Cr<sup>3+</sup> Pair Emission*, ACS Applied Materials & Interfaces, 2024, 16, 47, 64976-64987, (IF = 8.5, MNiSW Points: 200)

- P7. **M. Szymczak**, W.M. Piotrowski, U.R. Rodríguez-Mendoza, P. Wozny, M. Runowski, L. Marciniak, *Highly sensitive ratiometric luminescence manometer based on the multisite emission of Cr<sup>3+</sup>*, Journal of Materials Chemistry C, 2025, 13, 4224-4235, (IF = 5.7, MNiSW Points: 140)

## PUBLICATIONS BEYOND THE SCOPE OF THE DOCTORAL DISSERTATION

---

- P8. M.T. Abbas, **M. Szymczak**, V. Kinzhybalo, D. Szymanski, M. Drozd, L. Marciniak, *Expanding the horizons of phase transition-based luminescence thermometry*, Journal of Materials Chemistry C, 13, 10013-10022, (IF = 5.7, MNiSW Points: 140)
- P9. A. Javaid, **M. Szymczak**, M. Kubicka, J. Zeler, V. Kinzhybalo, M. Drozd, D. Szymanski, L. Marciniak, *NIR-to-NIR ratiometric and lifetime based luminescence thermometer on a structural phase transition in Na<sub>3</sub>Sc<sub>2</sub>(PO<sub>4</sub>)<sub>3</sub>:Yb<sup>3+</sup>*, Journal of Materials Chemistry C, 2025, 13, 9174-9184, (IF = 5.7, MNiSW Points: 140)
- P10. M.T. Abbas, **M. Szymczak**, V. Kinzhybalo, M. Drozd, L. Marciniak, *NIR-to-NIR Lifetime Based Thermometry with the Thermally Elongated Luminescence Kinetics Driven by Structural Phase Transition in LiYO<sub>2</sub>:Yb<sup>3+</sup>*, Laser & Photonics Review, 2025, 19, 7, 2401108, (IF = 9.8, MNiSW Points: 200)
- P11. O. Bezkravnyi, **M. Szymczak**, L. Marciniak, V. Seminko, P. Kraszkiewicz, M. Malecka, M. Pawlyta, M. Vorochta, I. Matolínová, *Advances and Limitations of the Eu<sup>3+</sup> Luminescent Probe for Monitoring Ce<sup>4+</sup>/Ce<sup>3+</sup> Transitions in Ceria*, Journal of Physical Chemistry C, 2025, 129, 3, 1724-1732, (IF = 3.3, MNiSW Points: 140)
- P12. **M. Szymczak**, A. Mauri, S. Galli, L. Marciniak, M. Fandzloch, *Highly sensitive, multiparametric thermal history phosphor based on an Eu(BTC) architecture*, Advanced Functional Materials, 2024, 34, 19, 2313045, (IF = 18.5, MNiSW Points: 200)
- P13. L. Marciniak, W.M. Piotrowski, **M. Szymczak**, C.D.S. Brites, V. Kinzhybalo, H. Suo, L.D. Carlos, F. Wang, *The Butterfly Effect: Multifaceted Consequences of Sensitizer Concentration Change in Phase Transition-based Luminescent Thermometer of LiYO<sub>2</sub>:Er<sup>3+</sup>,Yb<sup>3+</sup>*, ACS Applied Materials & Interfaces, 2024, 16, 20, 26439-26449, (IF = 8.5, MNiSW Points: 200)
- P14. L. Marciniak, W.M. Piotrowski, **M. Szymczak**, M. Drozd, V. Kinzhybalo, M. Back, *Customizing thermometry: Optimizing the operating temperature range of phase transition-based ratiometric luminescence thermometers*, Chemical Engineering Journal, 2024, 487, 150363, (IF = 13.4, MNiSW Points: 200)

- P15.** L. Marciniak, P. Woźny, **M. Szymczak**, M. Runowski, *Optical pressure sensors for luminescence manometry: Classification, development status, and challenges*, Coordination Chemistry Reviews, 2024, 507, 215770, (IF = 20.3, MNiSW Points: 200)
- P16.** J. Jaśkielewicz, **M. Szymczak**, J. Zeler, L. Marciniak, *The Role of Host Material in the Design of Ratiometric Optical Density Meters Based on Cr<sup>3+</sup> Luminescence in Y<sub>3</sub>Al<sub>5-x</sub>Ga<sub>x</sub>O<sub>12</sub>:Cr<sup>3+</sup> Power meter*, Advanced Optical Materials, 2024, 13, 2, 2402039, (IF = 8.0, MNiSW Points: 140)
- P17.** **M. Szymczak**, M. Runowski, D. Kwiatek, S. Sobczak, P. Woźny, M. Kubicki, G. Dutkiewicz, A. Katrusiak, L. Marciniak, *Multimodal luminescence manometers based on a novel organic complex material - Eu(bpyO<sub>2</sub>)<sub>4</sub>(PF<sub>6</sub>)<sub>3</sub>*, Journal of Materials Chemistry C, 2024, 12, 18435-18445, (IF = 5.7, MNiSW Points: 140)
- P18.** O. Bezkravnyi, **M. Szymczak**, L. Marciniak, P. Kraszkiewicz, V. Boiko, M. Vorochta, I. Matolínová, L. Kepinski, *Eu<sup>3+</sup> Species as a Luminescent Probe for Fast Monitoring of the Chemical State of Ceria Catalysts*, Journal of Physical Chemistry C, 2024, 128, 25, 10465-10473, (IF = 3.3, MNiSW Points: 140)
- P19.** **M. Szymczak**, W.M. Piotrowski, P. Woźny, M. Runowski, L. Marciniak, *A highly sensitive lifetime-based luminescent manometer and bi-functional pressure-temperature sensor based on a spectral shift of the R-line of Mn<sup>4+</sup> in K<sub>2</sub>Ge<sub>4</sub>O<sub>9</sub>*, Journal of Materials Chemistry C, 2024, 12, 6793-6804, (IF = 5.7, MNiSW Points: 140)
- P20.** W.M. Piotrowski, **M. Szymczak**, E. M. Rodríguez, R. Marin, M. Henklewska, B. Poźniak, M. Damićanin, L. Marciniak, *Step by step optimization of luminescence thermometry in MgTiO<sub>3</sub>:Cr<sup>3+</sup>, Nd<sup>3+</sup>@SiO<sub>2</sub> nanoparticles towards bioapplications*, Materials Chemistry and Physics, 2024, 312, 128623, (IF = 4.3, MNiSW Points: 70)
- P21.** **M. Szymczak**, P. Du, M. Runowski, P. Woźny, J. Xue, T. Zheng, L. Marciniak, *Highly sensitive optical manometer based on the visible emissions of Ce<sup>3+</sup>-doped La<sub>6</sub>Sr<sub>4</sub>(SiO<sub>4</sub>)<sub>6</sub>F<sub>2</sub> multisite phosphors*, Advanced Optical Materials, 2024, 12, 2302147, (IF = 8.0, MNiSW Points: 140)
- P22.** K. Maciejewska, A. Paściak, **M. Szymczak**, K. Ledwa, A. Bednarkiewicz, L. Marciniak, *Bimodal role of Cr<sup>3+</sup> ions: the nanoscaled photothermal agent and luminescence thermometry*, Materials Today Chemistry, 2023, 30, 101579, (IF = 6.7, MNiSW Points: 70)
- P23.** W. Piotrowski, R. Marin, **M. Szymczak**, E.M. Rodríguez, D.H. Ortgies, P. Rodríguez, P. Bolek, M.D. Damićanin, D. Jaque Garcia, L. Marciniak, *Critical Evaluation of the Thermometric Performance of Ratiometric Luminescence Thermometers based on Ba<sub>3</sub>(VO<sub>4</sub>)<sub>2</sub>:Mn<sup>5+</sup>, Nd<sup>3+</sup> for Deep-Tissue Thermal Imaging*, Journal of Materials Chemistry C, 2023, 11, 6713-6723, (IF = 5.7, MNiSW Points: 140)
- P24.** W.M. Piotrowski, R. Marin, **M. Szymczak**, E. M. Rodríguez, D.H. Ortgies, P. Rodríguez-Sevilla, M.D. Damićanin, D. Jaque, L. Marciniak, *Mn<sup>5+</sup> Lifetime-Based Thermal Imaging*

*in the Optical Transparency Windows Through Skin-Mimicking Tissue Phantom*, Advanced Optical Materials, 2023, 11, 2202366, (IF = 8.0, MNI<sub>SW</sub> Points: 140)

- P25. Preprint, submitted to journal** - L. Marciniak, M. Szymczak, P. Wozny, M. Runowski, *Bridging Two Dimensions: Luminescent Sensors at the Intersection of Temperature and Pressure*, DOI: 10.48550/arXiv.2505.15170 - submitted on 21 May 2025
- P26. Preprint, submitted to journal** - M. Kubicka, M. Szymczak, M. Ptak, D. Szymanski, V. Kinzhybalo, M. Drozd, L. Marciniak, *Modulating Thermometric Performance via Dopant Concentration and Morphology in Luminescence Thermometer Exhibiting Dual Structural Phase Transitions*, DOI: 10.48550/arXiv.2505.13956 - submitted on 20 May 2025
- P27. Preprint, submitted to journal** - M.T. Abbas, M. Szymczak, M. Drozd, D. Szymanski, A. Owczarek, A. Musialek, L. Marciniak, *Breaking Sensitivity Barriers in Luminescence Thermometry: Synergy Between Structural Phase Transition and Luminescence Thermal Quenching*, DOI: 10.48550/arXiv.2505.12858 - submitted on 19 May 2025
- P28. Preprint, submitted to journal** - J. Papan Djaniš, M. Szymczak, J. Hočevár, J. Iskra, Boštjan Genorio, D. Lisjak, L. Marciniak, K. Elzbieciak-Piecka, *Exploring the Interplay Between Formation Mechanisms and Luminescence of Lignin Carbon Quantum Dots from Spruce Biomass*, DOI: 10.48550/arXiv.2505.10886 - submitted on 16 May 2025
- P29. Preprint, submitted to journal** - A. Javaid, M. Szymczak, M. Kubicka, V. Kinzhybalo, M. Drozd, D. Szymanski, L. Marciniak, *Luminescent Platform for Thermal Sensing and Imaging Based on Structural Phase-Transition*, DOI: 10.48550/arXiv.2505.05953 - submitted on 09 May 2025

## CHAPTERS

---

L. Marciniak, W.M. Piotrowski, M. Szymczak, M. Pieprz, K. Trejgis, *New Strategies to Improve Thermal Sensitivity and Temperature Resolution in Lanthanide-Doped Luminescent Thermometers*, In: J.J. Carvajal Martí, M.C. Pujol Baige, *Luminescent Thermometry*, Springer, Cham, 2023, 69-103

## PATENTS

---

**National Patent Nr 246589, Maja Szymczak, Łukasz Marciniak**

„Sposób bezkontaktowego pomiaru ciśnienia za pomocą czujnika luminescencyjnego bazującego na emisji jonów  $Cr^{3+}$ ” („Remote pressure measurement method using a luminescent sensor based on  $Cr^{3+}$  ions emission”)

## SUBMITTED PATENT APPLICATIONS

---

**National Patent Application P.446395, Maja Szymczak**, Marzena Fandzloch, Łukasz Marciniak „*Znacznik historii termicznej zawierający luminofor, jego zastosowanie i sposób bezkontaktowego odczytu temperatury z jego zastosowaniem*” („*Thermal history marker containing a phosphor, its utilization, and the technique for remote temperature measurement employing it*”)

**National Patent Application P.451932, Łukasz Marciniak, Maja Szymczak** „*Detektor luminescencyjny przeznaczony do optycznego pomiaru ciśnienia oraz sposób bezkontaktowego pomiaru ciśnienia obiektu*” („*Luminescence detector for optical pressure measurement and method for remote pressure measurement of an object*”)

## SCHOLARSHIPS AND AWARDS

---

- **Scholarship L'Oréal-UNESCO For Woman in Science** (11/2024)
- **Scholarship START 2025 from Foundation for Polish Science (FNP)** (05/2025)
- **“Young Talents” Award for Scientific Achievement**, granted by the Lower Silesian Capital Club (05/2025)
- **The Max Born Scholarship** awarded under The Student Scholarship Programme by the Wrocław Academic Centre (10/2024)
- **3<sup>rd</sup> place in 1<sup>st</sup> China-CEEC Youth Innovation and Entrepreneurship Competition** (member of a team) (05/2023)
- **Student Prize for Poster Presentation** on The 7<sup>th</sup> International Conference on the Physics of Optical Materials & The 4<sup>th</sup> International Conference on Phosphor Thermometry (08/2024)
- **Best Poster Award** for the poster presented at the Scientific Session of the doctoral students for academic year 2023/2024 in Wrocław Doctoral School of Institutes of Polish Academy of Sciences
- **Best Poster Award** for the poster presented at the Scientific Session of the doctoral students for academic year 2022/2023 in Wrocław Doctoral School of Institutes of Polish Academy of Sciences
- **Best Poster Award** for the poster presented at the Scientific Session of the doctoral students for academic year 2021/2022 in Wrocław Doctoral School of Institutes of Polish Academy of Sciences
- **The Rector's scholarship** for the Best Students of University of Wrocław (2020/2021, during the Master's studies)
- **The Rector's scholarship** for the Best Students of University of Wrocław (2018/2019, during the Bachelor's studies)

## PARTICIPATION IN CONFERENCES

---

1. **Pacific Rim Meeting on Electrochemical and Solid State Science (PRiME 2024)**, 06-11/10/2024, Honolulu, Hawaii - “*Multi-Modal Luminescence Manometer Based on  $\text{Cr}^{3+}$  Ions Luminescence in Doped  $\text{Li}_3\text{Sc}_2(\text{PO}_4)_3$* ” - poster presentation
2. **The 1st International Online Conference on Photonics**, 14-16/10/2024, online - „*Luminescence Manometry Based on  $\text{Ni}^{2+}$  Ions Emission in Doped Spinel*” - oral presentation
3. **The 7<sup>th</sup> International Conference on the Physics of Optical Materials & The 4<sup>th</sup> International Conference on Phosphor Thermometry**, 26-30/08/2024, Budva, Montenegro
  - “*Optical pressure sensors utilizing the  $^4\text{T}_{2g} \rightarrow ^4\text{A}_{2g}$  electronic transition of  $\text{Cr}^{3+}$  ions*” - oral presentation
  - “*Luminescence manometry based on  $\text{Ni}^{2+}$  ions emission*” - poster presentation
4. **The 8<sup>th</sup> International Workshop on Advanced Spectroscopy and Optical Materials (IWASOM)**, 07-12/07/2024, Gdansk, Poland - “*Tri-modal optical pressure sensor based on  $\text{Cr}^{3+}$  ions luminescence*” - oral presentation
5. **Symposium on Advanced Technologies and Materials (ATAM) and Materials Science Conference on Advanced Functional Materials (MASCA)**, 5-7/06/2024, Wroclaw, Poland - “ *$\text{Ni}^{2+}$ -doped phosphors - novel class of luminescent manometers*” - poster presentation
6. **The 20<sup>th</sup> International Conference on Luminescence**, 27/08-01/09/2023, Paris, France - “*Ultra-sensitive, multimodal luminescence pressure sensor based on  $\text{Cr}^{3+}$  ions emission*” - poster presentation
7. **The 11<sup>th</sup> International Conference on f Elements (ICFE-11)**, 22-26/08/2023, Strasbourg, France - “*Spectroscopic properties of  $\text{Eu}(\text{BTC})$  MOFs for highly sensitive thermal history sensing*” - poster presentation
8. **X Doctoral Symposium on Chemistry in Lodz**, 18/05-19/05/2023, Łódź, Poland, “*Luminescence manometer based on  $\text{Cr}^{3+}$  ions emission*” - poster presentation
9. **Phobia Annual Nanophotonics International Conference “PANIC” Summer School 2023**, 15/05-19/05/2023, Wroclaw, Poland - “*Bimodal, ratiometric luminescence manometer based on  $\text{Cr}^{3+}$  doped  $\text{MgO}$  nanoparticles*” - poster presentation
10. **The 1<sup>st</sup> Serbian Conference on Materials Application and Technology**, 20-21/10/2022, online, “*Temperature invariant luminescence manometer based on  $\text{Cr}^{3+}$  emission in  $\text{Li}_2\text{Mg}_3\text{TiO}_6$* ” - oral presentation
11. **SHIFT 2022 - Spectral sHapIng For biomedical and energy applicaTions**, 10-14/10/2022, Tenerife, Canary Islands, “*Novel luminescence manometer based on  $\text{Cr}^{3+}$  emission in  $\text{Li}_2\text{Mg}_3\text{TiO}_6$* ” - poster presentation

12. **21<sup>st</sup> International Conference on Dynamical Processes in Excited States of Solids**, 04-09/09/2022, Wroclaw, Poland, “*Spectroscopic properties of NIR-emitting MgO:Cr<sup>3+</sup> for luminescence thermometry*” - poster presentation
13. **The 6<sup>th</sup> International Conference on the Physics of Optical Materials and Devices and The 5<sup>th</sup> International Workshop of Persistent and Photostimulable Phosphors**, 29/08-02/09/2022, Belgrade, Serbia, “*Synthesis and spectroscopic properties of Cr<sup>3+</sup> ions doped Li<sub>2</sub>Mg<sub>3</sub>TiO<sub>6</sub> nanocrystals*” - poster presentation
14. **Phobia Annual Nanophotonics International Conference “PANIC” Summer School 2022**, 30/05-03/06/2022, Wroclaw, Poland - “*Spectroscopic properties of Li<sub>2</sub>Mg<sub>3</sub>TiO<sub>6</sub>:Cr<sup>3+</sup> for noncontact temperature sensing*” - poster presentation

## OTHER ACTIVITIES

---

- Participation in mentoring programme **TopMinds 2022** organized by the **Polish-U.S. Fulbright Commission and Top 500 Innovators** (01/2022 - 06/2022)
- **Representative of PhD Students in Scientific Council of ILTSR PAN** (02/2022 - 12/2022)
- **Member of the Appeals Committee for PhD Students of ILTSR PAN** (02/2025 - present)
- **Member of the Organizing Committee of International Nano-Optoelectronics Workshop (iNOW 2025)**
- **Ambassador of the “Dziewczyny do Nauki!” (“Girls into Science!”) progamme**, financed by the Minister of Science and Higher Education of Poland (2025)
- **Speaker at TopMinds 2025** during the BootCamp at session “**Mentoring in Practice - Insights from a Mentee**” (01/2025)
- **Speaker at the workshop “Effective Acquisition of Research Grants and Scientific Scholarships”** with the lecture “**Opportunities for Female PhD Students (Projects, Scholarships, Mentoring Programs)**”, organized at ILTSR PAS - (03/2025)
- **Chairwoman of the chemists' scientific association “Jeż” of University of Wroclaw** (11/2019 - 03/2021)





---

## BRIEF BACKGROUND & MOTIVATION FOR THE RESEARCH

---

Pressure has consistently demonstrated its capacity for destruction, often with far-reaching and devastating consequences. Two particularly striking examples are the Helios Airways Flight 522 disaster and the Deepwater Horizon oil spill. In the former, a failure to maintain appropriate cabin pressure during the aircraft's ascent resulted in hypoxia, ultimately leading to the death of more than 120 passengers and crew. In the latter, a sudden and uncontrolled increase in pressure within methane transport pipelines on the Deepwater Horizon drilling platform initiated a catastrophic sequence of events - resulting not only in significant loss of human life but also in severe environmental degradation. The ensuing oil spill caused the death of hundreds of marine animals and brought about lasting disruptions to the local microclimate.

These incidents prompt inevitable questions about their causes and whether they could have been prevented. The answers are complex, involving intricate chains of causality and multiple contributing factors. Nevertheless, pressure stands out as a common underlying element in both cases. This reinforces the urgent need for improved monitoring and control of this critical parameter. Enhancements in sensor responsiveness and sensitivity - particularly to detect even minor pressure fluctuations - could serve as early warning signals and help avert disaster.

In response to this need, various classes of pressure sensors are being actively researched and upgraded. Among these, luminescent pressure sensing has emerged as a particularly promising approach. This technique allows for pressure readouts based on pressure-induced changes in the luminescent properties of phosphor materials. Luminescent pressure sensors offer several distinct advantages: they enable real-time remote sensing, are resistant to mechanical degradation, and can ensure high readout precision. However, significant challenges remain, most notably their limited sensitivity to small pressure variations and the dual sensitivity of luminescent properties to both pressure and temperature. Since these two variables are often interrelated - for example, a spontaneous temperature increase resulting from elevated pressure - accurate interpretation of luminescent signals, and thus accurate pressure readout becomes increasingly difficult.

A classic example of a luminescent pressure sensor is ruby ( $\text{Al}_2\text{O}_3:\text{Cr}^{3+}$ ), which has served as the standard pressure calibrant in diamond anvil cell (DAC) experiments since the 1970s.<sup>1-3</sup> In this system, pressure inside the DAC is determined by monitoring the spectral position of the sharp  $R_1$  emission line, associated with the  ${}^2\text{E}_g \rightarrow {}^4\text{A}_{2g}$  electronic transition of  $\text{Cr}^{3+}$  ions. However, this method suffers from several drawbacks, particularly when considered for industrial implementation. The pressure sensitivity is relatively low, with the  $R_1$  band exhibiting a pressure-induced spectral shift rate of only  $0.365 \text{ nm GPa}^{-1}$ .<sup>1-3</sup> Moreover, the emission band position is also sensitive to temperature fluctuations.<sup>4</sup> At temperatures exceeding ambient conditions,

the calibration curve must be adjusted to reflect the precise thermal environment; otherwise, pressure readouts become unreliable. These limitations underscore the need to enhance the performance of luminescent manometers, either by developing alternative readout methodologies or by identifying phosphors with improved pressure responsiveness - an overarching goal of the research conducted in this doctoral dissertation. In this context, the proposed approaches and materials could find practical application in advanced pressure sensing technologies, particularly in demanding industrial environments.

Lanthanide ions are the most frequently employed in luminescent pressure sensing, primarily due to their sharp emission lines resulting from intra- $4f$  electronic transitions.<sup>5-16</sup> These transitions are relatively insensitive to the change in surrounding crystal field, making them reliable indicators under stable conditions. However,  $d-f$  transitions in lanthanide ions, which can yield broader emission bands, have been less extensively explored in a case of optical pressure sensing.<sup>17-24</sup> Although these broadband emissions typically exhibit stronger responses to pressure - due to the lack of shielding of the outer-shell electrons, which makes the energy levels more susceptible to changes in the local environment, and thus crystal field - this advantage comes at a cost. The broadness of the emission bands reduces the accuracy of pressure measurements based on spectral position monitoring, as it hinders the precise determination of the emission maximum.

On the other hand, transition metal ions such as  $\text{Cr}^{3+}$  and  $\text{Mn}^{4+}$  have also been investigated, particularly due to their narrow  ${}^2\text{E}_g \rightarrow {}^4\text{A}_{2g}$  emission lines.<sup>25-30</sup> In contrast,  $\text{Mn}^{2+}$  ions, despite their broadband emission and significant spectral shifts under pressure, have been less commonly studied in a case of pressure sensing.<sup>31-35</sup> The notable pressure sensitivity of  $\text{Mn}^{2+}$  arises from the strong dependence of the energy of the  ${}^4\text{T}_1$  excited level on the crystal field strength, which increases as the metal-oxygen distances decrease under compression (in the high spin configuration), as described by the Tanabe-Sugano diagram.<sup>36,37</sup> A comparable case applies to  $\text{Cr}^{3+}$  ions, whose broadband  ${}^4\text{T}_{2g} \rightarrow {}^4\text{A}_{2g}$  emission, although extensively studied as a function of pressure and showing significant potential for pressure sensing, has been largely overlooked in practical manometric applications.<sup>38-43</sup> This gap in the literature served as one of the central motivations for the research presented in this dissertation.

As outlined above, most pressure-sensing strategies involving luminescent materials rely on monitoring shift of emission band maximum. Less frequently employed methods include utilizing changes in emission intensity<sup>44</sup>, its full width at half maximum<sup>13-15,17,22,31,45-47</sup>, excited-state lifetimes<sup>26,28,29,48-50</sup> or luminescence intensity ratio (LIR)<sup>16,51-56</sup>. Among these, the ratiometric approach based on the LIR offers distinct advantages. It enables readouts using relatively simple and inexpensive equipment, as it does not require high-resolution spectral analysis or time-resolved measurements of luminescence kinetics. From the perspective of real-world applications,

LIR-based technique is especially attractive, as they can facilitate straightforward visualization of pressure changes across large surface areas. This stands in contrast to point-based techniques that rely on precise band shift measurements or kinetic analysis. The effectiveness of the LIR-based approach has been validated in luminescence thermometry.<sup>57-59</sup> This methodology offers a promising framework that can be readily adapted for spatially resolved pressure sensing.

Given the considerations outlined above, there was a strong scientific justification for investigating the  $^4T_{2g} \rightarrow ^4A_{2g}$  emission of  $Cr^{3+}$  ions as a potential platform for pressure sensing. In parallel, the LIR-based approach emerges as a particularly promising strategy for advancing luminescence manometry due to its practical advantages in terms of instrumentation and data visualization. This naturally leads to a pivotal research questions: **what is the potential of the emission associated with the  $^4T_{2g} \rightarrow ^4A_{2g}$  electronic transition of  $Cr^{3+}$  ions for use in luminescence-based pressure sensing exploiting various approaches? Can the LIR-based approach - scarcely applied in this domain - be further optimized to improve the functionality and broaden the applicability of luminescent manometers? And most importantly, is it possible to combine these two identified research gaps in luminescence manometry - the broadband  $^4T_{2g} \rightarrow ^4A_{2g}$  emission of  $Cr^{3+}$  ions and the LIR-based pressure-sensing methodology - into a unified and more effective sensing platform? What new opportunities might emerge from such a combination?** These questions constituted the central motivation and driving force behind the research presented in this doctoral dissertation. The series of experimental studies conducted, along with the resulting scientific publications, aim to provide a comprehensive and evidence-based response to this inquiry.

---

## DISSERTATION OBJECTIVES

---

The primary objective of this dissertation is to comprehensively investigate the pressure-dependent luminescence of  $\text{Cr}^{3+}$  ions and to develop highly sensitive luminescent manometers with strong potential for industrial application. Particular emphasis was placed on  $\text{Cr}^{3+}$  emission associated with the  ${}^4\text{T}_{2g} \rightarrow {}^4\text{A}_{2g}$  electronic transition.

Three manometric approaches were explored:

- monitoring pressure-induced spectral shift of emission band,
- analysis of luminescence decay kinetics,
- a ratiometric approach exploiting luminescence intensity ratio (LIR).

Among these, the LIR-based strategy was given the most attention and emerged as the most significant contribution of this dissertation. Multiple variations of this approach were investigated, including the intensity ratio between two spectral ranges of the emission band associated with  ${}^4\text{T}_{2g} \rightarrow {}^4\text{A}_{2g}$  electronic transition of  $\text{Cr}^{3+}$  as well as the ratio between emission bands corresponding to  ${}^4\text{T}_{2g} \rightarrow {}^4\text{A}_{2g}$  and  ${}^2\text{E}_g \rightarrow {}^4\text{A}_{2g}$  electronic transitions of  $\text{Cr}^{3+}$  ions.

In addition, the dissertation examined two alternative emission phenomena relevant to pressure sensing:

- emission from  $\text{Cr}^{3+}$  ions occupying multiple crystallographic sites, and
- broad-band emission arising from  $\text{Cr}^{3+}$ - $\text{Cr}^{3+}$  pair interactions.

By addressing these objectives, the dissertation aims to expand the methodological framework of luminescent manometry and establish a foundation for the development of  $\text{Cr}^{3+}$ -based optical pressure sensors characterized by high sensitivity, thermal stability, and practical applicability.

---

## ABBREVIATIONS

---

CFS - crystal field strength  
CFT - crystal field theory  
DAC - diamond anvil cell  
EDS - energy dispersive spectroscopy  
FWHM - full width at half maximum  
IR - infrared  
LFT - ligand field theory  
LIR - luminescence intensity ratio  
Ln - lanthanide  
MOT - molecular orbital theory  
NIR - near-infrared  
PDMS - polydimethylsiloxane  
PEG - polyethylene glycol  
PTM - pressure-transmitting medium  
SEM - scanning electron microscope  
TEM - transmission electron microscope  
TIMF - Thermal Invariability Manometric Factor  
TM - transition metal  
XRD - X-ray diffraction

## 1. Luminescent materials doped with transition metal ions

---

Transition metal (TM) ions are characterized by a high sensitivity to their local crystal environment, which makes them particularly valuable in optical sensing applications<sup>30,60–66</sup>. The underlying reason is that  $3d$  electrons of transition metal ions are not shielded by outer electron shells, unlike the  $4f$  electrons in lanthanide ions.<sup>67,68</sup> As a result, the optical properties of transition metal ions can be effectively tuned for specific applications requiring a tailored luminescent response - simply by modifying the host material, its composition or adjusting its physicochemical characteristics. These characteristics include not only crystal field parameters and local structural symmetry, but also morphological features such as particle size, shape, and degree of crystallinity.<sup>69–75</sup> These factors may influence the spatial arrangement and interatomic distances between the TM ion and the surrounding ligands. Their sensitivity to the local environment can be interpreted within the framework of crystal field theory (CFT), and more comprehensively through ligand field theory (LFT), which extends CFT by incorporating the principles of molecular orbital theory (MOT)<sup>67,76,77</sup>. To better illustrate this phenomenon, a schematic representation is shown in **Figure 1**.

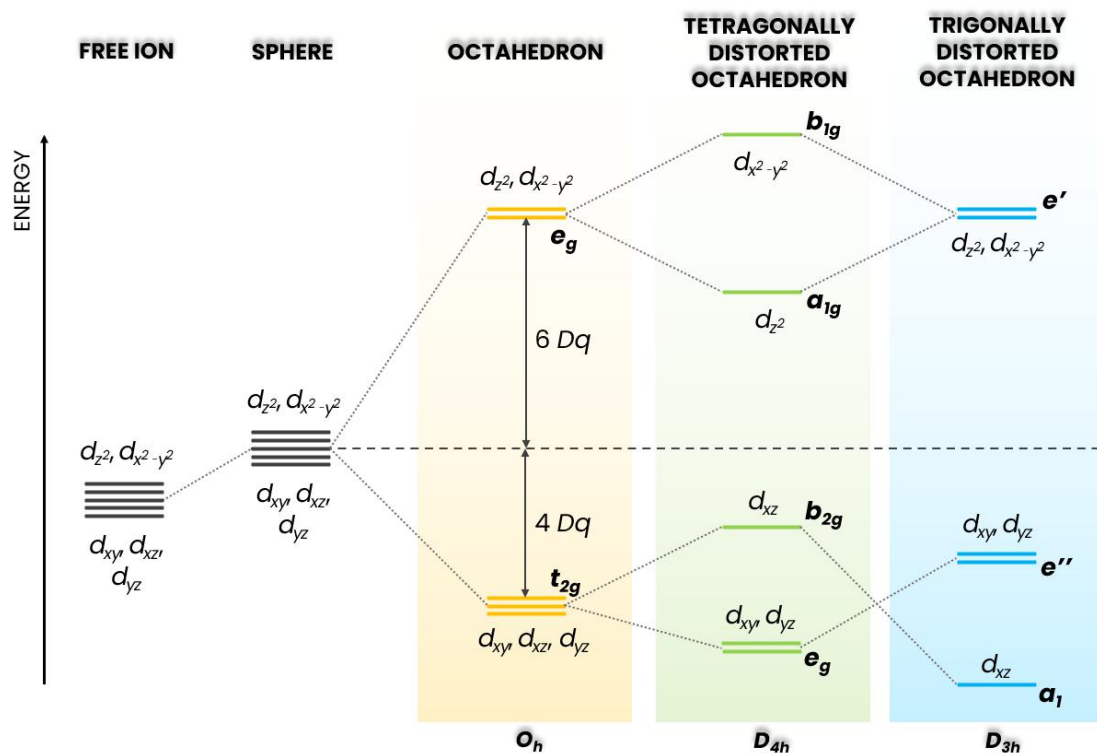


**Figure 1.** Schematic representation of  $d$ -orbital splitting in transition metal ions under various ligand field symmetries.

In the free-ion state, where no external field acts on the ion, the five  $d$ -orbitals ( $d_{xy}$ ,  $d_{xz}$ ,  $d_{yz}$ ,  $d_{z^2}$ ,  $d_{x^2-y^2}$ ) are degenerated, meaning they possess the same energy. When placed in a spherically symmetric field, their energy increases due to electrostatic repulsion between the ligand field and electron density, yet degeneracy is preserved. However, once the ion is embedded in an anisotropic field - such as one created by a specific ligand arrangement - the degeneracy is removed. When a TM ion is coordinated by six ligands arranged in a perfect octahedron, the five degenerate  $d$ -orbitals split into two distinct energy levels due to crystal field effects: the higher-energy  $e_g$  orbitals ( $d_{z^2}$ ,  $d_{x^2-y^2}$ ) and the lower-energy  $t_{2g}$  orbitals ( $d_{xy}$ ,  $d_{xz}$ ,  $d_{yz}$ ). The energy separation between these two groups of orbitals - defined by the crystal field splitting parameter  $\Delta$  or  $10Dq$  - is governed by the electrostatic interactions between the electron density of the orbitals and the surrounding ligand field, and it depends on the spatial orientation of each orbital relative to the ligands. The sensitivity of TM ions to their local environment becomes even more pronounced in the presence of deviations from ideal octahedral symmetry, such as tetragonal or trigonal distortions. As illustrated in the **Figure 1**, tetragonal or trigonal distortions, which lowers point symmetry from  $O_h$  to  $D_{4h}$  and  $D_{3h}$ , respectively, results in additional splitting or energy changing within both the  $e_g$  and  $t_{2g}$  orbitals.<sup>67,76,77</sup>

Mentioned changes are directly reflected in the luminescence behavior of TM ions. They influence not only the shape and complexity of emission spectra - such as the number and position of spectral lines - but also luminescence kinetics, due to shifts in the energy gaps between excited and ground states that affect the rates of radiative and non-radiative processes<sup>78-84</sup>. A more detailed analysis will be presented in the next subsection, with particular focus on the  $\text{Cr}^{3+}$  ion - one of the most widely researched TM ions and the central focus of this doctoral dissertation.

## 1.1. Introduction to spectroscopic properties of $\text{Cr}^{3+}$ ions

$\text{Cr}^{3+}$  ions are representatives of transition metal ions with a  $d^3$  electronic configuration. In the free-ion state, the lowest-energy term is  $^4F$ . When  $\text{Cr}^{3+}$  is affected by the octahedral ligand field, the  $^4F$  term splits into three components: the ground state  $^4A_{2g}$ , and two excited states -  $^4T_{2g}$  (lower energy) and  $^4T_{1g}$  (higher energy). In addition, another important excited state,  $^2E_g$  originates from the splitting of the higher-energy  $^2G$  term.<sup>67,77</sup> Electronic excitation typically occurs through spin-allowed transitions from the ground state  $^4A_{2g}$  to the excited states  $^4T_{2g}$  and  $^4T_{1g}$  and is manifested by broad bands in excitation spectrum. Following excitation, radiative depopulation may occur from two different excited states, depending on the crystal field strength (CFS), each exhibiting distinct emission characteristics: either narrow-band red emission associated with the spin-forbidden  $^2E_g \rightarrow ^4A_{2g}$  electronic transition, typically with emission maxima in the range

of around 680-720 nm<sup>85-87</sup>, or broad near-infrared (NIR) emission resulting from the spin-allowed  ${}^4T_{2g} \rightarrow {}^4A_{2g}$  transition, with emission maximum generally between around 750 nm and even up to 1100 nm<sup>88-93</sup>.

This crystal-field-dependent behavior of  $Cr^{3+}$  luminescence is well illustrated by the Tanabe-Sugano diagram for  $d^3$  ions in octahedral symmetry (**Figure 2**), which describes the evolution of electronic energy states as a function of crystal field strength, expressed by the parameter  $Dq/B$ . In this context, the octahedral coordination geometry is particularly favorable for  $Cr^{3+}$  luminescence, as the relatively large crystal field splitting results in lower probability of non-radiative multiphonon relaxation. By contrast, tetrahedral coordination leads to a much smaller crystal field splitting (approximately four-ninths of the crystal field splitting energy observed for an ideal octahedral geometry) increasing the probability of non-radiative processes thus making luminescence unobservable.<sup>67,94</sup>

Understanding the definition of the  $Dq$  parameter is essential for correctly interpreting the Tanabe-Sugano diagram and predicting the luminescent behavior of  $Cr^{3+}$  ions. As shown in **Figure 1**,  $Dq$  defines the magnitude of splitting between the energy of  $e_g$  and  $t_{2g}$  orbitals in an octahedral field. The  $Dq$  value depends on multiple factors, most notably the metal-ligand distance  $R$ , and follows the approximate relationship<sup>67</sup>:

$$Dq \sim \frac{r^4}{R^5} \quad (1)$$

where  $r$  is the average radius of the  $d$ -orbital. In addition to the metal-ligand distance,  $Dq$  also varies depending on the nature of the transition metal ion, the kind of ligand, and the coordination geometry. In the case of  $Cr^{3+}$  ions, the  $Dq$  value can be estimated using simplified crystal field models, based on the following equations<sup>95,96</sup>:

$$Dq = \frac{E({}^4A_{2g} \rightarrow {}^4T_{2g})}{10} \quad (2)$$

$$x = \frac{E({}^4A_{2g} \rightarrow {}^4T_{1g}) - E({}^4A_{2g} \rightarrow {}^4T_{2g})}{Dq} \quad (3)$$

$$\frac{Dq}{B} = \frac{15(x - 8)}{(x^2 - 10x)} \quad (4)$$

where  $B$  is the Racah parameter and  $E$  reflects energy of maximum of corresponding excitation bands. As mentioned above, **Figure 2** presents the Tanabe-Sugano diagram for  $d^3$  ions, which illustrates how the energies of various electronic states evolve as a function of crystal field strength,



expressed through the  $Dq/B$  ratio. In this representation, both the crystal field splitting and the state energies are normalized with respect to the Racah parameter  $B$ , allowing for generalization across different compounds.

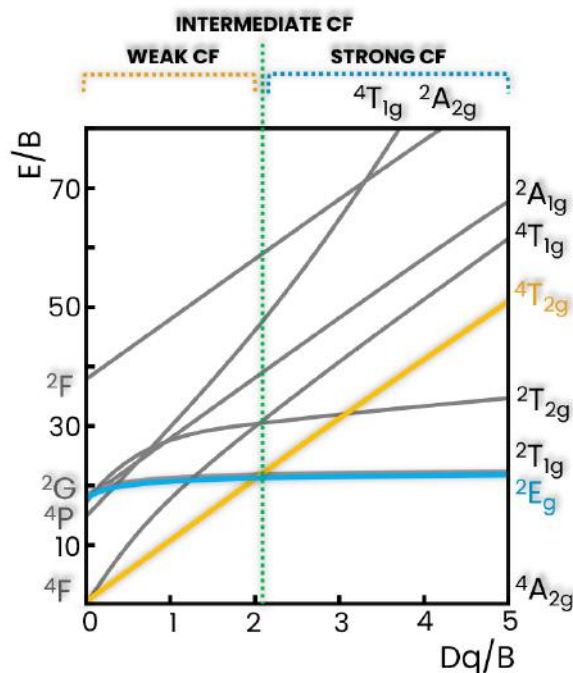


**Figure 2.** Tanabe-Sugano diagram for octahedrally-coordinated  $d^3$  ions.

In general, the first conclusion that can be drawn from the Tanabe-Sugano diagram is that the energy of the  $^2E_g$  level remains nearly constant with changes in crystal field strength. In contrast, the energy of the  $^4T_{2g}$  excited state is highly sensitive to variations in the local crystal field environment. At  $Dq/B$  values below approximately 2.2, the  $^4T_{2g}$  level is characterized by lower energy than  $^2E_g$ , while above this value,  $^2E_g$  becomes the lowest excited state. This phenomenon is of fundamental importance for understanding the luminescent behavior of  $\text{Cr}^{3+}$  ions and is schematically illustrated in **Figure 3**. When  $\text{Cr}^{3+}$  ions are incorporated into host lattices that ensures a strong crystal field - typically matrices where  $\text{Cr}^{3+}$  substitutes cations smaller in effective ionic radius, such as  $\text{Al}^{3+}$  - the lowest excited state is  $^2E_g$ . This results in narrow-band red emission arising from the  $^2E_g \rightarrow ^4A_{2g}$  electronic transition. Due to the nature of this transition, which is formally spin-forbidden, the radiative process is slow, yielding long luminescence decay time typically in the order of milliseconds.<sup>85,97</sup> On the other hand, when  $\text{Cr}^{3+}$  ions are affected by weak crystal field, the emission occurs predominantly via the spin-allowed  $^4T_{2g} \rightarrow ^4A_{2g}$  electronic transition. This results in a broad-band emission in the near-infrared region, typically accompanied by much shorter luminescence decay time - on the order of microseconds.<sup>88,89,98</sup> Importantly, under intermediate CFS near the crossover point ( $Dq/B \approx 2.2$ ), radiative depopulation of both excited

states occurs. This results in emission spectra that contain both narrow- and broad-band components.<sup>64,99,100</sup>

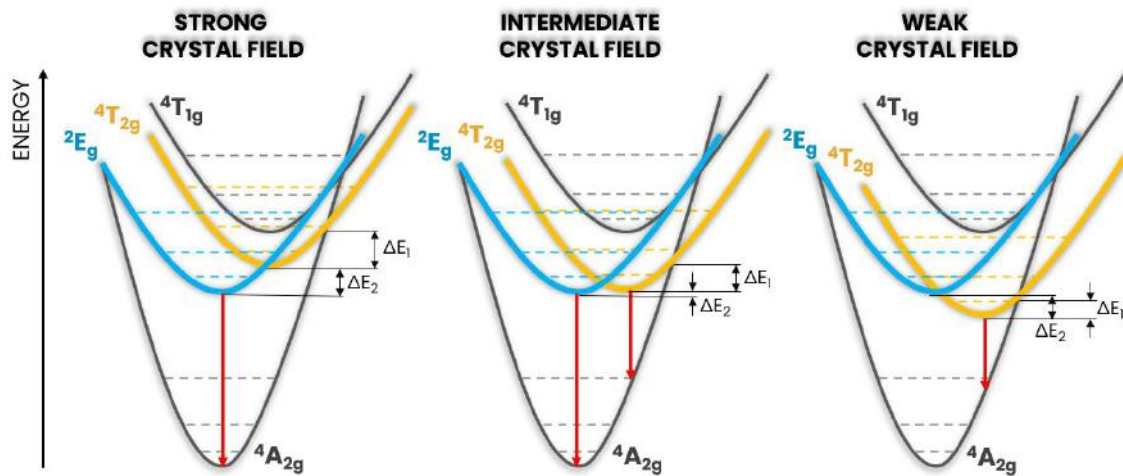


**Figure 3.** Configurational coordinate diagrams for octahedrally-coordinated  $\text{Cr}^{3+}$  ions affected by various crystal field.

The unique luminescent behavior of  $\text{Cr}^{3+}$  ions - resulting from their sensitivity to crystal field strength and the coexistence of both spin-allowed and spin-forbidden transitions - makes them highly versatile for a wide range of practical applications.<sup>3,101–105</sup> The dual nature of their emission, combined with tunability via the host material and external perturbations, allows  $\text{Cr}^{3+}$ -doped phosphors to be tailored to specific applications. In particular, the influence of various physical parameters - such as pressure and temperature - on the luminescent properties of  $\text{Cr}^{3+}$  ions is of critical importance. These dependencies not only affect emission wavelength and bandwidth, but also strongly influence luminescence decay time.<sup>106–109</sup> Understanding how these external factors modulate  $\text{Cr}^{3+}$  luminescence is essential for developing functional materials for advanced optical applications.

### 1.1.1. Pressure - dependent $\text{Cr}^{3+}$ luminescence

As mentioned above, the luminescence of  $\text{Cr}^{3+}$  ions is strongly dependent on the strength of the crystal field. To understand the pressure-dependent luminescent behavior of  $\text{Cr}^{3+}$ -doped materials, it is essential to first consider the relation between pressure and the CFS.<sup>110</sup> In general, the magnitude of  $Dq$  is inversely proportional to the metal-ligand distance raised to the fifth power, as described by the relation mentioned above (**Equation 1**).<sup>67</sup> Although pressure does not directly alter the electronic configuration of the  $\text{Cr}^{3+}$  ion, it induces structural compression, leading to a reduction in  $\text{Cr}^{3+}$ -ligand distances. This, in turn, enhances the crystal field strength. However, it is important to note that this simplified description does not account for structural stiffness, bond

compressibility, or other crystallographic factors that may limit the extent to which the structure responds to external pressure. In real materials, the pressure-induced changes in bond lengths and crystal field parameters can vary significantly depending on the lattice type and chemical composition.<sup>111–114</sup> When interpreting the luminescent behavior of  $\text{Cr}^{3+}$  under pressure, the Tanabe-Sugano diagram provides a valuable framework.<sup>115–117</sup> As discussed earlier, the energy of the  $^4\text{T}_{2g}$  level is strongly dependent on the  $Dq$  value, in contrast to the nearly crystal field-independent  $^2\text{E}_g$  level.<sup>94,95</sup> As a result, under increasing pressure - which leads to an increase in the  $Dq/B$  ratio -  $\text{Cr}^{3+}$ -doped phosphors that initially exhibit weak-field behavior are expected to display a progressive blue-shift of the broad emission band associated with the  $^4\text{T}_{2g} \rightarrow ^4\text{A}_{2g}$  transition<sup>38–41,43</sup>. This spectral shift reflects the increasing energy of the  $^4\text{T}_{2g}$  state, which dominates the emission spectrum in the weak- to intermediate-field regime. Furthermore, when a material providing a weak crystal field strength close to the critical  $Dq/B$  value of around 2.2 is studied under pressure, a gradual spectral evolution can be observed, in which the narrow emission band associated with the  $^2\text{E}_g \rightarrow ^4\text{A}_{2g}$  transition begins to dominate the spectrum with increasing pressure.<sup>118–120</sup> This effect arises from the pressure-induced crossover of the energy parabolas corresponding to the  $^2\text{E}_g$  and  $^4\text{T}_{2g}$  excited states (illustrated schematically in **Figure 4**, below).

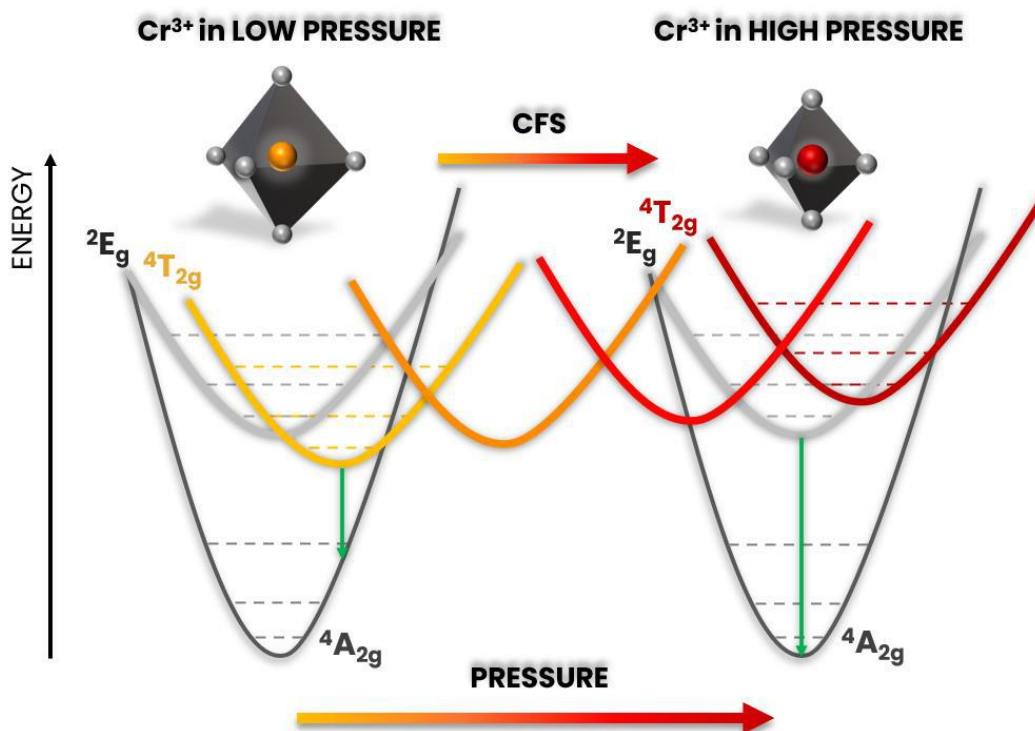


**Figure 4.** Schematic illustration one of the mechanism underlying pressure-induced luminescence variations in weak-crystal-field  $\text{Cr}^{3+}$ -doped phosphors: the applied pressure leads to a shortening of the  $\text{Cr}^{3+}\text{-O}^{2-}$  distances and increasing CFS, which in turn increases the energy of the  $^4\text{T}_{2g}$  level.

A pressure-induced blue shift is also predicted for the excitation bands, although experimental data on this phenomenon remain limited.<sup>121</sup> This is primarily due to the technical challenges of recording excitation spectra under high-pressure conditions. Nevertheless, this effect has been noted in analogous systems such as  $\text{Mn}^{4+}$ -doped materials, which share the same  $d^3$  electronic configuration as  $\text{Cr}^{3+}$ .<sup>28,122</sup>

In contrast to the  $^4\text{T}_{2g}$  level, the energy of the  $^2\text{E}_g$  state remains relatively stable with respect to variations in crystal field strength. Consequently, no significant spectral shift of the emission band associated with emission from this level is expected under pressure-induced changes in the  $Dq$  parameter. However, modification of the crystal field is not the only effect that pressure exerts on  $\text{Cr}^{3+}$  ions. One particularly important pressure-dependent phenomenon affecting their spectroscopic behavior is the alteration of bond covalency.<sup>123–125</sup> The energy of the  $^2\text{E}_g$  state is primarily determined by the Racah parameters  $B$  and  $C$ , which describe the intra-electronic Coulomb repulsion between electrons in the  $d$ -orbitals.<sup>95,126</sup> These parameters typically decrease under applied pressure, a consequence of increased metal-ligand bond covalency (nephelauxetic effect) and greater spatial delocalization of the  $d$ -orbitals.<sup>116,127</sup> As a result, a moderate lowering of the energy of the  $^2\text{E}_g$  level may occur, often manifesting as a red-shift of the  $^2\text{E}_g \rightarrow ^4\text{A}_{2g}$  narrow emission band.<sup>1,124,128,129</sup> However, this effect is generally weaker than the more pronounced pressure-induced blue-shift of the  $^4\text{T}_{2g} \rightarrow ^4\text{A}_{2g}$  emission band.<sup>41,130</sup> The aforementioned pressure-induced changes in the Racah parameters  $B$  and  $C$  indicate that, while spectroscopic properties at ambient pressure can be predicted using Tanabe-Sugano diagrams based on fixed  $B$  and  $C$  values, a more rigorous understanding of pressure effects requires the simultaneous measurement of excitation and emission spectra, from which the actual crystal field strength and pressure-modified Racah parameters can be determined.

Beyond spectral shift, pressure also influences the luminescence kinetics. In general, the lifetimes of both the  $^2\text{E}_g$  and  $^4\text{T}_{2g}$  excited states of  $\text{Cr}^{3+}$  are reported to elongate under pressure.<sup>120,131–134</sup> Due to the partial overlap of the  $^4\text{T}_{2g}$  and  $^2\text{E}_g$  wavefunctions, spin-orbit coupling between them may occur. In  $\text{Cr}^{3+}$ -doped materials characterized by a strong crystal field, the  $^4\text{T}_{2g}$  level is located energetically close to, or slightly above, the  $^2\text{E}_g$  level. Upon the application of external pressure, the  $^4\text{T}_{2g}$  state undergoes a more substantial energy shift than the relatively pressure-insensitive  $^2\text{E}_g$  level. This leads to an increasing energy separation between the two states, which weakens the spin-orbit coupling between them and consequently results in a prolongation of the luminescence decay time with increasing pressure. In materials exhibiting a weak crystal field, the  $^4\text{T}_{2g}$  state is characterized by a lower energy than the  $^2\text{E}_g$  state. Initially, with increasing pressure, the energy of  $^4\text{T}_{2g}$  level increase, progressively narrowing the energy gap between the two excited states, thereby enhancing the strength of spin-orbit coupling between them. The observed

lifetime elongation in this regime is primarily attributed to the enhanced contribution of the luminescence arising from the  $^2E_g$  state, which exhibits a longer lifetime. Once the  $^4T_{2g}$  level exceeds the  $^2E_g$  level in energy, the system follows the behavior typical of  $Cr^{3+}$  in a strong crystal field, as outlined above.<sup>135,136</sup>

Another important factor is the influence of pressure on the symmetry of the phosphors structure. Applied pressure frequently reduces structural symmetry, introducing local distortions and defects.<sup>137–140</sup> These changes can further affect orbital splitting within the octahedral environment, leading to the appearance of additional emission bands or enhanced splitting of existing bands. However, some studies report the opposite trend – an increase in structural symmetry under pressure – highlighting the complex and material-specific nature of these effects.<sup>141,142</sup>

Taking all of these factors into account,  $Cr^{3+}$  ions – particularly their emission associated with the  $^4T_{2g} \rightarrow ^4A_{2g}$  transition, which is highly sensitive to changes in crystal field strength and thus to applied pressure - offer considerable potential for use in pressure-responsive luminescent systems. This makes them promising candidates for the development optical pressure sensors capable of operating under extreme conditions.

## 1.2. Potential applications of $Cr^{3+}$ - doped phosphors

As outlined in the previous chapters,  $Cr^{3+}$  ions exhibit a unique set of properties that make them exceptionally versatile for a broad spectrum of applications.<sup>103,104,143–145</sup> Their ability to emit intense luminescence in both the visible and near-infrared regions greatly enhances their functional scope. Additionally, the broad absorption cross-section enables flexible excitation strategies, tailored to specific technological needs.<sup>146–148</sup> A distinctive advantage of  $Cr^{3+}$ -based phosphors lies in their pronounced sensitivity to the local coordination environment and to external stimuli acting on the doped material. Depending on the crystal field strength, it is possible to obtain either broad or narrow emission bands, and crucially these luminescent features can be precisely tuned through changes in the host material or synthesis conditions.<sup>70,148–151</sup> These combined advantages have led to an impressive array of proposed applications, ranging from NIR light-emitting devices, light-source for plant cultivation and bioimaging to luminescent sensors for physical quantities.<sup>100–103,145</sup> Among these applications, luminescence sensors stand out as a particularly compelling direction - not only because they take full advantage of the optical responsiveness and tunability of  $Cr^{3+}$  ions, but also due to the growing demand for precise, remote, and non-invasive sensing technologies.<sup>2,3,64,104,130,132,133,152–154</sup> Furthermore, the sensitivity of  $Cr^{3+}$  luminescence to changes in pressure, temperature, or chemical environment makes these materials especially suitable for

sensor development. For these reasons, the following section focuses specifically on this application area, which offers exceptional potential for the practical implementation of Cr<sup>3+</sup>-based phosphors in advanced sensing platforms.

### 1.2.1. Luminescence-based sensors

As mentioned in the previous section, the luminescent behavior of Cr<sup>3+</sup> ions has found widespread application in optical sensing, with temperature being the most common target parameter, and pressure sensing explored to a more limited extent. Cr<sup>3+</sup>-doped materials have emerged as promising candidates in the field of luminescence thermometry, owing not only to their typically high emission intensity, but also to a critical spectroscopic feature: their luminescence is highly sensitive to variations in crystal field strength. This characteristic renders Cr<sup>3+</sup>-doped phosphors particularly well-suited for the development of application-specific thermometric sensors. By tailoring the composition of the host material, the activation energy for non-radiative processes can be modulated, which in turn governs the thermal response of luminescence and enables the optimization of thermometric parameters, such as sensitivity, or operating temperature range of thermometer.<sup>70,99,108,155</sup>

The most widely utilized mechanism in Cr<sup>3+</sup>-based luminescence thermometry is the thermal coupling between the <sup>2</sup>E<sub>g</sub> and <sup>4</sup>T<sub>2g</sub> excited states. Consequently, host lattices with intermediate crystal field strength are typically preferred, as they give rise to emission spectra containing both a narrow band (associated with the <sup>2</sup>E<sub>g</sub>→<sup>4</sup>A<sub>2g</sub> electronic transition) and a broad band (<sup>4</sup>T<sub>2g</sub>→<sup>4</sup>A<sub>2g</sub> electronic transition).<sup>155–159</sup> The luminescence intensity ratio (LIR) of these two bands serves as a thermometric calibration curve. An important advantage of such systems is that they function as primary thermometers, as the LIR follows the Boltzmann distribution between thermally coupled energy levels. This means that the temperature can be directly determined from fundamental physical constants without the need for empirical calibration.<sup>155,160</sup>

Cr<sup>3+</sup> ions are also frequently employed as co-dopants in transition metal-lanthanide ions systems. In such systems, the lanthanide emission is less affected by thermal fluctuations - owing to the shielding of 4f electrons - acts as a reference, while the more thermally responsive <sup>4</sup>T<sub>2g</sub>→<sup>4</sup>A<sub>2g</sub> emission of Cr<sup>3+</sup> contributes a temperature-sensitive signal. Since the <sup>4</sup>T<sub>2g</sub> level is more susceptible to thermal quenching than the <sup>2</sup>E<sub>g</sub> level, these co-doped systems often achieve higher temperature sensitivities. However, this typically comes at the expense of a narrower operational temperature range, due to the rapid quenching of <sup>4</sup>T<sub>2g</sub>→<sup>4</sup>A<sub>2g</sub> emission of Cr<sup>3+</sup> at elevated temperatures.<sup>161–165</sup>

While LIR-based thermometric approach dominates the literature, temperature sensing via luminescence kinetics analysis represents a viable and complementary method. This technique relies on monitoring temperature-dependent changes in the decay dynamics of excited states.

In a case of  $\text{Cr}^{3+}$  ions, the  ${}^2\text{E}_g \rightarrow {}^4\text{A}_{2g}$  electronic transition is of particular interest, as its relatively long millisecond-scale lifetime contributes to enhanced accuracy in temperature determination. The temperature dependence of the  ${}^2\text{E}_g$  luminescence decay time arises primarily from the thermally activated non-radiative depopulation of the  ${}^2\text{E}_g$  state via the  ${}^4\text{T}_{2g}$  state. This mechanism enables precise lifetime-based thermometric readouts, especially in systems where the energy gap between the  ${}^2\text{E}_g$  and  ${}^4\text{T}_{2g}$  is narrow.<sup>108,166–168</sup>

In contrast to temperature sensing, the use of  $\text{Cr}^{3+}$  ions in luminescent pressure sensors remains relatively underexplored. Only a limited number of studies have been reported to date (aside from those presented in the publications constituting this doctoral dissertation<sup>130,132,133,152,154,169,170</sup>) - all of which rely on a single readout strategy: monitoring the spectral position of the narrow  ${}^2\text{E}_g \rightarrow {}^4\text{A}_{2g}$  emission band.<sup>1,3,171,172</sup> . On the other hand, given the broadband nature and strong responsiveness to pressure due to sensitivity on the CFS changes, the  ${}^4\text{T}_{2g} \rightarrow {}^4\text{A}_{2g}$  emission of  $\text{Cr}^{3+}$  holds significant potential for pronounced spectral shifts and variations in emission band shape, ultimately enabling higher pressure sensitivities than those achievable with conventional  $\text{Cr}^{3+}$ -based luminescent sensors based on narrowband  ${}^2\text{E}_g \rightarrow {}^4\text{A}_{2g}$  electronic transitions. This overlooked opportunity constitutes the central motivation of the present doctoral dissertation, which aims to investigate the potential of  $\text{Cr}^{3+}$  luminescence associated with the  ${}^4\text{T}_{2g} \rightarrow {}^4\text{A}_{2g}$  electronic transition in the context of its application in luminescent manometry.

## 2. Luminescence manometry

---

### 2.1. Manometric parameters

First, it is essential to clarify the key parameters that determine the manometric performance of phosphors. The most important among them is the relative sensitivity  $S_R$  of the manometer, defined by the equation:

$$S_R = \frac{1}{x} \frac{\Delta x}{\Delta p} \cdot 100\% \quad (5)$$

where  $\Delta x$  represents the change in the parameter  $x$  resulting from a pressure variation  $\Delta p$ . The choice of  $x$  depends on the specific manometric approach employed. In most cases, it refers to the LIR

or average lifetime of excited state  $\tau_{avr}$ . Another key parameter is the absolute sensitivity  $S_A$  given by:

$$S_A = \frac{\Delta x}{\Delta p} \quad (6)$$

where, again,  $\Delta x$  denotes the change in the measured parameter as a function of the pressure increment  $\Delta p$ . A third important metric is the Thermal Invariability Manometric Factor (TIMF), which quantifies the influence of temperature on pressure readouts. It reflects the ratio between pressure and temperature sensitivities and is defined as follows<sup>130</sup>:

$$TIMF = \frac{S_{R (pressure)}}{S_{R (temperature)}} \quad (7)$$

where,  $S_{R (pressure)}$  is pressure relative sensitivity as in **Equation 5**, and  $S_{R (temperature)}$  is temperature relative sensitivity defined analogously to **Equation 5**, substituting  $\Delta T$  for  $\Delta p$ . TIMF can be defined in various ways. In its original form, it was calculated as the ratio between the maximum pressure sensitivity achieved and the temperature sensitivity at room temperature. However, alternative approaches have also been proposed in the literature, in which TIMF is computed across the entire pressure range by dividing pressure sensitivity values by the temperature sensitivity obtained again at room temperature.<sup>152,170</sup>

## 2.2. Brief overview of phosphors and sensing approaches exploited in luminescence manometry

The publication of research presenting the calibration of the dependence between pressure and the spectral position of the narrow  $R_1$  emission band - associated with the  ${}^2E_g \rightarrow {}^4A_{2g}$  electronic transition of  $Cr^{3+}$  ions in doped ruby - is widely regarded as the conventional starting point of luminescence manometry.<sup>1-3</sup> For over five decades, this method has served as the gold standard for pressure determination in high-pressure research in diamond anvil cells. Throughout this period, extensive efforts have been devoted to the development of new phosphors and alternative strategies for pressure sensing based on pressure-dependent luminescence properties, especially for industry applications. Nevertheless, ruby remains the most commonly employed luminescent pressure indicator to this day. It would be misleading to claim that the field has not evolved. However, when evaluating the body of literature on luminescence manometry, one may conclude that progress has been limited. Most studies have focused on phosphor materials that exhibit emission characteristics similar to those of ruby (narrow-band emission), and the dominant methodology for pressure



determination continues to rely on monitoring the spectral position of a narrow emission band (**Figure 5a**) - just as it has since the ruby-based technique's implementation. Spectral shift-based approach still constitutes the basis of the majority of published work.<sup>6–8,47,49,173,174</sup> While the use of phosphors with narrow emission bands is justified in diamond DAC experiments - primarily due to the frequent overlap between the emission bands of the studied phosphors and those of the pressure calibrant - it is nonetheless worthwhile to explore new and improved solutions better suited for industrial applications. Nonetheless, alternative methods have also been explored<sup>175</sup>, including the monitoring of emission intensity changes<sup>44</sup>, intensity ratio between emission bands<sup>16,51–56</sup>, full width at half maximum (FWHM) of emission band<sup>13–15,17,22,31,45–47</sup> and variations in luminescence decay kinetics<sup>26,28,29,48–50</sup>. These different approaches are schematically illustrated in **Figure 5**, below.

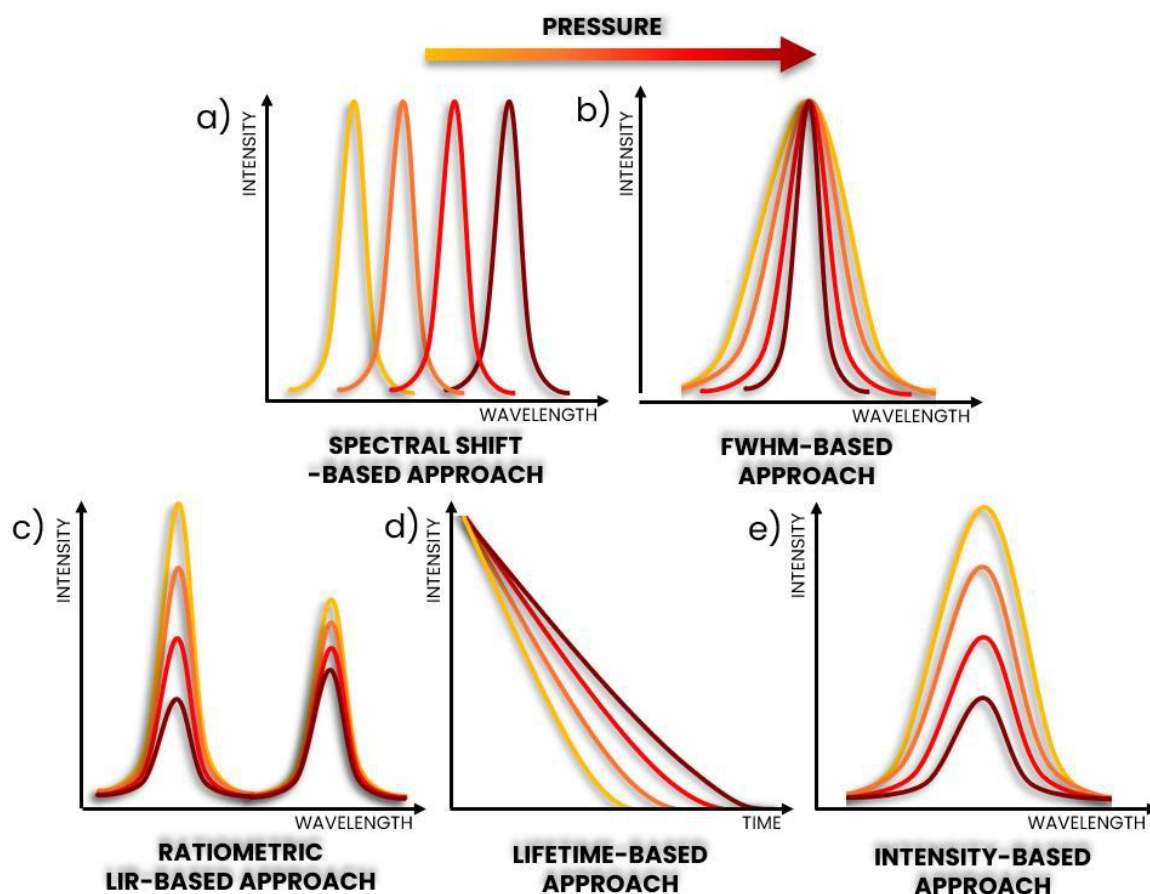


**Figure 5.** Schematic overview of pressure-sensing strategies in luminescence manometry.

In the context of pressure sensing, research most often focuses on inorganic phosphors that exhibit narrow emission bands associated with *f-f* electronic transitions of trivalent lanthanide ions, primarily  $\text{Nd}^{3+}$  and  $\text{Pr}^{3+}$ , or with up-converting systems based on  $\text{Yb}^{3+}/\text{Er}^{3+}$  co-doping.<sup>5–16</sup> Transition metal ions are investigated less frequently, typically limited to spin-forbidden *d-d* electronic

transition of  $\text{Cr}^{3+}$  and  $\text{Mn}^{4+}$ .<sup>1–3,25,26,28,30,129,171</sup> For the majority of these phosphors, the observed spectral shift rate does not exceed  $1 \text{ nm GPa}^{-1}$ , with only a few exceptions.<sup>28,30</sup> In the case of  $f-f$  transitions in Ln-doped materials, such small spectral shifts are mainly attributed to the shielding of the  $4f$  electrons by the outer  $5s$  and  $5p$  orbitals, which significantly reduces their sensitivity to the external environment. As a result, the reduction in interatomic distances under applied pressure leads only to minor changes. The interaction with ligands is also inherently weak, meaning that nephelauxetic effects do not significantly influence the luminescence either. More relevant in such systems are changes in spin-orbit coupling, which may induce multiplet splitting of the  $4f$  levels or mixing of  $4f$  orbitals with opposite-parity orbitals due to pressure-induced structural distortions. These mechanisms are typically responsible for the observed, generally modest red-shift of the narrow  $f-f$  emission band with increasing pressure.<sup>5–16</sup>

In the case of TM ions, the situation differs markedly from that of Ln ions. Here, changes in crystal field strength and metal-ligand interactions play a more pronounced role due to the unshielded nature of  $3d$  electrons, which are considerably more susceptible to external perturbations than the well-shielded  $4f$  electrons of Ln ions. Nevertheless, despite this higher sensitivity, the narrow emission bands of most commonly studied  $\text{Cr}^{3+}$  and  $\text{Mn}^{4+}$  ions - originating from the spin-forbidden  ${}^2\text{E}_g \rightarrow {}^4\text{A}_{2g}$  electronic transitions - are only weakly influenced by variations in the crystal field strength. This observation is in line with predictions from the Tanabe-Sugano diagram for  $d^3$  ions (see **Figure 2**). As a result, pressure-induced spectral shifts observed in these systems are primarily attributed to subtle variations in the covalency of metal-ligand bonds. Under increasing pressure, the enhanced orbital overlapping between the metal cation and surrounding ligands leads to a nephelauxetic effect. This effect lowers the energy of the  $d-d$  transitions, resulting in a red-shift of the emission band with increasing pressure.

In contrast, pressure sensing based on phosphors exhibiting broadband emission offers markedly enhanced responsiveness. Phosphors in this group include lanthanide ions undergoing  $d-f$  electronic transitions - most notably  $\text{Eu}^{2+}$  and  $\text{Ce}^{3+}$  - as well as transition metal ions exhibiting spin-allowed  $d-d$  transitions, which to date have been reported mainly for  $\text{Mn}^{2+}$ -doped phosphors.<sup>17–24,31–35,176</sup> In such systems, pressure-induced spectral modifications are significantly more pronounced, resulting in luminescent pressure sensors with much higher sensitivities. Reported values typically exceed  $1 \text{ nm GPa}^{-1}$ , and can reach up to nearly  $19 \text{ nm GPa}^{-1}$ , as demonstrated for  $\text{BaCN}_2\text{:Eu}^{2+}$ .<sup>19</sup> For Ln-based phosphors exhibiting emission associated with  $d-f$  electronic transition, the high sensitivity arises from the fact that the participating electrons are not shielded from external perturbations by outer electron shells, as is the case in  $f-f$  transitions. However, this approach also suffers from certain drawbacks, most notably the relatively low reliability of pressure readouts, a limitation that will be discussed in detail in the following subsection.

In the case of TM-doped phosphors exhibiting broadband emission, luminescent pressure sensing has focused on  $\text{Mn}^{2+}$  ions, where the pressure response is derived from the  ${}^4\text{T}_1 \rightarrow {}^6\text{A}_1$  electronic transition. A significant pressure-induced spectral shift rate of 21 nm  $\text{GPa}^{-1}$  for organic phosphor  $[(\text{CH}_3)_4\text{N}]\text{MnCl}_3$ <sup>176</sup> or change in FWHM exceeding 10 nm  $\text{GPa}^{-1}$  have been observed, for example, in  $\text{NaY}_9(\text{SiO}_4)_6\text{O}_2:\text{Mn}^{2+}$ <sup>31</sup>. This behavior results from the pronounced sensitivity of the  ${}^4\text{T}_1$  excited state of  $\text{Mn}^{2+}$  to variations in crystal field strength, as predicted by Tanabe-Sugano diagram for ions with  $d^5$  electronic configuration, which arise from the compression-induced shortening of metal-ligand bonds.<sup>176</sup> Nevertheless, the number of studies focusing on broadband-emission pressure sensing using TM ions remains limited. However, the research conducted within the framework of this doctoral dissertation demonstrated that the broad emission band of  $\text{Cr}^{3+}$  ions, associated with the  ${}^4\text{T}_{2g} \rightarrow {}^4\text{A}_{2g}$  electronic transition, can be effectively used for pressure sensing. A linear shift of the emission maximum as a function of pressure was observed, with a shift rate exceeding 23 nm  $\text{GPa}^{-1}$ .<sup>130,133</sup>

Luminescent pressure sensors operating in a ratiometric mode - based on monitoring changes in the luminescence intensity ratio under pressure - have also been reported (**Figure 5c**).<sup>16,51-56</sup> In this approach, the ratio of two emission bands of a luminescent ion is tracked, most commonly for lanthanide ions. The most frequently studied are the emission bands of  $\text{Er}^{3+}$  ions, specifically associated with the  ${}^4\text{S}_{3/2} \rightarrow {}^4\text{I}_{15/2}$  and  ${}^4\text{F}_{9/2} \rightarrow {}^4\text{I}_{15/2}$  electronic transitions. The relative pressure sensitivity achieved via this method typically ranges from approximately 0.2%  $\text{GPa}^{-1}$  to values between 10% and 20%  $\text{GPa}^{-1}$  with the notable exception of the  $\text{NaYF}_4@\text{NaYF}_4:\text{Yb}^{3+},\text{Er}^{3+}$  core-shell system, which has demonstrated a relative sensitivity of around 40%  $\text{GPa}^{-1}$ .<sup>51</sup> This approach centers on analyzing the luminescence intensity ratio of two narrow emission bands. The phosphors investigated in this doctoral dissertation represent an entirely new class of luminescent pressure sensors, in which pressure readouts are based on the ratiometric analysis of broad-band emission integrated into two spectral ranges. This approach enabled the achievement of pressure sensitivities as high as 120%  $\text{GPa}^{-1}$ .<sup>130</sup> As a continuation of this research, the methodology was also successfully extended to lanthanide-based phosphors.<sup>55,56</sup>

Another strategy employed in luminescence manometry involves the analysis of luminescence kinetics by recording decay curves under applied pressure (**Figure 5d**). This approach – although highly promising – remains significantly underexplored compared to spectral shift-based techniques. In the case of lanthanide-based phosphors, pressure typically leads to a shortening in the excited-state lifetime, primarily due to enhanced non-radiative relaxation processes enabled by reduced interatomic distances and increased electron-phonon coupling. Conversely, in TM-based systems - where  $\text{Mn}^{4+}$  luminescence kinetics have been the most widely studied - an elongation in lifetime with rising pressure is commonly observed. This effect

is attributed to the previously mentioned relaxation of spin-orbit coupling, which changes the probability of radiative depopulation of excited states.<sup>26,28,29,48–50</sup>

Luminescent pressure sensing based solely on monitoring changes in emission intensity is also reported (**Figure 5e**); however, this method has been explored only to a very limited extent, with just a handful of studies published to date.<sup>44</sup>

### **2.3. Advantages and disadvantages of the materials and approaches used in luminescence manometry**

Not everything that is most commonly used is necessarily the best. This is particularly true in the case of pressure determination based on monitoring the spectral position of a narrow emission band - a method that remains the most widely employed in luminescence manometry. This approach enables highly precise pressure readouts due to the sharp emission profiles, for which the maximum can be accurately determined. However, a fundamental limitation of this method lies in the typically small pressure-induced spectral shifts, which translate into low sensitivity of pressure sensors relying on this principle. While this approach is well-suited for monitoring pressure in controlled laboratory conditions, such as in diamond anvil cell experiments, it offers limited advantages for industrial applications due to its reliance on high-resolution spectral measurements and susceptibility to external interferences.

On the other hand, significantly higher pressure sensitivity can be achieved when utilizing broadband emission associated with *d-f* transitions of lanthanide ions or with *d-d* transitions of TM ions sensitive to crystal field strength – such as emissions from the  $^4T_2$  excited state of  $Cr^{3+}$ . For example, the pressure-induced spectral shift rate of  $BaCN_2:Eu^{2+}$  is more than 50-times greater than that observed for ruby.<sup>3,19</sup> Despite this advantage, the reliability of pressure determination using broadband emission is limited by the inherent ambiguity in defining the spectral maximum.<sup>154</sup> Moreover, both narrow and broad emission bands are typically subject to temperature-induced spectral shifts, which introduces additional error in pressure readouts-especially considering that increasing pressure can lead to spontaneous heating of the system. Another limitation of this method is its inherently localized nature: it allows only for point-based pressure measurements, making it unsuitable for fast large-area pressure mapping. Furthermore, narrow-band measurements require high-resolution detection systems to ensure accuracy, which significantly increases the overall cost. A similar drawback applies to pressure sensing strategies based on monitoring the FWHM of emission bands.

An alternative approach involves monitoring luminescence kinetics by analyzing luminescence decay curves. A key advantage of this method is the general insensitivity of decay profiles to the

measurement environment, including the medium in which the phosphor is embedded. This reduces readout errors, significantly enhancing the application versatility of such sensors. However, although this method can offer accurate and stable pressure readouts, it necessitates more complex detection setups compared to spectral shift or FWHM measurements - again increasing system cost. An additional challenge lies in the dual sensitivity of excited-state lifetimes to both pressure and temperature changes, which complicates data interpretation and limits the method's robustness.

In the case of the ratiometric approach based on the luminescence intensity ratio of  $f$ - $f$  narrow emission bands originating from Ln ions, it is important to note that the intensity ratio is also temperature dependent and is widely utilized in luminescence thermometry. Nonetheless, this method offers several distinct advantages, particularly from the perspective of luminescence manometry applications. Most notably, it enables the visualization of spatial distributions of the monitored parameter across larger areas, rather than being limited to single-point measurements. Additionally, the ratiometric approach does not require expensive or complex detection systems, representing a significant advantage over methods based on spectral position or decay kinetics. As a result, LIR-based pressure sensing strategy possess a high degree of application potential.

When critically evaluating the classes of luminophores used in luminescent manometry, inorganic phosphors emerge as the most promising candidates, primarily due to their structural robustness under high-pressure conditions. In contrast, organic compounds are typically limited to very low-pressure regimes, as they tend to undergo pressure-induced degradation.<sup>177</sup> Among inorganic phosphors, as mentioned above - the highest pressure sensitivity is generally observed for systems exhibiting broadband emission - either from  $d$ - $f$  transitions in lanthanide ions or from crystal-field-sensitive  $d$ - $d$  transitions in transition metal ions. For such systems, as mentioned above, classical pressure readout method based on monitoring spectral position of emission band is often inadequate and complicate the precise determination of the pressure value. Therefore, it is essential to explore new pressure readout strategies-or novel interpretations of existing ones-that enable the effective utilization of both the unique emission characteristics of various phosphor groups and the advantages of different sensing techniques. This concept forms the foundation of the present doctoral dissertation, in which the integration of the LIR-based ratiometric approach-characterized by a high potential for practical applications-with the pressure-responsive broadband emission of  $\text{Cr}^{3+}$  associated with the  ${}^4\text{T}_{2g} \rightarrow {}^4\text{A}_{2g}$  electronic transition was demonstrated for the first time.<sup>130,132,133,152,154,169,170</sup>

The scheme below (**Figure 6**) summarizes the key characteristics that define an ideal luminescent pressure sensor. Foremost among them is high sensitivity to pressure variations, which fundamentally determines the performance potential of the sensor. Equally important

is insensitivity to temperature fluctuations within the system, as this ensures that the measured pressure values are accurate and reliable under varying conditions. Another critical criterion is the ability to perform high-precision pressure measurements. In addition, the structural stability of the phosphor is essential-so that exposure to high pressure does not induce irreversible changes within the structure of material, which would otherwise limit the sensor to single-use operation. The ideal sensor should also allow for low-cost detection, supported by a strong luminescent signal from the phosphor. High emission intensity improves the signal-to-noise ratio and minimizes errors in pressure readout. Finally, as previously discussed, the capability to monitor pressure changes across a large area - not just point by point - adds substantial value to practical applications.

In principle, combining these desirable features from different approaches could yield the perfect sensor. However, in practice, such an all-encompassing solution remains unattainable. For this reason, intensive research continues, both on the optimization of proposed phosphor materials and on the development of new compounds or upgraded pressure-sensing strategies aimed at expanding the application potential of luminescence-based manometry.

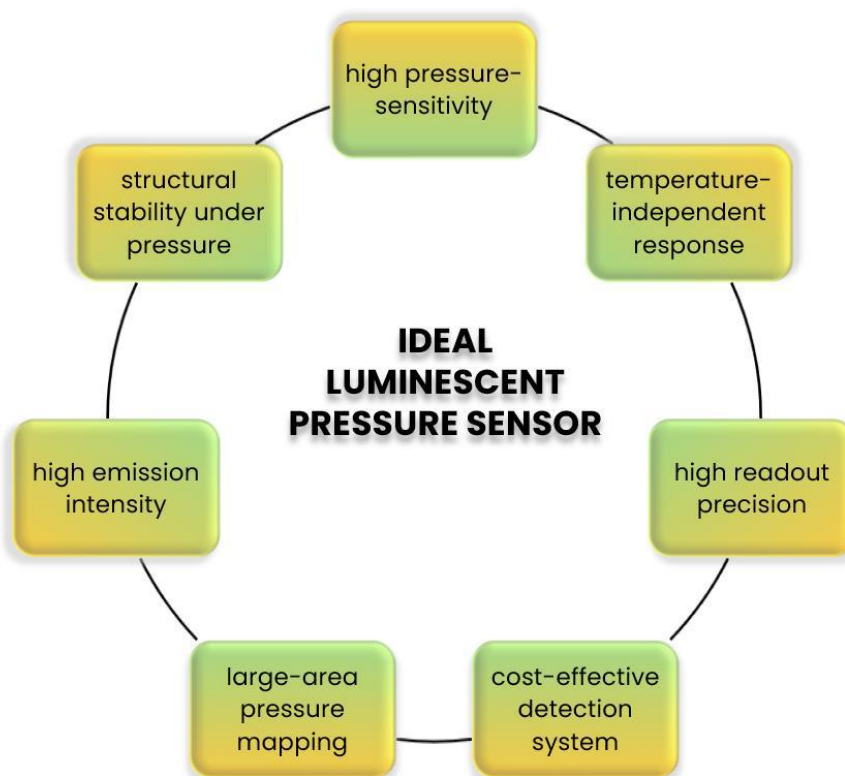


**Figure 6.** Schematic overview of the essential characteristics of a high-performance luminescent pressure sensor.

The schematic overview of the desired features of an ideal luminescent pressure sensor presented above not only aims to summarize the fundamental performance criteria, but also illustrates the broader research objectives that have guided the work carried out in this doctoral dissertation. It serves as a conceptual reference that connects the experimental efforts with the long-term vision of developing high-performance luminescent pressure sensors with high application potential.

### 3. High-pressure luminescence measurements in diamond anvil cell - construction and experimental methodology

---

The investigation of luminescent properties under variable pressure conditions constitutes a key methodological approach in the characterization of functional materials. Among the techniques available for this purpose, the diamond anvil cell stands out as the most widely adopted and versatile high-pressure tool. Since its development less than seven decades ago, the DAC has become a cornerstone of high-pressure research, enabling measurements across an exceptionally broad pressure range - extending up to 400 GPa - thereby surpassing natural pressure extremes such as those at the bottom of the Mariana Trench or even within the Earth's core.<sup>178–181</sup> One of the most significant advantages of the DAC lies in its ability to generate both ultra-high and relatively low pressures, depending on the geometric parameters of the anvils. In particular, the pressure  $p$  applied within the DAC is governed by the simple relationship:

$$p = \frac{F}{S} \quad (8)$$

where  $F$  is the applied mechanical force and  $S$  is the contact area between the diamond culets. Consequently, the use of diamonds with smaller culet diameters allows for the generation of significantly higher pressures with the same applied force. In addition, an important advantage of diamonds is their high transparency across a broad spectral range, which facilitates spectroscopic measurements without the risk of introducing significant alterations to the spectroscopic properties of the studied materials.<sup>182</sup> To fully appreciate the methodology of luminescence measurements conducted in a DAC, it is essential to understand both the structural design of the device and the experimental procedures that ensure accurate and reproducible results. These aspects are elaborated in the following subsections.

A standard DAC assembly consists of two opposing single-crystal diamond anvils mounted on metallic seats, as shown in the schematic representation in **Figure 7** below. Precise alignment of the anvils is critical to guarantee uniform compression of the sample and to ensure a stable and homogeneous pressure. Between the anvils, a pre-indented gasket, is placed. A small hole is drilled

at the center of the indented area. The hole is then loaded with the sample, a pressure calibrant, and a pressure-transmitting medium (PTM). The PTM is crucial for maintaining quasi-hydrostatic or hydrostatic conditions during compression.<sup>180</sup>

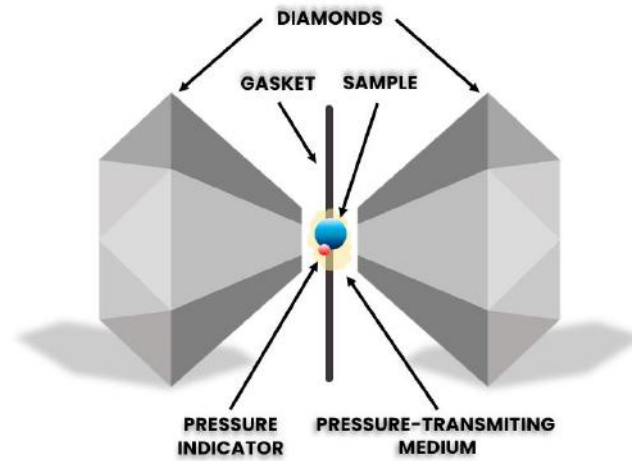


**Figure 7.** Schematic diagram of a diamond anvil cell.

Pressure can be applied in the DAC through several mechanisms. The most conventional approach involves the gradual tightening of metal screws, which incrementally increase the force acting on the anvils. In more advanced experimental setups, pressure control is achieved via a gas membrane mechanism, wherein an inert gas inflates a flexible membrane, compressing the anvils. This solution allows for remote and continuous pressure tuning without disassembling the optical system. While more complex and costly, membrane-driven systems significantly enhance experimental efficiency and precision.

The following sections provide a comprehensive overview of the DAC architecture and detail the step-by-step procedures for the high-pressure luminescence measurements using this technique.

### **3.1. Diamonds**

The selection of diamonds with appropriate optical and structural properties is a critical factor in pressure-dependent luminescence studies, as it directly impacts the quality, reliability, and sensitivity of the measured emission signals. Several key parameters must be considered when choosing suitable diamonds for high-pressure optical experiments, including culet size, crystal grade, and aperture. As previously discussed, the diameter of the culet of the diamond that comes into contact with the sample - is directly related to the maximum achievable pressure within the DAC. Specifically, larger culet sizes result in lower attainable pressures, due to the inverse



relationship between pressure and surface area (**Equation 8**). From an optical standpoint, diamond grade and aperture are crucial. Diamond grade refers primarily to the purity of the crystal, particularly with respect to nitrogen content. Nitrogen impurities absorb strongly in the visible region, introducing undesirable background fluorescence and reducing the signal-to-noise ratio in luminescence measurements. Therefore, diamonds with minimal nitrogen incorporation are preferred. Diamonds are typically classified into type *I* and type *II*, with further subdivision into subclasses (*a* and *b*), and in some cases, more specific designations such as *ac*, and *as*. Among these, type *IIas* and *IIac* diamonds are considered particularly well-suited for high-pressure luminescence studies. They exhibit exceptionally low fluorescence, minimal birefringence, and ultra-high optical transparency, all of which are essential for minimizing measurement artifacts and enabling the accurate collection of relatively weak luminescent signals, especially from low-emission systems.<sup>180,182,183</sup> Another important parameter is diamond alignment, particularly culet parallelism, which ensures uniform compression of the sample and optimal optical alignment along the excitation and emission pathways. Misalignment can lead to pressure gradients, non-hydrostatic conditions, and distortions in the optical path, all of which adversely affect spectral resolution and reproducibility.

In summary, diamonds constitute the most critical component of the diamond anvil cell assembly. Their optical quality, structural purity, and precise geometry directly determine the reliability and quality of luminescence data acquired under high-pressure conditions. The careful selection and preparation of diamonds are therefore foundational to the success of high-pressure luminescence experiments.<sup>180</sup>

### 3.2. Gasket

The gasket is a fundamental disposable component used during measurements in the DAC, playing a critical role in both pressure generation and its distribution within the sample. Despite its disposable nature, careful selection and meticulous preparation are essential to ensure stable and reliable high-pressure conditions throughout luminescence measurements. This applies equally to the accuracy and care required during gasket pre-indentation, the precise drilling of the hole, and the proper placement of both the sample and the pressure indicator.

Gaskets are typically fabricated from metals such as tungsten, rhenium, or stainless steel, with the choice of material dictated by the intended pressure range, chemical compatibility with the sample, and the required mechanical properties. Two key physical parameters govern gasket performance: thickness and hardness. The hardness of the gasket material is crucial for keeping the hole with sample stable and properly sealed during compression. If the gasket material is not sufficiently hard, it may deform and change a shape of a hole under compression,

leading to pressure loss, gasket rupture, or leakage of the PTM. Conversely, a material that is too hard may hinder the achievement of high pressures or induce non-hydrostatic conditions due to uneven deformation. Therefore, a balance must be struck to provide both sufficient mechanical strength and controlled compression. The initial thickness of a standard gasket is approximately  $200 \pm 50 \text{ }\mu\text{m}$ . The first step in gasket preparation is pre-indentation, during which the gasket is compressed using the DAC to a reduced thickness typically around  $70 \text{ }\mu\text{m}$  - within the intended measurement area. This pre-compression must be applied uniformly across the surface to ensure same thickness of gasket on entire surface and avoid the formation of stress concentrations, which could compromise gasket performance under high-pressure conditions. Following pre-indentation, a central hole is drilled into the pre-indentated gasket to form the place for sample and pressure indicator. This is most commonly accomplished using a laser drilling system or a precision micro-drilling tool, as spark erosion drilling machine. The hole diameter typically ranges from 30% to 50% of the culet diameter, depending on experimental requirements. Precision in this step is critical: the hole must be perfectly circular and centered within the indented area. Any deviation from this geometry can result in uneven pressure distribution, a reduction in the maximum achievable pressure, or even premature pressure release during the experiment.<sup>180,184</sup>

In summary, although often regarded as a secondary component, the gasket is in fact a crucial structural element that directly impacts the success of high-pressure luminescence measurements. Careful material selection, precise drilling, and meticulous preparation are indispensable for achieving reliable and reproducible results in DAC-based optical experiments.

### 3.3. Pressure Indicator

Another important element in high-pressure experiments using a DAC is the pressure calibrant, which enables precise determination of the pressure within the sample chamber. The most widely used pressure indicator is ruby ( $\text{Al}_2\text{O}_3:\text{Cr}^{3+}$ )<sup>1-3</sup>, which has been employed in this capacity since the lately 20th century. Its popularity stems from the exceptional structural stability of the oxide matrix and the high intensity of  $\text{Cr}^{3+}$  emission, which remains stable and detectable up to pressures achieving 150 GPa. Pressure determination using ruby relies on monitoring the spectral position of the sharp  $R_1$  emission line, associated with the  ${}^2\text{E}_g \rightarrow {}^4\text{A}_{2g}$  transition of  $\text{Cr}^{3+}$  ions occupying  $\text{Al}^{3+}$  crystallographic positions in the corundum lattice. At room temperature and ambient pressure, this line is centered at around 694.27 nm. With compression, the  $R_1$  line shifts to longer wavelengths in a well-characterized, quasi-linear manner (spectral-shift rate of  $0.364 \text{ nm GPa}^{-1}$ ), providing a reliable and precise method for in situ pressure calibration.<sup>1-3</sup> In addition to ruby, other luminescent materials have been proposed as pressure indicators, particularly in cases where the ruby emission overlaps with the emission spectrum of the sample under study. Phosphors such

as  $\text{SrB}_4\text{O}_7:\text{Sm}^{2+}$ ,<sup>185</sup> and various other rare-earth- or transition-metal-doped compounds have been investigated as alternatives, owing to their sharp emission lines and well-characterized pressure-dependent luminescence behavior.<sup>6,172,174</sup> The selection of an appropriate pressure indicator is therefore crucial in high-pressure experiments, especially when spectral overlap may hinder accurate measurements, this is particularly important when the investigated phosphor exhibits low emission intensity. For this reason, careful consideration of the spectral compatibility between the indicator and the sample is essential at the experimental design stage.

In typical DAC experiments, a small crystal or powder grain of the pressure indicator is placed at the edge of the gasket's hole. This positioning enables selective excitation of either the indicator or the sample by laterally shifting the excitation beam across the DAC aperture. By doing so, the relative intensity of the indicator and sample signals can be optimized.

### **3.4. Pressure-Transmitting Medium**

The pressure-transmitting medium plays a vital role in high-pressure experiments conducted using a DAC, as it ensures hydrostatic or quasi-hydrostatic pressure conditions for the sample under examination. The use of an appropriate PTM is essential for obtaining accurate and reproducible data, particularly when investigating pressure-dependent spectral shifts or intensity variations.

PTMs can be classified as either single-component or multi-component systems. Common single-component media include silicone-based compounds such as polydimethylsiloxane (PDMS) and inert oils like Daphne Oil. Frequently used multi-component PTMs are mixtures of methanol and ethanol, or methanol/ethanol/water, typically in volumetric ratios such as 4:1 or 16:3:1, respectively. The choice of composition depends on the desired pressure range and compatibility with the sample material. The primary selection criterion for any PTM is its chemical inertness toward the sample under investigation. The medium must not chemically react with, dissolve, or otherwise alter the physical state of the material. Additionally, an important practical consideration is the hydrostatic limit—that is, the maximum pressure at which the medium maintains hydrostatic conditions. Beyond this threshold, pressure distribution becomes anisotropic, resulting in non-hydrostatic conditions that may introduce unwanted spectral distortions or artificial shifts in luminescence behavior. From an experimental standpoint, care must be taken during DAC closure to ensure that the PTM is correctly introduced and remains inside the DAC throughout the measurement. Volatile media such as methanol/ethanol mixtures present an evaporation risk. To mitigate this, the chamber should be sealed immediately after the PTM is introduced. In contrast, oils like Daphne or PDMS exhibit negligible volatility, simplifying DAC preparation. During measurements, it is important to monitor the hole with sample visually, typically through

a microscope. One useful indicator of non-hydrostatic conditions is deformation of the gasket's hole, such as changes in its round shape or its diameter.<sup>180,186,187</sup>

In summary, luminescence measurements under high-pressure conditions impose stringent requirements not only on instrumentation but also on sample preparation protocols. Achieving reliable and reproducible results necessitates the use of high-quality, chemically and physically well-defined components, carefully selected pressure indicators and PTMs, and meticulous control over all stages of preparation and the measurement process. By adhering to these standards and continuously monitoring the behavior of the DAC components during both compression and decompression, high-quality optical data can be obtained even under extreme conditions.

---

## EXPERIMENTAL PART

---

### 4. Experimental methods

---

#### 4.1. Syntheses

Two synthesis methods were employed for the preparation of Cr<sup>3+</sup>-doped phosphors: the conventional high-temperature solid-state reaction method and the modified Pechini method.<sup>188</sup> The solid-state method was selected for the majority of the studied materials (compounds presented in **publications P3-P7**), primarily due to the demanding nature of pressure-dependent luminescence measurements. In such experiments, only a very small quantity of sample - typically placed in a 140 µm diameter gasket hole - is measured in DAC. Therefore, materials with strong luminescence are required to ensure sufficient signal intensity. The solid-state synthesis method is particularly suitable for this purpose, as it allows for high-temperature treatment, which promotes the growth of larger crystallites, typically in the micrometer size range, often resulting in enhanced emission intensity due to reduced surface-related quenching effects.

In general, the solid-state method involves thorough mixing and grinding of solid precursors - usually metal oxides or carbonates - in a mortar with the addition of a volatile medium. This medium must be chemically inert toward the reactants (i.e., it does not dissolve or react with the precursors), and its role is to facilitate the homogeneous distribution of precursors during grinding. Commonly used media include acetone, alcohols and hexane. After homogenization, the mixture is transferred into a crucible or another solid surface and subjected to high-temperature annealing, typically in air, although reducing or inert gas atmospheres (e.g., Ar, N<sub>2</sub>) may also be used depending on the synthesized material or precursors properties. In the case of the samples synthesized within the framework of this doctoral thesis using the solid-state reaction method, materials reported in **publications P3, P4, P5 and P7** were annealed in powder form using corundum crucibles as reaction vessels. An exception was the material described in **publication P6**, which was pelleted after grinding and annealed on platinum foil, due to undesirable interactions with the standard corundum crucible during synthesis. All the samples were annealed in air.

In contrast, the modified Pechini method was employed for the synthesis of phosphors described in **publications P1 and P2**. Pechini method allows to obtain nanoparticles, due to its ability to operate at lower annealing temperatures and to promote enhanced homogeneity of the material by suspending the precursors in a polymeric resin. However, it is important to note that the resulting crystallites often exhibit an aggregated morphology.

The modified Pechini method involves the preparation of a homogeneous solution - usually aqueous or alcohol-based - that enables complete dissolution of the starting precursors, most commonly inorganic or organic salts (e.g., nitrates, chlorides or acetates). Alternatively, in cases where suitable salts are unavailable, soluble precursors may be synthesized by dissolving metal oxides in concentrated acids, most frequently nitric or hydrochloric acid. This process involves gradual acid addition to a suspension of the oxide in distilled water, as the dissolution reaction is strongly exothermic. The mixture is gently heated to accelerate the dissolution, and once a clear solution is obtained, the resulting salt is recrystallized multiple times to remove excess acid and ensure purity.

Once the soluble metal salts are prepared, they are combined with citric acid, which acts as a chelating agent, forming stable metal-citrate complexes that improve the spatial distribution of metal ions within the precursor solution. This step is critical to achieving high homogeneity in the final phosphor. Subsequently, PEG is added as a polymerizing agent, which reacts with citric acid via esterification, leading to the formation of a crosslinked resin. The mixture is then heated to remove the solvent, yielding a resin, which is subsequently subjected to annealing in a furnace to form the desired powders.

The samples described in **publications P1** and **P2** were synthesized using the modified Pechini method in accordance with the protocol outlined above. In both cases, soluble salts of the desired cations were employed as starting materials. An exception was the source of  $\text{Ti}^{4+}$  ions used in the synthesis of the samples for **publication P1**, where titanium(IV) n-butoxide was utilized. To ensure its stability and prevent premature hydrolysis, the Ti-precursor was first stabilized by complexation with 2,4-pentanedione in a 1:1 molar ratio. In both syntheses, water served as the solvent medium.

A summary of the  $\text{Cr}^{3+}$ -doped phosphors synthesized for the doctoral dissertation - along with the detailed composition, synthesis conditions including annealing temperature, time, and heating rate are presented below in **Figure 8**. Phosphors prepared using the modified Pechini method marked in blue, while those obtained via the solid-state reaction method are indicated in green.

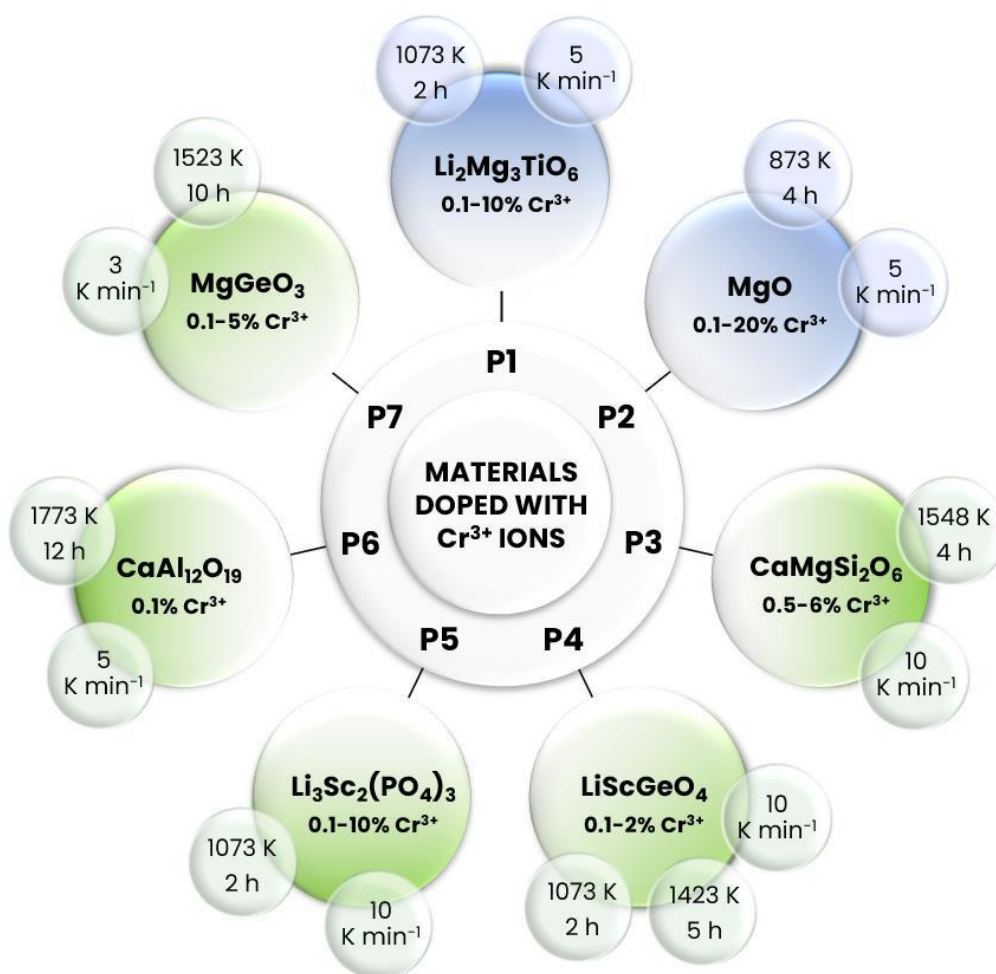


**Figure 8.** Summary of the  $\text{Cr}^{3+}$ -doped phosphors studies within the framework of this dissertation, along with corresponding synthesis conditions: temperature, time and heating rate of annealing. Phosphors prepared via modified Pechini method are marked in blue, while those synthesized by the solid-state reaction method are indicated in green.

## 4.2. Measurement methods and apparatus

### Investigation of the phase purity and structure

The X-ray diffraction (XRD) patterns were obtained using:

- **P1, P2, P4, P5 and P7:** Panalytical X'Pert Pro diffractometer equipped with an Anton Paar TCU1000 N Temperature Control Unit, using Ni-filtered  $\text{Cu K}\alpha$  radiation ( $V = 40 \text{ kV}$ ,  $I = 30 \text{ mA}$ )
- **P3 and P6:** D8 Advance diffractometer, Bruker Corporation, with  $\text{Cu K}\alpha$  radiation ( $V = 40 \text{ kV}$  and  $40 \text{ mA}$ ).

## Investigation of the morphology and elemental distribution

Transmission or scanning electron microscopy images were obtained using:

- **P1, P2, P4:** Philips CM-20 SuperTwin transmission electron microscope (TEM) (CCD FEI Eagle 2 K camera with a HAADF detector, LaB6 cathode). The studies were conducted using a 160 kV parallel beam electron energy. Sample preparation involved dispersing the powders in methanol, depositing the resulting suspension onto a copper grid, and subsequently drying the samples under an infrared (IR) lamp for 40 minutes.
- **P5, P6, P7:** FEI NOVA NanoSEM 230 scanning electron microscope (SEM) equipped with an EDAX Genesis XM4 energy-dispersive spectrometer. The powder sample was dispersed in a few drops of methanol, and a drop of the resulting suspension was deposited onto a carbon stub and subsequently dried under an IR lamp.
- **P3:** JSM-6701F scanning electron microscope, Hitachi. The sample was dispersed in a few drops of alcohol, and a drop of the resulting suspension was deposited onto a carbon stub and subsequently dried.

## Investigation of pressure-dependent Raman spectroscopy

Pressure-dependent Raman spectra were acquired using a Renishaw InVia confocal micro-Raman system operating in backscattering geometry. Excitation was provided by a 532 nm laser diode (100 mW), with the beam focused onto the sample through an Olympus  $\times 20$  SLMPlan N long working distance objective. The high-pressure experiments were carried out using a screw-driven diamond anvil cell equipped with ultra-low fluorescence type *IIa*s diamond anvils. A methanol/ethanol/water mixture in a 16:3:1 volume ratio was used as the pressure-transmitting medium.

## Investigation of the initial spectroscopic properties

**P1, P2, P4, P5, P6, P7:** Excitation and emission spectra, as well as luminescence decay profiles, were measured using an FLS1000 Fluorescence Spectrometer (Edinburgh Instruments). An R5509-72 photomultiplier tube (Hamamatsu), housed in a nitrogen-flow-cooled enclosure, was employed for infrared detection. Excitation spectra were recorded using a 450 W xenon lamp, while a 445 nm laser operated in either pulsed or continuous mode, depending on the measurement type - served as the excitation source for luminescence decay and emission spectra.

**P3:** Complementary measurements as above were conducted using a Hitachi F-4700 fluorescence spectrophotometer equipped with a 450 W xenon lamp to record excitation and emission spectra at room temperature. Luminescence decay profiles were obtained using an FS5 fluorescence spectrometer (Edinburgh Instruments).



The luminescence decay profiles were fitted using a biexponential function:

$$I(t) = I_0 + A_1 \cdot \exp\left(-\frac{t}{\tau_1}\right) + A_2 \cdot \exp\left(-\frac{t}{\tau_2}\right) \quad (9)$$

The average luminescence lifetime was then calculated according to **Equation 10**:

$$\tau_{avr} = \frac{A_1 \tau_1^2 + A_2 \tau_2^2}{A_1 \tau_1 + A_2 \tau_2} \quad (10)$$

where  $\tau_1$  and  $\tau_2$  denote the individual luminescence decay components, and  $A_1$  and  $A_2$  are their corresponding amplitudes, obtained from the parameters of the biexponential fit.

### Investigation of temperature-dependent luminescent properties

For temperature-dependent measurements of emission spectra and luminescence decay profiles, a 445 nm laser diode was employed as the excitation source. Temperature control during the experiments was provided by a THMS 600 heating-cooling stage (Linkam Scientific Instruments), with a temperature stability and set point resolution of 0.1 K. Prior to each measurement, the system was allowed to stabilize for 2 minutes at the target temperature. The signal was collected from the heating-cooling stage, positioned outside the FLS1000 spectrometer, and transferred to the detection system via a bifurcated fiber optic bundle supplied by Edinburgh Instruments.

### Investigation of pressure-dependent luminescent properties

Pressure-dependent luminescence studies were performed using an FLS1000 fluorescence spectrometer (Edinburgh Instruments), equipped with a 450 W xenon lamp and an R5509-72 photomultiplier tube (Hamamatsu) housed in a nitrogen-flow-cooled enclosure. The excitation was provided by a 445 nm laser diode. **For the purposes of this doctoral research, a custom optical setup was constructed for the measurement of luminescent properties under variable pressure conditions, and its calibration was performed.** Pressure-dependent luminescence studies were conducted using a Druck PACE 5000 pressure controller. High-pressure luminescence measurements were carried out in a diamond anvil cell purchased from Almax easyLab (Diacell  $\mu$ ScopeDAC-RT(G)). Pressure was applied via a nitrogen-fed gas membrane system. The DAC was equipped with ultra-low fluorescence type *IIa*s diamonds with 0.4 mm culets. A 250  $\mu$ m thick stainless-steel gasket (10 mm in diameter) was placed between the diamond anvils. A 140  $\mu$ m diameter hole was drilled at the center of the gasket to form the sample chamber. Into this chamber, an appropriate amount of pressure indicator, sample material, and a drop of pressure-transmitting medium (PTM) were introduced. A methanol:ethanol mixture in a 4:1 (v/v) ratio was used as the PTM, and ruby was used as the pressure indicator.

## 5. Results and discussion

---

### 5.1. Development of a pioneering ratiometric LIR-based luminescent manometer based on the ${}^4T_{2g} \rightarrow {}^4A_{2g}$ electronic transition of $Cr^{3+}$ in doped $Li_2Mg_3TiO_6$

The objective of the **publication P1** was to introduce, for the first time, the feasibility of utilizing the broadband emission associated with the  ${}^4T_{2g} \rightarrow {}^4A_{2g}$  electronic transition of  $Cr^{3+}$  ions for luminescence pressure sensing through a ratiometric approach based on the luminescence intensity ratio. The selected material for this study was  $Li_2Mg_3TiO_6:Cr^{3+}$ , a phosphor exhibiting unique spectroscopic properties due to the presence of two distinct crystallographic sites available for  $Cr^{3+}$  ion incorporation: octahedrally coordinated  $Mg^{2+}$  and  $Ti^{4+}$  ions.<sup>148</sup> To verify this possibility and determine the optimal composition of  $Li_2Mg_3TiO_6:Cr^{3+}$  for further pressure-dependent studies,  $Li_2Mg_3TiO_6:Cr^{3+}$  powders with varying  $Cr^{3+}$  concentrations (ranging from 0.1% to 10%) were synthesized. These samples were then subjected to comprehensive structural and spectroscopic analyses to gain deeper insight into their luminescence behavior under applied pressure, thereby assessing their potential for manometric applications.

Rietveld refinement of the XRD patterns collected at room temperature demonstrated an increase in unit cell volume - from  $73.1 \text{ \AA}^3$  to  $73.8 \text{ \AA}^3$  as the  $Cr^{3+}$  concentration increased up to 1%. This observation suggests that  $Cr^{3+}$  ions were successfully incorporated into  $Ti^{4+}$  positions, which possess a slightly smaller effective ionic radius ( $r_{Cr^{3+}} = 0.615 \text{ \AA}$ ,  $r_{Ti^{4+}} = 0.605 \text{ \AA}$ )<sup>189</sup>. However, as  $Cr^{3+}$  ions progressively replaced  $Mg^{2+}$  - which have a larger ionic radius ( $r_{Mg^{2+}} = 0.72 \text{ \AA}$ ) in respect to the  $Cr^{3+}$  ions - the unit cell exhibited contraction, ultimately leading to a volume reduction to approximately  $72.75 \text{ \AA}^3$  at a  $Cr^{3+}$  concentration of 10%. This structural evolution was corroborated by luminescence studies, which demonstrated a gradual change in spectra shape by an increasing dominance of a broad emission band associated with the  ${}^4T_{2g} \rightarrow {}^4A_{2g}$  electronic transition of  $Cr^{3+}$  ions with increasing  $Cr^{3+}$  concentration. The  $Mg^{2+}$  and  $Ti^{4+}$  crystallographic positions impose distinct crystal field strengths affecting  $Cr^{3+}$  due to differences in their ionic radii.  $Ti^{4+}$  ions, being smaller in radius than  $Cr^{3+}$ , induce a stronger crystal field, manifested in the luminescence spectrum as a narrow emission band associated with the  ${}^2E_g \rightarrow {}^4A_{2g}$  electronic transition. Similar emission features were observed for samples doped up to 2% of  $Cr^{3+}$ . As the  $Cr^{3+}$  concentration increased, the broad emission band corresponding to the  ${}^4T_{2g} \rightarrow {}^4A_{2g}$  electronic transition became progressively dominant, ultimately dominating the narrow emission band in the sample with 5%  $Cr^{3+}$ , where only a residual signal of the narrow emission remained. Such a luminescent response suggests the initial incorporation of  $Cr^{3+}$  ions into  $Ti^{4+}$  crystallographic sites, which possess a smaller ionic radius than  $Cr^{3+}$ . This substitution is reflected by the presence of a narrow emission band originating from the spin-forbidden  ${}^2E_g \rightarrow {}^4A_{2g}$  electronic transition,

characteristic of  $\text{Cr}^{3+}$  ions in a relatively strong crystal field. Once all available  $\text{Ti}^{4+}$  sites were occupied,  $\text{Cr}^{3+}$  ions began to substitute into  $\text{Mg}^{2+}$  positions, which generate a weaker crystal field environment. As the  $\text{Cr}^{3+}$  concentration increased, a progressive dominance of the  ${}^4\text{T}_{2g} \rightarrow {}^4\text{A}_{2g}$  emission band was observed, attributed to the growing proportion of  $\text{Cr}^{3+}$  ions occupying  $\text{Mg}^{2+}$  positions relative to  $\text{Ti}^{4+}$  crystallographic positions. The hypothesis of  $\text{Cr}^{3+}$  substitution into two distinct crystallographic positions was further validated by differences in maximum position of excitation bands associated with  ${}^4\text{A}_{2g} \rightarrow {}^4\text{T}_{1g}$  and  ${}^4\text{A}_{2g} \rightarrow {}^4\text{T}_{2g}$  electronic transitions of  $\text{Cr}^{3+}$ , which were measured by monitoring luminescence signal at maximum of broad and narrow band. The calculation of the  $Dq/B$  parameter based on excitation spectra was performed, which was determined to be 2.62 for  $\text{Cr}^{3+}$  in  $\text{Ti}^{4+}$  sites and 2.25 for  $\text{Cr}^{3+}$  in  $\text{Mg}^{2+}$  positions, what was in correlation with mentioned relation between intensity  ${}^4\text{T}_{2g} \rightarrow {}^4\text{A}_{2g}$  and  ${}^2\text{E}_g \rightarrow {}^4\text{A}_{2g}$  emission bands.

Given that the broad emission band exhibited significantly higher intensity than the narrow band associated with the  ${}^2\text{E}_g \rightarrow {}^4\text{A}_{2g}$  transition of  $\text{Cr}^{3+}$  ions, a sample with 5%  $\text{Cr}^{3+}$  was selected for further studies aimed at evaluating the potential use of the  ${}^4\text{T}_{2g} \rightarrow {}^4\text{A}_{2g}$  emission for luminescence manometry. As a first step, Raman spectroscopy was employed to examine the structural stability of  $\text{Li}_2\text{Mg}_3\text{TiO}_6$  under applied pressure. The results indicated that the  $\text{Li}_2\text{Mg}_3\text{TiO}_6$  structure remained stable up to approximately 8 GPa. Beyond this pressure, a nonlinear shift in one of the Raman modes was observed (with maximum at around  $400\text{ cm}^{-1}$ ), suggesting a pressure-induced phase transition, which could potentially introduce hysteresis effects in luminescence-based pressure readings. To further assess pressure-induced spectroscopic changes, emission spectra were recorded over a pressure range of 0-7.75 GPa.

With increasing pressure, a non-linear blue shift of the emission band associated with the  ${}^4\text{T}_{2g} \rightarrow {}^4\text{A}_{2g}$  transition of  $\text{Cr}^{3+}@ \text{Mg}^{2+}$  was observed. Consequently, the classical approach to optical pressure sensing - monitoring the spectral shift of the emission band - was evaluated as an initial strategy for developing a luminescence manometer. Between ambient pressure and 7.75 GPa, the emission band maximum shifted from 850.5 nm to 782 nm. Despite the relatively large spectral shift, a significant limitation in pressure readout was identified: the difficulty in precisely determining the emission band maximum resulted in substantial reading errors. This uncertainty was quantified by identifying the wavelength range in which the intensity remained above 95% of the peak value. It was found that, in the case of pressure-induced spectral shift, the pressure could be determined with an uncertainty of  $\pm 4$  GPa using the  $\text{Li}_2\text{Mg}_3\text{TiO}_6:\text{Cr}^{3+}$  luminescence. To mitigate this limitation, a ratiometric approach based on the LIR parameter was proposed, based on the ratio of the integrated intensities of two selected spectral ranges within the  ${}^4\text{T}_{2g} \rightarrow {}^4\text{A}_{2g}$  emission band:

$$LIR = \frac{\int_{825 \text{ nm}}^{935 \text{ nm}} I(\text{Cr}^{3+}; {}^4T_{2g} \rightarrow {}^4A_{2g}) d\lambda}{\int_{1005 \text{ nm}}^{1095 \text{ nm}} I(\text{Cr}^{3+}; {}^4T_{2g} \rightarrow {}^4A_{2g}) d\lambda} \quad (11)$$

The LIR values exhibited a monotonic increase from 4.88 at ambient pressure to 6.82 at 7.75 GPa. The maximum relative sensitivity was observed at ambient pressure, reaching 4.7% GPa<sup>-1</sup>, and decreased gradually to approximately 3.3% GPa<sup>-1</sup> at 7.75 GPa. Moreover, the measurement uncertainty in this ratiometric approach, estimated based on the signal-to-noise ratio, was significantly lower compared to the conventional spectral shift method. Importantly, the observed spectroscopic changes were fully reversible upon decompression, as confirmed through three compression-decompression cycles, ensuring the reproducibility of the measurements.

Another crucial aspect presented in **publication P1** was the investigation of temperature effect on pressure readouts. Emission spectra were recorded as a function of temperature in the range of 123-563 K, under identical measurement conditions to those used in the pressure experiments (same excitation source and detection parameters). A decrease in emission intensity was observed with increasing temperature; however, in contrast to pressure-dependent studies, no significant shift in the emission band maximum was detected. To assess the thermometric properties of the sample, the LIR curve was plotted as a function of temperature, following the same spectral ranges for LIR calculations as used in a case of manometric analysis. The temperature sensitivity across the studied temperature range did not exceed 0.11% K<sup>-1</sup>, which, according to literature reports, indicated poor thermometric performance.<sup>190</sup> This suggests that temperature variations do not significantly affect the pressure readouts of the developed ratiometric LIR-based manometer.

---

### **The most important scientific significance of publication P1 for the advancement of the research field**

---

The findings presented in **publication P1** led to the establishment of a novel class of luminescent manometers employing ratiometric LIR-based sensing through a monitoring a broadband emission band, with the first-ever demonstration based on the <sup>4</sup>T<sub>2g</sub>→<sup>4</sup>A<sub>2g</sub> emission of Cr<sup>3+</sup> ions. The proposed sensor demonstrated not only high sensitivity, excellent precision and reproducibility but also temperature-independent performance - a significant advantage over conventional optical pressure sensors that rely on pressure-induced spectral shifts. Therefore, this study represents a breakthrough in the field of luminescence manometry, paving the way for the development of practical, high-performance optical pressure sensors.

---

synthesis of samples with varying concentrations of  $\text{Cr}^{3+}$  ions; spectroscopic characterization of phosphors, including luminescence measurements; investigation of emission as a function of temperature and pressure; data analysis and preparation of the first draft of the manuscript

### 5.2. Validation of two LIR-based ratiometric approaches utilizing emission from $^2\text{E}_g$ and $^4\text{T}_{2g}$ excited states of $\text{Cr}^{3+}$ - studies of $\text{MgO}$ and $\text{CaMgSi}_2\text{O}_6$ doped with $\text{Cr}^{3+}$

In light of the findings presented in **publication P1**, it became necessary to further validate the superior potential of utilizing the broadband emission associated with the  $^4\text{T}_{2g} \rightarrow ^4\text{A}_{2g}$  electronic transition of  $\text{Cr}^{3+}$  ions for ratiometric LIR-based pressure sensing, in comparison to the approach based on the intensity ratio between the narrow and broad emission bands of  $\text{Cr}^{3+}$ , associated with the  $^2\text{E}_g \rightarrow ^4\text{A}_{2g}$  and the  $^4\text{T}_{2g} \rightarrow ^4\text{A}_{2g}$  electronic transitions, respectively, typically used in luminescence thermometry. To confirm this hypothesis,  $\text{MgO}:\text{Cr}^{3+}$  (**publication P2**) and  $\text{Ca}_{0.8}\text{Sr}_{0.2}\text{MgSi}_2\text{O}_6:\text{Cr}^{3+}$  (**publication P3**) phosphors were selected, both exhibiting emission spectra characterized by the presence of a narrow  $^2\text{E}_g \rightarrow ^4\text{A}_{2g}$  emission band at ambient pressure or under elevated pressure.

At the time the present study on  $\text{MgO}:\text{Cr}^{3+}$  was undertaken, published research on the pressure dependence of its luminescence was limited and predominantly focused on emission originating from the  $^2\text{E}_g$  energy level of  $\text{Cr}^{3+}$  ions.<sup>191,192</sup> Moreover, many reports were theoretical in nature or restricted in experimental scope.<sup>193</sup> Given its simple crystallographic structure, well-defined chemical composition, and excellent chemical, thermal, and mechanical stability,  $\text{MgO}$  remained a promising host material for  $\text{Cr}^{3+}$  ions, particularly in the context of luminescence manometry under extreme environmental conditions. Taking these aspects into consideration, a more comprehensive experimental investigation - especially one focusing on the broadband  $^4\text{T}_{2g} \rightarrow ^4\text{A}_{2g}$  emission, which had not previously been explored in the context of pressure-induced spectroscopic characteristics, was considered highly relevant for evaluating the potential of  $\text{MgO}:\text{Cr}^{3+}$  as a potential material for luminescence-based pressure sensing.

Given the scarcity of luminescence studies on this material,  $\text{MgO}:\text{Cr}^{3+}$  samples with  $\text{Cr}^{3+}$  concentrations ranging from 0.1% to 10% were synthesized to identify the optimal composition for pressure sensing. The Pechini method was employed for synthesis, accompanied by optimization of the annealing temperature. Structural analysis revealed that annealing above 873 K leads to the formation of an undesirable  $\text{MgCr}_2\text{O}_6$  phase. Consequently, all samples were annealed at 873 K to ensure phase purity and to maximize emission intensity, which benefits from the increased particle size achieved at this temperature.

Despite its structural simplicity, the MgO host material is characterized by an interesting environment for Cr<sup>3+</sup> incorporation. Owing to the charge imbalance between Mg<sup>2+</sup> and Cr<sup>3+</sup>, charge compensation occurs through the substitution of three Mg<sup>2+</sup> ions by two Cr<sup>3+</sup> ions, which results in local lattice distortions. As a consequence, three types of crystallographic positions for Cr<sup>3+</sup> ions may exist in the MgO structure: cubic, tetragonal, and rhombic. Given the preference of Cr<sup>3+</sup> ions for sixfold coordination, they predominantly occupy cubic and rhombic sites. This is spectroscopically manifested at 83 K as a combination of a narrow emission band corresponding to the <sup>2</sup>E<sub>g</sub>→<sup>4</sup>A<sub>2g</sub> electronic transition of Cr<sup>3+</sup> in cubic positions (observed in the 680-720 nm range) and a broad emission band arising from the <sup>4</sup>T<sub>2g</sub>→<sup>4</sup>A<sub>2g</sub> electronic transition of Cr<sup>3+</sup> located in rhombic sites (with maxima between 820-900 nm). At higher doping levels, an additional broad band centered around 1190 nm was observed, attributed probably to the formation of Cr<sup>3+</sup>-Cr<sup>3+</sup> pairs. For pressure-dependent emission studies, the sample with 1% Cr<sup>3+</sup> concentration was selected, as it exhibited both the narrow <sup>2</sup>E<sub>g</sub>→<sup>4</sup>A<sub>2g</sub> and broad <sup>4</sup>T<sub>2g</sub>→<sup>4</sup>A<sub>2g</sub> bands at room temperature. The emission band assigned to Cr<sup>3+</sup>-Cr<sup>3+</sup> pairs was also considered for analysis due to its rare nature and potential relevance to pressure sensing. However, its intensity was insufficient for reliable measurements in a diamond anvil cell. As a result, further investigations focused exclusively on the emission bands associated with emission from <sup>2</sup>E<sub>g</sub> and <sup>4</sup>T<sub>2g</sub> excited states of Cr<sup>3+</sup> in doped MgO.

Due to the weak Raman signal of MgO, pressure-dependent Raman spectroscopy studies were not performed. Nevertheless, literature data confirm the structural stability of the MgO lattice under pressures higher than 100 GPa<sup>194</sup> Emission measurements were conducted across a pressure range from ambient conditions up to 7.9 GPa. With increasing pressure, a gradual enhancement of the intensity ratio of <sup>2</sup>E<sub>g</sub>→<sup>4</sup>A<sub>2g</sub> and <sup>4</sup>T<sub>2g</sub>→<sup>4</sup>A<sub>2g</sub> emission bands was observed. This effect was expected - shortening of the Cr-O distances under increasing pressure leads to a strengthening of the crystal field, resulting in a gradual increase in the energy of the <sup>4</sup>T<sub>2g</sub> state. Consequently, emission from the <sup>2</sup>E level becomes energetically more favorable. Additionally, the blue-shift of broad emission band associated with <sup>4</sup>T<sub>2g</sub>→<sup>4</sup>A<sub>2g</sub> electronic transition was observed. These pressure-induced spectroscopic changes enabled the proposition of two independent LIR-based ratiometric readout strategies. Accordingly, the LIR parameter was calculated in two distinct ways. The first approach based on LIR<sub>1</sub> (Mode I), was based on the ratio of integral intensities from two spectral ranges of the broad <sup>4</sup>T<sub>2g</sub>→<sup>4</sup>A<sub>2g</sub> emission band - a novel concept in the field of luminescence manometry, as indicated in **publication P1**. Hence, LIR<sub>1</sub> was defined as follows:

$$LIR_I = \frac{\int_{760 \text{ nm}}^{850 \text{ nm}} I(\text{Cr}^{3+}: ^4T_{2g} \rightarrow ^4A_{2g}) d\lambda}{\int_{877 \text{ nm}}^{940 \text{ nm}} I(\text{Cr}^{3+}: ^4T_{2g} \rightarrow ^4A_{2g}) d\lambda} \quad (12)$$

and the second readout approach (Mode II), based on LIR<sub>2</sub>, was expressed as the ratio of the integral intensities of the  ${}^2E_g \rightarrow {}^4A_{2g}$  and  ${}^4T_{2g} \rightarrow {}^4A_{2g}$  emission bands, using followed spectral ranges selected to isolate each emission contribution:

$$LIR_2 = \frac{\int_{714 \text{ nm}}^{728 \text{ nm}} I(\text{Cr}^{3+}; {}^2E_g \rightarrow {}^4A_{2g}) d\lambda}{\int_{877 \text{ nm}}^{940 \text{ nm}} I(\text{Cr}^{3+}; {}^4T_{2g} \rightarrow {}^4A_{2g}) d\lambda} \quad (13)$$

In the case of LIR<sub>1</sub>, a monotonic increase in its value was observed - from approximately 2.1 to 3.4 as pressure increased from ambient to 5.9 GPa. At higher pressures, up to 7.9 GPa, the rate of increase progressively diminished, deviating from the initial linear trend. In contrast, LIR<sub>2</sub> exhibited a continuous and monotonic increase across the entire pressure range studied, rising from 0.18 to 0.67. The maximum relative sensitivity values based on LIR<sub>1</sub> and LIR<sub>2</sub> calibration curves were determined to be 9.83% GPa<sup>-1</sup> at 1.15 GPa and 40% GPa<sup>-1</sup> at ambient pressure, respectively. As previously emphasized, the suitability of a material for pressure sensing applications depends not only on its pressure response but also on its resistance to temperature-induced interferences. Consequently, the emission spectra were recorded as a function of temperature, and the temperature-dependent characteristic of the LIR-based ratiometric response was performed analogous to pressure-dependent studies using the same spectral ranges .

For both LIR<sub>1</sub> and LIR<sub>2</sub>, a gradual change in their values was observed between 123 K and approximately 350 K. Above this temperature, the increase in LIRs became more pronounced, continuing up to 680 K. The maximal  $S_R$  of 0.11% K<sup>-1</sup> for LIR<sub>1</sub> at 530 K and 0.25% K<sup>-1</sup> for LIR<sub>2</sub> at 470 K were achieved. At room temperature (300 K), the sensitivities were equal to 0.0056% K<sup>-1</sup> and 0.056% K<sup>-1</sup> for LIR<sub>1</sub> and LIR<sub>2</sub>, respectively. The enhanced temperature sensitivity of LIR<sub>2</sub> is attributed to the thermal coupling between the  ${}^2E_g$  and  ${}^4T_{2g}$  energy levels of Cr<sup>3+</sup>, an effect that is commonly exploited in luminescence thermometry. As such, readout Mode II, based on LIR<sub>2</sub>, may be suitable for applications operating under well-controlled, isothermal conditions. In contrast, Mode I, based on the broad band associated with emission from the  ${}^4T_{2g}$  level (LIR<sub>1</sub>), exhibited approximately 10-fold lower temperature sensitivity, making it significantly less susceptible to thermal fluctuations. Despite its approximately fourfold lower pressure sensitivity compared to Mode II, the 9.83% GPa<sup>-1</sup> value achieved in Mode I still places it among the highest sensitivity values reported in the literature. This, combined with its greater thermal invariability, renders Mode I of MgO:Cr<sup>3+</sup> more versatile and practical for broader real-world applications.

Additionally, a traditional pressure sensing method based on monitoring the spectral shift of the narrow emission band associated with the  ${}^2E_g \rightarrow {}^4A_{2g}$  electronic transition of Cr<sup>3+</sup> in doped

MgO was also evaluated. The  $S_A$  was determined to be  $0.504 \text{ nm GPa}^{-1}$ , which is approximately 40% higher than that of the commonly used  $R_1$  ruby's line<sup>1-3</sup>, associated with the same electronic transition of  $\text{Cr}^{3+}$  ions. This highlights the potential of  $\text{MgO}:\text{Cr}^{3+}$  not only as a high-performance ratiometric pressure sensor but also as a viable alternative to traditional ruby-based indicator in spectral-shift-based manometry.

Another phosphor employed to further validate the approach based on the broad emission band of  $\text{Cr}^{3+}$  ions was the pyroxene-type compound  $\text{Ca}_{0.8}\text{Sr}_{0.2}\text{MgSi}_2\text{O}_6$  (**publication P3**). Compared to the previously investigated  $\text{MgO}:\text{Cr}^{3+}$ ,  $\text{Ca}_{0.8}\text{Sr}_{0.2}\text{MgSi}_2\text{O}_6:\text{Cr}^{3+}$  was characterized by a weaker crystal field strength, as evidenced by the presence of only a broad emission band with a maximum at  $780 \pm 2 \text{ nm}$  under ambient conditions across all synthesized  $\text{Cr}^{3+}$ -doped samples (ranging from 0.5% to 6%). Due to the absence of significant differences in the position of the emission and excitation bands across all the samples, the selection of the optimal composition was primarily based on the sample exhibiting the highest emission intensity, which corresponded to the phosphor doped with 2%  $\text{Cr}^{3+}$ .

To confirm the structural stability of this material under pressure, Raman spectroscopy was performed up to 7.18 GPa. The observed Raman modes shifts were fully reversible during decompression, and no new Raman modes appeared upon compression, indicating the absence of pressure-induced phase transitions or structural degradation. Based on these results, luminescence measurements as a function of pressure were carried out for  $\text{Ca}_{0.8}\text{Sr}_{0.2}\text{MgSi}_2\text{O}_6:2\%\text{Cr}^{3+}$  within a similar pressure range. The pressure-dependent emission spectra showed the expected shape changes with increasing pressure: a narrow emission band with maximum at around 680 nm associated with the  ${}^2\text{E}_g \rightarrow {}^4\text{A}_{2g}$  electronic transition gradually appeared around 1.9 GPa and began to dominate the spectrum at approximately 5 GPa. Simultaneously, a blue shift of the  ${}^4\text{T}_{2g}$  broad emission band from 781.3 nm to 740.7 nm was observed. By plotting the dependence of the emission maximum position on applied pressure and fitting the data accordingly, the calculated  $S_A$  was determined, yielding a maximum value of  $6.8 \text{ nm GPa}^{-1}$ .

Following a detailed analysis of the pressure-induced changes in emission intensity within selected spectral ranges, two calibration curves were proposed, based on  $\text{LIR}_1$  and  $\text{LIR}_2$  parameters. As defined below,  $\text{LIR}_1$  corresponds to the intensity ratio between the  ${}^2\text{E}_g \rightarrow {}^4\text{A}_{2g}$  and  ${}^4\text{T}_{2g} \rightarrow {}^4\text{A}_{2g}$  emission bands, while  $\text{LIR}_2$  utilizes only spectral ranges within the broad band associated with the  ${}^4\text{T}_{2g} \rightarrow {}^4\text{A}_{2g}$  transition, following the same ratiometric strategy employed in earlier studies:



$$LIR_1 = \frac{\int_{678.5 \text{ nm}}^{688.5 \text{ nm}} I(\text{Cr}^{3+}: {}^2E_g \rightarrow {}^4A_{2g}) d\lambda}{\int_{842 \text{ nm}}^{852 \text{ nm}} I(\text{Cr}^{3+}: {}^4T_{2g} \rightarrow {}^4A_{2g}) d\lambda} \quad (14)$$

$$LIR_2 = \frac{\int_{700 \text{ nm}}^{720 \text{ nm}} I(\text{Cr}^{3+}: {}^4T_{2g} \rightarrow {}^4A_{2g}) d\lambda}{\int_{900 \text{ nm}}^{910 \text{ nm}} I(\text{Cr}^{3+}: {}^4T_{2g} \rightarrow {}^4A_{2g}) d\lambda} \quad (15)$$

A calibration curve based on the  $LIR_1$  was proposed for the pressure range of 1.9 GPa to 7.55 GPa, as the narrow emission band associated with the  ${}^2E_g \rightarrow {}^4A_{2g}$  electronic transition appeared only above 1.9 GPa. In contrast, the readout method based solely on the broad emission band ( $LIR_2$ ), attributed to the  ${}^4T_{2g} \rightarrow {}^4A_{2g}$  electronic transition of  $\text{Cr}^{3+}$ , was applicable across the entire studied pressure range. As the  ${}^4T_{2g}$  broad emission band represents a key spectroscopic feature for ratiometric pressure sensing, the optimization of spectral ranges used in the calculation of the  $LIR_2$  parameter was carried out by analyzing pressure-dependent changes in the integrated emission intensity within the 730-960 nm spectral range. The 700-720 nm spectral gate was selected as the reference range due to the pronounced distortion in the emission band shape observed in this region under increasing pressure. For each spectral pair - comprising 700-720 nm range in the numerator of LIR and another 10 nm spectral gates between 730 and 960 nm in the denominator - a calibration curves were constructed, and the corresponding relative sensitivities were calculated. The final  $LIR_2$  definition represented a compromise between high  $S_R$  value and acceptable readout precision. For instance, the utilization of 950-960 nm range for LIR calculation yielded a relative sensitivity of 55.9%  $\text{GPa}^{-1}$ , but the signal in this spectral range was approximately ten times weaker than that of the 900-910 nm region, resulting in a significantly lower signal-to-noise ratio and higher readout error.

Both  $LIR_2$  and  $LIR_1$  increased monotonically with applied pressure by a whole operating pressure range, resulting in corresponding maximum relative sensitivities of 50.7%  $\text{GPa}^{-1}$  at ambient pressure and 41.9%  $\text{GPa}^{-1}$  at 1.9 GPa, respectively. A notable advantage of the  $LIR_2$ -based readout is its broader usable pressure range, despite the lower  $S_R$  (e.g. approximately 25%  $\text{GPa}^{-1}$  at 1.9 GPa), compared to  $LIR_1$ . However, it is important to emphasize that the temperature stability of the readout is equally critical when assessing the overall application potential of a luminescent pressure sensor. To evaluate the effect of temperature on pressure readings, emission spectra of  $\text{Ca}_{0.8}\text{Sr}_{0.2}\text{MgSi}_2\text{O}_6:2\%\text{Cr}^{3+}$  were recorded over a wide temperature range, from 83 to 763 K. Throughout the entire temperature range studied, only the broad emission band associated with the  ${}^4T_{2g} \rightarrow {}^4A_{2g}$  electronic transition was observed - even at low temperatures. Consequently, the thermometric analysis focused exclusively on the broadband  ${}^4T_{2g} \rightarrow {}^4A_{2g}$  emission

and the temperature dependence of the  $LIR_2$ . In contrast to the pressure-induced trend,  $LIR_2$  exhibited an inverse monotonic behavior between 83 K and approximately 300 K. Beyond this temperature, the  $LIR_2$  values remained relatively stable up to 450 K. The maximum temperature sensitivity based on  $LIR_2$  was determined to be  $0.18\% K^{-1}$  at 83 K, and only  $0.033\% K^{-1}$  at room temperature. These values indicate that the material does not exhibit sufficient thermal responsiveness to function as a reliable luminescent thermometer. Nevertheless, when the TIMF was calculated its value reached  $1558 K GPa^{-1}$  at ambient pressure - indicating the excellent thermal stability of the pressure readout. With increasing pressure, the TIMF value gradually decreased but remained above  $300 K GPa^{-1}$  across the entire pressure range. For comparison,  $LIR_1$  exhibited a temperature sensitivity of  $0.26\% K^{-1}$  at room temperature, and a corresponding TIMF value of  $160.8 K GPa^{-1}$  at 1.9 GPa, which decreased to around  $17.5 K GPa^{-1}$  at 7.55 GPa. These results clearly demonstrate that the use of  ${}^4T_{2g} \rightarrow {}^4A_{2g}$  emission band of  $Cr^{3+}$  ions enables highly temperature-stable pressure sensing, validating the LIR-based ratiometric approach as an effective strategy for luminescence manometry.

In **publication P3**, luminescence kinetic was also investigated based on the  ${}^4T_{2g} \rightarrow {}^4A_{2g}$  emission band of  $Cr^{3+}$  ions. The average lifetime of the  ${}^4T_{2g}$  excited state, calculated from pressure-dependent luminescence decay curves, elongates from  $31 \mu s$  at ambient pressure to  $45.7 \mu s$  at 7.55 GPa. Due to the overlap of the wave functions associated with the  ${}^4T_{2g}$  and  ${}^2E_g$  levels, these states are coupled through spin-orbit interaction. As pressure increases, leading to an enhancement of the crystal field strength, the energy of the  ${}^4T_{2g}$  level increases. This leads to reduction in the energy separation between the  ${}^4T_{2g}$  and  ${}^2E_g$  states resulting in increase in the strength of the spin-orbit coupling between them. Consequently, an increase in the average lifetime with increasing pressure was observed.

The corresponding  $S_R$  derived from the  $\tau_{avr}$  vs. pressure dependence reached  $7.95\% GPa^{-1}$  at 5 GPa. Importantly, this result demonstrated that the sensor ensures a sensitivity exceeding  $3\% GPa^{-1}$  even in the high-pressure regime (above 5 GPa), which positioned it favorably compared to other luminescence decay time-based manometers reported at the time. The thermometric response of the sensor, evaluated from  $\tau_{avr}$  changes induced by temperature, yielded a sensitivity of  $0.16\% K^{-1}$  at room temperature, corresponding to a TIMF value of  $48.5 K GPa^{-1}$ . This relatively low TIMF indicates a non-negligible influence of temperature on lifetime-based pressure readouts. Therefore, for this particular material, a ratiometric readout based on the LIR parameter is recommended as the more reliable and temperature-independent mode of readout.

### **The most important scientific significance of publications P2 and P3 for the advancement of the research field**

The studies conducted within the scope of **publications P2** and **P3** clearly confirmed the potential of utilizing the band associated with emission from the  $^4T_{2g}$  level of  $Cr^{3+}$  for ratiometric pressure sensing based on the LIR approach. Both research demonstrated that although a readout based on the intensity ratio of bands associated with the  $^2E_g \rightarrow ^4A_{2g}$  and  $^4T_{2g} \rightarrow ^4A_{2g}$  transitions offers higher pressure sensitivity, it is significantly more susceptible to temperature-induced variations, due to the thermal coupling of  $^2E_g$  and  $^4T_{2g}$  states of  $Cr^{3+}$ , thereby limiting its practical applicability under non-isothermal conditions.

---

#### **Author's contribution to the publication P2**

---

synthesis of samples with varying concentrations of  $Cr^{3+}$  ions; spectroscopic characterization of phosphors, including luminescence measurements; investigation of emission as a function of temperature and pressure; data analysis and preparation of the first draft of the manuscript

#### **Author's contribution to the publication P3**

---

spectroscopic characterization of phosphors, including luminescence measurements; investigation of emission and luminescence kinetics as a function of temperature and pressure; data analysis and preparation of the first draft of the manuscript

### **5.3. Confirmation of manometric potential of matrices providing weak crystal field for $Cr^{3+}$ ions: multimodal luminescent manometer based on $LiScGeO_4:Cr^{3+}$ and $Li_3Sc_2(PO_4)_3:Cr^{3+}$ as an optical pressure sensor operating on three spectroscopic parameters**

In light of the exceptionally high manometric potential of the ratiometric approach based on  $Cr^{3+}$  ion emission associated with the  $^4T_{2g} \rightarrow ^4A_{2g}$  electronic transition, as evidenced in **publications P1, P2, and P3**, the subsequent phase of this doctoral research focused on further enhancing the effectiveness of this strategy through the design and development of pressure sensors exhibiting outstanding manometric performance to improve application potential. For this purpose, two host materials -  $LiScGeO_4$  (**publication P4**) and  $Li_3Sc_2(PO_4)_3$  (**publication P5**) - were selected, as they provide extremely weak crystal field for  $Cr^{3+}$  ions, with the  $Dq/B$  values of approximately 1.44 and 1.7, respectively.<sup>88,89</sup> This crystal field environment results in  $Cr^{3+}$  emission spectra characterized by the  $^4T_{2g} \rightarrow ^4A_{2g}$  broadband emission, significantly red-shifted into the near-infrared spectral range, with maxima at approximately 1100 nm for  $LiScGeO_4:Cr^{3+}$  and at 980 nm

for  $\text{Li}_3\text{Sc}_2(\text{PO}_4):\text{Cr}^{3+}$ . For both phosphors, the optimization of  $\text{Cr}^{3+}$  doping concentration was performed to identify the composition exhibiting the most favorable spectroscopic characteristics for pressure-dependent measurements in the DAC and for pressure sensing application. In the case of  $\text{LiScGeO}_4:\text{Cr}^{3+}$ , no significant changes were observed in the position or FWHM of the emission band across the samples with different  $\text{Cr}^{3+}$  concentration (0.1-2%). However, an increase in emission intensity was observed with rising  $\text{Cr}^{3+}$  concentration, reaching an optimum at 0.5%, after which a decrease was observed, likely due to concentration quenching effects. As a result, the 0.5%  $\text{Cr}^{3+}$ -doped sample was chosen for further pressure-dependent analysis.

The structural stability of  $\text{LiScGeO}_4:\text{Cr}^{3+}$  under pressure was evaluated using Raman spectroscopy. No signs of structural deformation or pressure-induced phase transitions were observed up to 7.5 GPa. Above this pressure, new Raman modes appeared in the spectrum. The full reversibility of the observed changes upon decompression suggests their origin in pressure-induced phase transitions, rather than irreversible structural degradation, which would otherwise undermine the material's suitability for use in pressure sensing. To ensure reliable and repeatable performance, the operational pressure range of the developed manometer was conservatively limited to 7 GPa in order to avoid possible hysteresis effects resulting from pressure-induced phase transitions.

Emission spectra were recorded as a function of pressure up to 7.87 GPa, revealing a pronounced hypsochromic (blue) shift of the  ${}^4\text{T}_{2g} \rightarrow {}^4\text{A}_{2g}$  broadband emission with increasing pressure. This shift exhibited a linear dependence across the entire investigated pressure range, with a rate of 23.63 nm  $\text{GPa}^{-1}$  representing the highest spectral shift rate reported among all luminescent manometers at the time the results were published in **publication P4**. The observed spectral behavior is attributed to the shortening of  $\text{Cr}^{3+}-\text{O}^{2-}$  bond length by applied pressure, which enhances the crystal field strength affected on  $\text{Cr}^{3+}$  ions. As a result, the energy of the  ${}^4\text{T}_{2g}$  excited state increases, leading to a blue-shift of the  ${}^4\text{T}_{2g} \rightarrow {}^4\text{A}_{2g}$  emission band. This pronounced pressure-induced spectral shift highlighted the exceptional suitability of the proposed phosphor for ratiometric pressure sensing using the LIR-based approach. To fully harness the ratiometric sensing potential, the emission spectra were integrated over 10 nm intervals, and multiple options for the LIR calculation were systematically evaluated to identify the configuration yielding the highest relative sensitivity. Among the tested intervals, the 870-880 nm range exhibited the most pronounced pressure-dependent intensity change. This range was subsequently fixed as the numerator in the LIR expression, while the denominator was varied across other 10 nm spectral gates. For each resulting LIR definition, a calibration curve was constructed, and the corresponding relative sensitivity was determined. This approach enabled the generation of two-dimensional sensitivity maps, providing a comprehensive visualization of how the LIR-based pressure sensitivity depends on the choice of spectral ranges - thereby guiding the selection of the most optimal spectral configuration. These

sensitivity maps serve as an effective basis for the rational optimization of luminescent manometers, allowing precise adjustment of the LIR to match the targeted pressure sensing range.

To demonstrate the performance of this approach, several LIR-based configurations were proposed:

$$LIR_1 = \frac{\int_{870 \text{ nm}}^{880 \text{ nm}} I(\text{Cr}^{3+}; {}^4T_{2g} \rightarrow {}^4A_{2g}) d\lambda}{\int_{1450 \text{ nm}}^{1460 \text{ nm}} I(\text{Cr}^{3+}; {}^4T_{2g} \rightarrow {}^4A_{2g}) d\lambda} \quad (16)$$

$$LIR_2 = \frac{\int_{870 \text{ nm}}^{880 \text{ nm}} I(\text{Cr}^{3+}; {}^4T_{2g} \rightarrow {}^4A_{2g}) d\lambda}{\int_{1220 \text{ nm}}^{1230 \text{ nm}} I(\text{Cr}^{3+}; {}^4T_{2g} \rightarrow {}^4A_{2g}) d\lambda} \quad (17)$$

$$LIR_3 = \frac{\int_{850 \text{ nm}}^{860 \text{ nm}} I(\text{Cr}^{3+}; {}^4T_{2g} \rightarrow {}^4A_{2g}) d\lambda}{\int_{1300 \text{ nm}}^{1310 \text{ nm}} I(\text{Cr}^{3+}; {}^4T_{2g} \rightarrow {}^4A_{2g}) d\lambda} \quad (18)$$

The analysis of LIR versus pressure calibration curves clearly demonstrates that the sensor response can be precisely tailored by selecting the appropriate LIR. This enables the development of pressure sensors optimized for specific sensitivity ranges or operational conditions, for example:

- LIR<sub>1</sub>: Provided  $S_R$  exceeding 40% GPa<sup>-1</sup> from ambient pressure up to ~4 GPa, with a maximum value of 121.14% GPa<sup>-1</sup> at 2.55 GPa.
- LIR<sub>2</sub>: Enabled  $S_R$  above 40% GPa<sup>-1</sup> across the entire operating range of the sensor (0-7 GPa), reaching a maximum of 99.57% GPa<sup>-1</sup> at 2.4 GPa.
- LIR<sub>3</sub>: Also yielded  $S_R$  above 40% GPa<sup>-1</sup> over the full range of pressure, with a peak value of approximately 80% GPa<sup>-1</sup> at ~4 GPa.

The temperature response of LiScGeO<sub>4</sub>:Cr<sup>3+</sup> was also assessed in the range of 83-443 K. Aside from typical thermal quenching, no significant changes were observed in the spectral shape or the position of the emission maximum as a function of temperature. The temperature dependence of the previously optimized LIR was analyzed, and the maximum temperature  $S_R$  of 0.75% K<sup>-1</sup> ( $S_{R1}$ ) and 0.87% K<sup>-1</sup> ( $S_{R2}$ ) were observed at 363.7 K and 343.15 K, respectively. To quantitatively assess the robustness of pressure readouts in the presence of temperature fluctuations, a Thermal Invariability Manometric Factor was proposed in **publication P4**

(Equation 7), and calculated for both LIR modes. The resulting values  $TIMF_1 = 241.1 \text{ K GPa}^{-1}$  and  $TIMF_2 = 128.4 \text{ K GPa}^{-1}$  - clearly indicated the high thermal stability of the manometric response, confirming the suitability of this system for use under variable-temperature conditions.

The pressure-induced spectral shift rate and relative sensitivity values reported in this study represented, at the time the results were published in **publication P4**, the highest obtained among all known luminescent manometers. Owing to the exceptional application potential of the developed  $\text{LiScGeO}_4\text{:Cr}^{3+}$  pressure sensor, patent application was prepared, resulting in the granting of National Patent No. 246589 entitled “*Sposób bezkontaktowego pomiaru ciśnienia za pomocą czujnika luminescencyjnego bazującego na emisji jonów  $\text{Cr}^{3+}$* ” („Remote pressure measurement method using a luminescent sensor based on  $\text{Cr}^{3+}$  ion emission”) **Maja Szymczak**, Łukasz Marciniak by Patent Office of the Republic of Poland.

---

#### **The most important scientific significance of publication P4 for the advancement of the research field**

The findings reported in **publication P4** unequivocally demonstrated the high applicability potential and scientific relevance of exploiting the broadband  ${}^4T_{2g} \rightarrow {}^4A_{2g}$  emission of  $\text{Cr}^{3+}$  ions in the development of luminescent pressure sensors. Moreover within the framework of **publication P4**, a novel strategy was proposed for visualization of luminescent manometer performance - two-dimensional sensitivity maps as a function of the LIR definition. This approach enables the flexible design of luminescent manometers by allowing the response of sensor to be precisely tuned to a specific operational pressure range and the desired region of maximum sensitivity. Additionally, **publication P4** introduced a new manometric-performance-metric - the Thermal Invariability Manometric Factor, which quantitatively expresses the ratio between pressure sensitivity and susceptibility to temperature-induced variations, and thus assess manometric potential of phosphors.

---

To further confirm the manometric potential of host materials providing a weak crystal field for  $\text{Cr}^{3+}$  ions within the ratiometric LIR-based sensing approach, the second compound investigated was the previously introduced  $\text{Li}_3\text{Sc}_2(\text{PO}_4)_3$ , described in **publication P5**. As with  $\text{LiScGeO}_4$ , the undoped  $\text{Li}_3\text{Sc}_2(\text{PO}_4)_3$  host material was subjected to pressure-dependent Raman spectroscopy to evaluate its structural stability under compression. The measurements revealed changes in the shape of selected Raman modes above 3 GPa, suggesting the occurrence of a pressure-induced phase transition. However, these changes were fully reversible upon decompression, and thus did not preclude the application of this material in pressure sensor development. A powders of  $\text{Li}_3\text{Sc}_2(\text{PO}_4)_3$  with various  $\text{Cr}^{3+}$  concentrations ranging from 0.1% to 10% were synthesized. As the luminescence properties remained relatively unchanged across all the samples,

the composition with 1% Cr<sup>3+</sup> was selected for further investigation. Although samples with higher Cr<sup>3+</sup> content exhibited slightly stronger emission intensities, local heating effects under laser excitation were observed - manifested as fluctuations in emission intensity during continuous illumination - which became increasingly pronounced at elevated dopant levels. Due to the elevated temperature of the samples, the pressure-dependent luminescence measurements could be affected by thermal influence, potentially compromising the reliability of the results for pressure sensor development. This was an additional factor motivating the selection of a sample with lower Cr<sup>3+</sup> concentration and thus lower emission intensity.

Emission spectra recorded as a function of pressure in range from ambient pressure to 3.79 GPa revealed a substantial blue shift of the broadband emission band associated with <sup>4</sup>T<sub>2g</sub> → <sup>4</sup>A<sub>2g</sub> electronic transition of Cr<sup>3+</sup>. The pressure-induced shift of the emission maximum reached 23.9 nm GPa<sup>-1</sup> (linear dependence) in the pressure range from ambient to 2.6 GPa, representing - at the time of the study's publication - the highest reported value among luminescent manometers reported in the literature. A deviation from the linear trend was observed above 2.6 GPa, suggesting a pressure-induced phase transition, consistent with structural changes identified in the same pressure range by Raman spectroscopy.

To establish an optimal LIR-based calibration curve, integrated intensities of emission band over 10 nm spectral gates were analyzed, and the most responsive spectral ranges were selected for the calculation of the LIR, as indicated in **Equation 19**, below:

$$LIR = \frac{\int_{700 \text{ nm}}^{720 \text{ nm}} I(\text{Cr}^{3+}; {}^4T_{2g} \rightarrow {}^4A_{2g}) d\lambda}{\int_{900 \text{ nm}}^{919 \text{ nm}} I(\text{Cr}^{3+}; {}^4T_{2g} \rightarrow {}^4A_{2g}) d\lambda} \quad (19)$$

The resulting LIR values increased monotonically with pressure up to 2.6 GPa, by almost 3-times respect to ambient pressure. Above this pressure an increase in the slope of the LIR-pressure dependence was observed, which coincided with the structural changes indicated by Raman spectroscopy. Consequently, the operational pressure range of the manometer was defined from ambient conditions up to 2.6 GPa. Emission spectra recorded during decompression confirmed the reversibility of the luminescence response, while the excellent reproducibility of the LIR values over three pressure compression attempts, demonstrated the robustness and application potential of Li<sub>3</sub>Sc<sub>2</sub>(PO<sub>4</sub>)<sub>3</sub>:Cr<sup>3+</sup> as a pressure-sensitive material. Based on pressure-dependent LIR, the relative sensitivity achieved for Li<sub>3</sub>Sc<sub>2</sub>(PO<sub>4</sub>)<sub>3</sub>:Cr<sup>3+</sup> was 56.86% GPa<sup>-1</sup>, which, although lower than that of LiScGeO<sub>4</sub>:Cr<sup>3+</sup> described in **publication P4**, was accompanied by a notable advantage: significantly reduced sensitivity to temperature variations. This conclusion was drawn from

temperature-dependent emission spectra measured in range 203 to 403 K, from which analogous LIR and  $S_R$  values were determined as in the case of pressure-dependent studies. The superior thermal stability of the  $\text{Li}_3\text{Sc}_2(\text{PO}_4)_3:\text{Cr}^{3+}$  luminescence was quantitatively expressed by the TIMF, which reached a value of  $1386.8 \text{ K GPa}^{-1}$ , nearly six times higher than that observed for the  $\text{LiScGeO}_4:\text{Cr}^{3+}$  based sensor (**publication P4**).

Beyond the ratiometric LIR-based approach, two additional readout strategies were proposed for the  $\text{Li}_3\text{Sc}_2(\text{PO}_4)_3:\text{Cr}^{3+}$  manometer. The second proposed readout method was based on luminescence kinetics and represented the first reported utilization of luminescence decay time of  $^4\text{T}_{2g}$  excited state of  $\text{Cr}^{3+}$  for pressure sensing. The average lifetimes of the  $^4\text{T}_{2g}$  excited state, determined through double-exponential fitting of the luminescence decay curves, prolonged significantly with applied pressure - from  $2.42 \mu\text{s}$  under ambient conditions to  $10.65 \mu\text{s}$  at 2.6 GPa. Above a pressure of 2.6 GPa, a rapid shortening of the luminescence decay time was observed - most likely caused by a pressure-induced phase transformation, consistent with results discussed in earlier sections. The pronounced and monotonic change in  $\tau_{\text{avr}}$  observed up to 2.6 GPa resulted in an exceptionally high  $S_R$  of  $93.56\% \text{ GPa}^{-1}$ , which, at the time of submission of this doctoral dissertation, represented the highest reported sensitivity value for any pressure sensor based on luminescence kinetics. Moreover, the pressure-induced elongation of the excited-state lifetime observed for  $\text{Cr}^{3+}$  ions is particularly noteworthy from an application-oriented perspective. This behavior contrasts sharply with that of lanthanide ions, for which increasing pressure typically leads to a reduction in luminescence lifetime. In lanthanide-based systems, such a decrease in lifetime reduces the signal-to-noise ratio and increases the uncertainty in pressure readout - especially at higher pressures - thereby limiting their effectiveness in lifetime-based manometric applications. In contrast, the prolongation of the luminescence lifetime with increasing pressure in TM-doped systems improves the precision and reliability of lifetime-based pressure sensing.

In addition to the pressure response, the temperature dependence of the luminescence decay time was also investigated. As expected, an opposite trend was observed: with increasing temperature,  $\tau_{\text{avr}}$  values decreased due to thermally activated non-radiative depopulation processes from the excited state. Specifically, between 183 K and 403 K, the average lifetime shortened from  $12.56 \mu\text{s}$  to  $0.97 \mu\text{s}$ . Based on the  $\tau_{\text{avr}}$  versus temperature relationship, the temperature sensitivity of the sensor at room temperature was determined to be  $0.83\% \text{ K}^{-1}$ , which yielded a TIMF value of  $112.72 \text{ K GPa}^{-1}$ . This relatively high TIMF value clearly indicates the minor influence of temperature on the pressure readout, highlighting the suitability of this approach for practical applications under varying thermal conditions. Furthermore, this readout mode confirmed the reversibility of the pressure response, as the average lifetime values returned to their initial state after decompression of the system - providing additional evidence of the reliability and robustness



of the proposed pressure-sensing mechanism. The proposed readout mode based on monitoring luminescence kinetics is highly attractive for luminescence manometry, primarily due to the inherent independence of lifetime values from external environmental factors - such as the surrounding medium in which the phosphor is embedded. However, it should be noted that equipment required for accurate decay time measurements is more demanding compared to that used for LIR-based readout. Moreover, the relatively short lifetimes of the  $^4T_2$  excited state, typically on the microsecond scale, may result in increased measurement uncertainty due to limitations in temporal resolution and signal stability.

The third readout mode was based on the spectral shift of the emission band, which not only exhibited a large and linear response to pressure up to 2.6 GPa, but also showed minimal sensitivity to temperature, with a shift of less than  $0.001 \text{ nm K}^{-1}$ , approximately seven times lower than that of the widely used ruby pressure standard. Nonetheless, this approach should be regarded with caution, as the determination of the emission band maximum is subject to considerable uncertainty, particularly in the case of broad spectral features. Consequently, the two alternative readout modes discussed above are considered more suitable for practical implementation.

An additional, crucial advantage of the  $\text{Li}_3\text{Sc}_2(\text{PO}_4)_3:\text{Cr}^{3+}$  manometer was the rare effect of increasing emission intensity with increasing pressure. This behavior is particularly desirable, as emission intensity typically decreases under compression, which leads to larger readout errors and greater demands on detection sensitivity. In contrast, a 3.3-fold increase in emission intensity of  $\text{Li}_3\text{Sc}_2(\text{PO}_4)_3:\text{Cr}^{3+}$  was observed at 2.6 GPa compared to ambient pressure. At the time the study was published, this effect represented the strongest reported increase in luminescence intensity under pressure, highlighting the uniqueness of the developed system among known pressure-sensitive phosphors. The most plausible explanation for the observed increase in emission intensity is a pressure-induced blue shift of the excitation band, which maximum is centered around 500 nm under ambient conditions. At ambient pressure, the 445 nm laser line excites the phosphor at the high-energy edge of the excitation band. As pressure increases, the excitation band blue-shifts, aligning more closely with the 445 nm laser wavelength and thereby improving absorption efficiency and, consequently, the emission intensity. Nevertheless, this mechanism remains hypothetical, as pressure-dependent excitation spectra cannot be directly recorded with the current experimental setup. Such measurements are technically demanding, requiring high excitation power and signal collection efficiency to overcome the inherent limitations imposed by the optical access and sample volume in diamond anvil cell experiments.

---

### **The most important scientific significance of publication P5 for the advancement of the research field**

---

**Publication P5** provides further compelling evidence of the exceptional suitability of  $\text{Cr}^{3+}$  emission from the  $^4\text{T}_{2g}$  excited state for the development of high-performance luminescent pressure sensors, complementing the outcomes reported in previous mentioned publications. A key advantage of the developed sensor was the implementation of three distinct pressure readout modes, each offering high sensitivity to pressure changes - including a first-time reported mode based on luminescence kinetics of  $^4\text{T}_{2g}$  state of  $\text{Cr}^{3+}$ . For instance, in scenarios where instrumental constraints prevent the implementation of kinetics measurements, the ratiometric LIR-based mode may serve as the most practical option. Conversely, in cases where the phosphor is dispersed in a liquid medium or embedded within a solid matrix, monitoring pressure-induced variations in luminescence decay time may provide a more robust and reliable readout method. The trimodal nature of the pressure sensor offers exceptional versatility, allowing it to be tailored to a broad spectrum of potential applications.

---

### **Author's contribution to the publications P4 and P5**

---

synthesis of samples with varying concentrations of  $\text{Cr}^{3+}$  ions; spectroscopic characterization of phosphors, including luminescence measurements; investigation of emission spectra and luminescence decay profiles (**publication P5**) as a function of temperature and pressure; data analysis and preparation of the first draft of the manuscript

### **5.4. Studies of the potential of $\text{Cr}^{3+}\text{-Cr}^{3+}$ pairs emission in doped $\text{CaAl}_{12}\text{O}_{19}$ - development of a luminescent bifunctional pressure-temperature sensor**

Due to the inability to measure the emission band associated with  $\text{Cr}^{3+}\text{-Cr}^{3+}$  pair emission in a case of  $\text{MgO}:\text{Cr}^{3+}$  (**publication P2**) - resulting from insufficient emission intensity at room temperature - identifying a phosphor exhibiting a more intense  $\text{Cr}^{3+}\text{-Cr}^{3+}$  emission band was of particular interest in the context of evaluating its manometric potential. This was especially relevant given the limited number of studies in the literature addressing the pressure-dependent behavior of  $\text{Cr}^{3+}\text{-Cr}^{3+}$  pair emission.

The  $\text{CaAl}_{12}\text{O}_{19}:\text{Cr}^{3+}$  phosphor was employed to investigate the aforementioned emission band, owing to its crystal structure, which provides three distinct types of non-equivalent  $\text{Cr}^{3+}$  centers:

- $\text{Cr}^{3+}$  ions located in crystallographic positions of  $\text{Al}^{3+}$  that provide a strong crystal field, resulting in a sharp, narrowband emission in the spectrum, attributed to the spin-forbidden  $^2\text{E}_g \rightarrow ^4\text{A}_{2g}$  electronic transition ( $\text{Cr}^{3+}(\text{C})$ ).

- $\text{Cr}^{3+}$  ions occupying  $\text{Al}^{3+}$  positions with a weaker crystal field, manifested by a broad emission band associated with the spin-allowed  ${}^4\text{T}_{2g} \rightarrow {}^4\text{A}_{2g}$  electronic transition ( $\text{Cr}^{3+}(\text{C})$ ) (also attributed to  $\text{Cr}^{3+}(\text{C})$ , but in a different local environment).
- $\text{Cr}^{3+}\text{-Cr}^{3+}$  pairs in crystallographic positions of  $\text{Al}^{3+}$ , whose emission, arising from the coupled electronic transitions  ${}^4\text{A}_{2g}, {}^4\text{T}_{2g} \rightarrow {}^4\text{A}_{2g}, {}^4\text{A}_{2g}$   $\text{Cr}^{3+}(\text{A})\text{-Cr}^{3+}(\text{A})$  was manifested as a broad emission band.

Raman spectroscopy studies have confirmed that pressures up to approximately 7.25 GPa do not induce any permanent structural changes or decomposition of the compound, indicating a high degree of pressure stability in the crystal structure - an important property for the development of reliable luminescent pressure sensors.

Emission spectra recorded as a function of pressure revealed a particularly interesting phenomenon. The broad emission band corresponding to the  ${}^4\text{A}_{2g}, {}^4\text{T}_{2g} \rightarrow {}^4\text{A}_{2g}, {}^4\text{A}_{2g}$  electronic transition of  $\text{Cr}^{3+}\text{-Cr}^{3+}$  pairs exhibited negligible sensitivity to applied pressure: the position of the emission maximum remained almost unchanged throughout the entire pressure range investigated. Several potential mechanisms may explain this behavior. First, it is important to recognize that this emission originates from  $\text{Cr}^{3+}\text{-Cr}^{3+}$  pairs, rather than isolated  $\text{Cr}^{3+}$  ions. While the emission from single  $\text{Cr}^{3+}$  centers is strongly dependent on the  $\text{Cr}^{3+}\text{-O}^{2-}$  bond length and, hence, sensitive to pressure, the  $\text{Cr}^{3+}\text{-Cr}^{3+}$  pair emission is also influenced by the  $\text{Cr}^{3+}\text{-Cr}^{3+}$  distance, which influences interionic energy transfer processes. Changes in  $\text{Cr}^{3+}\text{-Cr}^{3+}$  distances under pressure may not significantly perturb the relevant excited-state energy levels, resulting in a weak spectral response. Another plausible explanation involves a simultaneous pressure-induced shift of both the excited and ground levels of  $\text{Cr}^{3+}\text{-Cr}^{3+}$ , which would result in a negligible change in transition energy. A similarly low sensitivity of  $\text{Cr}^{3+}\text{-Cr}^{3+}$  pair emission to pressure changes has been reported for the analogous  $\text{SrAl}_{12}\text{O}_{19}$  phosphor.<sup>195</sup> Nevertheless, additional advanced spectroscopic investigations are required to fully elucidate the origin of this effect, particularly considering other host matrices in which variations in local structure and crystal field strength may influence the pressure-dependent behavior.

In contrast, temperature-dependent luminescence measurements revealed pronounced spectral changes in the  $\text{Cr}^{3+}\text{-Cr}^{3+}$  emission band. A significant thermally-induced blue-shift of the emission band was observed. This distinct dual sensitivity - weak dependence on pressure but strong sensitivity to temperature - suggested the feasibility of development a bifunctional optical sensor capable of simultaneous temperature and pressure sensing. This concept was realized by proposing two independent LIR parameters, each tailored to respond selectively to either temperature or pressure, as expressed by the following formulas:

$$LIR_1 = \frac{\int_{732 \text{ nm}}^{750 \text{ nm}} I(\text{Cr}^{3+}(\text{C}): {}^4\text{T}_{2g} \rightarrow {}^4\text{A}_{2g}) d\lambda}{\int_{680 \text{ nm}}^{692 \text{ nm}} I(\text{Cr}^{3+}(\text{C}): {}^2\text{E}_g \rightarrow {}^4\text{A}_{2g}) d\lambda} \quad (20)$$

$$LIR_2 = \frac{\int_{732 \text{ nm}}^{750 \text{ nm}} I(\text{Cr}^{3+}(\text{C}): {}^4\text{T}_{2g} \rightarrow {}^4\text{A}_{2g}) d\lambda}{\int_{840 \text{ nm}}^{860 \text{ nm}} I(\text{Cr}^{3+}(\text{A}): {}^4\text{A}_{2g}, {}^4\text{T}_{2g} \rightarrow {}^4\text{A}_{2g}, {}^4\text{A}_{2g}) d\lambda} \quad (21)$$

LIR<sub>1</sub> was the ratio of emission intensities originating from the  ${}^4\text{T}_{2g} \rightarrow {}^4\text{A}_{2g}$  ( $\text{Cr}^{3+}(\text{C})$ ) and  ${}^2\text{E}_g \rightarrow {}^4\text{A}_{2g}$  ( $\text{Cr}^{3+}(\text{C})$ ) emission bands, whereas LIR<sub>2</sub> was based on the ratio between the broad emission band corresponding to the  ${}^4\text{T}_{2g} \rightarrow {}^4\text{A}_{2g}$  electronic transition of  $\text{Cr}^{3+}(\text{C})$  and the  ${}^4\text{A}_{2g}, {}^4\text{T}_{2g} \rightarrow {}^4\text{A}_{2g}, {}^4\text{A}_{2g}$   $\text{Cr}^{3+}$ - $\text{Cr}^{3+}$  pair emission band. LIR<sub>1</sub> exhibited high sensitivity to pressure, reaching a maximum value of 70% GPa<sup>-1</sup> at ambient conditions. However, its sensitivity to temperature was considerably lower, with a maximum of approximately 1% K<sup>-1</sup> at 83 K. Furthermore, due to the non-monotonic behavior of LIR<sub>1</sub> as a function of temperature, it was not well suited for use for luminescence thermometry. This limitation was further confirmed by the analysis of the TIMF across the entire pressure range studied: while the TIMF reached a maximum of 150 K GPa<sup>-1</sup> at ambient pressure, it dropped sharply up to around 15 K GPa<sup>-1</sup> for pressure around 0.3 GPa. These observations indicate that the pressure-sensing capability of LIR<sub>1</sub> is most effective at low-pressure regimes (up to ~0.3 GPa). In contrast, LIR<sub>2</sub> demonstrated monotonic behavior with temperature, exhibiting a temperature sensitivity of 1.2% K<sup>-1</sup> at 83 K. However, its response to pressure was significantly weaker (maximal  $S_R = 4.5\%$  GPa<sup>-1</sup>) than that of LIR<sub>1</sub>. The TIMF values based on LIR<sub>2</sub> reached maximal value of 11 K GPa<sup>-1</sup> at ambient pressure and gradually decreased to 6 K GPa<sup>-1</sup> at a pressure of 6.76 GPa. Although neither LIR<sub>1</sub> nor LIR<sub>2</sub> showed exceptionally high pressure sensitivity, their distinct selectivity toward pressure and temperature, respectively, enabled the implementation of a bifunctional sensor based on  $\text{CaAl}_{12}\text{O}_{19}:\text{Cr}^{3+}$ , capable of simultaneously monitoring both parameters using LIR<sub>1</sub> for pressure and LIR<sub>2</sub> for temperature. To date, several phosphor materials have been reported that have been investigated for their performance under simultaneous pressure and temperature sensing conditions.<sup>14,16,52,196,197</sup>

In addition, the pressure and temperature dependence of the luminescence decay kinetics of the  ${}^2\text{E}_g \rightarrow {}^4\text{A}_{2g}$  transition in doped  $\text{CaAl}_{12}\text{O}_{19}$  was studied. A monotonic prolongation of the average lifetime of the  ${}^2\text{E}_g$  excited state was observed under pressure, rising from 2.3 ms at ambient pressure to 5.1 ms at 6.76 GPa. Conversely, temperature caused a substantial shortening of the  $\tau_{\text{avr}}$  - from 5.1 ms at 83 K to 0.3 ms at 633 K. These variations resulted in maximal pressure

sensitivity of 16% GPa<sup>-1</sup> at ambient pressure, and a temperature sensitivity of 0.75% K<sup>-1</sup> at 325 K. The corresponding TIMF reached 24 K GPa<sup>-1</sup> at ambient pressure, decreasing to 10 K GPa<sup>-1</sup> at 6.76 GPa. While pressure sensitivity is lower than those achieved using the previously discussed Li<sub>3</sub>Sc<sub>2</sub>(PO<sub>4</sub>)<sub>3</sub>:Cr<sup>3+</sup> phosphor - whose <sup>4</sup>T<sub>2g</sub>→<sup>4</sup>A<sub>2g</sub> emission yielded pressure sensitivities nearly four times higher - the CaAl<sub>12</sub>O<sub>19</sub>:Cr<sup>3+</sup> benefits from significantly longer luminescence decay time (on the millisecond scale), which enhance readout precision and may be advantageous for certain practical applications.

---

**The most important scientific significance of publication P6 for the advancement of the research field**

---

The emission associated with <sup>4</sup>A<sub>2g</sub>, <sup>4</sup>T<sub>2g</sub>→<sup>4</sup>A<sub>2g</sub>, <sup>4</sup>A<sub>2g</sub> electronic transition of Cr<sup>3+</sup>-Cr<sup>3+</sup> pairs exhibits limited potential for use in luminescent manometry due to its weak sensitivity to pressure. However, as demonstrated in **Publication P6**, it is possible to develop a bifunctional luminescent sensor capable of simultaneously measuring both temperature and pressure. This is achieved by carefully selecting spectral ranges to calculate LIRs, each tailored to be selectively responsive to either temperature or pressure, enabling reliable decoupling of the two effects.

---

**Author's contribution to the publication P6**

---

spectroscopic characterization of phosphors, including luminescence measurements; investigation of emission spectra and luminescence kinetics as a function of temperature and pressure; contribution to the data analysis and preparation of the first draft of the manuscript.

**5.5. Comparative analysis of ratiometric LIR-based strategies for phosphors with two distinct crystallographic positions for Cr<sup>3+</sup> ions - studies of MgGeO<sub>3</sub>:Cr<sup>3+</sup>**

Given the previously demonstrated suitability of broadband emission associated with the <sup>4</sup>T<sub>2g</sub>→<sup>4</sup>A<sub>2g</sub> electronic transition of Cr<sup>3+</sup> ions for ratiometric pressure sensing, it appeared particularly compelling to investigate a material in which the observed broadband emission arises from the two spectrally distinct Cr<sup>3+</sup> centers occupying inequivalent crystallographic positions and affected by weak crystal field. It was hypothesized that such a system could exhibit enhanced pressure-induced luminescence changes, as the overall response would reflect the combined spectral shifts of two separate emission bands originating from structurally distinct environments.

To verify this hypothesis, MgGeO<sub>3</sub> was selected as a compound containing two crystallographically inequivalent Mg<sup>2+</sup> sites, differentiated by their local coordination

environments. Specifically, the average  $\text{Mg}^{2+}\text{-O}^{2-}$  bond length is 2.088 Å for the Mg(1) and 2.129 Å for the Mg(2), suggesting distinct crystal field strengths that may differently influence  $\text{Cr}^{3+}$  and its spectroscopic behavior. To identify the composition with the highest manometric potential,  $\text{MgGeO}_3\text{:Cr}^{3+}$  samples with different  $\text{Cr}^{3+}$  concentration were synthesized (from 0.1% to 5%). Emission spectra recorded at room temperature revealed progressive broadening of the  ${}^4\text{T}_{2g} \rightarrow {}^4\text{A}_{2g}$  emission band with increasing  $\text{Cr}^{3+}$  content. Furthermore, when the emission spectra were represented in the energy domain ( $\text{cm}^{-1}$ ), the profiles deviated significantly from a single Gaussian shape, suggesting the presence of multiple emissive centers. Spectral deconvolution of the emission spectrum for the 5%  $\text{Cr}^{3+}$ -doped sample confirmed this assumption, revealing two distinct Gaussian components centered at  $11271 \text{ cm}^{-1}$  ( $\text{Cr}^{3+}(2)$ ) and  $12528 \text{ cm}^{-1}$  ( $\text{Cr}^{3+}(1)$ ). These results strongly supported the presence of two optically active  $\text{Cr}^{3+}$  centers, each associated with one of the two  $\text{Mg}^{2+}$  positions in the  $\text{MgGeO}_3$  structure. To further confirm this hypothesis, excitation spectra were recorded while monitoring two emission wavelengths corresponding to the low- and high-energy regions of the emission band –  $\lambda_{\text{em}} = 1000 \text{ nm}$  and  $750 \text{ nm}$ , respectively. The excitation spectra differed significantly in the position of the observed  ${}^4\text{A}_{2g} \rightarrow {}^4\text{T}_{1g}$  and  ${}^4\text{A}_{2g} \rightarrow {}^4\text{T}_{2g}$  absorption bands, indicating different crystal field environments experienced by  $\text{Cr}^{3+}(1)$  and  $\text{Cr}^{3+}(2)$ . Deconvolution of these excitation spectra enabled the calculation of the  $Dq/B$  values, yielding 1.97 for  $\text{Cr}^{3+}(1)$  and 1.90 for  $\text{Cr}^{3+}(2)$ , confirming the presence of two crystallographically distinct  $\text{Cr}^{3+}$  centers in the  $\text{MgGeO}_3$  host lattice.

Raman spectra as a function of pressure showed the stability of the  $\text{MgGeO}_3$  structure up to about 5 GPa. Above this value, a change in the shape of the Raman modes and the appearance of new ones were observed. According to the literature, the observed changes were due to a pressure-induced phase transformation of  $\text{MgGeO}_3$  from orthorhombic to monoclinic structure. However, even after compressing the sample to 11 GPa, the changes observed in the Raman spectra were reversible.

Pressure-dependent emission spectra were recorded for the  $\text{MgGeO}_3\text{:5\%Cr}^{3+}$  sample in the pressure range from ambient conditions up to 6.93 GPa. As the pressure increased, significant changes were observed in the shape of the emission spectra - most notably, a progressive spectral separation of the two broad emission bands associated with the  ${}^4\text{T}_{2g} \rightarrow {}^4\text{A}_{2g}$  electronic transition of  $\text{Cr}^{3+}(1)$  and  $\text{Cr}^{3+}(2)$ . In order to analyze this effect quantitatively, spectral deconvolution was performed. The two deconvoluted emission bands exhibited almost linear blue shifts with increasing pressure. The band attributed to  $\text{Cr}^{3+}(1)$  showed a shift rate of  $197 \text{ cm}^{-1} \text{ GPa}^{-1}$ , while the band associated with  $\text{Cr}^{3+}(2)$  shifted with a rate of  $105 \text{ cm}^{-1} \text{ GPa}^{-1}$ . Based on these deconvoluted components, the  $\text{LIR}_1$  was expressed as the intensity ratio between the emission bands corresponding to  $\text{Cr}^{3+}(2)$  and  $\text{Cr}^{3+}(1)$ . From ambient pressure up to approximately 4 GPa,  $\text{LIR}_1$

increased monotonically from 0.6 to 1.1. Between 4 and 5.2 GPa, the  $LIR_1$  value plateaued, after which it resumed a monotonic increase, reaching a value of 1.5 at 6.93 GPa. The observed plateau in  $LIR_1$  was likely associated with a pressure-induced phase transition, as confirmed by Raman spectroscopy studies. Although a maximal  $S_{R1}$  value of 22%  $GPa^{-1}$  was achieved at 1.3 GPa, the use of the  $LIR_1$ -based readout may be hindered by its pronounced susceptibility to pressure-induced structural transformations and the need for spectral deconvolution, which can complicate signal processing and impose additional requirements on the measurement setup. To address these limitations, three alternative ratiometric parameters -  $LIR_2$ ,  $LIR_3$  and  $LIR_4$  were introduced. These were calculating using 10 nm spectral ranges, making them compatible with 2D luminescence imaging systems based on cameras and optical bandpass filters, and thus highly applicable in real-time and spatially resolved sensing platforms. The  $LIR_2$ ,  $LIR_3$  and  $LIR_4$  were expressed as presented below:

$$LIR_2 = \frac{\int_{670 \text{ nm}}^{680 \text{ nm}} I(Cr^{3+}: ^4T_{2g} \rightarrow ^4A_{2g})d\lambda}{\int_{810 \text{ nm}}^{820 \text{ nm}} I(Cr^{3+}: ^4T_{2g} \rightarrow ^4A_{2g})d\lambda} \quad (22)$$

$$LIR_3 = \frac{\int_{710 \text{ nm}}^{720 \text{ nm}} I(Cr^{3+}: ^4T_{2g} \rightarrow ^4A_{2g})d\lambda}{\int_{810 \text{ nm}}^{820 \text{ nm}} I(Cr^{3+}: ^4T_{2g} \rightarrow ^4A_{2g})d\lambda} \quad (23)$$

$$LIR_4 = \frac{\int_{710 \text{ nm}}^{720 \text{ nm}} I(Cr^{3+}: ^4T_{2g} \rightarrow ^4A_{2g})d\lambda}{\int_{910 \text{ nm}}^{920 \text{ nm}} I(Cr^{3+}: ^4T_{2g} \rightarrow ^4A_{2g})d\lambda} \quad (24)$$

All three LIRs exhibited increases with applied pressure. Among them,  $LIR_2$  showed the largest pressure-dependent variation, yielding a maximum  $S_{R2}$  of 62%  $GPa^{-1}$  at 4.8 GPa, and maintaining a sensitivity above 10%  $GPa^{-1}$  across the entire studied pressure range.  $LIR_3$  and  $LIR_4$  provided lower sensitivities, but within lower pressure ranges:  $S_{R3} = 40\% GPa^{-1}$  at 1.5 GPa and  $S_{R4} = 43\% GPa^{-1}$  at 0.9 GPa. To assess the temperature stability of the proposed ratiometric approaches, thermal response studies were also conducted. While  $LIR_2$  demonstrated the highest pressure sensitivity, it was also found to be most sensitive to temperature variations, with a TIMF not exceeding 150 K  $GPa^{-1}$  throughout the entire tested pressure range. In contrast,  $LIR_4$  proved to be the most thermally-invariant option. It maintained TIMF values above 200 K  $GPa^{-1}$  from ambient pressure up to 5 GPa, reaching a maximum TIMF of 577 K  $GPa^{-1}$  at 0.66 GPa. These results clearly demonstrate that  $LIR_4$  represents the optimal balance between pressure sensitivity

and thermal invariability, making it the most suitable readout parameter for practical manometric applications using  $\text{MgGeO}_3\text{:Cr}^{3+}$ .

---

**The most important scientific significance of publication P7 for the advancement of the research field**

---

The research findings presented in **publication P7** offer a critical comparison of various LIR-based readout strategies. It was demonstrated that calculating the LIR parameter based on post-deconvolution emission components does not lead to a significant increase in sensitivity. Moreover, such an approach may reduce the practical applicability of the sensor due to the requirement for more complex and compact detection equipment, which may limit its use in real-world applications. Importantly, the results also emphasize that in evaluating the manometric potential of a luminescent material, one must consider not only its pressure sensitivity, but also its temperature sensitivity, as both factors directly influence the reliability of pressure readout in varying environments. In addition, the results presented in **publication P7** highlighted the critical importance of correctly defining the LIR parameter. By carefully selecting the spectral ranges used for its calculation, it is possible to modulate the manometric performance parameters, thereby facilitating the adjustment of sensor characteristics to meet specific application requirements.

---

**Author's contribution to the publication P7**

---

spectroscopic characterization of phosphors, including luminescence measurements; investigation of emission as a function of temperature and pressure; contribution to the data analysis and preparation of the first draft of the manuscript



---

## SUMMARY

---

### Conclusions

---

As part of this doctoral dissertation, the spectroscopic properties of  $\text{Cr}^{3+}$  ions were comprehensively investigated from multiple perspectives to assess their applicability in luminescent manometry. Three distinct manometric strategies were employed:

- spectral shift of the emission band as a function of pressure,
- ratiometric approach based on luminescence intensity ratio,
- analysis of luminescence decay kinetics.

This doctoral dissertation primarily focuses on the luminescence associated with the  ${}^4\text{T}_{2g} \rightarrow {}^4\text{A}_{2g}$  electronic transition of  $\text{Cr}^{3+}$  ions, which has remained underexplored in the context of luminescence manometry. In **publication P1**, using the  $\text{Li}_2\text{Mg}_3\text{TiO}_6:\text{Cr}^{3+}$  phosphor, it was demonstrated that the conventional manometric approach, based on monitoring the spectral position of the emission maximum, leads to significant readout errors due to the difficulty in accurately determining the maximum of a broad band. To overcome the limitations of conventional approach, a novel strategy for luminescence manometry was introduced: the use of the luminescence intensity ratio derived from the integration of a broad  $\text{Cr}^{3+}$  emission band over two selected spectral regions. This method was first validated for the  $\text{Li}_2\text{Mg}_3\text{TiO}_6:\text{Cr}^{3+}$  (**publication P1**), yielding a relative pressure sensitivity of 4.63%  $\text{GPa}^{-1}$ . Crucially, this approach allowed pressure readouts to remain unaffected by temperature variations - an important advantage over classical spectral shift method, in which emission bands are inherently sensitive to both pressure and temperature changes. To systematically evaluate the thermal robustness of different pressure readout strategies, the Thermal Invariability Manometric Factor was introduced in **publication P3** (see **Equation 7**). The strong potential of the LIR-based methodology exploiting broadband  $\text{Cr}^{3+}$  emission was further confirmed across multiple phosphor systems, including those reported in **publications P2, P3, P4, P5, and P7**, as illustrated in **Figure 9**, below.

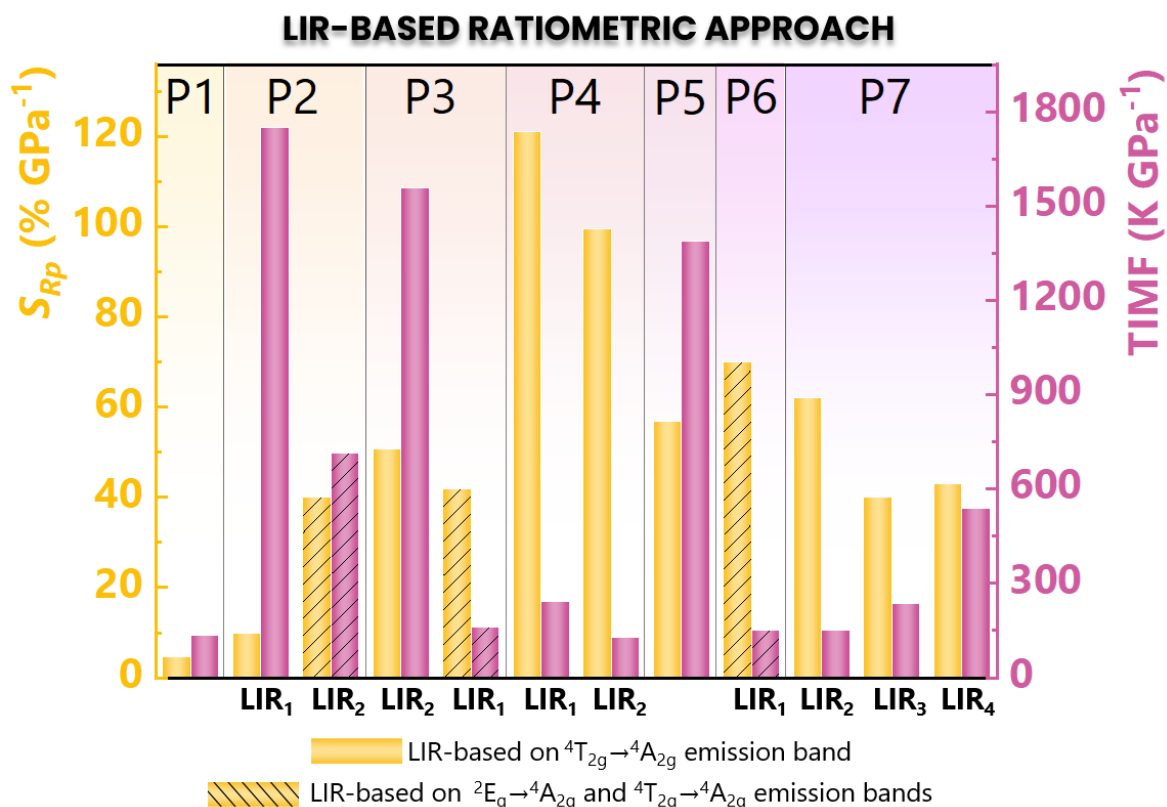


**Figure 9.** Comparison of the performance of the developed ratiometric LIR-based luminescent manometers, evaluated in terms of maximal relative pressure sensitivity ( $S_{Rp}$ ) and TIMF.

Among the investigated phosphors,  $\text{LiScGeO}_4:\text{Cr}^{3+}$  (**publication P4**) demonstrated the highest pressure sensitivity, accompanied by a TIMF value exceeding the critical threshold of  $100 \text{ K GPa}^{-1}$ , which was established as the benchmark for adequate thermal robustness. In contrast,  $\text{Li}_3\text{Sc}_2(\text{PO}_4)_3:\text{Cr}^{3+}$  (**publication P5**) and  $\text{CaMgSi}_2\text{O}_6:\text{Cr}^{3+}$  (**publication P3**) exhibited lower pressure sensitivities, however, their TIMF values were more than six times higher, significantly mitigating the influence of temperature fluctuations on pressure readouts and enhancing the reliability of pressure sensing under variable thermal conditions. Similarly,  $\text{Li}_2\text{Mg}_3\text{TiO}_6:\text{Cr}^{3+}$  (**publication P1**) and  $\text{MgO}:\text{Cr}^{3+}$  (**publication P2**) showed moderate sensitivities of  $4.63\% \text{ GPa}^{-1}$  and  $9.83\% \text{ GPa}^{-1}$ , respectively, with  $\text{MgO}:\text{Cr}^{3+}$  emerging as the most thermally robust material, achieving an exceptionally high TIMF of  $1750 \text{ K GPa}^{-1}$ . In the case of  $\text{MgGeO}_3:\text{Cr}^{3+}$  (**publication P6**), where  $\text{Cr}^{3+}$  ions occupy two distinct  $\text{Mg}^{2+}$  crystallographic positions, three LIRs were proposed based on the  ${}^4T_{2g} \rightarrow {}^4A_{2g}$  electronic transition. All yielded pressure sensitivities exceeding  $40\% \text{ GPa}^{-1}$ , though their thermal responses varied. Notably, adjusting the integration spectral window to express the LIR<sub>4</sub> resulted in nearly a threefold increase in thermal insensitivity. **This case highlights the critical role of spectral range selection in LIR-based sensing, as both pressure and temperature sensitivities can be effectively tuned through careful spectral design. All of the above phosphors demonstrated the potential of utilizing**

**the broad-band  $^4T_{2g} \rightarrow ^4A_{2g}$  emission of  $Cr^{3+}$  ions for the development of highly sensitive, thermally invariant pressure sensors.**

Additionally, **publications P<sub>2</sub> and P<sub>3</sub>** explored an alternative LIR-based approach involving the intensity ratio between the  $^4T_{2g} \rightarrow ^4A_{2g}$  and  $^2E_g \rightarrow ^4A_{2g}$  emission bands of  $Cr^{3+}$ . This dual-band method, commonly employed in luminescence thermometry for  $Cr^{3+}$ -doped phosphors with host lattices providing an intermediate crystal field strength, was compared with the LIR-based approach relying exclusively on the  $^4T_{2g} \rightarrow ^4A_{2g}$  emission band. Comparative studies conducted on  $MgO:Cr^{3+}$  and  $CaMgSi_2O_6:Cr^{3+}$  revealed that although both dual-band systems exhibited high pressure sensitivity, their TIMF values were significantly lower than those obtained using the broadband-only approach. **These findings underscore the superior thermal invariability of the strategy based on  $^4T_{2g} \rightarrow ^4A_{2g}$  emission and reinforce its position as the highly promising LIR-based method for luminescent manometry.**

Building upon this demonstrated potential, the dissertation further explores strategies to enhance the applicability of the  $^4T_{2g} \rightarrow ^4A_{2g}$  electronic transition of  $Cr^{3+}$ . For  $LiScGeO_4:Cr^{3+}$  (**publication P4**), relative sensitivity maps were proposed as a function of the spectral range used for LIR calculation, enabling the development of tailor-made luminescent manometers optimized for specific pressure regimes.

Furthermore, in **publication P5**, a tri-modal readout strategy was introduced for  $Li_3Sc_2(PO_4)_3:Cr^{3+}$  combining LIR-based ratiometry, spectral shift tracking, and luminescence decay time analysis. **This approach significantly expanded the functional versatility of the sensor and established it as the most pressure-sensitive kinetic-based luminescent manometer reported to date, with a relative sensitivity of 93.56% GPa<sup>-1</sup> and a TIMF value exceeding 100 K GPa<sup>-1</sup>. Notably, this was the first reported manometer utilizing the lifetime of the  $^4T_{2g}$  excited state of  $Cr^{3+}$  ions.** The lifetime of the  $^4T_{2g}$  level was also investigated for  $CaMgSi_2O_6:Cr^{3+}$  (**publication P3**), yielding a relative sensitivity of 7.95% GPa<sup>-1</sup> (**Figure 10a**). However, this material exhibited a TIMF below 50 K GPa<sup>-1</sup>, indicating a higher susceptibility to thermal fluctuations. The poorest performance in both pressure sensitivity and thermal robustness was recorded for  $CaAl_{12}O_{19}:Cr^{3+}$  whose pressure sensing relied on the kinetics of the  $^2E_g \rightarrow ^4A_{2g}$  electronic transition. **This result further emphasized the advantages of utilizing the broadband  $^4T_{2g} \rightarrow ^4A_{2g}$  emission in achieving thermally invariant luminescent pressure readouts.**

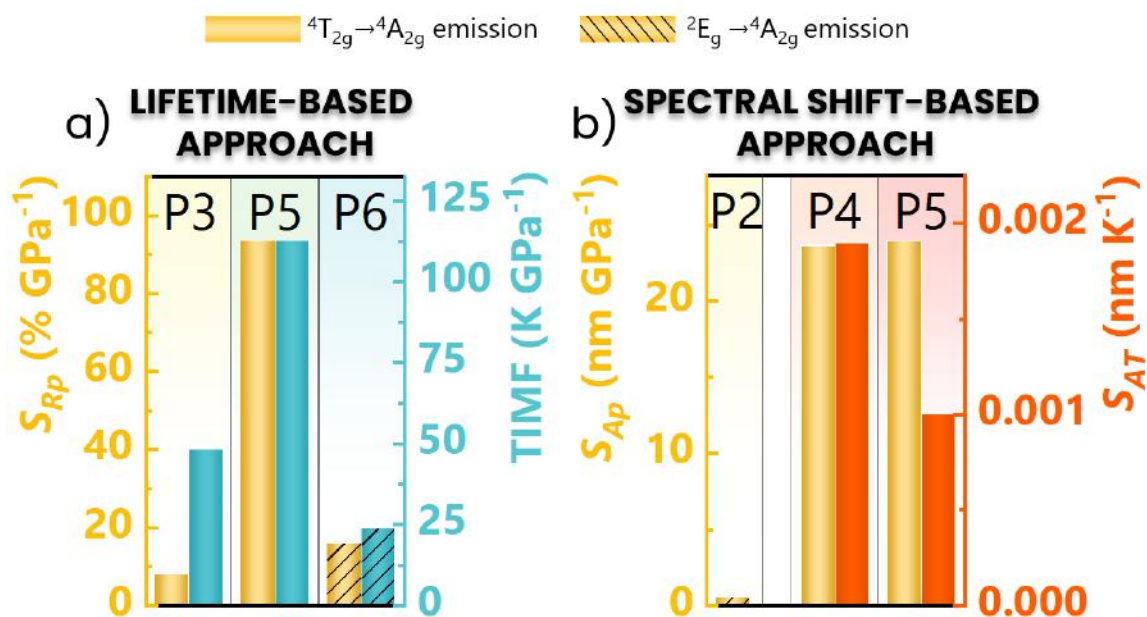


**Figure 10.** Comparison of the performance of the developed luminescent manometers employing a) lifetime- and b) spectral shift-based readout approaches, evaluated in terms of relative ( $S_{Rp}$ ) or absolute ( $S_{Ap}$ ) maximal pressure sensitivity and TIMF or absolute temperature sensitivity ( $S_{AT}$ ), respectively.

Monitoring the luminescence kinetics associated with the  ${}^4T_{2g} \rightarrow {}^4A_{2g}$  transition of  $\text{Cr}^{3+}$  ions, despite their greater susceptibility to temperature variations - resulting from the inherent sensitivity of luminescence decay times to both pressure and temperature - offers additional opportunities for application. One of the key advantages of this approach lies in the fact that luminescence kinetics are largely unaffected by external factors such as the physical or chemical nature of the surrounding medium, which can be a significant limitation in intensity-based methods. **For this reason, luminescence decay time-based manometry, although less thermally robust than the ratiometric LIR-based approach, merits further exploration.**

The manometric potential of alternative  $\text{Cr}^{3+}$ -based systems, based on doped  $\text{CaAl}_{12}\text{O}_{19}$  was investigated. One of its observed emission bands was attributed to  $\text{Cr}^{3+}$ - $\text{Cr}^{3+}$  pairs interactions. It was found that this  $\text{Cr}^{3+}$ - $\text{Cr}^{3+}$  pair emission was slightly sensitive to pressure changes. However, the material also exhibited a narrow emission band associated with the  ${}^2E_g \rightarrow {}^4A_{2g}$  electronic transition of  $\text{Cr}^{3+}$ , which allowed for the implementation of a dual-mode temperature-pressure sensing strategy. In this case, the manometric calibration curve based ratio of  ${}^2E_g \rightarrow {}^4A_{2g}$  and  ${}^4T_{2g} \rightarrow {}^4A_{2g}$  emissions bands resulted in a pressure sensitivity of approximately 70%  $\text{GPa}^{-1}$ , accompanied by a TIMF value of  $\sim 150 \text{ K GPa}^{-1}$ . On the other hand, the LIR based on band associated with  $\text{Cr}^{3+}$ - $\text{Cr}^{3+}$  pairs emission, owing to its negligible response to pressure, proved to be

a good thermometric indicator. The underlying mechanism of pressure insensitivity in  $\text{Cr}^{3+}$ - $\text{Cr}^{3+}$  pair emissions remains poorly understood due to the limited literature available on the subject. Nevertheless, this phenomenon may pave the way for the development of wider group of bifunctional sensors that simultaneously enable temperature and pressure readout, thus expanding the potential application scope of  $\text{Cr}^{3+}$ -doped phosphors.

Additionally, in **publications P4** and **P5**, a spectral shift-based pressure readout mode was proposed, capitalizing on the exceptionally high pressure-induced spectral shift rates of 23.63 nm GPa<sup>-1</sup> and 23.90 nm GPa<sup>-1</sup> for  $\text{LiScGeO}_4\text{:Cr}^{3+}$  and  $\text{Li}_3\text{Sc}_2(\text{PO}_4)_3\text{:Cr}^{3+}$ , respectively (**Figure 10b**). At the time of publication of **P4** and **P5**, these values represented the highest reported pressure-induced shift rates for  $\text{Cr}^{3+}$ -based luminescent manometers. Moreover, temperature-induced spectral shifts were found to be minimal, amounting to only 0.0019 nm K<sup>-1</sup> for  $\text{LiScGeO}_4\text{:Cr}^{3+}$  and 0.0010 nm K<sup>-1</sup> for  $\text{Li}_3\text{Sc}_2(\text{PO}_4)_3\text{:Cr}^{3+}$ , supporting the thermal robustness in spectral shift-based detection. A similar approach was evaluated for the  ${}^2\text{E}_g \rightarrow {}^4\text{A}_{2g}$  emission band of  $\text{MgO:Cr}^{3+}$ , which yielded a spectral shift rate of 0.504 nm GPa<sup>-1</sup> - notably higher than that of the commonly used ruby standard (0.365 nm GPa<sup>-1</sup>). However, despite these promising results, the practical applicability of shift-based manometry in industrial or real-world settings remains limited. This limitation stems from the fact that such measurements enable only point-wise pressure readout and require high-resolution spectrometers to minimize readout error, thereby increasing the cost and complexity of the sensing system. In contrast, ratiometric LIR-based approach offer more versatile and cost-effective alternatives, particularly for applications requiring robust and spatially-resolved pressure monitoring.

**In summary, the most promising approach proved to be the ratiometric method based on the luminescence intensity ratio of the broad  ${}^4\text{T}_{2g} \rightarrow {}^4\text{A}_{2g}$  emission band of  $\text{Cr}^{3+}$  ions, integrated over two selected spectral regions. This strategy was demonstrated for the first time in the publications constituting this doctoral dissertation.**

The luminescence of  $\text{Cr}^{3+}$  ions in weak-field host matrices and the LIR-based ratiometric methodology based on broad emission bands independently hold substantial potential for pressure sensing applications. However, when these two concepts are combined, they enable the development of luminescent pressure sensors with outstanding performance characteristics. These sensors exhibit exceptionally high pressure sensitivity, insensitivity to temperature variations, and practical benefits such as lower system costs and the capability to monitor pressure distributions across extended surfaces, rather than at isolated points. Such a combination of properties makes these sensors truly unique. The ability to simultaneously achieve high pressure sensitivity, temperature-independent operation, and cost-effective implementation sets them apart

from existing luminescent pressure sensing systems. The results obtained in this doctoral dissertation not only confirm the validity and robustness of this integrated approach but also demonstrate its scalability and adaptability across various host materials and pressure ranges. It opens new prospects for high-resolution, non-invasive pressure mapping in dynamic environments, offering critical advantages in sectors such as aerospace, manufacturing, energy systems, and materials diagnostics. In this context, the work presented in this dissertation constitutes a pivotal step in bridging the gap between academic innovation and technological application in the field of pressure sensing. Moreover, these findings significantly accelerate the transition of luminescent manometers from laboratory-based experimental concepts to practical, industrial-grade technologies with real-world applicability.

### Further research directions

---

The solutions presented in this dissertation demonstrate significant application potential, positioning the research topic as a compelling foundation for further exploration. One particularly important direction involves the systematic investigation of pressure-dependent luminescence across a broader temperature range, extending well beyond ambient conditions. Such studies would considerably expand the scope of practical applications. In the present work, this aspect remained unexplored due to instrumental limitations - specifically, the employed diamond anvil cell allowed for reliable operation only at room temperature.

Moreover, the LIR-based ratiometric approach utilizing broad emission bands proves to be a highly promising strategy not only in  $\text{Cr}^{3+}$ -doped systems but also in materials incorporating other luminescent centers. Research conducted outside the scope of this dissertation (**publication P21**) has already confirmed the feasibility of  $\text{Ce}^{3+}$ -doped phosphors as optical pressure sensors operating in the visible spectral range. Therefore, it is particularly worthwhile to investigate another phosphors exhibiting broadband emission, such as  $\text{Mn}^{2+}$ , as well as lanthanide ions exhibiting *d-f* electronic transitions. This research direction is currently being pursued for  $\text{Ni}^{2+}$ -doped phosphors within the framework of the NCN PRELUDIUM project, for which I serve as the principal investigator.

An especially promising but thus far only briefly illustrated direction is the development of ratiometric LIR-based sensors capable of monitoring multiple parameters simultaneously. In the example presented in this dissertation, a  $\text{Cr}^{3+}$ -doped phosphor was employed in which  $\text{Cr}^{3+}$  ions exhibited both broadband emission from the  $^4\text{T}_{2g}$  level and additional band attributed to  $\text{Cr}^{3+}$ - $\text{Cr}^{3+}$  pairs emission. This dual-emission behavior highlights the potential of such materials for temperature-pressure sensing applications. Further exploration of this concept - particularly through a detailed study of pressure-dependent luminescence arising from  $\text{Cr}^{3+}$ - $\text{Cr}^{3+}$  pairs -

is warranted. Expanding this research to other transition metal ion pairs, such as  $\text{Mn}^{2+}\text{--Mn}^{2+}$ , could also yield valuable insights, especially considering the limited number of publications available on the subject. Advancing this research direction could enable the development of next-generation optical sensors characterized by high functionality and broad application relevance.

Another essential yet underexplored research direction concerns the relationship between the structural characteristics of host lattices and their manometric performance. High-pressure X-ray diffraction studies would be particularly valuable in this context. Performing Rietveld refinements on high-pressure XRD data could allow for precise tracking of unit cell parameter evolution under pressure and their correlation with luminescent behavior. Although technically demanding - due to challenges such as parasitic reflections from diamond anvils and weak diffraction signals from small sample volumes - such studies could offer critical insights into the structural mechanisms governing pressure-sensitive luminescence.

Ultimately, establishing a deeper understanding of these structural-optical correlations could pave the way for the development of predictive models capable of estimating the pressure response of phosphors without the need for extensive synthesis and characterization. A particularly forward-looking strategy involves the creation of a curated database of luminescent materials evaluated under high-pressure conditions, including their structural parameters, emission profiles, and pressure and temperature sensitivities. Such a base would form a solid foundation for the application of machine learning algorithms to uncover hidden patterns and correlations that may elude conventional analytical approaches. By leveraging data-driven methods, it would become possible to predict the behavior of unexplored compositions, enabling the rational design of advanced phosphors. This approach could significantly shorten development cycles, minimize material consumption, and promote the emergence of sustainable, application-oriented luminescent pressure sensing technologies.

Taken together, the directions outlined above highlight the multifaceted nature and vast potential of luminescence-based pressure sensing. Building upon the foundations established in this dissertation, future studies integrating advanced structural characterization, exploration of a broader range of chemical compositions and dopant systems, and modern data-driven approaches may unlock new frontiers in luminescent manometers development. Such progress would not only enhance our fundamental understanding of pressure-sensitive luminescent phenomena in a view of sensing but also facilitate the translation of laboratory-scale innovations into robust, real-world technologies with meaningful industrial and scientific impact.

LIST OF PUBLICATIONS:

- P1. **M. Szymczak**, P. Wozny, M. Runowski, M. Pieprz, V. Lavín, L. Marciniak, *Temperature invariant ratiometric luminescence manometer based on Cr<sup>3+</sup> ions emission*, Chemical Engineering Journal, 2023, 453, 139632
- P2. **M. Szymczak**, M. Runowski, V. Lavín, L. Marciniak, *Highly Pressure-Sensitive, Temperature Independent Luminescence Ratiometric Manometer Based on MgO:Cr<sup>3+</sup> Nanoparticles*, Laser & Photonics Reviews, 2023, 17, 2200801
- P3. **M. Szymczak**, K. Su, L. Mei, M. Runowski, P. Woźny, Q. Guo, L. Liao, L. Marciniak, *Investigating the Potential of Cr<sup>3+</sup>-Doped Pyroxene for Highly Sensitive Optical Pressure Sensing*, ACS Applied Materials & Interfaces 2024, 16, 44, 60491-60500
- P4. **M. Szymczak**, M. Runowski, M.G. Brik, L. Marciniak, *Multimodal, super-sensitive luminescent manometer based on giant pressure-induced spectral shift of Cr<sup>3+</sup> in the NIR range*, Chemical Engineering Journal, 2023, 466, 143130
- P5. **M. Szymczak**, J. Jaśkielewicz, M. Runowski, J. Xue, S. Mahlik, L. Marciniak, *Highly-Sensitive, Tri-Modal Luminescent Manometer Utilizing Band-Shift, Ratiometric and Lifetime-Based Sensing Parameters*, Advanced Functional Materials, 2024, 34, 22, 2314068,
- P6. **M. Szymczak**, A. Antuzevics, P. Rodionovs. M. Runowski, U.R. Rodríguez-Mendoza, D. Szymanski, V. Kinzhybalo, L. Marciniak, *Bifunctional Luminescent Thermometer-Manometer Based on Cr<sup>3+</sup>-Cr<sup>3+</sup> Pair Emission*, ACS Applied Materials & Interfaces, 2024, 16, 47, 64976-64987
- P7. **M. Szymczak**, W.M. Piotrowski, U. R. Rodríguez-Mendoza, P. Wozny, M. Runowski, L. Marciniak, *Highly sensitive ratiometric luminescence manometer based on the multisite emission of Cr<sup>3+</sup>*, Journal of Materials Chemistry C, 2025, 13, 4224-4235





# Temperature invariant ratiometric luminescence manometer based on $\text{Cr}^{3+}$ ions emission

M. Szymczak<sup>a</sup>, P. Woźny<sup>b</sup>, M. Runowski<sup>b,c</sup>, M. Pieprz<sup>a</sup>, V. Lavín<sup>c</sup>, L. Marciniak<sup>a,\*</sup>

<sup>a</sup> Institute of Low Temperature and Structure Research, Polish Academy of Sciences, Okólna 2, 50-422 Wrocław, Poland

<sup>b</sup> Adam Mickiewicz University, Faculty of Chemistry, Uniwersytetu Poznańskiego 8, 61-614 Poznań, Poland

<sup>c</sup> Departamento de Física, IUEA and MALTA-Consilider Team, Universidad de La Laguna, Apartado de Correos 456, E-38200 San, Cristóbal de La Laguna, Santa Cruz de Tenerife, Spain

## ARTICLE INFO

### Keywords:

Luminescent manometry

Pressure sensor

$\text{Cr}^{3+}$

Chromium(III)

Thermal quenching

Crystal field strength

## ABSTRACT

The dependence of the spectroscopic properties of the phosphor on the applied pressure enables the development of luminescent manometers that allow remote readout and imaging of the pressure. Although the most widely used manometers for years have been those using pressure-induced spectral shift of the emission band, their main limitations are relatively low sensitivity for spectrally narrow emission lines or low readout precision for broadband phosphors. Taking advantage of the benefits of both these approaches, this paper proposes a ratiometric pressure-readout strategy that exploits spectral shift of the  ${}^4\text{T}_2 \rightarrow {}^4\text{A}_2$  emission band of  $\text{Cr}^{3+}$  ions in  $\text{Li}_2\text{Mg}_3\text{TiO}_6$ . The luminescent manometer developed in this way is characterized by a linear dependence of LIR on pressure in the range of 0–7.75 GPa pressure range and a relative sensitivity of  $S_R = 4.7\%/\text{GPa}$ . Importantly, this manometer is characterized by insensitivity to temperature changes in the 123–563 K. This novel approach will allow the development of a new group of highly sensitive luminescent manometers.

## 1. Introduction

Luminescent materials, in addition to their natural application in the lighting industry, are recently gaining popularity in detection systems and sensing applications [1–7]. This is due to the fact that the proper design of the phosphor allows to boost the susceptibility of its luminescent properties to variations in the physical or chemical parameters of the medium in which the phosphor is located [6,8–11]. Therefore, by the analysis of the change in energy, intensity of the emission band, its half-width or luminescence intensity ratio (LIR) of two bands and luminescence kinetics, allows the development of luminescence thermometers, pH meters, optical power meters or luminescence manometers [12–17]. While luminescence thermometry is a technique that has been developed very intensively in recent years, the literature devoted to luminescence manometers is rather scarce [16,18–25]. Most reports describe optical manometers based on emission line shift, whereas less common are manometers using full width at half maximum (FWHM) [26], luminescence lifetimes [22] or band intensity [16]. Although luminescence manometers based on the LIR of two bands have been reported for lanthanide ions or transition metal ions doped phosphors, the simultaneous dependence of this parameter on other factors such as

temperature limits their application potential [16,17,22,27–32]. Therefore, one of the most widely used techniques is manometry based on spectral band shift. For nearly 50 years the key indicator of isostatic pressure here is  $\text{Al}_2\text{O}_3:\text{Cr}^{3+}$  commonly used as a luminescent reference during measurements in the diamond anvil cell (DAC), which, depending on the used pressure-transmitting medium, allows ultra-high static pressures up to 150 GPa to be obtained [33]. In this case, the monotonic blue shift of the  $\text{R}_2$ -line of the  ${}^2\text{E} \rightarrow {}^4\text{A}_2$  transition allows for a readout of the pressure. However, this parameter is characterized by low sensitivity to pressure changes (a change in pressure from ambient to 2.7 GPa causes a change in band position by only 1 nm) [33]. On the other hand, a more spectacular spectral shift is observed in the case of wide bands such as  $\text{Ca}_9\text{NaZn}_{1-y}\text{Mg}_y(\text{PO}_4)_7:\text{Eu}^{2+}$  [34],  $\text{Ca}_2\text{Gd}_8\text{Si}_6\text{O}_{26}:\text{Ce}^{3+}$  [17],  $\text{BaLi}_2\text{Al}_2\text{Si}_2\text{N}_6:\text{Eu}^{2+}$  [35], etc. However, although the pressure dependence of the band position facilitates achieving high pressure sensitivity, the broad nature of the band hinders the reliable read of the emission maximum, thus limiting measurement precision. Therefore, in this work, a new strategy for ratiometric pressure readout in a manometer based on broadband emission of  $\text{Cr}^{3+}$  ion in  $\text{Li}_2\text{Mg}_3\text{TiO}_6$  (LMTO) phosphor is proposed. The main idea of the proposed strategy is schematically shown in Fig. 1.

\* Corresponding author.

E-mail address: [l.marciniak@intibs.pl](mailto:l.marciniak@intibs.pl) (L. Marciniak).

<https://doi.org/10.1016/j.cej.2022.139632>

Received 31 July 2022; Received in revised form 16 September 2022; Accepted 3 October 2022

Available online 8 October 2022

1385-8947/© 2022 The Author(s). Published by Elsevier B.V. This is an open access article under the CC BY license (<http://creativecommons.org/licenses/by/4.0/>).

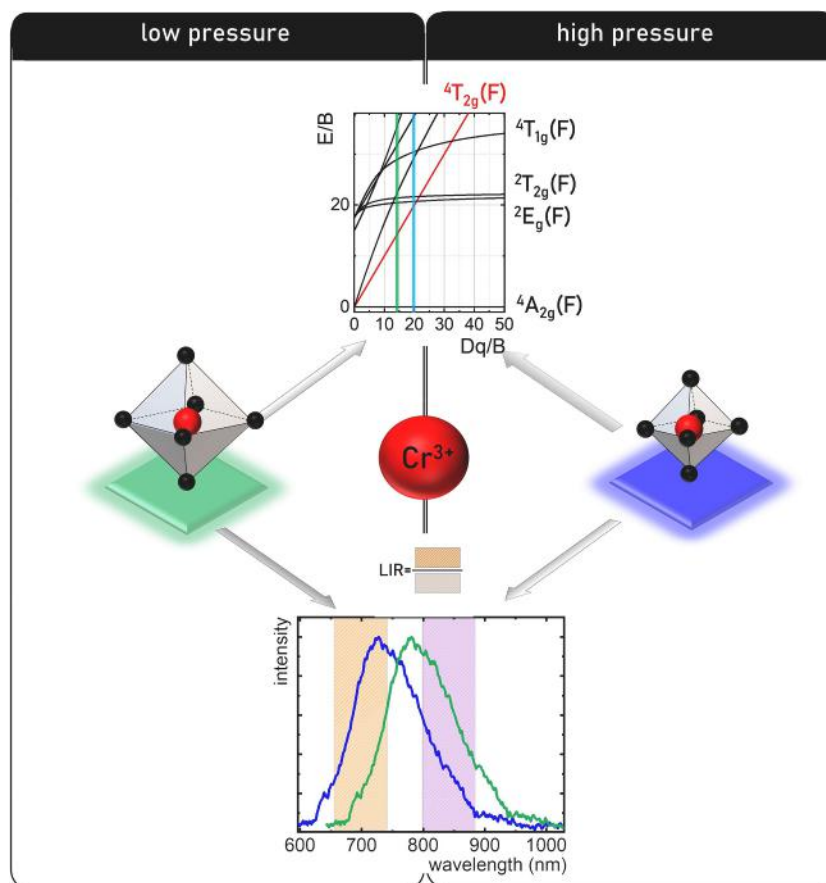


**Fig. 1.** The conceptual image shows the main idea of the work: the applied pressure causes a shrinkage of the  $\text{Cr}^{3+}\text{--O}^{2-}$  distance and thus modifying the energy of the excited states. As a result, the spectral position of the emission band related to the  ${}^4\text{T}_2 \rightarrow {}^4\text{A}_2$  undergoes a blue shift at elevated hydrostatic pressure. Therefore, the luminescence intensity ratio (LIR) of the signals integrated into the spectral ranges marked in the Figure can be used as a manometric parameter.

The luminescent properties of  $\text{Cr}^{3+}$  ions are associated with radiative depopulation of  ${}^2\text{E}$  and/or  ${}^4\text{T}_2$  levels [36–40]. The spin-forbidden  ${}^2\text{E} \rightarrow {}^4\text{A}_2$  transition is represented by a spectrally narrow band that is dominant when a strong crystal field affects  $\text{Cr}^{3+}$  ions. The spectrally broad band associated with the spin-allowed  ${}^4\text{T}_2 \rightarrow {}^4\text{A}_2$  transition dominates in a weak crystal field host materials. In contrast to the  ${}^2\text{E}$  level, the energy of the  ${}^4\text{T}_2$  level changes very strongly with a change in the strength of the crystal field. Taking into account that in the case of  $\text{Cr}^{3+}$  ions in octahedral coordination the strength of the crystal field ( $\text{Dq/B}$ ) increases strongly with the shortening of the metal–oxygen ( $R$ ) distance ( $\text{Dq/B} \sim R^{-5}$ ) [41,42], the spectral position of the  ${}^4\text{T}_2 \rightarrow {}^4\text{A}_2$  band is expected to change much more significantly with increasing pressure compared to the  ${}^2\text{E} \rightarrow {}^4\text{A}_2$  band. Therefore, from a manometric perspective, it is beneficial to exploit the  $\text{Cr}^{3+}$  doped materials with a dominant  ${}^4\text{T}_2 \rightarrow {}^4\text{A}_2$  emission band. As will be demonstrated in the further part of this article,  $\text{Li}_2\text{Mg}_3\text{TiO}_6\text{:Cr}^{3+}$  belongs to such a group of phosphors [43–46]. In order to eliminate the low precision of pressure measurement based on the broad band emission maximum, it is proposed to develop a ratiometric manometer using LIR integrated into two spectral ranges. Additional advantages of using the LMTO as a ratiometric luminescent manometer are the monotonic, sublinear variation of the LIR in the pressure range of 0–7.75 GPa and the independence of pressure measurement from temperature changes in the range of 123–563 K.

In the present work, the effect of the steepness of spectroscopic properties of  $\text{Cr}^{3+}$  ions in LMTO was investigated. In addition, the effect of temperature and hydrostatic pressure on the spectral positions of the  ${}^4\text{T}_2 \rightarrow {}^4\text{A}_2$  band was determined.

## 2. Experimental section

### 2.1. Materials

The  $\text{LMTO:Cr}^{3+}$  with different concentrations of  $\text{Cr}^{3+}$  ions were synthesized using a modified Pechini method [47]. The following reagents were used as precursors for the synthesis: lithium carbonate ( $\text{Li}_2\text{CO}_3$ , min. 99.0 %, Chempur), magnesium nitrate hydrate ( $\text{Mg}(\text{NO}_3)_2 \cdot x\text{H}_2\text{O}$ ,  $x \approx 6$ , 99.999 %, Alfa Aesar), titanium(IV) *n*-butoxide ( $\text{Ti}[\text{O}(\text{CH}_2)_3\text{CH}_3]_4$ , 99+%, Alfa Aesar), chromium(III) nitrate nonahydrate ( $\text{Cr}(\text{NO}_3)_3 \cdot 9\text{H}_2\text{O}$ , min. 99.99 %, Alfa Aesar), 2,4-pentanedione ( $\text{C}_5\text{H}_8\text{O}_2$ , 99 %, Alfa Aesar), polyethylene glycol 200 ( $\text{H}(\text{OCH}_2\text{CH}_2)_n\text{OH}$ ,  $n = 200$ , Alfa Aesar) and citric acid ( $\text{HOC}(\text{COOH})(\text{CH}_2\text{COOH})_2$ ,  $\geq 99.5$  %, Sigma-Aldrich). All reagents were used without further purification.

### 2.2. Synthesis

Stoichiometric amounts of lithium, magnesium(II) and chromium (III) salts were dissolved in 50 ml of distilled water with a sixfold molar excess (respect to all metals) of citric acid. The number of moles of lithium carbonate was always equal to  $8.5 \cdot 10^{-4} \text{ mol}$ , while the number of moles of magnesium(II) and chromium(III) nitrates was varied, depending on the amount of dopant chromium(III) in the sample, which was calculated with respect to the stoichiometric amount of  $\text{Mg}^{2+}$  ions in the host. Meanwhile, in another glass was placed  $8.5 \cdot 10^{-4} \text{ mol}$  of  $\text{Ti}(\text{OC}_4\text{H}_9)_4$ , which was stabilised with 2,4-pentanedione in a molar ratio of 1:1. The resulting yellow, clear solution was mixed with the previously prepared citrate complexes. Subsequently, PEG-200 was added in the molar ratio 1:1 with respect to the citric acid. The reaction mixture

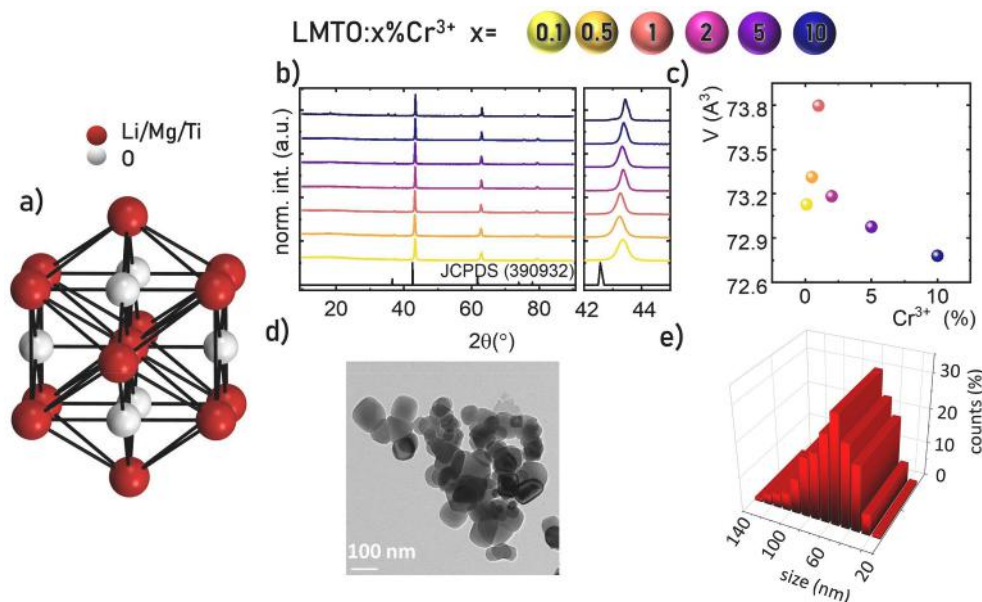


**Fig. 2.** Visualization of cubic structure of LMTO – a); XRD patterns of LMTO:Cr<sup>3+</sup> ( $x = 0.1$ –50) and zoom on angles ca. 42–45° – b); calculated cell unit volume as a function of Cr<sup>3+</sup> concentration – c); the representative TEM images of LMTO:10%Cr<sup>3+</sup> – d); and corresponding histogram of nanoparticle size distribution obtained from TEM images – e).

was stirred at 330 K for 2 h. After this time, the solution was dried for 5 days at 360 K in the air. The obtained LMTO resins with different Cr<sup>3+</sup> concentrations (0.1–50 %) were annealed in a ceramic crucible at the temperature range 673–1173 K in air for 2 h.

Stoichiometric amounts of chromium(III), magnesium(II) and lithium salts were dissolved in distilled water with a sixfold molar excess (to all metals) of citric acid. The mass of the dopant (Cr<sup>3+</sup>) was calculated with respect to the stoichiometric amount of Mg<sup>2+</sup> ions in the host. Meanwhile, in another glass Ti(OC<sub>4</sub>H<sub>9</sub>)<sub>4</sub>, stabilized by mixing with 2, 4-pentanedione, a complex is formed (1:1 M ratio) was placed. The resulting yellow, clear solution was mixed with the previously prepared citrate complexes. Subsequently, PEG-200 was added in the molar ratio 1:1 with respect to the citric acid. The reaction mixture was stirred at 330 K for 2 h. After this time, the solution was dried for 5 days at 360 K in the air. The obtained LMTO resins with different Cr<sup>3+</sup> concentrations (0.1–50 %) were annealed in a ceramic crucible at the temperature range 673–1173 K in air for 2 h.

### 3. Methods

Examination of the crystal structure by X-ray powder diffraction (XRD) was carried out using a PANalytical X'Pert Pro diffractometer in Bragg-Brentano geometry equipped with an Anton Paar TCU1000 N Temperature Control Unit using Ni-filtered Cu K  $\alpha$  radiation ( $V = 40$  kV,  $I = 30$  mA). Measurements were taken in the range 10–90°. Transmission electron microscopy images were obtained using a Philips CM-20 SuperTwin TEM microscope (CCD FEI Eagle 2 K camera with a HAADF detector, LaB<sub>6</sub> cathode). Studies were performed with 160 kV parallel beam electron energy. Samples were prepared by dispersing the powders in methanol, then applying the resulting suspension to a copper grid and drying under an IR lamp for 40 min. The prepared grid with sample was purified in a plasma cleaner. Samples for EDS measurements were prepared by putting a droplet of sample dispersion in methanol on a carbon stub. Measurements were performed using EDAX Genesis XM4 spectrometer installed on FEI NovaNanoSEM 230 microscope.

The excitation spectra were measured with FLS1000 Fluorescence Spectrometer from Edinburgh Instruments. The source of the excitation was a 450 W Xenon lamp and R5509-72 photomultiplier tube from Hamamatsu in nitrogen-flow cooled housing was used as the infrared

detector. The temperature and pressure-dependent emission spectra of the synthesized phosphors and luminescence decay profiles were measured with the aforementioned system, using a 445 nm laser diode operating in a continuous and pulsed work regimes, respectively. The temperature of the sample was controlled by a THMS 600 heating-cooling stage from Linkam (0.1 °C temperature stability and 0.1 °C set point resolution). Measurements were performed with the 1 min interval between measurements in order to obtain the thermal equilibrium.

The Raman spectra were recorded in a backscattering geometry using a Renishaw InVia confocal micro-Raman system with a power-controlled 100 mW 532 nm laser diode. The laser beam was focused using an Olympus x20 SLMPlan N long working distance objective. Raman spectra of the sample compressed in a Daphne Oil 7575 (pressure transmitting medium) were measured in a DAC equipped with the ultra-low fluorescence (Ilas) diamond anvils.

The pressure-dependent emission spectra were measured using a gas membrane driven diamond anvil cell Diacell  $\mu$ ScopeDAC-RT(G) diamond anvil cell (DAC) from Almax easyLab with 0.4 mm diamond culets. The sample was loaded into a 140  $\mu$ m hole drilled in a stainless steel gasket (thickness 250  $\mu$ m, diameter 10 mm). As the pressure transmitting medium was used methanol-ethanol solution (V:V/4:1). Pressure was controlled using a Druck PACE 5000 and ruby crystals were chosen as the pressure indicator, the value of which was determined by the spectral shift of R<sub>2</sub> line [48].

### 4. Results and discussion

LMTO crystallizes in a cubic structure with  $Fm\bar{3}m$  (225) space group [43–46,49–54]. All cations (Li<sup>+</sup>, Mg<sup>2+</sup> and Ti<sup>4+</sup>) are in the Wyckoff position coordinated by six oxygen ions in octahedral symmetry (Fig. 2a). Therefore, LMTO is an especially interesting host material for doping with Cr<sup>3+</sup> ions, which preferentially occupy octahedral sites. Based on the value of the ionic radii of the metals ( $R_{Li^+} > R_{Mg^{2+}} > R_{Cr^{3+}} > R_{Ti^{4+}}$ ), Cr<sup>3+</sup> ion is expected to occupy preferentially the crystallographic position of Ti<sup>4+</sup> ions, due to the smaller percentage difference in the value of ionic radii ( $D_R$ ) calculated from the formula [55]:

$$D_R = \frac{(R_H - R_D)}{R_H} \cdot 100\% \quad (1)$$

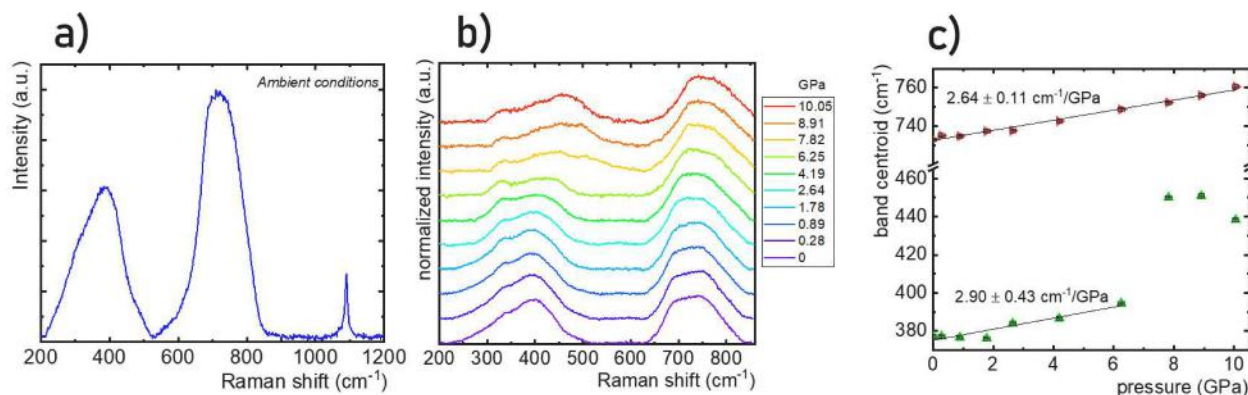


**Fig. 3.** The room temperature Raman spectra of LMTO measured at ambient conditions-a); and measured as a function of pressure -b); the band centroid as a function of applied pressure-c).

where  $R_H$  and  $R_D$ , are the ionic radii of the cations of the host material and dopant, respectively. For  $Ti^{4+}$  this difference is 1.65 %, while the radius of  $Mg^{2+}$  differs from that of  $Cr^{3+}$  by c.a. 14.6 %. Additionally a difference in the ionic charge occurs between substituted  $Ti^{4+}$  and  $Mg^{2+}$  ions and dopant ion  $Cr^{3+}$ . However, as it is considered in the literature the fact that  $Mg^{2+}$  and  $Ti^{4+}$  are neighboring sites it is expected that when the two ions occupy both sites simultaneously the charge compensation occurs [46]. The phase purity of LMTO: $Cr^{3+}$  powders was examined by

XRD technique. Due to the absence of the LMTO compound in the ICSD database, a compound with a similar structure,  $Li_2Mg_3SnO_6$  (JCPDS No. 390932), was used as a reference. The lack of additional reflection in the XRD patterns confirms the complete reactions of the synthesis precursors and phase purity of the synthesized powders annealed in the 673–1173 K temperature range (Figure S1). However, diffractograms of samples annealed below 973 K indicate the presence of an amorphous phase, the amount of which decreases with increasing annealing

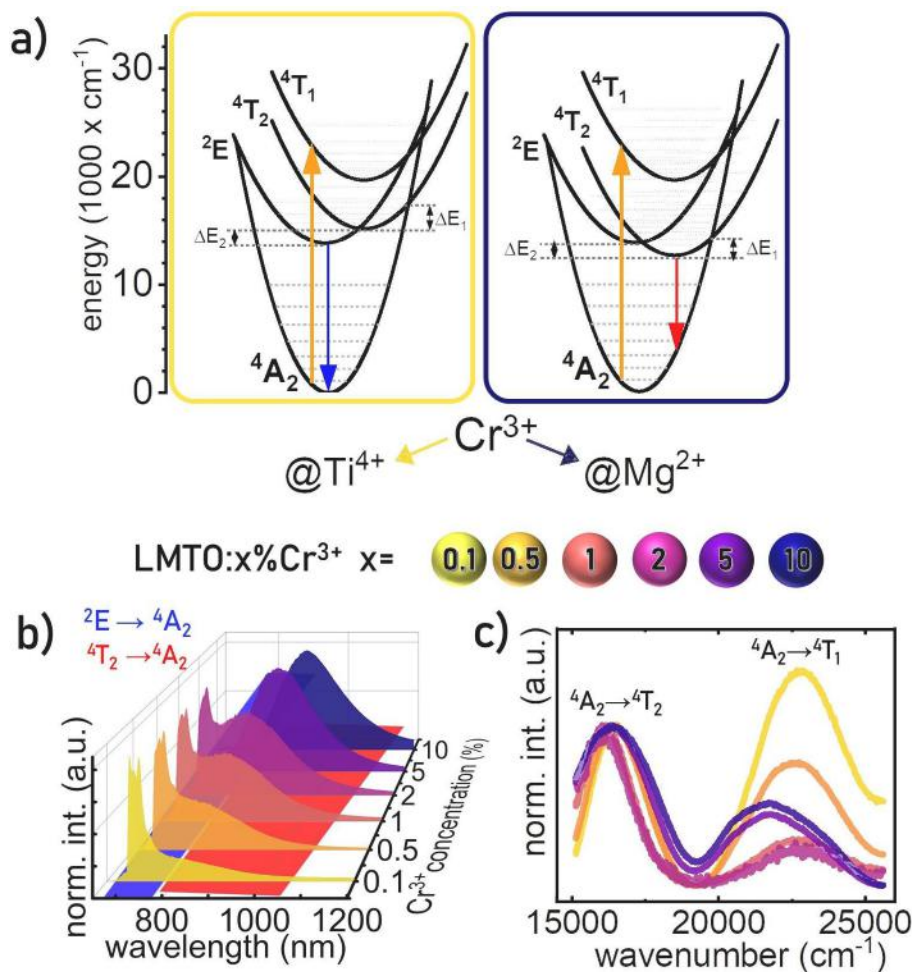


**Fig. 4.** Configurational coordinate diagram for  $Cr^{3+}$  ions substituted at  $Ti^{4+}$  and  $Mg^{2+}$  crystallographic sites - a); the comparison of the emission ( $\lambda_{exc} = 445$  nm) - b); and excitation ( $\lambda_{em} = 718$  nm for 0.1–2 %  $Cr^{3+}$  and on  $\lambda_{em} = 900$  nm for 5 and 10 %  $Cr^{3+}$ ). c) spectra of LMTO: $x\%Cr^{3+}$  powders for different concentration of  $Cr^{3+}$  ions ( $x = 0.1$ –10) measured at 123 K upon  $\lambda_{exc} = 445$  nm.



temperature and saturates at 973 K. Moreover the residues of carbon, formed during the high-temperature decomposition of the organic phase (citric acid, PEG), are present in samples annealed at 873 K and lower temperatures (Figure S2). The annealing temperature was too low for oxidation of all carbon to carbon dioxide in 120 min. Moreover, the decrease in the FWHM of the reflections with increasing annealing temperature was observed, indicating enlargement of the particle size. In view of the abovementioned observations, the temperature of 1073 K was selected as an optical annealing temperature that provides a balance between the high crystallinity of the sample and the small size of the particles. The diffractograms of samples with different dopant concentration (Fig. 2b) indicates that for up to 10 %Cr<sup>3+</sup>, there is a convergence of the diffraction peaks with both the reference pattern and the LMTO analyses reported previously. The detailed analysis reveals that, as the Cr<sup>3+</sup> doping increases, the XRD reflections initially shift towards smaller angles, for concentrations of 0.1 and 0.5 %, indicating an increase in crystallographic unit cell size followed by the opposite shift for higher Cr<sup>3+</sup> concentration (Fig. 2b). This suggests the substitution of Cr<sup>3+</sup> ions with a smaller ionic radius, in this case, Ti<sup>4+</sup> for low dopant concentration and the larger ionic site (like Mg<sup>2+</sup>) for higher dopant concentration. Since the R distance for Ti<sup>4+</sup> and Mg<sup>2+</sup> sites differ, the luminescent properties of Cr<sup>3+</sup> will strongly depend on the type of the crystallographic site which will be occupied by dopant ions. The unit cell volume determined based on the Rietveld refinement method initially increases up to 1 % of Cr<sup>3+</sup> and then decreases with increase of concentration (Fig. 2c, Figure S3). The analysis of the TEM images reveals that synthesized powders consist of aggregated particles of around 50 nm in diameter and the concentration of Cr<sup>3+</sup> does not significantly affect the particle size (Fig. 2d, e). As confirmed by the EDS studies (Figure S4) the dopant ions are uniformly distributed in the phosphor.

To understand the structural changes in the LMTO upon high isostatic pressure the Raman spectra were measured for the undoped sample. The measured Raman spectrum at ambient conditions reveals three bands, associated with Raman active modes, centered around 380, 730 and 1090 cm<sup>-1</sup> (Fig. 3a). However, in the case of the experiments performed under high-pressure conditions in a DAC, only the first two of them were clearly recognizable, because at higher wavenumber values the third band (at ≈1090 cm<sup>-1</sup>) overlapped with some artificial peaks originating mainly from the diamonds and pressure transmitting medium of the DAC (mainly from the diamonds and pressure transmitting medium) (Fig. 3b). Moreover, due to the typically observed deterioration of the Raman signal in the compressed materials, related to increased strains and crystal defects under pressure leading to the lower signal intensity, the signal-to-noise ratio decreased significantly with pressure, making observations of the low-intensity Raman modes difficult. Together with the compression of the materials, i.e., with increasing pressure values, the energy of the phonon modes increased, which is manifested by the shift of the Raman bands toward higher energy values (higher wavenumbers). This effect is due to the shortening of the average distances between the ions, namely, the bonds shortening in the compressed structure. The peak situated initially around 380 cm<sup>-1</sup>, exhibits an estimated shift rate of ≈2.9 cm<sup>-1</sup>/GPa, using a linear fit of the band centroids, whereas the one located at around 730 cm<sup>-1</sup> shifts with a rate of ≈2.6 cm<sup>-1</sup>/GPa (Fig. 3c). Please note, that the low-energy band at ≈380 cm<sup>-1</sup> shifts linearly up to ≈8 GPa. Above 8 GPa a sudden change of the band centroid is observed. The origin of this behaviour is not clear and it can be associated with the structural phase transition of the material. However, this is just hypothesis and further investigations are required to verify this. However this is not essential from the perspective of this manuscript since the spectroscopic properties of this material will be analyzed in the 0–7.75 GPa pressure range.

The spectroscopic properties of the Cr<sup>3+</sup> ions depend significantly on the crystal field strength [56,57]. Therefore, the change in the crystallographic position occupied by the Cr<sup>3+</sup> ions in the LMTO with an increase in the dopant concentration modifies their luminescence. To understand the change in the luminescence spectra of LMTO:Cr<sup>3+</sup>

**Table 1**Calculated crystal field parameters for LMTO:0.1 %Cr<sup>3+</sup> and 5 %Cr<sup>3+</sup> powders.

Position	E(4A <sub>2</sub> → <sup>4</sup> T <sub>2</sub> ) (cm <sup>-1</sup> )	Dq (cm <sup>-1</sup> )	E( <sup>4</sup> A <sub>2</sub> → <sup>4</sup> T <sub>1</sub> ) (cm <sup>-1</sup> )	x	Dq/B
Cr <sup>3+</sup> @ Ti <sup>4+</sup> site (0.1 %Cr <sup>3+</sup> )	16,574	1657.4	22,976	3.86	2.62
Cr <sup>3+</sup> @ Mg <sup>2+</sup> site (5 %Cr <sup>3+</sup> )	15,296	1529.6	21,896	4.31	2.25

induced either by dopant concentration or applied pressure the coordination configurational diagrams of Cr<sup>3+</sup> at Ti<sup>4+</sup> and Mg<sup>2+</sup> sites are presented in Fig. 4a. Short R distance at the Ti<sup>4+</sup> site results in a strong crystal field affecting Cr<sup>3+</sup> ions. Therefore the <sup>4</sup>T<sub>2</sub> state is localized above the minimum of the <sup>2</sup>E state and the dominant emission band observed for the LMTO:0.1 %Cr<sup>3+</sup> is a narrow line associated with the <sup>2</sup>E → <sup>4</sup>A<sub>2</sub> electronic transition. On the other hand, a much longer R distance for Cr<sup>3+</sup> at Mg<sup>2+</sup> results in the reduction of the energy of the <sup>4</sup>T<sub>2</sub> state below the <sup>2</sup>E ones. Hence the emission spectrum of LMTO:Cr<sup>3+</sup> for Cr<sup>3+</sup> concentration above 5 %Cr<sup>3+</sup> is dominated by the broad <sup>4</sup>T<sub>2</sub> → <sup>4</sup>A<sub>2</sub> emission band. The comparison of the emission spectra of LMTO:Cr<sup>3+</sup> measured at 123 K reveals that the change in the dopant concentration gradually changes the contribution ratio of the emission intensity from Cr<sup>3+</sup> in Ti<sup>4+</sup> to Mg<sup>2+</sup> sites. Observed change can be also observed in the comparison of the excitation spectra of LMTO:Cr<sup>3+</sup> (Fig. 4c). The change in the energy of the excitation bands with Cr<sup>3+</sup> concentration indicates modification of the crystal field strength. To quantify those changes the Dq/B parameter was calculated as follows [40]:

$$Dq = \frac{E(^4A_2 \rightarrow ^4T_2)}{10} \quad (2)$$

$$x = \frac{E(^4A_2 \rightarrow ^4T_1) - E(^4A_2 \rightarrow ^4T_2)}{Dq} \quad (3)$$

$$\frac{Dq}{B} = \frac{15(x - 8)}{(x^2 - 10x)} \quad (4)$$

The results presented in Table 1 indicate that the crystal field strength (Dq/B) parameter decreases from Dq/B = 2.62 for 0.1 %Cr<sup>3+</sup> to Dq/B = 2.25 for 5 %Cr<sup>3+</sup>. This is according to the expectations since the due to the difference in the ionic radii between dopant and replaced ions discussed above, lower crystal field strength is expected when Cr<sup>3+</sup> ions occupy Ti<sup>4+</sup> site.

The analysis of the luminescence kinetics of emitting state of Cr<sup>3+</sup> corresponds to the changes observed in the emission spectra and shortens from 875.15 μs for 0.1 %Cr<sup>3+</sup> to the 47.85 μs for 10 %Cr<sup>3+</sup> clearly indicating the change of the dominant emitting state from <sup>2</sup>E to <sup>4</sup>T<sub>2</sub> state (Figure S3).

The isostatic pressure applied to the host material causes the shrinkage of the crystallographic unit cell volume and thus the reduction of the R value. Hence, it is expected that the crystal field strength affecting Cr<sup>3+</sup> ions will increase with pressure. Therefore, in order to develop a highly sensitive ratiometric luminescence manometer based on the Cr<sup>3+</sup> luminescence a host material with a weak crystal field affecting the Cr<sup>3+</sup> ions is desirable. Since, as shown in Fig. 4b, the broad <sup>4</sup>T<sub>2</sub> → <sup>4</sup>A<sub>2</sub> emission band dominates in the emission spectrum of LMTO:Cr<sup>3+</sup> above 5 % of Cr<sup>3+</sup> ions and the increase of the dopant concentration reduced the integral emission intensity, the LMTO:5%Cr<sup>3+</sup> was found to be the optimal sample to be used in the further studies (the value of the applied pressure was readout based on the spectral position of the emission band of the pressure indicator Al<sub>2</sub>O<sub>3</sub>:Cr<sup>3+</sup> microcrystal Figure S4). As shown in Fig. 5a, the emission spectra of the analyzed sample consist of a broad emission band the centroid of which undergoes the spectral shift from 850 nm to 780 nm when the applied pressure increases from ambient to 7.75 GPa. The sharp line observed at around 694.3 nm is related to the pressure indicator signal of Cr<sup>3+</sup> in ruby

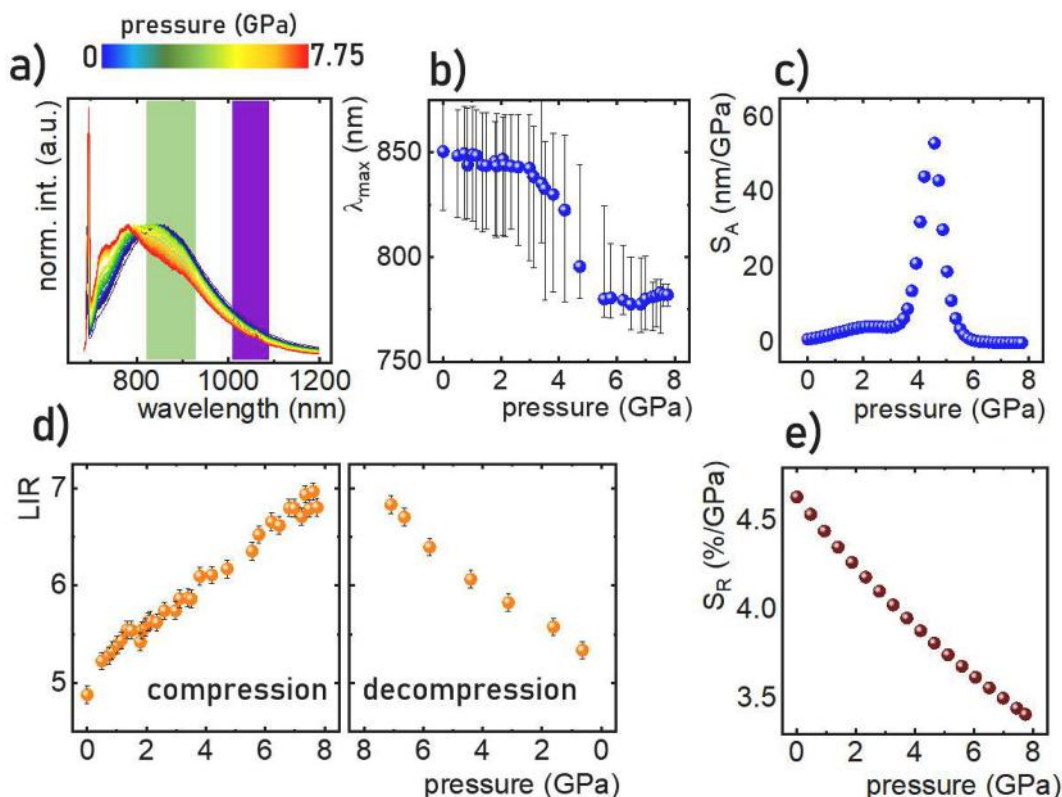


**Fig. 5.** The emission spectra of LMTO:5%Cr<sup>3+</sup> measured as a function of applied isostatic pressure ( $\lambda_{exc} = 445$  nm) -a);  ${}^4T_2 \rightarrow {}^4A_2$  band centroid as a function of applied pressure-b) and corresponding  $S_A$ -c); the LIR calculated as a function of applied pressure during compression and decompression-d) and the corresponding  $S_R$ -e).

(Al<sub>2</sub>O<sub>3</sub>:Cr<sup>3+</sup>). Besides the spectral shift of the emission band, it can be found that, for the pressure values above 4 GPa, the narrow emission band starts to rise up, which can be assigned to the  ${}^2E \rightarrow {}^4A_2$  transition. The occurrence of this emission band results from the increase of the crystal field strength and, since the  ${}^2E \rightarrow {}^4A_2$  emission band of the Cr<sup>3+</sup> ions localized at the Ti<sup>4+</sup> site as shown previously is localized around 720 nm, the band observed at high pressure can be assigned to the Cr<sup>3+</sup> ions localized at the Mg<sup>2+</sup> site.

When the shift of the band centroid is used as a manometric parameter, the change of its value by around 70 nm can be observed in the analyzed pressure range (Fig. 5b, see also data after Jacobian conversion Figure S10). However, the most prominent changes in its value are found in the relatively narrow range of pressures (3.1–5.0 GPa). The broad nature of the emission band results in the high value of uncertainty of the band centroid determination represented as error bars in Fig. 5b (error bars were determined as a spectral range in which the  $I_{max} \pm 5\%I_{max}$  was found, where  $I_{max}$  represents the maximal emission intensity for a given spectrum). Usually the relative sensitivity of luminescence sensors is determined to compare the sensing ability of given sensor. However, in the case of the spectral shift-based luminescent sensor, its usefulness is limited because the values obtained are largely dependent on the spectral range in which the band is present, which obviously does not carry practical information about sensing capabilities. Therefore, to quantify observed changes the absolute pressure sensitivity can be determined as follows:

$$S_A = \frac{\Delta\lambda_{max}}{\Delta p} \quad (5)$$

where  $\Delta\lambda_{max}$  represents the change of band centroid corresponding to the change of the pressure by  $\Delta p$ . As expected, the maximal value of  $S_A$  was found at 4.51 GPa and equals  $S_A = 53.66$  nm/GPa (Fig. 5c).

However, it should be noted here that below 3.3 GPa and above 5.5 GPa the  $S_A$  is very low as for the broad emitting pressure-sensitive phosphors. Moreover, low precision in the band centroid determination hinders the practical application of LMTO:Cr<sup>3+</sup> as a pressure sensor in this approach.

Therefore, the ratiometric approach is proposed, in which the luminescence intensity ratio of the integral emission intensities, calculated in the marked in Fig. 5a spectral ranges, (Figure S5) is used as a manometric parameter:

$$LIR = \frac{\int_{825nm}^{935nm} {}^4T_2 \rightarrow {}^4A_2 d\lambda}{\int_{1005nm}^{1095nm} {}^4T_2 \rightarrow {}^4A_2 d\lambda} \quad (6)$$

In the case of the LMTO:Cr<sup>3+</sup> the LIR increases monotonically from 5 to 7 (Fig. 5d), in the whole pressure range studied. An additional advantage of this optical manometer is a linear trend of the LIR vs pressure, which facilitates the interpolation of the pressure readouts in the analyzed pressure range. The observed changes in the spectroscopic properties of the LMTO:Cr<sup>3+</sup> are associated only with the shrinkage of the R distance, and not with the decomposition of the material, which is confirmed by the excellent reproduction of the pressure dependence of LIR during the decompression process (Fig. 5d, Figure S6, Figure S11, see also Figure S12 for LIR analysis with 3 cycles of compression and decompression). The relative sensitivity of LIR to pressure changes can be determined using the following equation:

$$S_R = \frac{1}{LIR} \frac{\Delta LIR}{\Delta p} 100\% \quad (7)$$

As shown in Fig. 5e, the LMTO:5%Cr<sup>3+</sup> is characterized by the high value of the  $S_R$  in the whole analyzed pressure range. The  $S_R$  decreases linearly from  $S_R = 4.7$  %/GPa at ambient pressure to 3.3 %/GPa at 7.5 GPa. This confirms the good sensing performance of the proposed manometer. Additionally, the error in the determination of LIR is associated with the emission intensity and is much lower comparing to the

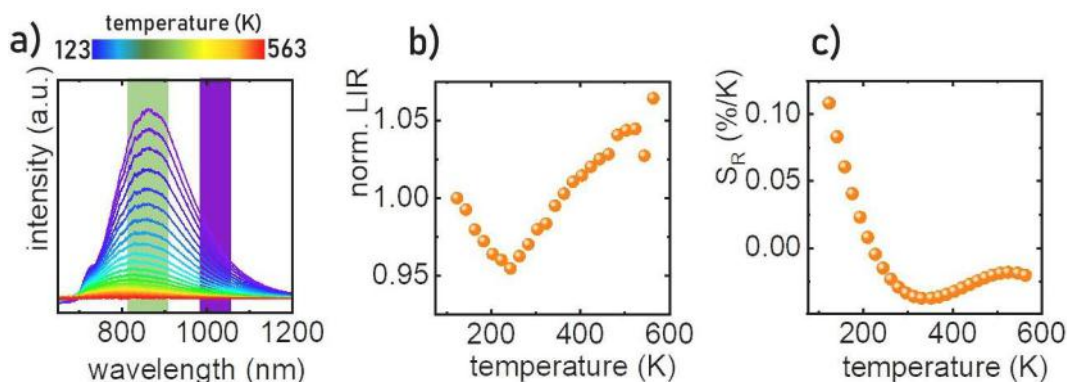


**Fig. 6.** The emission spectra of LMTO:5%Cr<sup>3+</sup> measured as a function of temperature ( $\lambda_{\text{exc}} = 445$  nm) -a); the normalized LIR values as a function of temperature-b) and corresponding thermal dependence of  $S_R$  -c).

centroid shift approach. Another important manometric parameter is the pressure determination uncertainty  $\delta p$ , which can be determined using eq. S1. As shown in Figure S13 for LMTO:5%Cr<sup>3+</sup> the  $\delta p$  increases at an elevated pressure which is expected since both emission signal and  $S_R$  decreases at higher applied temperatures. Nevertheless, the  $\delta p$  remains  $< 0.18$  GPa is the analyzed 0–7.75 GPa pressure range.

The key aspect of the pressure-sensitive luminescent materials is to provide a pressure readout that is independent of other experimental conditions. Among them, the temperature may most significantly affect the spectroscopic properties of the phosphor. Therefore in order to verify the influence of the temperature on the spectroscopic properties of the LMTO:5%Cr<sup>3+</sup>, its emission spectra were measured at temperatures changed in the 123–563 K range (Fig. 6a, Figure S7). It can be clearly seen that the increase in temperature results in the gradual lowering of the emission intensity, whereas the spectral position of the band maxima remains almost unchanged. To verify the influence of temperature on LIR the emission intensities integrated into exactly the same spectral range as in the manometric part of the analysis (see eq. (6)) were calculated and their ratio was plotted in a function of temperature (Fig. 6b). It was found that the LIR changes its value by only 5 % when the temperature was changed from 123 K to 563 K. This results in the relative thermal sensitivity lower than  $S_R = 0.1$  %/K and above 200 K  $S_R < 0.05$  %/K (Fig. 6c). This confirms that using the ratiometric approach for the LMTO:5%Cr<sup>3+</sup>, the pressure readouts are almost not affected by the temperature variations.

## 5. Conclusions

Spectral shift is one of the most widely used manometric parameters in luminescence manometry. Therefore, to redout the pressure values either narrow or broad band emitting luminescence manometer are developed. In a response to the limitations of both of these approaches related to low sensitivity in the former case and low precision of the later one, a new approach is proposed in this work. It is based on the ratiometric readout of emission intensities integrated in two spectral regions for the broad emission band  ${}^4T_2 \rightarrow {}^4A_2$  of Cr<sup>3+</sup> ions in LMTO. An increase in the pressure causing a leads to the reduction in the Cr<sup>3+</sup>–O<sup>2-</sup> distance causing an enhancement in the strength of the crystal field affecting Cr<sup>3+</sup> ions. Thus, the energy of the  ${}^4T_2$  band changes and consequently the position of the band associated with the depopulation of this level spectrally shifts. As has been shown, in order to design such a manometer, it is advantageous to exploit a high concentration of Cr<sup>3+</sup> ions, because in the case of low concentrations Cr<sup>3+</sup> ions occupy Ti<sup>4+</sup> positions characterized by a strong crystal field. For high concentrations of Cr<sup>3+</sup> ions, the luminescence spectrum is dominated by the  ${}^4T_2 \rightarrow {}^4A_2$  band coming from Cr<sup>3+</sup> ions occupying the position of Mg<sup>2+</sup> ions. As shown, this approach allows monotonic LIR variation in the range of 0–7.75 GPa and  $S_R = 4.7$  %/GPa sensitivity. In addition, the temperature

change in the range of 123–563 K hardly affects the readouts of pressure values. Moreover, the fact that the LIR shows the same pressure dependence during both compression and decompression cycles, suggests the high application potential of this luminescent manometer.

## Declaration of Competing Interest

The authors declare the following financial interests/personal relationships which may be considered as potential competing interests: Lukasz Marciniak reports financial support was provided by National Science Centre Poland.

## Data availability

Data will be made available on request.

## Acknowledgements

This work was supported by the National Science Center (NCN) Poland under project no. DEC-UMO- 2020/37/B/ST5/00164. This work was also supported by the Spanish Ministerio de Economía y Competitividad (MINECO) under the National Program of Sciences and Technological Materials (PID2019-106383GB-44), and by EU-FEDER funds. M.R. acknowledges support from Fondo Social Europeo and Agencia Estatal de Investigación (RYC2020-028778-I/AEI/10.13039/501100011033).

## Appendix A. Supplementary data

Supplementary data to this article can be found online at <https://doi.org/10.1016/j.cej.2022.139632>.

## References

- [1] A. Kumari, M.K. Mahata, Chapter 12 - Upconversion nanoparticles for sensing applications, in: S. Thomas, K. Upadhyay, R.K. Tamrakar, N.B.T.-U.N. Kalarikkal (Eds.), *Micro Nano Technol.*, Elsevier, 2022: pp. 311–336.
- [2] C.B.T.-R.M. in M.S. and M.E. Ronda, *Rare-Earth Phosphors: Fundamentals and Applications*, in: Elsevier, 2017.
- [3] C.C. Klick, J.H. Schulman, *Luminescence in Solids*, in: F. SEITZ, D.B.T.-S.S.P. TURNBULL (Eds.), *Solid State Phys. - Adv. Res. Appl.*, Academic Press, 1957: pp. 97–172.
- [4] M.D. Drmicin, *Sensing temperature via downshifting emissions of lanthanide-doped metal oxides and salts. A review*, *Methods Appl. Fluoresc.* 4 (2016) 42001.
- [5] S. Wang, S. Westcott, W. Chen, *Nanoparticle luminescence thermometry*, *J. Phys. Chem. B.* 106 (43) (2002) 11203–11209.
- [6] C.D.S. Brites, A. Millán, L.D. Carlos, *Lanthanides in Luminescent Thermometry*, in: B. Jean-Claude, P.B.T.-H. on the P. and C. of R.E. Vitalij K. (Eds.), *Handb. Phys. Chem. Rare Earths*, Elsevier, 2016: pp. 339–427.
- [7] J. Zhou, B. del Rosal, D. Jaque, S. Uchiyama, D. Jin, *Advances and challenges for fluorescence nanothermometry*, *Nat. Methods.* 17 (10) (2020) 967–980.



- [8] D. Jaque, C. Jacinto, Luminescent nanoprobes for thermal bio-sensing: Towards controlled photo-thermal therapies, *J. Lumin.* 169 (2016) 394–399.
- [9] X.D. Wang, O.S. Wolfbeis, R.J. Meier, Luminescent probes and sensors for temperature, *Chem. Soc. Rev.* 42 (2013) 7834–7869.
- [10] A. Bednarkiewicz, J. Drabik, K. Trejgis, D. Jaque, E. Ximendes, L. Marciniak, Luminescence based temperature bio-imaging: Status, challenges, and perspectives, *Appl. Phys. Rev.* 8 (1) (2021) 011317.
- [11] L. Marciniak, K. Kniec, K. Elżbieciak-Piecka, K. Trejgis, J. Stefanska, M. Dramićanin, Luminescence thermometry with transition metal ions. A review, *Coord. Chem. Rev.* 469 (2022), 214671.
- [12] A.M. Kaczmarek, M. Suta, H. Rijckaert, A. Abalymov, I. Van Driessche, A. G. Skirtach, A. Meijerink, P. Van Der Voort, Visible and NIR Upconverting  $\text{Er}^{3+}$ - $\text{Yb}^{3+}$  Luminescent Nanorattles and Other Hybrid PMO-Inorganic Structures for In Vivo Nanothermometry, *Adv. Funct. Mater.* 30 (2020) 2003101.
- [13] A. Bednarkiewicz, L. Marciniak, L.D. Carlos, D. Jaque, Standardizing luminescence nanothermometry for biomedical applications, *Nanoscale*. 12 (27) (2020) 14405–14421.
- [14] B. del Rosal, E. Ximendes, U. Rocha, D. Jaque, In Vivo Luminescence Nanothermometry: from Materials to Applications, *Adv. Opt. Mater.* 5 (1) (2017) 1600508.
- [15] K. Kniec, L. Marciniak, A ratiometric luminescence pH sensor based on  $\text{YAG}:\text{V}^{3+}$ ,  $\text{V}^{5+}$  nanoparticles, *New J. Chem.* 46 (2022) 11562–11569.
- [16] M. Runowski, A. Shyichuk, A. Tyminiński, T. Gryzb, V. Lavín, S. Lis, Multifunctional Optical Sensors for Nanomanometry and Nanothermometry: High-Pressure and High-Temperature Upconversion Luminescence of Lanthanide-Doped Phosphates -  $\text{LaPO}_4/\text{YPO}_4:\text{Yb}^{3+}, \text{Tm}^{3+}$ , *ACS Appl. Mater. Interfaces*. 10 (2018) 17269–17279.
- [17] T. Zheng, L. Luo, P. Du, S. Lis, U.R. Rodríguez-Mendoza, V. Lavín, I.R. Martín, M. Runowski, Pressure-triggered enormous redshift and enhanced emission in  $\text{Ca}_2\text{Gd}_2\text{Si}_2\text{O}_6:\text{Ce}^{3+}$  phosphors: Ultrasensitive, thermally-stable and ultrafast response pressure monitoring, *Chem. Eng. J.* 443 (2022), 136414.
- [18] B.R. Jovanic, J.P. Andreeta,  $\text{GdAlO}_3:\text{Cr}^{3+}$  as a New Pressure Sensor, *Phys. Scr.* 59 (1999) 274–276.
- [19] J.D. Barnett, S. Block, G.J. Piermarini, An optical fluorescence system for quantitative pressure measurement in the diamond-anvil cell, *Rev. Sci. Instrum.* 44 (1) (1973) 1–9.
- [20] U.R. Rodríguez-Mendoza, S.F. León-Luis, J.E. Muñoz-Santiuste, D. Jaque, V. Lavín,  $\text{Nd}^{3+}$ -doped  $\text{Ca}_3\text{Ga}_2\text{Ge}_3\text{O}_{12}$  garnet: A new optical pressure sensor, *J. Appl. Phys.* 113 (2013), 213517.
- [21] M. Runowski, P. Woźny, I.R. Martín, Optical pressure sensing in vacuum and high-pressure ranges using lanthanide-based luminescent thermometer-manometer, *J. Mater. Chem. C*. 9 (13) (2021) 4643–4651.
- [22] M. Runowski, J. Marciniak, T. Gryzb, D. Przybylska, A. Shyichuk, B. Barszcz, A. Katrusiak, S. Lis, Lifetime nanomanometry – high-pressure luminescence of up-converting lanthanide nanocrystals –  $\text{SrF}_2:\text{Yb}^{3+}$ ,  $\text{Er}^{3+}$ , *Nanoscale*. 9 (41) (2017) 16030–16037.
- [23] C. Hernandez, S.K. Gupta, J.P. Zuniga, J. Vidal, R. Galvan, M. Martinez, H. Guzman, L. Chavez, Y. Mao, K. Lozano, Performance evaluation of  $\text{Ce}^{3+}$  doped flexible PVDF fibers for efficient optical pressure sensors, *Sensors Actuators A Phys.* 298 (2019), 111595.
- [24] J. Barzowska, T. Lesniewski, S. Mahlik, H.J. Seo, M. Grinberg,  $\text{KMgF}_3:\text{Eu}^{2+}$  as a new fluorescence-based pressure sensor for diamond anvil cell experiments, *Opt. Mater. (Amst)* 84 (2018) 99–102.
- [25] F. Datchi, R. LeToullec, P. Loubeyre, Improved calibration of the  $\text{SrB}_4\text{O}_7:\text{Sm}^{2+}$  optical pressure gauge: advantages at very high pressures and high temperatures, *J. Appl. Phys.* 81 (1997) 3333–3339.
- [26] M. Runowski, P. Woźny, N. Stopikowska, Q. Guo, S. Lis, Optical pressure sensor based on the emission and excitation band width (FWHM) and luminescence shift of  $\text{Ce}^{3+}$ -doped fluorapatite—high-pressure sensing, *ACS Appl. Mater. Interfaces*. 11 (4) (2019) 4131–4138.
- [27] M.D. Wisser, M. Chea, Y.u. Lin, D.M. Wu, W.L. Mao, A. Salleo, J.A. Dionne, Strain-induced modification of optical selection rules in lanthanide-based upconverting nanoparticles, *Nano Lett.* 15 (3) (2015) 1891–1897.
- [28] A. Lay, D.S. Wang, M.D. Wisser, R.D. Mehlenbacher, Y.u. Lin, M.B. Goodman, W. L. Mao, J.A. Dionne, Upconverting nanoparticles as optical sensors of nano- to micro-newton forces, *Nano Lett.* 17 (7) (2017) 4172–4177.
- [29] M. Back, J. Ueda, H. Hua, S. Tanabe, Predicting the optical pressure sensitivity of  $^2\text{E} \rightarrow ^4\text{A}_2$  spin-flip transition in  $\text{Cr}^{3+}$ -doped crystals, *Chem. Mater.* 33 (9) (2021) 3379–3385.
- [30] T. Zheng, M. Sójka, P. Woźny, I.R. Martín, V. Lavín, E. Zych, S. Lis, P. Du, L. Luo, M. Runowski, Supersensitive Ratiometric Thermometry and Manometry Based on Dual-Emitting Centers in  $\text{Eu}^{2+}/\text{Sm}^{2+}$ -Doped Strontium Tetraborate Phosphors, *Adv. Opt. Mater.* n/a (2022) 2201055. <https://doi.org/10.1002/adom.202201055>.
- [31] T. Zheng, M. Runowski, P. Rodríguez-Hernández, A. Muñoz, F.J. Manjón, M. Sójka, M. Suta, E. Zych, S. Lis, V. Lavín, Pressure-driven configurational crossover between  $4f^7$  and  $4f^65d^1$  states – giant enhancement of narrow  $\text{Eu}^{2+}$  UV-emission lines in  $\text{SrB}_4\text{O}_7$  for luminescence manometry, *Acta Mater.* 231 (2022), 117886.
- [32] T. Zheng, M. Sójka, M. Runowski, P. Woźny, S. Lis, E. Zych,  $\text{Tm}^{2+}$  Activated  $\text{SrB}_4\text{O}_7$  bifunctional sensor of temperature and pressure—highly sensitive, multi-parameter luminescence thermometry and manometry, *Adv. Opt. Mater.* 9 (2021) 2101507.
- [33] H.K. Mao, P.M. Bell, J.W. Shaner, D.J. Steinberg, Specific volume measurements of Cu, Mo, Pd, and Ag and calibration of the ruby R1 fluorescence pressure gauge from 0.06 to 1 Mbar, *J. Appl. Phys.* 49 (6) (1978) 3276–3283.
- [34] D. Zhang, B. Zheng, Z. Zheng, L. Li, Q. Yang, Y. Song, B. Zou, H. Zou, Multifunctional  $\text{Ca}_9\text{NaZn}_{1-3}\text{Mg}_3(\text{PO}_4)_7:\text{Eu}^{2+}$  phosphor for full-spectrum lighting, optical thermometry and pressure sensor applications, *Chem. Eng. J.* 431 (2022), 133805.
- [35] Y. Wang, T. Seto, K. Ishigaki, Y. Uwatoke, G. Xiao, B. Zou, G. Li, Z. Tang, Z. Li, Y. Wang, Pressure-driven  $\text{Eu}^{2+}$ -doped  $\text{BaLi}_2\text{Al}_2\text{Si}_2\text{N}_6$ : a new color tunable narrow-band emission phosphor for spectroscopy and pressure sensor applications, *Adv. Funct. Mater.* 30 (2020) 2001384.
- [36] C. Garapon, A. Brenier, R. Moncorgé, Site-selective optical spectroscopy of  $\text{Cr}^{3+}$  doped non-stoichiometric green spinel  $\text{MgO}-2.6 \text{ Al}_2\text{O}_3$ , *Opt. Mater. (Amst)*. 10 (3) (1998) 177–189.
- [37] G. Walker, A. El Jaer, R. Sherlock, T.J. Glynn, M. Czaja, Z. Mazurak, Luminescence spectroscopy of  $\text{Cr}^{3+}$  and  $\text{Mn}^{2+}$  in spodumene ( $\text{LiAlSi}_2\text{O}_6$ ), *J. Lumin.* 72–74 (1997) 278–280.
- [38] D.R. Lee, T.P.J. Han, B. Henderson, Charge compensation and the spectroscopy of  $\text{Cr}^{3+}$  in  $\text{KMgF}_3$ , *Radiat. Eff. Defects Solids*. 136 (1-4) (1995) 51–55.
- [39] A. Lucì, M. Casalboni, T. Castrignanò, U.M. Grassano, A.A. Kaminskii, Optical properties of  $\text{Cr}^{3+}$ -ions in  $\text{LaSr}_2\text{Ga}_{11}\text{O}_{20}$ , *Radiat. Eff. Defects Solids*. 135 (1-4) (1995) 227–230.
- [40] M. Casalboni, A. Lucì, U.M. Grassano, B.V. Mill, A.A. Kaminskii, Optical spectroscopy of  $\text{La}_3\text{Ga}_5\text{SiO}_{14}:\text{Cr}^{3+}$  crystals, *Phys. Rev. B*. 49 (1994) 3781–3790.
- [41] J.E. House, Chapter 17 - Ligand Fields and Molecular Orbitals, in: J.E.B.T.-I.C. (Second E. House (Ed.), Academic Press, 2013: pp. 591–616.
- [42] M.G. Brik, N.M. Avram, Microscopic analysis of the crystal field strength and electron-vibrational interaction in cubic  $\text{SrTiO}_3$  doped with  $\text{Cr}^{3+}$ ,  $\text{Mn}^{4+}$  and  $\text{Fe}^{5+}$  ions, *J. Phys. Condens. Matter*. 21 (2009), 155502.
- [43] K. Ye, Z. Yan, X. Yang, S. Xiao, Enhanced red emission in  $\text{Li}_2\text{Mg}_3\text{TiO}_6:\text{Mn}^{4+}$  phosphor via  $\text{Na}^+$  and  $\text{Ge}^{4+}$  doping, *Opt. Mater. (Amst)*. 121 (2021) 111480.
- [44] Y. Zhao, P. Zhang, Microstructure and microwave dielectric properties of low loss materials  $\text{Li}_3(\text{Mg}_{0.95}\text{Al}_{0.05})_2\text{NbO}_6$  ( $A = \text{Ca}^{2+}, \text{Ni}^{2+}, \text{Zn}^{2+}, \text{Mn}^{2+}$ ) with rock-salt structure, *J. Alloys Compd.* 658 (2016) 744–748.
- [45] Z. Fu, P. Liu, J. Ma, X. Zhao, H. Zhang, Novel series of ultra-low loss microwave dielectric ceramics:  $\text{Li}_2\text{Mg}_3\text{BO}_6$  ( $B = \text{Ti}, \text{Sn}, \text{Zr}$ ), *J. Eur. Ceram. Soc.* 36 (3) (2016) 625–629.
- [46] T. Tan, S. Wang, J. Su, W. Yuan, H. Wu, R. Pang, J. Wang, C. Li, H. Zhang, Design of a novel near-infrared luminescence material  $\text{Li}_2\text{Mg}_3\text{TiO}_6:\text{Cr}^{3+}$  with an ultrawide tuning range applied to near-infrared light-emitting diodes, *ACS Sustain. Chem. Eng.* 10 (2022) 3839–3850.
- [47] M.P. Pechini, Method of preparing lead and alkaline earth titanates and niobates and coating method using the same to form a capacitor, 1967.
- [48] G. Shen, Y. Wang, A. Dewaele, C. Wu, D.E. Fratanduono, J. Eggert, S. Klotz, K.F. Dziubek, P. Loubeyre, O. V. Fat'yanov, P.D. Asimow, T. Mashimo, R.M.M. Wentzcovitch, Toward an international practical pressure scale: A proposal for an IPPS ruby gauge (IPPS-Ruby2020), 40 (2020) 299–314.
- [49] M. Ma, J. Guo, W. Ma, H. Zhao, Y. Yang, J. Gao, Synthesis, characterization and microwave dielectric properties of rock-salt structure  $\text{Li}_2\text{Mg}_3\text{TiO}_6$  via aqueous sol-gel method, *J. Mater. Sci. Mater. Electron.* 29 (6) (2018) 4955–4960.
- [50] Z. Fu, P. Liu, J. Ma, X. Chen, H. Zhang, New high Q low-fired  $\text{Li}_2\text{Mg}_3\text{TiO}_6$  microwave dielectric ceramics with rock salt structure, *Mater. Lett.* 164 (2016) 436–439.
- [51] H. Zhou, X. Tan, J. Huang, N. Wang, G. Fan, X. Chen, Phase structure, sintering behavior and adjustable microwave dielectric properties of  $\text{Mg}_{1-x}\text{Li}_{2x}\text{Ti}_x\text{O}_{1+2x}$  solid solution ceramics, *J. Alloys Compd.* 696 (2017) 1255–1259.
- [52] J. Ma, Z. Fu, P. Liu, L. Zhao, B. Guo, Ultralow-fired  $\text{Li}_2\text{Mg}_3\text{TiO}_6$ - $\text{Ca}_{0.8}\text{Sr}_{0.2}\text{TiO}_3$  composite ceramics with temperature stable at microwave frequency, *J. Alloys Compd.* 709 (2017) 299–303.
- [53] F. Luo, B. Tang, Z. Fang, Y. Yuan, H. Li, S. Zhang, Effects of coupling agent on dielectric properties of PTFE based and  $\text{Li}_2\text{Mg}_3\text{TiO}_6$  filled composites, *Ceram. Int.* 45 (16) (2019) 20458–20464.
- [54] X. Shi, H. Zhang, D. Zhang, F. Xu, Y. Zheng, G. Wang, C. Liu, L. Jin, J. Li, L. Jia, Correlation between structure characteristics and dielectric properties of  $\text{Li}_2\text{Mg}_3\text{TiO}_6$  ceramics based on complex chemical bond theory, *Ceram. Int.* 45 (17) (2019) 23509–23514.
- [55] M. Peng, Z. Pei, G. Hong, Q. Su, The reduction of  $\text{Eu}^{3+}$  to  $\text{Eu}^{2+}$  in  $\text{BaMgSiO}_4:\text{Eu}$  prepared in air and the luminescence of  $\text{BaMgSiO}_4:\text{Eu}^{2+}$  phosphor, *J. Mater. Chem.* 13 (2003) 1202–1205.
- [56] B. Struve, G. Huber, The effect of the crystal field strength on the optical spectra of  $\text{Cr}^{3+}$  in gallium garnet laser crystals, *Appl. Phys. B*. 36 (4) (1985) 195–201.
- [57] K. Elzbieciak, A. Bednarkiewicz, L. Marciniak, Temperature sensitivity modulation through crystal field engineering in  $\text{Ga}^{3+}$  co-doped  $\text{Gd}_3\text{Al}_{5-x}\text{Ga}_x\text{O}_{12}:\text{Cr}^{3+}, \text{Nd}^{3+}$  nanothermometers, *Sensors Actuators, B Chem.* 269 (2018) 96–102.



## Supporting Information

### Temperature invariant ratiometric luminescence manometer based on Cr<sup>3+</sup> ions emission

**M. Szymczak<sup>1</sup>, P. Woźny<sup>2</sup>, M. Runowski<sup>2,3</sup>, M. Pieprz<sup>1</sup>, V. Lavín<sup>3</sup>, L.**

**Marciniak<sup>1\*</sup>**

<sup>1</sup> Institute of Low Temperature and Structure Research, Polish Academy of Sciences,

Okólna 2, 50-422 Wrocław, Poland

<sup>2</sup> Adam Mickiewicz University, Faculty of Chemistry, Uniwersytetu Poznańskiego 8,

61-614 Poznań, Poland

<sup>3</sup> Departamento de Física, Universidad de La Laguna, Apartado de Correos 456, E-38200 San

Cristóbal de La Laguna, Santa Cruz de Tenerife, Spain

\* corresponding author: [l.marciniak@intibs.pl](mailto:l.marciniak@intibs.pl)

*KEYWORDS luminescent manometry, pressure sensor, Cr<sup>3+</sup>, chromium(III), thermal  
quenching, crystal field strength*

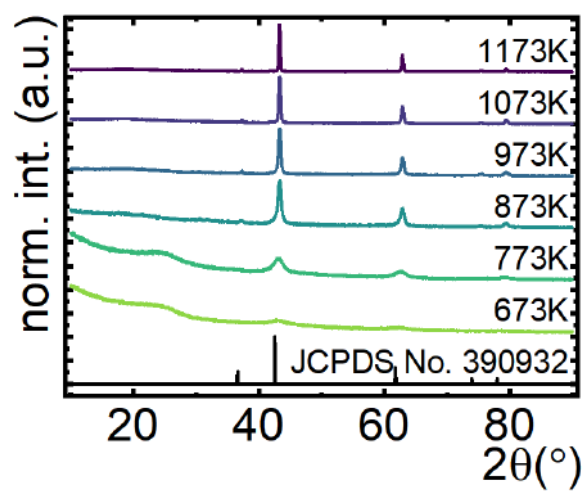


**Figure S1.** XRD patterns of LMTO:5%Cr<sup>3+</sup> powders annealed at different temperatures.

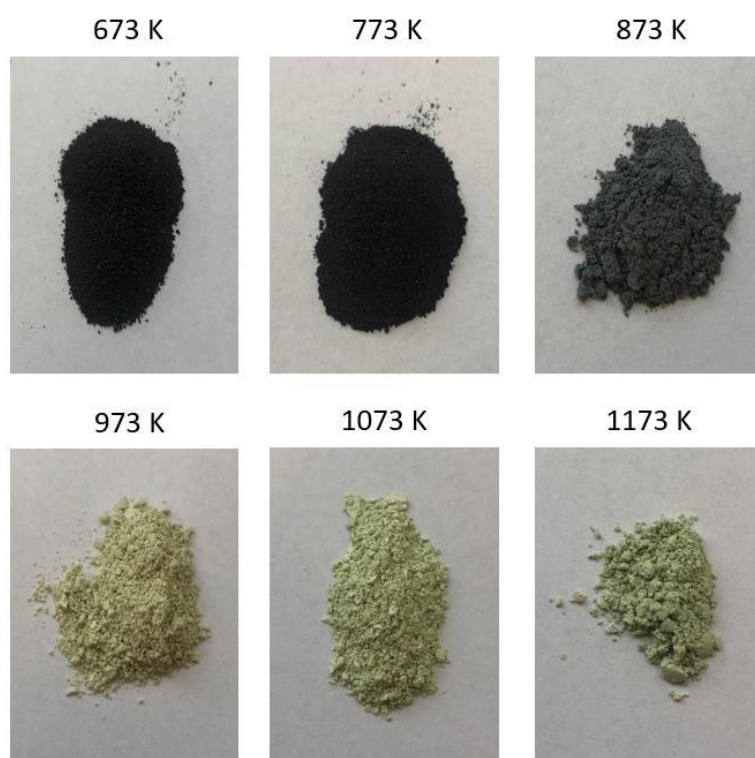
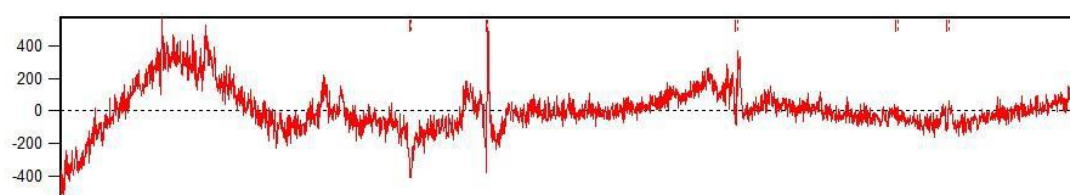
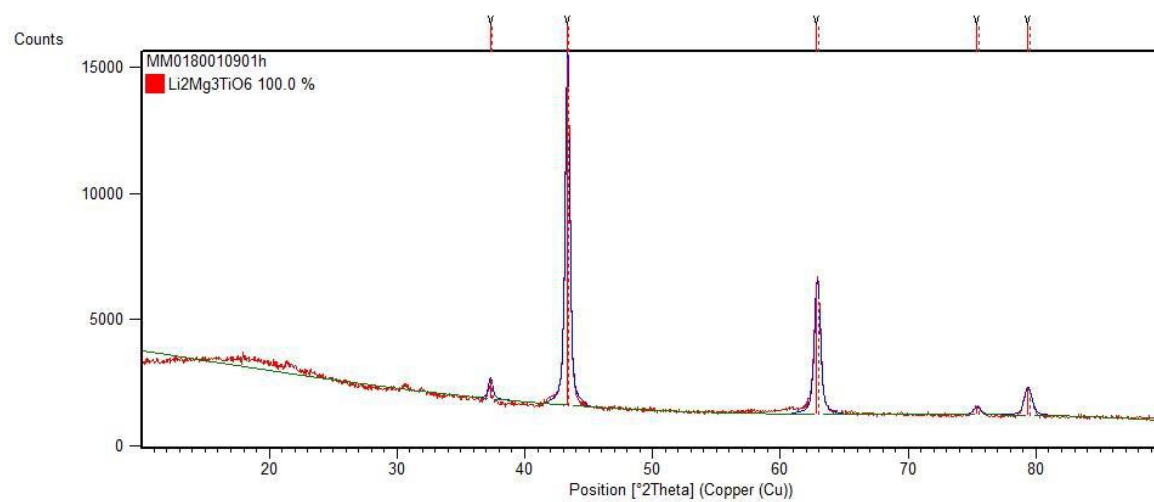
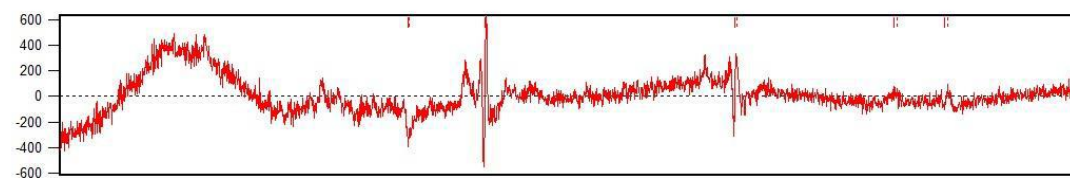
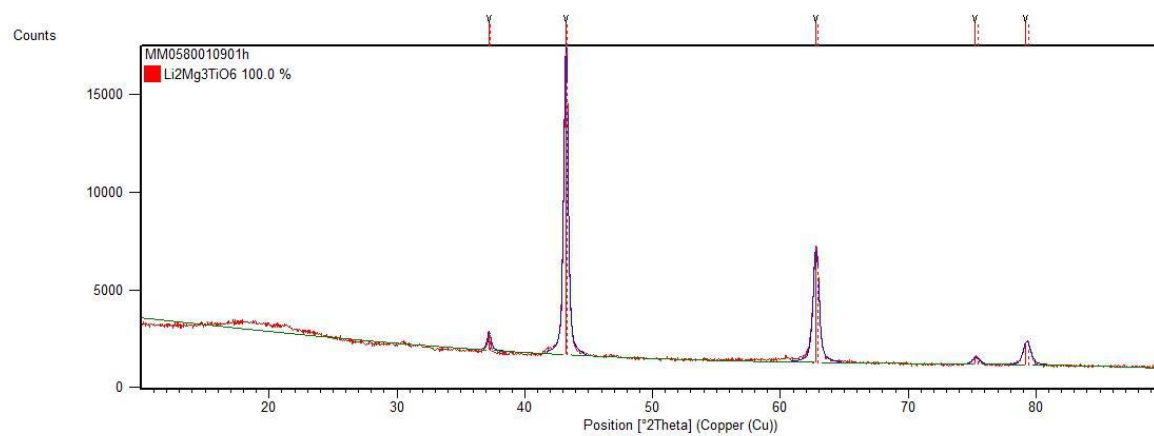


**Figure S2.** Photos of LMTO:5%Cr<sup>3+</sup> powders annealed at different temperatures.

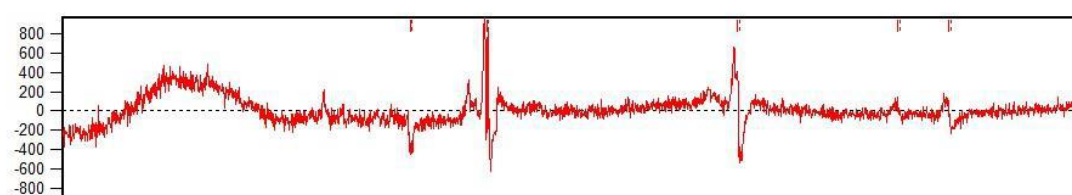
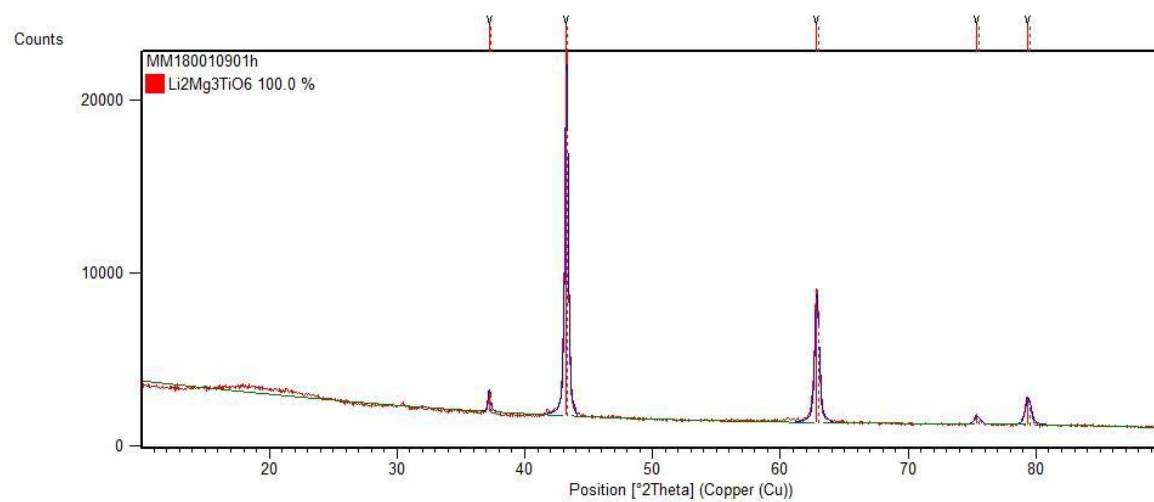
a)



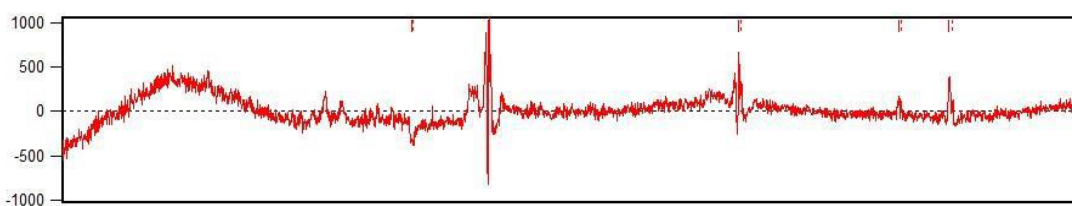
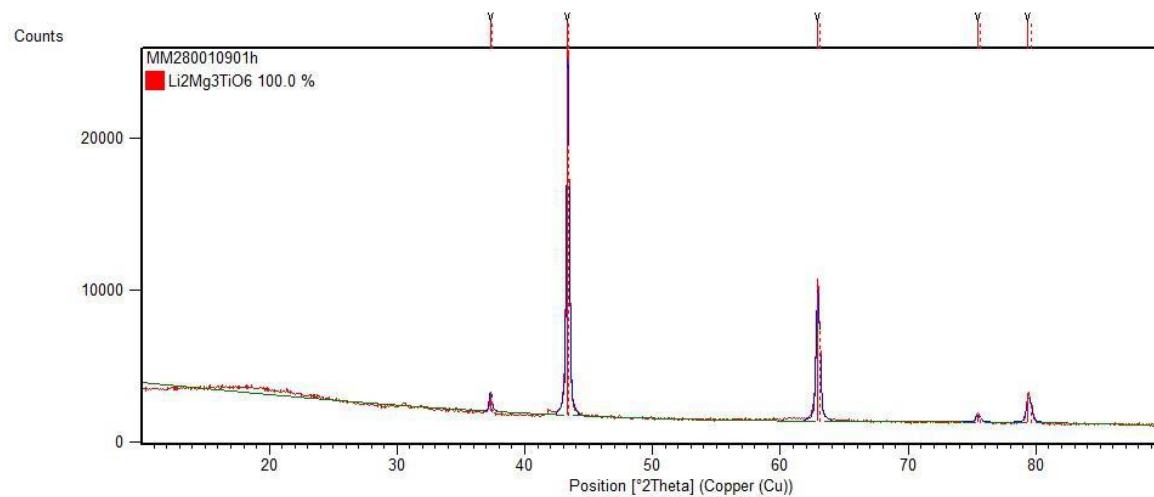
b)



c)



d)



e)

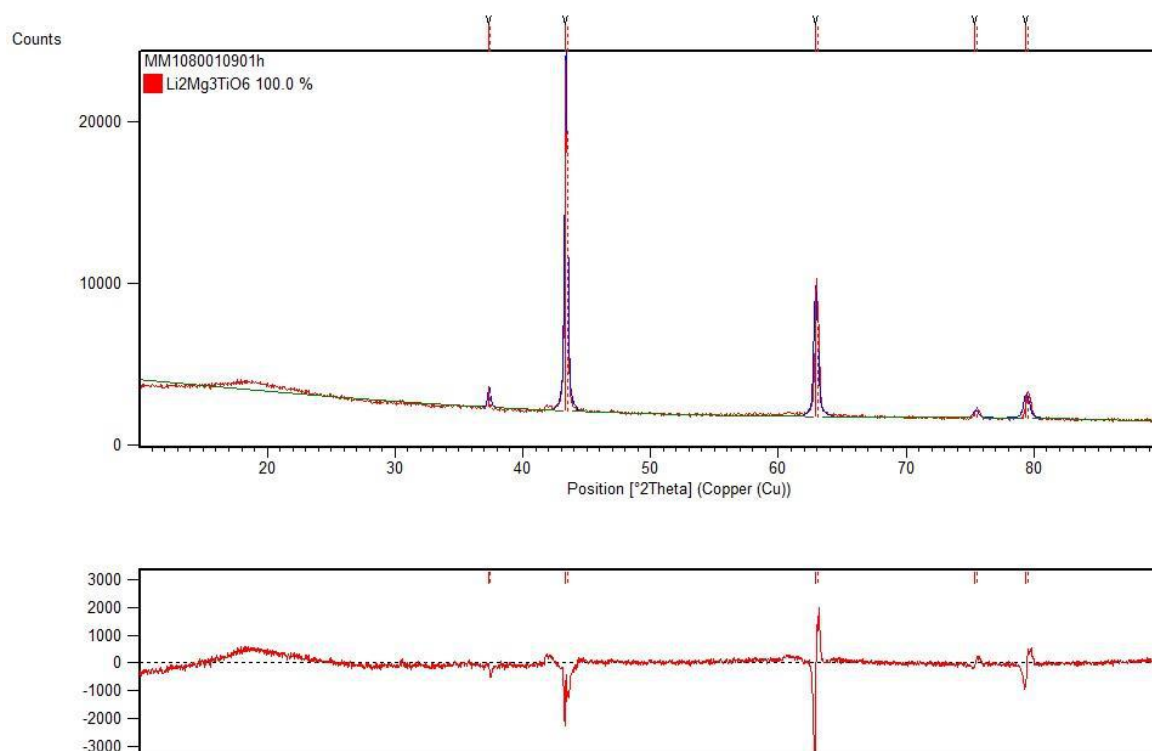


**Figure S3.** The results of the Rietveld refinement of the XRD patterns of LMTO:Cr<sup>3+</sup> with: 0.1% Cr<sup>3+</sup>-a); 0.5% Cr<sup>3+</sup>-b); 1% Cr<sup>3+</sup>-c); 2% Cr<sup>3+</sup>-d) and 5% Cr<sup>3+</sup>-e).

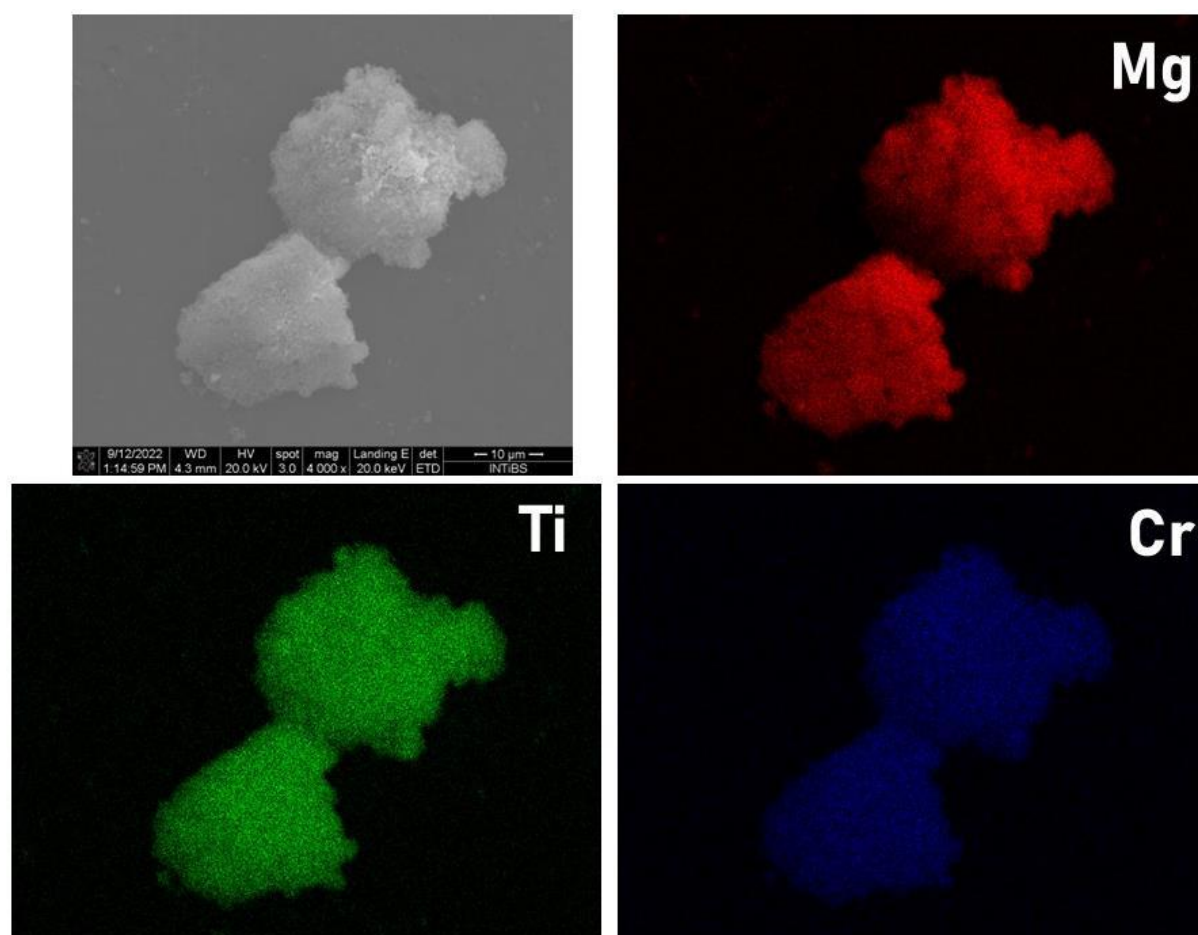


**Figure S4.** The representative SEM image of LMTO:5%Cr<sup>3+</sup> and the atom distribution maps of Mg, Ti and Cr.

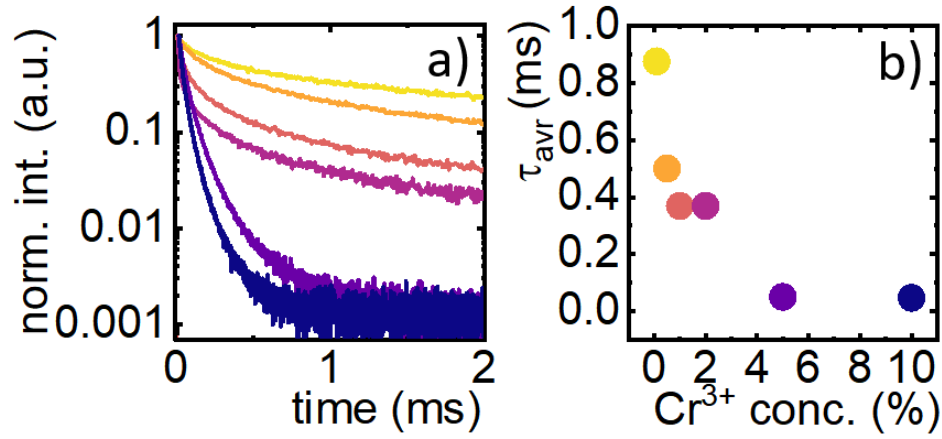


**Figure S5.** Luminescence decay profiles of LMTO: $x\%$ Cr<sup>3+</sup> ( $x = 0.1-10$ ) measured at 123K upon  $\lambda_{exc} = 445$  nm-a) and corresponding  $\tau_{avr}$ -b).

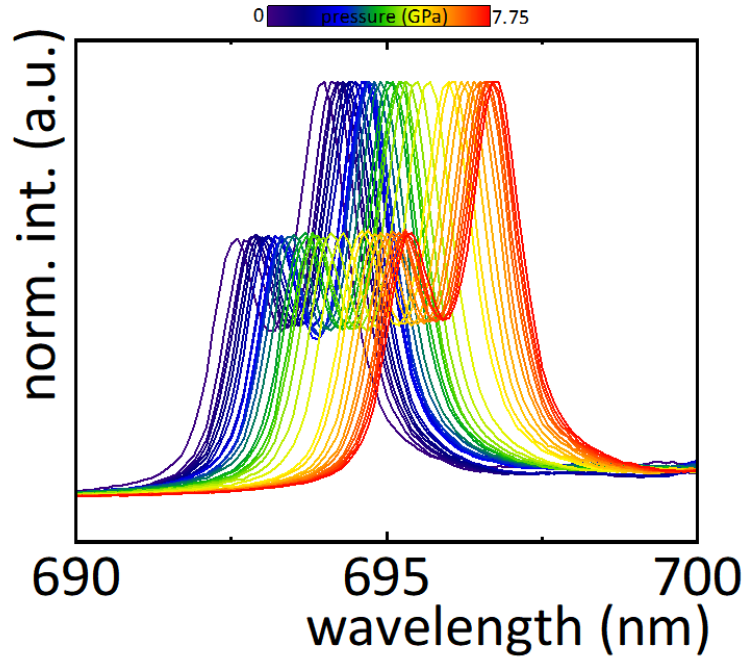


**Figure S6.** Emission spectra of Al<sub>2</sub>O<sub>3</sub>:Cr<sup>3+</sup> (pressure indicator during LMTO measurement) as function of pressure, measured upon  $\lambda_{exc} = 445$  nm.

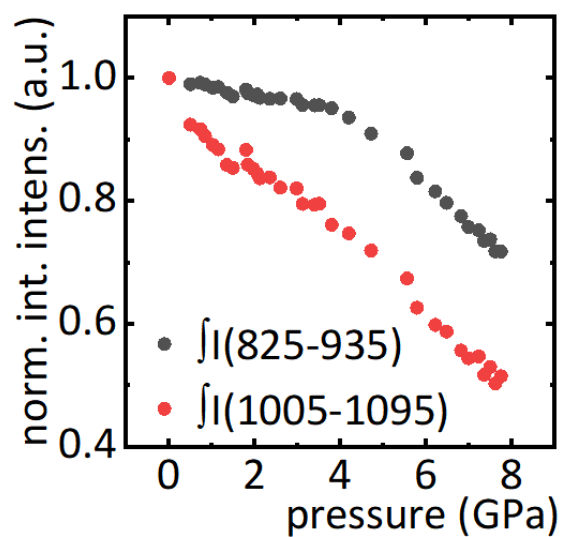


**Figure S7.** Pressure dependence of the emission intensity of  $\text{Cr}^{3+}$  integrated into two spectral ranges

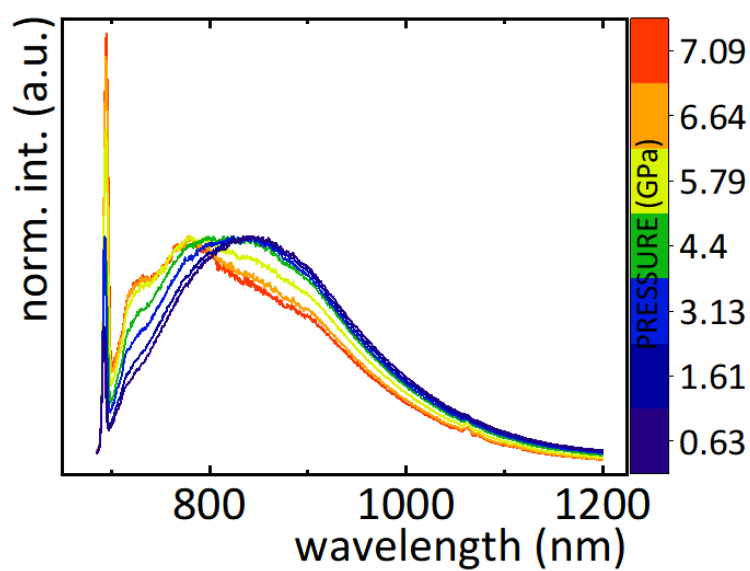


**Figure S8.** Emission spectra of LMTO:5% $\text{Cr}^{3+}$  nanoparticles measured as a function of pressure (decompression), upon  $\lambda_{\text{exc}} = 445$  nm.

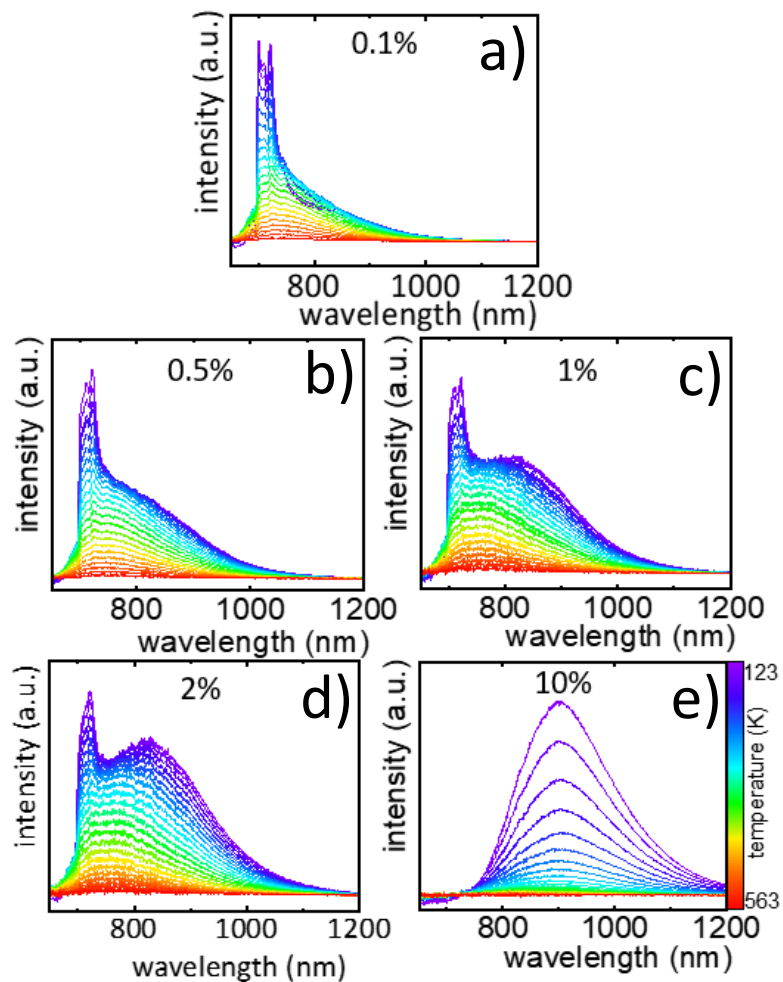


**Figure S9.** Emission spectra of LMTO:Cr<sup>3+</sup> powders measured as a function of temperature upon  $\lambda_{\text{exc}} = 445$  nm for 0.1%Cr<sup>3+</sup>-a), 0.5%Cr<sup>3+</sup>-b); 1%Cr<sup>3+</sup>-c); 2%Cr<sup>3+</sup>-d) and 10%Cr<sup>3+</sup>-e).

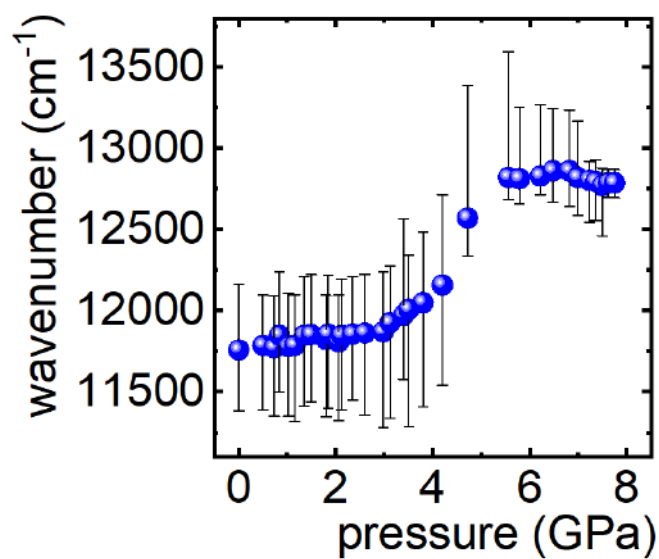


**Figure S10.** Barycenter of the emission band of LMTO:5%Cr<sup>3+</sup> as a function of applied pressure.



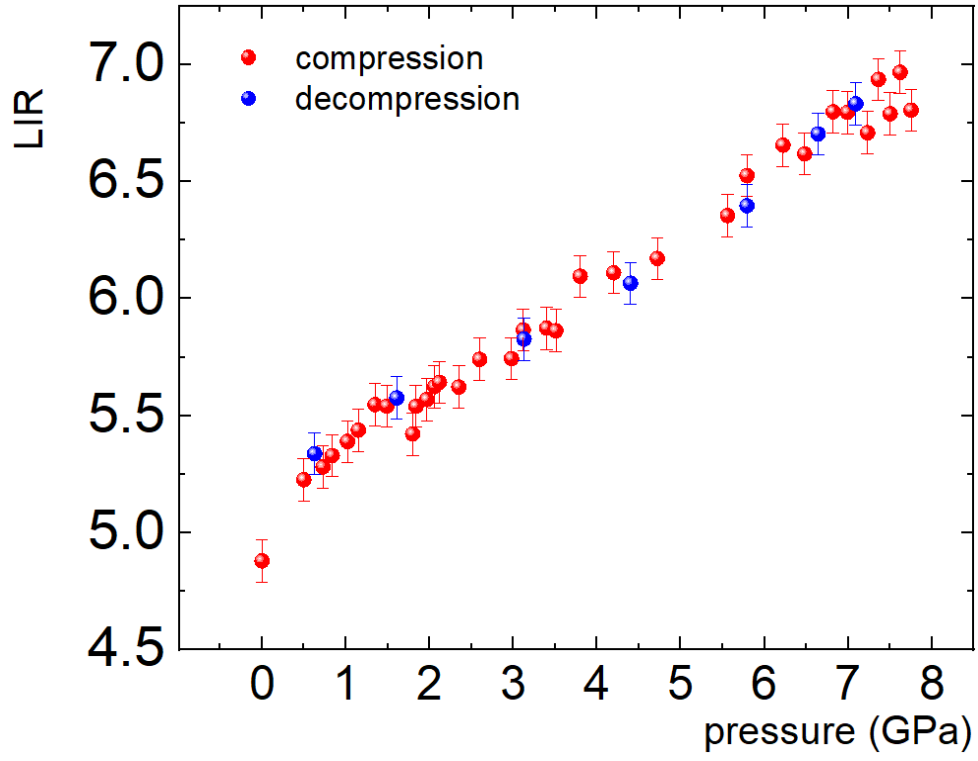


**Figure S11.** The LIR as a function of applied and released pressure for LMTO:5%Cr<sup>3+</sup>.

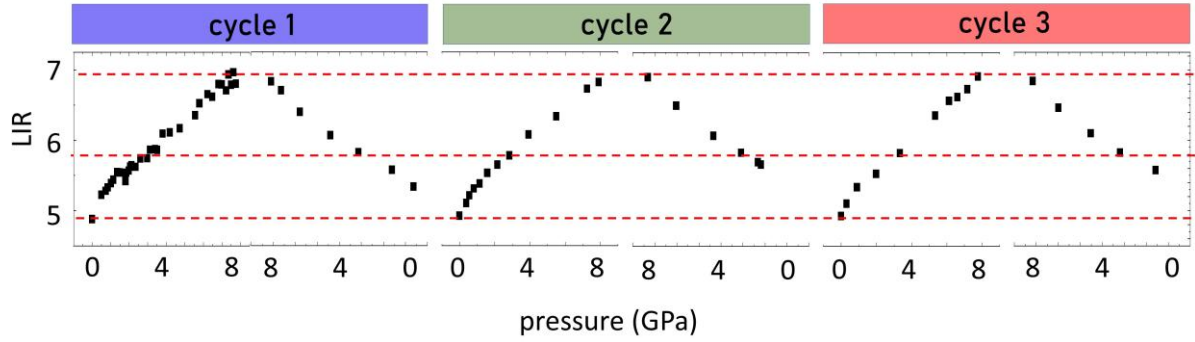


**Figure S12.** The LIR for LMTO:5%Cr<sup>3+</sup> measured within 3 cycles of compression and decompression.

The pressure determination uncertainty was calculated according to the methodology commonly used in luminescence thermometry:

$$\delta p = \frac{1}{S_R} \frac{\delta LIR}{LIR} \quad (S1)$$

$$\frac{\delta LIR}{LIR} = \sqrt{\left(\frac{\delta I_1}{I_1}\right)^2 + \left(\frac{\delta I_2}{I_2}\right)^2} \quad (S2)$$

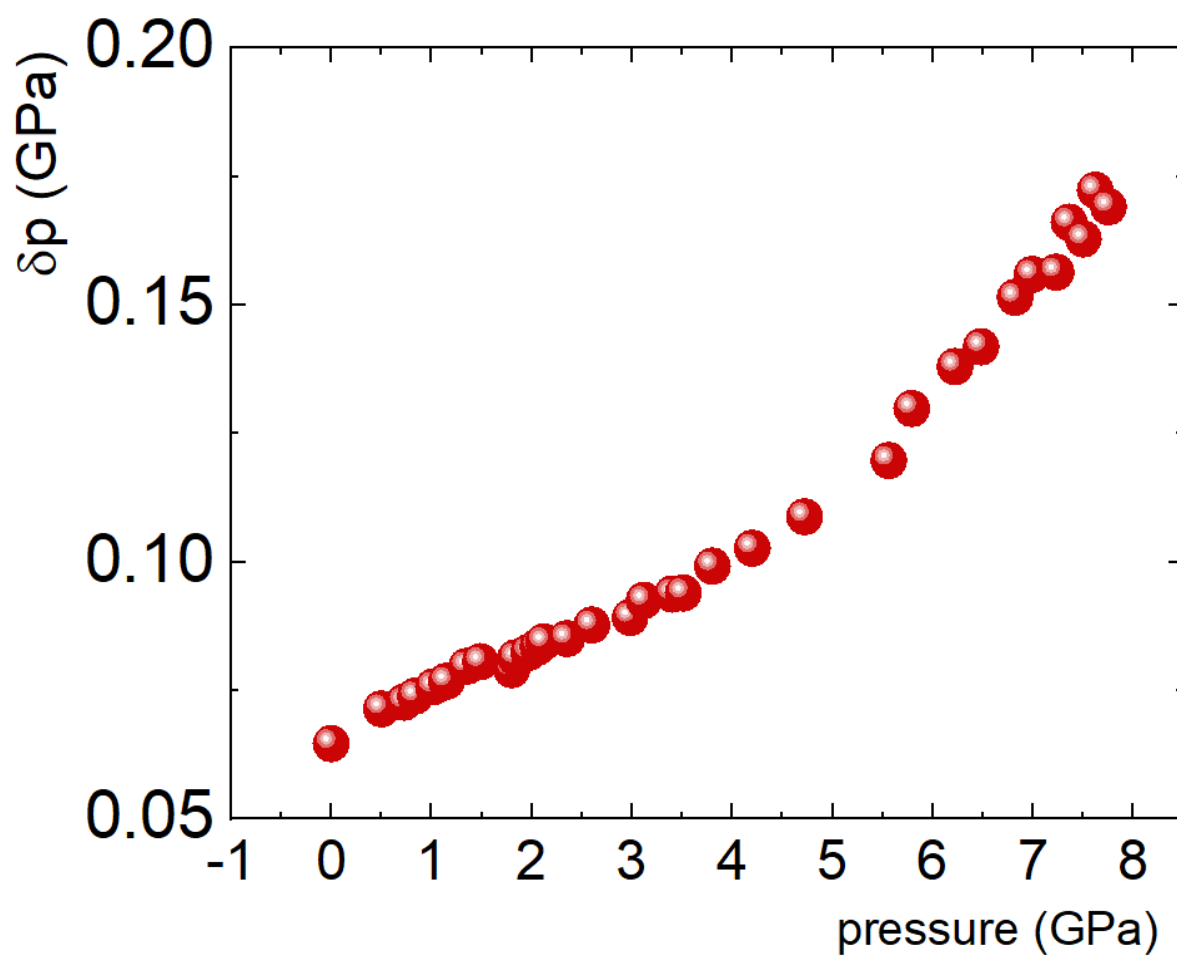


**Figure S13.** Pressure determination uncertainty determined using eq. S1 for LMTO:5%Cr<sup>3+</sup> as a function of applied pressure.

# Highly Pressure-Sensitive, Temperature Independent Luminescence Ratiometric Manometer Based on $\text{MgO}:\text{Cr}^{3+}$ Nanoparticles

Maja Szymczak,\* Marcin Runowski, Victor Lavín, and Lukasz Marciniak\*

Reliable remote pressure readout is possible only if high sensitivity of the measurement and independence from other physical factors are ensured. Among the parameters most strongly affecting measurements, temperature plays the most important role. In luminescence manometry, ratiometric measurement facilitates rapid pressure measurement ensuring high sensitivity of measurement while maintaining accuracy. Therefore, this paper compares the manometric performance of two ratiometric approaches in the material based on the luminescence of  $\text{Cr}^{3+}$  ions: using the intensity ratio of  ${}^2\text{E} \rightarrow {}^4\text{A}_2$  to  ${}^4\text{T}_2 \rightarrow {}^4\text{A}_2$  and a new approach based on the luminescence intensity ratio of  ${}^4\text{T}_2 \rightarrow {}^4\text{A}_2$  band recorded in two spectral ranges. Using the first approach, a manometer with an unprecedented sensitivity of  $S_R = 40\% \text{ GPa}^{-1}$  is developed. However, the second approach provides completely temperature-invariant pressure measurement with a sensitivity of  $S_R = 9.8\% \text{ GPa}^{-1}$ . The presented results indicate that the  $\text{MgO}:\text{Cr}^{3+}$  nanoparticles are a highly reliable and sensitive candidate for a new luminescent manometer.

lines offers high precision of the readout.<sup>[7,13,14]</sup> However, a small change in the value of manometric parameter corresponding to the high change in the pressure causes low sensitivity and thus accuracy of pressure readout. On the other hand, broad band emitting manometers are often characterized by a large high-pressure sensitivity, while readout error of the band maxima limits the precision of this approach.<sup>[10,15–17]</sup> Therefore, in order to provide a highly precise and accurate pressure readout the strategy in which spectral shift of the broad emission band of  $\text{Cr}^{3+}$  ions was analyzed in the ratiometric approach is proposed. Although different types of dopant ions can be used for luminescence manometry, the high susceptibility of the luminescence properties

## 1. Introduction

Pressure, along with temperature, is one of the most important physical parameters determining the dynamics and nature of physical processes and chemical reactions.<sup>[1–6]</sup> Therefore, its accurate reading is of vital importance. Most of the currently used luminescence-based pressure indicators exploit pressure-induced spectral shift of the emission band as a manometric parameter.<sup>[7–12]</sup> Luminescence manometer of narrow emission

of transition metal ions to the change in the crystallographic environment (represented by the crystal field strength;  $\text{Dq/B}$  parameter)<sup>[18,19]</sup> makes them perfect candidates for pressure sensing. Actually, the most well-established pressure indicator is also based on the  $\text{Cr}^{3+}$  emission ( $\text{Al}_2\text{O}_3:\text{Cr}^{3+}$ ).<sup>[13]</sup> The shape of the emission spectra of the octahedrally coordinated  $\text{Cr}^{3+}$  ions is strongly dependent on the crystal field strength.<sup>[20]</sup> The emission spectrum is dominated by a narrow band corresponding to the spin-forbidden  ${}^2\text{E} \rightarrow {}^4\text{A}_2$  transition in a strong crystal field site or broadband associated with the spin-allowed  ${}^4\text{T}_2 \rightarrow {}^4\text{A}_2$  transition in a weak crystal field site. The coexistence of both bands can be observed in the spectrum for the crystal field of intermediate strength. Furthermore, the spectral positions of the  ${}^4\text{T}_2 \rightarrow {}^4\text{A}_2$  and  ${}^2\text{E} \rightarrow {}^4\text{A}_2$  emission bands alter with the change of the  $\text{Dq/B}$  value (strong change in the band centroid is expected for the  ${}^4\text{T}_2 \rightarrow {}^4\text{A}_2$  band comparing to the  ${}^2\text{E} \rightarrow {}^4\text{A}_2$  one).<sup>[18]</sup> Since the strength of this field is proportional to the 5th-power of the distance between  $\text{Cr}^{3+}$  and ligand (R), namely ( $\text{Dq/B} \sim R^{-5}$ ), even a small change of the R value (for instance by the applied pressure) is significantly manifested in the luminescence spectra.<sup>[20]</sup>

In general, the ratiometric pressure readouts using  $\text{Cr}^{3+}$ -doped phosphors can be accomplished in two modes, in which luminescence intensity ratio (LIR) integrated into two spectral ranges, corresponding to the sidebands of the  ${}^4\text{T}_2 \rightarrow {}^4\text{A}_2$  emission band (mode I,  $\text{LIR}_1$  in Figure 1) or the LIR of  ${}^2\text{E} \rightarrow {}^4\text{A}_2$  to the  ${}^4\text{T}_2 \rightarrow {}^4\text{A}_2$  (mode II,  $\text{LIR}_2$  in Figure 1),<sup>[21]</sup> so both of them can be used as manometric parameters (Figure 1). Although the mode II is more

M. Szymczak, L. Marciniak  
Institute of Low Temperature and Structure Research  
Polish Academy of Sciences  
Okólna 2, Wrocław 50-422, Poland  
E-mail: m.szymczak@intibs.pl; l.marciniak@intibs.pl

M. Runowski  
Adam Mickiewicz University  
Faculty of Chemistry  
Uniwersytetu Poznańskiego 8, Poznań 61-614, Poland

M. Runowski, V. Lavín  
Departamento de Física  
IUdEA and MALTA-Consolider Team  
Universidad de La Laguna  
Apartado de Correos 456  
E-38200 San Cristóbal de La Laguna, Santa Cruz de Tenerife, Spain

The ORCID identification number(s) for the author(s) of this article can be found under <https://doi.org/10.1002/lpor.202200801>

DOI: 10.1002/lpor.202200801

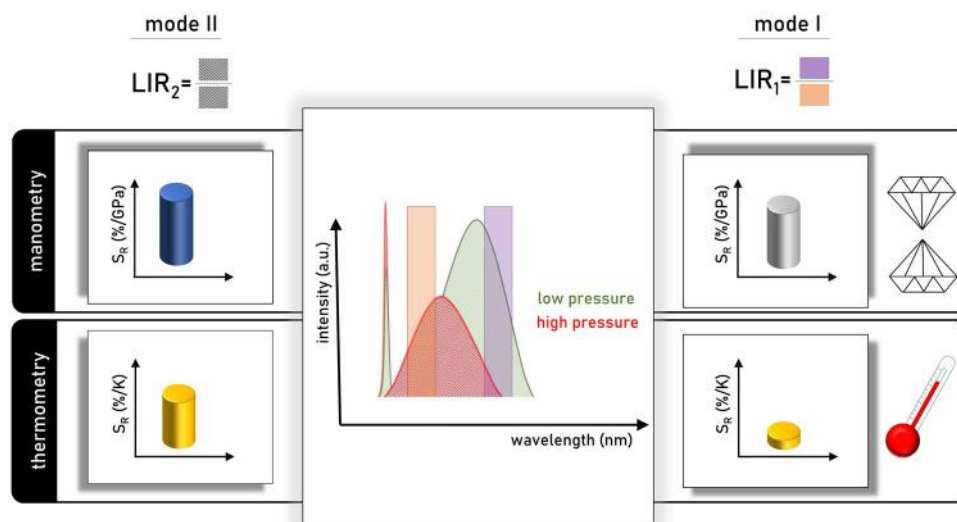


**Figure 1.** The conceptual image of the presented approach: two different modes were examined for luminescence manometry. In the mode I, the LIR integrated in two spectral ranges is used as a manometric parameter; whereas in mode II the  ${}^2\text{E} \rightarrow {}^4\text{A}_2$  to the  ${}^4\text{T}_2 \rightarrow {}^4\text{A}_2$  LIR is considered. The disadvantage of mode II approach is its higher sensitivity to temperature changes.

frequently used, its main limitation that affects the pressure readout reliability is its high sensitivity to temperature changes. This thermal coupling between  ${}^4\text{T}_2$  and the  ${}^2\text{E}$  states, which is exploited in luminescence thermometry leads to the thermal dependence of LIR according to the Boltzmann distribution. On the other hand, when only the  ${}^4\text{T}_2 \rightarrow {}^4\text{A}_2$  emission band is considered, an increase in temperature affects only the intensity of the band and not the spectral position. Hence the  $\text{LIR}_1$  becomes independent of temperature variations. Therefore, the use of mode I enables the development of a highly sensitive and temperature-invariant luminescence manometer.

To verify this hypothesis, the luminescence properties of the  $\text{Cr}^{3+}$  doped phosphor of the intermediate crystal field should be analyzed. In order to do this the spectroscopic properties of the  $\text{MgO}:\text{Cr}^{3+}$  materials are analyzed as a function of temperature and pressure. Although the  $\text{MgO}:\text{Cr}^{3+}$  is a well-known phosphor of strong crystal field, as it will be shown the increase of  $\text{Cr}^{3+}$  significantly modifies the crystal field strength affecting the  $\text{Cr}^{3+}$  ions. Because of the high symmetry and great structural stability, magnesium oxide—MgO is a well-known internal (direct) and primary (absolute) pressure standard/calibrant, allowing pressure readouts by monitoring its density/volume with X-ray powder diffraction (XRD) technique, alike for the diamond anvil cell and large-volume press experiments.<sup>[22]</sup> Hence, its P-V-T diagrams (equation of state) are carefully analyzed/investigated by the researchers, and constructed up to very high pressure ( $\approx 800$  GPa) and extreme temperature values ( $\approx 20\,000$  K).<sup>[23]</sup> The importance of understanding of fundamental properties of MgO is related to the discovery of super-Earth planets (exoplanets), and the possibility of using this material as sensors of ultrahigh pressures.<sup>[22]</sup> MgO, which is isostructural with cubic NaCl crystals at ambient conditions, under high-pressure conditions (above  $\approx 400$  GPa) transforms from the rocksalt structure (B1) to the caesium chloride-type structure (B2),<sup>[22]</sup> which has already been confirmed by XRD experiments and theoretical calculations.<sup>[22,24]</sup> The increase of temperature leads to the

decreasing pressure value of the phase transition. However, even at temperature as high as 8000 K, the mentioned phase transition occurs above  $\approx 250$  GPa. So the structure of MgO is very stable under extreme conditions of high-pressure and temperature.<sup>[22]</sup> Moreover, at ambient pressure, the solid phase of a bulk MgO is stable up to  $\approx 3000$  K, and at least up to  $\approx 1000$  K for the small nanoparticles ( $\approx 10$  nm).<sup>[25,26]</sup> These features of the MgO makes it excellent candidate as a host material for luminescence manometry.

$\text{Al}_2\text{O}_3:\text{Cr}^{3+}$  is undoubtedly the most widely used pressure indicator, and its high application potential results from its high luminescence intensity, chemical and mechanical stability, and spectrally narrow emission line offering high measurement precision. The purpose of this work is not to search for a better pressure indicator than  $\text{Al}_2\text{O}_3:\text{Cr}^{3+}$  but to propose an alternative-ratiometric pressure readout. This is in many cases (especially for 2D imaging of pressure changes) an approach that is easier to implement than an approach based on spectral band centroid shift.

## 2. Results and Discussion

MgO crystallizes in the cubic system and belongs to the space group  $Fm\bar{3}m$  (No. 225).<sup>[27–31]</sup> In this structure  $\text{Mg}^{2+}$  ions are located in the center of the octahedron coordinated with the six oxygen ions, as shown in Figure 2a. The comparison of the XRD patterns of synthesized nanocrystals with the standard XRD data of MgO (ICSD No. 19755) reveals the doping of MgO with  $\text{Cr}^{3+}$  ions up to 10% neither causes a deformation of the structure nor results in the formation of an additional phase (Figure 2b; and Figure S1, Supporting Information). In the case of the  $\text{MgO}:\text{20\%Cr}^{3+}$  additional reflection at  $2\theta = 36^\circ$  was found. This excludes this sample from further analysis. The increase of dopant concentration results in a gradual shift of the diffraction reflections toward higher angles, which usually corresponds to

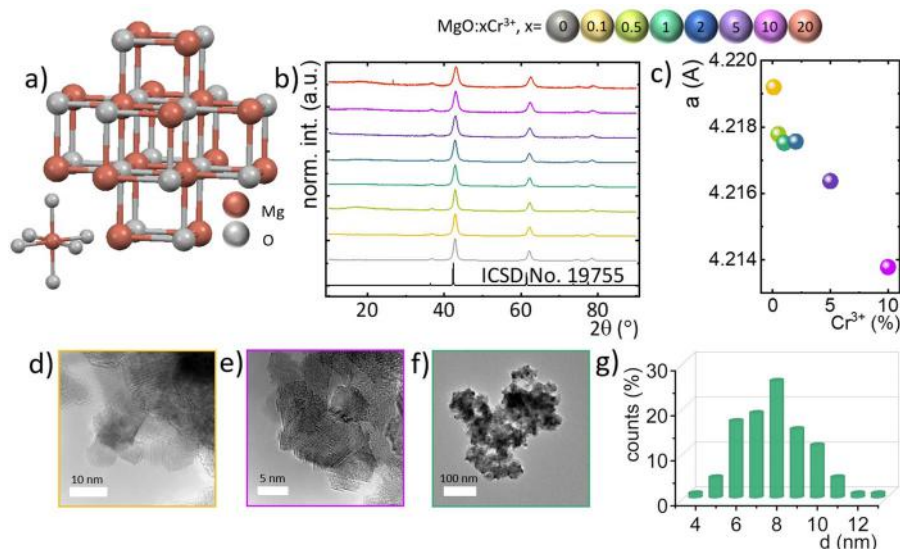


**Figure 2.** The visualization of the cubic structure of MgO and single octahedron of Mg<sup>2+</sup> ion coordinated by six oxygen ions (a). X-ray diffraction patterns of the MgO:Cr<sup>3+</sup> nanocrystals doped with different concentration of Cr<sup>3+</sup> ions (b). The calculated unit cell parameter *a* as a function of Cr<sup>3+</sup> concentration (c). The HRTEM images of MgO:0.1%Cr<sup>3+</sup> (d), and 10% Cr<sup>3+</sup> (e). The representative TEM image of MgO:1%Cr<sup>3+</sup> (f) and corresponding histogram of nanoparticle size distribution calculated from TEM images (g).

the shrinkage of the unit cell. Indeed, a Rietveld refinement indicates that the cell parameter decreases from 4.2192 Å for the sample with 0.1% of Cr<sup>3+</sup> to 4.21378 Å for the one with 10% of Cr<sup>3+</sup>. As is known, changes in the elemental unit cell are usually related to the difference in the ionic radii between the host and dopant ions. In this case, Cr<sup>3+</sup> ions have smaller ionic radii than Mg<sup>2+</sup> ( $r_{\text{Mg}^{2+}} = 0.72 \text{ Å}$ ,  $r_{\text{Cr}^{3+}} = 0.615 \text{ Å}$ ). It should be mentioned here that the difference in the ionic charge between substituted and dopant ions occurs, which might lead to the occurrence of the defect states, ionic pairs, or the decomposition of host material. The analysis of the TEM images of MgO:Cr<sup>3+</sup> reveals that the synthesized powders consist of the well-crystallized and strongly aggregated particles of around 10 nm in diameter (Figure 2d,e; and Figure S2, Supporting Information). The increase of the Cr<sup>3+</sup> concentration results in a small reduction of the particle size, from around 11 nm for the 0.1%Cr<sup>3+</sup> sample to around 7 nm for the 10%Cr<sup>3+</sup> one (Figure S3, Supporting Information). This effect is probably caused by the difference in the ionic radii between Mg<sup>2+</sup> and Cr<sup>3+</sup> and thus shrinkage of the particle size. The particle size distribution of the MgO:Cr<sup>3+</sup> is relatively narrow for all samples. For the representative sample—MgO:1%Cr<sup>3+</sup>, the particle size of  $10 \pm 5 \text{ nm}$  was determined (Figure 2f).

As is well-known, the emission spectrum of Cr<sup>3+</sup> ions is strongly dependent on the crystal field strength and this effect can be explained by using a configurational coordinate diagram (Figure 3a). When the Cr<sup>3+</sup> ions are affected by a weak crystal field interaction, the bottom of the <sup>4</sup>T<sub>2</sub> state parabola is localized below the bottom of the <sup>2</sup>E parabola, resulting in a dominating broadband emission associated with the <sup>4</sup>T<sub>2</sub> → <sup>4</sup>A<sub>2</sub> transition (see Tanabe–Sugano diagram for 3d<sup>3</sup> electronic configuration<sup>[18]</sup>). An increase in the crystal field strength results in the increase of the energy of the <sup>4</sup>T<sub>2</sub> state parabola, up to the situation when the <sup>2</sup>E one becomes a lower energetically state and thus <sup>2</sup>E → <sup>4</sup>A<sub>2</sub> emission band starts to dominate in the spectrum.

The comparison of the emission spectra of the MgO:Cr<sup>3+</sup> samples (measured at 123 K;  $\lambda_{\text{exc}} = 445 \text{ nm}$ ) for different concentrations of Cr<sup>3+</sup> ions reveals a significant impact of dopant concentration. In the case of the MgO:0.1%Cr<sup>3+</sup>, the emission spectrum consists of the <sup>2</sup>E → <sup>4</sup>A<sub>2</sub> emission band characteristic of the strong crystal field.<sup>[18,29]</sup> However, an increase in dopant concentration results in a gradual increase of the contribution of the broad <sup>4</sup>T<sub>2</sub> → <sup>4</sup>A<sub>2</sub> emission band up to the 10% of Cr<sup>3+</sup>, for which the narrow band <sup>2</sup>E → <sup>4</sup>A<sub>2</sub> completely disappeared. Additionally, the centroid of the broad emission band undergoes a redshift from 820 nm for the MgO:0.5%Cr<sup>3+</sup> to 905 nm for the MgO:10%Cr<sup>3+</sup>. This indicates the reduction of the energy between the ground and excited state, which is in agreement with the reduction of the crystal field strength. Further increase in the dopant amount results in the occurrence of an additional broad band, centered at around 1250 nm, associated with the Cr<sup>3+</sup>–Cr<sup>3+</sup> pair emission.<sup>[30]</sup> This emission was already observed in a several compounds and is fully understandable since the growing amount of Cr<sup>3+</sup> leads to an increase in pair formation. The change of the shape of the Cr<sup>3+</sup> emission spectrum of MgO:Cr<sup>3+</sup> with an increase of dopant concentration reveals that the crystallographic sites of lower crystal field stats to be more favorable occupied for higher Cr<sup>3+</sup> amount. MgO is seemingly a compound with an uncomplicated structure, and the only site into which the Cr<sup>3+</sup> ion can be incorporated is at the Mg<sup>2+</sup> one. However, due to the difference in charge of these two ions, and the consequent charge compensation, every three Mg<sup>2+</sup> ions are substituted by two Cr<sup>3+</sup> ions, and in addition a vacant site remains, leading to the structure deformations. Therefore, in fact, Cr<sup>3+</sup> ions can be located in three types of crystallographic sites, i.e., in cubic, tetragonal, and rhombic sites of MgO host.<sup>[18,19,31,28,29,32,33]</sup> Since a very small energy gap separates excited and ground states of Cr<sup>3+</sup> in the tetragonal site, its emission is not expected to be observed. Hence only cubic and rhombic sites occupied by the Cr<sup>3+</sup> will be considered in the



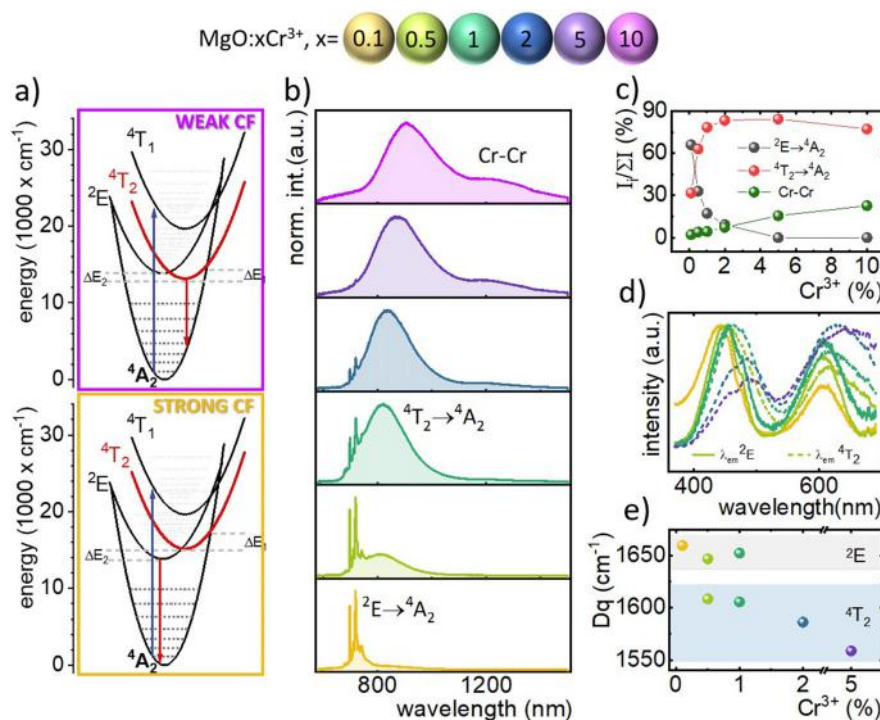


**Figure 3.** Configurational coordinate diagrams for the Cr<sup>3+</sup> ions in octahedral symmetry, in a weak and strong crystal field (a). The comparison of emission spectra of MgO:Cr<sup>3+</sup> with different concentration of dopant ions measured at 123 K upon  $\lambda_{\text{exc}} = 445$  nm (b). The percentage contribution of the integrated intensities of particular bands in the emission spectrum of MgO:Cr<sup>3+</sup> as a function of Cr<sup>3+</sup> concentration (c). Excitation spectra of MgO:Cr<sup>3+</sup> measured at 123 K (d), and Dq value as a function of Cr<sup>3+</sup> concentration, determined from the excitation spectra for the  ${}^2\text{E} \rightarrow {}^4\text{A}_2$  and  ${}^4\text{T}_2 \rightarrow {}^4\text{A}_2$  emission band (e).

further discussion. As can be seen in Figure 3b, for low concentration (0.1%) only a narrow emission lines corresponding to the  ${}^2\text{E} \rightarrow {}^4\text{A}_2$  transitions of Cr<sup>3+</sup> in cubic sites are observed (centered at  $\approx 680$ –720 nm). The higher the Cr<sup>3+</sup> concentration, the more dominant becomes the broadband emission from the  ${}^4\text{T}_2$  level of Cr<sup>3+</sup> in a rhombic site (maximum of emission from  $\approx 820$ –900 nm).<sup>[19]</sup> Since the average Cr<sup>3+</sup>–O<sup>2-</sup> distance is larger in the rhombic site comparing to the cubic one an increase in the rhombic site occupation is expected for higher Cr<sup>3+</sup> ions concentration. The detailed analysis of the percentage contribution of emission intensity of a particular band ( $I_i$ ) to the total emission intensity ( $\Sigma I$ ) reveals that the  ${}^2\text{E} \rightarrow {}^4\text{A}_2$  emission rapidly decreases with Cr<sup>3+</sup> concentration. On the contrary, contribution of the  ${}^4\text{T}_2 \rightarrow {}^4\text{A}_2$  transition increases to 80% for the MgO:2%Cr<sup>3+</sup> sample, and with further increase of Cr<sup>3+</sup> concentration it slightly decreases to 75%, due to the growing intensity of Cr<sup>3+</sup> pairs emission (Figure 3c). Such a correlation may suggest that increasing amounts of dopant ions cause greater distortion of the structure, or that the pair states are located on the surface state of the nanoparticle. The second hypothesis is supported by the correlation noted earlier between Cr<sup>3+</sup> ions concentration and nanoparticle size, namely, the more Cr<sup>3+</sup> ions as a dopant, the smaller the nanoparticle. As the size of the nanoparticle decreases, the surface-to-volume ratio increases. The reduction of the crystal field strength with dopant concentration is clearly manifested in the excitation spectra of MgO:Cr<sup>3+</sup>. When monitoring the  ${}^2\text{E} \rightarrow {}^4\text{A}_2$  emission intensity ( $\lambda_{\text{em}} = 718$  nm) the spectral position of the  ${}^4\text{A}_2 \rightarrow {}^4\text{T}_2$  and  ${}^4\text{A}_2 \rightarrow {}^4\text{T}_1$  absorption bands for the samples containing 0.1–1%

of Cr<sup>3+</sup> remains almost unchanged. On the contrary, when the  ${}^4\text{T}_2 \rightarrow {}^4\text{A}_2$  emission intensity ( $\lambda_{\text{em}} \approx 800$  nm) appeared, the gradual redshift of the  ${}^4\text{A}_2 \rightarrow {}^4\text{T}_2$  and  ${}^4\text{A}_2 \rightarrow {}^4\text{T}_1$  absorption bands was found, as well. This is clearly reflected in the Dq trend as a function of Cr<sup>3+</sup> concentration (calculation procedure is presented in the Supporting Information, Figure 3e).

As stated in the introduction to develop a bi-modal (mode I and mode II) luminescence-based pressure sensor the phosphors of the intermediate crystal fields are required. Therefore, the MgO:1%Cr<sup>3+</sup> was selected for manometric studies (Figure 4a). As stated above in the MgO, there is only one structural phase but two dominant crystallographic sites occupied by the Cr<sup>3+</sup> ions: cubic and rhombic. The influence of the applied pressure on both sites results in a very similar way: a pressure-induced shortening of the metal-oxygen distance (R) results in an increase in the crystal field strength. In the case of the strong crystal field affecting the Cr<sup>3+</sup> ions in the cubic site this change of R results in less spectacular changes in the shape of the emission spectrum- only a slight spectral shift of the  ${}^2\text{E} \rightarrow {}^4\text{A}_2$ . On the other hand in the case of the Cr<sup>3+</sup> ions located in the rhombic site the strong spectral shift of the  ${}^4\text{T}_2 \rightarrow {}^4\text{A}_2$  emission band is found. The room temperature emission spectra measured as a function of the applied pressure reveal two main effects: I) spectral blueshift of the  ${}^4\text{T}_2 \rightarrow {}^4\text{A}_2$  centroid; and II) the change in the intensity of the  ${}^4\text{T}_2 \rightarrow {}^4\text{A}_2$  with respect to the  ${}^2\text{E} \rightarrow {}^4\text{A}_2$  band one.

The compression of the MgO:Cr<sup>3+</sup> structure results in the shortening of the R distance between Cr<sup>3+</sup> and O<sup>2-</sup> ions. Hence, the associated enhancement of the crystal field strength is

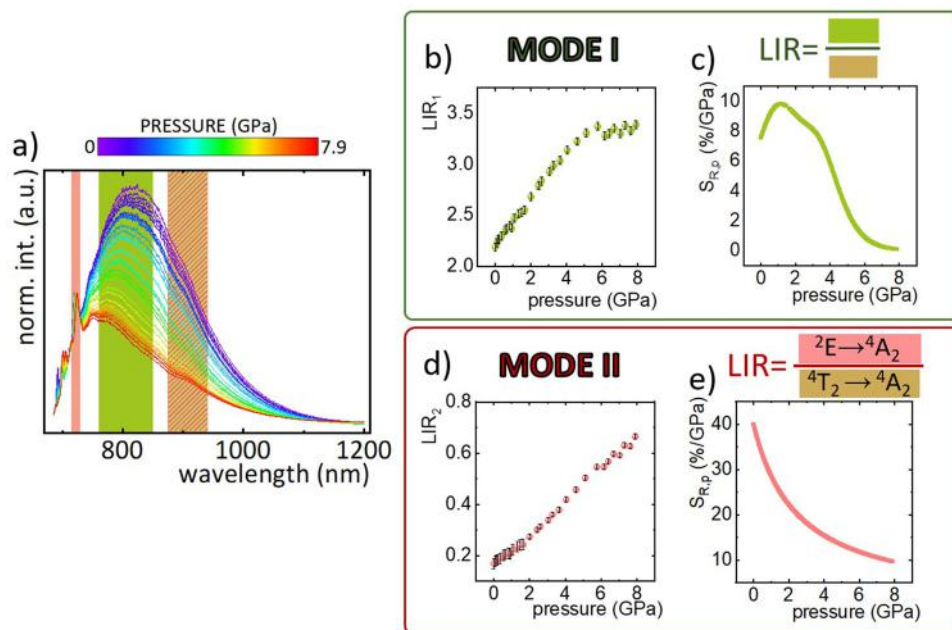


**Figure 4.** The emission spectra of the MgO:1%Cr<sup>3+</sup> nanomaterial measured as a function of pressure (0–8 GPa) upon  $\lambda_{\text{exc}} = 445$  nm excitation, with the schematically marked spectral ranges used for LIR<sub>1</sub> and LIR<sub>2</sub> calculations (a). The LIR<sub>1</sub> as a function of pressure (b) and corresponding pressure dependence of  $S_R$  (c) for mode I; and LIR<sub>2</sub> values (d) and corresponding  $S_R$  (e) for mode II.

reflected in the shape and position of the emission spectra of MgO:1%Cr<sup>3+</sup>. To investigate whether the changes occurring in the luminescence of MgO:Cr<sup>3+</sup> are due to changes in the crystal structure, luminescence measurements were performed during decompression. As can be seen in Figure S4 (Supporting Information), with decreasing pressure, the emission spectrum of the sample returned to its original shape and position, confirming that the pressure does not cause irreversible structural changes (plastic deformations), and therefore, the material has a great potential to be used as a highly sensitive luminescent manometer. Instead of the analysis of the position of the  ${}^4T_2 \rightarrow {}^4A_2$  band centroid, which could be as mentioned earlier of low precision, the ratiometric representation was proposed. Therefore, the LIR<sub>1</sub> was calculated as follows

$$\text{LIR}_1 = \frac{\int_{760 \text{ nm}}^{850 \text{ nm}} {}^4T_2 \rightarrow {}^4A_2 d\lambda}{\int_{877 \text{ nm}}^{940 \text{ nm}} {}^4T_2 \rightarrow {}^4A_2 d\lambda} \quad (1)$$

The LIR<sub>1</sub> monotonically increases with applied pressure from ambient to around 6 GPa, above which some saturation of the LIR<sub>1</sub> parameter was observed (Figure 4b; and Figure S5, Supporting Information). This dependence indicates that MgO:1%Cr<sup>3+</sup> can be applied in mode I as a pressure sensor in the 0–6 GPa range. To quantify the observed changes, the relative pressure sensitivity ( $S_R$ ) was calculated according to the following equation

$$S_{R,p} = \frac{1}{\text{LIR}} \frac{\Delta \text{LIR}}{\Delta p} 100\% \quad (2)$$

As shown in Figure 4c, the  $S_R$  initially increases, reaching the maximal value of 9.83% GPa<sup>−1</sup> at 1.15 GPa, followed by the lowering of  $S_R$  up to ≈6 GPa (Figure 4c). The obtained maximum  $S_R$  value is significantly higher compared to the previously reported for Cr<sup>3+</sup> in ratiometric approach, i.e.,  $S_R = 4.7\%$  GPa<sup>−1</sup> for the Li<sub>2</sub>Mg<sub>3</sub>TiO<sub>6</sub>:Cr<sup>3+</sup> material.<sup>[34]</sup>

In the second mode, the  ${}^2E \rightarrow {}^4A_2$  to the  ${}^4T_2 \rightarrow {}^4A_2$  luminescence intensity ratio was calculated as follows

$$\text{LIR}_2 = \frac{\int_{714 \text{ nm}}^{728 \text{ nm}} {}^2E \rightarrow {}^4A_2 d\lambda}{\int_{877 \text{ nm}}^{940 \text{ nm}} {}^4T_2 \rightarrow {}^4A_2 d\lambda} \quad (3)$$

In this case, the monotonic change of LIR<sub>2</sub> parameter was observed in the whole analyzed pressure range (0–8 GPa), which is wider compared to mode I. Moreover, the corresponding  $S_R$  reached significantly much higher values with maximal  $S_R = 40\%$  GPa<sup>−1</sup> at ambient pressure (Figure 4e). Currently this value is the highest reported one in the literature for the ratiometric pressure sensing (compared to 8 and 13.8% GPa<sup>−1</sup> for Tm<sup>3+</sup> and Eu<sup>2+</sup>/Sm<sup>2+</sup> system, respectively),<sup>[35,36]</sup> making the developed nano-manometer a leader in sensitivity among all other luminescent materials using such approach (Table 1). Additionally it should be noticed that strong spectral overlap between  ${}^2E \rightarrow {}^4A_2$  and the  ${}^4T_2 \rightarrow {}^4A_2$  emission bands occurs in this material. This significantly affects the calculated  ${}^2E \rightarrow {}^4A_2$  emission intensity. These two signals can be separated by deconvolution. However, this procedure additionally complicates the pressure imaging process and limits the applicative potential of the mode II approach.

**Table 1.** Comparison of the manometric performance of the ratiometric luminescence manometers.

Compound	Dopant ions	LIR	$\lambda_{\text{exc}}$ [nm]	Maximal $S_R$ [% GPa <sup>-1</sup> ]	P @ $S_R$ max [GPa]	Refs.
SrB <sub>4</sub> O <sub>7</sub>	Eu <sup>2+</sup> /Sm <sup>2+</sup>	Eu <sup>2+</sup> (5d-4f) / Sm <sup>3+</sup> ( <sup>5</sup> D <sub>0</sub> → <sup>7</sup> F <sub>0</sub> )	280	13.8	40	[36]
Li <sub>2</sub> Mg <sub>3</sub> TiO <sub>6</sub>	Cr <sup>3+</sup>	Cr <sup>3+</sup> ( <sup>4</sup> T <sub>2</sub> → <sup>4</sup> A <sub>2</sub> ) / Cr <sup>3+</sup> ( <sup>4</sup> T <sub>2</sub> → <sup>4</sup> A <sub>2</sub> )	445	4.7	Ambient	[34]
MgO	Cr <sup>3+</sup>	Cr <sup>3+</sup> ( <sup>4</sup> T <sub>2</sub> → <sup>4</sup> A <sub>2</sub> ) / Cr <sup>3+</sup> ( <sup>4</sup> T <sub>2</sub> → <sup>4</sup> A <sub>2</sub> )	445	9.83	1.15	This work
MgO	Cr <sup>3+</sup>	Cr <sup>3+</sup> ( <sup>2</sup> E → <sup>4</sup> A <sub>2</sub> ) / Cr <sup>3+</sup> ( <sup>4</sup> T <sub>2</sub> → <sup>4</sup> A <sub>2</sub> )	445	40	Ambient	This work

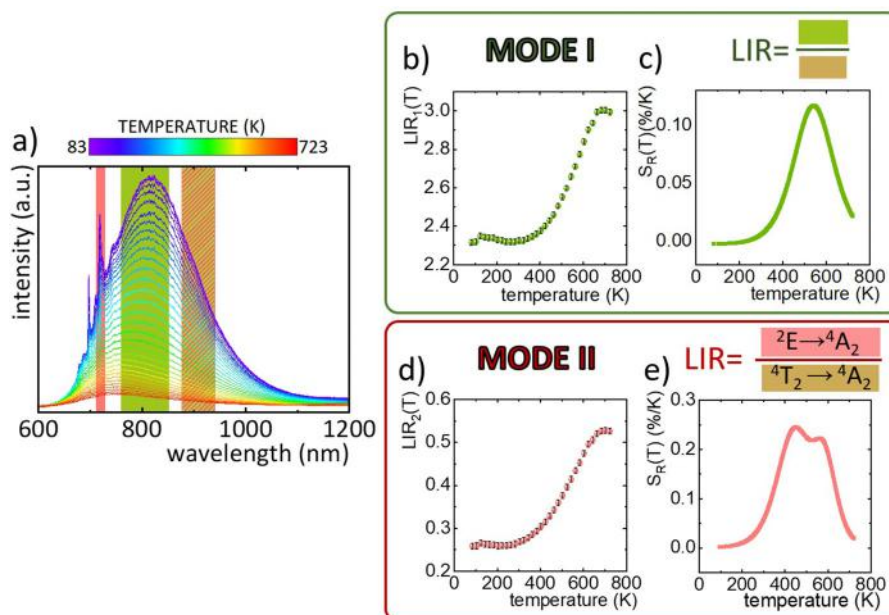


**Figure 5.** Emission spectra of the MgO:1%Cr<sup>3+</sup> measured as a function of temperature (83–723 K,  $\lambda_{\text{exc}}$  = 445 nm), with the schematically marked spectral ranges used for the LIR<sub>1</sub> and LIR<sub>2</sub> calculations (a). The LIR<sub>1</sub>(T) as a function of temperature (b), and the corresponding thermal dependence of  $S_R(T)$  (c), for mode I; the LIR<sub>2</sub>(T) (d), and the corresponding  $S_R(T)$  (e) for mode II as a function of temperature.

Since the spectroscopic properties of phosphors are usually strongly affected by temperature change, it is crucial to investigate how temperature affect the determined spectroscopic parameters, because the thermally-invariant pressure readouts are always favorable. Therefore, the thermal variability of LIR<sub>1</sub> in mode I and LIR<sub>2</sub> in mode II were examined. In order to do this, the emission spectra of MgO:1%Cr<sup>3+</sup> were measured as a function of temperature, in the T-range of 83–723 K (Figure 5; and Figure S6, Supporting Information). The analysis of the emission spectra for the MgO:1%Cr<sup>3+</sup> nanomaterial reveals that the spectral position of the <sup>4</sup>T<sub>2</sub> → <sup>4</sup>A<sub>2</sub> emission band remains almost unchanged up to around 500 K, above which a gradual blueshift was observed. This is associated with the thermalization of the higher vibronic states of the <sup>4</sup>T<sub>2</sub> level and consequently an increase in the energy of the emitted photons. Hence the LIR<sub>1</sub> value is temperature invariant in the 83–450 K T-range, above which it increases by around 25% of its initial value. This is reflected in the low value of the relative thermal sensitivity— $S_{R,T}$  (calculated using Equation (4)) that reaches the maximal value of only 0.1% K<sup>-1</sup> at 570 K (Figure 5c)

$$S_{R,T} = \frac{1}{\text{LIR}} \frac{\Delta \text{LIR}}{\Delta T} 100\% \quad (4)$$

On the other hand, in the case of the change in the relative emission intensities of <sup>2</sup>E → <sup>4</sup>A<sub>2</sub> and the <sup>4</sup>T<sub>2</sub> → <sup>4</sup>A<sub>2</sub> bands more significant changes were observed in the whole analyzed temperature range (Figure 5a). This results from the thermal coupling between the <sup>4</sup>T<sub>2</sub> and <sup>2</sup>E states. Hence although the integral emission intensity decreases at elevated temperature, the <sup>4</sup>T<sub>2</sub> → <sup>4</sup>A<sub>2</sub> band is quenched faster compared to the <sup>2</sup>E → <sup>4</sup>A<sub>2</sub> one. Therefore, the LIR<sub>2</sub> value starts to increase already above 270 K and reached 220% of its initial value at 700 K. The  $S_{R,T}$  reached 2.5 times higher values ( $S_{R,T} = 0.25\% \text{ K}^{-1}$  at 470 K) compared to the one obtained using mode I. It should be also noted that in the whole analyzed T-range the mode II is thermally more sensitive than mode I. Additionally, in the 360–660 K T-range, the thermal sensitivity of mode II exceeds the maximal value obtained in mode I. The low thermal sensitivity ( $S_{R,T} < 0.2\% \text{ K}^{-1}$ ) of the luminescence manometer is beneficial and guarantees a more reliable pressure readout. Hence although higher pressure sensitivities were achieved in mode II mode, it is recommended to use the mode I as a manometric parameter for sensing, in order to guarantee much more accurate, reliable and almost temperature-independent pressure readouts. Additionally, what is important for the 2D pressure changes imaging is the fact that the <sup>2</sup>E → <sup>4</sup>A<sub>2</sub>



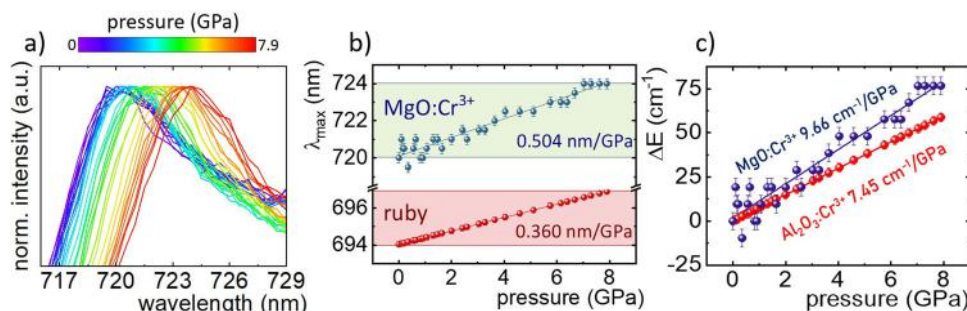


**Figure 6.** The influence of the applied pressure on the spectral position of the  ${}^2\text{E} \rightarrow {}^4\text{A}_2$  emission band for the  $\text{MgO:1\%Cr}^{3+}$  sample ( $\lambda_{\text{exc}} = 445 \text{ nm}$ ) (a). The comparison of the pressure induced changes in the spectral positions of the  ${}^2\text{E} \rightarrow {}^4\text{A}_2$  emission bands for the  $\text{MgO:1\%Cr}^{3+}$  and ruby ( $\text{Al}_2\text{O}_3:\text{Cr}^{3+}$ ) (b); and corresponding changes in the energy of the emission lines (c).

emission line is relatively spectrally narrow. Since the readout used in mode II relies on the spectral separation of the  ${}^2\text{E} \rightarrow {}^4\text{A}_2$  and  ${}^4\text{T}_2 \rightarrow {}^4\text{A}_2$  emission bands, the accuracy of pressure readout in this approach is limited by the optical filters available. In the case of the mode I, however, the spectrally wide ranges used for analysis overlap well with commercially available bandpass filters.

Beside the spectral shift of the  ${}^4\text{T}_2 \rightarrow {}^4\text{A}_2$  band, a slight change in the band centroid was also found in the case of the  ${}^2\text{E} \rightarrow {}^4\text{A}_2$  line (Figure 6a; and Figure S7, Supporting Information). Analogously to the  $\text{Al}_2\text{O}_3:\text{Cr}^{3+}$ , this luminescent feature of  $\text{Cr}^{3+}$  ions in  $\text{MgO:1\%Cr}^{3+}$  can be used for pressure sensing. When the pressure increases from 0 to 7.9 GPa this emission line shifts from 720 to 724 nm, whereas the emission line of  $\text{Al}_2\text{O}_3:\text{Cr}^{3+}$  shifts from 694 to 696 nm (Figure 6b). Hence the corresponding change in the energy of the  ${}^2\text{E} \rightarrow {}^4\text{A}_2$  transition increases by  $77 \text{ cm}^{-1}$  ( $0.504 \text{ nm GPa}^{-1}$ ) compared to the  $59 \text{ cm}^{-1}$  ( $0.36 \text{ nm GPa}^{-1}$ ) for  $\text{Al}_2\text{O}_3:\text{Cr}^{3+}$ . In both phosphors, monotonic spectral shift with pressure was observed, however with different rates ( $9.66 \text{ cm}^{-1} \text{ GPa}^{-1}$  for the  $\text{MgO:1\%Cr}^{3+}$ , and  $7.45 \text{ cm}^{-1} \text{ GPa}^{-1}$  for  $\text{Al}_2\text{O}_3:\text{Cr}^{3+}$ ). A higher slope observed for the  $\text{MgO:1\%Cr}^{3+}$  nanosensor is actually expected when the Tanabe Sugano diagram for  $3d^3$  electronic configuration is analyzed.<sup>[19,37]</sup> The energy of the  ${}^2\text{E}$  state exhibits an almost parallel trend with respect to the ground  ${}^4\text{A}_2$  state with an increase of  $\text{Dq/B}$ . Therefore, for the phosphors with a strong crystal field, the further increase of the strength induced with applied pressure affects only barely the energy of the  ${}^2\text{E}$  state. On the other hand, in the case of the phosphors of intermediate crystal field strength, the applied pressure meaningfully changes the position of the  ${}^2\text{E} \rightarrow {}^4\text{A}_2$  emission band. It should be also noted that in the pressure range between 0 and 2 GPa the trend presented in Figure 6 is very noisy and the band centroid strongly fluctuates. Nevertheless, it should be noticed here that for  $\text{MgO:1\%Cr}^{3+}$  some variation of the band centroid was observed which may result from the morphology of this phosphor (nanoparticles) compared to microcrystals of  $\text{Al}_2\text{O}_3:\text{Cr}^{3+}$  and the difference in the emission intensities between those two phosphors.

Although  $\text{Al}_2\text{O}_3:\text{Cr}^{3+}$  is an excellent pressure indicator commonly used in diamond chambers, it should be noted that it is extremely difficult to use it for 2D pressure imaging. In many applications, not only the local pressure reading but also its surface distribution is important. Such a measurement using  $\text{Al}_2\text{O}_3:\text{Cr}^{3+}$  would require luminescence spectrum measure-

ments at every point in the imaged area, which would require a spectrally high-resolution detection system as well as being very time-consuming. The approach presented in this manuscript (mode I) not only allows to combine high precision and high sensitivity, but above all extremely facilitates pressure imaging. The ability to read pressure using intensity ratios measured in two relatively broad spectral ranges that do not occur in close proximity precludes the need to measure emission spectra. Additionally, the detection system does not even need to be equipped with a monochromator—it is enough to use the commercially available bandpass filters instead (decreasing the cost and simplifying the system). 2D pressure imaging in this case will be possible by dividing two images/intensity maps by each other.

### 3. Conclusions

In this work, we have developed a new optical manometer, allowing temperature-independent pressure readout with unprecedentedly high sensitivity ( $S_R = 40\% \text{ GPa}^{-1}$ ), which makes it currently the most sensitive luminescent high-pressure sensor operating in the ratiometric mode. The spectroscopic properties of the  $\text{MgO:Cr}^{3+}$  nanoparticles were investigated as a function of dopant concentration, applied pressure, and temperature, to develop a highly sensitive and temperature invariant luminescence manometer. The detailed spectroscopic studies revealed that the increase of  $\text{Cr}^{3+}$  results in the change of the emission spectra shape for the  $\text{MgO:Cr}^{3+}$  samples, from the narrow emission band ( ${}^2\text{E} \rightarrow {}^4\text{A}_2$  transition) for the  $\text{MgO:0.1\%Cr}^{3+}$  through the spectrum that consists of both  ${}^2\text{E} \rightarrow {}^4\text{A}_2$  and  ${}^4\text{T}_2 \rightarrow {}^4\text{A}_2$  bands for a higher (intermediate) concentration of dopants ( $>0.5\% \text{Cr}^{3+}$ ), finally to the broadband ( ${}^4\text{T}_2 \rightarrow {}^4\text{A}_2$ ) luminescence for the  $\text{MgO:10\%Cr}^{3+}$ . Additionally, the spectral position of the  ${}^4\text{T}_2 \rightarrow {}^4\text{A}_2$  emission band shifts toward longer wavelengths with increasing dopant amount. Since two crystallographic sites are observed in the structure, namely cubic and rhombic sites that can be occupied by  $\text{Cr}^{3+}$  ions the observed changes are related to the growing number of  $\text{Cr}^{3+}$  in rhombic site for higher dopant concentration. Due to the weaker crystal field strength affecting the  $\text{Cr}^{3+}$  in this crystallographic position the higher contribution of the broad emission band in the spectrum is observed. The investigations of the spectroscopic studies of  $\text{MgO:1\%Cr}^{3+}$  as a function of applied pressure reveal i) strong the pressure-induced spectral blue shift of the  ${}^4\text{T}_2 \rightarrow {}^4\text{A}_2$  band; ii) slight spectral blueshift of the  ${}^2\text{E} \rightarrow {}^4\text{A}_2$  band, and iii) change in the  ${}^2\text{E} \rightarrow {}^4\text{A}_2$  to the  ${}^4\text{T}_2 \rightarrow {}^4\text{A}_2$  emission

intensity ratio. Thus the two ratiometric modes were considered to develop a highly sensitive ratiometric manometer. It was found that although in the LIR of  ${}^2\text{E} \rightarrow {}^4\text{A}_2$  to the  ${}^4\text{T}_2 \rightarrow {}^4\text{A}_2$  much higher pressure relative sensitivity was found ( $S_R = 40\%/ \text{GPa}$ ) compared to ( $S_R = 9.83\% \text{ GPa}^{-1}$ ) for the LIR of two spectral ranges of  ${}^4\text{T}_2 \rightarrow {}^4\text{A}_2$  transition the much higher thermal variability of this former approach reduces its applicative potential.

At least for this phosphor, it is evident that the spectral shift of the  ${}^4\text{T}_2 \rightarrow {}^4\text{A}_2$  emission band represented as the ratio of intensities integrated into two spectral ranges is, due to its thermal invariability, more reliable manometric parameter comparing to the LIR of the  ${}^2\text{E} \rightarrow {}^4\text{A}_2$  to the  ${}^4\text{T}_2 \rightarrow {}^4\text{A}_2$  bands. Concluding the  $\text{MgO}:1\%\text{Cr}^{3+}$  nanoparticles are very promising luminescence-based pressure probes that operate in the ratiometric approach.

## 4. Experimental Section

The nanocrystals of MgO (MO) doped with chromium(III) ions were synthesized using a modified Pechini method.<sup>[38]</sup> Magnesium nitrate hydrate ( $\text{Mg}(\text{NO}_3)_2 \cdot x\text{H}_2\text{O}$ ,  $x \approx 6$ , 99.999% of purity, Alfa Aesar), chromium(III) nitrate nonahydrate ( $\text{Cr}(\text{NO}_3)_3 \cdot 9\text{H}_2\text{O}$ , min. 99.99%, Alfa Aesar), polyethylene glycol 200 (PEG,  $\text{H}(\text{OCH}_2\text{CH}_2)_n\text{OH}$ ,  $n = 200$ , Alfa Aesar), and citric acid ( $\text{HOC}(\text{COOH})(\text{CH}_2\text{COOH})_2$ ,  $\geq 99.5\%$ , Sigma-Aldrich) were used as precursors for the synthesis. All reagents were used without further purification.

Appropriate amounts of magnesium(II) and chromium(III) nitrate were placed in a beaker with a sixfold molar excess of citric acid, dissolved in distilled water and stirred for 2 h at 320 K. After this time, PEG (1:1 in molar ratio respect to citric acid) was added and stirred again for 1 h at 320 K. The solutions were then dried for 3 days at 360 K in air. The resulting resins of  $\text{MgO}:x\%\text{Cr}^{3+}$  ( $x = 0.1\text{--}20$ ) were annealed in ceramic crucibles at 873 K for 4 h in air.

Structural studies by XRD were carried out using a PANalytical X'Pert Pro diffractometer equipped with an Anton Paar TCU1000 N Temperature Control Unit using Ni-filtered Cu  $\text{K}\alpha$  radiation ( $V = 40 \text{ kV}$ ,  $I = 30 \text{ mA}$ ). Measurements were taken in the range  $10^\circ\text{--}90^\circ$ . Transmission electron microscopy images were obtained using a Philips CM-20 SuperTwin TEM microscope (CCD FEI Eagle 2K camera with a HAADF detector, LaB6 cathode). Samples were prepared by dispersing the powders in methanol, then applying the resulting suspension to a copper grid and drying under an IR lamp for 40 min. The prepared grid with the sample was purified in a plasma cleaner.

The excitation spectra were measured with FLS1000 Fluorescence Spectrometer from Edinburgh Instruments. The 450 W Xenon lamp was used as a source of the excitation and R5509-72 photomultiplier tube from Hamamatsu in nitrogen-flow cooled housing was used as the detector. All the emission spectra were corrected to the detector response curve. The temperature and pressure-dependent emission spectra of the synthesized phosphors were measured with the aforementioned system, using a 445 nm laser diode. The temperature of the sample was controlled by a THMS 600 heating-cooling stage from Linkam ( $0.1^\circ\text{C}$  temperature stability and  $0.1^\circ\text{C}$  set point resolution). Measurements were performed with an interval of 1 min between measurements to obtain the thermal equilibrium. The pressure-dependent emission spectra were measured using a gas membrane driven diamond anvil cell Diacell  $\mu\text{ScopeDAC-RT(G)}$  from Almax easyLab with 0.4 mm diamond culets. The sample was loaded into a  $140 \mu\text{m}$  hole drilled in a stainless steel gasket (thickness  $250 \mu\text{m}$ , diameter  $10 \text{ mm}$ ). As the pressure transmitting medium was used methanol-ethanol solution ( $V:V/4:1$ ). Pressure was controlled using a Druck PACE 5000. Ruby ( $\text{Al}_2\text{O}_3:\text{Cr}^{3+}$ ) crystals were chosen as the pressure indicator, the value of which was determined by the spectral shift of  $\text{R}_2$  line.<sup>[14]</sup>

## Supporting Information

Supporting Information is available from the Wiley Online Library or from the author.

## Acknowledgements

This work was supported by the National Science Center (NCN) Poland under Project No. DEC-UMO- 2020/37/B/ST5/00164. M.R. acknowledges support from Fondo Social Europeo and Agencia Estatal de Investigación (RYC2020-028778-I/AEI/10.13039/501100011033). This work was also supported by the Spanish Ministerio de Economía y Competitividad (MINECO) under the National Program of Sciences and Technological Materials (PID2019-106383GB-44) and by EU-FEDER funds.

## Conflict of Interest

The authors declare no conflict of interest.

## Data Availability Statement

The data that support the findings of this study are available from the corresponding author upon reasonable request.

## Keywords

$\text{Cr}^{3+}$ , crystal field strength, luminescence intensity ratio, luminescent manometer, manometry, pressure sensors

Received: October 21, 2022

Revised: November 29, 2022

Published online: January 11, 2023

- [1] A. P. Zhilyaev, T. G. Langdon, *Prog. Mater. Sci.* **2008**, *53*, 893.
- [2] D. C. Elliott, T. R. Hart, G. G. Neuenschwander, *Ind. Eng. Chem. Res.* **2006**, *45*, 3776.
- [3] H. Mújica-Paz, A. Valdez-Fragoso, C. T. Samson, J. Welti-Chanes, J. A. Torres, *Food Bioprocess Technol.* **2011**, *4*, 969.
- [4] S. Schultz, G. Wagner, K. Urban, J. Ulrich, *Chem. Eng. Technol.* **2004**, *27*, 361.
- [5] S. Rapagná, H. Provendier, C. Petit, A. Kiennemann, P. U. Foscolo, *Biomass Bioenergy* **2002**, *22*, 377.
- [6] M. F. Patterson, K. B. T.-R. M. in F. S. Knoerzer, Elsevier, **2016**.
- [7] J. D. Barnett, S. Block, G. J. Piermarini, *Rev. Sci. Instrum.* **1973**, *44*, 1.
- [8] M. Runowski, P. Woźny, V. Lavín, S. Lis, *Sens. Actuators, B* **2018**, *273*, 585.
- [9] F. Datchi, R. LeToullec, P. Loubeyre, *J. Appl. Phys.* **1997**, *81*, 3333.
- [10] M. Runowski, P. Woźny, N. Stopikowska, Q. Guo, S. Lis, *ACS Appl. Mater. Interfaces* **2019**, *11*, 4131.
- [11] B. R. Jovanić, J. P. Andreeta, *Phys. Scr.* **1999**, *59*, 274.
- [12] U. R. Rodríguez-Mendoza, S. F. León-Luis, J. E. Muñoz-Santiuste, D. Jaque, V. Lavín, *J. Appl. Phys.* **2013**, *113*, 213517.
- [13] H. K. Mao, J. Xu, P. M. Bell, *J. Geophys. Res. Solid Earth* **1986**, *91*, 4673.
- [14] G. Shen, Y. Wang, A. Dewaele, C. Wu, D. E. Fratanduono, J. Eggert, S. Klotz, K. F. Dziubek, P. Loubeyre, O. V. Fat'yanov, P. D. Asimow, T. Mashimo, R. M. M. Wentzcovitch, *High Pressure Res.* **2020**, *40*, 299.
- [15] T. Zheng, L. Luo, P. Du, S. Lis, U. R. Rodríguez-Mendoza, V. Lavín, I. R. Martín, M. Runowski, *Chem. Eng. J.* **2022**, *443*, 136414.
- [16] J. Barzowska, T. Lesniewski, S. Mahlik, H. J. Seo, M. Grinberg, *Opt. Mater.* **2018**, *84*, 99.

- [17] C. Hernandez, S. K. Gupta, J. P. Zuniga, J. Vidal, R. Galvan, M. Martinez, H. Guzman, L. Chavez, Y. Mao, K. Lozano, *Sens. Actuators. A* **2019**, 298, 111595.
- [18] Y. Y. Yeung, *J. Phys. Condens. Matter* **1990**, 2, 2461.
- [19] S. Adachi, *J. Lumin.* **2021**, 232, 117844.
- [20] B. Struve, G. Huber, *Appl. Phys. B* **1985**, 36, 195.
- [21] M. Back, J. Ueda, H. Hua, S. Tanabe, *Chem. Mater.* **2021**, 33, 3379.
- [22] J. Bouchet, F. Bottin, V. Recoules, F. Remus, G. Morard, R. M. Bolis, A. Benuzzi-Mounaix, *Phys. Rev. B* **2019**, 99, 94113.
- [23] R. S. McWilliams, D. K. Spaulding, J. H. Eggert, P. M. Celliers, D. G. Hicks, R. F. Smith, G. W. Collins, R. Jeanloz, *Science* **2012**, 338, 1330.
- [24] F. Coppari, R. F. Smith, J. H. Eggert, J. Wang, J. R. Rygg, A. Lazicki, J. A. Hawreliak, G. W. Collins, T. S. Duffy, *Nat. Geosci.* **2013**, 6, 926.
- [25] A. C. Victor, T. B. Douglas, *J. Res. Natl. Bur. Stand., Sect. A* **1963**, 67A, 325.
- [26] S. Kleiman, R. Chaim, *Mater. Lett.* **2007**, 61, 4489.
- [27] C.-Y. Huang, *Phys. Lett. A* **1968**, 28, 461.
- [28] A. M. Glass, *J. Chem. Phys.* **1967**, 46, 2080.
- [29] M. G. Brik, *J. Lumin.* **2005**, 60, 437.
- [30] V. Rajendran, M.-H. Fang, W.-T. Huang, N. Majewska, T. Lesniewski, S. Mahlik, G. Leniec, S. M. Kaczmarek, W. K. Pang, V. K. Peterson, K.-M. Lu, H. Chang, R.-S. Liu, *J. Am. Chem. Soc.* **2021**, 143, 19058.
- [31] A. Boyrivent, E. Duval, R. Louat, *Solid State Commun.* **1976**, 19, 1221.
- [32] D. Ma, D. E. Ellis, *J. Lumin.* **1997**, 71, 329.
- [33] J. E. Wertz, P. Auzins, *Phys. Rev.* **1957**, 106, 484.
- [34] M. Szymczak, P. Woźny, M. Runowski, M. Pieprz, V. Lavín, L. Marciniak, *Chem. Eng. J.* **2023**, 139632.
- [35] M. Runowski, A. Shyichuk, A. Tyimiński, T. Grzyb, V. Lavín, S. Lis, *ACS Appl. Mater. Interfaces* **2018**, 10, 17269.
- [36] T. Zheng, M. Sójka, P. Woźny, I. R. Martín, V. Lavín, E. Zych, S. Lis, P. Du, L. Luo, M. Runowski, *Adv. Opt. Mater.* **2022**, n/a, 2201055.
- [37] M. G. Brik, N. M. Avram, C. N. Avram, in *Optical Properties of 3d-Ions in Crystals Spectroscopy and Crystal Field Analysis* (Eds: N. M. Avram, M. G. Brik), Springer, Berlin **2013**, pp. 29–94.
- [38] M. P. Pechini, (Sprague Electric Co), US33330697A3 **1963**.
- [39] M. O. Henry, J. P. Larkin, G. F. Imbusch, *Phys. Rev. B* **1976**, 13, 1893.



## Supporting Information

for *Laser Photonics Rev.*, DOI 10.1002/lpor.202200801

Highly Pressure-Sensitive, Temperature Independent Luminescence Ratiometric Manometer  
Based on MgO:Cr<sup>3+</sup> Nanoparticles

*Maja Szymczak\*, Marcin Runowski, Victor Lavín and Lukasz Marciniak\**

## Supporting Information

### Highly pressure-sensitive, temperature independent luminescence ratiometric manometer based on MgO:Cr<sup>3+</sup> nanoparticles

M. Szymczak<sup>1\*</sup>, M. Runowski<sup>2,3</sup>, V. Lavín<sup>3</sup>, L. Marciniak<sup>1\*</sup>

<sup>1</sup> Institute of Low Temperature and Structure Research, Polish Academy of Sciences,  
Okólna 2, 50-422 Wrocław, Poland

<sup>2</sup> Adam Mickiewicz University, Faculty of Chemistry, Uniwersytetu Poznańskiego 8,  
61-614 Poznań, Poland

<sup>3</sup> Departamento de Física, IUdEA and MALTA-Consolider Team, Universidad de La Laguna, Apartado de  
Correos 456, E-38200 San Cristóbal de La Laguna, Santa Cruz de Tenerife, Spain

\* corresponding author: [l.marciniak@intibs.pl](mailto:l.marciniak@intibs.pl); [m.szymczak@intibs.pl](mailto:m.szymczak@intibs.pl)

**KEYWORDS** *luminescent manometer, pressure sensor, Cr<sup>3+</sup>, chromium(III) ions, crystal field  
strength, luminescence intensity ratio*

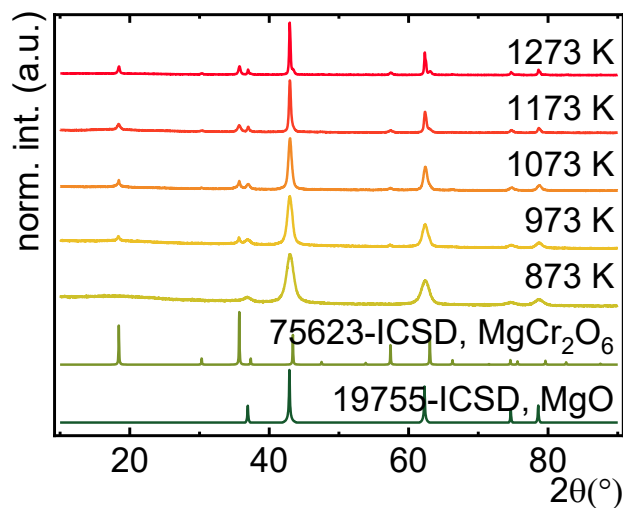


**Figure S1.** XRD patterns of MgO:10%Cr<sup>3+</sup> powders annealed at different temperatures (873-1273 K) and reference samples (MgCr<sub>2</sub>O<sub>6</sub> and MgO).

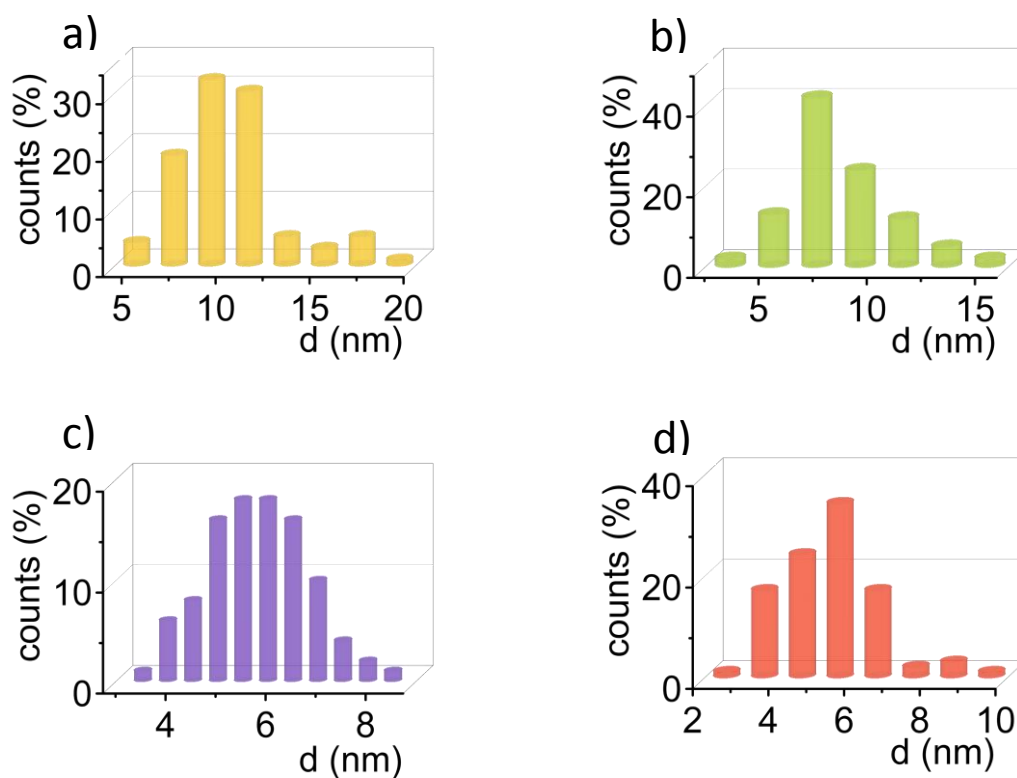


**Figure S2.** Histograms of nanoparticle size distribution obtained from TEM images of MgO:x%Cr<sup>3+</sup> x = 0.1-a), 0.5-b), 5-c), 10-d).

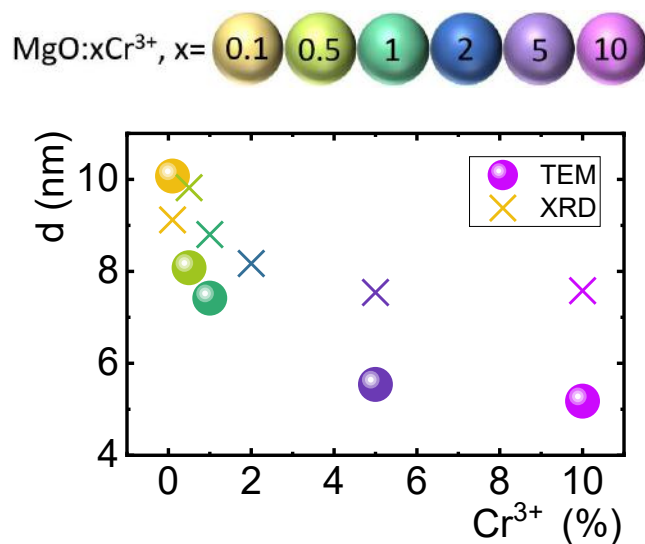


**Figure S3.** Average size ( $d$ ) of nanoparticles obtained, determined from TEM images and Rietveld analysis, of MgO nanoparticles as a function of  $\text{Cr}^{3+}$  ions concentration.

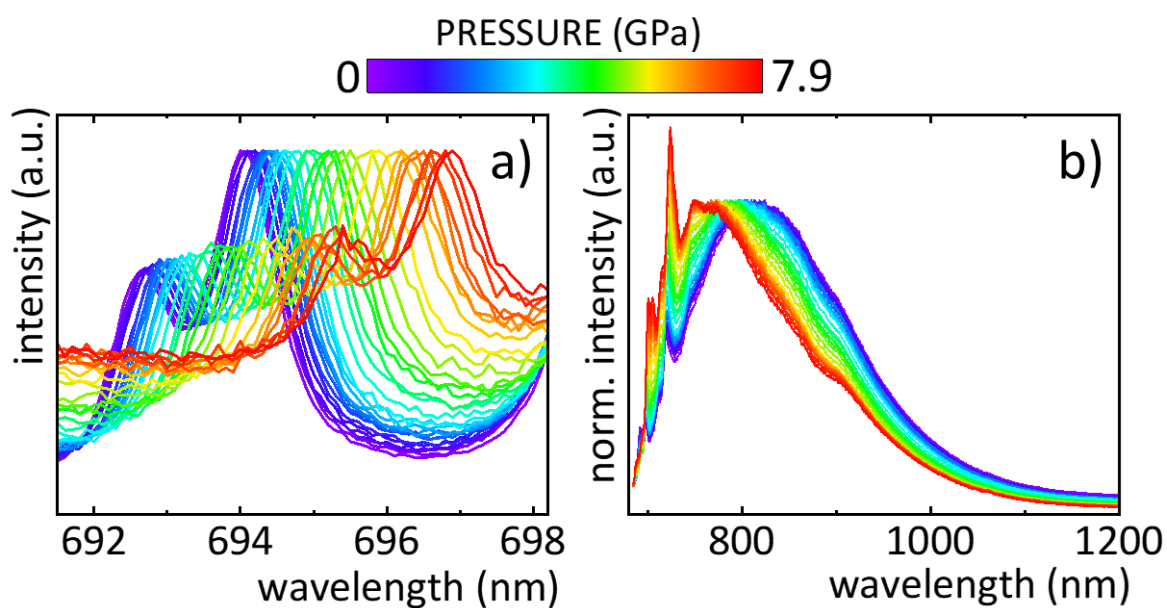


**Figure S4.** Pressure-dependent emission spectra of  $\text{Al}_2\text{O}_3:\text{Cr}^{3+}$  (pressure indicator)-a) and  $\text{MgO}:1\%\text{Cr}^{3+}$  nanoparticles-b), measured upon  $\lambda_{\text{exc}} = 445$  nm at RT.



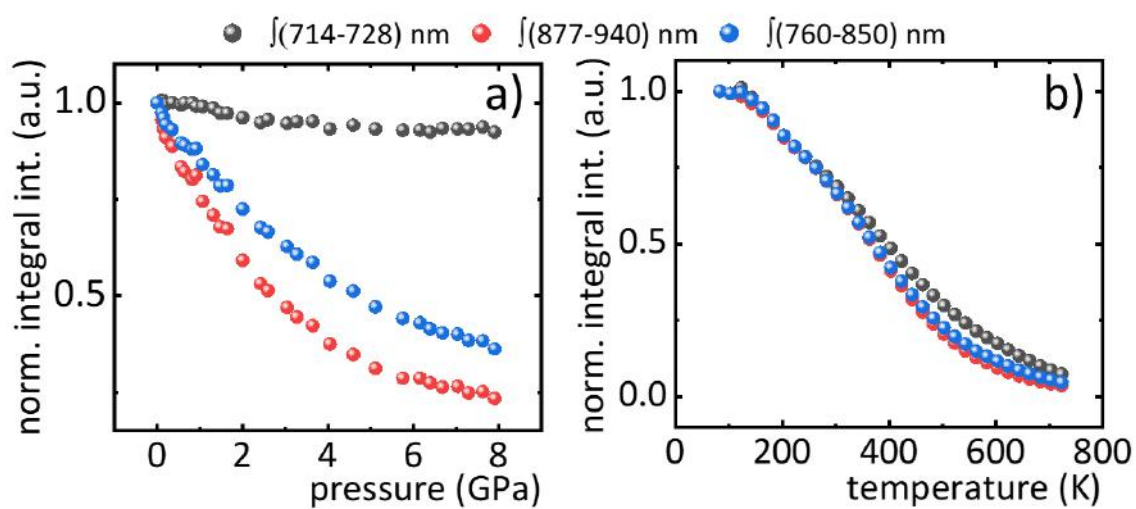


**Figure S5.** Normalised integral intensities of emission band of MgO:1%Cr<sup>3+</sup> nanoparticles as a function of pressure-a) and temperature-b).

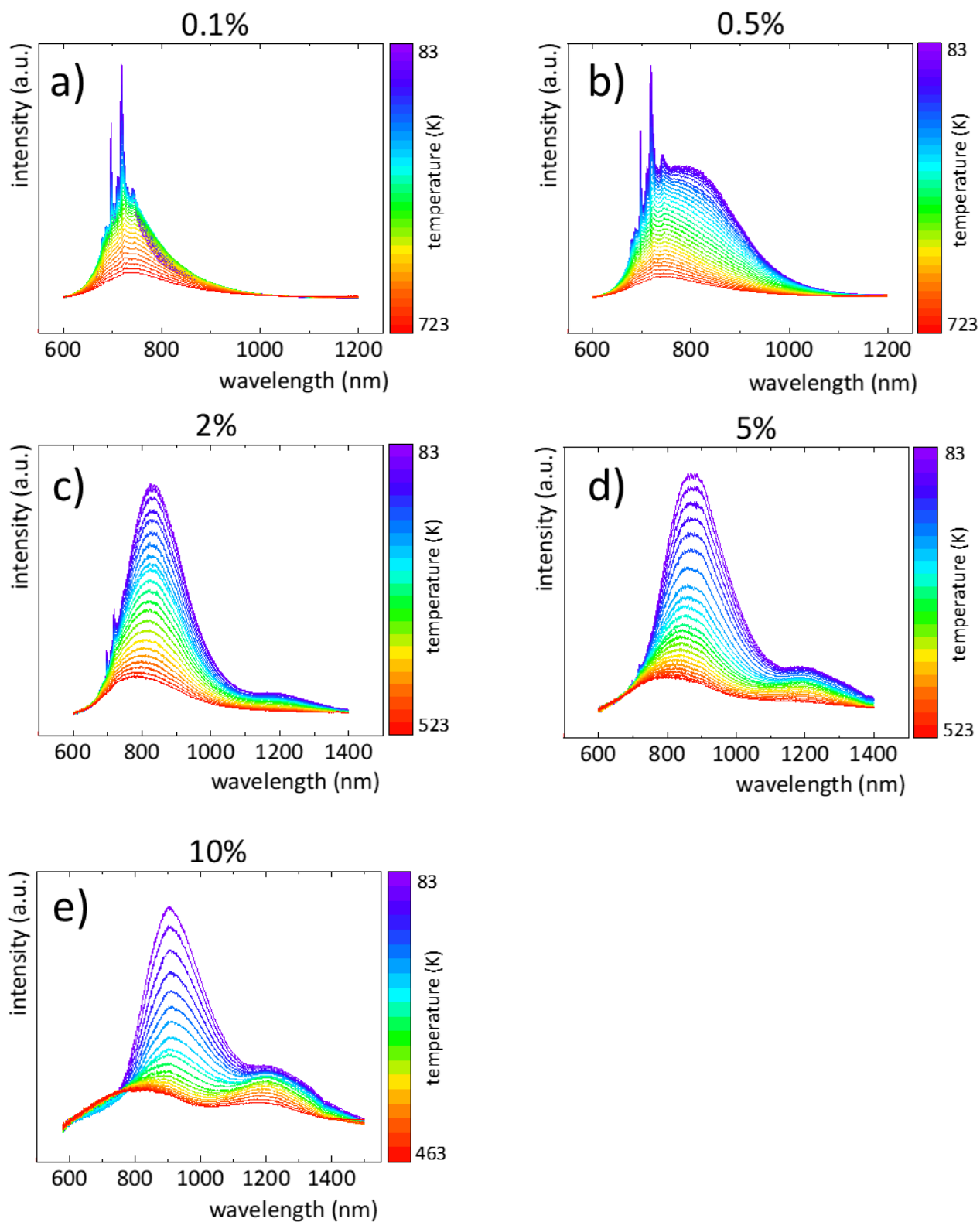


**Figure S6.** Temperature-dependent emission spectra of MgO:x%Cr<sup>3+</sup> x = 0.1-a), 0.5-b), 2-c), 5-d), 10-e) powders, measured upon  $\lambda_{\text{exc}} = 445$  nm.

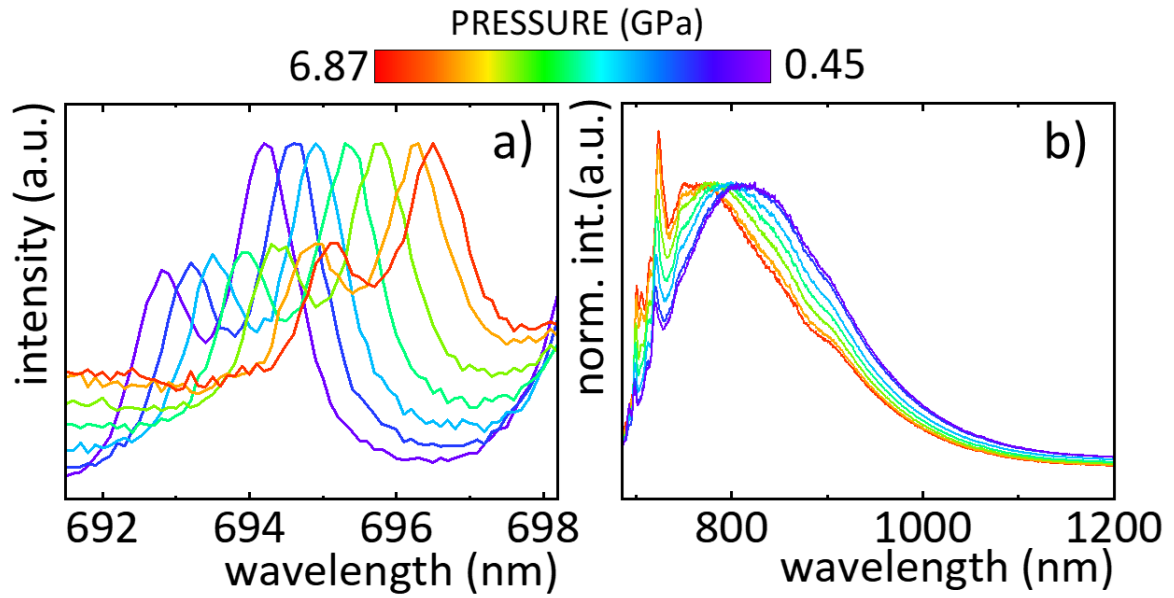


**Figure S7.** Pressure-dependent emission spectra of  $\text{Al}_2\text{O}_3:\text{Cr}^{3+}$  (pressure indicator)-a) and  $\text{MgO}:1\%\text{Cr}^{3+}$  nanoparticles-b) (decompression), measured upon  $\lambda_{\text{exc}} = 445$  nm at RT.

Crystal field strength parameter  $Dq/B$  was calculated with the use of following equations:

$$Dq = \frac{E(^4A_{2(g)} \rightarrow ^4T_{2(g)})}{10} \quad (1)$$

$$\frac{Dq}{B} = \frac{15(x-8)}{(x^2-10x)} \quad (2)$$

where  $Dq$  is the magnitude of crystal field splitting,  $B$  is the Racah parameter and  $x$  could be described as:

$$x = \frac{E(^4A_{2(g)} \rightarrow ^4T_{1(g)}) - E(^4A_{2(g)} \rightarrow ^4T_{2(g)})}{10} \quad (3)$$

# Investigating the Potential of Cr<sup>3+</sup>-Doped Pyroxene for Highly Sensitive Optical Pressure Sensing

Maja Szymczak,<sup>#</sup> Ke Su,<sup>#</sup> Lefu Mei,<sup>\*</sup> Marcin Runowski, Przemyslaw Woźny, Qingfeng Guo, Libing Liao, and Lukasz Marciniak<sup>\*</sup>



Cite This: *ACS Appl. Mater. Interfaces* 2024, 16, 60491–60500



Read Online

ACCESS |



Metrics & More



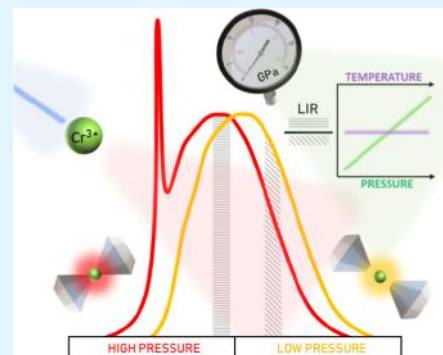
Article Recommendations



Supporting Information

**ABSTRACT:** Luminescent manometry has gained significant popularity in recent years due to its capability to provide in situ pressure measurements in a remote manner. Therefore, there is a growing need to identify phosphors with pressure-dependent spectroscopic properties that can be utilized to develop highly sensitive pressure sensors operating over a wide pressure range. Hence, we present a novel temperature-invariant luminescent manometer based on Cr<sup>3+</sup> ion emission in pyroxene Ca<sub>0.8</sub>Sr<sub>0.2</sub>MgSi<sub>2</sub>O<sub>6</sub>:Cr<sup>3+</sup>. We utilized two readout modes, including an innovative luminescent pressure sensing ratiometric approach based on the broad emission band associated with the <sup>4</sup>T<sub>2g</sub> → <sup>4</sup>A<sub>2g</sub> electronic transition of Cr<sup>3+</sup> ions. This approach provided an exceptionally high sensitivity of S<sub>R</sub> = 50.7 ± 0.5% GPa<sup>-1</sup> and ensured temperature-independent pressure measurements, thus offering highly reliable readouts. Furthermore, the proposed readout mode, which leverages changes in luminescence kinetics, demonstrated high sensitivity at high pressure at around 5 GPa (S<sub>R</sub> ~ 8 ± 0.2% GPa<sup>-1</sup>) surpassing the performance of luminescence kinetics-based manometers reported to date. Consequently, Ca<sub>0.8</sub>Sr<sub>0.2</sub>MgSi<sub>2</sub>O<sub>6</sub>:Cr<sup>3+</sup> emerges as a highly promising phosphor with significant application potential for pressure sensing across a broad pressure range.

**KEYWORDS:** luminescent manometer, optical pressure sensor, luminescence manometry, Cr<sup>3+</sup> luminescence, luminescence intensity ratio, pressure-dependent luminescence kinetics, pressure-dependent spectral shift, temperature-independent pressure sensing



## 1. INTRODUCTION

Since the 1960s, ruby (Al<sub>2</sub>O<sub>3</sub>:Cr<sup>3+</sup>)<sup>1</sup> known for its high chemical and thermal stability has been considered as an irreplaceable, gold standard for pressure indication for measurements in a diamond anvil cell (DAC).<sup>2–5</sup> The widely used approach exploits analysis of the spectral position of the R<sub>1</sub> or R<sub>2</sub> spectral lines of Cr<sup>3+</sup> for pressure determination. Generally, the spectral-shift method stands as the most renowned, traditional, and extensively researched technique in pressure sensing based on the luminescence properties of phosphors.<sup>3,6</sup> Consequently, in subsequent years, researchers predominantly focused on refining this method, endeavoring to develop increasingly sensitive luminescent manometers using different types of dopant ions.<sup>7–13</sup> Thus far, narrow emission lines of lanthanide or transition metal ions have predominantly been explored for pressure sensing.<sup>2,9,10,12,14,15</sup> While this method facilitates highly accurate and precise pressure readouts, due to the unequivocal determination of the position of the narrow emission band, the sensitivity of pressure readouts remains a persistent challenge. Moreover, a reliable pressure reading imposes the necessity of insensitivity of the manometric parameter to changes in other physical parameters among which the most significant is temperature.<sup>2,10,15</sup> For instance, in the case of ruby, the anisotropy of the material's

thermal expansion coefficient alters the covalency of the Cr<sup>3+</sup>–O<sup>2–</sup> bond, leading to a thermal shift in the spectral bands.<sup>16</sup> This may significantly affect the reliability of the pressure readout. Addressing one of these challenges, namely, low sensitivity, involves leveraging the broad emission band of lanthanide and transition metal ions. The sensitivities achieved, for instance, for BaCN<sub>2</sub>:Eu<sup>2+</sup>,<sup>17</sup> Sr<sub>8</sub>Si<sub>4</sub>O<sub>12</sub>C<sub>18</sub> microspheres,<sup>18</sup> or Li<sub>3</sub>Sc<sub>2</sub>(PO<sub>4</sub>)<sub>3</sub>:Cr<sup>3+</sup><sup>19</sup> far surpassed those of mentioned ruby.<sup>1</sup> However, this approach posed a trade-off, namely, while the sensitivity of the pressure readouts is significantly improved, the precision decreased due to larger maximum determination error.<sup>20</sup> Consequently, alternative manometric approaches enabling the elimination of the presented limitations are sought.

A potential solution to the described issue is the recently proposed ratiometric manometric approach based on broad-band phosphors doped with lanthanide ions (Ce<sup>3+</sup>)<sup>21</sup> or

Received: July 23, 2024

Revised: October 21, 2024

Accepted: October 21, 2024

Published: October 29, 2024



transition metals ( $\text{Cr}^{3+}$ ).<sup>19,22–24</sup> In this approach, instead of analyzing the position of the emission band maximum, the luminescence intensity ratio (LIR), analyzed in two spectral regions within the emission band of the phosphor, is considered as a superior manometric parameter. In this case, the change in the strength of the crystal field affecting the luminescent ion, due to the compression of the material, is altered modulating the energy of the emitting level.<sup>25–27</sup> Thus, the spectral position of the band can be shifted, inducing a monotonic change in the LIR parameter. On the other hand, using such a method, a change in temperature should not induce a change in the strength of the crystal field. A temperature increase, due to luminescence thermal quenching, would lead to the parallel change of the intensity recorded in both analyzed spectral ranges, making the LIR thermally independent.<sup>20–22,24</sup>

The applicative potential of the ratiometric LIR-based approach has been showcased in few very recent publications, predominantly employing  $\text{Cr}^{3+}$  ions as the optically active ions.<sup>22–24</sup> Due to the unique spectroscopic features of  $\text{Cr}^{3+}$  ions, their deliberate exploration in pressure sensing is highly reasonable. In addition to their relatively high emission intensity and numerous advantages derived from the  $3d^3$  electronic configuration, the energy of the  ${}^4\text{T}_{2(\text{g})}$  excited state is strongly dependent on the strength of the crystal field, as evidenced by the Tanabe–Sugano diagram.<sup>28</sup> Exposure of the  $\text{Cr}^{3+}$ -doped phosphor to high pressure alters the ion's local environment by modifying the distance between  $\text{Cr}^{3+}$  and the ligands. Consequently, significant spectral changes in the emission band associated with the  ${}^4\text{T}_{2(\text{g})} \rightarrow {}^4\text{A}_{2(\text{g})}$  transition are expected. Despite the prevalence of studies focusing on the behavior of the  ${}^2\text{E}_{(\text{g})} \rightarrow {}^4\text{A}_{2(\text{g})}$  emission band under pressure,<sup>1–5,7,29,30</sup> it is the  ${}^4\text{T}_{2(\text{g})} \rightarrow {}^4\text{A}_{2(\text{g})}$  electronic transition that merits deeper exploration due to its significantly greater sensitivity to pressure variations comparing to the  ${}^2\text{E}_{(\text{g})}$  state.

As previous studies have shown,<sup>31</sup> the two ratiometric approaches that can be implemented for  $\text{Cr}^{3+}$ -doped luminescence manometers take into account (i) LIR of the  ${}^2\text{E} \rightarrow {}^4\text{A}_2$  band to the  ${}^4\text{T}_2 \rightarrow {}^4\text{A}_2$  band and (ii) the ratio of emission intensities recorded in two spectral ranges corresponding to the  ${}^4\text{T}_2 \rightarrow {}^4\text{A}_2$  emission band. The performed study of  $\text{MgO}/\text{Cr}^{3+}$  showed that although the relative sensitivity values for approach (ii) were significantly lower [ $S_{\text{R}} \sim 40\% \text{ GPa}^{-1}$  for (i) and  $S_{\text{R}} \sim 9.8\% \text{ GPa}^{-1}$  for (ii)], its use allows providing low sensitivity of the pressure readout to temperature changes. Considering the high sensitivity of the spectroscopic properties of materials doped with  $\text{Cr}^{3+}$  ions to host material composition in this work, we show that by using  $\text{Ca}_{0.8}\text{Sr}_{0.2}\text{MgSi}_2\text{O}_6:\text{Cr}^{3+}$ , the manometric relative sensitivity can be significantly increased compared to the results obtained for  $\text{MgO}/\text{Cr}^{3+}$ .<sup>31</sup> Accordingly, we have studied the potential of pyroxene  $\text{Ca}_{0.8}\text{Sr}_{0.2}\text{MgSi}_2\text{O}_6:\text{Cr}^{3+}$  in pressure sensing utilizing pressure-affected luminescence properties. Pyroxenes of the  $\text{ABC}_2\text{O}_6$  type are generally regarded as ideal phosphor materials owing to their six-coordinated B crystallographic positions<sup>32,33</sup> suitable for  $\text{Cr}^{3+}$  incorporation and their high structural tunability. Previous research has shown that the partial substitution of  $\text{Ca}^{2+}$  ions with  $\text{Sr}^{2+}$  ions positively influences<sup>34</sup> the properties of  $\text{CaMgSi}_2\text{O}_6$ . Furthermore, the introduction of  $\text{Sr}^{2+}$  ions influences the strength of the crystal field that affects the  $\text{Cr}^{3+}$  ions. The larger ionic radii of  $\text{Sr}^{2+}$  ions, compared to  $\text{Ca}^{2+}$  ions, result in weaker interactions between ligands and  $\text{Sr}^{2+}$  ions in the  $\text{Ca}_{1-x}\text{Sr}_x\text{MgSi}_2\text{O}_6$

structure. Consequently, this increases the  $\text{Cr}^{3+}-\text{O}^{2-}$  distances, thereby weakening the crystal field that influences the  $\text{Cr}^{3+}$  ions. Prior studies on the utilization of  $\text{Cr}^{3+}$  for pressure sensing indicate that sensors exhibiting the highest sensitivity rely on the luminescence of  $\text{Cr}^{3+}$  ions affected by a weak crystal field [9].

To assess the effectiveness of  $\text{Ca}_{0.8}\text{Sr}_{0.2}\text{MgSi}_2\text{O}_6:\text{Cr}^{3+}$  in pressure sensing, both its emission spectra and luminescence kinetics were studied as a function of pressure. Based on the obtained results, two readout modes were proposed: (I) ratiometric and (II) luminescence kinetics approach (lifetime-based). Within the ratiometric LIR-based approach, two methods were explored: (1) utilizing the emission bands associated with  ${}^2\text{E}_{(\text{g})} \rightarrow {}^4\text{A}_{2(\text{g})}$  and  ${}^4\text{T}_{2(\text{g})} \rightarrow {}^4\text{A}_{2(\text{g})}$  electronic transitions of  $\text{Cr}^{3+}$  and (2) an approach based solely on the  ${}^4\text{T}_{2(\text{g})} \rightarrow {}^4\text{A}_{2(\text{g})}$  emission band of  $\text{Cr}^{3+}$ . The studies revealed that the second mentioned method provides a high sensitivity of pressure readout ( $S_{\text{R}} = 50.7\% \text{ GPa}^{-1}$ ), while maintaining temperature independence, as confirmed by the temperature-invariant manometric factor (TIMF) value of  $1558 \text{ K GPa}^{-1}$ . The results underscore the significant role of  $\text{Cr}^{3+}$  ions in highly sensitive, precise, and accurate pressure sensing, representing progress in increasing the application potential of luminescence manometry.

## 2. EXPERIMENTAL SECTION

**2.1. Materials.**  $\text{CaCO}_3$  (Aladdin, 99.00%),  $\text{SrCO}_3$  (Aladdin, 99.00%),  $\text{MgO}$  (Aladdin, 99.00%),  $\text{SiO}_2$  (Aladdin, 99.00%), and  $\text{Cr}_2\text{O}_3$  (Aladdin, 99.99%) were used as the initial materials without additional purification.

**2.2. Synthesis.** A series of  $\text{Ca}_{0.8}\text{Sr}_{0.2}\text{MgSi}_2\text{O}_6:x\text{Cr}^{3+}$ , where  $x = 0.5, 1, 2, 3, 5$ , and  $6\%$ , were prepared using the traditional high-temperature solid-state synthesis. The stoichiometric amount of initial materials with few drops of ethanol was mixed evenly in the agate mortar and then was put into the alumina crucibles. The compounds were sintered in a tubular furnace at  $1275^\circ\text{C}$  for 4 h. The sintered samples were naturally cooled and ground into powder for further characterization.

**2.3. Methods.** The X-ray diffraction (XRD) patterns of the synthesized powders were obtained by the use of an X-ray diffractometer (D8 ADVANCE diffractometer, Bruker Corporation, Germany) with  $\text{Cu K}\alpha$  ( $\lambda = 1.5406 \text{ \AA}$ ) at 40 kV and 40 mA. A fluorescence spectrophotometer (F-4700, Hitachi, Japan) supplied with a 450 W Xe lamp for monitoring room-temperature emission and excitation spectra was applied in the experiment. A fluorescence spectrometer (FSS, Edinburgh) was used for measuring the luminescence decay curves of the samples under ambient conditions. The morphology was characterized by a field-emission scanning electron microscope (SEM, JSM-6701F, Hitachi, Japan) operated at 10 kV.

Scattering Raman spectra were recorded in the pressure range from ambient pressure to 7.18 GPa in a backscattering geometry using a Renishaw InVia confocal micro-Raman system with a 100 mW 532 nm diode laser and an optical system with an Olympus  $\times 20$  SLMPlan N long working distance objective to focus the laser beam on the material. Raman spectra of the compressed sample were recorded in a DAC equipped with the IIa type, low fluorescence diamonds in methanol/ethanol/water (16:3:1) solution as a pressure transmitting medium (PTM).

The pressure- and temperature-dependent emission spectra and luminescence decay profiles were measured using an FLS1000 fluorescence spectrometer (Edinburgh Instruments), equipped with the 450 W xenon lamp and R5509-72 photomultiplier tube from Hamamatsu in nitrogen-flow cooled housing as the detector. A continuous/pulse laser diode with a wavelength of 445 nm was used as the excitation source for measuring the emission spectra and luminescence decay profiles, respectively. A THMS 600 heating–



cooling stage from Linkam was used to set and control the temperature during measurements with 0.1 K temperature stability and 0.1 K set point resolution. To stabilize the temperature of the measured sample, it was incubated at the set temperature for 2 min, and the results were collected after this time. A Druck PACE 5000 was used to apply a pressure during pressure-dependent luminescence studies. The high-pressure luminescence measurements were carried out in a DAC purchased from Almax EasyLab Diacell  $\mu$ ScopeDAC-RT(G). The pressure in the DAC was applied through a nitrogen-fed gas membrane. The DAC was equipped with ultralow fluorescence IIas type diamonds, with 0.4 mm culets. A 250  $\mu$ m stainless-steel gasket with a diameter of 10 mm was placed between the diamonds. A hole of 140  $\mu$ m in diameter was drilled centrally in the gasket, into which an appropriate amount of pressure indicator, sample, and drop of a PTM were placed. The mixture of methanol and ethanol in a volume ratio of 4:1 was used as the PTM and a  $R_2$  line of  $\text{Cr}^{3+}$  in doped  $\text{Al}_2\text{O}_3$  (ruby) was used as a pressure indicator. Thermal and pressure dependences of LIR and  $\tau_{\text{avr}}$  were fitted using polynomial eqs S6–S10 given in the Supporting Information file.

### 3. RESULTS AND DISCUSSION

$\text{CaMgSi}_2\text{O}_6$ , commonly known as diopside, is a naturally occurring mineral with good thermal and mechanical properties.<sup>35–40</sup>  $\text{CaMgSi}_2\text{O}_6$  is characterized by a monoclinic crystal structure with the  $C12/c2$  space group.<sup>35–41</sup> Within this structure,  $\text{Ca}^{2+}$  ions are 8-fold-coordinated, while  $\text{Mg}^{2+}$  ions form octahedra with six  $\text{O}^{2-}$  ligands (Figure 1a). Simulta-

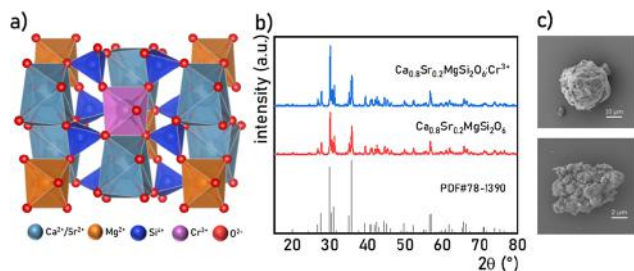


**Figure 1.** Visualized crystal structure of  $\text{Ca}_{0.8}\text{Sr}_{0.2}\text{MgSi}_2\text{O}_6:\text{Cr}^{3+}$  (a); comparison of powder X-ray diffractograms of  $\text{Ca}_{0.8}\text{Sr}_{0.2}\text{MgSi}_2\text{O}_6$  and  $\text{Ca}_{0.8}\text{Sr}_{0.2}\text{MgSi}_2\text{O}_6$  doped with 2%  $\text{Cr}^{3+}$  ions, as well as undoped sample and reference patterns (PDF#78-1390) (b); SEM images of the  $\text{Ca}_{0.8}\text{Sr}_{0.2}\text{MgSi}_2\text{O}_6:2\%\text{Cr}^{3+}$  microcrystals (c).

neously,  $\text{Si}^{4+}$  ions form  $(\text{SiO}_4)$  tetrahedra, linking planes composed of coordinated  $\text{Ca}^{2+}$  and  $\text{Mg}^{2+}$  polyhedra. The incorporation of 20% of  $\text{Sr}^{2+}$  ions (in respect to  $\text{Ca}^{2+}$  ions) into the  $\text{CaMgSi}_2\text{O}_6$  structure does not disrupt its crystal structure,<sup>34</sup> as evidenced by the absence of any additional reflections in the XRD patterns (Figure 1b). Moreover, no reflections of the tetragonal crystal structure of  $\text{SrMgSi}_2\text{O}_6$  with space group  $P421m$  were observed. Prior studies revealed that doping the  $\text{CaMgSi}_2\text{O}_6$  diopside structure with  $\text{Sr}^{2+}$  ions up to 30% ensures<sup>42</sup> the formation of a diopside solid solution. Hence, it can be concluded that the pure phase of  $\text{Ca}_{0.8}\text{Sr}_{0.2}\text{MgSi}_2\text{O}_6$  was obtained. The influence of the  $\text{Cr}^{3+}$  dopant on the  $\text{Ca}_{0.8}\text{Sr}_{0.2}\text{MgSi}_2\text{O}_6$  structure was also examined. In Figure 1b, a powder diffractogram of the sample doped with 2 mol % of  $\text{Cr}^{3+}$  is depicted. The mentioned sample was selected for further analysis based on preliminary spectroscopic studies, which will be described in detail in subsequent sections (also see diffractograms for other samples with varying  $\text{Cr}^{3+}$  concentration in Figure S1). The reflexes of  $\text{Ca}_{0.8}\text{Sr}_{0.2}\text{MgSi}_2\text{O}_6:2\%\text{Cr}^{3+}$  are in good agreement with the reference pattern (PDF#78-1390), indicating that the doping

of  $\text{Cr}^{3+}$  ions does not introduce any structural distortion or additional impurities. Despite the charge difference between the 6-fold-coordinated  $\text{Mg}^{2+}$  and  $\text{Cr}^{3+}$  ions,  $\text{Mg}^{2+}$  crystallographic positions will be plausibly occupied by  $\text{Cr}^{3+}$  ions, due to the similar ionic radii ( $r_{\text{Mg}^{2+}} = 0.72$  Å and  $r_{\text{Cr}^{3+}} = 0.615$  Å)<sup>43</sup> and preferential octahedral surroundings of the oxygen ligands. This assumption is consistent with previously reported results.<sup>44,45</sup> In general, doping of  $\text{Cr}^{3+}$  ions up to 6% allows the formation of a pure diopside phase, without any additional impurities (see Figure S1). The substitution of  $\text{Mg}^{2+}$  ions by  $\text{Cr}^{3+}$  ions is also proved by the unit cell size obtained from the Rietveld refinement (see Figure S2 in Supporting Information), which shows that as the concentration of  $\text{Cr}^{3+}$  ions increases, the unit cell volume decreases from 440.782 to 440.480 Å<sup>3</sup> for undoped and 2%  $\text{Cr}^{3+}$ -doped sample, respectively (Table 1). This effect occurs due to the smaller ionic radius of  $\text{Cr}^{3+}$  compared to that of substituted  $\text{Mg}^{2+}$ .

**Table 1.** Lattice Parameters of  $\text{Ca}_{0.8}\text{Sr}_{0.2}\text{MgSi}_2\text{O}_6$  Undoped and Doped with 2% of  $\text{Cr}^{3+}$  Ions<sup>a</sup>

compound	$\text{Ca}_{0.8}\text{Sr}_{0.2}\text{MgSi}_2\text{O}_6$	$\text{Ca}_{0.8}\text{Sr}_{0.2}\text{MgSi}_2\text{O}_6:2\%\text{Cr}^{3+}$
Sp.Gr.	$C2/c$	$C2/c$
$a$ , Å	$9.749 \pm 0.02$	$9.747 \pm 0.03$
$b$ , Å	$8.951 \pm 0.02$	$8.94 \pm 0.03$
$c$ , Å	$5.252 \pm 0.02$	$5.251 \pm 0.03$
beta	$105.896 \pm 1$	$105.902 \pm 1$
$V$ , Å <sup>3</sup>	$440.782 \pm 3$	$440.480 \pm 3$
$2\theta$ interval, °	5–120	5–120
$R_{\text{wp}}$ , %	4.340%	3.692%
$R_p$ , %	5.881%	4.861%
$\chi^2$	3.446	2.47

<sup>a</sup>Results obtained from the Rietveld refinement.

The microscopic analysis of SEM images of the  $\text{Ca}_{0.8}\text{Sr}_{0.2}\text{MgSi}_2\text{O}_6:2\%\text{Cr}^{3+}$  crystals revealed that the synthesized powders consist of microcrystallites, with a size distribution ranging from a few to tens of micrometers (Figure 1c). The agglomerated morphology with a wide size distribution is a result of the solid-state synthesis method employed.

The vibrational Raman spectra were recorded to analyze the structural stability of the  $\text{Ca}_{0.8}\text{Sr}_{0.2}\text{MgSi}_2\text{O}_6:\text{Cr}^{3+}$  material under high pressure. The recorded Raman scattering spectrum for the  $\text{Ca}_{0.8}\text{Sr}_{0.2}\text{MgSi}_2\text{O}_6:\text{Cr}^{3+}$  material at ambient conditions presents four main intense Raman modes at around 320, 390, 670, and 1010  $\text{cm}^{-1}$  and a few less intense modes as a result of the inelastic scattering of photons. Four mentioned modes were chosen for further analysis. The relative intensity of the Raman modes does not change drastically, and the formation of new Raman modes was not observed in the compression process, which is evidence of the structural stability of the  $\text{Ca}_{0.8}\text{Sr}_{0.2}\text{MgSi}_2\text{O}_6:\text{Cr}^{3+}$  material under pressure up to 7.18 GPa (Figure 2a). The energies of the phonon modes increase under the compression process, and the corresponding Raman mode centroids shift linearly toward higher wavenumbers, as presented in Figure 2b. The observed tendencies of the Raman mode shifts are an effect of decreasing interatomic distances (the bonds shortening) in the crystal structure under high pressure. The calculated Raman mode shift rates ( $\text{cm}^{-1} \text{GPa}^{-1}$ ) are collected in Table 2 (see also Table S1). Observed changes of the Raman spectra at around 1030  $\text{cm}^{-1}$ , i.e., elevation and broadening, are results of artifacts of the Raman

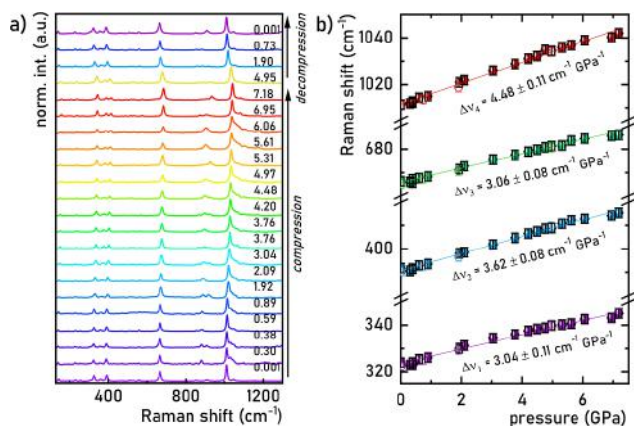


**Figure 2.** Normalized vibrational Raman spectra for the  $\text{Ca}_{0.8}\text{Sr}_{0.2}\text{MgSi}_2\text{O}_6:\text{Cr}^{3+}$  material in a compression and decompression cycle (a); calculated peak centroids of the four most intense Raman modes as a function of high pressure (b); spheres indicate Raman peaks in compression cycles, and empty ones indicate Raman peaks in decompression cycles; the colored lines are fitted linear functions for determination of the Raman mode shift rates under pressure.

**Table 2. Approximated Peak Centroids of the Most Intense Raman Modes around Starting Pressure Values and the Corresponding Shift Rates of the Raman Modes for the  $\text{Ca}_{0.8}\text{Sr}_{0.2}\text{MgSi}_2\text{O}_6:\text{Cr}^{3+}$  Material under Pressure**

peak centroid (cm <sup>-1</sup> )	shift rate (cm <sup>-1</sup> GPa <sup>-1</sup> )
≈320	3.04 ± 0.11
≈390	3.62 ± 0.08
≈670	3.06 ± 0.08
≈1010	4.48 ± 0.11

signal from diamonds in the DAC. In the decompression process, the reverse tendency of the vibrational Raman mode shift to the initial state was observed (empty spheres, Figure 2b). The same position of Raman modes in the decompression process indicates reversibility of the structural changes caused by the compression of the material under high pressure. The fitting details and information about the centroid determination method are given in the Supporting Information.

To identify the  $\text{Ca}_{0.8}\text{Sr}_{0.2}\text{MgSi}_2\text{O}_6:\text{Cr}^{3+}$  sample with the highest potential for pressure sensing, the spectroscopic properties under ambient conditions of samples with varying concentration of  $\text{Cr}^{3+}$  ions (0.5–6%) were studied. The emission spectra obtained upon  $\lambda_{\text{exc}} = 457$  nm were recorded (Figure 3a; see also Figure 3b for excitation spectra). The emission spectra of all samples consist of a broad emission band associated with the  $^4\text{T}_{2g} \rightarrow ^4\text{A}_{2g}$  electronic transitions of  $\text{Cr}^{3+}$ , which confirms that  $\text{Cr}^{3+}$  ions are located in the weak crystal field in  $\text{Ca}_{0.8}\text{Sr}_{0.2}\text{MgSi}_2\text{O}_6$ . The maximum of each band is at around 780 nm (12,818 cm<sup>-1</sup>), with the full-width at half-maximum increasing from 184.6 nm (3076 cm<sup>-1</sup>) to 211.6 nm (3541 cm<sup>-1</sup>) for 0.5% and 5%  $\text{Cr}^{3+}$ , respectively, and then decreasing to 188.8 nm for the sample with the highest concentration of 6%  $\text{Cr}^{3+}$ . Although reliable quantitative comparison of luminescence intensity of phosphors is challenging, measurements made for all  $\text{Ca}_{0.8}\text{Sr}_{0.2}\text{MgSi}_2\text{O}_6:\text{Cr}^{3+}$  samples under comparable conditions allowed a rough determination of the effect of  $\text{Cr}^{3+}$  ion concentration on room-temperature emission intensity from  $\text{Ca}_{0.8}\text{Sr}_{0.2}\text{MgSi}_2\text{O}_6:\text{Cr}^{3+}$ . It can be found that the concentration

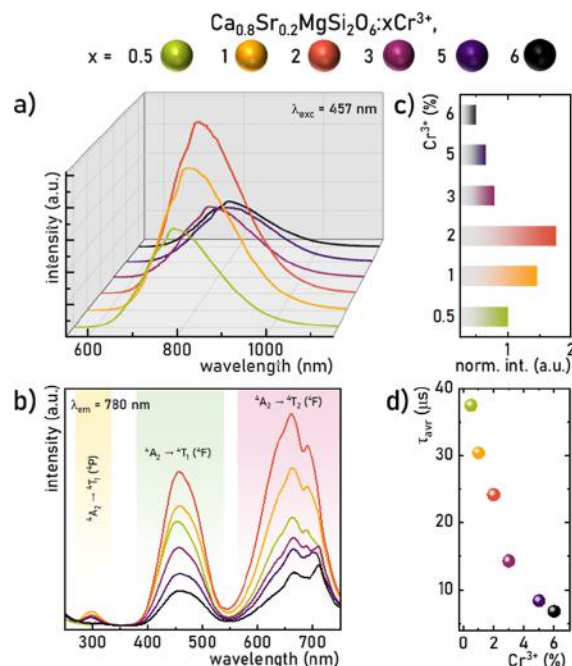


**Figure 3.** Room-temperature luminescence characteristics: emission ( $\lambda_{\text{exc}} = 457$  nm) (a) and excitation ( $\lambda_{\text{em}} = 780$  nm) (b) spectra; comparison of the intensity of emission (c) and calculated  $\tau_{\text{avr}}$  of the  $^4\text{T}_{2(g)}$  state of  $\text{Cr}^{3+}$  (d) of the  $\text{Ca}_{0.8}\text{Sr}_{0.2}\text{MgSi}_2\text{O}_6$  powders doped with various  $\text{Cr}^{3+}$  contents.

increases with  $\text{Cr}^{3+}$  concentration up to 2%, reaching a value about twice higher than that of the sample with the lowest dopant concentration (0.5%  $\text{Cr}^{3+}$ ) (Figure 3c). Above 2% of  $\text{Cr}^{3+}$ , the intensity gradually decreases due to the interionic interactions. The recorded room-temperature excitation spectra, obtained by monitoring an emission at 780 nm, revealed two intense bands associated with the  $^4\text{A}_2 \rightarrow ^4\text{T}_1$  and  $^4\text{A}_2 \rightarrow ^4\text{T}_2$  electronic transitions of  $\text{Cr}^{3+}$ , with maxima at about  $454 \pm 3$  nm ( $22,026 \pm 145$  cm<sup>-1</sup>) and  $653 \pm 3$  nm ( $15,314 \pm 70$  cm<sup>-1</sup>), respectively (Figure 3b). Additionally, a low-intensity band corresponding to the  $^4\text{A}_2 \rightarrow ^4\text{T}_1$  (P) transition of  $\text{Cr}^{3+}$  with a maximum at about 298 nm ( $33,560$  cm<sup>-1</sup>) is also observed in the excitation spectra.

To analyze the influence of  $\text{Cr}^{3+}$  ion concentration on luminescence kinetics, room-temperature luminescence decay profiles were recorded for all studied  $\text{Ca}_{0.8}\text{Sr}_{0.2}\text{MgSi}_2\text{O}_6:\text{Cr}^{3+}$  samples, monitoring an emission maximum at 780 nm upon  $\lambda_{\text{exc}} = 457$  nm (Figure S3). Based on data obtained by fitting curves with a double-exponential function (eq 1), the average lifetimes of the  $^4\text{T}_{2g}$  excited state were determined using eq 2

$$I(t) = I_0 + A_1 \cdot \exp\left(-\frac{t}{\tau_1}\right) + A_2 \cdot \exp\left(-\frac{t}{\tau_2}\right) \quad (1)$$

$$\tau_{\text{avr}} = \frac{A_1 \tau_1^2 + A_2 \tau_2^2}{A_1 \tau_1 + A_2 \tau_2} \quad (2)$$

where  $I_0$  is the initial intensity,  $A_1$  and  $A_2$  are the amplitudes, and  $\tau_1$  and  $\tau_2$  are the decay time components. The biexponential function was used due to the nonexponential shape of the decay profiles of samples doped with higher  $\text{Cr}^{3+}$  concentrations. The calculated average lifetimes are in the microsecond range, which is characteristic of the kinetics of the



$^4T_{2(g)}$  state of  $Cr^{3+}$  (Figure 3d). The  $\tau_{avr}$  was observed to shorten with increasing  $Cr^{3+}$  ion concentration in  $Ca_{0.8}Sr_{0.2}MgSi_2O_6:Cr^{3+}$ , from 37.51 to 6.82  $\mu s$  for 0.5% and 6% of  $Cr^{3+}$ , respectively.

Based on the structural and spectroscopic studies discussed above, a sample  $Ca_{0.8}Sr_{0.2}MgSi_2O_6$  doped with 2%  $Cr^{3+}$  was selected for investigating its potential for pressure sensing applications. This choice was mainly due to the highest emission intensity required to conduct high-resolution luminescence measurements in a DAC. Therefore, the emission spectra of the sample  $Ca_{0.8}Sr_{0.2}MgSi_2O_6:Cr^{3+}$  were measured upon 445 nm excitation, ranging from ambient pressure up to 7.55 GPa during compression (Figure 4a;

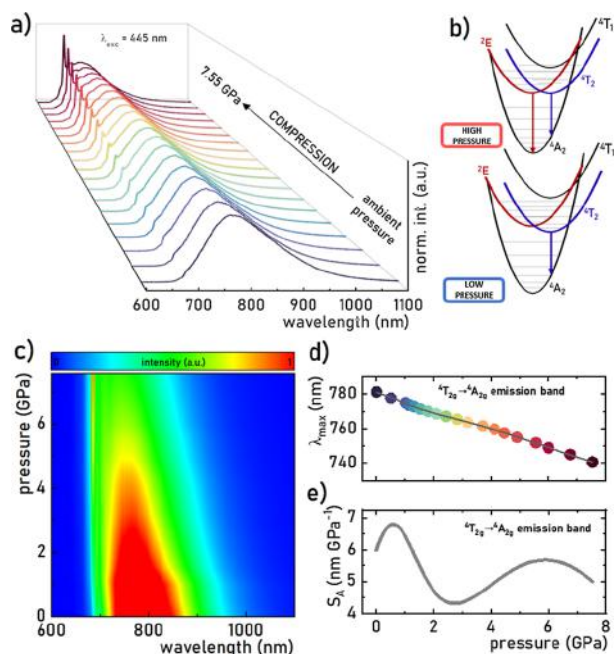


**Figure 4.** Pressure-dependent emission spectra (normalized to the maximum of the  $^4T_{2(g)} \rightarrow ^4A_{2(g)}$  emission band) (a); configuration coordinate diagrams of  $Cr^{3+}$  ions affected by low and high pressure (b); pressure-dependent emission intensity map (c); spectral position of the  $^4T_{2(g)} \rightarrow ^4A_{2(g)}$  emission band as a function of pressure (d) and corresponding  $S_A$  (e) of  $Ca_{0.8}Sr_{0.2}MgSi_2O_6:Cr^{3+}$  measured from ambient pressure to 7.55 GPa.

normalized spectra are available in Supporting Information in Figure S4a,b) and decompression of the material (see Figure S5 in the Supporting Information). As described earlier, a broad emission band was observed at ambient conditions, indicating the electron transitions from the  $^4T_{2(g)}$  excited state to the  $^4A_{2(g)}$  ground state (Figure 4b) of  $Cr^{3+}$  ions. At approximately 2 GPa, a narrow emission band associated with the  $^2E_{(g)} \rightarrow ^4A_{2(g)}$  electronic transition of  $Cr^{3+}$  becomes discernible in the emission spectrum. The intensity of the mentioned band gradually increases with an increasing pressure and starts to dominate the emission spectrum above 5 GPa. This phenomenon results from the shortening in distance  $R$  between  $Cr^{3+}$  and  $O^{2-}$  ligands associated with the compression, which is inversely proportional to the crystal field strength parameter  $Dq/B$  ( $Dq/B \sim R^{-5}$ ).<sup>46</sup> Based on the Tanabe–Sugano diagram for ions with  $3d^3$  electronic configuration, with increasing crystal field strength, the energy of the  $^4T_{2(g)}$  state rises in respect to the energy of the  $^2E_{(g)}$

level, which remains almost constant. Beyond a value of  $Dq/B$  approximately 2.2, the  $^2E_{(g)}$  state becomes energetically lower compared to the  $^4T_{2(g)}$  state of  $Cr^{3+}$ . Consequently, the predominant emission is observed from the  $^2E_{(g)}$  level, manifested by domination of the emission spectrum by the narrow band associated with the  $^2E_{(g)} \rightarrow ^4A_{2(g)}$  electronic transition of  $Cr^{3+}$ . This effect is also clearly visible in the pressure-dependent map of the emission intensity shown in Figure 4c, whereas the two-dimensional (2D) pressure-dependent emission spectra are depicted in Figure S6 in the Supporting Information file. The described pressure-driven change in the energy of the  $^4T_{2(g)}$  state results in the high sensitivity of the spectral position of the  $^4T_{2(g)} \rightarrow ^4A_{2(g)}$  emission band to pressure (Figure 4d). The observed blue shift of this band upon material compression demonstrates a monotonic and nearly linear trend. From ambient pressure to 7.55 GPa, the maximum of this broad band shifts from  $781.3 \pm 0.4$  to  $740.7 \pm 0.4$  nm (from 12,799 to 13,500  $cm^{-1}$ ). Given a significant shift in the  $^4T_{2(g)} \rightarrow ^4A_{2(g)}$  band, a readout mode based on this spectral shift was proposed to determine absolute sensitivity using the formula (eq 3)

$$S_A = \frac{\Delta\lambda_{max}}{\Delta p} \quad (3)$$

where  $\Delta\lambda_{max}$  is the change of maximum of emission band corresponding to the change of the pressure  $\Delta p$ . The maximal  $S_A = 6.8$  nm  $GPa^{-1}$  ( $112.9$   $cm^{-1}$   $GPa^{-1}$ ) was obtained at a pressure of 0.57 GPa (Figure 4e) and is approximately 18 times greater than the commonly used  $Al_2O_3:Cr^{3+}$  (ruby) pressure indicator.<sup>47–49</sup> However, while achieving high sensitivity to pressure variations, there is a trade-off with readout precision due to ambiguity in determination of the maximum of the broad emission band. Additionally, the bandwidth of the  $^4T_{2(g)} \rightarrow ^4A_{2(g)}$  transitions narrows with the applied pressure which may suggest that the curvature of the  $^4T_{2(g)}$  parabola starts to be slightly modified. Furthermore, with the  $Ca_{0.8}Sr_{0.2}MgSi_2O_6:Cr^{3+}$  compression, a subtle decrease in the half-bandwidth of the  $^4T_2 \rightarrow ^4A_2$  band can be observed (from 2510 to 2412  $cm^{-1}$  and in wavelength units: from 158.34 to 138.97 nm at ambient pressure and at 7.55 GPa, respectively). Several mechanisms could account for this phenomenon.<sup>50</sup> One potential explanation is the alteration in the curvature of the  $^4T_2$  state parabola under applied pressure, which affects the energy of the  $^4T_2$  level. Additionally, the fwhm of the  $^4T_2 \rightarrow ^4A_2$  band is influenced by the displacement between the  $^4A_2$  and  $^4T_2$  state parabolas in the configurational coordination diagram.<sup>51,52</sup> Consequently, the reduction in the  $Cr^{3+}-O^{2-}$  bond distance associated with material compression may reduce this displacement, leading to a spectral narrowing of the band. It is plausible that both mechanisms concurrently contribute to the observed changes in  $Ca_{0.8}Sr_{0.2}MgSi_2O_6:Cr^{3+}$ .

As briefly mentioned earlier, due to the low precision in the determination of the band maxima of the broad band emitting phosphors, the analysis of its spectral position for pressure determination has some drawbacks and limitations.<sup>23</sup> Therefore, for the  $Ca_{0.8}Sr_{0.2}MgSi_2O_6:Cr^{3+}$  phosphor, a ratiometric approach was adopted utilizing the LIR parameter as a manometric parameter (Figure 5a). Given the presence of both narrow and broad emission bands in the emission spectrum at high pressures, corresponding to electronic transitions to  $^4A_2$  the ground state from  $^2E_{(g)}$  and  $^4T_{2(g)}$  excited states of  $Cr^{3+}$ , respectively, two approaches were compared in the context of

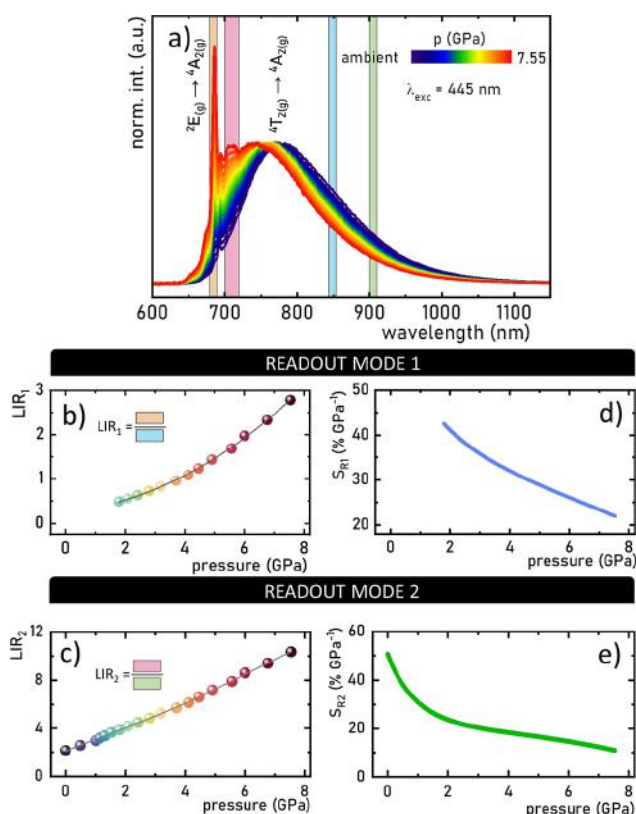


**Figure 5.** Normalized emission spectra of  $\text{Ca}_{0.8}\text{Sr}_{0.2}\text{MgSi}_2\text{O}_6:\text{Cr}^{3+}$  as a function of pressure (spectral ranges used for  $\text{LIR}_1$  and  $\text{LIR}_2$  determination are marked by the color bars) (a); comparison of manometric performance of  $\text{Ca}_{0.8}\text{Sr}_{0.2}\text{MgSi}_2\text{O}_6:\text{Cr}^{3+}$ , based on two ratiometric pressure readout modes: (1) based on the  ${}^2\text{E}_{\text{g}} \rightarrow {}^4\text{A}_{2\text{g}}$  and  ${}^4\text{T}_{2\text{g}} \rightarrow {}^4\text{A}_{2\text{g}}$  emission intensity ratios (b,d) and (2) based on the  ${}^4\text{T}_{2\text{g}} \rightarrow {}^4\text{A}_{2\text{g}}$  emission band (c,e); pressure dependence of  $\text{LIR}_1$  (b) and  $\text{LIR}_2$  (c) and corresponding  $S_{\text{R}_1}$  (d) and  $S_{\text{R}_2}$  (e).

pressure sensing. The first approach utilizes both narrow and broad emission bands, a method frequently employed in the development of luminescent thermometers due to the thermal coupling of  ${}^2\text{E}_{\text{g}}$  and  ${}^4\text{T}_{2\text{g}}$  levels of  $\text{Cr}^{3+}$ .<sup>53</sup> Conversely, the second approach utilizes the spectral ranges of only the  ${}^4\text{T}_{2\text{g}} \rightarrow {}^4\text{A}_{2\text{g}}$  broad emission band. Our previous work has demonstrated the efficacy of this approach in developing highly sensitive pressure sensors.<sup>21,23,24</sup> Consequently, the LIR parameters were defined as follows and are schematically marked in Figure 5a

$$\text{LIR}_1 = \frac{\int_{678.5 \text{ nm}}^{688.5 \text{ nm}} I(\text{Cr}^{3+}: {}^2\text{E} \rightarrow {}^4\text{A}_2) d\lambda}{\int_{842 \text{ nm}}^{852 \text{ nm}} I(\text{Cr}^{3+}: {}^4\text{T}_2 \rightarrow {}^4\text{A}_2) d\lambda} \quad (5)$$

$$\text{LIR}_2 = \frac{\int_{700 \text{ nm}}^{720 \text{ nm}} I(\text{Cr}^{3+}: {}^4\text{T}_{2\text{g}} \rightarrow {}^4\text{A}_{2\text{g}}) d\lambda}{\int_{900 \text{ nm}}^{910 \text{ nm}} I(\text{Cr}^{3+}: {}^4\text{T}_{2\text{g}} \rightarrow {}^4\text{A}_{2\text{g}}) d\lambda} \quad (6)$$

Both  $\text{LIR}_1$  (eq 5) and  $\text{LIR}_2$  (eq 6) exhibit a monotonic enhancement with increasing applied pressure across the entire analyzed range of pressure, so at least up to 7.55 GPa (Figure 5b,c). Based on the obtained LIR values as a function of pressure, a manometric performance of  $\text{Ca}_{0.8}\text{Sr}_{0.2}\text{MgSi}_2\text{O}_6:\text{Cr}^{3+}$  was assessed by calculating the relative pressure sensitivity ( $S_{\text{R}}$ ) of the determined LIRs using the following formula (eq 7)

$$S_{\text{R}} = \left| \frac{1}{\text{LIR}} \frac{\Delta \text{LIR}}{\Delta p} 100\% \right| \quad (7)$$

where  $\Delta \text{LIR}$  represents the change of LIR for the  $\Delta p$  change in pressure. Since the  ${}^2\text{E}_{\text{g}} \rightarrow {}^4\text{A}_{2\text{g}}$  emission band can be observed only above 1.8 GPa, the operating pressure range is very limited. Moreover, the manometric sensitivity in this case is reduced due to the spectral overlap between the  ${}^2\text{E}_{\text{g}} \rightarrow {}^4\text{A}_{2\text{g}}$  and  ${}^4\text{T}_{2\text{g}} \rightarrow {}^4\text{A}_{2\text{g}}$  emission bands. Nevertheless, the relative sensitivity decreases monotonically from  $40 \pm 0.5\% \text{ GPa}^{-1}$  at 2 GPa to around  $20 \pm 0.5\% \text{ GPa}^{-1}$  at 7.55 GPa (Figure 5d). On the other hand, the operating range of the approach based on the  ${}^4\text{T}_{2\text{g}} \rightarrow {}^4\text{A}_{2\text{g}}$  bands is much wider and the maximal  $S_{\text{R}} = 50.7 \pm 0.5\% \text{ GPa}^{-1}$  at ambient pressure is achieved (Figure 5e). However, the relative sensitivity above 2 GPa is lower compared to the  $\text{LIR}_1$  approach and decreases up to  $11 \pm 0.5\% \text{ GPa}^{-1}$  at 7.5 GPa. To fully explore the potential of the proposed optical pressure sensor based on emission associated with the  ${}^4\text{T}_2 \rightarrow {}^4\text{A}_2$  electronic transition of  $\text{Cr}^{3+}$  ions, several combinations of spectral ranges used to define the LIR parameter were analyzed. The 700–720 nm range, exhibiting significant changes in band shape and its intensity, was selected as the numerator for LIR. For the denominator, 10 nm-wide ranges from 730 to 960 nm of the  ${}^4\text{T}_2$  emission band were examined. The corresponding sensitivities, based on the LIR pressure dependencies, are provided in Figures S7 and S8. To further illustrate the results, the  $S_{\text{R}_x}$  values obtained were presented in a 2D map, with the y axis representing the spectral range used to define the LIR denominator. The 900–910 nm range, selected as the LIR denominator, did not yield the highest relative sensitivity, with better results observed for spectral ranges above 900 nm, where the relative sensitivity increased by up to 5% for the monitored 950–960 nm range. However, the 900–910 nm range was chosen as a compromise between sensor sensitivity and measurement reliability. At 950 nm, the point intensity of the band is below 10% of the maximum intensity of the  ${}^4\text{T}_2$  band, while at 900 nm, this value approaches 20% at the highest applied pressure of 7.55 GPa, leading to a lower signal-to-noise ratio and reduced error in pressure values derived from the calibration curve of the potential manometer. Therefore, the 700–720 and 900–910 nm spectral ranges were selected to define LIR, optimizing both sensitivity and reliability of pressure readouts.

To date, research on utilizing spectroscopic properties for pressure sensing has primarily focused on assessing their potential based solely on the magnitude of parameter variations induced by applied pressure. However, it is crucial to acknowledge that very often, the same spectroscopic properties are also significantly influenced by the temperature.<sup>2,7</sup> Therefore, when the sensing properties of a potential luminescence manometer are evaluated, it is vital to investigate the impact of temperature on the spectroscopic parameters used for pressure sensing.

Consequently, emission spectra of the  $\text{Ca}_{0.8}\text{Sr}_{0.2}\text{MgSi}_2\text{O}_6:\text{Cr}^{3+}$  material were studied as a function of temperature within the range of 83–763 K upon 445 nm excitation (Figure 6a). Throughout the entire temperature range, only a broad emission band associated with the radiative transition of electrons from the  ${}^4\text{T}_{2\text{g}}$  excited state to the  ${}^4\text{A}_2$  ground state of  $\text{Cr}^{3+}$  was observed. Therefore, the  $\text{LIR}_1$  approach was excluded from further analysis. A characteristic

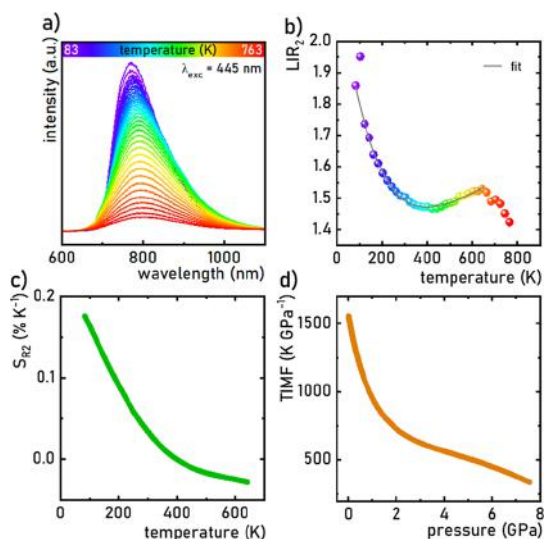


**Figure 6.** Temperature characterization of the developed luminescent manometer  $\text{Ca}_{0.8}\text{Sr}_{0.2}\text{MgSi}_2\text{O}_6:\text{Cr}^{3+}$ : emission spectra as a function of temperature ( $\lambda_{\text{exc}} = 445$  nm) (a), thermal evolution of  $\text{LIR}_2$  (b), and corresponding  $S_{R_2}$  (c); pressure dependence of TIMF (d).

thermal quenching of  $\text{Cr}^{3+}$  emission associated with the nonradiative depopulation of the  $^4\text{T}_{2(\text{g})}$  state through the intersection point between the  $^4\text{T}_{2(\text{g})}$  and  $^4\text{A}_{2(\text{g})}$  state parabolas was observed. The thermal evolution of  $\text{LIR}_2$  is illustrated in Figure 6b. As can be clearly seen, the  $\text{LIR}_2$  decreases from 1.86 at 83 K to 1.5 at around 300 K and oscillates around those values during further increase of temperature. The results of thermal relative sensitivities (determined analogous to eq 7, by replacing pressure with temperature) presented in Figure 6c

indicate that the maximal  $S_R = 0.18 \pm 0.03\% \text{ K}^{-1}$  at 83 K was achieved, and its value decreases with temperature. In the 300–700 K temperature range, the  $S_R$  does not exceed  $0.05\% \pm 0.04\% \text{ K}^{-1}$  (with  $S_R = 0.033\% \text{ K}^{-1}$  at room temperature). According to the well-established standardization, thermal sensitivity below  $1\% \text{ K}^{-1}$  excludes the material from potential thermal sensing applications,<sup>54</sup> which in this particular case confirms its thermal invariability. To further evaluate thermal independence of pressure readout using  $\text{Ca}_{0.8}\text{Sr}_{0.2}\text{MgSi}_2\text{O}_6:\text{Cr}^{3+}$ , the TIMF parameter<sup>22</sup> proposed previously was determined (eq 8)

$$\text{TIMF} = \left| \frac{S_{R,p,\text{max}}}{S_{R,T,\text{(RT)}}} \right| \quad (8)$$

where  $S_{R,p,\text{max}}$  represents the maximum pressure sensitivity and  $S_{R,T,\text{(RT)}}$  is the temperature relative sensitivity achieved at room temperature. TIMF's value represents the change in the temperature which is required to induce the change of  $\text{LIR}_2$  that corresponds to its change observed for  $\Delta p = 1$  GPa (Figure 6d). In the case of the  $\text{Ca}_{0.8}\text{Sr}_{0.2}\text{MgSi}_2\text{O}_6:\text{Cr}^{3+}$  material,  $\text{TIMF} = 1558 \text{ K GPa}^{-1}$  was found. This guarantees high reliability of pressure readouts obtained from the developed manometer.<sup>6</sup>

The influence of pressure on luminescence kinetics of  $\text{Ca}_{0.8}\text{Sr}_{0.2}\text{MgSi}_2\text{O}_6:\text{Cr}^{3+}$  was also investigated. Luminescence decay curves were thus recorded across the entire pressure range, i.e., from ambient to 7.55 GPa during the compression (Figure 7a) and decompression (Figure S9) cycles. The sample was measured upon  $\lambda_{\text{exc}} = 445$  nm and the maximum of the  $^4\text{T}_{2(\text{g})} \rightarrow ^4\text{A}_{2(\text{g})}$  emission band was monitored. Due to the nonexponential character of the recorded decay profiles, the luminescence decay curves were fitted using a biexponential function, as described by eq 1, and the average lifetime of the

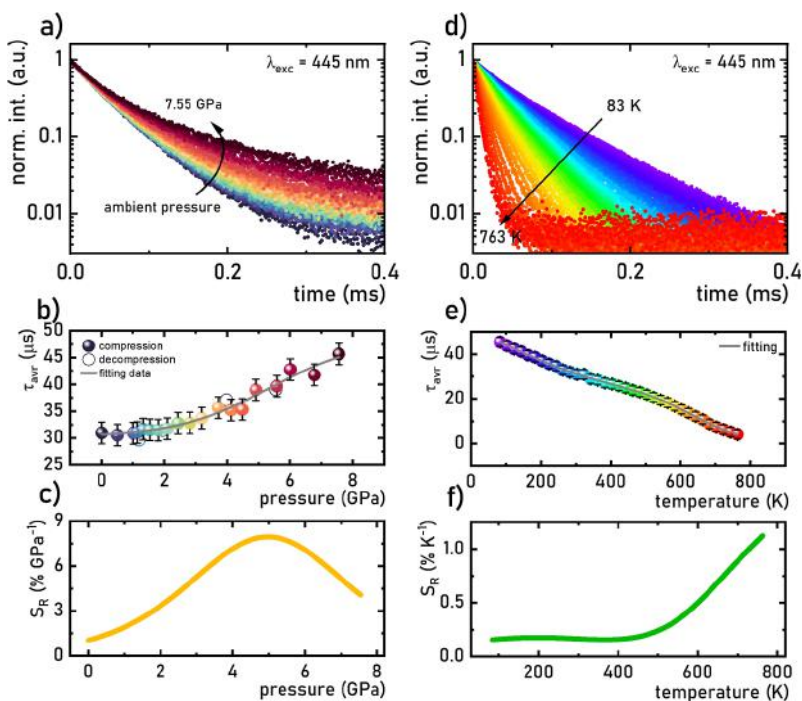


**Figure 7.** Pressure- and temperature-dependent luminescence decay curves ( $\lambda_{\text{exc}} = 445$  nm;  $\lambda_{\text{em}}$  was maximum of the emission band associated with the  $^4\text{T}_{2(\text{g})} \rightarrow ^4\text{A}_{2(\text{g})}$  electronic transition of  $\text{Cr}^{3+}$ ) (a,d), respectively; average lifetime of the  $^4\text{T}_{2(\text{g})}$  excited state of  $\text{Cr}^{3+}$  as a function of pressure (b) (filled symbols correspond to compression and open symbols to decompression) and temperature (e) and corresponding  $S_R$  (c,f), respectively, for  $\text{Ca}_{0.8}\text{Sr}_{0.2}\text{MgSi}_2\text{O}_6:\text{Cr}^{3+}$ .



${}^4T_{2(g)}$  excited state was calculated using eq 2. The  $\tau_{\text{avr}}$  evidently and reversibly prolongs from  $31.0 \pm 2 \mu\text{s}$  at ambient pressure to  $45.7 \pm 2 \mu\text{s}$  at 7.55 GPa (Figure 7b, fitting results presented in Figures S10–S15). Figure 7b also presents the results obtained during the decompression. There is a strong agreement with the values obtained during compression of the material, which further confirms the results derived from Raman spectroscopy, indicating that the observed spectral changes are not attributed to permanent structural alterations or the formation of structural defects.

Due to the overlap of the wave functions of the  ${}^4T_{2(g)}$  and  ${}^2E_{(g)}$  states, their spin–orbital coupling is expected.<sup>55,56</sup> Therefore, when the energy of the  ${}^4T_{2(g)}$  state increases, the coupling gradually becomes relaxed and thus the radiative probability of the depopulation of the  ${}^4T_{2(g)}$  increases.<sup>19</sup> Consequently, the  $\tau_{\text{avr}}$  is prolonged at elevated pressures. Therefore, the manometric relative sensitivity  $S_R$  for the lifetime-based approach was determined as follows (eq 9)

$$S_R = \frac{1}{\tau_{\text{avr}}} \frac{\Delta\tau_{\text{avr}}}{\Delta p} 100\% \quad (9)$$

where  $\Delta\tau_{\text{avr}}$  represents the change of the average  $\tau$  for the  $\Delta p$  change of pressure. The maximal relative sensitivity equal to  $7.95 \pm 0.2\%$  GPa<sup>−1</sup> was obtained at 5 GPa (Figure 7c). As previously mentioned, evaluating the influence of temperature on the observed pressure-induced changes is also crucial; hence,  $\text{Ca}_{0.8}\text{Sr}_{0.2}\text{MgSi}_2\text{O}_6:\text{Cr}^{3+}$  was consequently studied analogously as a function of temperature. Figure 7d illustrates the temperature-dependent luminescence decay curves recorded over the  $T$  range from 83 to 763 K. The determined  $\tau_{\text{avr}}$  shortened from  $45.6 \pm 2 \mu\text{s}$  at 83 K to  $4.1 \pm 2 \mu\text{s}$  at 763 K (Figure 7e). Additionally, the relative thermal sensitivity  $S_R$  (calculated based on eq 9) was determined, and the value achieved at room temperature was  $0.16\% \pm 0.1 \text{ K}^{-1}$  (Figure 7f). To assess the impact of the temperature on pressure readouts, the TIMF parameter was calculated using eq 8, reaching a value of 48.5 K GPa<sup>−1</sup>.

To date, the TIMF parameter has only been determined for two luminescent manometers operating at lifetime-based mode, namely,  $\text{SrGdAlO}_4:\text{Mn}^{4+}$ <sup>8</sup> and  $\text{Sr}_4\text{Al}_{11}\text{O}_{25}:\text{Mn}^{4+}$ ,<sup>57</sup> for which the TIMF was equal to 134 and 187 K GPa<sup>−1</sup>, respectively. The value obtained for  $\text{Ca}_{0.8}\text{Sr}_{0.2}\text{MgSi}_2\text{O}_6:\text{Cr}^{3+}$  is comparatively lower than those for the mentioned manometers. However, the proposed manometer offers the advantage of superior readout sensitivity in the higher pressure ranges, specifically above 3 GPa, whereas the mentioned manometers based on  $\text{Mn}^{4+}$  luminescence are most effective at pressures below 3 GPa.

#### 4. CONCLUSIONS

In this work, we conducted a detailed study to investigate the manometric potential of pyroxene  $\text{Ca}_{0.8}\text{Sr}_{0.2}\text{MgSi}_2\text{O}_6$  doped with  $\text{Cr}^{3+}$  ions. We analyzed the spectroscopic and structural properties to identify the optimal concentration of the  $\text{Cr}^{3+}$  dopant of the studied phosphors. A pressure-dependent study of the spectroscopic properties of  $\text{Ca}_{0.8}\text{Sr}_{0.2}\text{MgSi}_2\text{O}_6:2\%\text{Cr}^{3+}$  revealed that from approximately 2 GPa, a narrow emission band related to the  ${}^2E_g \rightarrow {}^4A_{2g}$  electronic transition of  $\text{Cr}^{3+}$  appeared in the spectrum, indicating an increase in the crystal field strength affecting  $\text{Cr}^{3+}$  ions. The emergence of the  ${}^2E_g \rightarrow {}^4A_{2g}$  emission band, which is not visible at ambient pressure, enabled the possibility of developing a luminescent manometer

operating in ratiometric readout mode using two approaches: the LIR defined by the ratio of the spectral ranges corresponding to  ${}^2E_g \rightarrow {}^4A_{2g}$  and  ${}^4T_{2g} \rightarrow {}^4A_{2g}$  emission bands and a relatively new approach for luminescence manometry based on the LIR integrated into two spectral ranges of the broad emission band associated with  ${}^4T_{2g} \rightarrow {}^4A_{2g}$  electronic transition of  $\text{Cr}^{3+}$ . Using the first approach, we achieved a remarkably high manometric sensitivity of  $40 \pm 0.5 \text{ GPa}^{-1}$  at 2 GPa. However, due to thermal coupling between the  ${}^2E_g$  and  ${}^4T_{2g}$  levels of  $\text{Cr}^{3+}$ , and thermal variability of this parameter, the second approach was analyzed in the further part of the presented research. We demonstrated that the second approach ensures a very high readout sensitivity of  $S_R = 50.7 \pm 0.5\%$  GPa<sup>−1</sup> while providing a temperature-invariant pressure readout, as evidenced by the unprecedented high value of the TIMF over the entire pressure range tested—decreasing from approximately 1550 K GPa<sup>−1</sup> at ambient conditions to 300 K GPa<sup>−1</sup> at 7.55 GPa. Additionally, we investigated the luminescence kinetics of the  ${}^4T_2$  state as a function of applied pressure, allowing the proposal of an alternative pressure reading mode with high sensitivity ( $S_R \sim 8 \pm 0.2\%$  GPa<sup>−1</sup>) in the high-pressure range, around 5 GPa. Based on the results obtained, it is evident that the developed pressure sensor  $\text{Ca}_{0.8}\text{Sr}_{0.2}\text{MgSi}_2\text{O}_6:2\%\text{Cr}^{3+}$  is characterized by innovation in a case of utilized approach and by high application potential, providing high sensitivity in pressure measurements that are independent of temperature variations, which has been a significant challenge in the development of reliable luminescent pressure sensors.

#### ■ ASSOCIATED CONTENT

##### Supporting Information

The Supporting Information is available free of charge at <https://pubs.acs.org/doi/10.1021/acsami.4c12145>.

XRD patterns for samples with different concentrations of  $\text{Cr}^{3+}$ ; luminescence decay profiles and fittings; and emission spectra measured at different temperatures and pressures (PDF)

#### ■ AUTHOR INFORMATION

##### Corresponding Authors

Lefu Mei – Engineering Research Center of Ministry of Education for Geological Carbon Storage and Low Carbon Utilization of Resources, Beijing Key Laboratory of Materials Utilization of Nonmetallic Minerals and Solid Wastes, National Laboratory of Mineral Materials, School of Materials Science and Technology, China University of Geosciences, Beijing 100083, China; [orcid.org/0000-0003-1420-2351](https://orcid.org/0000-0003-1420-2351); Email: [mlf@cugb.edu.cn](mailto:mlf@cugb.edu.cn)

Lukasz Marciniak – Institute of Low Temperature and Structure Research, Polish Academy of Sciences, 50-422 Wrocław, Poland; [orcid.org/0000-0001-5181-5865](https://orcid.org/0000-0001-5181-5865); Email: [l.marciniak@intibs.pl](mailto:l.marciniak@intibs.pl)

##### Authors

Maja Szymczak – Institute of Low Temperature and Structure Research, Polish Academy of Sciences, 50-422 Wrocław, Poland

Ke Su – School of Science, China University of Geosciences, Beijing 100083, China

**Marcin Runowski** – Adam Mickiewicz University, Faculty of Chemistry, 61-614 Poznań, Poland; [orcid.org/0000-0002-9704-2105](https://orcid.org/0000-0002-9704-2105)

**Przemysław Woźny** – Adam Mickiewicz University, Faculty of Chemistry, 61-614 Poznań, Poland

**Qingfeng Guo** – Jewelry and Mineral Materials Laboratory of Experimental Teaching Demonstration Center, Beijing, School of Gemology, China University of Geosciences, Beijing 100083, China

**Libing Liao** – Engineering Research Center of Ministry of Education for Geological Carbon Storage and Low Carbon Utilization of Resources, Beijing Key Laboratory of Materials Utilization of Nonmetallic Minerals and Solid Wastes, National Laboratory of Mineral Materials, School of Materials Science and Technology, China University of Geosciences, Beijing 100083, China; [orcid.org/0000-0001-5312-8487](https://orcid.org/0000-0001-5312-8487)

Complete contact information is available at:

<https://pubs.acs.org/10.1021/acsami.4c12145>

## Author Contributions

\*M.S. and K.S. contributed equally to this work.

## Notes

The authors declare no competing financial interest.

## ACKNOWLEDGMENTS

This work was supported by the National Science Center (NCN), Poland, under project no. DEC-UMO-2020/37/B/ST5/00164. Lefu Mei acknowledges support from the National Natural Science Foundation of China (grant no. 52274273).

## REFERENCES

- (1) Mao, H. K.; Xu, J.; Bell, P. M. Calibration of the Ruby Pressure Gauge to 800 Kbar under Quasi-hydrostatic Conditions. *J. Geophys. Res. Solid Earth* **1986**, 91 (B5), 4673–4676.
- (2) Shen, G.; Smith, J. S.; Kenney-Benson, C.; Klotz, S. Calibration of Ruby ( $\text{Cr}^{3+}:\text{Al}_2\text{O}_3$ ) and  $\text{Sm}^{2+}:\text{SrFCl}$  Luminescence Lines from the Melting of Mercury: Constraints on the Initial Slopes. *High Pressure Res.* **2021**, 41 (2), 175–183.
- (3) Forman, R. A.; Piermarini, G. J.; Barnett, J. D.; Block, S. Pressure Measurement Made by the Utilization of Ruby Sharp-Line Luminescence. *Science* **1972**, 176 (4032), 284–285.
- (4) Piermarini, G. J.; Block, S.; Barnett, J. D.; Forman, R. A. Calibration of the Pressure Dependence of the R1 Ruby Fluorescence Line to 195 Kbar. *J. Appl. Phys.* **1975**, 46 (6), 2774–2780.
- (5) Chijioke, A. D.; Nellis, W. J.; Soldatov, A.; Silvera, I. F. The Ruby Pressure Standard to 150 GPa. *J. Appl. Phys.* **2005**, 98 (11), 114905.
- (6) Marciniak, L.; Woźny, P.; Szymczak, M.; Runowski, M. Optical Pressure Sensors for Luminescence Manometry: Classification, Development Status, and Challenges. *Coord. Chem. Rev.* **2024**, 507, 215770.
- (7) Barnett, J. D.; Block, S.; Piermarini, G. J. An Optical Fluorescence System for Quantitative Pressure Measurement in the Diamond-Anvil Cell. *Rev. Sci. Instrum.* **1973**, 44 (1), 1–9.
- (8) Pieprz, M.; Runowski, M.; Woźny, P.; Xue, J.; Marciniak, L. Temperature Invariant Lifetime Based Luminescent Manometer on  $\text{Mn}^{4+}$  Ions. *J. Mater. Chem. C Mater.* **2023**, 11 (33), 11353–11360.
- (9) Lorenz, B.; Shen, Y. R.; Holzapfel, W. B. Characterization of the New Luminescence Pressure Sensor  $\text{SrFCl}:\text{Sm}^{2+}$ . *High Pressure Res.* **1994**, 12 (2), 91–99.
- (10) Rashchenko, S. V.; Kurnosov, A.; Dubrovinsky, L.; Litasov, K. D. Revised Calibration of the  $\text{Sm}:\text{SrB}_4\text{O}_7$  Pressure Sensor Using the Sm-Doped Yttrium-Aluminum Garnet Primary Pressure Scale. *J. Appl. Phys.* **2015**, 117 (14), 145902.
- (11) Shen, Y. R.; Gregorian, T.; Holzapfel, W. B. Progress in Pressure Measurements with Luminescence Sensors. *High Pressure Res.* **1991**, 7 (1–6), 73–75.
- (12) Liu, J.; Vohra, Y. K. Sm:YAG Optical Pressure Sensor to 180 GPa: Calibration and Structural Disorder. *Appl. Phys. Lett.* **1994**, 64 (25), 3386–3388.
- (13) Arashi, H.; Ishigame, M. Diamond Anvil Pressure Cell and Pressure Sensor for High-Temperature Use. *Jpn. J. Appl. Phys.* **1982**, 21 (11R), 1647–1649.
- (14) Penhouet, T.; Hagemann, H.  $\text{Sm}^{2+}$  as a Probe of Crystal Field in Fluorides and Fluorohalides: Effect of Pressure and Temperature. *J. Alloys Compd.* **2008**, 451 (1–2), 74–76.
- (15) Chen, G.; Hölsä, J.; Peterson, J. R. A Luminescence Study of Single-Crystal  $\text{EuPO}_4$  at High Pressure. *J. Phys. Chem. Solids* **1997**, 58 (12), 2031–2037.
- (16) Grabowski, G.; Lach, R.; Pędzich, Z.; Świerczek, K.; Wojteczko, A. Anisotropy of Thermal Expansion of 3Y-TZP,  $\alpha\text{-Al}_2\text{O}_3$  and Composites from 3Y-TZP/ $\alpha\text{-Al}_2\text{O}_3$  System. *Arch. Civ. Mech. Eng.* **2018**, 18 (1), 188–197.
- (17) Masubuchi, Y.; Nishitani, S.; Miyazaki, S.; Hua, H.; Ueda, J.; Higuchi, M.; Tanabe, S. Large Red-Shift of Luminescence from  $\text{BaCN}_2:\text{Eu}^{2+}$  Red Phosphor under High Pressure. *Appl. Phys. Express* **2020**, 13 (4), 042009.
- (18) Zheng, T.; Runowski, M.; Xue, J.; Luo, L.; Rodríguez-Mendoza, U. R.; Lavín, V.; Martín, I. R.; Rodríguez-Hernández, P.; Muñoz, A.; Du, P. Giant Pressure-Induced Spectral Shift in Cyan-Emitting  $\text{Eu}^{2+}$ -Activated  $\text{Sr}_5\text{Si}_4\text{O}_{12}\text{Cl}_8$  Microspheres for Ultrasensitive Visual Manometry. *Adv. Funct. Mater.* **2023**, 33 (26), 2214663.
- (19) Szymczak, M.; Jaśkielewicz, J.; Runowski, M.; Xue, J.; Mahlik, S.; Marciniak, L. Highly-Sensitive, Tri-Modal Luminescent Manometer Utilizing Band-Shift, Ratiometric and Lifetime-Based Sensing Parameters. *Adv. Funct. Mater.* **2024**, 34, 2314068.
- (20) Szymczak, M.; Runowski, M.; Lavín, V.; Marciniak, L. Highly Pressure-Sensitive, Temperature Independent Luminescence Ratiometric Manometer Based on  $\text{MgO}:\text{Cr}^{3+}$  Nanoparticles. *Laser Photon. Rev.* **2023**, 17 (4), 2200801.
- (21) Szymczak, M.; Du, P.; Runowski, M.; Woźny, P.; Xue, J.; Zheng, T.; Marciniak, L. Highly Sensitive Optical Manometer Based on the Visible Emissions of  $\text{Ce}^{3+}$ -Doped  $\text{La}_2\text{Sr}_4(\text{SiO}_4)_6\text{F}_2$  Multisite Phosphors. *Adv. Opt. Mater.* **2023**, 12 (7), 2302147.
- (22) Szymczak, M.; Runowski, M.; Brik, M. G.; Marciniak, L. Multimodal, Super-Sensitive Luminescent Manometer Based on Giant Pressure-Induced Spectral Shift of  $\text{Cr}^{3+}$  in the NIR Range. *Chem. Eng. J.* **2023**, 466, 143130.
- (23) Szymczak, M.; Runowski, M.; Lavín, V.; Marciniak, L. Highly Pressure-Sensitive, Temperature Independent Luminescence Ratiometric Manometer Based on  $\text{MgO}:\text{Cr}^{3+}$  Nanoparticles. *Laser Photon. Rev.* **2023**, 17 (4), 2200801.
- (24) Szymczak, M.; Woźny, P.; Runowski, M.; Pieprz, M.; Lavín, V.; Marciniak, L. Temperature Invariant Ratiometric Luminescence Manometer Based on  $\text{Cr}^{3+}$  Ions Emission. *Chem. Eng. J.* **2023**, 453, 139632.
- (25) Brik, M. G.; Avram, N. M.; Avram, C. N. Exchange Charge Model of Crystal Field for 3d Ions. In *Optical Properties of 3d-Ions in Crystals: Spectroscopy and Crystal Field Analysis*; Avram, N. M., Brik, M. G., Eds.; Springer Berlin Heidelberg: Berlin, Heidelberg, 2013; Vol. 9783642308, pp 29–94.
- (26) Solé, J. G.; Bausá, L. E.; Jaque, D. Applications: Rare Earth and Transition Metal Ions, and Color Centers. *Opt. Spectrosc. Inorg. Solid.* **2005**, 199–234.
- (27) Tanabe, Y.; Sugano, S. On the Absorption Spectra of Complex Ions. I. *J. Phys. Soc. Jpn.* **1954**, 9 (5), 753–766.
- (28) Adachi, S. Spectroscopy of  $\text{Cr}^{3+}$  Activator: Tanabe–Sugano Diagram and Racah Parameter Analysis. *J. Lumin.* **2021**, 232, 117844.
- (29) Beales, T. P.; H, L.; Goodman, C.; Scarrott, K. A New High Pressure Calibrant:  $\beta\text{-Ga}_2\text{O}_3:\text{Cr}$ . *Solid State Commun.* **1990**, 73 (1), 1–3.
- (30) Mao, H. K.; Bell, P. M.; Shaner, J. W.; Steinberg, D. J. Specific Volume Measurements of Cu, Mo, Pd, and Ag and Calibration of the

Ruby R<sub>1</sub> Fluorescence Pressure Gauge from 0.06 to 1 Mbar. *J. Appl. Phys.* **1978**, *49* (6), 3276–3283.

(31) Szymczak, M.; Runowski, M.; Lavín, V.; Marciniak, L. Highly Pressure-Sensitive, Temperature Independent Luminescence Ratiometric Manometer Based on MgO:Cr<sup>3+</sup> Nanoparticles. *Laser Photon. Rev.* **2023**, *17* (4), 2200801.

(32) Mi, H.; Huang, Y.; Lin, Z.; Zhang, L.; Wang, G. Cr<sup>3+</sup>-Doped CaMgSi<sub>2</sub>O<sub>6</sub> Crystal: A Promising Tunable Laser and Ultrashort Laser Crystal. *CrystEngComm* **2014**, *16* (5), 763–765.

(33) Wen, Y.; He, C.; Wen, Y.; Dong, B.; Deng, C.; Li, Q.; Lu, Y. Fabrication, Structure, and Luminescent Properties of Cr-Doped CaMgSi<sub>2</sub>O<sub>6</sub> Fluorescent Ceramics. *Mod. Phys. Lett. B* **2023**, *37* (07), 2250207.

(34) Shahrouzifar, M. R.; Salahinejad, E. Strontium Doping into Diopside Tissue Engineering Scaffolds. *Ceram. Int.* **2019**, *45* (8), 10176–10181.

(35) Bellucci, L.; Cassetta, M.; Skogby, H.; Nazzareni, S. Pure and Sc-Doped Diopside (CaMgSi<sub>2</sub>O<sub>6</sub>) Vibrational Spectra: Modelling and Experiments. *Phys. Chem. Chem. Phys.* **2024**, *26* (5), 4029–4038.

(36) Takei, H.; Miura, T.; Morioka, M. Czochralski Growth of Diopside (CaMgSi<sub>2</sub>O<sub>6</sub>) Crystals. *J. Cryst. Growth* **1982**, *60* (2), 453–456.

(37) Sherikar, B. N.; Sahoo, B.; Umarji, A. M. One-Step Synthesis of Diopside (CaMgSi<sub>2</sub>O<sub>6</sub>) Ceramic Powder by Solution Combustion Method. *Adv. Powder Technol.* **2020**, *31* (8), 3492–3499.

(38) Lindsley, D. H.; Grover, J. E.; Davidson, P. M. In *The Thermodynamics of the Mg<sub>2</sub>Si<sub>2</sub>O<sub>6</sub>-CaMgSi<sub>2</sub>O<sub>6</sub> Join: A Review and an Improved Model BT—Thermodynamics of Minerals and Melts*; Newton, R. C., Navrotsky, A., Wood, B. J., Eds.; Springer New York: New York, NY, 1981; pp 149–175.

(39) Chandrakar, P.; Baghel, R. N.; Bisen, D. P.; Chandra, B. P. Characterization and Luminescence Properties of CaMgSi<sub>2</sub>O<sub>6</sub>:Eu<sup>2+</sup> Blue Phosphor. *Luminescence* **2015**, *30* (7), 1034–1040.

(40) Tseng, Y.-S.; Su, Y.-H.; Chen, C.-L.; Zhang, J.; Wang, C.-K.; Hanaor, D. A. H.; Chen, W.-F. Bioceramics in the CaMgSi<sub>2</sub>O<sub>6</sub>-Li<sub>2</sub>O System: A Glass-Ceramic Strategy for Excellent Mechanical Strength and Enhanced Bioactivity by Spontaneous Elemental Redistribution. *Adv. Mater. Interfaces* **2023**, *10* (12), 2202491.

(41) Su, F.; Zhou, W.; Yang, Y.; Ou, Y.; Qi, Z.; Duan, C.-K.; Brik, M. G.; Dorenbos, P.; Liang, H. Structure, Luminescence of Eu<sup>2+</sup> and Eu<sup>3+</sup> in CaMgSi<sub>2</sub>O<sub>6</sub> and Their Co-Existence for the Excitation-Wavelength/Temperature Driven Colour Evolution. *Dalton Trans.* **2021**, *50* (29), 10050–10058.

(42) Benna, P. Ca–Sr Substitution in Clinopyroxenes along the Join CaMgSi<sub>2</sub>O<sub>6</sub>–SrMgSi<sub>2</sub>O<sub>6</sub>. *Tschermaks Mineral. Petrogr. Mittl.* **1982**, *30* (1), 37–46.

(43) Shannon, R. D. Revised Effective Ionic Radii and Systematic Studies of Interatomic Distances in Halides and Chalcogenides. *Acta Crystallogr., Sect. A* **1976**, *32* (5), 751–767.

(44) Dong, X.; Chen, Z.; Liu, L.; Yuan, F.; Huang, Y.; Zhang, L.; Lin, Z. Tuning the Emission Half-Peak Width of CaMgSi<sub>2</sub>O<sub>6</sub>:Cr<sup>3+</sup> from 138 nm to 393 nm by Controlling the Cr<sup>3+</sup> Concentration. *J. Alloys Compd.* **2024**, *981*, 173746.

(45) Mi, H.; Huang, Y.; Lin, Z.; Zhang, L.; Wang, G. Cr<sup>3+</sup>-Doped CaMgSi<sub>2</sub>O<sub>6</sub> Crystal: A Promising Tunable Laser and Ultrashort Laser Crystal. *CrystEngComm* **2014**, *16* (5), 763–765.

(46) House, J. E. Ligand Fields and Molecular Orbitals. In *Inorganic Chemistry*, 2nd ed.; Academic Press, 2013; pp 591–616.

(47) Mao, H. K.; Xu, J.; Bell, P. M. Calibration of the Ruby Pressure Gauge to 800 Kbar under Quasi-Hydrostatic Conditions. *J. Geophys. Res. Solid Earth* **1986**, *91* (B5), 4673–4676.

(48) Katrusiak, A. Lab in a DAC – High-Pressure Crystal Chemistry in a Diamond-Anvil Cell. *Acta Crystallogr. B Struct. Crystallogr. Cryst. Chem.* **2019**, *75* (6), 918–926.

(49) Tröster, T. Optical Studies of Non-Metallic Compounds under Pressure. *Handb. Phys. Chem. Rare Earths* **2003**, *33*, 515–589.

(50) Sugano, S.; Tanabe, Y.; Kamimura, H. Multiplets of Transition-Metal Ions in Crystals. In *Pure and Applied Physics*; Elsevier, 1970; Vol. 33, p 333.

(51) Reber, C.; Güdel, H. U.; Spiccia, L.; Marty, W. Ferromagnetic Exchange Interaction in a Binuclear Chromium (III) Complex: Magnetic and Spectroscopic Properties of [(H<sub>2</sub>O)<sub>4</sub>Cr(OH)<sub>2</sub>Cr(H<sub>2</sub>O)<sub>4</sub>][(CH<sub>3</sub>)<sub>3</sub>C<sub>6</sub>H<sub>2</sub>SO<sub>3</sub>]<sub>4</sub>·4H<sub>2</sub>O. *Inorg. Chem.* **1987**, *26* (19), 3186–3191.

(52) Knochenmuss, R.; Reber, C.; Rajasekharan, M. V.; Güdel, H. U. Broadband Near-infrared Luminescence of Cr<sup>3+</sup> in the Elpasolite Lattices Cs<sub>2</sub>NaInCl<sub>6</sub>, Cs<sub>2</sub>NaYCl<sub>6</sub>, and Cs<sub>2</sub>NaYBr<sub>6</sub>. *J. Chem. Phys.* **1986**, *85* (8), 4280–4289.

(53) Back, M.; Ueda, J.; Hua, H.; Tanabe, S. Predicting the Optical Pressure Sensitivity of <sup>2</sup>E → <sup>4</sup>A<sub>2</sub> Spin-Flip Transition in Cr<sup>3+</sup>-Doped Crystals. *Chem. Mater.* **2021**, *33* (9), 3379–3385.

(54) Bednarkiewicz, A.; Marciniak, L.; Carlos, L. D.; Jaque, D. Standardizing Luminescence Nanothermometry for Biomedical Applications. *Nanoscale* **2020**, *12* (27), 14405–14421.

(55) Grinberg, M.; Suchocki, A. Pressure-Induced Changes in the Energetic Structure of the 3d<sup>3</sup> Ions in Solid Matrices. *J. Lumin.* **2007**, *125* (1–2), 97–103.

(56) Galanciak, D.; Grinberg, M.; Gryk, W.; Kobayakov, S.; Suchocki, A.; Boulon, G.; Brenier, A. Influence of High Pressure on the Luminescence Transitions of Mn<sup>4+</sup>-Doped Gadolinium Gallium Garnet. *J. Phys.: Condens. Matter* **2005**, *17* (46), 7185–7197.

(57) Pieprz, M.; Piotrowski, W.; Woźny, P.; Runowski, M.; Marciniak, L. Highly Sensitive Lifetime-Based Luminescent Manometer on Mn<sup>4+</sup> Luminescence in Sr<sub>4</sub>Al<sub>14</sub>O<sub>25</sub> Mn<sup>4+</sup>. *Adv. Opt. Mater.* **2023**, *12*, 2301316.

## Supporting Information

### Investigating the Potential of Cr<sup>3+</sup>-Doped Pyroxene for Highly-Sensitive Optical Pressure Sensing

**Maja Szymczak<sup>1,a</sup>, Ke Su<sup>2,a</sup>, Lefu Mei<sup>3,\*</sup>, Marcin Runowski<sup>4</sup>, Przemysław  
Woźny<sup>4</sup>, Qingfeng Guo<sup>5</sup>, Libing Liao<sup>3</sup>, Lukasz Marciniak<sup>1,\*</sup>**

<sup>1</sup> Institute of Low Temperature and Structure Research, Polish Academy of Sciences,

Okólna 2, 50-422 Wrocław, Poland

<sup>2</sup> School of Science, China University of Geosciences, Beijing 100083, China

<sup>3</sup> Engineering Research Center of Ministry of Education for Geological Carbon Storage and Low Carbon Utilization  
of Resources, Beijing Key Laboratory of Materials Utilization of Nonmetallic Minerals and Solid Wastes, National  
Laboratory of Mineral Materials, School of Materials Science and Technology, China University of Geosciences  
(Beijing), 100083, China

<sup>4</sup> Adam Mickiewicz University, Faculty of Chemistry, Uniwersytetu Poznańskiego 8,

61-614 Poznań, Poland

<sup>5</sup> Jewelry and mineral materials Laboratory of experimental teaching demonstration center, Beijing. School of  
Gemology, China University of Geosciences, Beijing 100083, China

<sup>a</sup> They are contributed equally to this work

**\*corresponding author:** L. Mei (E-mail: [mlf@cugb.edu.cn](mailto:mlf@cugb.edu.cn)), and L. Marciniak  
([l.marciniak@intibs.pl](mailto:l.marciniak@intibs.pl))



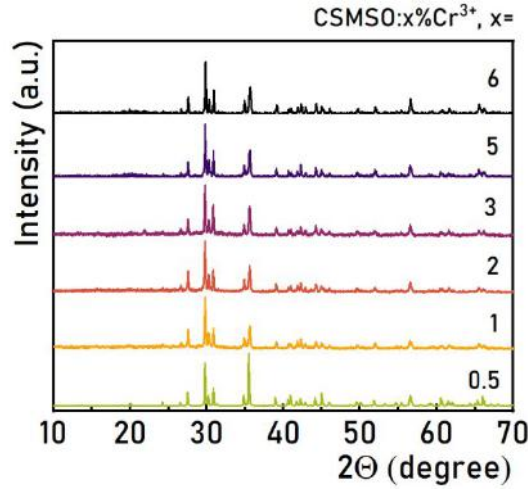


**Figure S1.** XRD patterns of the  $\text{Ca}_{0.8}\text{Sr}_{0.2}\text{MgSi}_2\text{O}_6:\text{xCr}^{3+}$ , where  $x = 0.5, 1, 2, 3, 5$  and  $6\%$ .

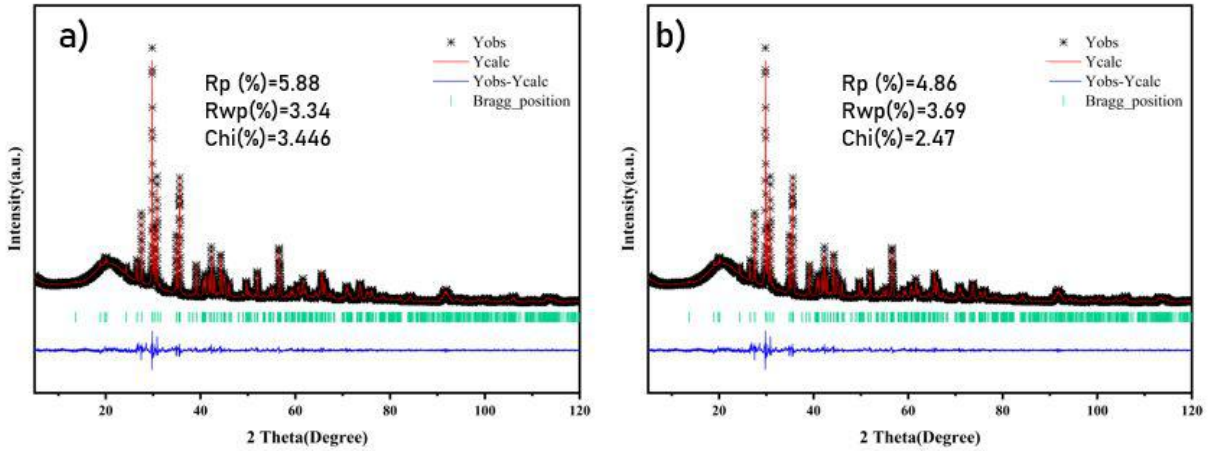


**Figure S2.** Rietveld refinement for the  $\text{Ca}_{0.8}\text{Sr}_{0.2}\text{MgSi}_2\text{O}_6$  undoped -a) and doped with 2% of  $\text{Cr}^{3+}$  -b).

### Fitting of the Raman spectra and centroid determination

In order to determine the centroid of the observed Raman bands we used a standard Lorentz fitting:

$$y(x) = y_0 + \frac{2A}{\pi} \frac{w}{4(x - x_c)^2 + w^2} \quad (\text{S1})$$

where  $y_0$  is the offset intensity,  $x_c$  represents the peak centroid and  $w$  is the FWHM. The selected fitting (integration) ranges differed for different pressures, due to the observed spectral shift for the compressed material, i.e. shift to higher wavenumbers with pressure. Hence, we provide below



(Table S1) the exact values of spectral ranges used for fitting at extreme pressures, i.e. at ambient and 7.18 GPa.

Table S1. Raman peak centroids and the corresponding integration ranges at ambient pressure and 7.18 GPa.

Centroid (cm <sup>-1</sup> )	Spectral range used for fitting (cm <sup>-1</sup> )	
	Ambient pressure	- High pressure (7.18 GPa)
320	290 to 345	310 to 365
390	375 to 410	400 to 435
670	640 to 695	660 to 715
1010	985 to 1030	1020 to 1065

Finally, we used the following formulas and fitting parameters to correlate the determine data points (Raman peak centroids) with pressure values *via* simple linear fits, resulting in the shift rates (in cm<sup>-1</sup> GPa<sup>-1</sup>), discussed in the manuscript.

$$\text{Centroid } 320 \text{ cm}^{-1}: y(p) = 3.043 \pm 0.113p + 323.736 \pm 0.462 \quad (\text{S2})$$

$$\text{Centroid } 390 \text{ cm}^{-1}: y(p) = 3.624 \pm 0.079p + 390.785 \pm 0.319 \quad (\text{S3})$$

$$\text{Centroid } 670 \text{ cm}^{-1}: y(p) = 3.062 \pm 0.081p + 665.875 \pm 0.330 \quad (\text{S4})$$

$$\text{Centroid } 1010 \text{ cm}^{-1}: y(p) = 4.479 \pm 0.106p + 1011.646 \pm 0.433 \quad (\text{S5})$$

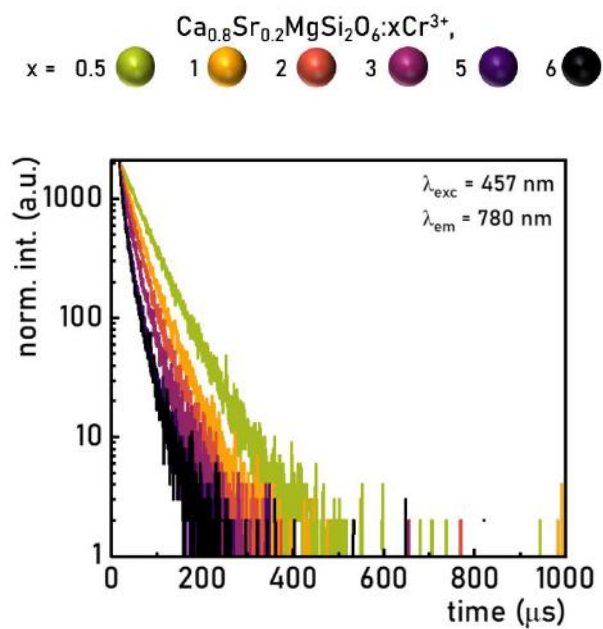


**Figure S3.** Luminescence decay curves of the  $\text{Ca}_{0.8}\text{Sr}_{0.2}\text{MgSi}_2\text{O}_6:\text{xCr}^{3+}$ , where  $\text{x} = 0.5, 1, 2, 3, 5$  and  $6\%$ .

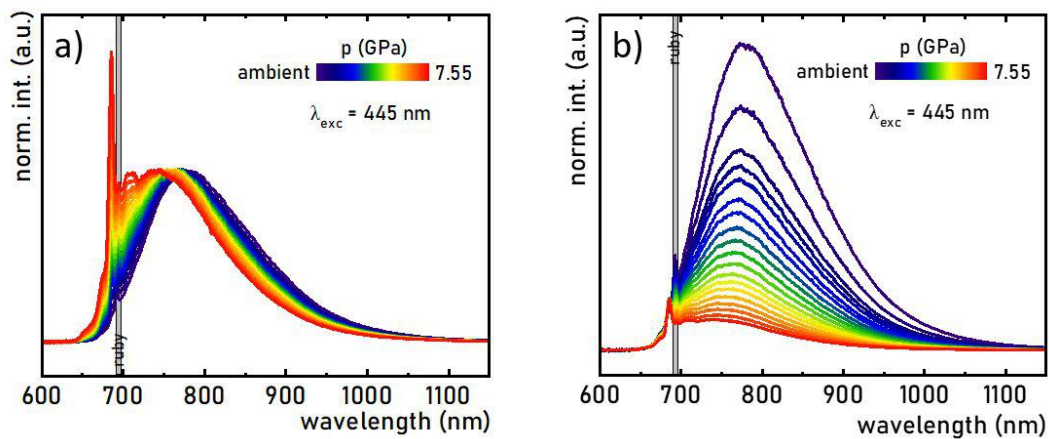


**Figure S4.** Normalized to  ${}^4\text{T}_2$  band -a) and to  ${}^2\text{E}$  band -b) emission spectra of the  $\text{Ca}_{0.8}\text{Sr}_{0.2}\text{MgSi}_2\text{O}_6:2\%\text{Cr}^{3+}$  measured as a function of pressure upon  $\lambda_{\text{exc}} = 445 \text{ nm}$ .

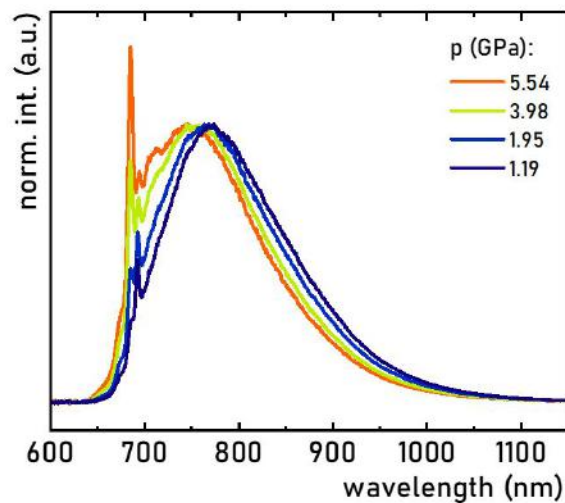


**Figure S5.** Pressure-dependent emission spectra of the  $\text{Ca}_{0.8}\text{Sr}_{0.2}\text{MgSi}_2\text{O}_6:2\%\text{Cr}^{3+}$  measured during decompression upon  $\lambda_{\text{exc.}} = 445$  nm

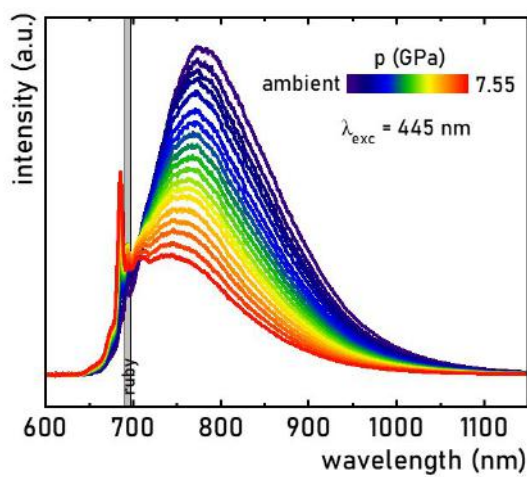


**Figure S6.** Emission spectra of the  $\text{Ca}_{0.8}\text{Sr}_{0.2}\text{MgSi}_2\text{O}_6:2\%\text{Cr}^{3+}$  measured as a function of pressure upon  $\lambda_{\text{exc.}} = 445$  nm.

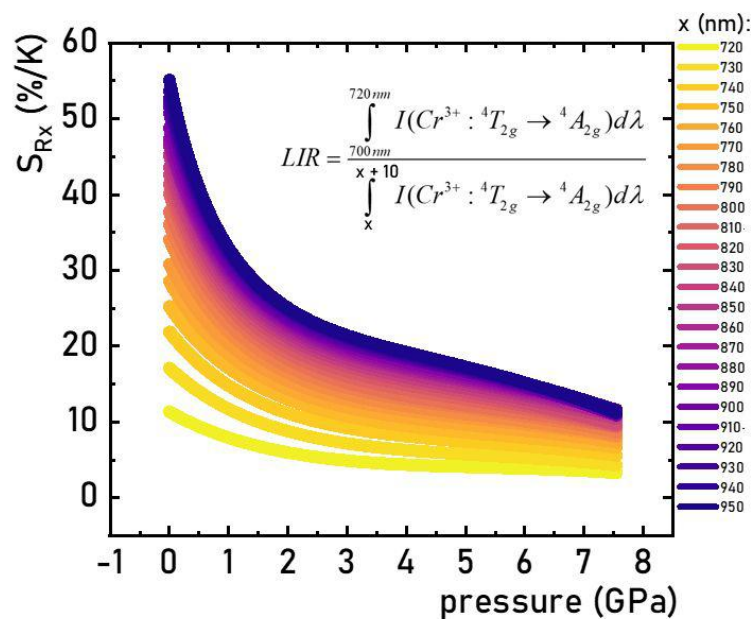


**Figure S7.** Relative sensitivity as a function of monitored spectral range to define LIR parameter.

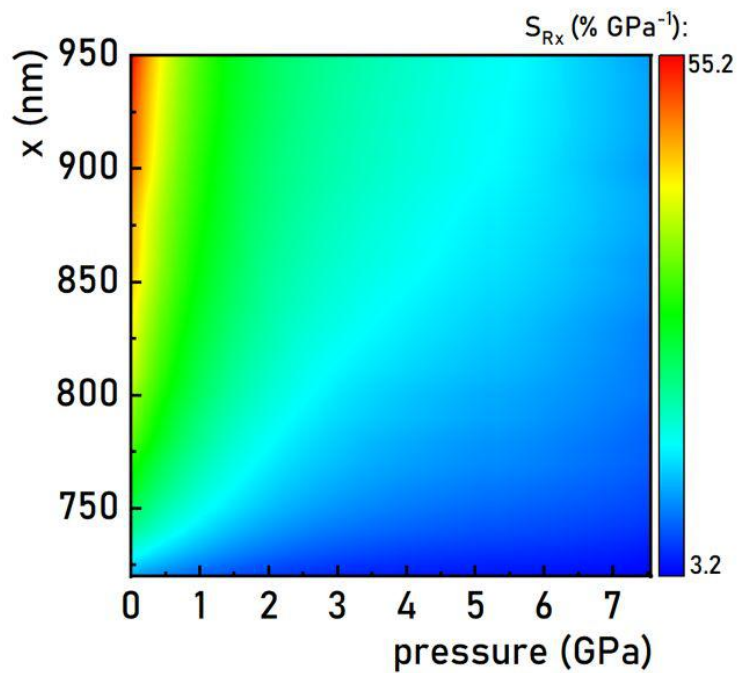


**Figure S8.** 2D map of relative sensitivity as a function of monitored spectral range to define LIR parameter.

Thermal and pressure dependences of LIR and  $\tau_{avr}$  were fitted using polynomial equation as follows:

$$\tau_{avr}(T) = A_0 + A_1T + A_2T^2 + A_3T^3 + A_4T^4 \quad (S6)$$

where  $A_0=56.14$ ,  $A_1=-0.149$ ,  $A_2=3.55 \cdot 10^{-4}$ ,  $A_3=-5.089 \cdot 10^{-7}$ ,  $A_4=2.63 \cdot 10^{-10}$

$$\tau_{avr}(p) = A_0 + A_1p + A_2p^2 + A_3p^3 + A_4p^4 \quad (S7)$$

where  $A_0=30.84$ ,  $A_1=-0.08$ ,  $A_2=0.23$ ,  $A_3=0.038$ ,  $A_4=-0.0045$

$$\lambda_{em}(p) = A_0 + A_1p + A_2p^2 + A_3p^3 + A_4p^4 \quad (S7)$$

where  $A_0=781.32$ ,  $A_1=-8.23$ ,  $A_2=1.55$ ,  $A_3=-0.26$ ,  $A_4=0.014$

$$LIR(p) = A_0 + A_1p + A_2p^2 + A_3p^3 + A_4p^4 \quad (S9)$$

where  $A_0=-0.089$ ,  $A_1=0.49$ ,  $A_2=-0.13$ ,  $A_3=0.028$ ,  $A_4=-0.0157$  for LIR 1

and  $A_0=2.09$ ,  $A_1=1.058$ ,  $A_2=-0.083$ ,  $A_3=0.0234$ ,  $A_4=-0.00155$  for LIR 2

$$LIR(T) = A_0 + A_1T + A_2T^2 + A_3T^3 + A_4T^4 \quad (S10)$$

where for LIR 2  $A_0=2.36$ ,  $A_1=-0.00698$ ,  $A_2=2.004 \cdot 10^{-5}$ ,  $A_3=-2.54 \cdot 10^{-8}$ ,  $A_4=1.25 \cdot 10^{-11}$

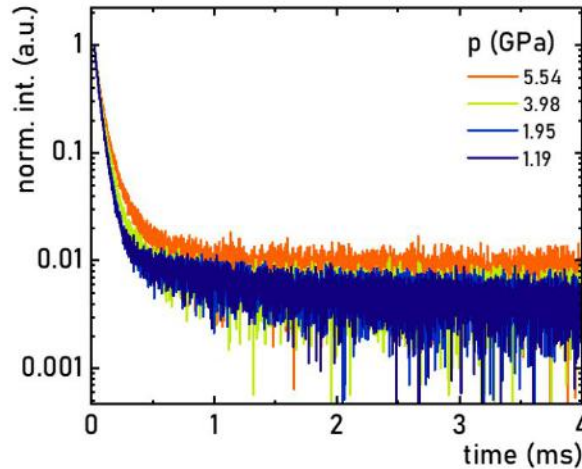


**Figure S9.** Luminescence decay profiles of the  $\text{Ca}_{0.8}\text{Sr}_{0.2}\text{MgSi}_2\text{O}_6:2\%\text{Cr}^{3+}$  measured as a function of pressure during decompression and upon  $\lambda_{\text{exc.}} = 445 \text{ nm}$ .

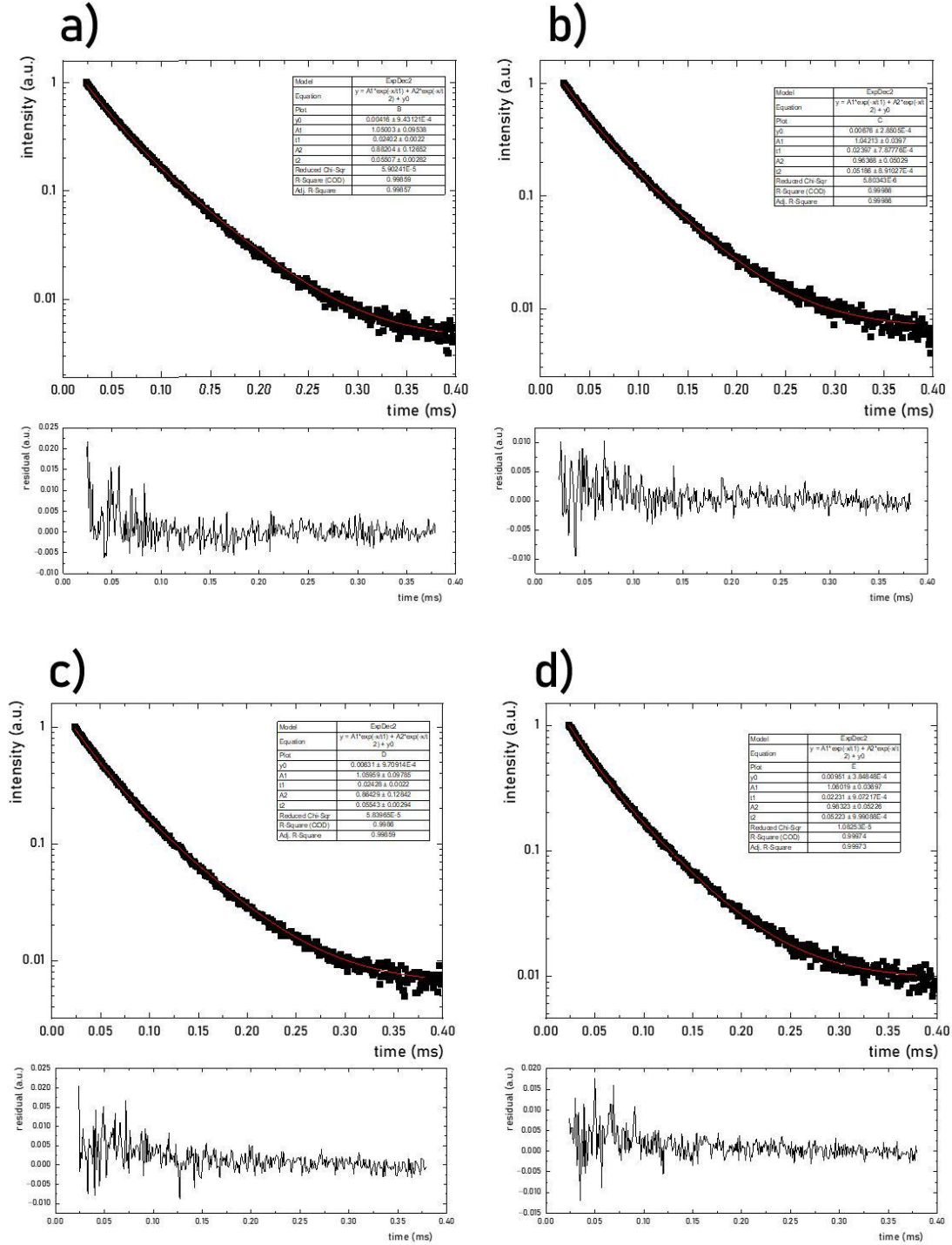


**Figure S10.** Room temperature luminescence decay profile of  $\text{Ca}_{0.8}\text{Sr}_{0.2}\text{MgSi}_2\text{O}_6:2\%\text{Cr}^{3+}$  under  $\lambda_{\text{exc}} = 445$  nm (black points) and bi-exponential fitting curve (red line) with residuals measured as a function of pressure at: ambient pressure-a); 0.5 GPa -b); 1.01 GPa -c); 1.14 GPa -d).

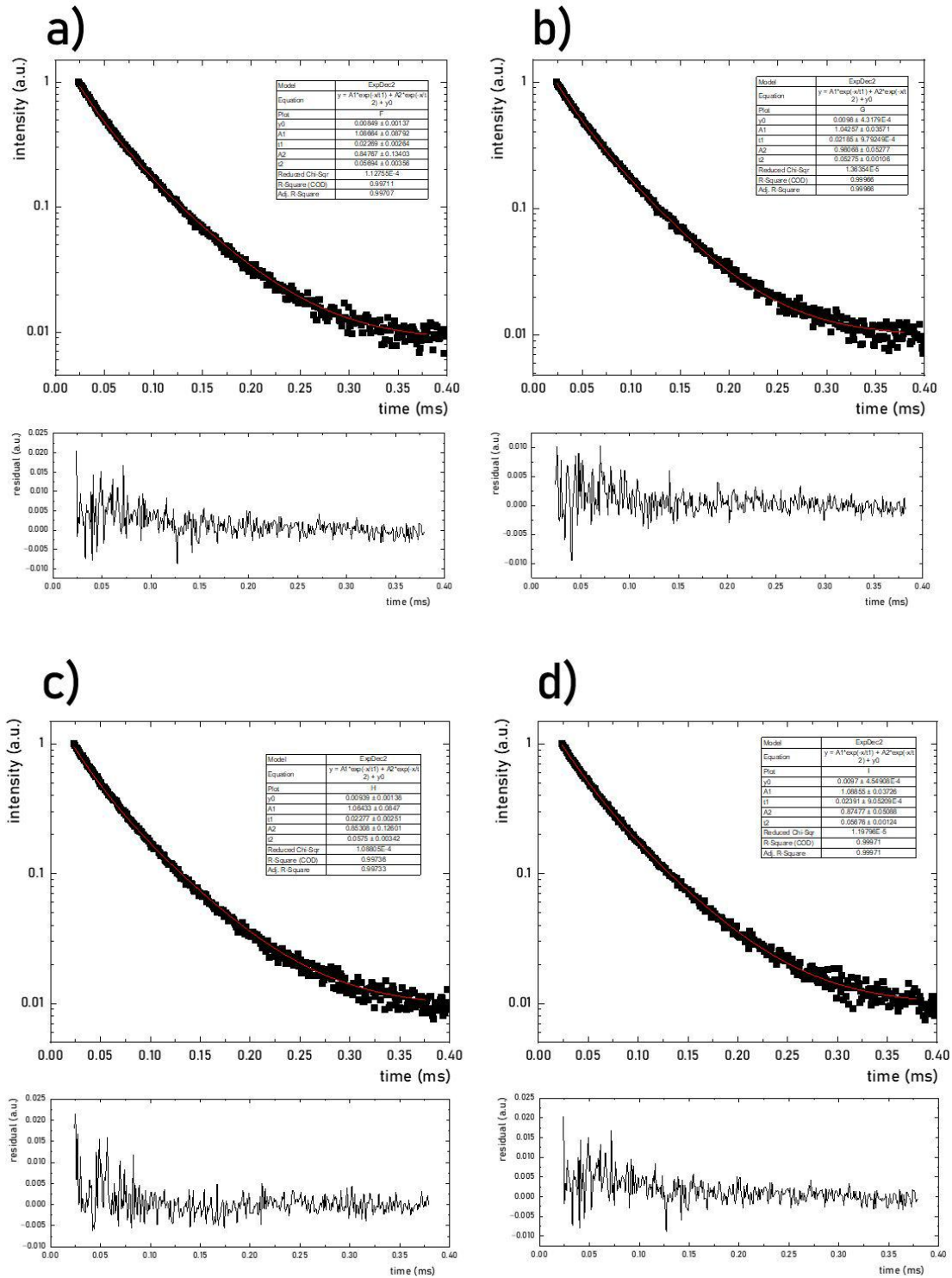


**Figure S11.** Room temperature luminescence decay profile of  $\text{Ca}_{0.8}\text{Sr}_{0.2}\text{MgSi}_2\text{O}_6:2\%\text{Cr}^{3+}$  under  $\lambda_{\text{exc.}} = 445$  nm (black points) and bi-exponential fitting curve (red line) with residuals measured as a function of pressure at: 1.32 GPa -a); 1.53 GPa -b); 1.8 GPa -c); 2.09 GPa -d).



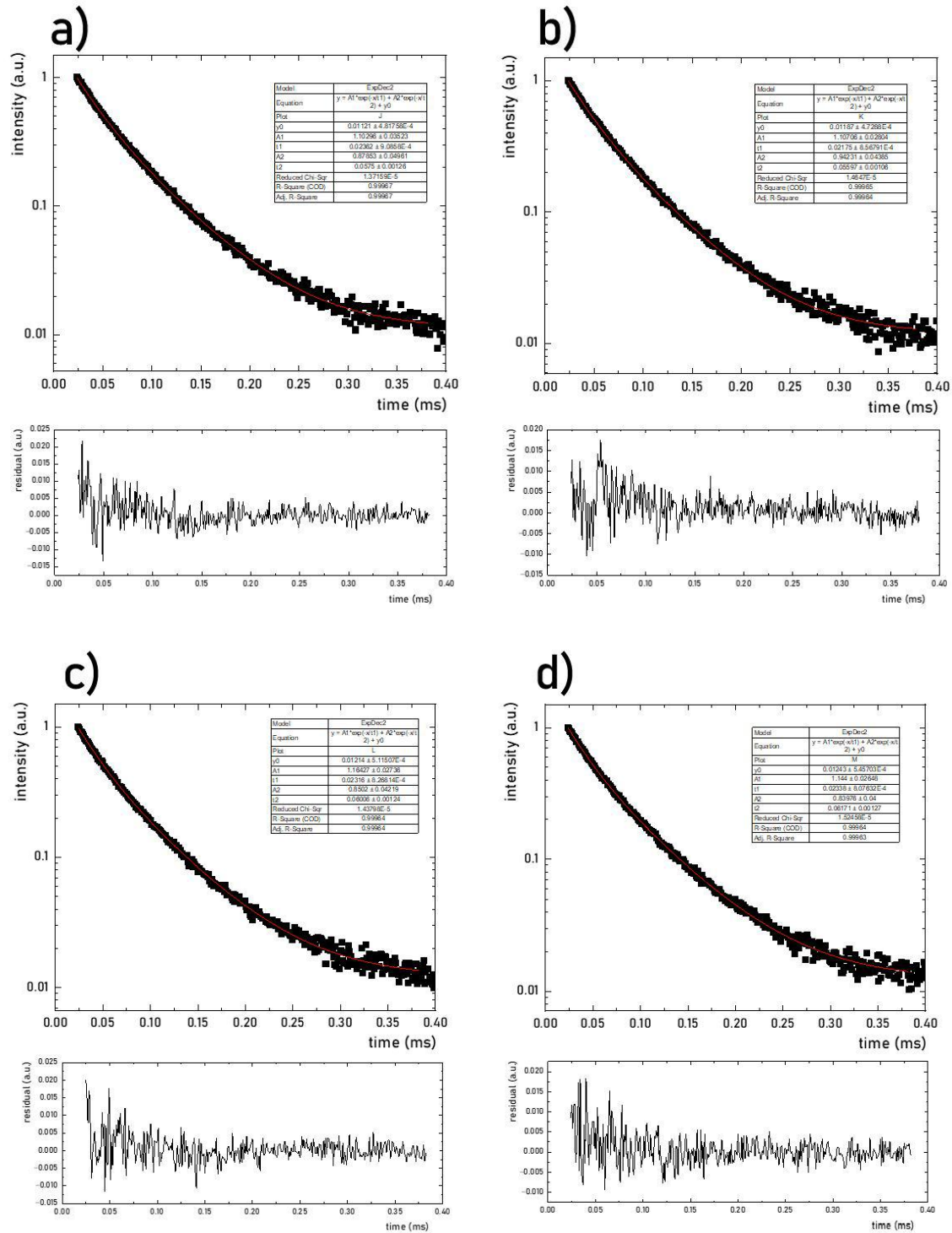


**Figure S12.** Room temperature luminescence decay profile of  $\text{Ca}_{0.8}\text{Sr}_{0.2}\text{MgSi}_2\text{O}_6:2\%\text{Cr}^{3+}$  under  $\lambda_{\text{exc.}} = 445$  nm (black points) and bi-exponential fitting curve (red line) with residuals measured as a function of pressure at: 2.43 GPa -a); 2.81 GPa -b); 3.19 GPa -c); 3.71 GPa -d).



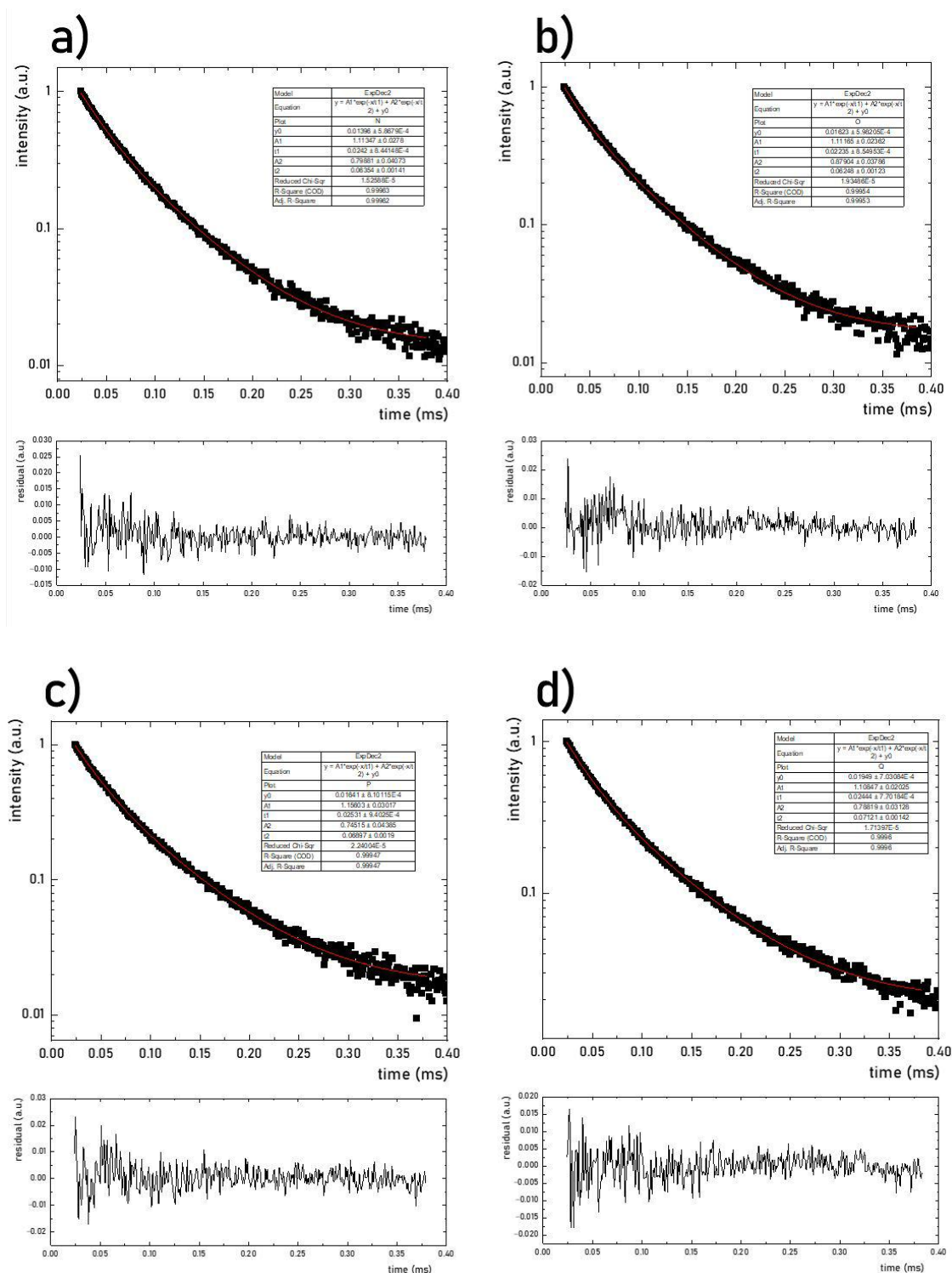


**Figure S13.** Room temperature luminescence decay profile of  $\text{Ca}_{0.8}\text{Sr}_{0.2}\text{MgSi}_2\text{O}_6:2\%\text{Cr}^{3+}$  under  $\lambda_{\text{exc}} = 445$  nm (black points) and bi-exponential fitting curve (red line) with residuals measured as a function of pressure at: 4.12 GPa -a); 4.47 GPa -b); 4.91 GPa -c); 5.57 GPa -d).

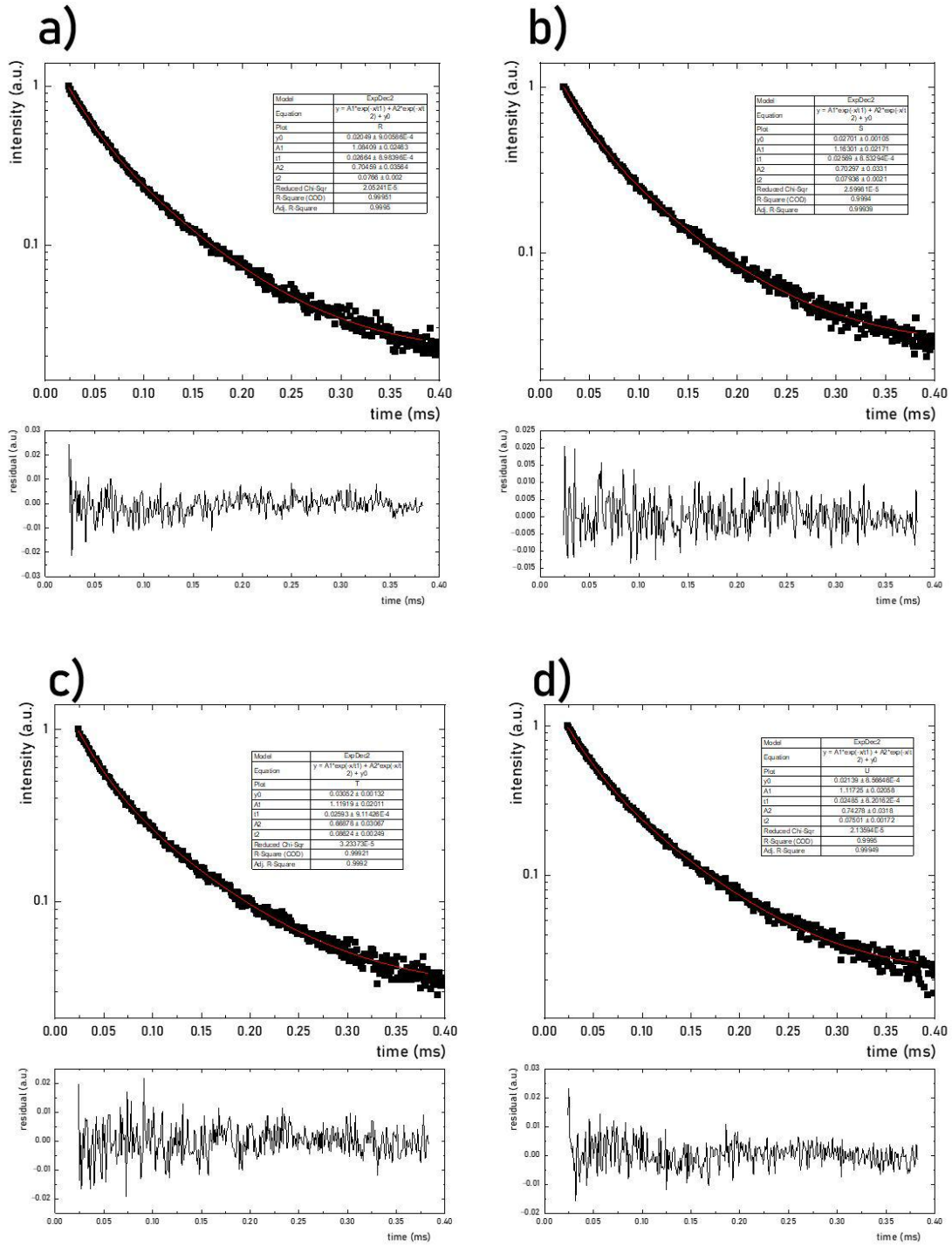


**Figure S14.** Room temperature luminescence decay profile of  $\text{Ca}_{0.8}\text{Sr}_{0.2}\text{MgSi}_2\text{O}_6:2\%\text{Cr}^{3+}$  under  $\lambda_{\text{exc}} = 445$  nm (black points) and bi-exponential fitting curve (red line) with residuals measured as a function of pressure at: 6.01 GPa -a); 6.77 GPa -b); 7.55 GPa -c); 5.54 GPa [decompression]-d).

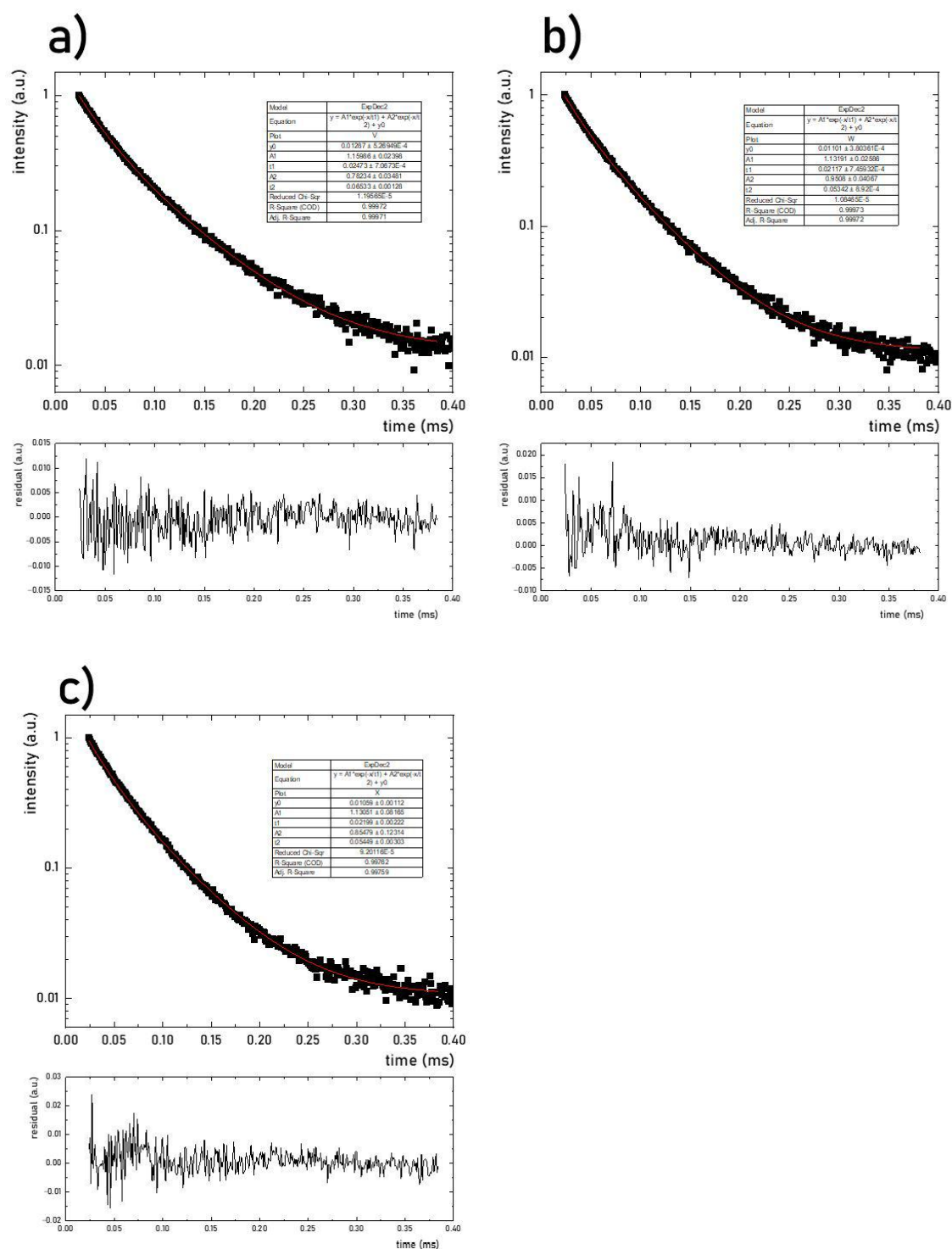


**Figure S15.** Room temperature luminescence decay profile of  $\text{Ca}_{0.8}\text{Sr}_{0.2}\text{MgSi}_2\text{O}_6:2\%\text{Cr}^{3+}$  under  $\lambda_{\text{exc.}} = 445$  nm (black points) and bi-exponential fitting curve (red line) with residuals measured as a function of pressure at: 3.98 GPa [decompression] -a); 1.95 GPa [decompression] -b); 1.19 GPa [decompression] -c).





# Multimodal, super-sensitive luminescent manometer based on giant pressure-induced spectral shift of $\text{Cr}^{3+}$ in the NIR range

M. Szymczak<sup>a</sup>, M. Runowski<sup>b,c</sup>, M.G. Brik<sup>d,e,f,g,h</sup>, L. Marciniak<sup>a,\*</sup>

<sup>a</sup> Institute of Low Temperature and Structure Research, Polish Academy of Sciences, Okólna 2, 50-422 Wrocław, Poland

<sup>b</sup> Adam Mickiewicz University, Faculty of Chemistry, Uniwersytetu Poznańskiego 8, 61-614 Poznań, Poland

<sup>c</sup> Departamento de Física, IUEA and MALTA-Consolider Team, Universidad de La Laguna, Apartado de Correos 456, E-38200 San Cristóbal de La Laguna, Santa Cruz de Tenerife, Spain

<sup>d</sup> College of Sciences & CQUPT-BUL Innovation Institute, Chongqing University of Posts and Telecommunications, Chongqing 400065, People's Republic of China

<sup>e</sup> Institute of Physics, University of Tartu, W. Ostwald Str. 1, Tartu 50411, Estonia

<sup>f</sup> Centre of Excellence for Photoconversion, Vinča Institute of Nuclear Sciences - National Institute of the Republic of Serbia, University of Belgrade, Belgrade, Serbia

<sup>g</sup> Faculty of Science and Technology, Jan Długosz University, 42200 Częstochowa, Poland

<sup>h</sup> Academy of Romanian Scientists, 050044 Bucharest, Romania

## ARTICLE INFO

### Keywords:

Luminescent manometer

Pressure sensor

$\text{Cr}^{3+}$

Luminescence intensity ratio

Pressure induced spectral shift

## ABSTRACT

The remote pressure readout is of vital application importance as it will facilitate and in many cases enable rapid diagnostics. For most of the luminescent manometers described to date, the sensitivity of the pressure readout is limited by the relatively small pressure-induced spectral shift of the emission band. In response to this limitation, in this work, we present a super-sensitive and temperature-invariant NIR emitting luminescent manometer based on  $\text{LiScGeO}_4:\text{Cr}^{3+}$ . The  ${}^4\text{T}_2 \rightarrow {}^4\text{A}_2$  emission band of  $\text{Cr}^{3+}$  ions undergoes in this manometer a linear spectral shift with a rate of  $d\lambda/dp = 23.63 \text{ nm/GPa}$ , which is the highest value reported in the literature to date. In addition, by using a ratiometric approach, this manometer has a relative sensitivity exceeding  $120\%/ \text{GPa}$ . Importantly, the developed optical manometer operates in the NIR spectral region, providing good light permeability in the non-transparent systems, having high absorption in the visible range. Moreover, in the case of high-pressure luminescence experiments, the use of the developed sensor will eliminate spectral overlapping issues, as the vast majority of the organic and inorganic phosphors emitting in the visible range.

## 1. Introduction

One of the most rapidly developing branches of the remote, optical sensors are those based on luminescence [1–8]. The deliberative and thoughtful design of such sensors allows for the development of luminescent materials with selective sensitivity to changes in a physical or chemical parameter of the environment [9–17]. In addition, by taking advantage of the luminescence phenomenon, the exclusionary sensing of parameters only for an element of the interest (that exhibits luminescence) is provided. This comprises a significant advantage over other noncontact measurement methods. A vast majority of luminescent sensors are luminescent thermometers [13,18–22]. However, besides temperature, the other crucial physical parameter that affects physical and biological processes and chemical reactions is pressure, which is rather underestimated in the literature in the context of optical sensing [23,24,33,25–32].

Among luminescent manometers, those based on the pressure induced spectral band shifts are the most widely used [23,24,33–42,25,43,44,26–32]. Amongst them, the supreme role is played by  $\text{Al}_2\text{O}_3:\text{Cr}^{3+}$  (ruby), whose spectrally narrow  $\text{R}_1$  emission line associated with the  ${}^2\text{E}_g \rightarrow {}^4\text{A}_{2g}$  electronic transition monotonically shifts with increasing pressure up to  $\approx 150 \text{ GPa}$  [45]. Although this sensor provides high measurement precision, its main limitation is relatively low sensitivity to pressure changes ( $d\lambda/dP = 0.365 \text{ nm/GPa}$ ) [25,37]. Moreover, the application potential of the approach based on band maximum analysis in 2-dimensional or 3-dimensional pressure imaging is relatively low due to the requirement to measure the spectrum at every point in the analyzed area. Therefore, the ratiometric pressure measurement approach has been intensively explored recently. While promising results are reported for manometers based on lanthanide ions ( $\text{Ln}^{3+}$ ) their high susceptibility to temperature changes limits the reliability of the pressure measurements. Therefore, ratiometric

\* Corresponding author.

E-mail address: [l.marciniak@intibs.pl](mailto:l.marciniak@intibs.pl) (L. Marciniak).

<https://doi.org/10.1016/j.cej.2023.143130>

Received 15 February 2023; Received in revised form 24 March 2023; Accepted 19 April 2023

Available online 24 April 2023

1385-8947/© 2023 Elsevier B.V. All rights reserved.

luminescent manometers that involve pressure-induced spectral shift of the broad  ${}^4T_{2g} \rightarrow {}^4A_{2g}$  emission band of  $Cr^{3+}$  ions have recently been proposed [46,47]. In this approach, the manometric parameter is the emission intensity ratio recorded in two spectral regions, which partially overlap with the  ${}^4T_{2g} \rightarrow {}^4A_{2g}$  emission band. Although this approach is universal and can be applied to any broadband emitting luminescent manometer [39,47–54], the  $Cr^{3+}$  ions possess unique features that predestinate them for this kind of application. Optical properties of the transition metal ions of  $3d^3$  electronic configuration, which include  $Cr^{3+}$ , directly depend on the crystal field strength ( $Dq/B$ ), that changes proportionally to the  $Cr^{3+}-O^{2-}$  distance ( $R$ ) according to the relation  $Dq/B \sim R^{-5}$ . Hence, according to the Tanabe-Sugano diagram [55] the applied isostatic pressure affects the  $R$  distance and causes the change in

the energy of the  ${}^4T_2$  state (Fig. 1). Thus, in the case of the  $Cr^{3+}$ -doped phosphors of weak crystal field strength, for which the emission spectrum is dominated by the  ${}^4T_2 \rightarrow {}^4A_2$  emission band, a change in the applied pressure shifts the position of the emission band barycenter. Since the spectral position of this band is almost independent of the temperature changes, this approach provides temperature invariant pressure readouts.

In order to develop a highly sensitive manometer operating in the ratiometric approach, it is necessary to select a host material of a weak crystal field that affects  $Cr^{3+}$  ions ( $Dq/B < 2.3$ ). For any host material meeting this criterion, it is expected that an increase in applied pressure will result in a spectral shift of the  ${}^4T_2 \rightarrow {}^4A_2$  band towards shorter wavelengths. However, if the applied pressure leads to the increase in

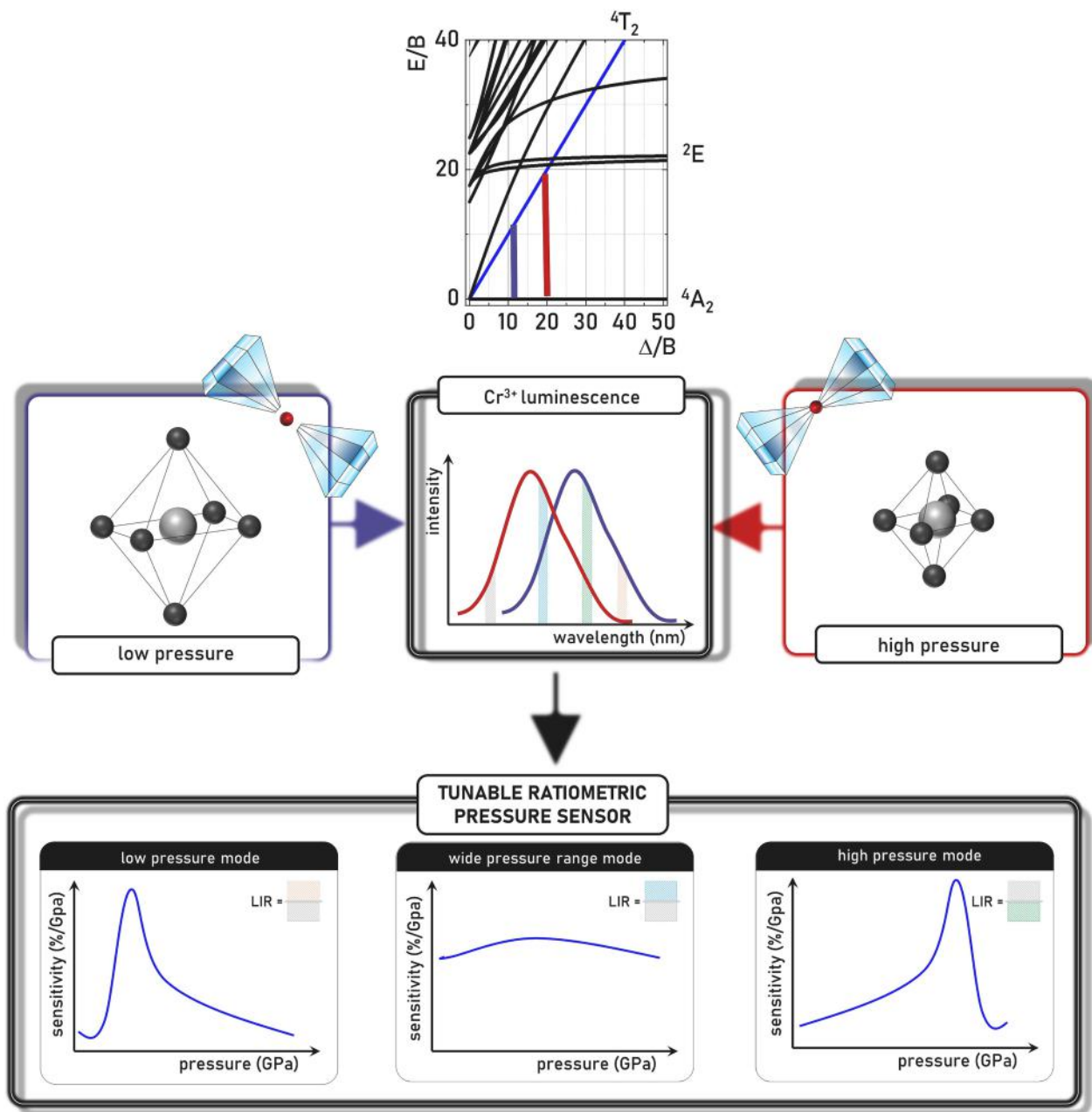


**Fig. 1.** Schematic representation of the proposed approach: as shown in the Tanabe-Sugano diagram the increase in the crystal field strength causes the increase of the energy of the  ${}^4T_2$  state. Therefore, the applied pressure that causes the shortening of the  $Cr^{3+}-O^{2-}$  distances in the  $LiScGeO_4:Cr^{3+}$  crystal structure, affects the emission spectrum of the  $Cr^{3+}$  and thus leads to the blue-shift of the  ${}^4T_2 \rightarrow {}^4A_2$  emission band. Hence, the luminescence intensity ratio (LIR) of signals integrated into two different spectral ranges can be used for ratiometric pressure readout. The pressure operating range of the such a luminescent manometer can be modified by the spectral ranges used. (For interpretation of the references to colour in this figure legend, the reader is referred to the web version of this article.)



the crystal field strength above  $\approx 2.3$ , it is expected that an additional  ${}^2E \rightarrow {}^4A_2$  emission line will appear in the emission spectrum, which due to the overlapping of both bands will negatively affect the accuracy of the pressure readouts. Therefore, in order to extend the useful pressure range in which the luminescent manometer can be applied, it is beneficial to select a host material of very low value of  $Dq/B$ . In addition, previous studies suggest that the lower the crystal field strength interacting with  $Cr^{3+}$  ions, the higher the sensitivity of the ratiometric manometer [46,47]. The above criteria motivated the selection of the  $LiScGeO_4$  host material, for which a weak crystal field was reported in the present studies [56–61]. As will be proved in this work, an additional advantage of the ratiometric approach based on the ratio of emission intensity integrated into two spectral gates for broadband emitting phosphor, is the possibility to tune the manometric properties by optimizing the choice of the spectral range analyzed. This unique feature allows the development of both: a super-sensitive manometer operating in the low/high pressure ranges and a highly sensitive manometer operating in a wide pressure range using the same luminescent material.

In this work, the abovementioned hypothesis was verified and evaluated on the  $LiScGeO_4:Cr^{3+}$  materials. It was shown that the  ${}^4T_2 \rightarrow {}^4A_2$  emission band undergoes huge pressure-induced blue-shift, i.e.,  $d\lambda/dP = 23.63$  nm/GPa (absolute sensitivity) in the 0–7 GPa  $p$ -range, which is currently the largest spectral shift reported in the literature. These unique features allow the development of a ratiometric luminescent manometer of unprecedentedly high relative sensitivity, i.e., over 120%/GPa, classifying it as the most sensitive pressure gauge. In addition, crystal field calculations of the  $Cr^{3+}$  energy levels in  $LiScGeO_4$  were performed to analyze the influence of the host structure on the impurity ion's optical properties.

## 2. Experimental section

### 2.1. Materials

All precursors for the synthesis were purchased from Alfa Aesar and were used without further purification:  $Li_2CO_3$  (99.998% of purity),  $Sc_2O_3$  (99.99% of purity),  $GeO_2$  (99.999% of purity) and  $Cr(NO_3)_3 \cdot 9H_2O$  (min. 99.99% of purity).

### 2.2. Synthesis

The  $LiScGeO_4:0-2\%Cr^{3+}$  (LSGO) microcrystalline powders were synthesized using a conventional high-temperature solid-state-reaction method. All reagents, i.e.  $GeO_2$  and  $Sc_2O_3$ , as well as  $Li_2CO_3$  and  $Cr(NO_3)_3 \cdot 9H_2O$  in stoichiometric amounts, were meticulously ground in an agate mortar. To increase the degree of homogeneity of precursors throughout the mixture,  $n$ -hexane was used for the grinding process. The mixed precursors were transferred to a corundum crucible and preheated at 1073 K for 2 h, followed by a final annealing at 1423 K for 5 h (heating 10 K/min), in air. The cooled to room temperature in the air powders were ground again in an agate mortar and left for subsequent analysis.

### 2.3. Methods

X-ray powder diffraction (XRD) measurements were performed on a PANalytical X'Pert Pro diffractometer equipped with an Anton Paar TCU1000 N Temperature Control Unit using Ni-filtered  $Cu\ K\alpha$  radiation ( $V = 40$  kV,  $I = 30$  mA).

The morphology of obtained samples was studied using Transmission Electron Microscopy (TEM) and Scanning Electron Microscopy (SEM), measurements were carried out with FEI TECNAI G2 X-TWIN microscope (300 keV parallel beam electron energy) equipped with an EDS detector and with FEI Nova NanoSEM 230 equipped with an energy dispersive spectrometer EDAX Genesis XM4, respectively. EDS maps were obtained using the SEM system. The sample was prepared by

grinding in an agate mortar, dispersing in a small amount of methanol and then a drop of the obtained suspension was applied on the carbon stub (SEM) or on a copper grid (TEM) and dried under an infrared lamp.

The Raman spectra were measured in the pressure range from  $\approx 0$  to 10 GPa, in a backscattering geometry using a Renishaw InVia confocal micro-Raman system with a power-controlled 100 mW 532 nm laser diode. The laser beam was focused using an Olympus x20 SLMPlan N long working distance objective. Raman spectra of the sample compressed in a methanol/ethanol/water – 16/3/1 (pressure transmitting medium) were measured in a DAC equipped with the ultra-low fluorescence (Iias) diamond anvils.

The excitation spectra were recorded using FLS1000 Fluorescence Spectrometer (Edinburgh Instruments), equipped with the 450 W Xenon lamp as a source of the excitation and R5509-72 photomultiplier tube from Hamamatsu in nitrogen-flow cooled housing as the detector. The temperature and pressure-dependent emission spectra and luminescence decay profiles were measured using the aforementioned setup, and a 445 nm laser diode excitation. The temperature of the sample during photoluminescence measurements was controlled by a THMS 600 heating-cooling stage from Linkam (0.1 °C temperature stability and 0.1 °C set point resolution). To achieve a stable set temperature, intervals of 1 min were taken between measurements.

The high-pressure measurements were performed with a gas (nitrogen) membrane driven diamond anvil cell Diacell  $\mu$ ScopeDAC-RT(G) from Almax easyLab. The pressure was applied using a controller Druck PACE 5000. Between the diamond anvils (ultra-low fluorescence; Iias type; 0.4 mm culets), a stainless steel gasket with a thickness of 250  $\mu$ m was placed, in which a hole with a diameter of 140  $\mu$ m was previously drilled (after preindentation). A sample was placed in the hole together with a small crystal of ruby, which acted as a pressure indicator (pressure readout based on the spectral shift of  $R_1$  line [25,45]). As the pressure transmitting medium was used methanol-ethanol solution (V:V/4:1).

## 3. Results and discussion

### 3.1. Experimental spectroscopic measurements at ambient and elevated pressure and temperature sensing

The  $LiScGeO_4$  crystallizes in an orthorhombic crystal structure with a  $Pnma$  (No. 62) space group [56–61]. Their structure consists of octahedra formed by 6-fold coordinated  $Sc^{3+}$  and  $Li^+$  sites and the  $(GeO_4)^{4-}$  tetrahedra (Fig. 2a). The  $Cr^{3+}$  dopant ions preferentially occupy the  $Sc^{3+}$  sites, due to their octahedral coordination and the similarity in ionic radii:  $R(Li^+) = 0.76\text{\AA} > R(Sc^{3+}) = 0.745\text{\AA} > R(Cr^{3+}) = 0.615\text{\AA} > R(Ge^{4+}) = 0.39\text{\AA}$  [62]. A relatively small difference in the ionic radii of dopant ions and  $Sc^{3+}$  results in the lack of the additional diffraction reflexes in the XRD patterns of the  $LiScGeO_4$  powders with  $Cr^{3+}$  concentrations up to 2%, and as shown in Fig. 2b all observed reflexes correspond to the reference pattern of the pure host (ICSD 62481). The analysis of the morphology of the synthesized phosphor reveals that resulting powders consist of the particles with the average size of  $\sim 3\text{ }\mu$ m in diameter. However, some small fraction of the submicron-sized particles can be found as well. The wide distribution of the crystals' size is due to the applied solid state synthesis method. The uniform distribution of the Sc, Ge and Cr elements was revealed by the EDS analysis, which confirms the lack of clusterification of the dopant ions in the  $LiScGeO_4:Cr^{3+}$  (EDS data can be found in Figure S1).

In order to study the effect of applied isostatic pressure on the  $LiScGeO_4$  structure, Raman spectra were measured as a function of pressure for the undoped sample. The measured Raman spectra for the  $LiScGeO_4$  sample at ambient pressure revealed several bands (Raman active modes), and the most intense ones were initially centered at  $\approx 400, 450, 500, 660, 720$  and  $790\text{ cm}^{-1}$  (Fig. 3a). The compression of the material, i.e., with increasing pressure values, results in the increase of the energy of the phonon modes, which is manifested by the shift of

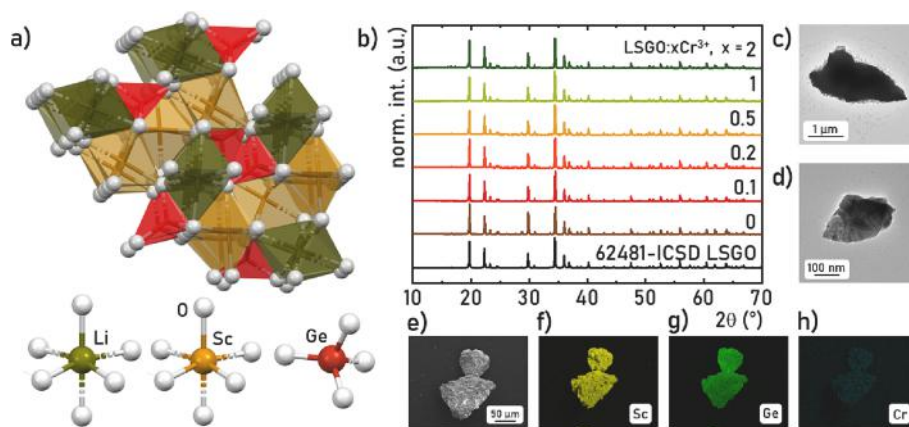


**Fig. 2.** 3D visualization of the LiScGeO<sub>4</sub> structure and octahedral/tetrahedral surrounding of cations in host material -a), X-ray diffraction patterns of LiScGeO<sub>4</sub> with different Cr<sup>3+</sup> ions concentration -b), representative TEM -c)-d) and SEM images -e) with EDS maps of Sc -f), Ge -g) and Cr -h) elements of LiScGeO<sub>4</sub>:0.5 %Cr<sup>3+</sup>.

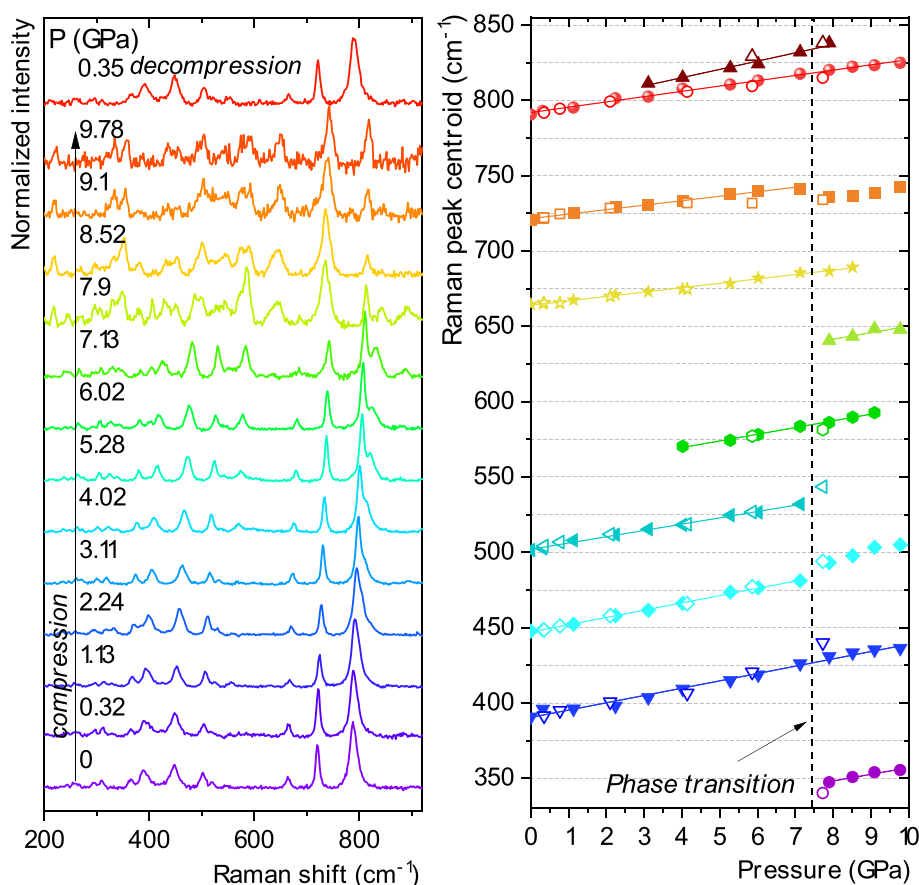


**Fig. 3.** Normalized Raman spectra for the LiScGeO<sub>4</sub> material measured for different pressure values, during the compression and after the decompression cycle -a). Determined energies (peak centroids) of the most intense phonon modes as a function of pressure -b); filled symbols represent compression data, and empty ones represent decompression data; the continuous lines are the linear fits applied for determination of the pressure shift rates of the corresponding Raman modes.

the Raman bands toward higher energy values (higher wavenumbers) (Fig. 3b). This effect is due to the shortening of the average distances between the ions, namely, the bonds shortening in the compressed structure. Around 3–4 GPa, there start to appear new band centered at  $\approx 570$  cm<sup>-1</sup>, as well as the most intense, high-energy band ( $\approx 790$  cm<sup>-1</sup>) seems to “split” into two peaks, resulting in the appearance of the new band centered at  $\approx 820$  cm<sup>-1</sup>. Nevertheless, it is worth noting that other Raman modes originating from the crystal structure of the LSGO material neither change their shape/intensity nor the shift rate. However, around  $\approx 7.5$ –8 GPa the Raman spectrum changes completely for the

investigated compound, manifested in a form of the appearance of several new peaks (e.g. at  $\approx 350$  and  $640$  cm<sup>-1</sup>) and disappearance (e.g. at  $\approx 500$ ,  $660$  and  $820$  cm<sup>-1</sup>) or huge spectral shift of the initial Raman modes (e.g. at  $\approx 450$  and  $720$  cm<sup>-1</sup>). The observed drastic changes in the Raman spectra in the mentioned high-pressure region are most plausibly associated with some phase transition of the compressed material. Moreover, due to the typically observed deterioration of the Raman signal in the compressed materials (increasing strains and crystal defects under pressure, leading to the lower signal intensity), the signal-to-noise ratio significantly decreased with pressure, hampering observations of



the low-intensity Raman modes. Importantly, the postulated phase transition is fully reversible, because during the decompression process (pressure release) all of the peaks return to their initial positions/energies, showing very good agreement with the compression data, especially in the 0–7 GPa range. The reversibility of structural changes in the compression-decompression cycles is crucial for the pressure sensing applications, indicating the possibility of using the LiScGeO<sub>4</sub> material as an optical pressure sensor. The determined peak centroids both for compression (filled symbols) and decompression (empty symbols) are presented in Fig. 3b, and the Raman spectra recorded during decompression cycle are given in Figure S2, whereas, the determined shift rates (using linear fits) for the most intense Raman modes are listed in Table S1.

The spectroscopic properties of Cr<sup>3+</sup> ions are strongly governed by the strength of the crystal field of the host material as shown in the Tanabe-Sugano diagram for transition metal ions with 3d<sup>3</sup> electron configuration (Fig. 1). According to this diagram, depending on the value of the Dq/B parameter, the lowest excited level is the <sup>4</sup>T<sub>2</sub> level for Dq/B < 2.2 (weak crystal field) or the <sup>2</sup>E level for Dq/B > 2.4 (strong crystal field). This effect is manifested in a change in the shape of the phosphor emission spectrum, from broadband emission associated with the <sup>4</sup>T<sub>2</sub> → <sup>4</sup>A<sub>2</sub> transition to narrowband emission assigned to the <sup>2</sup>E → <sup>4</sup>A<sub>2</sub> transition. For the intermediate crystal field approximation case, the emission spectrum consists of both these bands. As shown in Fig. 4a, in the case of the LiScGeO<sub>4</sub>:Cr<sup>3+</sup> materials, for which a weak crystal field is expected, the emitting state is the <sup>4</sup>T<sub>2</sub> energy level. Hence, upon photoexcitation, the resulting <sup>4</sup>T<sub>2</sub> → <sup>4</sup>A<sub>2</sub> radiative transition in the LiScGeO<sub>4</sub>:Cr<sup>3+</sup> compound leads to a broad emission band, centered at about 1100 nm (Fig. 4c). The concentration of Cr<sup>3+</sup> ions affects emission intensity, which decreases with the dopant concentration above 0.5 %Cr<sup>3+</sup>, but it does not influence on the spectral position of this band. This confirms that Cr<sup>3+</sup> ions, regardless of dopant concentration, consistently substitute only one crystallographic position in the LiScGeO<sub>4</sub> structure. As shown in the excitation spectra of the LiScGeO<sub>4</sub>:Cr<sup>3+</sup> (Fig. 4b), broadband emission can be obtained upon excitation into any of the

three observed excitation bands at about 330 nm, 590 nm and 780 nm corresponding to the <sup>4</sup>A<sub>2</sub> → <sup>4</sup>T<sub>1</sub> (P), <sup>4</sup>A<sub>2</sub> → <sup>4</sup>T<sub>1</sub>(<sup>4</sup>F) and <sup>4</sup>A<sub>2</sub> → <sup>4</sup>T<sub>2</sub> electron transitions, respectively. The spectral position of these bands indicates that the Cr<sup>3+</sup> ion is located in a weak crystal field. To verify this, Dq/B calculations were performed according to a well-known procedure [63]:

$$Dq = \frac{E(^4A_2 \rightarrow ^4T_2)}{10} \quad (1)$$

$$x = \frac{E(^4A_2 \rightarrow ^4T_1) - E(^4A_2 \rightarrow ^4T_2)}{Dq} \quad (2)$$

$$\frac{Dq}{B} = \frac{15(x - 8)}{(x^2 - 10x)} \quad (3)$$

where Dq is the crystal field splitting energy and B is Racah parameter. The obtained value of Dq/B = 1.44 is independent of dopant concentration and is in a good agreement with the previously reported value [56]. As expected, the luminescence of Cr<sup>3+</sup> ions in LiScGeO<sub>4</sub> is characterized by fast kinetics (Fig. 4d, Figure S3). The average lifetimes (τ<sub>avr</sub>) slightly shorten with increasing Cr<sup>3+</sup> concentration, from 8.59 μs for the LiScGeO<sub>4</sub>:0.1 %Cr<sup>3+</sup> to 7.7 μs for the LiScGeO<sub>4</sub>:2% Cr<sup>3+</sup>. This effect is probably related to the interionic interactions. Since the shape of the emission spectrum is not affected by the dopant concentration and the most intense luminescence was observed for LiScGeO<sub>4</sub>:0.5 %Cr<sup>3+</sup> this sample was selected for further studies.

To investigate the manometric properties of the LiScGeO<sub>4</sub>:Cr<sup>3+</sup>, room temperature pressure-dependent emission spectra were measured in the 0–7.87 GPa pressure range (Fig. 5a). The measurements during compression (Fig. 5a) and decompression (Figure S4) were carried out in a diamond anvil cell, upon λ<sub>exc</sub> = 445 nm. Additionally, low intensity bands at around 800 nm are associated with the luminescence of Al<sub>2</sub>O<sub>3</sub>:Cr<sup>3+</sup> pressure indicator (ruby), which was used during measurements (see Fig. S4a and S5). During the compression of the LiScGeO<sub>4</sub>:Cr<sup>3+</sup> material, the broad <sup>4</sup>T<sub>2</sub> → <sup>4</sup>A<sub>2</sub> emission band, initially centered at around 1100 nm undergoes a huge, linear blue-shift by ≈170 nm in the analyzed

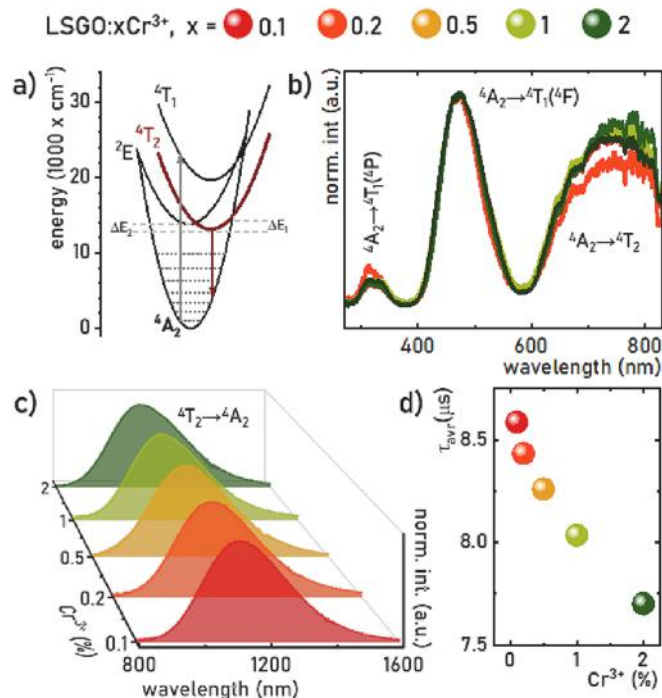


**Fig. 4.** Configurational coordinate diagram for the octahedrally coordinated Cr<sup>3+</sup> ions in a weak crystal field -a); the comparison of room temperature excitation spectra (λ<sub>em</sub> = 1110 nm) -b); emission spectra (λ<sub>exc</sub> = 445 nm) -c); and τ<sub>avr</sub> -d) of LiScGeO<sub>4</sub> doped with different concentrations of Cr<sup>3+</sup> ions.

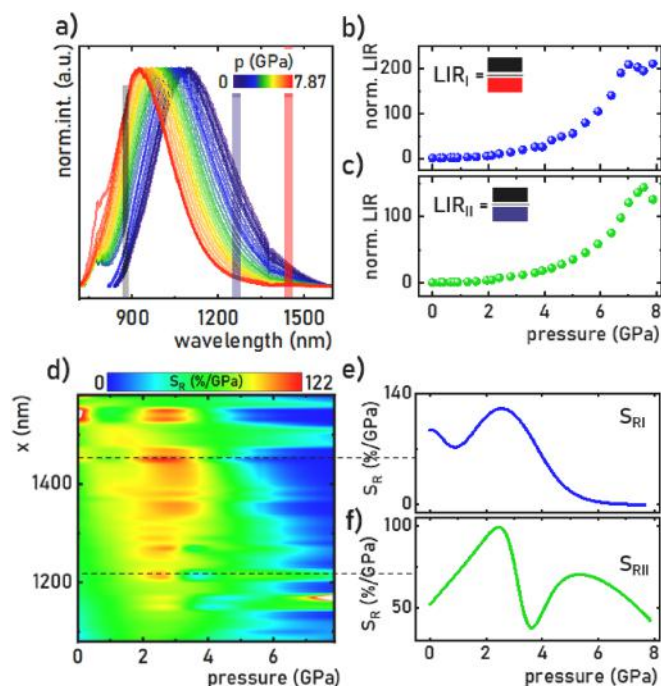


**Fig. 5.** The pressure-dependent emission spectra (λ<sub>exc</sub> = 445 nm) of LiScGeO<sub>4</sub>:0.5 %Cr<sup>3+</sup>, with marked spectral ranges used to calculate LIR<sub>I</sub> and LIR<sub>II</sub> parameters -a); normalized LIR<sub>I</sub> -b) and LIR<sub>II</sub> -c); pressure dependent S<sub>R</sub> -d); S<sub>RI</sub> -e) and S<sub>RII</sub> -f) as a function of pressure (0–7.87 GPa).

pressure range, resulting in a shift rate  $d\lambda/dp = 23.63 \text{ nm/GPa}$  ( $231 \text{ cm}^{-1}/\text{GPa}$  - Figure S6). This is an unprecedentedly large spectral shift among all luminescent materials reported in the literature. However, beside analyzing only the change in the emission band centroid as a manometric parameter the ratiometric approach is presented here. The dynamics of the LIR changes as a function of pressure depend on the considered spectral range used for LIR calculation. Therefore, to evaluate thoroughly this effect the LIR was calculated in 10 nm-width spectral intervals as follows (Figure S7):

$$LIR_x = \frac{\int_{870\text{nm}}^{880\text{nm}} {}^4T_2 \rightarrow {}^4A_2 d\lambda}{\int_{x-10\text{nm}}^{x+10\text{nm}} {}^4T_2 \rightarrow {}^4A_2 d\lambda} \quad (4)$$

where  $x = (1080\text{--}1580) \text{ nm}$ . All of obtained pressure dependencies of LIR are presented in Figure S8, whereas here two representative cases will be considered (Fig. 5b and 5c):

$$LIR_I = \frac{\int_{870\text{nm}}^{880\text{nm}} {}^4T_2 \rightarrow {}^4A_2 d\lambda}{\int_{1450\text{nm}}^{1460\text{nm}} {}^4T_2 \rightarrow {}^4A_2 d\lambda} \quad (5)$$

$$LIR_{II} = \frac{\int_{870\text{nm}}^{880\text{nm}} {}^4T_2 \rightarrow {}^4A_2 d\lambda}{\int_{1220\text{nm}}^{1230\text{nm}} {}^4T_2 \rightarrow {}^4A_2 d\lambda} \quad (6)$$

The  $LIR_I$  is characterized by the highest slope as a function of pressure and increases 200-times in the 0–7 GPa pressure range, while in the case of  $LIR_{II}$  less dynamic but gradual in the whole analyzed pressure range enhancement of LIR was observed (verified also within additional compression-decompression cycles Figure S9).  $LIR_I$  and  $LIR_{II}$  can be fitted using empirical equations using eq. S1 and S2. Actually, as shown in Figure S7 and Figure S8 the manometric parameters of this optical pressure indicator can be tuned by the appropriate selection of the integrated spectral range used for the LIR determination. To quantify the pressure induced changes in  $LIR_x$  values of the relative manometric sensitivity was calculated as follows:

$$S_{R,px} = \frac{1}{LIR_x} \frac{\Delta LIR_x}{\Delta p} 100\% \quad (7)$$

The obtained results presented in a form of a 2-dimensional map (Fig. 5d) indicate that the selection of  $x$  significantly affects the maximal sensitivity, usable pressure range and the pressure at which the  $S_{R,max}$  was obtained. For  $x \sim 1080 \text{ nm}$  the developed manometer provides the high sensitivity of pressure readout above 6 GPa, while for the  $x = 1450 \text{ nm}$  the highest  $S_R$  was reached at pressure around 2.5 GPa. Actually, for  $LIR_I$  the maximal  $S_R$  reached  $121.14 \text{ \%/GPa}$  at 2.55 GPa which is the highest reported value of the sensitivity of the ratiometric luminescent manometer of both transition metal ion based ( $S_{R,p} = 4.7\%/GPa$  for  $\text{Li}_2\text{Mg}_3\text{TiO}_6:\text{Cr}^{3+}$  and  $S_{R,p} = 40/9.83\%/GPa$  for  $\text{MgO}:\text{Cr}^{3+}$ ) and on materials doped with lanthanide ions ( $S_{R,p} = 13.8\%/GPa$  for  $\text{SrB}_4\text{O}_7:\text{Eu}^{2+}/\text{Sm}^{2+}$ ) up to date (Fig. 5e)[42,46,47]. It is also possible to obtain readout mode that is highly sensitive at both low and high pressures ( $S_{R,p} = 99.57\%/GPa$  at 2.39 GPa and  $S_{R,p} = 70.56\%$  at 5.33 GPa) by using  $LIR_{II}$  (Fig. 5f, see also Figure S10 and S11). On the other hand, when the  $x \sim 1500 \text{ nm}$  a high  $S_R \sim 50\%/GPa$  can be obtained in the whole analyzed pressure range. The presented tuning of the manometric properties reveals high versatility of the  $\text{LiScGeO}_4:\text{Cr}^{3+}$  material as an optical manometer.

Despite, the extraordinary manometric properties of the developed  $\text{LiScGeO}_4:\text{Cr}^{3+}$  sensor, it is important to investigate how temperature affects pressure readouts, i.e., determine the thermal dependence for the spectroscopic (manometric) parameters used. This is critical for the experiments performed simultaneously under changes in pressure and temperature, where the applied pressure sensor should exhibit a negligible or small and well-defined temperature dependence. Therefore, the spectroscopic properties of the  $\text{LiScGeO}_4:0.5 \text{ \%Cr}^{3+}$  were studied as a function of temperature in the range of 83–443 K. As expected, an increase in temperature causes a decrease in emission intensity, which is

associated with the overcoming of the intersection point of  ${}^4T_2$  and  ${}^4A_2$  states by the electrons occupying  ${}^4T_2$  state (Fig. 4a). However, the position of the band maximum does not change significantly with increasing temperature, which is illustrated by the small temperature variation of  $LIR_I$  and  $LIR_{II}$  (only a 2-fold increase for  $LIR_I$  and 5.5-fold for  $LIR_{II}$ ) in the analyzed temperature range (Fig. 6b,c). This is an expected result since  $\text{Cr}^{3+}$  ions occupy only one crystallographic position in the  $\text{LiScGeO}_4$  host, and therefore, no significant temperature-induced changes in the spectral position (and shape) of the emission band are expected (Fig. 6a, S12). The determined relative temperature sensitivities clearly indicate that the temperature changes of LIR are small. The maximum  $S_{R,T}$  reach about  $S_{R,T,max} = 0.75 \text{ \%/K}$  at 363.7 K and  $0.87 \text{ \%/K}$  at 343.15 K for  $LIR_I$  and  $LIR_{II}$ , respectively (Fig. 6e, f). Although from a thermometric perspective, the obtained  $S_{R,T}$  values are not very high, they indicate that the LIR can be affected by temperature to some extent. Nevertheless, the  $S_{R,p}$  value exceeds the  $S_{R,T}$  by more than two orders of magnitude. In order to determine how much more sensitive is the LIR parameter in the  $\text{LiScGeO}_4:\text{Cr}^{3+}$  to changes of pressure, with respect to its temperature sensitivity, the Thermal Invariability Manometric Factor (TIMF) was introduced according to the equation:

$$TIMF = \left| \frac{S_{R,p}}{S_{R,T}} \right| \quad (8)$$

This is a very important parameter that can designate the range of applications for a given luminescent manometer. In the case of applications for which the temperature changes of the system are not expected during the measurement (e.g. materials compression experiments at ambient temperature), the selection of a suitable manometer can be based predominantly on the criterion of high relative sensitivity. However, if there is a risk of temperature changes during the measurement, the TIMF value should also be considered. It can be assumed that for a reliable luminescent manometer should  $TIMF > 100$ . This value is adopted arbitrarily but fully justified because it determines, that changes in pressure will cause two orders of magnitude higher changes than temperature changes. At room temperature, for

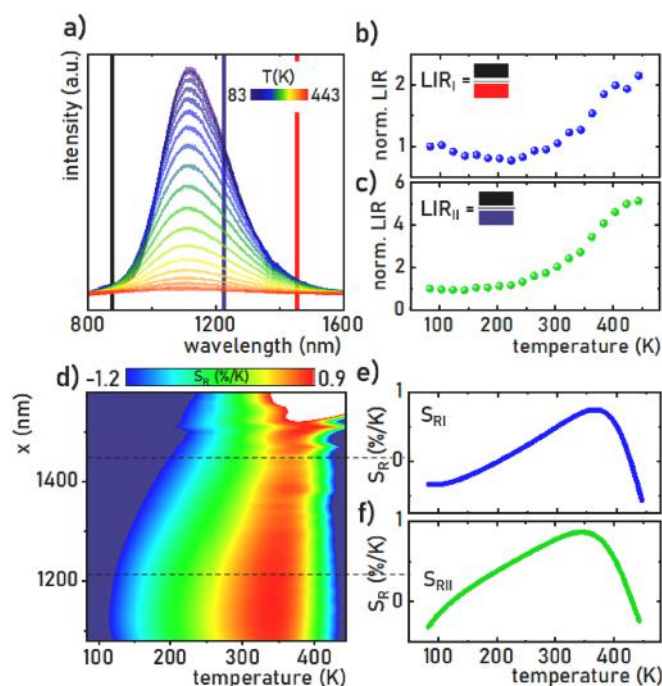


Fig. 6. Thermal evolution of emission spectra ( $\lambda_{exc} = 445 \text{ nm}$ ) of  $\text{LiScGeO}_4:0.5 \text{ \%Cr}^{3+}$ , with marked spectral ranges used to define  $LIR_I$  and  $LIR_{II}$  -a); normalized  $LIR_I$  -b) and  $LIR_{II}$  -c),  $S_{R,T}$  map -d),  $S_{RI}$  -e) and  $S_{RII}$  -f) as a function of temperature (83–443 K).

LiScGeO<sub>4</sub>:0.5 %Cr<sup>3+</sup> the value of TIMF<sub>LIRI</sub> = 241.1 and TIMF<sub>LIRII</sub> = 128.4. In both cases, the criterion of TIMF > 100 is met, but as can be seen from a comparison of the TIMF parameter for other ratiometric manometers based on the <sup>4</sup>T<sub>2</sub>→<sup>4</sup>A<sub>2</sub> band shift, this is not the highest value (Table 1).

As indicated above, ratiometric pressure readout in many cases facilitates multidimensional imaging of pressure changes in the objects under study. However, the spectral band shift approach is currently commonly used for pressure sensing. Therefore, the pressure-induced band shift observed in the LiScGeO<sub>4</sub>:Cr<sup>3+</sup> was analyzed. As can be seen, the band centroid monotonically decreases by ≈170 nm, from around 1100 to 930 nm, with the shift rate ≈23.6 nm/GPa in the 0–7 GPa pressure range. This slope of the emission band maxima (which is also equal to 231 cm<sup>-1</sup>/GPa) can be used for modeling the positions of other energy levels of Cr<sup>3+</sup> in LiScGeO<sub>4</sub>, assuming (as the first approximation) that the Stokes shift between the excitation and emission band maxima and Racah parameters are pressure independent, at least, for the values of pressure close to the ambient one. Comparing the absolute sensitivity S<sub>A</sub> in both the wavelength domain (nm), as well as the wavenumbers domain (cm<sup>-1</sup>), it is clear that the developed LiScGeO<sub>4</sub>:Cr<sup>3+</sup> sensor material can work as an optical manometer with the highest rate of change among all reports described in the literature to date [39,48–52,54] (see Fig. 7)

### 3.2. Crystal field calculations and comparison with the experimental spectra

A deeper insight into the spectroscopic properties of impurity ions in solids can be gained by applying crystal field theory to the analysis of the energy levels splitting. In the present work, we used the exchange charge model (ECM) [65] of the crystal field to calculate the crystal field parameters (CFP) and energy level scheme of the Cr<sup>3+</sup> ions in LiScGeO<sub>4</sub>. Detailed description of the ECM foundations, along with all equations, can be easily found in the literature [66–68], they will not be repeated here again for the sake of brevity. The main advantages of the ECM can be just underlined:

- possibility to calculate directly the CFP values from the real crystal structure data without making any *a priori* assumptions on the point symmetry of the impurity ion site;
- calculations of the complete energy level scheme of the impurity ion using the obtained CFP values;
- a small number of fitting parameters (which is only one in the simplest case). Its introduction is related to the fact that the pure atomic (ionic) wave functions are used to calculate the overlap integrals between the wave functions of an impurity ion and ligands. The value of this fitting parameter is evaluated from the position of the first (lowest in energy) absorption maximum. The ECM has been successfully applied to various combinations of dopants and host matrices to yield good agreement between the

**Table 1**

Comparison of the manometric parameter of different ratiometric luminescent manometers based on the pressure induced spectral shift of the <sup>4</sup>T<sub>2</sub>→<sup>4</sup>A<sub>2</sub> emission band.

Manometer	S <sub>R,p</sub> max [%/GPa]	p @ S <sub>R,p</sub> max [GPa]	S <sub>R,T</sub> @ 300 K [%/K]	TIMF	Ref.
Li <sub>2</sub> Mg <sub>3</sub> TiO <sub>6</sub> :Cr <sup>3+</sup>	4.63	ambient	0.034	136.2	[47]
MgO:Cr <sup>3+</sup> mode I	9.8	1.16	0.0056	1750	[46]
MgO:Cr <sup>3+</sup> mode II	40	ambient	0.056	714.3	[46]
LiScGeO <sub>4</sub> :Cr <sup>3+</sup> LIRI	121.14	2.55	0.502	241.3	This work
LiScGeO <sub>4</sub> :Cr <sup>3+</sup> LIRII	99.57	2.39	0.775	128.5	This work

calculated impurity ions' energy level schemes and experimental spectroscopic data (an extensive list of corresponding references can be found in Ref. [68])

The Cr<sup>3+</sup> ions substitute for the 6-fold coordinated Sc ions. To take into account the influence of ions in remote coordination spheres and ensure proper convergence of the crystal lattice sums needed for calculations of the CFP, a large cluster consisting of 80,170 ions around a Cr<sup>3+</sup> ion was constructed using the VESTA software [69]. The calculated values of the non-zero CFP (Stevens normalization, in cm<sup>-1</sup>) are as follows: B<sub>2</sub><sup>0</sup> = -2189; B<sub>2</sub><sup>1</sup> = 6521; B<sub>2</sub><sup>2</sup> = 291; B<sub>4</sub><sup>0</sup> = -2344; B<sub>4</sub><sup>1</sup> = -5014; B<sub>4</sub><sup>2</sup> = -1944; B<sub>4</sub><sup>3</sup> = 73695; B<sub>4</sub><sup>4</sup> = 5412. Diagonalization of the crystal field Hamiltonian with these CFPs and Racah parameters B = 500 cm<sup>-1</sup>, C = 3600 cm<sup>-1</sup> allowed to calculate all energy levels of Cr<sup>3+</sup> ions in LiScGeO<sub>4</sub> shown by vertical lines in Fig. 8.

Comparison of the calculated results with the experimental excitation spectrum yields good agreement, as is evidenced by Fig. 8a. All orbital triplet states are split into three singlet levels each (two upper levels from the <sup>4</sup>T<sub>2</sub> state are close to each other, so they seem to merge in Fig. 8a) and each orbital doublet is split into two singlet states, which indicates complete removal of degeneracy in low-symmetry crystal field. A conclusion about low symmetry of crystal field in this particular case can be also drawn from the structure of the crystal field Hamiltonian with above-listed non-zero CFPs. The width of both broad excitation bands that correspond to the transition from the <sup>4</sup>A<sub>2</sub> ground state of the Cr<sup>3+</sup> ions to the <sup>4</sup>T<sub>2</sub> and <sup>4</sup>T<sub>1</sub> triplets (all arising from the ground <sup>4</sup>F term of a free ion) correlates with large crystal field splitting of these triplet states induced by the low-symmetry component of crystal field. We note that the dip at the <sup>4</sup>T<sub>2</sub> excitation band at about 14500 cm<sup>-1</sup> corresponds to the <sup>2</sup>E state of the Cr<sup>3+</sup> ions, which was also detected as a Fano anti-resonance by Sharonov et al at about 14540 cm<sup>-1</sup> in the same host [58]. Another mechanism that is responsible for the broadening of the spectral bands of transition metal ions is the electron-vibrational interaction (EVI), which manifests itself not only in the appearance of broad spectral bands but also in the shift of the first emission band maxima in respect to the corresponding excitation band (the so called Stokes shift). Using well-known relations [70] between the full width at half maximum (FWHM) of the emission band Γ, Stokes shift ΔE (2418 cm<sup>-1</sup> and 4295 cm<sup>-1</sup>, respectively, according to the experimental data) and effective phonon energy ħω, we found the following values of Huang-Rhys factor S = 9.08 and effective phonon energy ħω = 250 cm<sup>-1</sup> (this value cannot be directly compared with the Raman or vibrational spectroscopic data, because it is determined in the framework of the single configurational coordinate model and represents the result of the interaction of the impurity ion's electronic states with all normal modes at the same time). The validity of the obtained in this way parameters can be checked by plotting the emission band with the help of the following equation. The intensity I of the emission band at energy E can be approximated by the following expression [70]:

$$I = \frac{e^{-S} S^p}{p!} \left( 1 + S^2 \frac{e^{-\hbar\omega/kT}}{p+1} \right), p = \frac{E_0 - E}{\hbar\omega} \quad (9)$$

where E<sub>0</sub> is the zero phonon line (ZPL) energy, which is located in the vicinity of the point of intersection of the excitation and emission spectra, and p is the number of the effective phonons with the energy ħω involved into the emission transition. With the above given values of S and ħω and the position of the ZPL at 11050 cm<sup>-1</sup>, the shape of the <sup>4</sup>T<sub>2</sub>→<sup>4</sup>A<sub>2</sub> emission band can be modeled. Fig. 8b shows good agreement between the experimental and fitted (by means of Eq. (9)) emission band shapes in terms of the position of their maxima and overall appearance. The width of the calculated band shape is smaller than the experimental one, it often happens when Eq. (9) is used, because of simplified assumptions made for its derivation.



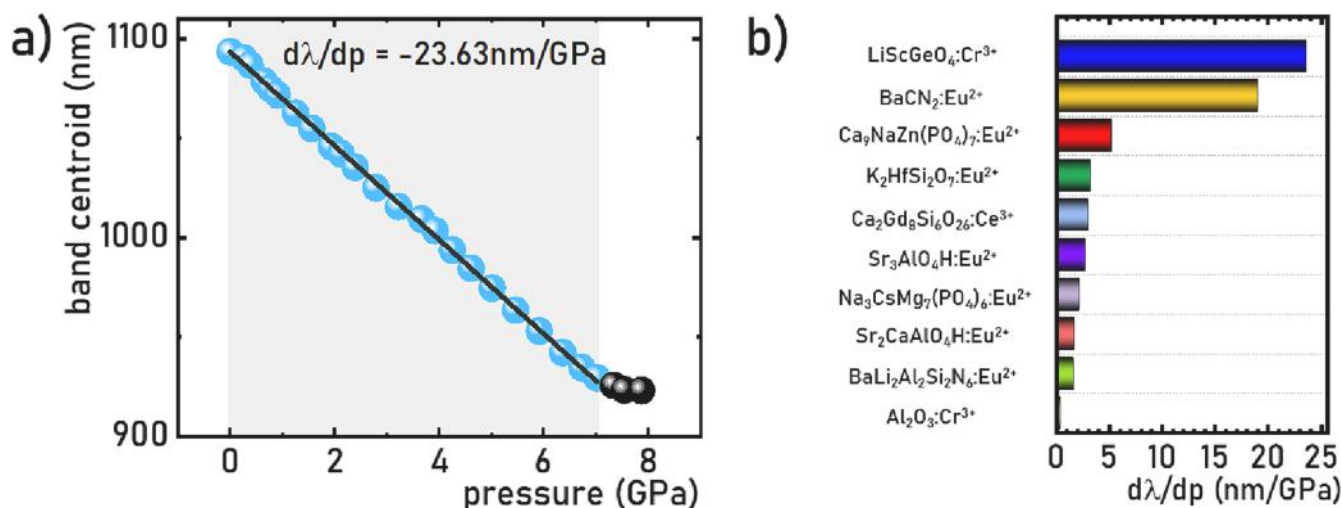


Fig. 7. The band centroid of the  ${}^4T_2 \rightarrow {}^4A_2$  emission band for the  $\text{LiScGeO}_4:0.5\% \text{Cr}^{3+}$  with marked usable pressure range and linear fit in range 0–7 GPa -a); the comparison of  $d\lambda/dp$  of the pressure induced spectral shift calculated in the wavelength domain of the broadband emitting luminescent manometers and ruby-b) [25,38,39,48–52,54,64].

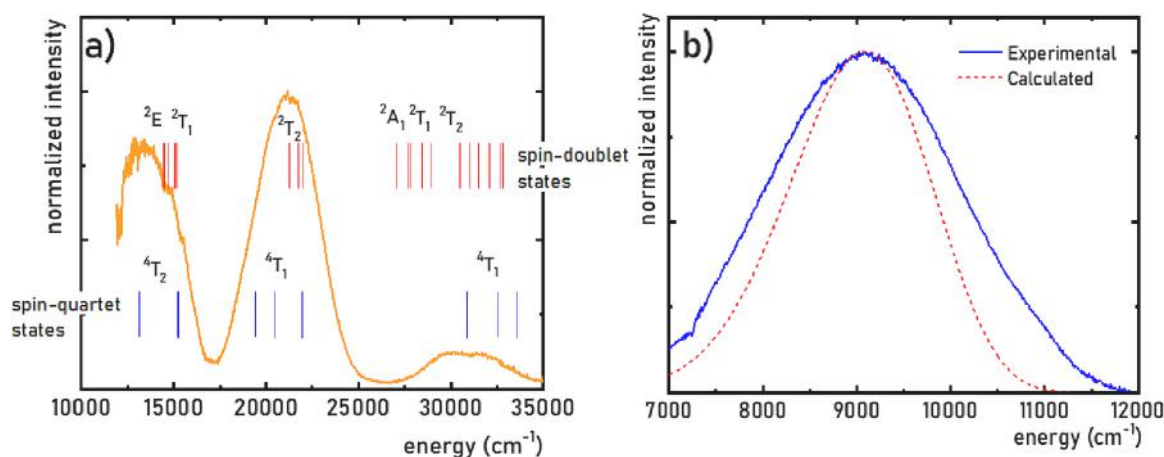


Fig. 8. Calculated energy levels of  $\text{Cr}^{3+}$  (vertical lines) in  $\text{LiScGeO}_4$  in comparison with the experimental excitation spectrum (solid line)-a); Calculated  ${}^4T_2 - {}^4A_2$  emission band energy levels of  $\text{Cr}^{3+}$  (vertical lines) in  $\text{LiScGeO}_4$  in comparison with the experimental emission spectrum (solid line)-b).

#### 4. Conclusions

In summary, this paper describes the development and spectroscopic properties of a new luminescent manometer with unprecedentedly high sensitivity in the ratiometric readout mode and the absolute sensitivity in the spectral shift mode of  $d\lambda/dp = 23.63 \text{ nm/GPa}$ , which is the highest shift rate reported elsewhere.  $\text{Cr}^{3+}$  ions incorporated in the  $\text{LiScGeO}_4$  crystal structure are characterized by broadband emission associated with the  ${}^4T_2 \rightarrow {}^4A_2$  electron transition. Increasing pressure, this emission band, initially centered at about 1100 nm, undergoes a linear spectral blue-shift by  $\approx 170 \text{ nm}$  in the 0–7 GPa range. Therefore, the developed ratiometric luminescent manometer based on this emission is characterized by a record relative sensitivity of  $S_R = 121.14 \text{ \% /GPa}$ . In addition, as demonstrated by the appropriate selection of the integrated spectral ranges considered in the LIR calculations, it is possible to develop a ratiometric manometer with super-sensitivity either in low or high-pressure range, or a wide-range sensor with sensitivity exceeding 50%/GPa. Beneficially, the spectral shift of the band and the derived LIR parameters have low sensitivity to temperature changes, indicating the possibility of using the developed sensor for the experiments under extreme conditions (simultaneous compression and heating/cooling of the material studied). Importantly, the

developed sensor material  $\text{LiScGeO}_4:\text{Cr}^{3+}$  exhibits record sensitivity in both ratiometric and spectral shift based approaches. The ability to tune the manometric properties of the luminescent manometer together with unprecedented high relative sensitivity and a TIMF parameter exceeding 240 make  $\text{LiScGeO}_4:\text{Cr}^{3+}$  an excellent candidate for remote, super-sensitive optical pressure readouts and multi-dimensional imaging. Importantly, the developed sensor works in the NIR range of the spectrum, which is available for monitoring both by the silicon and InGaAs detectors, ensuring no overlapping with emission of the luminescent materials studied. Thanks to the NIR operating range of the sensor, it provides great penetrability of light in the systems/surroundings which are opaque, i.e., highly absorbing in the visible but are transparent in the NIR region. Crystal field calculations of the  $\text{Cr}^{3+}$  energy levels and analysis of the electron-vibrational interaction were also performed to gain a deeper insight into the influence of crystal structure and local symmetry on the optical properties of the studied material.

#### Declaration of Competing Interest

The authors declare that they have no known competing financial interests or personal relationships that could have appeared to influence the work reported in this paper.

## Data availability

Data will be made available on request.

## Acknowledgements

This work was supported by the National Science Center (NCN) Poland under project no. DEC-UMO- 2020/37/B/ST5/00164. M.R. acknowledges support from Fondo Social Europeo and Agencia Estatal de Investigación (RYC2020-028778-I/AEI/10.13039/501100011033). M. G.B. appreciates support from the Program for the Foreign Experts (Grant No. W2017011) offered by Chongqing University of Posts and Telecommunications, the National Foreign Experts Program for “Belt and Road Initiative” Innovative Talent Exchange (Grant No. DL2021035001L), and NCN project 2018/31/B/ST4/00924.

## Appendix A. Supplementary data

Supplementary data to this article can be found online at <https://doi.org/10.1016/j.cej.2023.143130>.

## References

- [1] X. Liu, A. Skripka, Y. Lai, C. Jiang, J. Liu, F. Vetrone, J. Liang, Fast wide-field upconversion luminescence lifetime thermometry enabled by single-shot compressed ultrahigh-speed imaging, *Nat. Commun.* 12 (2021) 6401.
- [2] R. An, Y. Liang, R. Deng, P. Lei, H. Zhang, Hollow nanoparticles synthesized via Ostwald ripening and their upconversion luminescence-mediated Boltzmann thermometry over a wide temperature range, *Light Sci. Appl.* 11 (2022) 217.
- [3] E. Ximendes, R. Marin, L.D. Carlos, D. Jaque, Less is more: dimensionality reduction as a general strategy for more precise luminescence thermometry, *Light Sci. Appl.* 11 (2022) 237.
- [4] Z. Hu, B.J. Deibert, J. Li, Luminescent metal-organic frameworks for chemical sensing and explosive detection, *Chem. Soc. Rev.* 43 (16) (2014) 5815–5840.
- [5] S.V. Eliseeva, J.-C. Bünzli, Lanthanide luminescence for functional materials and bio-sciences, *Chem. Soc. Rev.* 39 (1) (2010) 189–227.
- [6] Y. Yang, Q. Zhao, W. Feng, F. Li, Luminescent Chemodosimeters for Bioimaging, *Chem. Rev.* 113 (1) (2013) 192–270.
- [7] J. Rocha, L.D. Carlos, F.A.A. Paz, D. Ananias, Luminescent multifunctional lanthanides-based metal-organic frameworks, *Chem. Soc. Rev.* 40 (2) (2011) 926–940.
- [8] M.D. Dramićanin, L. Marciniak, S. Kuzman, W. Piotrowski, Z. Ristić, J. Periša, I. Evans, J. Mitrić, V. Đorđević, N. Romčević, M.G. Brik, C.G. Ma, Mn<sup>5+</sup>-activated Ca<sub>6</sub>Ba(PO<sub>4</sub>)<sub>4</sub>O near-infrared phosphor and its application in luminescence thermometry, *Light Sci. Appl.* 11 (2022) 279.
- [9] C. Hoera, A. Kiontke, M. Pahl, D. Belder, A chip-integrated optical microfluidic pressure sensor, *Sensors Actuators B Chem.* 255 (2018) 2407–2415.
- [10] O.S. Wolfbeis, Fiber-Optic Chemical Sensors and Biosensors, *Anal. Chem.* 78 (12) (2006) 3859–3874.
- [11] M.D. Dramićanin, Trends in luminescence thermometry, *J. Appl. Phys.* 128 (2020) 40902.
- [12] K. Kniec, L. Marciniak, A ratiometric luminescence pH sensor based on YAG:V<sup>3+</sup>, v<sup>s</sup> + nanoparticles, *New J. Chem.* 46 (2022) 11562–11569.
- [13] L. Marciniak, K. Kniec, K. Elżbieciak-Piecka, K. Trejgis, J. Stefanska, M. Dramićanin, Luminescence thermometry with transition metal ions. A review, *Coord. Chem. Rev.* 469 (2022), 214671.
- [14] O.S. Wolfbeis, Optical Technology until the Year 2000: An Historical Overview BT - Optical Sensors: Industrial Environmental and Diagnostic Applications, in: R. Narayanaswamy, O.S. Wolfbeis (Eds.), Springer, Berlin Heidelberg, Berlin, Heidelberg, 2004, pp. 1–34.
- [15] D. Parker, Luminescent lanthanide sensors for pH, pO<sub>2</sub> and selected anions, *Coord. Chem. Rev.* 205 (2000) 109–130.
- [16] X. Jia, J. Li, E. Wang, One-pot green synthesis of optically pH-sensitive carbon dots with upconversion luminescence, *Nanoscale.* 4 (2012) 5572–5575.
- [17] X.D. Wang, O.S. Wolfbeis, R.J. Meier, Luminescent probes and sensors for temperature, *Chem. Soc. Rev.* 42 (2013) 7834–7869.
- [18] X. Wang, Q. Liu, Y. Bu, C.-S. Liu, T. Liu, X. Yan, Optical temperature sensing of rare-earth ion doped phosphors, *RSC Adv.* 5 (105) (2015) 86219–86236.
- [19] L.H. Fischer, G.S. Harms, O.S. Wolfbeis, Upconverting nanoparticles for nanoscale thermometry, *Angew. Chemie - Int. Ed.* 50 (20) (2011) 4546–4551.
- [20] Q. Wang, M. Liao, Q. Lin, M. Xiong, Z. Mu, F. Wu, A review on fluorescence intensity ratio thermometer based on rare-earth and transition metal ions doped inorganic luminescent materials, *J. Alloys Compd.* 850 (2021), 156744.
- [21] D. Jaque, F. Vetrone, Luminescence nanothermometry, *Nanoscale.* 4 (2012) 4301–4326.
- [22] C.D.S. Brites, S. Balabhadra, L.D. Carlos, Lanthanide-Based Thermometers: At the Cutting-Edge of Luminescence Thermometry, *Adv. Opt. Mater.* 7 (2019) 1801239.
- [23] B.R. Jovanić, J.P. Andreetta, GdAlO<sub>3</sub>:Cr<sup>3+</sup> as a New Pressure Sensor, *Phys. Scr.* 59 (1999) 274–276.
- [24] M. Runowski, A. Shyichuk, A. Tyminiński, T. Grzyb, V. Lavín, S. Lis, Multifunctional Optical Sensors for Nanomanometry and Nanothermometry: High-Pressure and High-Temperature Upconversion Luminescence of Lanthanide-Doped Phosphates - LaPO<sub>4</sub>/YPO<sub>4</sub>:Yb<sup>3+</sup>-Tm<sup>3+</sup>, *ACS Appl. Mater. Interfaces.* 10 (2018) 17269–17279.
- [25] H.K. Mao, J. Xu, P.M. Bell, Calibration of the ruby pressure gauge to 800 kbar under quasi-hydrostatic conditions, *J. Geophys. Res.* 91 (1986) 4673.
- [26] M. Back, J. Ueda, H. Hua, S. Tanabe, Predicting the Optical Pressure Sensitivity of <sup>2</sup>E → <sup>4</sup>A<sub>2</sub> Spin-Flip Transition in Cr<sup>3+</sup>-Doped Crystals, *Chem. Mater.* 33 (9) (2021) 3379–3385.
- [27] U.R. Rodríguez-Mendoza, S.F. León-Luis, J.E. Muñoz-Santiuste, D. Jaque, V. Lavín, Nd<sup>3+</sup>-doped Ca<sub>3</sub>Ga<sub>2</sub>Ge<sub>3</sub>O<sub>12</sub> garnet: A new optical pressure sensor, *J. Appl. Phys.* 113 (2013), 213517.
- [28] J. Barzowska, T. Lesniewski, S. Mahlik, H.J. Seo, M. Grinberg, KMgF<sub>3</sub>:Eu<sup>2+</sup> as a new fluorescence-based pressure sensor for diamond anvil cell experiments, *Opt. Mater. (Amst)* 84 (2018) 99–102.
- [29] F. Datchi, R. LeToullec, P. Loubeyre, Improved calibration of the SrB<sub>4</sub>O<sub>7</sub>:Sm<sup>2+</sup> optical pressure gauge: Advantages at very high pressures and high temperatures, *J. Appl. Phys.* 81 (1997) 3333–3339.
- [30] N.J. Hess, G.J. Exarhos, Temperature and Pressure Dependence of Laser Induced Fluorescence in Sm: Yag “A New Pressure Calibrant, *High Press. Res.* 2 (1) (1989) 57–64.
- [31] C. Hernandez, S.K. Gupta, J.P. Zuniga, J. Vidal, R. Galvan, M. Martinez, H. Guzman, L. Chavez, Y. Mao, K. Lozano, Performance evaluation of Ce<sup>3+</sup> doped flexible PVDF fibers for efficient optical pressure sensors, *Sensors Actuators, A Phys.* 298 (2019), 111595.
- [32] H. Arashi, M. Ishigame, Diamond Anvil Pressure Cell and Pressure Sensor for High-Temperature Use, *Jpn. J. Appl. Phys.* 21 (1982) 1647.
- [33] M. Runowski, P. Woźny, I.R. Martín, Optical pressure sensing in vacuum and high-pressure ranges using lanthanide-based luminescent thermometer-manometer, *J. Mater. Chem. C* 9 (13) (2021) 4643–4651.
- [34] M. Runowski, J. Marciniak, T. Grzyb, D. Przybylska, A. Shyichuk, B. Barszcz, A. Katusiak, S. Lis, Lifetime nanomanometry-high-pressure luminescence of up-converting lanthanide nanocrystals-SrF<sub>2</sub>:Yb<sup>3+</sup>, Er<sup>3+</sup>, *Nanoscale.* 9 (41) (2017) 16030–16037.
- [35] M. Runowski, P. Woźny, N. Stopikowska, Q. Guo, S. Lis, Optical Pressure Sensor Based on the Emission and Excitation Band Width (fwhm) and Luminescence Shift of Ce<sup>3+</sup>-Doped Fluorapatite - High-Pressure Sensing, *ACS Appl. Mater. Interfaces.* 11 (4) (2019) 4131–4138.
- [36] S.F. León-Luis, J.E. Muñoz-Santiuste, V. Lavín, U.R. Rodríguez-Mendoza, Optical pressure and temperature sensor based on the luminescence properties of Nd<sup>3+</sup> ion in a gadolinium scandium gallium garnet crystal, *Opt. Express.* 20 (2012) 10393–10398.
- [37] H.K. Mao, P.M. Bell, J.W. Shaner, D.J. Steinberg, Specific volume measurements of Cu, Mo, Pd, and Ag and calibration of the ruby R1 fluorescence pressure gauge from 0.06 to 1 Mbar, *J. Appl. Phys.* 49 (6) (1978) 3276–3283.
- [38] Q. Lv, C. Wang, S. Chen, H. Zheng, E. Dong, G. Zhu, Ultrasensitive Pressure-Induced Optical Materials: Europium-Doped Hafnium Silicates with a Khibinskite Structure for Optical Pressure Sensors and WLEDs, *Inorg. Chem.* 61 (2022) 3212–3222.
- [39] D. Zhang, B. Zheng, Z. Zheng, L. Li, Q. Yang, Y. Song, B. Zou, H. Zou, Multifunctional Ca<sub>9</sub>NaZn<sub>1-y</sub>Mg<sub>y</sub>(PO<sub>4</sub>)<sub>7</sub>:Eu<sup>2+</sup> phosphor for full-spectrum lighting, optical thermometry and pressure sensor applications, *Chem. Eng. J.* 431 (2022), 133805.
- [40] B. Zheng, X. Zhang, D. Zhang, F. Wang, Z. Zheng, X. Yang, Q. Yang, Y. Song, B. Zou, H. Zou, Ultra-wideband phosphor Mg<sub>2</sub>Gd<sub>8</sub>(SiO<sub>4</sub>)<sub>6</sub>O<sub>2</sub>:Ce<sup>3+</sup>, Mn<sup>2+</sup>: Energy transfer and pressure-driven color tuning for potential applications in LEDs and pressure sensors, *Chem. Eng. J.* 427 (2022), 131897.
- [41] T. Zheng, M. Sójka, M. Runowski, P. Woźny, S. Lis, E. Zych, Tm<sup>2+</sup> Activated SrB<sub>4</sub>O<sub>7</sub> Bifunctional Sensor of Temperature and Pressure—Highly Sensitive, Multi-Parameter Luminescence Thermometry and Manometry, *Adv. Opt. Mater.* 9 (2021) 2101507.
- [42] T. Zheng, M. Sójka, P. Woźny, I.R. Martín, V. Lavín, E. Zych, S. Lis, P. Du, L. Luo, M. Runowski, Supersensitive Ratiometric Thermometry and Manometry Based on Dual-Emitting Centers in Eu<sup>2+</sup>/Sm<sup>2+</sup>-Doped Strontium Tetraborate Phosphors, *Adv. Opt. Mater.* 10 (2022) 2201055.
- [43] M.A. Antoniak, S.J. Zelewski, R. Oliva, A. Żak, R. Kudrawiec, M. Nyk, Combined Temperature and Pressure Sensing Using Luminescent NaBiF<sub>4</sub>:Yb, Er Nanoparticles, *ACS Appl. Nano Mater.* 3 (5) (2020) 4209–4217.
- [44] M. Sójka, M. Runowski, P. Woźny, L.D. Carlos, E. Zych, S. Lis, Y<sub>2</sub>(Ge, Si)<sub>5</sub>O<sub>5</sub>: Pr phosphors: multimodal temperature and pressure sensors shaped by bandgap management, *J. Mater. Chem. C* 9 (2021) 13818–13831.
- [45] G. Shen, Y. Wang, A. Dewaele, C. Wu, D.E. Fratanduno, J. Eggert, S. Klotz, K.F. Dziubek, P. Loubeyre, O. V. Fat'yanov, P.D. Asimow, T. Mashimo, R.M.M. Wentzcovitch, Toward an international practical pressure scale: A proposal for an IPPS ruby gauge (IPPS-Ruby2020), *High Press. Res.* (2020) 299–314.
- [46] M. Szymczak, M. Runowski, V. Lavín, L. Marciniak, Highly pressure-sensitive, temperature independent luminescence ratiometric manometer based on MgO:Cr<sup>3+</sup> nanoparticles, *Laser Photonics Rev.* 17 (4) (2023).
- [47] M. Szymczak, P. Woźny, M. Runowski, M. Pieprz, V. Lavín, L. Marciniak, Temperature invariant ratiometric luminescence manometer based on Cr<sup>3+</sup> ions emission, *Chem. Eng. J.* 453 (2023), 139632.
- [48] Y. Masubuchi, S. Nishitani, S. Miyazaki, H. Hua, J. Ueda, M. Higuchi, S. Tanabe, Large red-shift of luminescence from BaCn<sub>2</sub>:Eu<sup>2+</sup> red phosphor under high pressure, *Appl. Phys. Express.* 13 (2020) 42009.
- [49] T. Zheng, L. Luo, P. Du, S. Lis, U.R. Rodríguez-Mendoza, V. Lavín, I.R. Martín, M. Runowski, Pressure-triggered enormous redshift and enhanced emission in

- $\text{Ca}_2\text{Gd}_3\text{Si}_6\text{O}_{26}:\text{Ce}^{3+}$  phosphors: Ultrasensitive, thermally-stable and ultrafast response pressure monitoring, *Chem. Eng. J.* 443 (2022), 136414.
- [50] T. Kobayashi, T. Sekine, K. Takemura, T. Dykhne, Emission Spectroscopy of Eu-Doped  $\text{CaF}_2$  under Static and Dynamic High Pressures, *Jpn. J. Appl. Phys.* 46 (2007) 6696.
- [51] T. Wu, H. Hua, J. Ueda, S. Tanabe, S. Matsuishi, Pressure-dependent photoluminescence of Eu-activated aluminate hydride  $\text{Sr}_{3-x}\text{AlO}_4\text{H}:\text{Eu}^{2+}$  ( $A = \text{Ca}, \text{Ba}; x = 0, 1$ ): Application of advanced U-determination technique for luminescence wavelength prediction, *J. Appl. Phys.* 132 (2022) 83104.
- [52] Y. Wang, T. Seto, K. Ishigaki, Y. Uwatoko, G. Xiao, B. Zou, G. Li, Z. Tang, Z. Li, Y. Wang, Pressure-Driven  $\text{Eu}^{2+}$ -Doped  $\text{BaLi}_2\text{Al}_2\text{Si}_2\text{N}_6$ : A New Color Tunable Narrow-Band Emission Phosphor for Spectroscopy and Pressure Sensor Applications, *Adv. Funct. Mater.* 30 (2020) 2001384.
- [53] A. Baran, S. Mahlik, M. Grinberg, E. Zych, High pressure and time-resolved luminescence spectra of  $\text{Ca}_3\text{Y}_2(\text{SiO}_4)_3$  doped with  $\text{Eu}^{2+}$  and  $\text{Eu}^{3+}$ , *J. Phys. Condens. Matter.* 25 (2013) 25603.
- [54] W. Chen, G. Li, J.-O. Malm, Y. Huang, R. Wallenberg, H. Han, Z. Wang, J.-O. Bovin, Pressure dependence of  $\text{Mn}^{2+}$  fluorescence in  $\text{ZnS}:\text{Mn}^{2+}$  nanoparticles, *J. Lumin.* 91 (2000) 139–145.
- [55] M.D. Seltzer, Interpretation of the Emission Spectra of Trivalent Chromium-Doped Garnet Crystals Using Tanabe-Sugano Diagrams, *J. Chem. Educ.* 72 (1995) 886.
- [56] S. Miao, Y. Liang, Y. Zhang, D. Chen, X.-J. Wang, Broadband Short-Wave Infrared Light-Emitting Diodes Based on  $\text{Cr}^{3+}$ -Doped  $\text{LiScGeO}_4$  Phosphor, *ACS Appl. Mater. Interfaces.* 13 (30) (2021) 36011–36019.
- [57] Z. Ye, Z. Wang, Q. Wu, X. Huo, H. Yang, Y. Wang, D. Wang, J. Zhao, H. Suo, P. Li, A single luminescence center ultra-broadband near-infrared  $\text{LiScGeO}_4$ : Cr phosphor for biological tissue penetration, *Dalt. Trans.* 50 (2021) 10092–10101.
- [58] M.Y. Sharonov, A.B. Bykov, P. Rojas, V. Petricevic, R.R. Alfano, Spectroscopy of chromium centers in  $\text{LiScGeO}_4$  and  $\text{LiInGeO}_4$  single crystals, *Phys. Rev. B.* 72 (2005), 115111.
- [59] A.A. Galeev, N.M. Khasanova, C. Rudowicz, G.S. Shakurov, A.B. Bykov, G.R. Bulka, N.M. Nizamutdinov, V.M. Vinokurov, Multifrequency EPR study of  $\text{Cr}^{3+}$  ions in  $\text{LiScGeO}_4$ , *J. Phys. Condens. Matter.* 12 (2000) 4465.
- [60] M. Sharonov, V. Petricevic, A. Bykov, R.R. Alfano, Ultra-wideband near-infrared laser operation of  $\text{Cr}^{3+}$  centers in chromium doped  $\text{Li}(\text{In}, \text{Sc})\text{GeO}_4$  olivines, in: *Conf. Lasers Electro-Optics/Quantum Electron. Laser Sci. Photonic Appl. Syst. Technol.*, Optica Publishing Group, Baltimore, Maryland, 2005: p. CTuA1.
- [61] Z. Zhou, P. Xiong, H. Liu, M. Peng, Ultraviolet-A Persistent Luminescence of a  $\text{Bi}^{3+}$ -Activated  $\text{LiScGeO}_4$  Material, *Inorg. Chem.* 59 (17) (2020) 12920–12927.
- [62] R.D. Shannon, Revised effective ionic radii and systematic studies of interatomic distances in halides and chalcogenides, *Acta Crystallogr. Sect. A.* 32 (5) (1976) 751–767.
- [63] M. Casalbón, A. Luci, U.M. Grassano, B.V. Mill, A.A. Kaminskii, Optical spectroscopy of  $\text{La}_3\text{Ga}_5\text{SiO}_{14}:\text{Cr}^{3+}$  crystals, *Phys. Rev. B.* 49 (1994) 3781–3790.
- [64] H. Chen, T. Seto, Y. Wang, An efficient blue phosphor with high thermal stability for lighting and optical pressure sensor applications, *Inorg. Chem. Front.* 9 (8) (2022) 1644–1654.
- [65] B.Z. MALKIN, CHAPTER 2 - Crystal field and Electron-Phonon Interaction in Rare-Earth Ionic Paramagnets, in: A.A. KAPLYANSKII, R.M.B.T.-M.P. in C.M.S. MACFARLANE (Eds.), *Spectrosc. Solids Contain. Rare Earth Ions*, Elsevier, 1987: pp. 13–50.
- [66] C. Jousseau, D. Vivien, A. Kahn-Harari, B.Z. Malkin, Long-lifetime fluorescence and crystal field calculation in  $\text{Cr}^{4+}$ -doped  $\text{Li}_2\text{MSiO}_4$ ,  $M = \text{Mg}, \text{Zn}$ , *Opt. Mater. (Amst)* 24 (1-2) (2003) 143–150.
- [67] X.-K. Hu, B. Wu, Y. Yang, Y.Y. Yeung, C.-G. Ma, M.G. Brik, An old system revisited:  $\text{Al}_2\text{O}_3:\text{Ti}^{3+}$  - Microscopic crystal field effects explored by the crystal field and first-principles calculations, *J. Alloys Compd.* 847 (2020), 156459.
- [68] M.G. Brik, C.-G. Ma, *Theoretical Spectroscopy of Transition Metal and Rare Earth Ions*, 2019.
- [69] K. Momma, F. Izumi, VESTA 3 for three-dimensional visualization of crystal, volumetric and morphology data, *J. Appl. Crystallogr.* 44 (2011) 1272–1276.
- [70] B. Henderson, G.F. Imbusch, Optical spectroscopy of inorganic solids, in (1989).

## Supporting Information

### Multimodal, super-sensitive luminescent manometer based on giant pressure-induced spectral shift of Cr<sup>3+</sup> in the NIR range

**M. Szymczak<sup>1</sup>, M.Runowski<sup>2,3</sup>, M.G. Brik<sup>4,5,6,7,8</sup>, L. Marciniak<sup>1\*</sup>**

<sup>1</sup> Institute of Low Temperature and Structure Research, Polish Academy of Sciences,  
Okólna 2, 50-422 Wrocław, Poland

<sup>2</sup> Adam Mickiewicz University, Faculty of Chemistry, Uniwersytetu Poznańskiego 8,  
61-614 Poznań, Poland

<sup>3</sup> Departamento de Física, IUdEA and MALTA-Consilider Team, Universidad de La Laguna, Apartado de Correos 456, E-38200 San Cristóbal de La Laguna, Santa Cruz de Tenerife, Spain

<sup>4</sup> College of Sciences & CQUPT-BUL Innovation Institute, Chongqing University of Posts and Telecommunications, Chongqing 400065, People's Republic of China

<sup>5</sup> Institute of Physics, University of Tartu, W. Ostwald Str. 1, Tartu 50411, Estonia

<sup>6</sup> Centre of Excellence for Photoconversion, Vinča Institute of Nuclear Sciences - National Institute of the Republic of Serbia, University of Belgrade, Belgrade, Serbia

<sup>7</sup> Faculty of Science and Technology, Jan Długosz University, 42200 Częstochowa, Poland

<sup>8</sup> Academy of Romanian Scientists, 050044 Bucharest, Romania

\* corresponding author: [l.marciniak@intibs.pl](mailto:l.marciniak@intibs.pl)

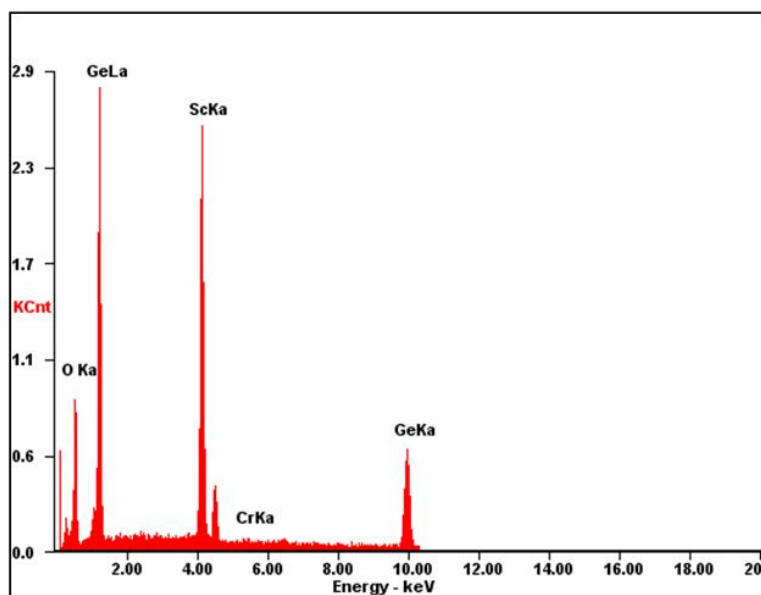


**Figure S1.** EDS analysis of the LSGO:2%Cr<sup>3+</sup>.

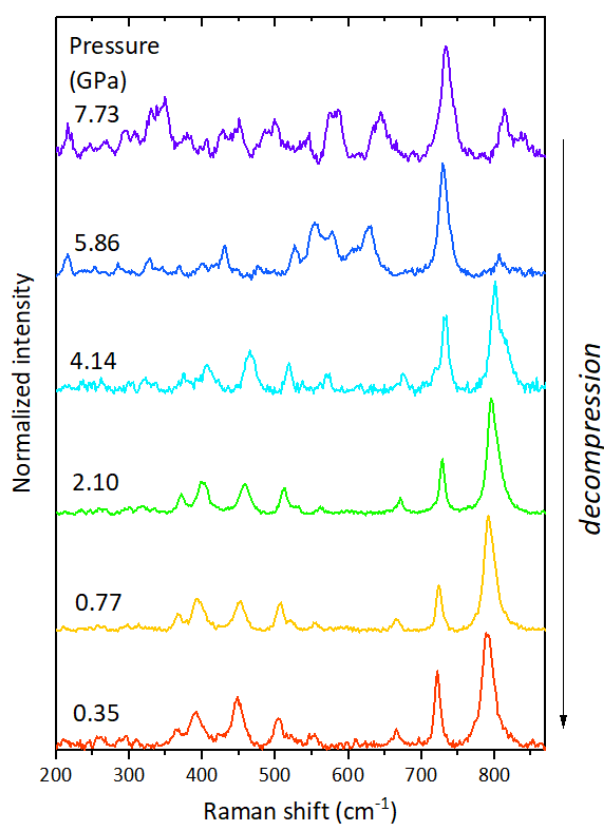


**Figure S2.** Normalized Raman spectra for the LSGO material measured for different pressure values, during the decompression cycle.



**Table S1.** Approximated energies (peak centroids) of the main Raman modes at ambient pressure, and the corresponding pressure shift rates of the corresponding bands.

Peak centroid at ambient pressure ( $\text{cm}^{-1}$ )	Shift rate ( $\text{cm}^{-1}/\text{GPa}$ )
$\approx 350$	$4.42 \pm 0.61$
$\approx 400$	$4.86 \pm 0.17$
$\approx 450$	$4.82 \pm 0.08$
$\approx 500$	$4.19 \pm 0.1$
$\approx 570$	$4.44 \pm 0.15$
$\approx 640$	$4.35 \pm 1.3$
$\approx 660$	$2.91 \pm 0.07$
$\approx 720$	$2.97 \pm 0.11$
$\approx 790$	$3.51 \pm 0.08$
$\approx 820$	$5.49 \pm 0.35$

LSGO: $x\text{Cr}^{3+}$ ,  $x =$  ● 0.1 ● 0.2 ● 0.5 ● 1 ● 2

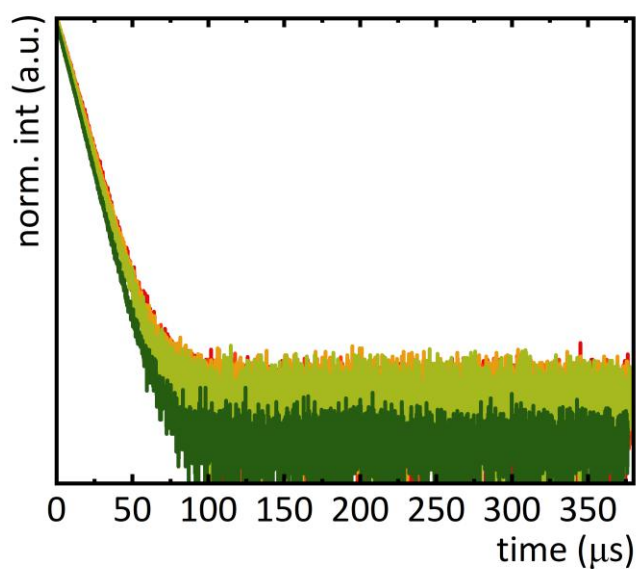


**Figure S3.** Room temperature luminescence decay profiles of LSGO:0.1-2% $\text{Cr}^{3+}$  measured upon  $\lambda_{\text{exc}} = 445 \text{ nm}$ .

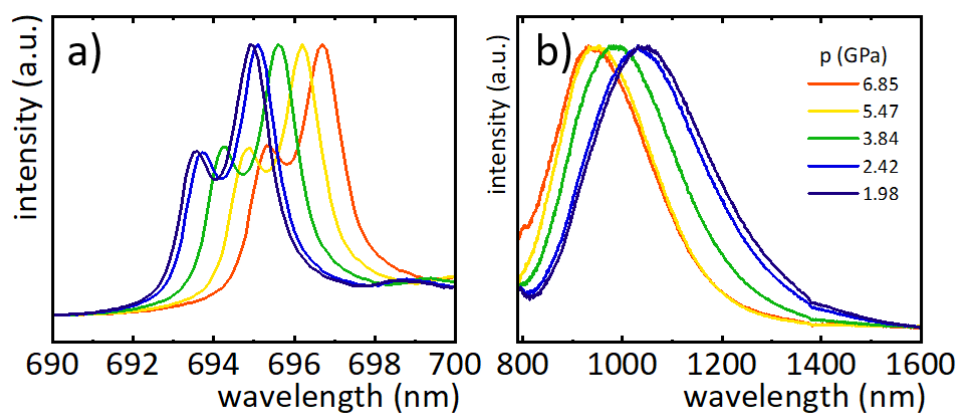


**Figure S4.** Emission spectra of pressure indicator  $\text{Al}_2\text{O}_3:\text{Cr}^{3+}$  (a) and  $\text{LSGO}:0.5 \text{Cr}^{3+}$  (b) ( $\lambda_{\text{exc}} = 445 \text{ nm}$ ) as a function of pressure during decompression.

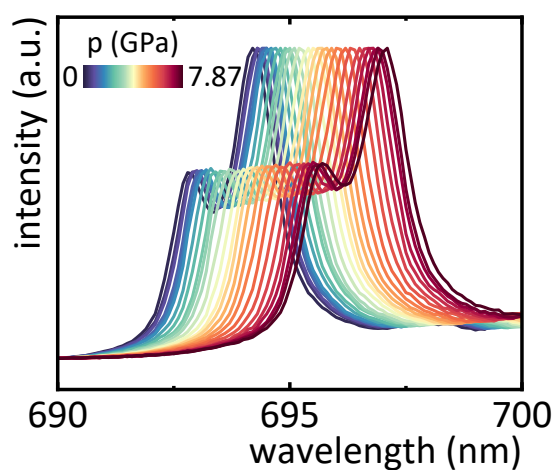


**Figure S5.** Emission spectra of pressure indicator  $\text{Al}_2\text{O}_3:\text{Cr}^{3+}$  used during pressure-dependent emission measurement of  $\text{LSGO}:\text{Cr}^{3+}$  ( $\lambda_{\text{exc}} = 445 \text{ nm}$ ).

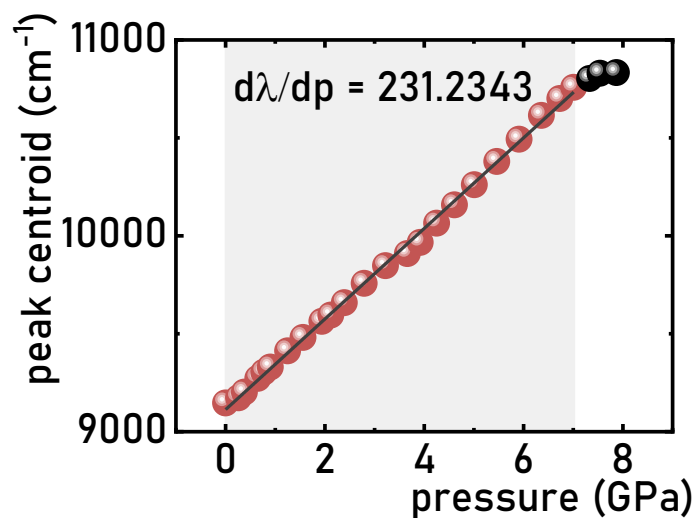


**Figure S6.** The position of the peak centroid of LSGO:2%Cr<sup>3+</sup> as a function of pressure in wavenumbers.

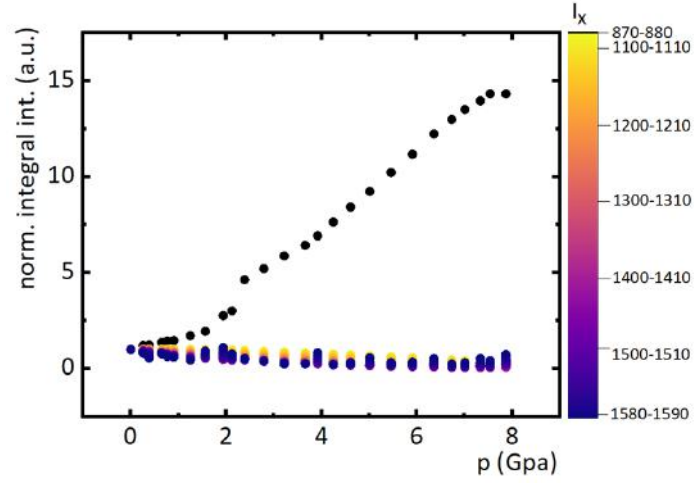


**Figure S7.** The integral intensities used to count LIR<sub>x</sub>, as a function of pressure.

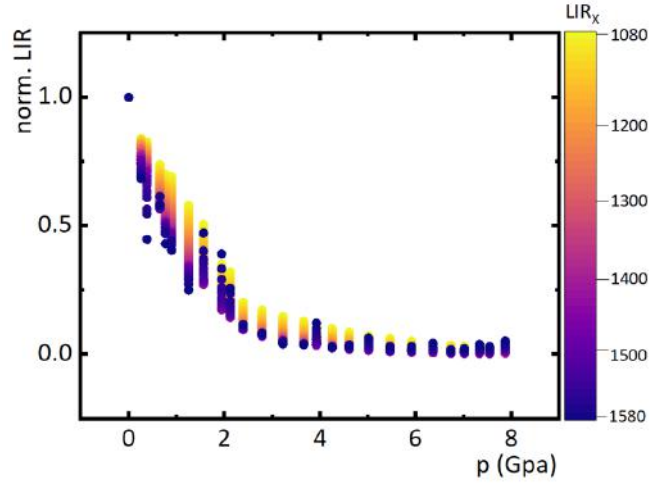


**Figure S8.** The LIR<sub>x</sub> as a function of pressure.

Pressure dependence of LIR<sub>I</sub> and LIR<sub>II</sub> can be empirically determined using the following equations:

$$LIR_I(p) = 6.11247 - 31.077p + 38.8777p^2 - 16.099p^3 + 2.80368p^4 - 0.16135p^5 \quad (S1)$$

$$LIR_{II}(p) = 5.29989 - 24.29349p + 28.38403p^2 - 11.02392p^3 + 1.79884p^4 - 0.09811p^5 \quad (S2)$$

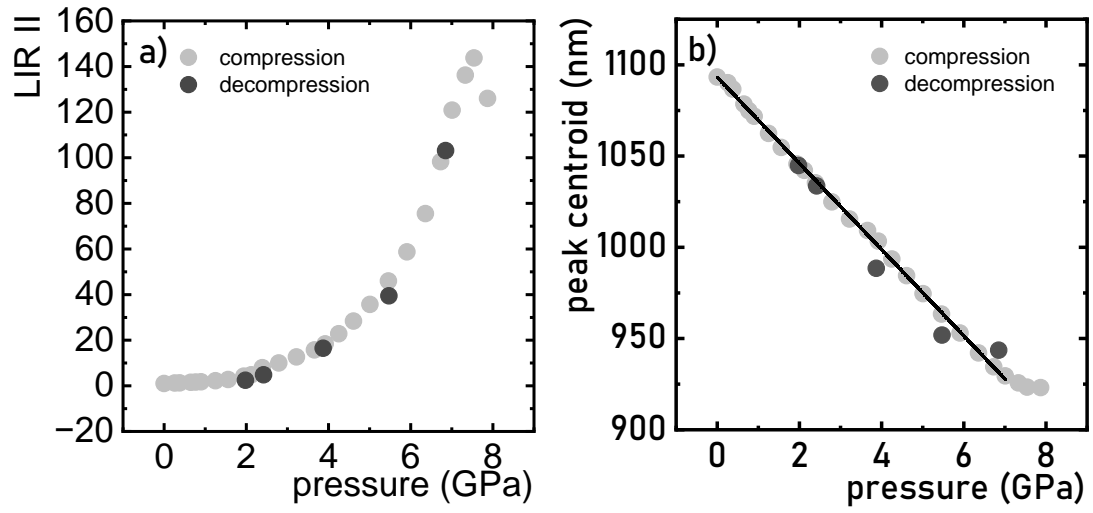


**Figure S9:** The LIR<sub>II</sub> parameter and the centroid of the  ${}^4T_2 \rightarrow {}^4A_2$  emission band as a function of pressure during compression and decompression cycle for  $\text{LiScGeO}_4:0.5\% \text{Cr}^{3+}$ .

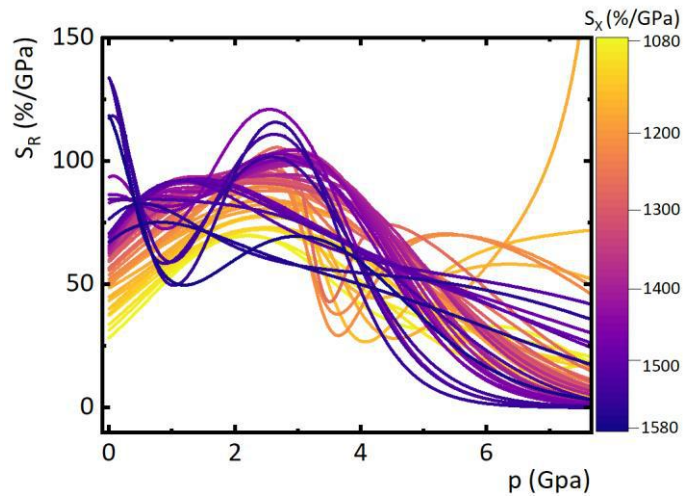


**Figure S10.** The  $S_{RX}$  as a function of pressure.

$$LIR_x = \frac{\int_{1310nm}^{(x+10)nm} {}^4T_2 \rightarrow {}^4A_2 d\lambda}{\int_{1300nm}^{1310nm} {}^4T_2 \rightarrow {}^4A_2 d\lambda}$$

X = 850, 870, 890, 920, 970, 1020, 1070, 1120, 1180, 1240, 1450, 1540

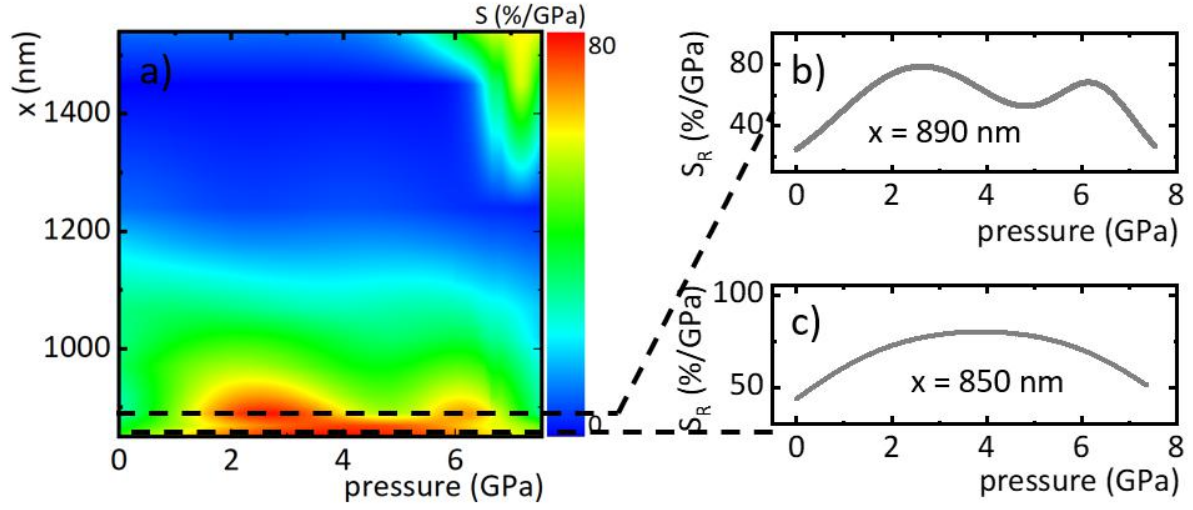


**Figure S11.** The  $S_R$  map (a) with listed two sensitivities determined from LIRx ( $x=850$  (b) and 890 (c) nm) as a function of pressure.

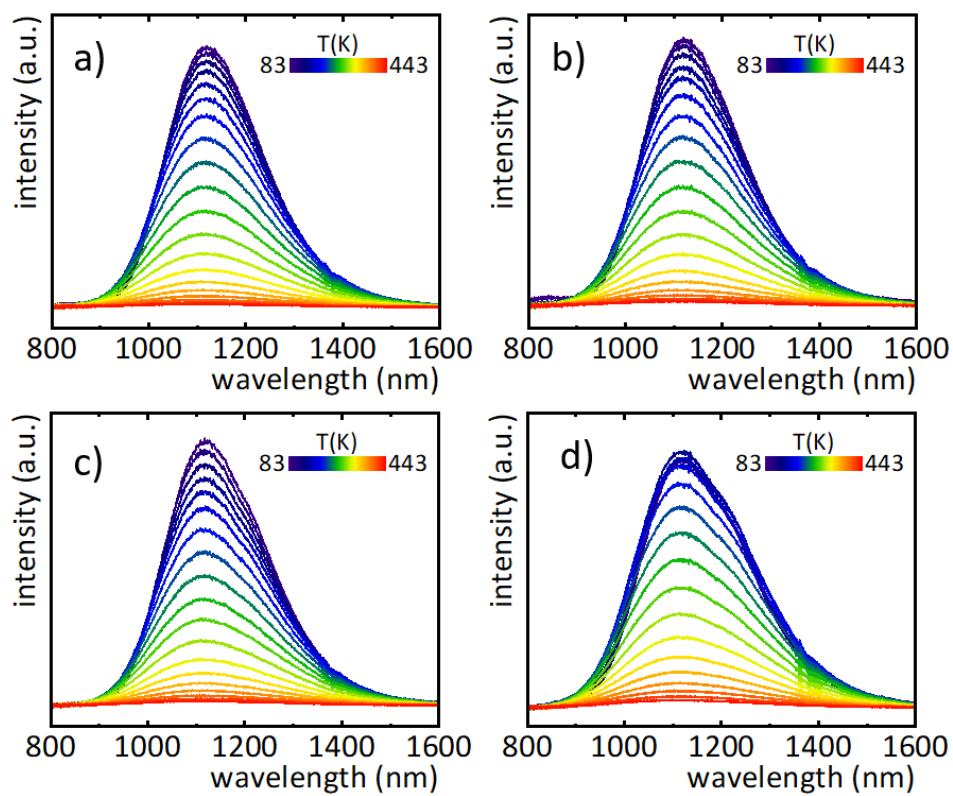


**Figure S12.** Temperature-dependent emission spectra of LSGO: $x\text{Cr}^{3+}$  powders,  $x=0.1\%\text{Cr}^{3+}$ -a),  $0.2\%\text{Cr}^{3+}$ -b);  $1\%\text{Cr}^{3+}$ -c) and  $2\%\text{Cr}^{3+}$ -d).

# Highly-Sensitive, Tri-Modal Luminescent Manometer Utilizing Band-Shift, Ratiometric and Lifetime-Based Sensing Parameters

Maja Szymczak, Julia Jaśkielewicz, Marcin Runowski, Junpeng Xue, Sebastian Mahlik, and Lukasz Marciniak\*

In addressing the broad spectrum of applications for optical pressure sensors, their predominant drawback lies in their limited sensitivity to pressure fluctuations. To overcome these constraints, this study introduces a luminescent manometer harnessing the emission properties of  $\text{Cr}^{3+}$  ions in  $\text{Li}_3\text{Sc}_2(\text{PO}_4)_3$ , operational in three distinct reading modes: spectral shift, ratiometric, and lifetime-based. Notably, the conducted research establishes this luminescent manometer as the most sensitive reported to date in both spectra shift ( $\lambda/\text{dp} = 23.9 \text{ nm/GPa}$ ) and lifetime-based ( $S_R = 93.56\%/ \text{GPa}$ ) modes. A departure from conventional lifetime-based luminescent pressure gauges,  $\text{Li}_3\text{Sc}_2(\text{PO}_4)_3:\text{Cr}^{3+}$  exhibits a prolongation of lifetime of the  $^4\text{T}_2$  state correlated with increasing pressure. The advantages extend beyond sensitivity, encompassing a three-fold surge in emission intensity with pressure escalation from ambient to 3 GPa, coupled with minimal susceptibility to temperature-induced fluctuations. Unquestionably,  $\text{Li}_3\text{Sc}_2(\text{PO}_4)_3:\text{Cr}^{3+}$  showcases remarkable manometric performance, validating its significant application potential in diverse scenarios within the realm of optical pressure sensors.

## 1. Introduction

As illustrated by the largest marine oil spill in world history – the Deepwater Horizon oil spill in 2010, an uncontrolled pressure increase can lead to catastrophic consequences. The explosion on the Deepwater Horizon platform in the Gulf of Mexico was caused by a methane leak under tremendous pressure. This accident brought devastating consequences for the environment and the economy. At the same time, it showed the importance of accurate and continuous pressure monitoring, but also demonstrated the need to implement effective pressure control methods to prevent potential disasters. Accurate pressure control holds significance across various industries. In biomedicine, ensuring a precise regulation of gas flow within respiratory systems is crucial for maintaining patient health.<sup>[1,2]</sup> Pressure variations can serve as symptomatic indicators for a

diverse range of diseases, with cardiovascular system disease and Alzheimer's disease ranking among the most severe.<sup>[3]</sup> In the food industry, meticulous pressure control is essential for facilitating an optimal packaging process, thereby ensuring the extended shelf life of products.<sup>[4]</sup> Additionally, the imperative to remotely monitor pressure in mechanical systems and gas tanks has been a driving force behind the development of pressure-sensitive paints.<sup>[5]</sup> Therefore, many scientists are focusing their attention on designing new pressure sensors that would provide the ability to control pressure in real-time, with sufficient readout precision and at a low cost of its production.<sup>[6–10]</sup> A class of sensors that meets all these requirements are luminescent pressure sensors, whose pressure readout is based on changes in spectroscopic properties of phosphors under the influence of applied pressure. Most of the luminescent manometers reported up to date exploit a change in the spectral position of the emission band,<sup>[6,9]</sup> lifetime<sup>[11,12]</sup> of excited state, and luminescence intensity ratio (LIR)<sup>[13–15]</sup> parameter. The effectiveness of the approaches mentioned above hinges on the choice of phosphor considered as the pressure sensor. The pressure sensing based on the spectral shift approach is advantageous in exploiting phosphors with a narrow emission band. It ensures high precision in pressure value determination, but it falls short in terms of

M. Szymczak, J. Jaśkielewicz, L. Marciniak  
Institute of Low Temperature and Structure Research  
Polish Academy of Sciences  
Okólna 2, Wrocław 50–422, Poland  
E-mail: [l.marciniak@intibs.pl](mailto:l.marciniak@intibs.pl)

M. Runowski  
Faculty of Chemistry  
Adam Mickiewicz University  
Uniwersytetu Poznańskiego 8  
Poznań 61-614, Poland

J. Xue  
School of Science  
Jiangsu University of Science and Technology  
Zhenjiang 212100, China  
S. Mahlik  
Institute of Experimental Physics  
Faculty of Mathematics  
Physics and Informatics  
University of Gdańsk  
Wita Stwosza 57, Gdańsk 80–308, Poland

The ORCID identification number(s) for the author(s) of this article can be found under <https://doi.org/10.1002/adfm.202314068>

DOI: 10.1002/adfm.202314068

sensitivity to pressure variations due to the limited band shift with applied pressure. On the other hand, for broadband-emitting phosphors, the sensitivity to pressure changes is significantly higher; however, the precision is limited.<sup>[16]</sup> Accordingly, achieving high sensitivity and precision in pressure sensing becomes challenging. Additionally, the pressure readout provided by the luminescence manometer should be temperature-invariant. To meet all these requirements a ratiometric approach was introduced, in which the ratio of luminescence intensities of broad  ${}^4T_2 \rightarrow {}^4A_2$  emission band of the  $Cr^{3+}$  integrated into two spectral gates is a manometric figure of merit. It has been proved that this approach ensures high sensitivity and temperature-invariant pressure readouts.<sup>[10,14,17]</sup>

On the other hand, in most the lifetime-based luminescence manometers reported up to date, the increase of the pressure results in the shortening of the lifetime of the excited state.<sup>[14]</sup> However, a similar effect corresponds to the change in temperature, which affects the reliability of pressure readout and limits its applicative potential. However, as shown recently in the case of the transition metal ions, the change in the covalency of the metal-oxygen distance affects the probability of the radiative transitions, thus causing the elongation of the lifetime of the excited state.<sup>[18–20]</sup> This was demonstrated for the  $Mn^{4+}$  based manometry but never proposed for the  $Cr^{3+}$  luminescence manometers.<sup>[11,12]</sup>

Therefore, in this work, an undeniably highly applicable multimodal luminescence manometer based on the emission of  $Cr^{3+}$  ions embedded in  $Li_3Sc_2(PO_4)_3$  host has been successfully developed. The multimodality of the proposed manometer involves a ratiometric approach, a lifetime-based approach and a spectral shift of the emission band. The selection of the  $Li_3Sc_2(PO_4)_3$  host lattice was intentional, aimed at ensuring a weak crystal field for the incorporated  $Cr^{3+}$  ions, which leads to a broad emission band associated with the  ${}^4T_2 \rightarrow {}^4A_2$  transition of  $Cr^{3+}$  ions.<sup>[21]</sup> It should be highlighted that the demonstrated pressure sensor exhibits the highest sensitivity ( $d\lambda/dp = 23.9$  nm/GPa) in the spectral shift and ( $S_R = 93.56\%/GPa$ ) in the lifetime-based modes reported so far.

## 2. Experimental Section

### 2.1. Materials

All precursors for the synthesis were used without additional purification:  $Li_2CO_3$  (Alfa Aesar, 99.998% of purity),  $Sc_2O_3$  (Alfa Aesar, 99.99% of purity),  $NH_4H_2PO_4$  (POL-AURA, 99% of purity), and  $Cr(NO_3)_3 \cdot 9H_2O$  (Alfa Aesar, min. 99.99% of purity).

### 2.2. Synthesis

The  $Li_3Sc_2(PO_4)_3$  doped with  $Cr^{3+}$  ions (0.1–10 molar %) materials in the form of micron-sized crystals were obtained using the solid-state method. All the above-mentioned reactants were thoroughly grinded in an agate mortar. In addition, hexane was used in the grounding process to obtain a highly homogeneous mixture. The resulting powders were transferred to ceramic crucibles and annealed in air at 1273 K for 6 h, with a heating rate

of 10 K min. After the annealing process, the powders were naturally cooled down and ground again in a mortar. The as-prepared samples were subjected to further analysis.

### 2.3. Methods

To assess phase purity and examine sample structure, the powder X-ray diffraction (PXRD) measurements were carried out by the use of a Panalytical X'Pert Pro diffractometer equipped with an Anton Paar TCU1000 N Temperature Control Unit, using Ni-filtered  $Cu\ K\alpha$  radiation ( $V = 40$  kV,  $I = 30$  mA). In turn, the morphology of the obtained powders and the distribution of elements (energy dispersive spectroscopy (EDS) maps) in microparticles were monitored with the help of scanning electron microscopy (SEM), which was carried out with FEI Nova NanoSEM 230 equipped with an energy dispersive spectrometer EDAX Genesis XM4. A standard procedure was used to prepare the sample for measurements – dispersing in a small amount of methanol, and then a drop of the obtained suspension was placed on the carbon stub and dried under an infrared lamp. The Raman spectra were measured under high-pressure conditions, up to  $\approx 9$  GPa, in a backscattering geometry using a Renishaw InVia confocal micro-Raman system with a power-controlled 100 mW 532 nm laser diode. The laser beam was focused using an Olympus x20 SLMPlan N long working distance objective. Raman spectra of the sample compressed in a methanol/ethanol/water – 16/3/1 (pressure transmitting medium) were measured in a diamond anvil cell (DAC) equipped with ultra-low fluorescence (IIas) diamond anvils. The excitation/emission spectra and luminescence decay profiles were recorded using FLS1000 Fluorescence Spectrometer (Edinburgh Instruments), equipped with the 450 W Xenon lamp (used only for excitation spectra) and R5509-72 photomultiplier tube from Hamamatsu in nitrogen-flow cooled housing as the detector. For measurements of the temperature- and pressure-dependent emission spectra and luminescence decay profiles, a 445 nm laser diode was used as an excitation source.

The temperature of the samples during the temperature-dependent emission and decay profile measurements was controlled by a THMS 600 heating-cooling stage from Linkam ( $0.1^\circ C$  temperature stability and  $0.1^\circ C$  set point resolution). Before each measurement, temperature stabilization was carried out for 2 min. Heating/cooling rate was established as  $20^\circ C\ min^{-1}$ . Luminescence signal was collected from the heating-cooling stage located outside the FLS 1000 spectrometer to the detection system via a bifurcated fiber bundle provided by Edinburgh instruments. The high-pressure emission spectra measurements were carried out in a gas (nitrogen) membrane driven diamond anvil cell, i.e., Diacell  $\mu Scope DAC-RT(G)$  from Almax easyLab (Figure S1, Supporting Information). The pressure was controlled and applied by a controller Druck PACE 5000. The ultra-low fluorescence IIas type diamonds, with 0.4 mm culets were used, and a stainless-steel gasket with a thickness of 250  $\mu m$  was placed between diamond anvils. In a gasket's drilled hole with a diameter of 140  $\mu m$ , the sample with pressure indicator ( $Al_2O_3:Cr^{3+}$ ) were placed. The applied pressure inside the DAC chamber was determined based on the spectral position of the R1 line of  $Cr^{3+}$  in a doped  $Al_2O_3$  (ruby) crystal. The following



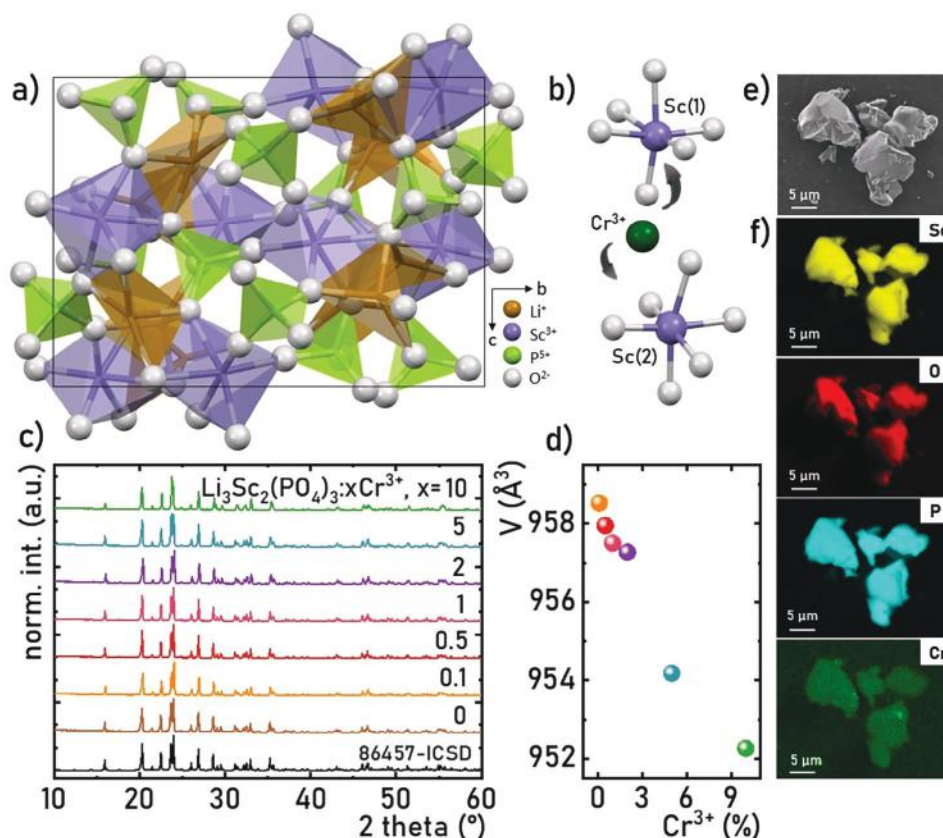


**Figure 1.** The visualization of the crystal structure of the  $\text{Li}_3\text{Sc}_2(\text{PO}_4)_3$  with marked unit cell a); the local coordination environment of two types of  $\text{Sc}^{3+}$  sites and schematically depicted incorporation of  $\text{Cr}^{3+}$  ions in  $(\text{ScO}_6)^{9-}$  octahedra b) PXRD patterns c) and unit cell volume d) for the  $\text{Li}_3\text{Sc}_2(\text{PO}_4)_3$  doped with various  $\text{Cr}^{3+}$  concentration from 0.1–10%; representative SEM image and EDS maps of Sc, P, O, and Cr elements for the  $\text{Li}_3\text{Sc}_2(\text{PO}_4)_3$ :1%  $\text{Cr}^{3+}$ .

pressure dependence of the  $R_1$  line of the  ${}^2\text{E} \rightarrow {}^4\text{A}_2$  emission band of  $\text{Al}_2\text{O}_3:\text{Cr}^{3+}$  was used as a calibration curve:

$$p[\text{GPa}] = 1.87(\pm 0.01) \cdot 10^3 \cdot \left( \frac{\Delta\lambda}{\lambda_0} \right) \cdot \left[ 1 + 5.63(\pm 0.03) \cdot \left( \frac{\Delta\lambda}{\lambda_0} \right) \right] \quad (1)$$

where  $\lambda_0 = 694.25 \text{ nm}$ .<sup>[22]</sup> A methanol–ethanol solution (V:V/4:1) was used as a pressure transmitting medium during the measurements. Pressure-dependent emission, excitation and luminescence decay time were measured within 3 cycles of compression–decompression to verify the stability of the system and reproducibility of the pressure measurements. Luminescence signal was collected from the DAC located outside the FLS 1000 spectrometer to the detection system via a bifurcated fiber bundle provided by Edinburgh instruments.

### 3. Results and Discussion

The  $\text{Li}_3\text{Sc}_2(\text{PO}_4)_3$  material can crystallize in three distinct crystal phases as a consequence of temperature-induced reversible phase transitions. The  $\alpha$ -phase, featuring a monoclinic structure, exists at temperatures below  $187^\circ\text{C}$ . The  $\beta$ -phase also has a mon-

oclinic structure but with different unit cell parameters than the  $\alpha$ -phase and emerges between  $187^\circ\text{C}$  and  $245^\circ\text{C}$ . Finally, the  $\gamma$ -phase, with an orthorhombic structure, is formed at a temperature exceeding  $245^\circ\text{C}$ .<sup>[23]</sup> This research primarily focuses on the  $\alpha$ -phase with a monoclinic structure, with a space group  $P2_1/c$  (No. 14), aligning with the subsequent research direction.

The  $\alpha$ -phase  $\text{Li}_3\text{Sc}_2(\text{PO}_4)_3$  structure consists of three types of differently coordinated inequivalent  $\text{Li}^+$  ions, three inequivalent  $\text{P}^{5+}$  ions forming  $(\text{PO}_4)^{3-}$  tetrahedra, and two types of  $(\text{ScO}_6)^{9-}$  distorted octahedrons, differentiated by bond lengths between  $\text{Sc}^{3+}$  and  $\text{O}^{2-}$  ions, as shown in Figure 1a.<sup>[21,24,25]</sup> The crystallographic positions of  $\text{Sc}^{3+}$  ions are the most significant from the perspective of the incorporation of  $\text{Cr}^{3+}$  ions into the  $\text{Li}_3\text{Sc}_2(\text{PO}_4)_3$  structure. Considering  $\text{Cr}^{3+}$  ions' preference to occupy six-fold-coordinated crystallographic positions, matching ionic charge and similar ionic radii –  $r$  (the difference of 17.45% –  $r_{\text{Cr}^{3+}} = 0.615 \text{ \AA}$  and  $r_{\text{Sc}^{3+}} = 0.745 \text{ \AA}$ )<sup>[26]</sup>, it becomes evident that the  $(\text{ScO}_6)^{9-}$  octahedrons are the preferable positions for the  $\text{Cr}^{3+}$  ion incorporation, as visually illustrated in Figure 1b. The synthesized  $\text{Li}_3\text{Sc}_2(\text{PO}_4)_3$  samples, varying in  $\text{Cr}^{3+}$  ions concentration (0–10%), were examined by PXRD to assess phase purity and the impact of dopant ions on the structural properties of the host lattice. As depicted in Figure 1c, the diffractograms reveal an absence of additional crystallographic phases beyond the

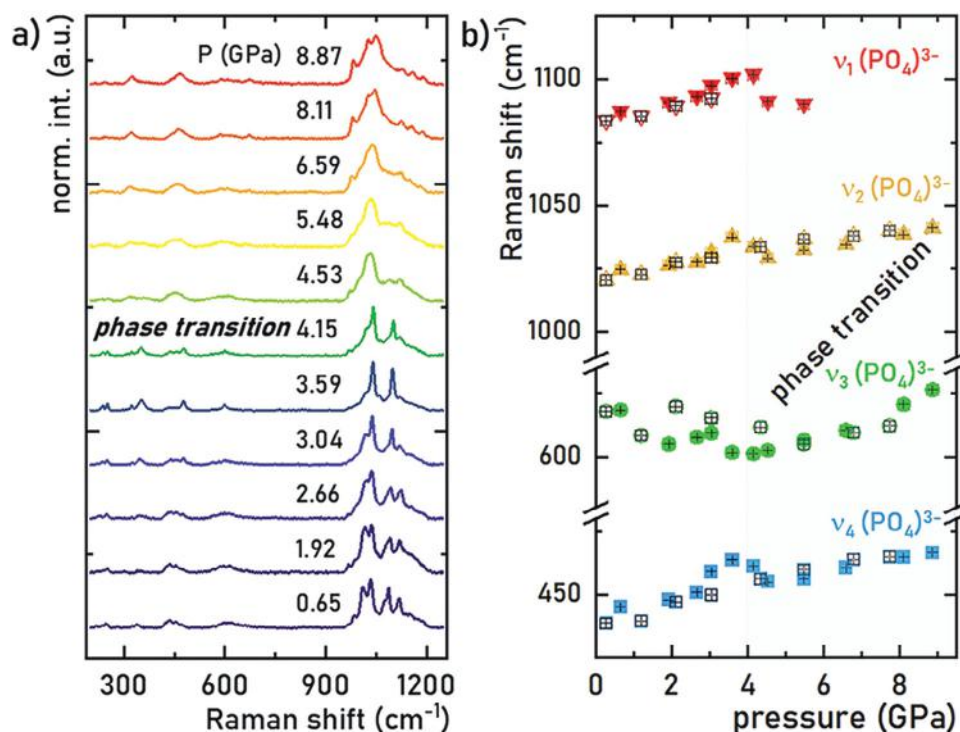


**Figure 2.** Normalized Raman spectra for the  $\text{Li}_3\text{Sc}_2(\text{PO}_4)_3$  material measured for different pressure values during the compression cycle a). Determined energies (peak centroids) of the most intense phonon modes as a function of pressure b); filled symbols represent compression data, and empty ones represent decompression data.

desired monoclinic  $\text{Li}_3\text{Sc}_2(\text{PO}_4)_3$  phase, as confirmed by comparison with reference patterns (ICSD-86457). However, for 10% of  $\text{Cr}^{3+}$ , the distortion of some XRPD reflections can be observed, which may indicate the presence of some additional peaks (see Figure S2, Supporting Information). Therefore, this sample was excluded from further spectroscopic studies.

Based on the diffractograms, a Rietveld refinement was performed to investigate the effect of  $\text{Cr}^{3+}$  incorporation on the unit cell parameters. The relationship between the unit cell volume and the  $\text{Cr}^{3+}$  content in the  $\text{Li}_3\text{Sc}_2(\text{PO}_4)_3$  host, as shown in Figure 2d, validates the earlier hypothesis that  $\text{Cr}^{3+}$  ions are replacing  $\text{Sc}^{3+}$  ions. Evidently, as the concentration of  $\text{Cr}^{3+}$  ions increases, there is a noticeable reduction in the volume of the unit cell, aligning with expectations based on the differing sizes of  $\text{Cr}^{3+}$  and  $\text{Sc}^{3+}$  ionic radii. The smaller  $\text{Cr}^{3+}$  ions increasingly occupy the  $\text{Sc}^{3+}$  ion crystallographic sites, resulting in a reduction of the unit cell volume from  $958.53 \text{ \AA}^3$  for a sample with 0.1% of  $\text{Cr}^{3+}$  to  $952.26 \text{ \AA}^3$  for  $\text{Li}_3\text{Sc}_2(\text{PO}_4)_3:10\% \text{ Cr}^{3+}$ . To investigate the morphology of the  $\text{Li}_3\text{Sc}_2(\text{PO}_4)_3:\text{Cr}^{3+}$  powders, the SEM technique was employed. Figure 2e displays a representative SEM image of the  $\text{Li}_3\text{Sc}_2(\text{PO}_4)_3:1\% \text{ Cr}^{3+}$  crystals, and additional images at various scales can be found in Figure S3 (Supporting Information). The obtained images reveal that the  $\text{Li}_3\text{Sc}_2(\text{PO}_4)_3$  materials, synthesized via the solid-state method, form aggregated microcrystals with an undefined shape. To assess the elemental distribution in the  $\text{Li}_3\text{Sc}_2(\text{PO}_4)_3:1\% \text{ Cr}^{3+}$  sample, elemental maps based on the EDS technique were determined for Sc, O, P, and Cr elements. As shown in Figure 2f, the distribution of the men-

tioned elements remains consistent throughout the surface of the crystals, indicating the uniform incorporation of  $\text{Cr}^{3+}$  ions, which is of particular significance from the perspective of luminescence studies.

To verify the mechanical stability of the analyzed system upon applied pressure, the Raman spectra of the undoped (to avoid the luminescence background from the activator ions) sample were measured. The recorded Raman spectra for the  $\text{Li}_3\text{Sc}_2(\text{PO}_4)_3$  material at initial pressure values have several Raman active modes, at  $240, 340 \text{ cm}^{-1}$  corresponding to the external (lattice) vibrations, at  $450 (\nu_4(\text{PO}_4)^{3-}), 610 \text{ cm}^{-1} (\nu_3(\text{PO}_4)^{3-})$  corresponding to the deformation vibrations and at  $1020 (\nu_2(\text{PO}_4)^{3-})$  and  $1100 \text{ cm}^{-1} (\nu_1(\text{PO}_4)^{3-})$  corresponding to the vibrations of the valency bonds of  $\text{PO}_4$  tetrahedra at (Figure 2a).<sup>[27]</sup> The most intense, broad and split band ranges from approx.  $1000$  to  $1200 \text{ cm}^{-1}$ . Together with increasing pressure values, i.e., material compression, the energies of the phonon modes increase, leading to the shift of the Raman peaks toward higher wavenumbers (higher energy values), as can be observed in Figure 2b. The observed phenomenon is related to the shortening of the average distances between the atoms, i.e., the shortening of the bonds in the compressed material. Notably, above 3 GPa, the shape of all bands starts to change clearly, and  $\approx 4.5 \text{ GPa}$  all bands are significantly altered and broadened, as shown in Figure 2a. Moreover, analyzing the plotted centroids of the most intense Raman bands, the evident bias, i.e., sudden change in the initial shift tendencies, can be noticed  $\approx 4 \text{ GPa}$ . These observations indicate the occurrence of some phase transition of the compressed material structure in the mentioned pressure range, i.e., from  $\approx 3$  to  $4.5 \text{ GPa}$ , as indicated

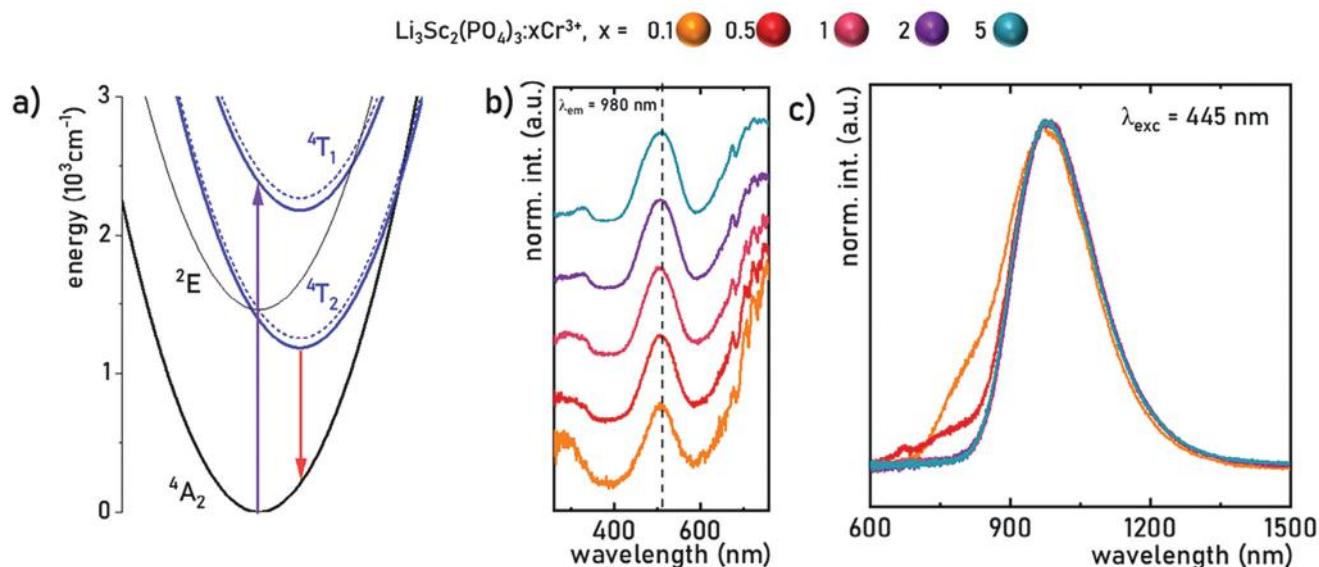


**Figure 3.** Configurational coordinate diagram of  $\text{Cr}^{3+}$  in  $\text{Li}_3\text{Sc}_2(\text{PO}_4)_3$  host. The dashed curves represent excited states at pressure 2.6 GPa a); excitation spectra ( $\lambda_{\text{em}} = 980 \text{ nm}$ ) and emission spectra ( $\lambda_{\text{exc}} = 445 \text{ nm}$ ) measured at 183 K for the  $\text{Li}_3\text{Sc}_2(\text{PO}_4)_3:\text{x}\%\text{Cr}^{3+}$ , where  $x = 0.1$ –5%.

in Figure 2a. It is worth noting that the observed phase transition is reversible, as the shape of the bands is recovered with pressure release during the decompression process, as seen in Figure S4 (Supporting Information). However, in a decompression cycle, both the spectra and determined energies of the Raman modes come back to the initial shape and positions at lower pressure values (below 2 GPa) compared to the compression run. Such hysteresis is frequently observed during high-pressure experiments performed in compression-decompression cycles, where the reversible phase transitions occur.<sup>[28]</sup>

One notable advantage of  $\text{Cr}^{3+}$  ions as luminescent dopants is their tunable luminescence adjusted by the strength of the crystal field of the host material, which is prominently illustrated in the Tanabe-Sugano diagram for  $3d^3$  electronic configuration.<sup>[29]</sup> Modulating the crystal field's strength enables it to achieve  $\text{Cr}^{3+}$  ions emission in a wide spectral range, extending from the visible range (deep-red emission) to even the NIR-II (near-infrared range; 1000–1700 nm)<sup>[30–32]</sup> Accordingly, when a strong crystal field ( $Dq/B > 2.2$ ) affects  $\text{Cr}^{3+}$  ions, it results in emission from the  $2E$  level, manifested by a narrow emission band in the deep-red spectral range. On the other hand, when the strength of the crystal field is weak ( $Dq/B < 2.2$ ), the energy of the bottom of the  $4T_2$  parabola is lower than the  $2E$  parabola (Figure 3a). This leads to the domination of the emission spectra by a broad band associated with the  $4T_2 \rightarrow 4A_2$  electronic transition of  $\text{Cr}^{3+}$  ions. The band associated with the emission from the  $4T_2$  state is particularly noteworthy in the context of developing highly sensitive luminescent pressure sensors. As evident from the Tanabe-Sugano diagram, the energy of the  $4T_2$  level is markedly affected by the strength of the crystal field  $10Dq$ , in contrast to the weakly dependent energy of the  $2E$  level.<sup>[33]</sup> Therefore, to develop a highly sensitive luminescent pressure sensor, it is crucial to exploit the emission band associated with the  $4T_2 \rightarrow 4A_2$  transition of  $\text{Cr}^{3+}$  ions.<sup>[10,14,17]</sup> The  $\text{Li}_3\text{Sc}_2(\text{PO}_4)_3:\text{Cr}^{3+}$  is an example of a phosphor, showcasing a broad emission band asso-

ciated with the  $4T_2 \rightarrow 4A_2$ .<sup>[21]</sup> In order to identify the most suitable sample for subsequent studies of spectroscopic properties under applied pressure, thereby determining the manometric characteristic of the  $\text{Li}_3\text{Sc}_2(\text{PO}_4)_3:\text{Cr}^{3+}$ , excitation and emission spectra were measured for the samples with varying concentrations of  $\text{Cr}^{3+}$  ions (0.1–5%). The spectra were measured at 183 K, as the emission intensity of  $\text{Li}_3\text{Sc}_2(\text{PO}_4)_3$  doped with the lowest concentration of  $\text{Cr}^{3+}$  ions (0.1%) was relatively weak at room temperature. The excitation spectra ( $\lambda_{\text{em}} = 980 \text{ nm}$ ) for samples doped with 0.1–5% of  $\text{Cr}^{3+}$  (Figure 3b) reveal no significant differences regarding the shape and position of the band (maximum at  $\approx 510 \text{ nm}$ ) associated with the  $4A_2 \rightarrow 4T_1$  transition of  $\text{Cr}^{3+}$  ions. Only slight band broadening was observed – full width at half maximum (FWHM) increased from  $\approx 90.5$  to  $98 \text{ nm}$  when the concentration of dopants rose from 0.1 to 5% of  $\text{Cr}^{3+}$ , respectively. On the other hand, the emission spectra ( $\lambda_{\text{exc}} = 445 \text{ nm}$ ) of the  $\text{Li}_3\text{Sc}_2(\text{PO}_4)_3:\text{Cr}^{3+}$  phosphors consist of a broad emission band associated with the  $4T_2 \rightarrow 4A_2$  transition of  $\text{Cr}^{3+}$  ions, the shape of which was independent of dopant concentration (each band's maximum remaining at  $980 \pm 5 \text{ nm}$ ). In the spectral range from  $\approx 630$  to  $850 \text{ nm}$ , artefacts stemming from the measurement setup are noticeable for  $\text{Li}_3\text{Sc}_2(\text{PO}_4)_3$  samples containing 0.1 and 0.5% of  $\text{Cr}^{3+}$  due to their relatively low emission intensity.

In a previously reported study of the  $\text{Li}_3\text{Sc}_2(\text{PO}_4)_3:\text{Cr}^{3+}$ ,<sup>[21]</sup> the incorporation of  $\text{Cr}^{3+}$  ions in two inequivalent  $\text{Sc}^{3+}$  crystallographic positions was proved. In this study, any significant variation in the shape of emission spectra of the  $\text{Li}_3\text{Sc}_2(\text{PO}_4)_3:1\%\text{Cr}^{3+}$  under different  $\lambda_{\text{exc}}$  was not observed. However, the di-exponential nature of the luminescence decays confirms this assumption (as presented in the further part of the manuscript). In this case, it should be assumed that the two  $\text{Cr}^{3+}$  centers have such a slight difference in crystal fields that the emission and excitation spectra obtained from them overlap entirely.



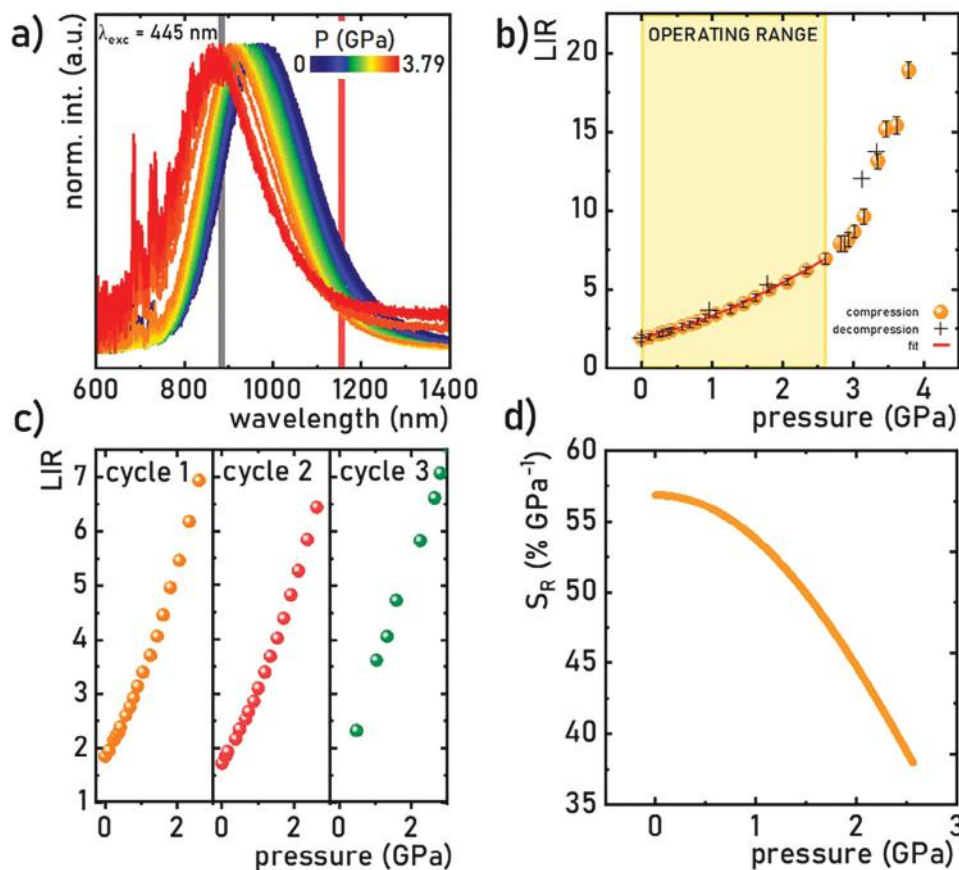


**Figure 4.** Normalized room temperature emission spectra recorded as a function of applied pressure from 0–3.79 GPa ( $\lambda_{\text{exc}} = 445 \text{ nm}$ ) for the  $\text{Li}_3\text{Sc}_2(\text{PO}_4)_3:1\% \text{Cr}^{3+}$  (spectral ranges marked in gray and red were used to calculate LIR according to the Equation 2) a); pressure-dependent LIR during compression (orange dots) and decompression (black crosses), with marked operating range of the manometer b); three compression cycles performed in operating range of pressures c);  $S_R$  as a function of pressure d) for the  $\text{Li}_3\text{Sc}_2(\text{PO}_4)_3:1\% \text{Cr}^{3+}$ .

Therefore, due to the lack of any influence of dopant concentration on spectroscopic properties of  $\text{Li}_3\text{Sc}_2(\text{PO}_4)_3:\text{Cr}^{3+}$  and weak emission intensity of 0.1% and 0.5%  $\text{Cr}^{3+}$ , the  $\text{Li}_3\text{Sc}_2(\text{PO}_4)_3:1\% \text{Cr}^{3+}$  was used for further analysis. This selection was driven by the requirement of sufficient emission intensity to conduct measurements in a DAC. Although  $\text{Li}_3\text{Sc}_2(\text{PO}_4)_3$  samples doped with a  $\text{Cr}^{3+}$  concentration higher than 1% exhibited slightly higher emission intensity, the high number of luminescence centers and the probability of nonradiative depopulation of excited states may lead to the self-heating of the  $\text{Cr}^{3+}$ -doped sample upon excitation, and consequently, in unreliable pressure-dependent spectroscopic properties.

To explore the manometric properties of the  $\text{Cr}^{3+}$ -doped  $\text{Li}_3\text{Sc}_2(\text{PO}_4)_3$  material and its potential for non-contact pressure sensing applications, the influence of applied pressure on the spectroscopic properties of the  $\text{Li}_3\text{Sc}_2(\text{PO}_4)_3:1\% \text{Cr}^{3+}$  was examined. As an initial step, pressure-dependent emission spectra, from ambient pressure to 3.79 GPa ( $\lambda_{\text{exc}} = 445 \text{ nm}$ ), were measured (before phase transition; see Figure 2). As illustrated in Figure 4a, the broad emission band associated with the  ${}^4\text{T}_{2g} \rightarrow {}^4\text{A}_{2g}$  transition of  $\text{Cr}^{3+}$  shifts toward shorter wavelengths with increasing pressure. The observed effect stems from the pressure-induced increase of the crystal field strength, attributed

to the reduction in the  $\text{Cr}^{3+}-\text{O}^{2-}$  distances  $R$  due to the applied pressure ( $10Dq \approx R^{-5}$ , where  $10Dq$  is the crystal field splitting energy). Consequently, the increase of the energy of the  ${}^4\text{T}_2$  state causes an enhancement of the energy distance between the  ${}^4\text{T}_2$  and ground  ${}^4\text{A}_2$  states, manifested by an observed pressure-induced blue shift of the emission band. This substantial spectral shift paved the way for the utilization of a ratiometric approach in developing the highly-sensitive manometer in which the luminescence intensity ratio (LIR) integrated into two spectral gates is a figure of merit. To facilitate broader applications of the  $\text{Li}_3\text{Sc}_2(\text{PO}_4)_3:\text{Cr}^{3+}$  material as an optical manometer in potential pressure imaging, the emission bands were integrated within a narrow 10 nm spectral ranges. The pressure-dependent integral intensities, obtained within the 880–1200 nm range, are presented in Figure S5 (Supporting Information). The most promising results were obtained for the following spectral ranges:

$$\text{LIR} = \frac{\int_{880\text{nm}}^{890\text{nm}} I(\text{Cr}^{3+} : {}^4\text{T}_{2g} \rightarrow {}^4\text{A}_{2g}) d\lambda}{\int_{1160\text{nm}}^{1170\text{nm}} I(\text{Cr}^{3+} : {}^4\text{T}_{2g} \rightarrow {}^4\text{A}_{2g}) d\lambda} \quad (2)$$

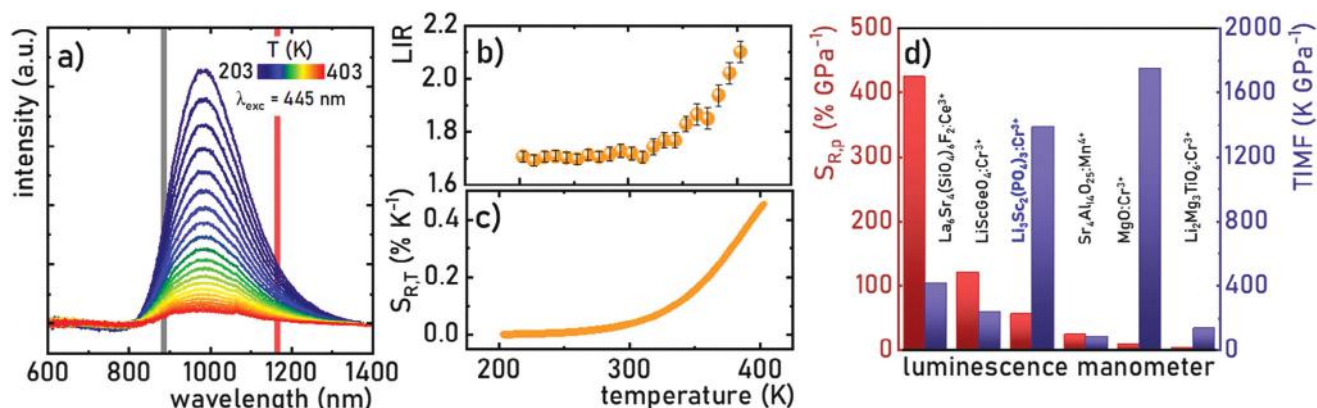


**Figure 5.** Temperature-dependent emission spectra ( $\lambda_{\text{exc}} = 445$  nm) a), thermal evolution of  $LIR$  b), and corresponding  $S_{R,T}$  c) in T-range from 203 to 403 K for the  $\text{Li}_3\text{Sc}_2(\text{PO}_4)_3:1\%\text{Cr}^{3+}$ ; comparison of  $TIMF$  and  $S_{R,p}$  for selected ratiometric luminescent manometers d).<sup>[11,17,39,40]</sup>

The evolution of the  $LIR$  as a function of pressure is illustrated in Figure 4b, where orange dots represent the results obtained during compression, while crosses denote data from the decompression cycle. As pressure rises to  $\approx 2.6$  GPa, a monotonic seven-fold increase in  $LIR$  is evident. Beyond applied pressure equal to 2.6 GPa, there is a distinct and sharp increase in  $LIR$ , which may be attributed to a reorganization of the structure preceding the pressure-induced phase transition, which was suggested by the analysis of Raman spectra as a function of pressure (Figure 2), and discussed above. Therefore, to prevent unreliable pressure readouts linked to the possible hysteresis of the  $LIR$  values during<sup>[34]</sup> compression and decompression of the material, as a result of the phase transition, the operating range of the  $\text{Li}_3\text{Sc}_2(\text{PO}_4)_3:\text{Cr}^{3+}$  manometer was established from ambient pressure to 2.6 GPa, as schematically indicated in Figure 4b. Furthermore, within this pressure range, the acquired  $LIR$  values exhibit excellent repeatability, as demonstrated during the decompression cycle (Figure 4b, black crosses) and over the three cycles of pressure-dependent emission spectra measurements (Figure 4c; pressure-dependent emission spectra are on Figures S6 and S7, Supporting Information). As a result, the  $\text{Li}_3\text{Sc}_2(\text{PO}_4)_3:\text{Cr}^{3+}$  sensor offers reliable pressure readouts, which holds significant relevance in terms of gauge design.

To determine the relative sensitivity ( $S_R$ ) of this ratiometric luminescence manometer the following equation was used:

$$S_R = \frac{1}{LIR} \frac{\Delta LIR}{\Delta p} 100\% \quad (3)$$

where  $\Delta LIR$  is the change of the  $LIR$ , which corresponds to the pressure change by  $\Delta p$ . The  $S_R$  obtained for the  $\text{Li}_3\text{Sc}_2(\text{PO}_4)_3:\text{Cr}^{3+}$  manometer reached  $56.86\% \text{ GPa}^{-1}$  at  $0.02 \text{ GPa}$  and monotonically decreases with the compression process. It is also important to mention that in the whole operating pressure range the developed  $\text{Li}_3\text{Sc}_2(\text{PO}_4)_3:\text{Cr}^{3+}$  manometer ensures highly sensitive pressure readouts, as the lowest sensitivity achieved was  $38\% \text{ GPa}^{-1}$  at  $2.61 \text{ GPa}$ . Up to date, only few ratiometric luminescence manometers operating in this mode have been reported so far, but  $\text{Li}_3\text{Sc}_2(\text{PO}_4)_3$  is one of the most sensitive to pressure variations.<sup>[11,12,35–37]</sup>

Apart from the manometer's response to variations in pressure, it is equally crucial to investigate the impact of temperature on the spectroscopic properties of the proposed manometer. Temperature, beyond pressure, also strongly influences the luminescence characteristic of phosphors. Therefore, to assess the influence of temperature on the pressure-dependent measurements and thus ensure the reliability of pressure readouts, emission spectra of the  $\text{Li}_3\text{Sc}_2(\text{PO}_4)_3:\text{Cr}^{3+}$  1% were recorded over a temperature range from 203 to 403 K (Figure 5a). Below 183 K change in the shape of the emission spectra and the results of the DSC analysis indicate the structural phase transition, which is not the subject of this work. Therefore, spectroscopic properties of the  $\text{Li}_3\text{Sc}_2(\text{PO}_4)_3:\text{Cr}^{3+}$  material were analyzed at higher temperature values. The recorded emission spectra reveal a temperature-induced quenching effect of the broadband associated with the  ${}^4\text{T}_2 \rightarrow {}^4\text{A}_2$  electronic transition of  $\text{Cr}^{3+}$  ions. Generally, no significant changes in the shape of the emission spectra with increasing temperature were observed. Consequently, a similar analysis was conducted for the aforementioned pressure-dependent emission studies. The temperature-dependent  $LIR$  parameter was determined (Figure 5b), utilizing the same spectral ranges as used for evaluating the  $\text{Li}_3\text{Sc}_2(\text{PO}_4)_3:\text{Cr}^{3+}$  manometer's response to pressure, based on Equation (2). The obtained dependence exhibits negligible variation in the  $LIR$  parameter up to  $\approx 310 \text{ K}$ . Based on the thermal evolution of the  $LIR$  values, the relative sensitivity  $S_R$  was determined using Equation (3), but concerning temperature change  $\Delta T$ , instead of  $\Delta p$ . At room temperature,  $S_R$  of  $0.041\% \text{ K}^{-1}$  was achieved (Figure 5b). Although this value is relatively low,<sup>[38]</sup> it does not indicate temperature's impact on the manometric properties of the developed sensor. Hence, the temperature invariant manometric factor ( $TIMF$ ) expressed by Equation (4):<sup>[14]</sup>

$$TIMF = \left| \frac{S_{R,p,\text{max}}}{S_{R,T}(RT)} \right| \quad (4)$$

was used, where  $S_{R,p,\text{max}}$  is the maximum pressure relative sensitivity and  $S_{R,T}$  is the temperature sensitivity achieved at room temperature. The  $TIMF$  parameter quantifies the sensitivity of a manometer to pressure variations (GPa) in respect to sensitivity to temperature changes (K). For the  $\text{Li}_3\text{Sc}_2(\text{PO}_4)_3:\text{Cr}^{3+}$

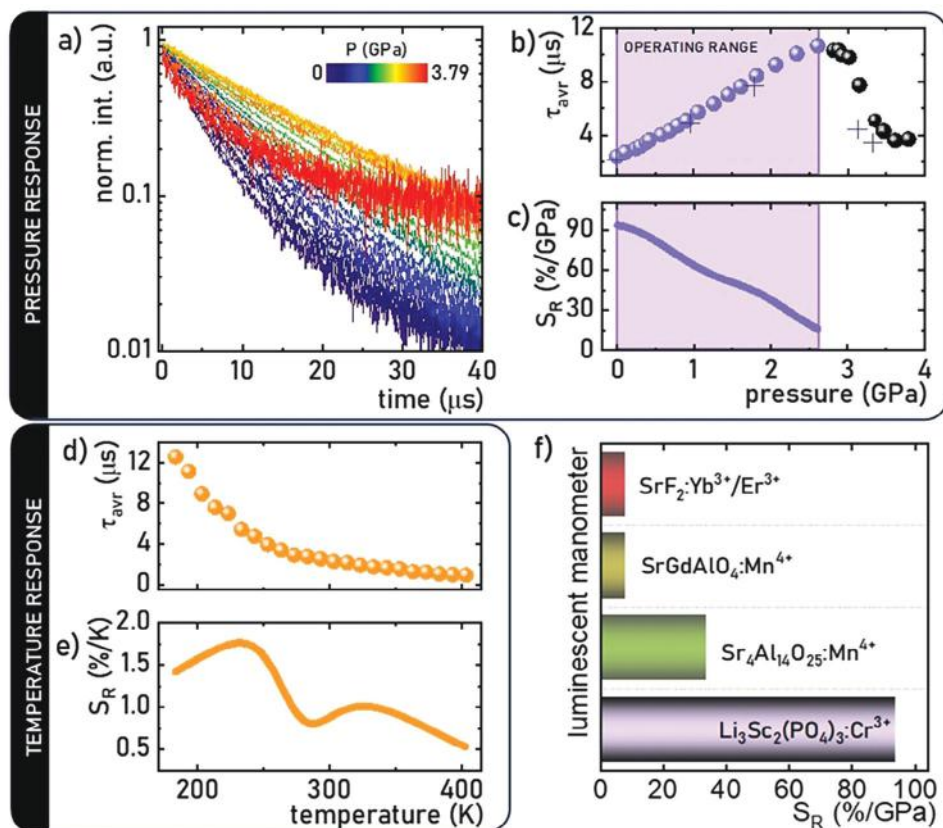


**Figure 6.** Pressure-dependent luminescence decay profiles ( $\lambda_{exc} = 445$  nm) a),  $\tau_{avr}$  of the  ${}^4T_2$  excited state of  $Cr^{3+}$ , with marked pressure range defined as an operating range of manometer (dots indicate results obtained during material compression, crosses indicate decompression cycle) b) and corresponding  $S_R$  c) as a function of pressure. The corresponding results obtained from the measurements as a function of temperature, i.e.,  $\tau_{avr}$  d) and corresponding  $S_R$  e) as a function of temperature for the  $Li_3Sc_2(PO_4)_3:1\%Cr^{3+}$ ; the comparison of the highest  $S_R$  for different lifetime based luminescence manometers f).

manometer, the  $TIMF$  value equals  $1386.8$  K GPa $^{-1}$ . In general, to ensure the high application potential of the developed manometer, the  $TIMF$  value should exceed  $\approx 100$  K GPa $^{-1}$ .<sup>[17]</sup> This value indicates the independence of the pressure readout from temperature. The obtained value was compared with other ratiometric luminescence manometers for which  $TIMF$  values have been determined, as depicted in Figure 5c, in which the  $S_{R,p}$  values are also included. It is evident that the  $Li_3Sc_2(PO_4)_3:1\%Cr^{3+}$  manometer achieves one of the highest  $TIMF$  values reported so far, all while maintaining an unquestionably high sensitivity to pressure variations.

In light of the substantial changes in emission spectra induced by applied pressure, the luminescence kinetics as a function of pressure was also investigated for the  $Li_3Sc_2(PO_4)_3:1\%Cr^{3+}$  sample. Luminescence decay curves were measured over the pressure range from ambient to 3.79 GPa, upon  $\lambda_{exc} = 445$  nm, while monitoring the maximum of the emission band determined at the given pressure. The recorded luminescence decay curves (Figure 6a; Figure S9, Supporting Information) were well-fitted using a double exponential function (Equation 5), proving that both  $Cr^{3+}$  centers are optically active.

$$I(t) = I_0 + A_1 \cdot \exp\left(-\frac{t}{\tau_1}\right) + A_2 \cdot \exp\left(-\frac{t}{\tau_2}\right) \quad (5)$$

The average lifetimes  $\tau_{avr}$  of the  $Cr^{3+}$  luminescence (during the compression and decompression cycle) were calculated as follows (Equation 6):

$$\tau_{avr} = \frac{A_1\tau_1^2 + A_2\tau_2^2}{A_1\tau_1 + A_2\tau_2} \quad (6)$$

where:  $\tau_1$  and  $\tau_2$  represent the luminescence decay time components and  $A_1$ ,  $A_2$  are amplitudes obtained from double exponential function parameters and  $I_0$  is the initial emission intensity. A remarkable prolongation of the  $\tau_{avr}$  was observed, increasing from 2.42 to 10.65 μs when the applied pressure increases from ambient to 2.6 GPa (Figure 6b). The prolongation of lifetime is a consequence of the pressure-induced reduction in  $Cr^{3+}-O^{2-}$  distances, which, in turn, alters the covalency of the bonds and the change in the activation energy of the  ${}^4T_2$  state. Consequently, the probability of radiative and nonradiative transitions changes. However, when the applied pressure is higher than 2.6 GPa, a rapid shortening of the  $\tau_{avr}$  becomes evident, reaching 3.62 μs at 3.6 GPa. This effect, i.e., an abrupt drop/bias in the monotonicity of changes of the lifetime values as a function of pressure, clearly confirms the postulated phase transition  $\approx 3$  GPa. The pressure driven change in the probability of the radiative and nonradiative transitions was already reported for the  $Mn^{4+}$  doped

phosphors.<sup>[11,12,41,42]</sup> The significant and reversible change in average lifetimes of the excited state as a function of applied pressure has enabled the possibility of developing a manometer operating with lifetime-based readout mode. Based on the obtained dependence of  $\tau_{avr}$  as a function of pressure, the  $S_R$  was determined using the formula:

$$S_R = \frac{1}{\tau_{avr}} \frac{\Delta\tau_{avr}}{\Delta p} 100\% \quad (7)$$

where  $\Delta\tau_{avr}$  represents the change of the  $\tau_{avr}$ , which corresponds to the change of pressure by  $\Delta p$ . The highest  $S_R$  value was achieved at ambient pressure, reaching 93.56% GPa<sup>-1</sup> (Figure 6c). Nevertheless, the manometer exhibits significant sensitivity across its entire operating range – at the  $S_R$  is equal to 63.75% GPa<sup>-1</sup> and 37.86% GPa<sup>-1</sup> at 1 and 2 GPa, respectively. The achieved  $S_R$  equal to 93.56% GPa<sup>-1</sup> is nearly three-times higher than the  $S_R$  of the most sensitive lifetime-based manometer reported so far – Sr<sub>4</sub>Al<sub>14</sub>O<sub>25</sub>:Mn<sup>4+</sup> ( $S_R$  = 33.6% GPa<sup>-1</sup>),<sup>[11]</sup> and over ten-times more sensitive than the second most sensitive lifetime-based manometer SrGdAlO<sub>4</sub>:Mn<sup>4+</sup> (7.85% GPa<sup>-1</sup>).<sup>[12]</sup>

As previously mentioned, to ensure reliable pressure readouts, the developed manometer must exhibit insensitivity to temperature fluctuations. Consequently, a study of luminescence kinetics as a function of temperature (183–403 K) for the Li<sub>3</sub>Sc<sub>2</sub>(PO<sub>4</sub>)<sub>3</sub>:1%Cr<sup>3+</sup> was conducted (see Figure S10, Supporting Information). The increase in temperature from 183 to 403 K results in the monotonic shortening of the  $\tau_{avr}$ , from 12.56 to 0.97 μs, respectively (Figure 6d). This effect is associated with the increase in the probability of the nonradiative depopulation of the <sup>4</sup>T<sub>2</sub> state. The calculated (by the analogy to Equation 7, when change in the temperature is considered instead of pressure) thermal sensitivity  $S_R$  of the  $\tau_{avr}$  for the Li<sub>3</sub>Sc<sub>2</sub>(PO<sub>4</sub>)<sub>3</sub>:1%Cr<sup>3+</sup> sensor reached the maximal value of 1.5%/K at 200 K, while at room temperature (temperature at which pressure dependent studies were performed) the  $S_R$  = 0.83% K<sup>-1</sup> was obtained (Figure 6e). It should be underlined that both stimuli (pressure and temperature) affect the  $\tau_{avr}$  in the opposite way, which is the advantage of the system. Additionally, for the pressure-dependent measurements performed at room temperature, the increase in pressure leads to more nonexponential decays, in contrast to the temperature effect. This is a highly desirable and unique feature of lifetime-based luminescent manometers, which are made of phosphor materials doped with transition metal ions. To assess the impact of temperature on pressure readouts and evaluate the manometer's application potential, the *TIMF* parameter was calculated, following Equation (4). For the Li<sub>3</sub>Sc<sub>2</sub>(PO<sub>4</sub>)<sub>3</sub>:Cr<sup>3+</sup> 1%, the *TIMF* value is equal to 112.72 K GPa<sup>-1</sup>, which indicates temperature-invariant pressure readouts. For comparison, the *TIMF* for the Sr<sub>4</sub>Al<sub>14</sub>O<sub>25</sub>:Mn<sup>4+</sup> manometer is 187 K GPa<sup>-1</sup>,<sup>[11]</sup> while the SrGdAlO<sub>4</sub>:Mn<sup>4+</sup> achieves a *TIMF* of 134 K GPa<sup>-1</sup>.<sup>[12]</sup> The comparison of the highest  $S_R$  of different lifetime-based luminescence manometers reported so far clearly indicates the extraordinary manometric performance of Li<sub>3</sub>Sc<sub>2</sub>(PO<sub>4</sub>)<sub>3</sub>:Cr<sup>3+</sup> 1% (Figure 6f). Although the thermal sensitivity of the  $\tau_{avr}$  is not negligible, the relatively high value of the *TIMF* parameter for Li<sub>3</sub>Sc<sub>2</sub>(PO<sub>4</sub>)<sub>3</sub>:Cr<sup>3+</sup> 1% indicates that the  $\tau_{avr}$  can be successfully used after pressure readings. However, it will be particularly ben-

eficial to use this parameter for conditions of small temperature changes.

Another significant feature of the Li<sub>3</sub>Sc<sub>2</sub>(PO<sub>4</sub>)<sub>3</sub>:Cr<sup>3+</sup> material, that distinguishes this phosphor from many other luminescent manometers, is the notable enhancement of emission intensity with applied pressure, as depicted in Figure 7a and Figure S8 (Supporting Information). The pressure-induced enhancement of the integrated emission intensity ( $I_p$ ) to the intensity obtained at ambient pressure ( $I_0$ ) is very significant (over three times), resulting in the monotonically increasing ratio  $I_p/I_0$  with pressure, reaching 3.3 at 2.6 GPa. This behavior is crucial from the applicative perspective since, in most phosphors, the applied pressure leads to a quenching of emission intensity, complicating and hampering the measurement and the whole sensing process. So far, this phenomenon has been reported for several phosphors in the context of luminescent manometers. For instance, Zheng et al.<sup>[43]</sup> developed a luminescent manometer based on Ca<sub>2</sub>Gd<sub>8</sub>Si<sub>6</sub>O<sub>26</sub>:Ce<sup>3+</sup> powder, in which the emission intensity increased more than twice at 9.5 GPa compared to 0.62 GPa.<sup>[43]</sup> In the case of the Li<sub>3</sub>Sc<sub>2</sub>(PO<sub>4</sub>)<sub>3</sub>:Cr<sup>3+</sup> material, two possible mechanisms can be responsible for this emission intensity increase: 1) the more efficient absorption of the excitation wavelength associated with the pressure-induced blue-shift of the Cr<sup>3+</sup> excitation bands; or 2) the change in the probability of the radiative and nonradiative depopulation of the emitting state, associated with the change in the activation energy. As indicated by the analysis of the kinetics of the <sup>4</sup>T<sub>2</sub> state as a function of pressure, the  $\tau_{avr}$  increases over three times in this pressure range. This correlated exactly with the enhancement factor of the emission intensity. However, beyond ≈2.6 GPa, a notable reduction in emission intensity is observed. This decrease is plausibly associated with the following factors: I) phase transition occurring ≈3 GPa, where the resulting phase can ensure an unfavorable local environment for Cr<sup>3+</sup> ions in terms of luminescence properties; II) above a pressure of 2.6 GPa, the excitation band maximum is located at less than 445 nm and continues to gradually shift toward shorter wavelengths, thus resulting in a reduction of the excitation efficiency. The significant quenching of emission may result from the cumulative effects mentioned above, which elucidate its more rapid change in  $I_p/I_0$  values, compared to change observed during the increase in intensity up to 2.6 GPa.

It is worth noting the remarkable spectral shift of the emission band associated with the <sup>4</sup>T<sub>2</sub>→<sup>4</sup>A<sub>2</sub> electron transition of Cr<sup>3+</sup> in the doped structure of Li<sub>3</sub>Sc<sub>2</sub>(PO<sub>4</sub>)<sub>3</sub>. A linear dependence between the maximum band and the applied pressure, spanning from ambient pressure to ≈2.6 GPa, was observed with the spectral shift rate of  $d\lambda/dp$  = 23.9 nm GPa<sup>-1</sup>, as shown in Figure 8a. Furthermore, as also depicted in Figure 8a, the full reversibility of the emission band centroid during the decompression cycle has been demonstrated, signifying that the spectral shift of the emission band is not caused by irreversible structure defects. The achieved rate of spectral shift is the highest value reported so far among high-pressure luminescence manometers, as illustrated in Figure 8b, where it is compared to the most sensitive luminescence manometers with a spectral shift rate exceeding 1 nm GPa<sup>-1</sup>. The ruby sensor, i.e., Al<sub>2</sub>O<sub>3</sub>:Cr<sup>3+</sup> was also included in the comparison in Figure 8b due to its crucial significance and common use in high-pressure experiments. It is worth



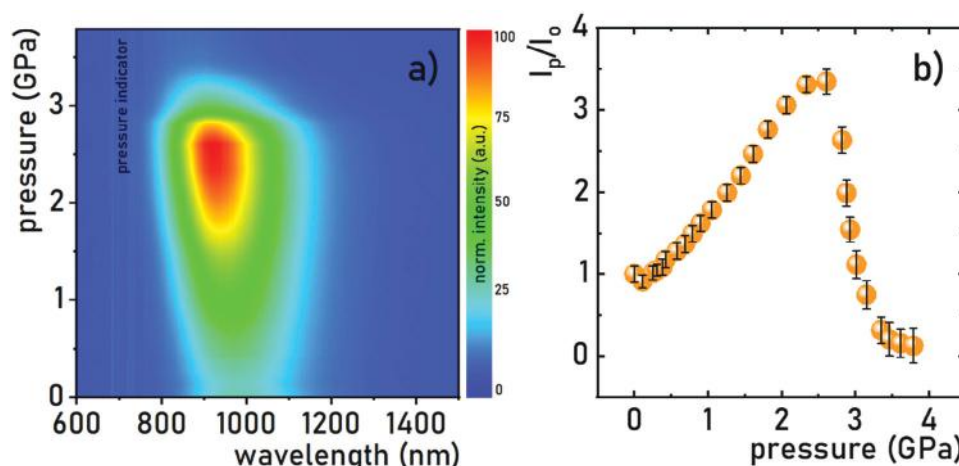


**Figure 7.** Pressure-dependent emission spectra map with marked spectral range of the emission of the pressure indicator  $\text{Al}_2\text{O}_3:\text{Cr}^{3+}$  a) and the  $I_p/I_0$  intensity ratio as a function of pressure b) for the  $\text{Li}_3\text{Sc}_2(\text{PO}_4)_3:1\%\text{Cr}^{3+}$ .

noting that the  $\text{Al}_2\text{O}_3:\text{Cr}^{3+}$  pressure indicator demonstrates a sensitivity nearly 80 times lower than the developed sensor  $\text{Li}_3\text{Sc}_2(\text{PO}_4)_3:\text{Cr}^{3+}$ .<sup>[44]</sup> The relevant manometric performance of  $\text{Li}_3\text{Sc}_2(\text{PO}_4)_3:\text{Cr}^{3+}$  can be also underlined when the  $d\lambda/dp$  versus  $d\lambda/dT$  plot for different luminescence manometers based on the spectral shift is analyzed (Figure 8c). This concludes the considerable potential of the  $\text{Li}_3\text{Sc}_2(\text{PO}_4)_3:\text{Cr}^{3+}$  for use as a luminescent manometer. Of course, it should be recalled that the high-pressure spectroscopy measurements were performed in DAC in a methanol–ethanol solution (V:V/4:1). Although  $\text{Li}_3\text{Sc}_2(\text{PO}_4)_3:1\%\text{Cr}^{3+}$  has a high chemical stability in real application, if other solvents or reactive gases are used, it would

be necessary to verify their effect on the emission intensity and calibration curves of the manometric parameters.

In conjunction with the indisputable advantages of  $\text{Li}_3\text{Sc}_2(\text{PO}_4)_3:1\%\text{Cr}^{3+}$  as a pressure sensor, it is imperative to acknowledge certain limitations that temper the broad applicability of the described techniques. The most important is the constrained range of pressures within which  $\text{Li}_3\text{Sc}_2(\text{PO}_4)_3:1\%\text{Cr}^{3+}$  can be used for pressure readout. The discernible changes in Raman spectra of  $\text{Li}_3\text{Sc}_2(\text{PO}_4)_3$  above 4 GPa indicate a critical threshold beyond which the utility of  $\text{Li}_3\text{Sc}_2(\text{PO}_4)_3:1\%\text{Cr}^{3+}$  as a pressure sensor diminishes. Moreover, the broadband nature of the emission introduces a potential source of imprecision when

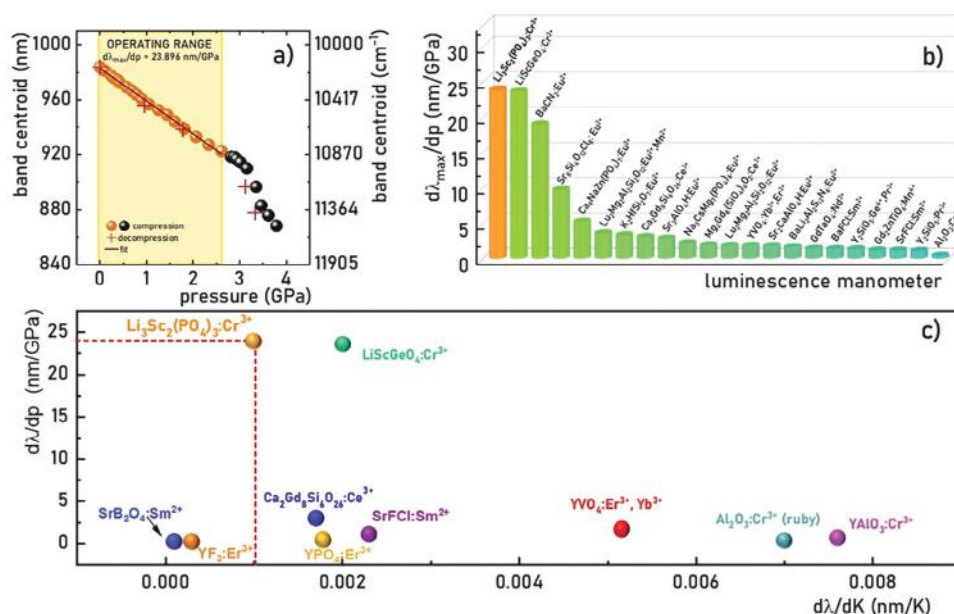


**Figure 8.** Pressure-dependent maximum of the emission band associated with the  ${}^4\text{T}_{2g} \rightarrow {}^4\text{A}_{2g}$  transition of  $\text{Cr}^{3+}$  ions in doped  $\text{Li}_3\text{Sc}_2(\text{PO}_4)_3$  (1%  $\text{Cr}^{3+}$ ), with the pressure range defined as the operating range, where a linear dependence of the band centroid as a function of pressure was obtained a); A summary of the most sensitive luminescence manometers in terms of pressure-induced spectral shift rate of the emission band ( $>1\text{ nm GPa}^{-1}$ ) b) [6,8,14,37,43–56] and a  $d\lambda/dp$  versus  $d\lambda/dT$  plot for representative luminescence manometers based on the spectral shift-c).



determining the band maximum, distinguishing it unfavorably from the narrowband emission characteristics observed in materials such as ruby. The observed reduction in emission intensity with increasing pressure above 3 GPa further complicates the accurate measurement of pressures above this value. Additionally, attention should also be paid to the morphology of the obtained powder. As shown in the SEM images, the obtained powder consists of aggregated crystallites, which may hinder its applicability. Therefore, before the final use of the described material, it would be beneficial to further optimize/modify the synthesis conditions to obtain a monodisperse powder and/or, depending on the requirements of the application, particles of smaller size. Consequently, future investigations should be directed toward identifying host materials with higher stability under high pressures, where the emission intensity remains less susceptible to significant quenching effects caused by increasing pressure.

## 4. Conclusion

In this work, the structural and spectroscopic studies of  $\text{Li}_3\text{Sc}_2(\text{PO}_4)_3:\text{Cr}^{3+}$  as a function of pressure and temperature were analyzed in order to evaluate its manometric performance. It was found that the  $\text{Li}_3\text{Sc}_2(\text{PO}_4)_3:\text{Cr}^{3+}$  reveals structural stability up to 3 GPa, above which a phase transition was observed. According to the predictions, the compression of the system leads to the increase of the crystal field strength affecting  $\text{Cr}^{3+}$  ions, and causing an increase in the energy of the  ${}^4\text{T}_2$  state. Consequently, the broad emission band associated with the  ${}^4\text{T}_2 \rightarrow {}^4\text{A}_2$  electronic transitions undergoes a blue shift with pressure. The performed analysis indicates that  $\text{Li}_3\text{Sc}_2(\text{PO}_4)_3:\text{Cr}^{3+}$  can be used for pressure sensing with three different modes: I) spectral shift of the emission band; II) ratiometric and III) lifetime-based approach. Importantly, the position of the maxima of the  ${}^4\text{T}_2 \rightarrow {}^4\text{A}_2$  reveals the highest up to date shift rate reaching  $d\lambda/dp = 23.9 \text{ nm GPa}^{-1}$ , from ambient to 2.6 GPa. In the ratiometric approach, the  $S_r$  is as high as  $56.86\% \text{ GPa}^{-1}$  at 0.02 GPa, which together with full reversibility of the readout and the high TIMF factor ( $\text{TIMF} = 1386.83 \text{ K GPa}^{-1}$ ), indicates the high applicative potential of this sensor. Additionally, the kinetics of the  ${}^4\text{T}_2$  state reveal high sensitivity to pressure changes. The  $\tau_{\text{avr}}$  increases linearly from 2.42 to 10.65  $\mu\text{s}$  in the ambient to 2.6 GPa pressure range, thus resulting in the highest up to date sensitivity value for the lifetime-based phosphor  $S_R = 93.56\% \text{ GPa}^{-1}$ . Importantly, in contrast to the temperature, the pressure increase leads to the rarely observed prolongation of the  $\tau_{\text{avr}}$  and the increase in the exponential character of the luminescence kinetics.

Moreover, the pressure-driven enhancement in the emission intensity was observed for the  $\text{Li}_3\text{Sc}_2(\text{PO}_4)_3:\text{Cr}^{3+}$ , which is highly beneficial for optical sensing, and it is a consequence of the co-existence of change in the nonradiative depopulation rate of the  ${}^4\text{T}_2$  state and the spectral shift of the absorption band of  $\text{Cr}^{3+}$  ions with pressure. All of the above observations indicate that the developed optical manometer  $\text{Li}_3\text{Sc}_2(\text{PO}_4)_3:\text{Cr}^{3+}$  shows high potential as an ultra-sensitive and multimode luminescent pressure gauge, operating at relatively low-pressure values, where, e.g. most of the interesting physicochemical effects and phase transformations occur in the case of soft, organic materials. It should be noticed that the advantage of employing luminescent

manometry for pressure measurement lies in its electrically passive nature, eliminating the need for an external electrical power supply to the sensor. Additionally, pressure-sensitive phosphors can be integrated with paints or varnishes, enabling their application onto surfaces exposed to elevated pressure conditions.

## Supporting Information

Supporting Information is available from the Wiley Online Library or from the author.

## Acknowledgements

This work was supported by the National Science Center (NCN) Poland under project no. DEC-UMO- 2020/37/B/ST5/00164.

## Conflict of Interest

The authors declare no conflict of interest.

## Data Availability Statement

The data that support the findings of this study are available from the corresponding author upon reasonable request.

## Keywords

$\text{Cr}^{3+}$  luminescence, luminescence intensity ratio, luminescence manometer, optical pressure sensor, pressure induced spectral shift, pressure sensing, pressure-dependent lifetime

Received: November 9, 2023

Revised: January 23, 2024

Published online: February 7, 2024

- [1] A. Siria, P. Poncharal, A. L. Biance, R. Fulcrand, X. Blase, S. T. Purcell, L. Bocquet, *Nature* **2013**, 494, 455.
- [2] V. Shanmugam, S. Selvakumar, C. S. Yeh, *Chem. Soc. Rev.* **2014**, 43, 6254.
- [3] R. A. A. de Heus, M. G. M. Olde Rikkert, P. J. Tully, B. A. Lawlor, J. A. H. R. Claassen, null, *Hypertension* **2019**, 74, 1172.
- [4] C. Grossiord, T. N. Buckley, L. A. Cernusak, K. A. Novick, B. Poulter, R. T. W. Siegwolf, J. S. Sperry, N. G. McDowell, *New Phytol.* **2020**, 226, 1550.
- [5] J. W. Gregory, K. Asai, M. Kameda, T. Liu, J. P. Sullivan, *Proc. Inst. Mech. Eng., Part C* **2008**, 222, 249.
- [6] Y. Wang, T. Seto, K. Ishigaki, Y. Uwatoko, G. Xiao, B. Zou, G. Li, Z. Tang, Z. Li, Y. Wang, *Adv. Funct. Mater.* **2020**, 30, 2001384.
- [7] M. Runowski, P. Woźny, S. Lis, V. Lavín, I. R. Martín, *Adv. Mater. Technol.* **2020**, 5, 1901091.
- [8] T. Zheng, M. Runowski, J. Xue, L. Luo, U. R. Rodríguez-Mendoza, V. Lavín, I. R. Martín, P. Rodríguez-Hernández, A. Muñoz, P. Du, *Adv. Funct. Mater.* **2023**, 33, 2214663.
- [9] T. Zheng, M. Runowski, I. R. Martín, K. Soler-Carracedo, L. Peng, M. Skwierczyńska, M. Sójka, J. Barzowska, S. Mahlik, H. Hemmerich, F. Rivera-López, P. Kulpiński, V. Lavín, D. Alonso, D. Peng, *Adv. Mater.* **2023**, 35, 2304140.

- [10] M. Szymczak, M. Runowski, V. Lavín, L. Marciniak, *Laser Photonics Rev.* **2023**, 17, 2200801.
- [11] M. Pieprz, W. Piotrowski, P. Woźny, M. Runowski, L. Marciniak, *Adv. Opt. Mater.* **2023**, 12, 2301316.
- [12] M. Pieprz, M. Runowski, P. Woźny, J. Xue, L. Marciniak, *J. Mater. Chem. C* **2023**, 11, 11353.
- [13] M. A. Antoniak, S. J. Zelewski, R. Oliva, A. Žak, R. Kudrawiec, M. Nyk, *ACS Appl. Nano Mater.* **2020**, 3, 4209.
- [14] M. Szymczak, M. Runowski, M. G. Brik, L. Marciniak, *Chem. Eng. J.* **2023**, 466, 143130.
- [15] T. Zheng, M. Sójka, P. Woźny, I. R. Martín, V. Lavín, E. Zych, S. Lis, P. Du, L. Luo, M. Runowski, *Adv. Opt. Mater.* **2022**, 10, 2201055.
- [16] L. Labrador-Páez, M. Pedroni, A. Speghini, J. García-Solé, P. Haro-González, D. Jaque, *Nanoscale* **2018**, 10, 22319.
- [17] M. Szymczak, P. Woźny, M. Runowski, M. Pieprz, V. Lavín, L. Marciniak, *Chem. Eng. J.* **2023**, 453, 139632.
- [18] N. Zhang, Y. T. Tsai, M. H. Fang, C. G. Ma, A. Lazarowska, S. Mahlik, M. Grinberg, C. Y. Chiang, W. Zhou, J. G. Lin, J. F. Lee, J. Zheng, C. Guo, R. S. Liu, *ACS Appl. Mater. Interfaces* **2017**, 9, 23995.
- [19] C. Y. Chang, N. Majewska, K. C. Chen, W. T. Huang, T. Leśniewski, G. Leniec, S. M. Kaczmarek, W. K. Pang, V. K. Peterson, D. H. Cherng, K. M. Lu, S. Mahlik, R. S. Liu, *Chem. Mater.* **2022**, 34, 10190.
- [20] R. S. Liu, X. J. Wang, in *Phosphor Handbook: Experimental Methods for Phosphor Evaluation and Characterization*, 3rd ed., CRC Press, Boca Raton **2022**.
- [21] S. Zhao, L. Lou, S. Yuan, D. Zhu, F. Wu, Z. Mu, *J. Lumin.* **2022**, 251, 119188.
- [22] G. Shen, Y. Wang, A. Dewaele, C. Wu, D. E. Fratanduono, J. Eggert, S. Klotz, K. F. Dziubek, P. Loubeyre, O. V. Fat'yanov, P. D. Asimow, T. Mashimo, R. M. M. Wentzcovitch, *High Pressure Res.* **2020**, 40, 299.
- [23] T. Suzuki, K. Yoshida, K. Uematsu, T. Kodama, K. Toda, Z. G. Ye, M. Ohashi, M. Sato, *Solid State Ionics* **1998**, 113–115, 89.
- [24] M. Jiao, Q. Xu, M. Liu, C. Yang, Y. Yu, *Phys. Chem. Chem. Phys.* **2018**, 20, 26995.
- [25] S. Xu, D. Zhu, D. Gong, F. Wu, H. Dong, Z. Mu, *Opt. Mater.* **2023**, 143, 114239.
- [26] R. D. Shannon, *Acta Crystallogr., Sect. A: Found. Crystallogr.* **1976**, 32, 751.
- [27] V. V. Kravchenko, V. I. Michailov, S. E. Sigaryov, *Solid State Ionics* **1992**, 50, 19.
- [28] M. Runowski, P. Woźny, N. Stopikowska, Q. Guo, S. Lis, *ACS Appl. Mater. Interfaces* **2019**, 11, 4131.
- [29] S. Adachi, *J. Lumin.* **2021**, 232, 117844.
- [30] S. Miao, Y. Liang, Y. Zhang, D. Chen, X. J. Wang, *ACS Appl. Mater. Interfaces* **2021**, 13, 36011.
- [31] J. P. Hehir, M. O. Henry, J. P. Larkin, G. F. Imbusch, *J. Phys. C Solid State Phys.* **1974**, 7, 2241.
- [32] V. Rajendran, M. H. Fang, G. N. De Guzman, T. Lesniewski, S. Mahlik, M. Grinberg, G. Leniec, S. M. Kaczmarek, Y. S. Lin, K. M. Lu, C. M. Lin, H. Chang, S. F. Hu, R. S. Liu, *ACS Energy Lett.* **2018**, 3, 2679.
- [33] N. Majewska, A. Muñoz, R. S. Liu, S. Mahlik, *Chem. Mater.* **2023**, 35, 4680.
- [34] M. Mączka, S. Sobczak, P. Ratajczyk, F. F. Leite, W. Paraguassu, F. Dybała, A. P. Herman, R. Kudrawiec, A. Katrusiak, *Chem. Mater.* **2022**, 34, 7867.
- [35] M. Tian, Y. Gao, P. Zhou, K. Chi, Y. Zhang, B. Liu, *Phys. Chem. Chem. Phys.* **2021**, 23, 20567.
- [36] M. Runowski, J. Marciniak, T. Grzyb, D. Przybylska, A. Shyichuk, B. Barszcz, A. Katrusiak, S. Lis, *Nanoscale* **2017**, 9, 16030.
- [37] P. Zhou, Q. Zhang, F. Peng, B. Sun, X. Dou, B. Liu, D. Han, Y. Xue, K. Ding, *J. Rare Earths* **2022**, 40, 870.
- [38] A. Bednarkiewicz, L. Marciniak, L. D. Carlos, D. Jaque, *Nanoscale* **2020**, 12, 14405.
- [39] M. Szymczak, P. Du, M. Runowski, P. Woźny, J. Xue, T. Zheng, L. Marciniak, *Adv. Opt. Mater.* **2023**, <https://doi.org/10.1002/adom.202302147>
- [40] M. Szymczak, M. Runowski, V. Lavín, L. Marciniak, *Laser Photonics Rev.* **2023**, 17, 2200801.
- [41] Y. Jin, M. H. Fang, M. Grinberg, S. Mahlik, T. Lesniewski, M. G. Brik, G. Y. Luo, J. G. Lin, R. S. Liu, *ACS Appl. Mater. Interfaces* **2016**, 8, 11194.
- [42] W. L. Wu, M. H. Fang, W. Zhou, T. Lesniewski, S. Mahlik, M. Grinberg, M. G. Brik, H. S. Sheu, B. M. Cheng, J. Wang, R. S. Liu, *Chem. Mater.* **2017**, 29, 935.
- [43] T. Zheng, L. Luo, P. Du, S. Lis, U. R. Rodríguez-Mendoza, V. Lavín, I. R. Martín, M. Runowski, *Chem. Eng. J.* **2022**, 443, 136414.
- [44] H. K. Mao, J. Xu, P. M. Bell, *J. Geophys. Res.: Solid Earth* **1986**, 91, 4673.
- [45] T. Wu, H. Hua, J. Ueda, S. Tanabe, S. Matsuishi, *J. Appl. Phys.* **2022**, 132, 83104.
- [46] H. Chen, T. Seto, Y. Wang, *Inorg. Chem. Front.* **2022**, 9, 1644.
- [47] B. Zheng, X. Zhang, D. Zhang, F. Wang, Z. Zheng, X. Yang, Q. Yang, Y. Song, B. Zou, H. Zou, *Chem. Eng. J.* **2022**, 427, 131897.
- [48] M. Runowski, T. Zheng, P. Woźny, P. Du, *Dalton Trans.* **2021**, 50, 14864.
- [49] P. Comodi, F. P. Zanazzi, *J. Appl. Crystallogr.* **1993**, 26, 843.
- [50] M. Sójka, M. Runowski, P. Woźny, L. D. Carlos, E. Zych, S. Lis, *J. Mater. Chem. C* **2021**, 9, 13818.
- [51] T. Zheng, L. Luo, P. Du, S. Lis, U. R. Rodríguez-Mendoza, V. Lavín, M. Runowski, *Chem. Eng. J.* **2022**, 446, 136839.
- [52] B. Lorenz, Y. R. Shen, W. B. Holzapfel, *High Pressure Res.* **1994**, 12, 91.
- [53] Y. Masubuchi, S. Nishitani, S. Miyazaki, H. Hua, J. Ueda, M. Higuchi, S. Tanabe, *Appl. Phys. Express* **2020**, 13, 042009.
- [54] D. Zhang, B. Zheng, Z. Zheng, L. Li, Q. Yang, Y. Song, B. Zou, H. Zou, *Chem. Eng. J.* **2022**, 431, 133805.
- [55] Z. Zheng, Y. Song, B. Zheng, Y. Zhao, Q. Wang, X. Zhang, B. Zou, H. Zou, *Inorg. Chem. Front.* **2023**, 10, 2788.
- [56] Q. Lv, C. Wang, S. Chen, H. Zheng, E. Dong, G. Zhu, *Inorg. Chem.* **2022**, 61, 3212.

# ADVANCED FUNCTIONAL MATERIALS

## Supporting Information

for *Adv. Funct. Mater.*, DOI 10.1002/adfm.202314068

Highly-Sensitive, Tri-Modal Luminescent Manometer Utilizing Band-Shift, Ratiometric and Lifetime-Based Sensing Parameters

*Maja Szymczak, Julia Jaśkielewicz, Marcin Runowski, Junpeng Xue, Sebastian Mahlik and Lukasz Marciniak\**

## Supporting Information

### Highly-sensitive, tri-modal luminescent manometer utilizing band-shift, ratiometric and lifetime-based sensing parameters

M. Szymczak<sup>1</sup>, J. Jaśkielewicz<sup>1</sup>, M. Runowski<sup>2</sup>, J. Xue<sup>3</sup>, S. Mahlik<sup>4</sup>, L.

Marciniak<sup>1\*</sup>

<sup>1</sup> Institute of Low Temperature and Structure Research, Polish Academy of Sciences, Okólna 2, 50-422 Wrocław, Poland

<sup>2</sup> Adam Mickiewicz University, Faculty of Chemistry, Uniwersytetu Poznańskiego 8, 61-614 Poznań, Poland

<sup>3</sup> School of Science, Jiangsu University of Science and Technology, Zhenjiang 212100, China

<sup>4</sup> Institute of Experimental Physics, Faculty of Mathematics, Physics and Informatics, University of Gdańsk, Wita Stwosza 57, 80-308 Gdańsk, Poland

\*corresponding author: l.marciniak@intibs.pl

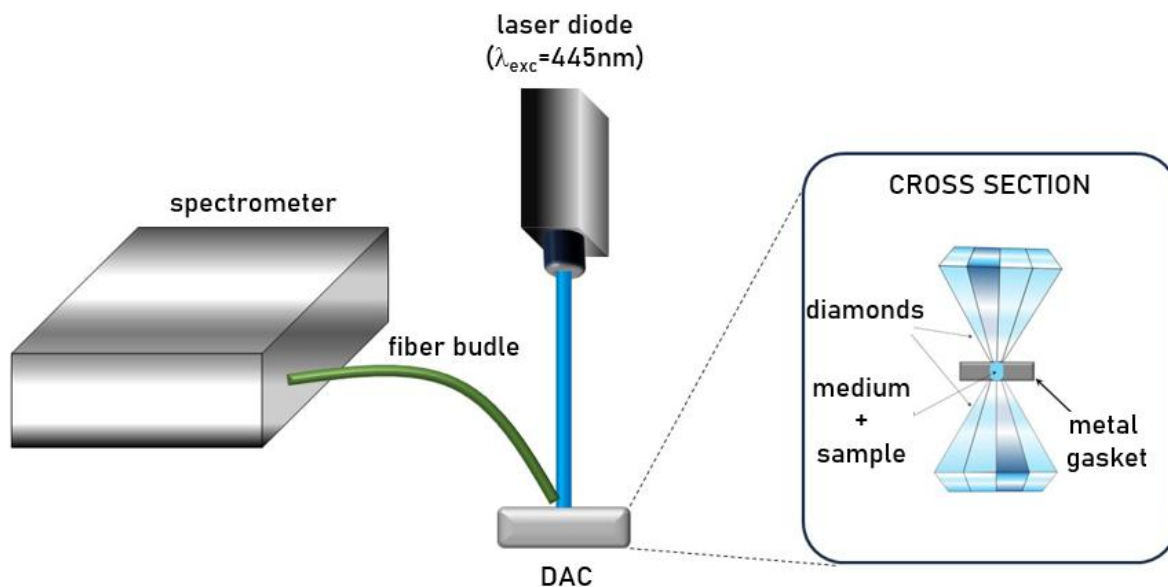


**Figure S1.** Schematic presentation of the experimental setup used for high-pressure measurements of luminescence properties of  $\text{Li}_3\text{Sc}_2(\text{PO}_4)_3:x\% \text{Cr}^{3+}$  (laser diode operating in a continuous work and pulsed work modes).

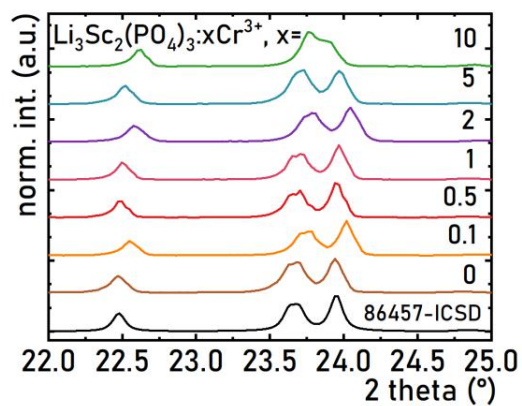


**Figure S2.** Zoom-in on the XRD patterns for the  $\text{Li}_3\text{Sc}_2(\text{PO}_4)_3:x\% \text{Cr}^{3+}$ ,  $x = 0.1$ -10%

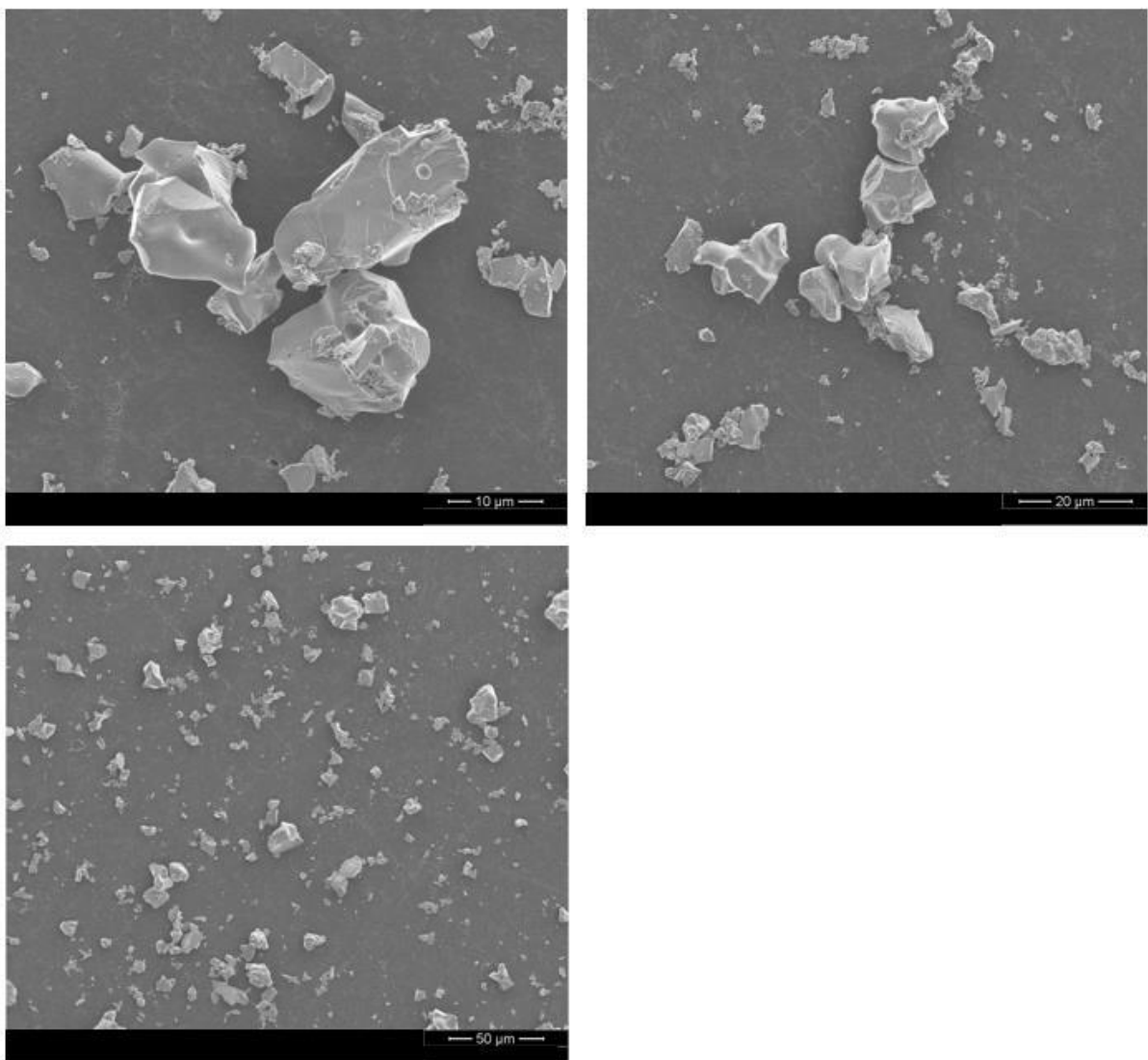


**Figure S3.** Representative SEM images of the  $\text{Li}_3\text{Sc}_2(\text{PO}_4)_3:1\% \text{Cr}^{3+}$ .

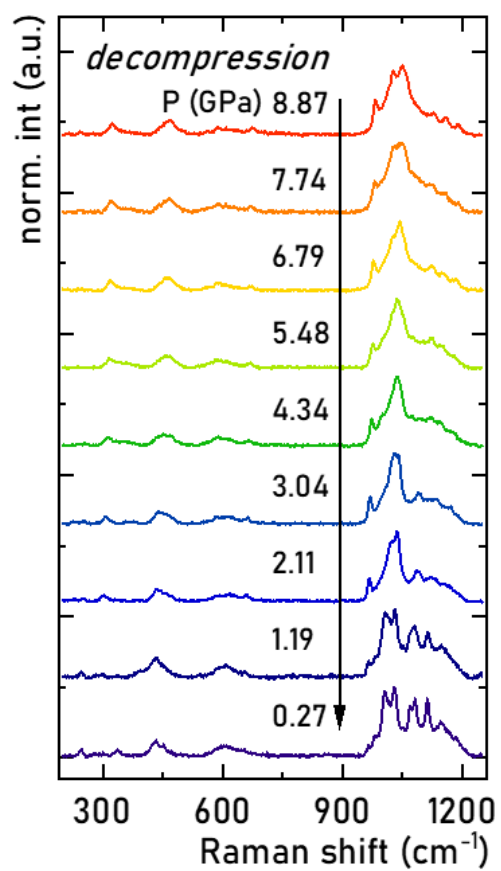


**Figure S4.** Normalized Raman spectra for the  $\text{Li}_3\text{Sc}_2(\text{PO}_4)_3$  material measured for different pressure values, during the decompression cycle.

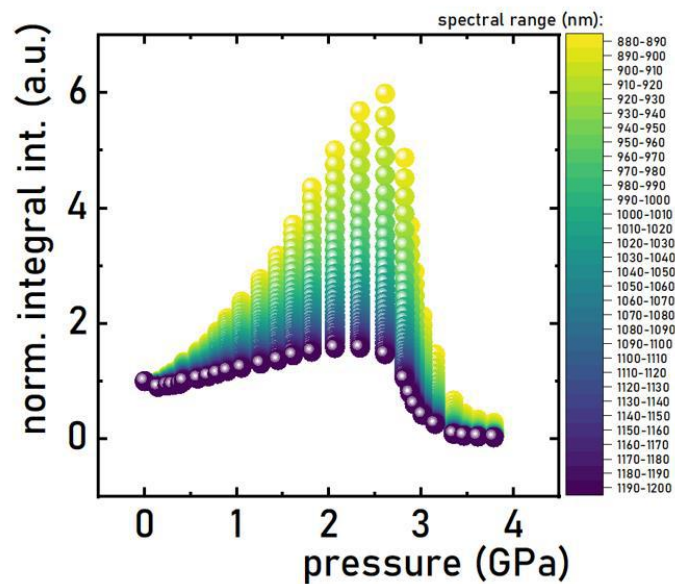


**Figure S5.** Integral emission intensity as a function of applied pressure integrated into different spectral ranges.

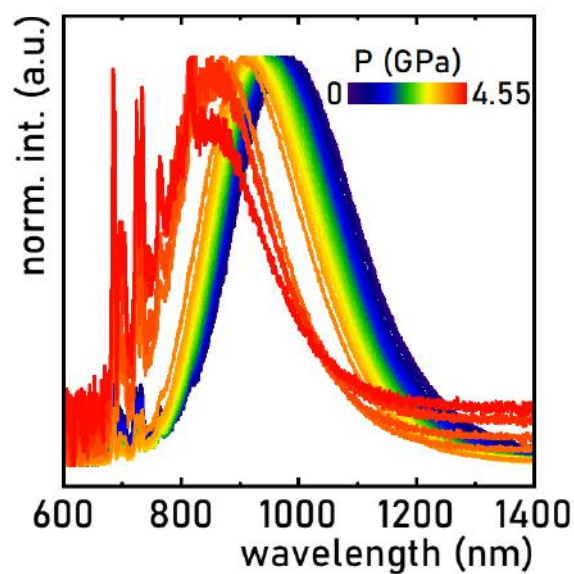


**Figure S6.** Pressure-dependent emission spectra for the  $\text{Li}_3\text{Sc}_2(\text{PO}_4)_3:1\% \text{Cr}^{3+}$  measured upon  $\lambda_{\text{exc}} = 445$  nm during cycle No. 2.



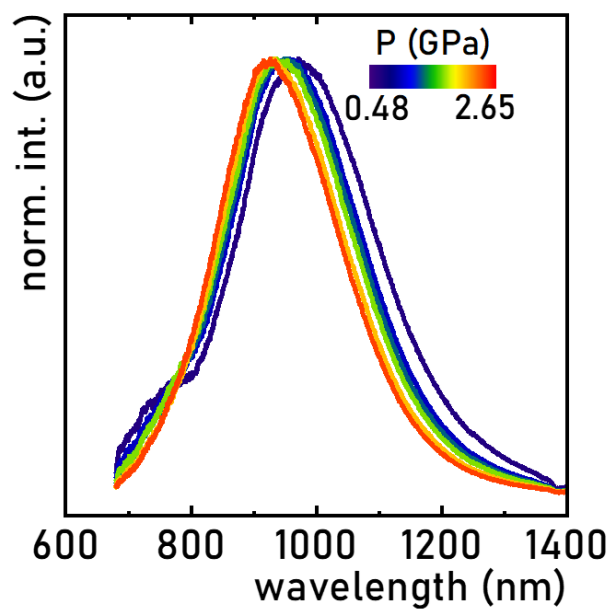


**Figure S7.** Pressure-dependent emission spectra for the  $\text{Li}_3\text{Sc}_2(\text{PO}_4)_3:1\% \text{Cr}^{3+}$  measured upon  $\lambda_{\text{exc.}} = 445$  nm during cycle No. 3.

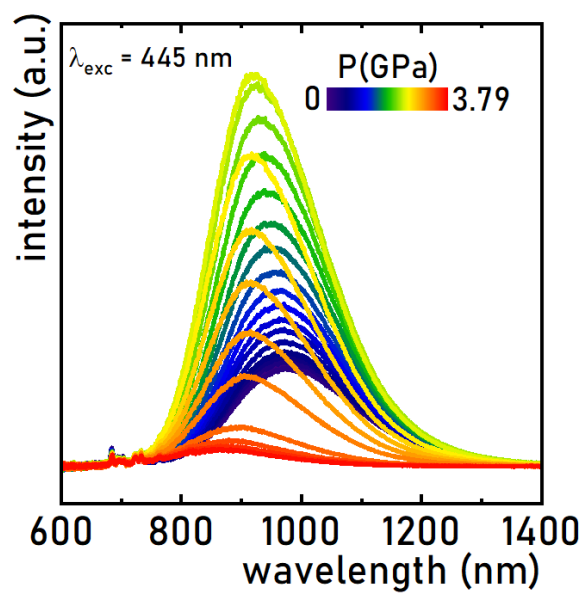


**Figure S8.** Pressure-dependent emission spectra for the  $\text{Li}_3\text{Sc}_2(\text{PO}_4)_3:1\% \text{Cr}^{3+}$  measured upon  $\lambda_{\text{exc.}} = 445$  nm.

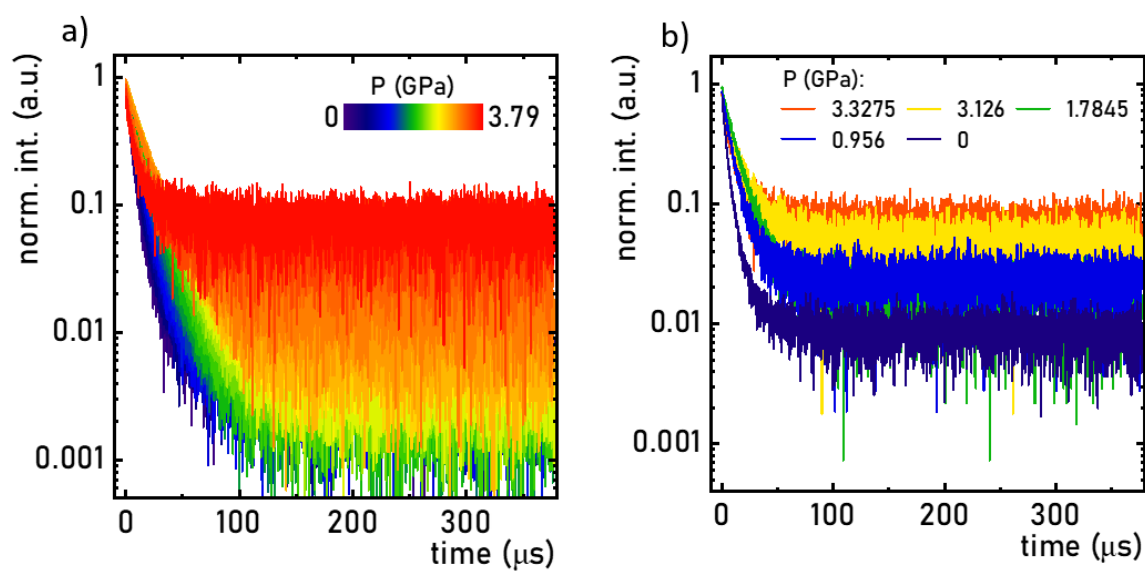


**Figure S9.** Pressure-dependent luminescence decay profiles measured during compression -a) and decompression -b) for the  $\text{Li}_3\text{Sc}_2(\text{PO}_4)_3:1\% \text{Cr}^{3+}$  ( $\lambda_{\text{exc}} = 445 \text{ nm}$ )

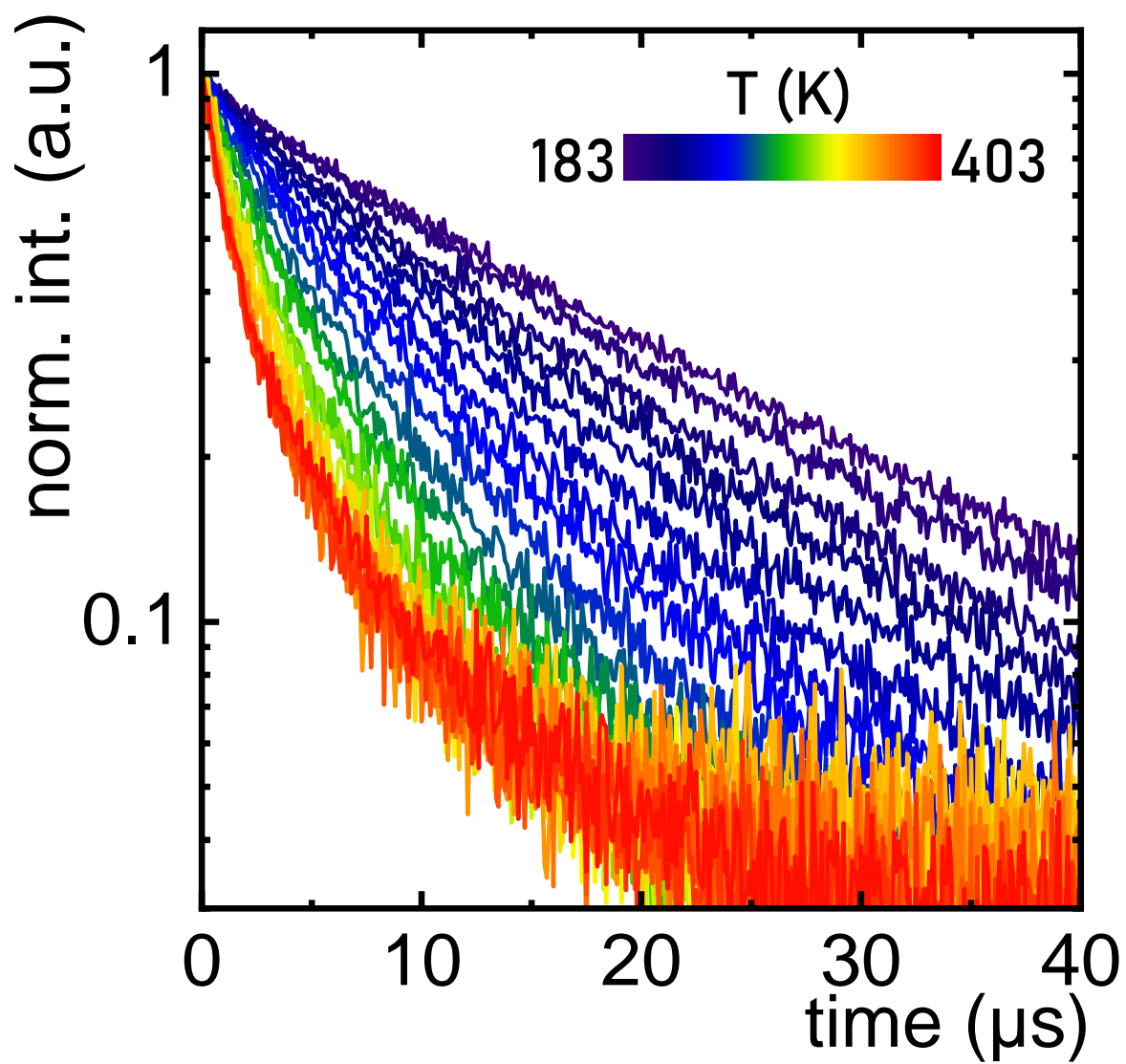


**Figure S10.** Temperature-dependent luminescence decay profiles for the  $\text{Li}_3\text{Sc}_2(\text{PO}_4)_3:1\% \text{Cr}^{3+}$  ( $\lambda_{\text{exc}} = 445$  nm)



# Bifunctional Luminescent Thermometer-Manometer Based on $\text{Cr}^{3+}$ – $\text{Cr}^{3+}$ Pair Emission

Maja Szymczak, Andris Antuzevics, Pavels Rodionovs, Marcin Runowski, Ulises R. Rodríguez-Mendoza, Damian Szymanski, Vasyi Kinzhybalo, and Lukasz Marciniak\*



Cite This: *ACS Appl. Mater. Interfaces* 2024, 16, 64976–64987



Read Online

ACCESS |



Metrics & More



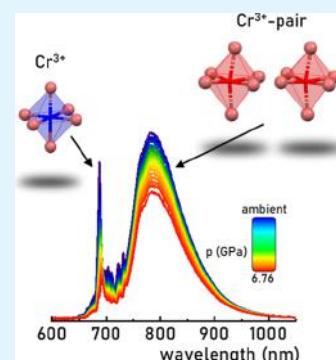
Article Recommendations



Supporting Information

**ABSTRACT:** Pressure dependence of spectral positions of the  ${}^2\text{E} \rightarrow {}^4\text{A}_2$  and  ${}^4\text{T}_2 \rightarrow {}^4\text{A}_2$  bands of  $\text{Cr}^{3+}$  ions, resulting from changes in  $\text{Cr}^{3+}$ – $\text{O}^{2-}$  covalency and variations in crystal field strength, respectively, is commonly utilized in luminescence manometry. However, as demonstrated in this paper, the luminescence of  $\text{Cr}^{3+}$ – $\text{Cr}^{3+}$  pairs shows insensitivity to pressure changes, making this signal suitable as a luminescence reference. The significant difference in the thermal and pressure dependences of luminescence with  $\text{Cr}^{3+}$  occupying different crystallographic positions in  $\text{CaAl}_2\text{O}_9:\text{Cr}^{3+}$  enables the development of a dual-function luminescence thermometer that operates in both ratiometric and lifetime-based readout modes. The presented first demonstration on utilization of  $\text{Cr}^{3+}$ – $\text{Cr}^{3+}$  pairs luminescence for sensing applications may rekindle interest in  $\text{Cr}^{3+}$ – $\text{Cr}^{3+}$  pairs for the development of optical sensors for physical quantities.

**KEYWORDS:** luminescent manometer, luminescence thermometry, optical sensors, ratiometric approach,  $\text{Cr}^{3+}$  pairs



## 1. INTRODUCTION

The spectroscopic characteristics of phosphors are susceptible to external factors such as temperature and pressure, making them viable candidates for luminescence-based remote sensing of physical parameters.<sup>1–5</sup> This measurement technique offers several advantages, including remote readout, rapid response times, real-time analysis without disrupting the observed system, as well as reduced electrical and magnetic interferences.<sup>2,6–9</sup> Additionally, by coating the investigated object with a layer of phosphor, both point measurements and two-dimensional (2D) imaging of physical quantities become feasible.<sup>10,11</sup>

Although luminescence thermometry and manometry techniques have demonstrated their effectiveness in many experiments over the years, one of the most significant limitations affecting the precision and reliability of the measurement is the cross-interdependence of the analyzed spectroscopic parameter on both pressure and temperature. Therefore, many of the luminescent thermometers and manometers described in the literature can be used only under constant pressure or temperature conditions.<sup>12–15</sup> Yet, in real-world scenarios, changes in temperature often coincide with alterations in pressure and vice versa, as seen, for instance, in the temperature–pressure relationship of gases during compression/decompression cycles.<sup>16,17</sup>

Hence, efforts are underway to address this challenge by either (1) developing selective sensors of a single state function, which remain unaffected by changes in other parameters<sup>18–20</sup> or (2) creating multifunctional materials

capable of simultaneous temperature and pressure readings.<sup>21–23</sup> While approach (1) holds significant importance, it limits the amount of information obtained during measurements, which, for certain applications, may limit functionality. Therefore, the second approach has been gaining popularity recently. However, it is extremely difficult to develop a sensor that provides such independent readouts of both physical quantities.

One of the most popular groups of phosphors used in sensor applications are inorganic materials doped with transition-metal ions, among which those with a  $3d^3$  electronic configuration, such as  $\text{Cr}^{3+}$  and  $\text{Mn}^{4+}$ , predominate.<sup>24–28</sup> This is attributed to the unusual sensitivity of their spectroscopic properties to changes in pressure and temperature, as well as the chemical composition of the material resulting from the electron configuration.<sup>4,9,29,30</sup> The intersection point between the parabolas of the excited and ground levels facilitates nonradiative depopulation of the excited states upon supplying the required thermal energy, a phenomenon commonly utilized in luminescence thermometry. On the other hand, the applied pressure causes a dual modification of the emission

**Received:** July 16, 2024

**Revised:** October 31, 2024

**Accepted:** November 8, 2024

**Published:** November 13, 2024



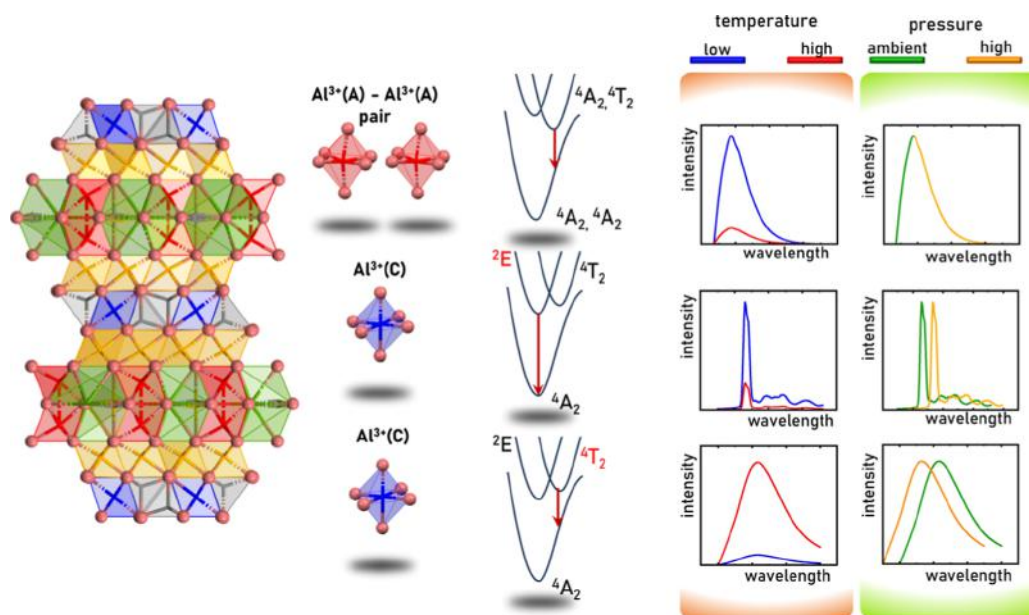


**Figure 1.** Schematic presentation of the main concept of the work.

spectrum of  $\text{Cr}^{3+}$  ions. For narrow-band emission associated with the  ${}^2\text{E} \rightarrow {}^4\text{A}_2$  electron transition, due to a change in the covalency of the  $\text{Cr}^{3+}-\text{O}^{2-}$  bond, the emission maximum is slightly spectrally shifted.<sup>12,14,31–34</sup> Meanwhile, broadband emission associated with the  ${}^4\text{T}_2 \rightarrow {}^4\text{A}_2$  electronic transition, observed in materials with intermediate and weak crystal fields, undergoes a spectral shift with material compression, driven by increased crystal field strength affecting the energy of the  ${}^4\text{T}_2$  level.<sup>4,35–38</sup>

However, in this work we present an alternative approach for simultaneous and independent pressure and temperature readouts using a single phosphor material. This approach is based on the unique structural properties of the hibonite-type  $\text{CaAl}_{12}\text{O}_{19}:\text{Cr}^{3+}$  crystals<sup>39–46</sup> facilitating  $\text{Cr}^{3+}-\text{Cr}^{3+}$  pairs creation even for low dopant concentration.

In this material, there are 3 inequivalent octahedral crystallographic positions of  $\text{Al}^{3+}$  ions (denoted here as A, B, and C) that can be occupied by  $\text{Cr}^{3+}$  ions (Figure 1). Due to the shortest bond lengths of  $\text{Cr}^{3+}-\text{O}^{2-}$  and the highest symmetry of the C site, the  ${}^2\text{E} \rightarrow {}^4\text{A}_2$  emission band can be observed for this site.<sup>47</sup> The luminescence of the C site reveals typical pressure dependence, resulting in a red spectral shift of the  ${}^2\text{E} \rightarrow {}^4\text{A}_2$  emission bands associated with the change in the covalency of the  $\text{Cr}^{3+}-\text{O}^{2-}$  bond. At elevated temperature, the thermalization of the  ${}^4\text{T}_2$  state results in the gradual enhancement of the  ${}^4\text{T}_2 \rightarrow {}^4\text{A}_2$  emission intensity with respect to the  ${}^2\text{E} \rightarrow {}^4\text{A}_2$  one. However, the close vicinity of the A sites of  $\text{Al}^{3+}$  facilitates the formation of the  $\text{Cr}^{3+}-\text{Cr}^{3+}$  ionic pairs, the emission intensity of which dominates the luminescence spectrum of  $\text{CaAl}_{12}\text{O}_{19}:\text{Cr}^{3+}$ . Hence, the independence of the spectral position of the  ${}^4\text{A}_2, {}^4\text{T}_2 \rightarrow {}^4\text{A}_2, {}^4\text{A}_2$  emission band on the applied pressure and strong thermal quenching of its luminescence is one of the available but previously unexplored approaches, which allows for the development of unique, bifunctional luminescence-based thermo-manometers.

## 2. EXPERIMENTAL SECTION

**2.1. Materials.** The  $\text{CaAl}_{11.9}\text{O}_{19}:\text{Cr}^{3+}$  samples were synthesized by the solid-state reaction method. Stoichiometric amounts of  $\text{CaCO}_3$

(99.95%),  $\text{Al}_2\text{O}_3$  (99.9%), and  $\text{Cr}_2\text{O}_3$  (99.97%) were ground in an agate mortar for 20 min with acetone as a mixing medium. The highest integral emission intensity of  $\text{Cr}^{3+}$  ions was obtained for 0.83%  $\text{Cr}^{3+}$ . Therefore, this dopant concentration was used for further analysis (Figure S1). The obtained homogeneous mixture was pelletized using a uniaxial hydraulic press, placed on a Pt foil, and heat treated at 1500 °C for 12 h with heating and cooling rate of 5 °C  $\text{min}^{-1}$ . After cooling, the ceramic sample was ground into a fine powder for further characterization.

**2.2. Methods.** The X-ray diffraction (XRD) patterns of the synthesized powders were obtained by the use of X-ray diffractometers (D8 Advance diffractometer, Bruker Corporation, Germany and X'Pert Pro diffractometer, PANalytical, Netherlands) with  $\text{Cu K}\alpha$  ( $\lambda = 1.5406$  Å) at 40 kV and 40 mA. The fluorescence spectrophotometer (F-4700, Hitachi, Japan) supplied with a 450 W Xe-lamp for monitoring room-temperature emission and excitation spectra were applied in the experiment. A fluorescence spectrometer (FSS, Edinburgh) was used for measuring the luminescence decay curves of the samples under ambient conditions. The morphology and chemical composition of the samples were determined by a field emission scanning electron microscopy (FE-SEM) FEI Nova NanoSEM 230 instrument (FEI Company as a part of Thermo Fisher Scientific, USA). Before SEM-EDS measurements, samples were mounted on metal stubs by using a sticky carbon disc, which increases conductivity. Finally, the SEM images were recorded at 5.0 kV in beam deceleration mode in order to show more detailed features of the examined samples. In the case of EDS elemental mapping measurements, the samples were scanned at 20.0 kV using an EDAX Apollo X Silicon Drift Detector (SDD) along with EDAX Genesis Software.

Electron paramagnetic resonance (EPR) spectra were measured at room temperature by using the Bruker ELEXSYS-II E500 CW-EPR system. The spectra were recorded at an X-band (9.83 GHz) microwave frequency using a 10 mW radiation power. Magnetic field modulation parameters were set at a 100 kHz frequency and 0.4 mT amplitude.

Scattering Raman spectra were recorded in the pressure range from ambient pressure to 7.18 GPa in a backscattering geometry using a Renishaw InVia confocal micro-Raman system with a 100 mW 532 nm diode laser and an optical system with Olympus  $\times 20$  SLMPlan N long working distance objective to focus the laser beam on the material. Raman spectra of the compressed sample were recorded in a diamond anvil cell (DAC) equipped with the IIas type, low



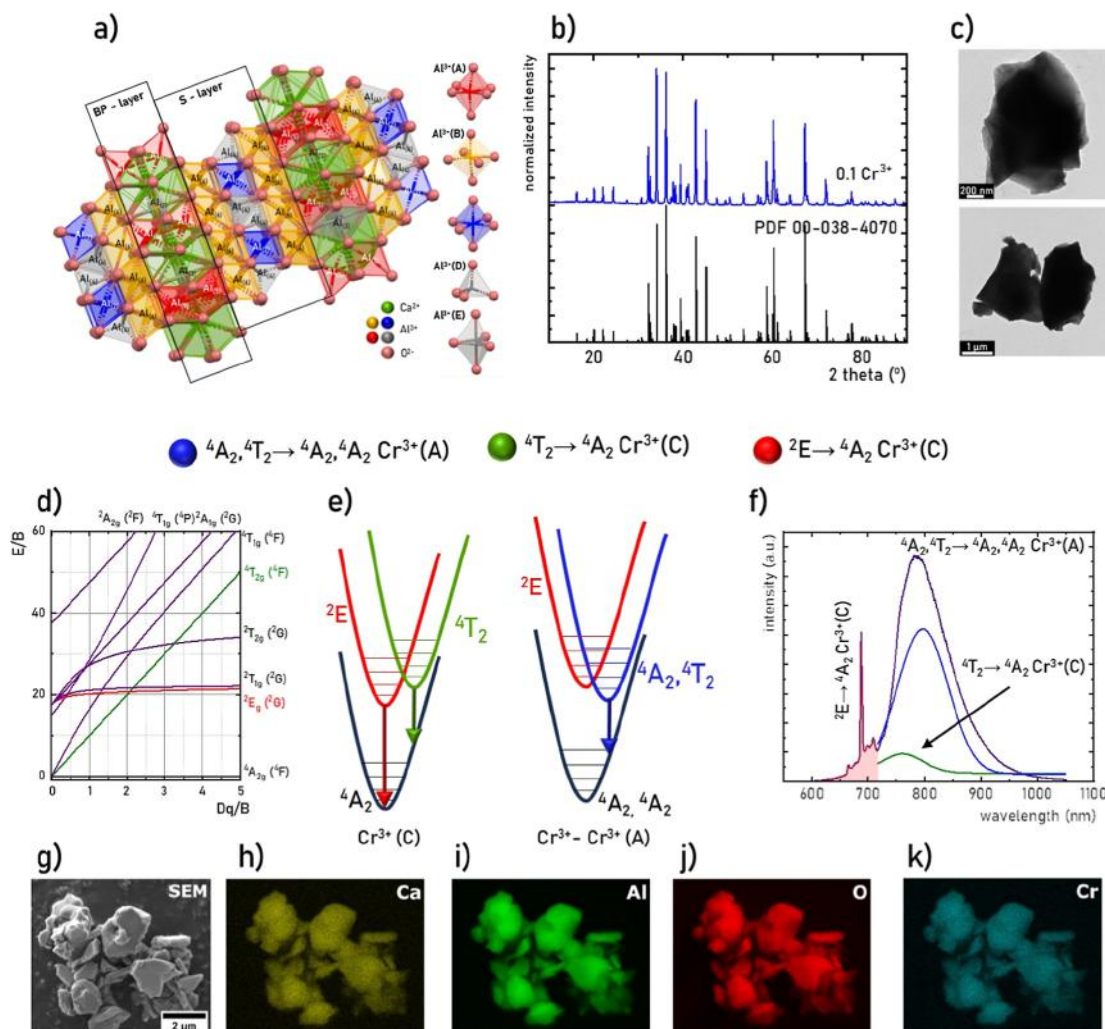


**Figure 2.** Visualization of the structure of  $\text{CaAl}_{12}\text{O}_{19}$  (a); XRD patterns of  $\text{CaAl}_{12}\text{O}_{19}:\text{Cr}^{3+}$  with different concentrations of  $\text{Cr}^{3+}$  ions (b) and representative TEM images for  $\text{CaAl}_{12}\text{O}_{19}:0.83\% \text{Cr}^{3+}$  (c); Tanabe–Sugano diagram for  $3d^3$  electronic configuration (d); simplified configurational coordination diagrams for  $\text{Cr}^{3+}$  in  $\text{Al}^{3+}(\text{C})$  site and for the  $\text{Cr}^{3+}-\text{Cr}^{3+}$  ionic pairs in  $\text{Al}^{3+}(\text{A})$  sites (e) and the room-temperature emission spectra of  $\text{CaAl}_{12}\text{O}_{19}:0.83\% \text{Cr}^{3+}$  (f); representative SEM image (g) and corresponding EDS elemental maps of Ca (h); Al (i); O (j); and Cr (k) in  $\text{CaAl}_{12}\text{O}_{19}:0.83\% \text{Cr}^{3+}$ .

fluorescence diamonds in methanol/ethanol/water (16:3:1) solution as a pressure transmitting medium.

The pressure- and temperature-dependent emission spectra and luminescence decay profiles were measured using an FLS1000 fluorescence spectrometer (Edinburgh Instruments), equipped with a 450 W xenon lamp and a R5509-72 photomultiplier tube from Hamamatsu in a nitrogen-flow cooled housing as the detector. A continuous/pulse laser diode with a wavelength of 445 nm was used as the excitation source for measuring emission spectra and luminescence decay profiles, respectively. A THMS 600 heating-cooling stage from Linkam was used to set and control temperature during measurements with  $0.1^\circ\text{C}$  temperature stability and  $0.1^\circ\text{C}$  set point resolution. To stabilize the temperature of the measured sample, it was incubated at the set temperature for 2 min, and the results were collected after this time. A Druck PACE 5000 was used to apply pressure during pressure-dependent luminescence studies. The high-pressure luminescence measurements were carried out in a DAC purchased from Almax easyLab Diacell  $\mu\text{ScopeDAC-RT(G)}$ . The pressure in the DAC was applied through a nitrogen-fed gas membrane. The DAC was equipped with ultralow fluorescence IIas type diamonds, with 0.4 mm culets. A 250  $\mu\text{m}$  stainless-steel gasket with a diameter of 10 mm was placed between the diamonds. A hole of 140  $\mu\text{m}$  diameter was drilled centrally in the gasket, into which an

appropriate amount of pressure indicator, sample, and drop of a pressure transmitting medium (PTM) were placed. The mixture of methanol/ethanol/water (16:3:1) was used as PTM, and an  $\text{R}_2$ -line of  $\text{Cr}^{3+}$  in doped  $\text{Al}_2\text{O}_3$  (ruby) was used as a pressure indicator.

### 3. RESULTS AND DISCUSSION

Hibonite  $\text{CaAl}_{12}\text{O}_{19}$ , with a magnetoplumbite-type structure, crystallizes in a hexagonal crystal system with a  $P6_3/mmc$  space group.<sup>39–41,43–46</sup> In the structure of  $\text{CaAl}_{12}\text{O}_{19}$ , as shown in its visualization in Figure 2a, there are 12-fold coordinated  $\text{Ca}^{2+}$  ions, as well as  $\text{Al}^{3+}$  ions occupying five different crystallographic positions. There are three types of 6-fold coordinated  $\text{Al}^{3+}$  ions: two of them form distorted octahedra [face-sharing— $\text{Al}^{3+}(\text{A})$  and edge-sharing— $\text{Al}^{3+}(\text{B})$ ] and third type of  $\text{Al}^{3+}$  forming a trigonal antiprism  $\text{Al}^{3+}(\text{C})$ . Additionally, there are also  $\text{Al}^{3+}$  ions which form tetrahedra  $\text{Al}^{3+}(\text{D})$  and trigonal bipyramids  $\text{Al}^{3+}(\text{E})$ . Generally, the structure of  $\text{CaAl}_{12}\text{O}_{19}$  can be described as layered, consisting of blocks alternating along the  $c$ -axis—the spinel layer (S-layer) is arranged alternately with the trigonal bipyramidal BP-layer.

The recorded diffractogram of the  $\text{CaAl}_{12}\text{O}_{19}:\text{Cr}^{3+}$  powder (Figure 2b, see also Figure S2) indicates a high phase purity referring to the reference pattern (PDF 00-038-4070). Additionally, the diffractogram shows that the proposed concentration of the  $\text{Cr}^{3+}$ -dopant was

successfully incorporated into the structure, as evidenced by the absence of additional reflections originating from possible Cr-containing phases. As a result of doping the  $\text{CaAl}_{12}\text{O}_{19}$  structure with  $\text{Cr}^{3+}$  ions, they are incorporated in positions of  $\text{Al}^{3+}$  ions due to their similar ionic radii and identical ionic charge. Specifically,  $\text{Cr}^{3+}$  ions may occupy the crystallographic positions of  $\text{Al}^{3+}(\text{A})$ ,  $\text{Al}^{3+}(\text{B})$ , and  $\text{Al}^{3+}(\text{C})$ , providing a 6-fold coordinated environment. However, as will be presented later, the luminescence of  $\text{Cr}^{3+}$  ions only from  $\text{Al}^{3+}(\text{A})$  and  $\text{Al}^{3+}(\text{C})$  was observed in the spectra of  $\text{CaAl}_{12}\text{O}_{19}:\text{Cr}^{3+}$ . The incorporation of  $\text{Cr}^{3+}$  ions into the crystallographic positions of the  $\text{Al}^{3+}$  ions is further supported by a shift in the reflections toward smaller angles relative to the reference pattern, indicating an expansion of the unit cell.  $\text{Cr}^{3+}$  ions in a 6-fold coordination have an ionic radius of 0.615 Å, while  $\text{Al}^{3+}$  ions in the same coordination are characterized by an ionic radius equal to 0.535 Å. This difference explains the substitution-induced expansion of the unit cell.

As shown in Figure 2c,  $\text{CaAl}_{12}\text{O}_{19}:\text{Cr}^{3+}$  powders exhibit a broad crystallite size distribution, with particles ranging from a few hundred nanometers to a few micrometers. The particles also vary in shape. The morphology of  $\text{CaAl}_{12}\text{O}_{19}:\text{Cr}^{3+}$  particles is typical for powders obtained by a solid-state reaction method. To understand the spectroscopic properties of  $\text{Cr}^{3+}$  ions, the Tanabe–Sugano diagram for the  $3d^3$  electronic configuration should be analyzed<sup>48,49</sup> (Figure 2d). Depending on the value of the crystal field (CF) strength, we can distinguish three regions of weak, intermediate, and strong CFs. Each of these approximations is characterized by different spectroscopic properties of  $\text{Cr}^{3+}$  ions. In the case of strong CF, the  ${}^2\text{E}$  level is the excited state of the lowest energy; hence the luminescence spectrum is dominated by the sharp emission band associated with the  ${}^2\text{E} \rightarrow {}^4\text{A}_2$  electronic transition (Figure 2e). In the case of weak CF, the situation is reversed and it is the  ${}^4\text{T}_2$  level that is the emitting level, and the emission spectrum consists of a broad band associated with the  ${}^4\text{T}_2 \rightarrow {}^4\text{A}_2$  transition. When the energy difference between  ${}^2\text{E}$  and  ${}^4\text{T}_2$  states is low at elevated temperatures, the  ${}^4\text{T}_2$  state can be thermalized, leading to the occurrence of the  ${}^4\text{T}_2 \rightarrow {}^4\text{A}_2$  emission band. For the intermediate situation, both bands are present in the emission spectrum. However, the classification of  $\text{Cr}^{3+}$  dopants interaction between neighboring  $\text{Cr}^{3+}$  ions may lead to the formation of the  $\text{Cr}^{3+}-\text{Cr}^{3+}$  pairs for which the broad emission band associated with  ${}^4\text{A}_2, {}^4\text{T}_2 \rightarrow {}^4\text{A}_2, {}^4\text{A}_2$  transition can be observed (Figure 2e).<sup>50,51</sup> While high concentrations of dopant ions typically promote the formation of ion pairs, clustering has been observed in certain materials even at low dopant ion levels. The interaction mechanisms between ion pairs that result in luminescence are generally explained in the literature through intervalence charge transfer<sup>52</sup> or magnetic exchange coupling.<sup>53,54</sup> Luminescence kinetics is commonly used to identify which mechanism is dominant. For intervalence charge transfer, the luminescence lifetime of the emitting state is expected to be longer compared with that of the isolated ion. In contrast, magnetic interactions between ions relax the selection rules, leading to a shorter excited-state lifetime.<sup>53</sup> The presence of ionic pairs is often indicated by the appearance of an additional emission band, a phenomenon increasingly utilized in recent years for the development of near-infrared light sources.<sup>55–57</sup>

Analysis of the room-temperature emission spectrum of  $\text{CaAl}_{12}\text{O}_{19}:\text{Cr}^{3+}$  shows that it consists of 3 bands: one narrow band associated with the  ${}^2\text{E} \rightarrow {}^4\text{A}_2$  transition (maximum at 686 nm) and two broad bands associated at 760 and 800 nm (Figure 2f). The emission band at 760 nm can be attributed to the  ${}^4\text{T}_2 \rightarrow {}^4\text{A}_2$  luminescence of the  $\text{Cr}^{3+}(\text{C})$  due to its close spectral vicinity to the  ${}^2\text{E} \rightarrow {}^4\text{A}_2$  and their relative thermal dependence described in the further part of the article. However, the assignment of the broad emission band at 800 nm requires closer examination. Although the shape of the  $\text{Cr}^{3+}-\text{Cr}^{3+}$  pairs' emission spectrum is very similar to the  ${}^4\text{T}_2 \rightarrow {}^4\text{A}_2$  band, there are certain unique properties of the  $\text{Cr}^{3+}-\text{Cr}^{3+}$  pairs' luminescence that allow them to be distinguished from the  ${}^4\text{T}_2$  radiative depopulation. In the case of magnetic coupling between  $\text{Cr}^{3+}-\text{Cr}^{3+}$  pairs, the lifetime of the excited level of the pair is much longer (ms range) relative to that observed for the  ${}^4\text{T}_2$  state (tens of

$\mu\text{s}$ ).<sup>50,58,59</sup> In addition, if the strength of the crystal field interacting with  $\text{Cr}^{3+}$  ions is reduced by increasing the average  $\text{Cr}^{3+}-\text{O}^{2-}$  distance, it should result in a red shift of the  ${}^4\text{T}_2 \rightarrow {}^4\text{A}_2$  emission band. However, for  $\text{Cr}^{3+}-\text{Cr}^{3+}$  pairs, such a distancing of the interacting ions should result in a slight blue shift of the emission band of  $\text{Cr}^{3+}-\text{Cr}^{3+}$  pairs. In the case of  $\text{CaAl}_{12}\text{O}_{19}:\text{Cr}^{3+}$ , luminescence kinetics measurements reveal very long luminescence decay times at around 800 nm ( $\tau = 1.79$  ms) and slightly longer times at 686 nm ( $\tau = 2.57$  ms) (Figure S4). The difference in the values of these two lifetimes indicates that they are related to the depopulation of different excited states, and the large values for luminescence at 800 nm unequivocally exclude the association of the observed band with  ${}^4\text{T}_2 \rightarrow {}^4\text{A}_2$  electronic transition. In addition, when  $\text{Al}^{3+}$  was gradually substituted with  $\text{Ga}^{3+}$  ions (causing, due to the difference in ionic radii, an elongation in the  $\text{Cr}^{3+}-\text{O}^{2-}$  distance), a slight blue shift of the broad emission band was observed (Figure S5). The described results clearly indicate that the observed luminescence is associated with  $\text{Cr}^{3+}-\text{Cr}^{3+}$  ionic pairs. In addition, the possibility of forming  $\text{Cr}^{3+}-\text{Cr}^{3+}$  pairs in  $\text{CaAl}_{12}\text{O}_{19}:\text{Cr}^{3+}$  was confirmed by EPR studies also for low concentrations of dopant ions.<sup>51</sup> The assignment of  $\text{Cr}^{3+}-\text{Cr}^{3+}$  pairs to the A  $\text{Al}^{3+}$  site is associated with the shortest interion distance for these ions of 2.7 Å.

The X-band EPR spectrum shown in Figure S6 reveals the incorporation of  $\text{Cr}^{3+}$  in several isolated sites and hints at the potential formation of  $\text{Cr}^{3+}-\text{Cr}^{3+}$  pairs within  $\text{CaAl}_{12}\text{O}_{19}$ . The powder spectrum features multiple signals in the 0–870 mT range, which originate from  $\text{Cr}^{3+}$ -related paramagnetic centers in different site symmetries. Based on the simulation results of multifrequency EPR data,<sup>60</sup> the signals observed at 190, 570, and 650 mT are assigned to axial symmetry  $\text{Al}^{3+}(\text{A})$  sites, whereas the resonances at 164, 208, 618, and 713 mT can be attributed to the highly distorted  $\text{Al}^{3+}(\text{B})$  sites. The interpretation of the symmetrically intensive line at 355 mT is ambiguous. On one hand, such  $\text{Cr}^{3+}$  signals are prevalent in cubic hosts,<sup>61</sup> and the  $\text{CaAl}_{12}\text{O}_{19}$  lattice has the high-symmetry  $\text{Al}^{3+}(\text{C})$  position. However, in a study of the isostructural  $\text{SrAl}_{11.88-x}\text{Ga}_x\text{O}_{19}:\text{Cr}^{3+}$  compound, a similar signal was linked to the interaction within  $\text{Cr}^{3+}-\text{Cr}^{3+}$  pairs.<sup>55</sup> Conversely, the two satellite lines flanking the 355 mT signal (marked with asterisks in the inset of Figure S6) could additionally indicate the presence of chromium pairs in  $\text{CaAl}_{12}\text{O}_{19}$ . A study of  $\text{Cr}^{3+}$ -doped  $\text{LaMgAl}_{11}\text{O}_{19}$  single crystals has analyzed the angular dependence of these small satellites, providing evidence for the occurrence of  $\text{Cr}^{3+}-\text{Cr}^{3+}$  pairs in these types of materials.<sup>62</sup> In summary,  $\text{Cr}^{3+}$  ions substitute the available octahedral Al sites in  $\text{CaAl}_{12}\text{O}_{19}$ , resulting in the formation of both isolated  $\text{Cr}^{3+}$  centers and pairs. However, further EPR studies of single-crystalline samples are necessary to gain more definitive conclusions. The EDS analysis of  $\text{CaAl}_{12}\text{O}_{19}:0.83\% \text{Cr}^{3+}$  revealed a homogeneous distribution of the elemental composition of obtained powders (Figure 2g–k).

To verify the structural stability of the synthesized material, Raman spectra for the studied material were measured as a function of the pressure. The obtained Raman spectrum for the  $\text{CaAl}_{12}\text{O}_{19}:\text{Cr}^{3+}$  material at ambient pressure has four bands, which are initially located at  $\approx 332$ , 395, 618, and 771  $\text{cm}^{-1}$ , as displayed in Figure 3a,b. In general, it is worth noting that the main bands in the Raman spectra of hibonite-type structures, such as the investigated  $\text{CaAl}_{12}\text{O}_{19}$  material, are associated with the Al–O vibrations within  $(\text{AlO}_4)^{5-}$  groups.<sup>63</sup> The character of the Raman spectra may depend on the crystal orientation relative to laser beam polarization;<sup>64</sup> however, this effect is of minor importance in the case of the small-sized polycrystalline materials. The Raman mode at around 332  $\text{cm}^{-1}$  corresponds to the bending vibrations ( $\nu_2$ ) within the  $(\text{AlO}_4)^{5-}$  groups; the one at 395  $\text{cm}^{-1}$  is assigned to the stretching vibrations ( $\nu$ ) of Al–O–Al in  $\text{Al}_2\text{O}_3^{12-}$  groups; on the other hand, the band at 618  $\text{cm}^{-1}$  originates from symmetric stretching vibrations ( $\nu_1$ ) in  $(\text{AlO}_6)^{9-}$  groups; whereas the last peak, centered around 771  $\text{cm}^{-1}$  is associated both with symmetric ( $\nu_1$ ) and asymmetric ( $\nu_3$ ) vibrations within  $(\text{AlO}_4)^{5-}$  groups.<sup>64</sup>

With pressure elevation (compression), the energies of the phonon modes increase, and the corresponding Raman bands shift toward



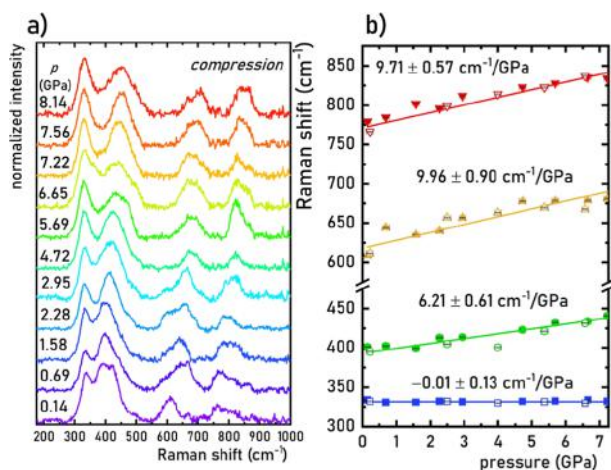


**Figure 3.** Normalized Raman spectra for the CaAl<sub>12</sub>O<sub>19</sub>:Cr<sup>3+</sup> material measured for different pressure values, during the compression cycle (a). Determined energies (peak centroids) of the most intense phonon modes as a function of pressure (b); filled symbols represent compression data, and empty ones represent decompression data; the continuous lines are the linear fits applied for determination of the pressure shift rates of the corresponding Raman modes.

higher wavenumbers, as presented in Figure 3b. The observed phenomenon originates from the bond shortening, namely, decrease of the interatomic distances in the compressed structures. It is worth noting that the determined spectral shifts are monotonous and linear, and the overall shape of the spectra does not significantly change, ensuring good structural stability of the examined material. Moreover, there are no effects of vanishing or appearing new peaks (Raman modes), which additionally confirms the phase stability of this crystal structure in the analyzed pressure range. It is worth noting that the peak around 332 cm<sup>-1</sup> negligibly shifts with pressure, resulting in improved splitting/separation from the second band centered initially at around 394 cm<sup>-1</sup> during the compression process. The calculated shift rates (cm<sup>-1</sup> GPa<sup>-1</sup>) for the observed Raman peaks are given in Table S1 in the Supporting Information data. Noteworthy, the observed deterioration of the Raman signal with pressure (lowering signal-to-noise ratio) is associated with the increasing strains and

crystal defects in the compressed crystal structures, which is a typical effect in Raman studies. Importantly, on releasing the pressure (decompression), spectral positions and shapes of all Raman bands return to the initial state (see Figures 3b and S6). The good agreement of the compression–decompression data indicates the reversibility of the high-pressure experiments, which is fundamental for optical sensing applications, i.e., development of new luminescent manometers.

High-pressure spectroscopic studies of Cr<sup>3+</sup>-based phosphors provide essential insights into dopant properties. Therefore, for CaAl<sub>12</sub>O<sub>19</sub>:Cr<sup>3+</sup>, investigations were conducted at room temperature across a pressure range from ambient to 6.76 GPa (Figure 4a). An increase in pressure results in a slight reduction of the CaAl<sub>12</sub>O<sub>19</sub>:Cr<sup>3+</sup> emission intensity, which is a common outcome for such kinds of compression experiments, due to the generation of strains and structural defects acting as quenching centers. Notably, this intensity change was fully reversible upon decompression, without any observed plastic deformations of the structure. Additionally, a slight red shift in the emission maximum of the <sup>2</sup>E<sub>g</sub> → <sup>4</sup>A<sub>2g</sub> (Cr<sup>3+</sup> (C)) band was detected as expected, being attributed to the increased covalency of the Cr<sup>3+</sup>–O<sup>2-</sup> bonds under compression, leading to the reduction of the energy between the corresponding ground and excited (emitting) state.<sup>12,65,66</sup>

Conversely, no spectral shift in the <sup>4</sup>A<sub>2</sub>, <sup>4</sup>T<sub>2</sub> → <sup>4</sup>A<sub>2</sub>, <sup>4</sup>A<sub>2</sub> emission band was detected with increasing pressure in the case of the Cr<sup>3+</sup>(A) site (Figure 4b). When the broad emission band observed in the emission spectrum of CaAl<sub>12</sub>O<sub>19</sub>:Cr<sup>3+</sup> was associated with the <sup>4</sup>T<sub>2</sub> → <sup>4</sup>A<sub>2</sub> electronic transition of Cr<sup>3+</sup> ions, the absence of shift would be unexpected, given the high sensitivity of the <sup>4</sup>T<sub>2g</sub> level energy to changes in crystal field strength according to the Tanabe–Sugano diagram for the 3d<sup>3</sup> electronic configuration, which would typically result in a significant blue shift upon compression of a given material.<sup>18,36,42,67,68</sup> The unusual behavior of the observed band is additional confirmation that it is related to the Cr<sup>3+</sup>–Cr<sup>3+</sup> pair luminescence. The simultaneous spectral shift of the <sup>2</sup>E<sub>g</sub> → <sup>4</sup>A<sub>2g</sub> band for the Cr<sup>3+</sup>(C) site in the same material corroborates the compression of CaAl<sub>12</sub>O<sub>19</sub>:Cr<sup>3+</sup> by applied pressure. Two effects may contribute to the insensitivity of the spectral position of the Cr<sup>3+</sup>–Cr<sup>3+</sup> band under compression. The first effect may be related to the fact that compression induces similar changes in the energy of both the ground <sup>4</sup>A<sub>2</sub>, <sup>4</sup>A<sub>2</sub> and the excited states <sup>4</sup>A<sub>2</sub>, <sup>4</sup>T<sub>2</sub>, thereby preserving the energy difference between them. The second effect may be associated with the small distance between interacting ions

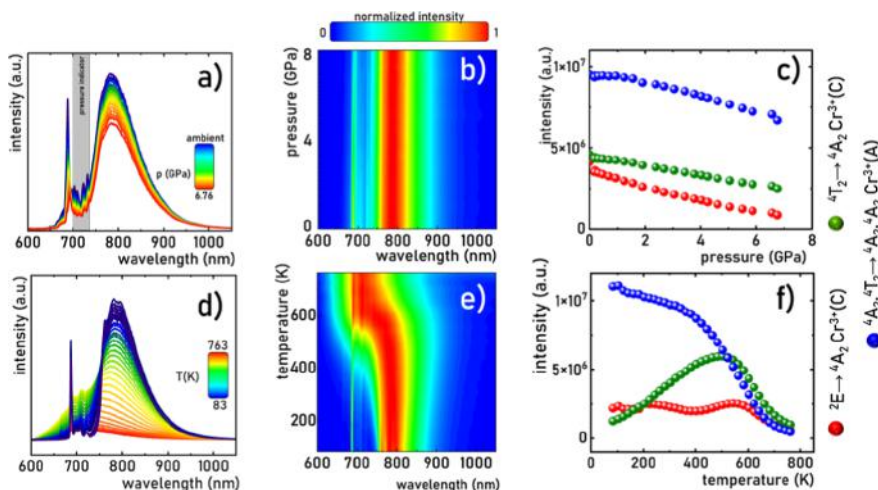


**Figure 4.** Room-temperature emission spectra of CaAl<sub>12</sub>O<sub>19</sub>:Cr<sup>3+</sup> measured as a function of the applied pressure (a) and the corresponding pressure maps of normalized emission spectra (b); the integrated emission intensities of <sup>4</sup>T<sub>2</sub> → <sup>4</sup>A<sub>2</sub> Cr<sup>3+</sup>(A), <sup>2</sup>E<sub>g</sub> → <sup>4</sup>A<sub>2</sub> Cr<sup>3+</sup>(C), and <sup>4</sup>A<sub>2</sub>, <sup>4</sup>T<sub>2</sub> → <sup>4</sup>A<sub>2</sub>, <sup>4</sup>A<sub>2</sub> Cr<sup>3+</sup>(A) determined based on the deconvolution of emission spectra as a function of pressure (c); the influence of temperature on the emission spectra of CaAl<sub>12</sub>O<sub>19</sub>:Cr<sup>3+</sup> (d) with corresponding thermal maps of normalized spectra (e); the influence of temperature on the integrated emission intensities of particular Cr<sup>3+</sup> positions (f).

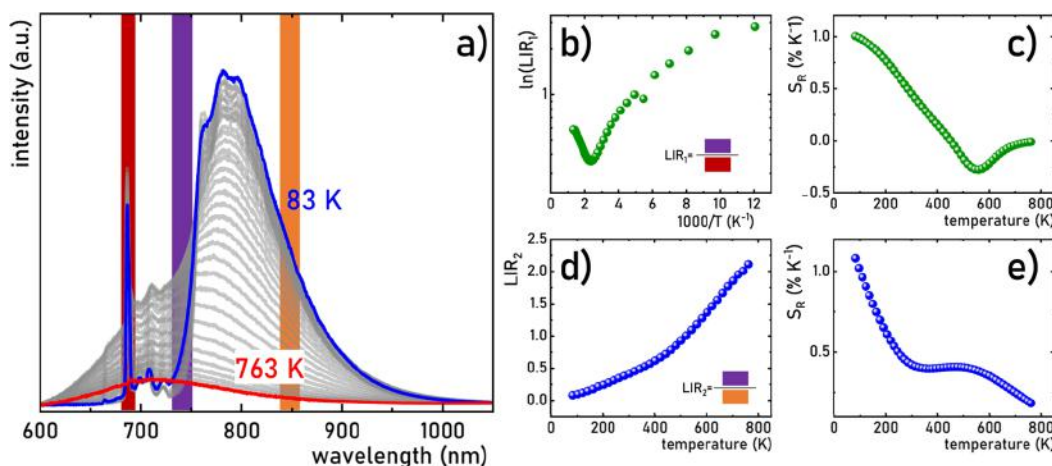


**Figure 5.** Temperature-dependent emission spectra of  $\text{CaAl}_{12}\text{O}_{19}:\text{Cr}^{3+}$ , with the marked spectral ranges analyzed for  $\text{LIR}_1$  and  $\text{LIR}_2$  determination (a); thermal variations of  $\text{LIR}_1$  (b) and  $\text{LIR}_2$  (d), including the corresponding relative sensitivities ( $S_R$ ) (c,e), respectively.

forming pairs, such that material compression does not cause a significant change in the magnetic coupling, which leads to the formation of the excited state  $^4\text{A}_2$ ,  $^4\text{T}_2$ . Regardless of the fact which of these effects dominates, this unusual phenomenon suggests high potential in sensing applications (Figure 4c).

On the other hand, temperature variations significantly alter the  $\text{CaAl}_{12}\text{O}_{19}:\text{Cr}^{3+}$  emission spectrum, not only by changing the ratio of the  $^2\text{E}_g \rightarrow ^4\text{A}_{2g}$   $\text{Cr}^{3+}(\text{C})$  to  $^4\text{A}_2$ ,  $^4\text{T}_2 \rightarrow ^4\text{A}_2$   $\text{Cr}^{3+}(\text{A})$  band intensities but also by spectrally shifting the  $^4\text{A}_2$ ,  $^4\text{T}_2 \rightarrow ^4\text{A}_2$ ,  $^4\text{A}_2$  band. At 83 K, the spectrum is dominated by the  $^4\text{A}_2$ ,  $^4\text{T}_2 \rightarrow ^4\text{A}_2$   $\text{Cr}^{3+}(\text{A})$  band, with a clear visibility of the  $^2\text{E}_g \rightarrow ^4\text{A}_{2g}$  emission line associated with  $\text{Cr}^{3+}(\text{C})$  (Figure 4d). An increase in temperature leads to the quenching of both  $\text{Cr}^{3+}(\text{C})$  and  $\text{Cr}^{3+}-\text{Cr}^{3+}(\text{A})$  luminescence through nonradiative depopulation of emitting levels. However, the thermal quenching of  $\text{Cr}^{3+}-\text{Cr}^{3+}(\text{A})$  is more rapid than that of  $\text{Cr}^{3+}(\text{C})$ , clearly indicating a lower activation energy for  $\text{Cr}^{3+}-\text{Cr}^{3+}(\text{A})$ . Above approximately 400 K, the luminescence intensity of  $^4\text{T}_2 \rightarrow ^4\text{A}_2$ ,  $\text{Cr}^{3+}(\text{C})$  begins to predominate, suggesting thermalization of the  $^4\text{T}_2$  state with respect to the  $^2\text{E}$   $\text{Cr}^{3+}(\text{C})$  ions (Figure 4e). This hypothesis is supported by the analysis of thermal variation of the integral emission intensity, associated with different  $\text{Cr}^{3+}$  sites, revealing a noticeable increase in the  $^4\text{T}_2 \rightarrow ^4\text{A}_2$   $\text{Cr}^{3+}(\text{C})$  luminescence intensity, corresponding to the range of dynamic quenching in  $\text{Cr}^{3+}(\text{C})$  luminescence intensity. The apparent low thermal sensitivity of the  $^2\text{E} \rightarrow ^4\text{A}_2$   $\text{Cr}^{3+}(\text{C})$  luminescence intensity, as illustrated in Figure 4f, results from the spectral overlap of signals from  $^4\text{T}_2 \rightarrow ^4\text{A}_2$  and  $^2\text{E} \rightarrow ^4\text{A}_2$ , affecting the measured values.

The pronounced changes in the shape of the emission spectrum under temperature indicate the high potential of the  $\text{CaAl}_{12}\text{O}_{19}:\text{Cr}^{3+}$  material for temperature sensing purposes. The clear difference in the thermal dependence of luminescence intensities associated with different crystallographic positions of  $\text{Cr}^{3+}$  ions enables a ratiometric approach for temperature readout (Figure 5a). The effect of temperature on the observed changes in the shape of emission spectra and thus the thermometric performance of  $\text{CaAl}_{12}\text{O}_{19}:\text{Cr}^{3+}$  can be analyzed by (1) deconvolution of emission spectra or (2) luminescence intensity analysis integrated in two spectral ranges. Deconvolution of the emission spectra clearly indicates that an increase in temperature alters the relative emission intensity of  $^4\text{A}_2$ ,  $^4\text{T}_2 \rightarrow ^4\text{A}_2$ ,  $^4\text{A}_2$   $\text{Cr}^{3+}-\text{Cr}^{3+}(\text{A})$  with respect to  $^4\text{T}_2 \rightarrow ^4\text{A}_2$   $\text{Cr}^{3+}(\text{C})$  (Figure S7). On the other hand, to implement the second approach of the analysis of the emission spectra of  $\text{CaAl}_{12}\text{O}_{19}:\text{Cr}^{3+}$ , luminescence intensities were integrated in the 680–692 nm, 732–750 nm, and 840–860 nm ranges, corresponding to  $^2\text{E} \rightarrow ^4\text{A}_2$   $\text{Cr}^{3+}(\text{C})$ ,  $^4\text{T}_2 \rightarrow ^4\text{A}_2$   $\text{Cr}^{3+}(\text{C})$ , and  $^4\text{A}_2$ ,  $^4\text{T}_2 \rightarrow ^4\text{A}_2$ ,  $^4\text{A}_2$   $\text{Cr}^{3+}-\text{Cr}^{3+}(\text{A})$ , respectively. Although this method of intensity analysis, unlike band deconvolution, limits the sensitivity of the readout due to partial overlap of emission bands, its main advantage is simplicity of application,

requiring no additional analytical procedures. In order to obtain a high relative sensitivity of the ratiometric luminescent thermometer, it is desirable to select spectral bands used for analysis that enable the opposite thermal monotonicity of the signals. Since thermal quenching of the luminescence with enhancement in the corresponding thermal range for  $\text{Cr}^{3+}(\text{C})$  and  $\text{Cr}^{3+}(\text{A})$  was observed, the following two luminescence intensity ratios were proposed

$$\text{LIR}_1 = \frac{\text{Cr}^{3+}(\text{C})}{\text{Cr}^{3+}(\text{A})} = \frac{\int_{732\text{nm}}^{750\text{nm}} ^4\text{T}_2 \rightarrow ^4\text{A}_2[\text{Cr}^{3+}(\text{C})]d\lambda}{\int_{680\text{nm}}^{692\text{nm}} ^2\text{E} \rightarrow ^4\text{A}_2[\text{Cr}^{3+}(\text{C})]d\lambda} \quad (1)$$

$$\text{LIR}_2 = \frac{\text{Cr}^{3+}(\text{C})}{\text{Cr}^{3+}(\text{A})} = \frac{\int_{732\text{nm}}^{750\text{nm}} ^4\text{T}_2 \rightarrow ^4\text{A}_2[\text{Cr}^{3+}(\text{C})]d\lambda}{\int_{840\text{nm}}^{860\text{nm}} ^4\text{T}_2, \text{A}_2 \rightarrow ^4\text{A}_2, \text{A}_2[\text{Cr}^{3+}(\text{A}) - \text{Cr}^{3+}(\text{A})]d\lambda} \quad (2)$$

In order to verify if the appearing at elevated temperature of the  $^4\text{T}_{2g} \rightarrow ^4\text{A}_{2g}$  band results from thermalization of the  $^4\text{T}_2$  state in  $\text{Cr}^{3+}(\text{C})$  site, the thermal dependence of the  $\text{LIR}_1$  parameter was presented in the form of  $\ln(\text{LIR}_1)$  vs.  $1000/T$  plot (Figure 5b). The almost linear  $\ln(\text{LIR}_1)$  relationship in the 2.0–4.1  $1000/T$  range (243–500 K) may, according to Boltzmann distribution,<sup>69</sup> suggest thermal coupling between these levels. Some deviations from linear trend above  $1000/T = 4.1$  result from the low emission intensity of the  $^2\text{E} \rightarrow ^4\text{A}_2$  and spectral overlapping of the signal with the  $^4\text{T}_2 \rightarrow ^4\text{A}_2$  band. The presented trend indicates a change in the monotonicity of the  $\ln(\text{LIR}_1)$  waveform for temperatures around 400 K ( $\ln(\text{LIR}_1) = 2$ ), and this is related to a significant thermal enhancement of the luminescence intensity of  $^4\text{T}_2 \rightarrow ^4\text{A}_2$   $\text{Cr}^{3+}(\text{C})$  whose emission band overlaps spectrally with that of  $\text{Cr}^{3+}-\text{Cr}^{3+}(\text{A})$ , disturbing the temperature reading. In general, change in the monotonicity of the thermal dependence of luminescence intensity ratio (LIR) prevents reliable temperature readout. Therefore, it is important to note that the operational temperature range of the  $\text{LIR}_1$ -based luminescence thermometer is restricted to 83–500 K. Thermal dependence of both  $\text{LIR}_1$  and  $\text{LIR}_2$  can be fitted using empirical polynomial curves (see eq S1 and Figure S8). Quantification of the observed thermal variation of  $\text{LIR}_1$  can be done by determining the relative temperature sensitivity according to the equation

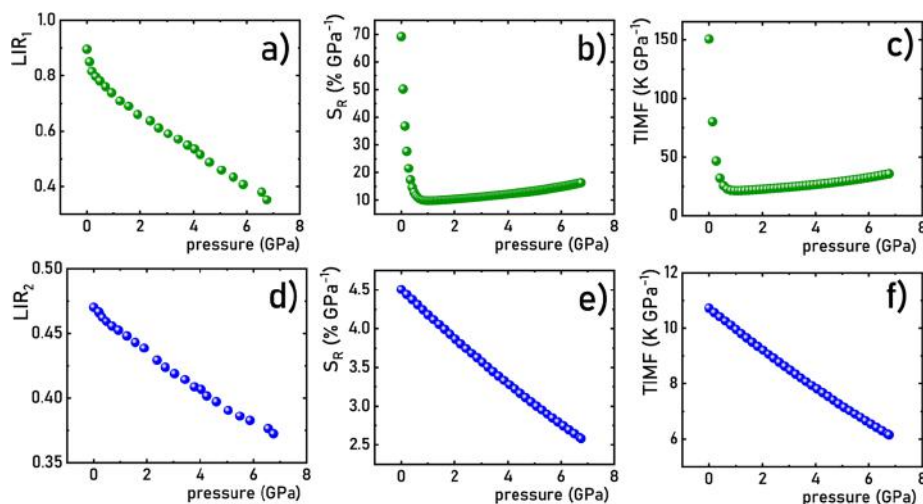


**Figure 6.** Influence of pressure on LIR<sub>1</sub> (a) and LIR<sub>2</sub> (d) and corresponding manometric  $S_R$  (b,e), respectively; the influence of pressure on TIMF parameter for LIR<sub>1</sub>- (c) and LIR<sub>2</sub>- (f) based ratiometric luminescent manometers.

$$S_R = \frac{1}{LIR} \frac{\Delta LIR}{\Delta T} \times 100\% \quad (3)$$

where  $\Delta LIR$  is the temperature change corresponding to a change in temperature by  $\Delta T$  (Figure 5c). Although many works on luminescence thermometry analyze the absolute value of relative sensitivity, information about the change in monotonicity of the LIR is lost in this way. However, the monotonicity of LIR (or any other thermometric parameter) is very important information because it directly determines the useful temperature range of the luminescence thermometer. A reliable temperature readout imposes the requirement that a given LIR value must correspond to only one temperature value. The change in monotonicity of the LIR is reflected in the change in the sign of the relative sensitivity. Therefore, in this work, the real values of  $S_R$  are analyzed. The initially positive values of relative sensitivity for LIR<sub>1</sub> successively decrease with temperature elevation, i.e., from ca. 1% K<sup>-1</sup>, reaching negative values above 400 K, which is due to the mentioned effect of the change in monotonicity in the case of LIR<sub>1</sub>. On the other hand, the described apparent spectral shift of the broadband luminescence associated with thermal enhancement of <sup>4</sup>T<sub>2</sub> → <sup>4</sup>A<sub>2</sub> Cr<sup>3+</sup>(C) emission allows the use of LIR<sub>2</sub> for temperature sensing (Figure 5d). LIR<sub>2</sub> successively increased over the entire analyzed temperature range. Therefore, the useful temperature range of this luminescence thermometer is much wider than that of LIR<sub>1</sub>, and it covers 83–763 K. The obtained sensitivities drop from 1.2% K<sup>-1</sup> for 83 K and rank at about 0.45% K<sup>-1</sup> in the 300–550 K range (Figure 5e). It is worth noticing that when the ratio of the emission intensities of <sup>4</sup>A<sub>2</sub>, <sup>4</sup>T<sub>2</sub> → <sup>4</sup>A<sub>2</sub>, <sup>4</sup>A<sub>2</sub> Cr<sup>3+</sup>-Cr<sup>3+</sup>(A) to <sup>4</sup>T<sub>2</sub> → <sup>4</sup>A<sub>2</sub> Cr<sup>3+</sup>(C) bands obtained from deconvolution of the emission spectra is used for temperature sensing, a higher  $S_R = 1.4\%$  K<sup>-1</sup> at 650 K can be reached (Figure S9).

To assess the manometric performance of CaAl<sub>12</sub>O<sub>19</sub>:Cr<sup>3+</sup>, both sensor parameters, namely LIR<sub>1</sub> and LIR<sub>2</sub>, were analyzed as a function of pressure during compression and decompression cycles (Figure S4). The results clearly show a monotonic, more than 2-fold decrease in the value of LIR<sub>1</sub> over the analyzed pressure range (Figure 6a). The complete reversibility of the observed course obtained within the framework of material decompression excludes the presence of plastic deformation of the material, confirming the reliability of the obtained readout. Pressure dependence of LIR<sub>1</sub> and LIR<sub>2</sub> can be fitted using experimental polynomial curves (see eq S2 and Figure S11). The relatively high change in the LIR<sub>1</sub> value, especially observed in the low pressure range (below 0.5 GPa), is reflected in the values of relative pressure sensitivity (determined by analogy with eq 3, substituting  $\Delta p$  for  $\Delta T$ ). The maximum sensitivity value of 70% GPa<sup>-1</sup> obtained at ambient conditions decreases gradually with increasing pressure, and above 1 GPa displays a slight increase, maintaining values exceeding

10% GPa<sup>-1</sup> throughout the analyzed pressure range (Figure 6b). Importantly, the obtained relative sensitivity values for LIR<sub>1</sub> should be compared to the relative thermal sensitivity of this parameter. For this purpose, the thermal invariability manometric factor (TIMF) was determined according to the following equation<sup>70</sup>

$$TIMF = \frac{S_{R,p}}{S_{R,T}} \quad (4)$$

where  $S_{R,p}$  and  $S_{R,T}$  represent manometric and thermometric relative sensitivities, respectively (the room-temperature  $S_{R,T}@T = 293$  K was used for TIMF calculations in this work). The value of this parameter defines the temperature change (in K) required to induce LIR changes corresponding to a pressure change of 1 GPa. The obtained relatively high values of this parameter (TIMF = 150 K GPa<sup>-1</sup>) indicate good reliability of this manometric parameter (Figure 6c). While some ratiometric luminescence manometers reported<sup>71,72</sup> to date exhibit significantly higher TIMF values than those of CaAl<sub>12</sub>O<sub>19</sub>:Cr<sup>3+</sup>, it is important to recognize that the suitability of TIMF values depends on the specific application requirements for achieving a thermally invariant pressure readout. In general, higher TIMF values are preferred; however, in cases where only small temperature fluctuations are expected within the system (on the order of a few degrees or tens of degrees), TIMF values exceeding 100 K GPa<sup>-1</sup> are sufficient to ensure reliable pressure measurement. A close analysis of the thermal variation thermometric relative sensitivity values for LIR<sub>1</sub> (Figure 5c) may suggest that a further increase in temperature, leading to a decrease in the thermal  $S_R$ , will allow additional amplification of the TIMF parameter, increasing the accuracy of the pressure reading. However, in order to ultimately verify the validity of such a hypothesis, it is necessary to perform experiments allowing for simultaneous changes in pressure and temperature, which are beyond our experimental capabilities. On the other hand, LIR<sub>2</sub> shows only small changes in the analyzed pressure range, which is related to the insensitivity of the spectral position of the <sup>4</sup>A<sub>2</sub>, <sup>4</sup>T<sub>2</sub> → <sup>4</sup>A<sub>2</sub>, <sup>4</sup>A<sub>2</sub> (Cr<sup>3+</sup>(A)) band to pressure changes described above (Figure 6d). Hence, the resulting  $S_R$  values are very small, decreasing from 4.5% GPa<sup>-1</sup> at 0.1 GPa to 2.6% GPa<sup>-1</sup> at 6.76 GPa (Figure 6e). The small TIMF values for LIR<sub>2</sub> (TIMF < 11 K GPa<sup>-1</sup>) confirm two main aspects, i.e., (1) LIR<sub>2</sub> is extremely sensitive to changes in temperature and (2) high pressure changes are required to bring out changes in LIR<sub>2</sub>, confirming its low manometric sensitivity (Figure 6f). Comparison of thermal and pressure variation analysis of LIR<sub>1</sub> and LIR<sub>2</sub> indicate that LIR<sub>1</sub> can be successfully used to read pressure with little thermal sensitivity, while LIR<sub>2</sub> shows good thermal sensing performance, insensitive to pressure changes.



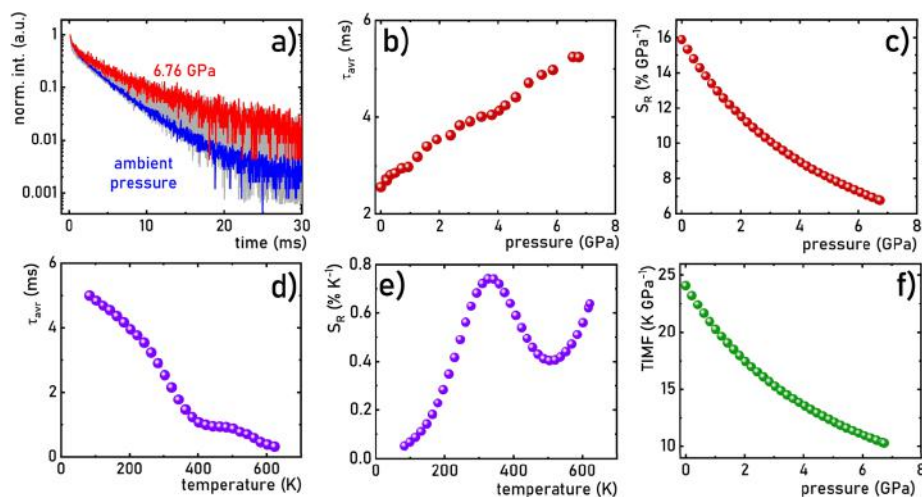


**Figure 7.** Luminescence decay profiles for the  ${}^2E_g$  state  $\text{Cr}^{3+}(\text{C})$  measured as a function of applied pressure (a) and the corresponding  $\tau_{\text{avr}}$  as a function of pressure (b) and temperature (c); relative pressure (d) and thermal (e) sensitivities of the lifetime-based sensor and the influence of pressure on the TIMF parameter for lifetime-based luminescence manometer based on  $\text{CaAl}_{12}\text{O}_{19}:\text{Cr}^{3+}$  (f).

An additional benefit of using the  $\text{CaAl}_{12}\text{O}_{19}:\text{Cr}^{3+}$  material for sensing applications lies in the balanced spectral distance between the analyzed areas used for  $\text{LIR}_1$  and  $\text{LIR}_2$  determination. As is well-known, too high proximity of the spectral windows analyzed in the LIR technique can impede an optical readout by making it difficult to select suitable optical filters. However, as demonstrated by Jaque et al.,<sup>73</sup> the dispersive dependence of light absorption and scattering by the medium present in the optical path between the detector and the phosphor can significantly modify the shape of the emission spectrum and thus the reliability of the readout. From this perspective, it is desirable to implement a ratiometric readout for spectral ranges with low relative separation allowing reduction of the described adverse effects. From this perspective, the distance between the first and last windows used to determine  $\text{LIR}_1$  and  $\text{LIR}_2$  for  $\text{CaAl}_{12}\text{O}_{19}:\text{Cr}^{3+}$  of 180 nm seems favorable. A comparison of the sensing performance of ratiometric manometers described in the literature makes it possible to conclude that the manometric relative sensitivities of  $\text{CaAl}_{12}\text{O}_{19}:\text{Cr}^{3+}$  for  $\text{LIR}_1$  are significantly higher than those obtained for most luminescent manometers based on the luminescence of  $\text{Ln}^{3+}$  ions<sup>74</sup> such as  $S_{\text{R,p}} = 2.09\% \text{ GPa}^{-1}$  for  $\text{NaBiF}_4:\text{Yb}^{3+}, \text{Er}^{3+}$ ,<sup>75</sup>  $S_{\text{R,p}} = 3.86\% \text{ GPa}^{-1}$  for  $\text{NaErF}_4:\text{Tm}@\text{NaLuF}_4:\text{Er}^{3+}$ ,<sup>76</sup>  $S_{\text{R,p}} = 18.5\% \text{ GPa}^{-1}$  for  $\text{CaLu}_{0.69}\text{Yb}_{0.28}\text{Er}_{0.03}\text{F}@\text{CaLuF}_4$ ,<sup>77</sup>  $S_{\text{R,p}} = 40\% \text{ GPa}^{-1}$  for  $\text{NaY}_{0.69}\text{Yb}_{0.28}\text{Er}_{0.03}\text{F}@\text{NaYF}_4$ ,<sup>77</sup> and  $S_{\text{R,p}} = 13.8\% \text{ GPa}^{-1}$  for  $\text{SrB}_4\text{O}_7:\text{Sm}^{3+}, \text{Eu}^{2+78}$  and significantly higher than those reported for other materials doped with  $\text{Cr}^{3+}$  ions such as  $S_{\text{R,p}} = 4.7\% \text{ GPa}^{-1}$  for  $\text{Li}_2\text{Mg}_3\text{TiO}_6:\text{Cr}^{3+}$ ,<sup>79</sup>  $S_{\text{R,p}} = 9.83\% \text{ GPa}$  for  $\text{MgO}/\text{Cr}^{3+}$ ,<sup>71</sup> and  $S_{\text{R,p}} = 57\% \text{ GPa}$  for  $\text{Li}_3\text{Sc}_2(\text{PO}_4)_3:\text{Cr}^{3+}$ .<sup>80</sup> On the other hand, reports of significantly higher relative sensitivity values, such as  $S_{\text{R,p}} = 120\% \text{ GPa}$  for  $\text{LiScGeO}_4:\text{Cr}^{3+}$ ,<sup>72</sup> can be found in the literature. The comparison performed allows us to conclude that  $\text{CaAl}_{12}\text{O}_{19}:\text{Cr}^{3+}$  presents extremely favorable manometric performance in a ratiometric approach.

In the case of the luminescence kinetics of phosphors doped with  $\text{Cr}^{3+}$ , the lifetime of the  ${}^2E_g$  excited level is expected to be longer than that for  ${}^4T_{2g}$  due to the spin-forbidden transition (Figure 7a, fitting curves presented in Figures S12–23). As is well-known, the compression of material not only alters the emission spectrum but also impacts luminescence kinetics. In the case of  $\text{Cr}^{3+}$  ions, the coupling between the  ${}^2E_g$  and  ${}^4T_{2g}$  levels modifies the probability of radiative depopulation of the emitting level, shortening the lifetime of the  ${}^2E_g$  level. Therefore, according to the Tanabe–Sugano diagram, the increase in the strength of the crystal field for  $\text{Cr}^{3+}(\text{C})$  associated with the compression of the material causes an increase in the energy of the  ${}^4T_{2g}$  level. Thus, the coupling strength between these levels is reduced, leading to an elongation of the luminescence kinetics.

Consequently, for  $\text{CaAl}_{12}\text{O}_{19}:\text{Cr}^{3+}$  an increase in pressure results in the elongation of  $\tau_{\text{avr}}$  from 2.3 ms at ambient pressure to 5.1 ms at 6.76 GPa (Figure 7b). Pressure dependence of  $\tau_{\text{avr}}$  can be fitted by a polynomial function as presented in Figure S24. This notable increase in lifetime can be used in luminescent manometers. The determined values of relative sensitivity to pressure changes indicate that it decreases from 16%  $\text{GPa}^{-1}$  at around ambient pressure, down to 7%  $\text{GPa}^{-1}$  at 6.76 GPa (Figure 7c). On the other hand, an increase in temperature leads to an increase in the probability of nonradiative depopulation of emitting levels through the intersection point between the  ${}^4A_{2g}$  and  ${}^2E_g$  parabolas. Therefore,  $\tau_{\text{avr}}$  shortens with temperature from 5.1 ms at 83 K to 0.3 ms at 633 K (Figures 7d, S25, fitting of thermal dependence of  $\tau_{\text{avr}}$  using polynomial function is presented in Figure S26). The fastest rate of  $\tau_{\text{avr}}$  shortening is observed in the 200–350 K range, which results in maximal thermal sensitivities of 0.75%  $\text{K}^{-1}$  at 325 K (Figure 7e).

Analysis of the TIMF values for the lifetime-based manometer indicates that as the pressure increases, its value decreases from about 24 K  $\text{GPa}^{-1}$  to about 10 K  $\text{GPa}^{-1}$  at 6.76 GPa (Figure 7f). A sensitivity comparison of the values obtained for other lifetime-based luminescence manometers indicates that the values obtained for  $\text{CaAl}_{12}\text{O}_{19}:\text{Cr}^{3+}$  exceed those obtained for lanthanide-doped phosphors (7.7%  $\text{GPa}^{-1}$  for  $\text{SrF}_2:\text{Er}^{3+}, \text{Yb}^{3+}$ )<sup>81</sup> and some  $\text{Mn}^{4+}$ -based phosphors (7.85%  $\text{GPa}^{-1}$  for  $\text{SrGaAlO}_4:\text{Mn}^{4+82}$  and 12%  $\text{GPa}^{-1}$  for  $\text{K}_2\text{Ge}_4\text{O}_9:\text{Mn}^{4+21}$ ). However, they are lower than those obtained for  $\text{Sr}_4\text{Al}_{14}\text{O}_{25}:\text{Mn}^{4+}$  (35%  $\text{GPa}^{-1}$ )<sup>83</sup> and  $\text{Li}_3\text{Sc}_2(\text{PO}_4)_3$  (93.56%  $\text{GPa}^{-1}$ ),<sup>35</sup> which places the manometric performance of  $\text{CaAl}_{12}\text{O}_{19}:\text{Cr}^{3+}$  in a high position among lifetime-based luminescent manometers. Furthermore, it is noteworthy that while TIMF values are not exceptionally high, the relatively low thermal sensitivities in the 400–500 K range suggest the potential for higher thermal invariability, in this temperature range, for the lifetime-based luminescence manometer.

## 4. CONCLUSIONS

In this work, spectroscopic properties of the hibonite-type crystals, i.e.,  $\text{CaAl}_{12}\text{O}_{19}:\text{Cr}^{3+}$ , were investigated as a function of pressure and temperature in order to develop a unique, bifunctional luminescent sensor (optical thermometer-manometer). The performed studies reveal that the  $\text{Cr}^{3+}$  ions luminescence can be observed from two distinct octahedral  $\text{Al}^{3+}$  sites in the synthesized  $\text{CaAl}_{12}\text{O}_{19}:\text{Cr}^{3+}$  crystals. Due to the variation in the average  $\text{Cr}^{3+}-\text{O}^{2-}$  distances at these sites, the narrowband luminescence associated with the  ${}^2E \rightarrow {}^4A_2$

transition for  $\text{Cr}^{3+}(\text{C})$  and broadband emission associated with the  ${}^4\text{T}_2 \rightarrow {}^4\text{A}_2$  transition for  $\text{Cr}^{3+}(\text{C})$  and  ${}^4\text{A}_2, {}^4\text{T}_2 \rightarrow {}^4\text{A}_2$ , and  ${}^4\text{A}_2$  of  $\text{Cr}^{3+}(\text{A})\text{--Cr}^{3+}(\text{A})$  pairs can be observed simultaneously. High-pressure studies revealed the unusual behavior of  $\text{Cr}^{3+}$  ions. It was found that the spectral position for the  ${}^4\text{A}_2, {}^4\text{T}_2 \rightarrow {}^4\text{A}_2, {}^4\text{A}_2$  band of  $\text{Cr}^{3+}\text{--Cr}^{3+}$  pairs remains insensitive to pressure changes up to 7 GPa. Conversely, the  ${}^2\text{E} \rightarrow {}^4\text{A}_2$  line of  $\text{Cr}^{3+}(\text{C})$  ions undergoes a monotonic spectral shift with increasing pressure due to changes in  $\text{Cr}^{3+}\text{--O}^{2-}$  bond covalency. Therefore, the ratio of luminescence intensities in the two proposed spectral ranges varies monotonically with pressure changes, achieving a maximum relative sensitivity of 70%  $\text{GPa}^{-1}$  at 0.05 GPa. Notably, this proposed luminescence intensity ratio (LIR) does not exhibit high sensitivity to temperature changes with a temperature invariant manometric factor (TIMF) of 150 K  $\text{GPa}^{-1}$ . Additionally, the thermal population of the  ${}^4\text{T}_2$  level for  $\text{Cr}^{3+}(\text{C})$  results in a successive increase in the intensity of this band with increasing temperature. The inverse thermal monotonicity of this band's intensity relative to the  ${}^2\text{E} \rightarrow {}^4\text{A}_2$  band of  $\text{Cr}^{3+}(\text{C})$  enables the development of a ratiometric luminescence thermometer with a sensitivity of 1%  $\text{K}^{-1}$  at 180 K. Importantly, the pressure-induced change in spin–orbit coupling between the  ${}^2\text{E}$  and  ${}^4\text{T}_2$  states prolongs the lifetime of the  ${}^4\text{T}_2$  level, facilitating remote pressure readings based on luminescence kinetics. Our study demonstrates that the unusual pressure behavior of the  $\text{Cr}^{3+}\text{--Cr}^{3+}$  pairs luminescence site allows for the development of a unique, remote, and bifunctional luminescent manometer-thermometer, based on the optically active  $\text{CaAl}_{12}\text{O}_{19}\text{:Cr}^{3+}$  material.

## ■ ASSOCIATED CONTENT

### Supporting Information

The Supporting Information is available free of charge at <https://pubs.acs.org/doi/10.1021/acsami.4c11806>.

Raman spectra as a function of pressure (decompression cycle), excitation spectra, emission spectra as a function of pressure (decompression cycle), luminescence decay profiles as a function of temperature, and deconvolution of emission spectra (PDF)

## ■ AUTHOR INFORMATION

### Corresponding Author

Lukasz Marciniak – Institute of Low Temperature and Structure Research, Polish Academy of Sciences, 50-422 Wrocław, Poland; [orcid.org/0000-0001-5181-5865](https://orcid.org/0000-0001-5181-5865); Email: [l.marciniak@intibs.pl](mailto:l.marciniak@intibs.pl)

### Authors

Maja Szymczak – Institute of Low Temperature and Structure Research, Polish Academy of Sciences, 50-422 Wrocław, Poland

Andris Antuzevics – Institute of Solid State Physics, University of Latvia, LV-1063 Riga, Latvia

Pavels Rodionovs – Institute of Solid State Physics, University of Latvia, LV-1063 Riga, Latvia

Marcin Runowski – Faculty of Chemistry, Adam Mickiewicz University, 61-614 Poznań, Poland; [orcid.org/0000-0002-9704-2105](https://orcid.org/0000-0002-9704-2105)

Ulises R. Rodríguez-Mendoza – Departamento de Física, Instituto de Materiales y Nanotecnología, IUdEA & MALTA Consolider Team, Universidad de La Laguna, E-38200 San

Cristóbal de La Laguna, Santa Cruz de Tenerife, Spain;

[orcid.org/0000-0002-1431-8488](https://orcid.org/0000-0002-1431-8488)

Damian Szymanski – Institute of Low Temperature and Structure Research, Polish Academy of Sciences, 50-422 Wrocław, Poland

Vasyl Kinzhybalo – Institute of Low Temperature and Structure Research, Polish Academy of Sciences, 50-422 Wrocław, Poland

Complete contact information is available at: <https://pubs.acs.org/doi/10.1021/acsami.4c11806>

## Notes

The authors declare no competing financial interest.

## ■ ACKNOWLEDGMENTS

This work was supported by the National Science Center (NCN), Poland, under project no. DEC-UMO-2020/37/B/ST5/00164. Institute of Solid State Physics, University of Latvia, Latvia, as the Center of Excellence has received funding from the European Union's Horizon 2020 Framework Programme H2020-WIDESPREAD-01-2016-2017-Teaming-Phase2 under grant agreement no. 739508, project CAMART.<sup>2</sup>

## ■ REFERENCES

- (1) Wang, X.; Liu, Q.; Bu, Y.; Liu, C. S.; Liu, T.; Yan, X. Optical Temperature Sensing of Rare-Earth Ion Doped Phosphors. *RSC Adv.* **2015**, *5* (105), 86219–86236.
- (2) Jaque, D.; Jacinto, C. Luminescent Nanoprobes for Thermal Bio-Sensing: Towards Controlled Photo-Thermal Therapies. *J. Lumin.* **2016**, *169*, 394–399.
- (3) Dramićanin, M. Luminescence: The Basics, Methods, and Instrumentation. In *Luminescence Thermometry*; Dramićanin, M. B., Ed.; Woodhead Publishing, 2018; pp 33–61.
- (4) Marciniak, L.; Woźny, P.; Szymczak, M.; Runowski, M. Optical Pressure Sensors for Luminescence Manometry: Classification, Development Status, and Challenges. *Coord. Chem. Rev.* **2024**, *507*, 215770.
- (5) Bednarkiewicz, A.; Marciniak, L.; Carlos, L. D.; Jaque, D. Standardizing Luminescence Nanothermometry for Biomedical Applications. *Nanoscale* **2020**, *12* (27), 14405–14421.
- (6) Rocha, U.; Jacinto, C.; Kumar, K. U.; López, F. J.; Bravo, D.; Solé, J. G.; Jaque, D. Real-Time Deep-Tissue Thermal Sensing with Sub-Degree Resolution by Thermally Improved  $\text{Nd}^{3+}\text{:LaF}_3$  Multi-functional Nanoparticles. *J. Lumin.* **2016**, *175*, 149–157.
- (7) Brites, C. D. S.; Lima, P. P.; Silva, N. J. O.; Millán, A.; Amaral, V. S.; Palacio, F.; Carlos, L. D. Thermometry at the Nanoscale. *Nanoscale* **2012**, *4* (16), 4799–4829.
- (8) Brites, C. D. S.; Balabhadra, S.; Carlos, L. D. Lanthanide-Based Thermometers: At the Cutting-Edge of Luminescence Thermometry. *Adv. Opt. Mater.* **2019**, *7* (5), 1801239.
- (9) Dramićanin, M. D. Trends in Luminescence Thermometry. *J. Appl. Phys.* **2020**, *128* (4), 40902.
- (10) Piotrowski, W.; Trejgis, K.; Maciejewska, K.; Ledwa, K.; Fond, B.; Marciniak, L. Thermochromic Luminescent Nanomaterials Based on  $\text{Mn}^{4+}/\text{Tb}^{3+}$  Codoping for Temperature Imaging with Digital Cameras. *ACS Appl. Mater. Interfaces* **2020**, *12* (39), 44039–44048.
- (11) Piotrowski, W. M.; Kniec-Stec, K.; Suta, M.; Bogiński, B.; Pozniak, B.; Marciniak, L. Positive Luminescence Thermal Coefficient of  $\text{Mn}^{2+}$  Ions for Highly Sensitive Luminescence Thermometry. *Chem. Eng. J.* **2023**, *464*, 142492.
- (12) Forman, R. A.; Piermarini, G. J.; Barnett, J. D.; Block, S. Pressure Measurement Made by the Utilization of Ruby Sharp-Line Luminescence. *Science* **1972**, *176* (4032), 284–285.
- (13) León-Luis, S. F.; Muñoz-Santisteban, J. E.; Lavín, V.; Rodríguez-Mendoza, U. R. Optical Pressure and Temperature Sensor Based on

the Luminescence Properties of Nd<sup>3+</sup> Ion in a Gadolinium Scandium Gallium Garnet Crystal. *Opt. Express* **2012**, *20* (9), 10393.

(14) Penhouet, T.; Hagemann, H. Sm<sup>2+</sup> as a Probe of Crystal Field in Fluorides and Fluorohalides: Effect of Pressure and Temperature. *J. Alloys Compd.* **2008**, *451* (1–2), 74–76.

(15) Back, M.; Ueda, J.; Hua, H.; Tanabe, S. Predicting the Optical Pressure Sensitivity of <sup>2</sup>E → <sup>4</sup>A<sub>2</sub> Spin-Flip Transition in Cr<sup>3+</sup>-Doped Crystals. *Chem. Mater.* **2021**, *33* (9), 3379–3385.

(16) Ishaq, H.; Dincer, I.; Crawford, C. A Review on Hydrogen Production and Utilization: Challenges and Opportunities. *Int. J. Hydrogen Energy* **2022**, *47* (62), 26238–26264.

(17) Aghaie, M.; Rezaei, N.; Zendejboudi, S. A Systematic Review on CO<sub>2</sub> Capture with Ionic Liquids: Current Status and Future Prospects. *Renew. Sustain. Energy Rev.* **2018**, *96*, 502–525.

(18) Szymczak, M.; Runowski, M.; Lavín, V.; Marciniak, L. Highly Pressure-Sensitive, Temperature Independent Luminescence Ratiometric Manometer Based on MgO:Cr<sup>3+</sup> Nanoparticles. *Laser Photon. Rev.* **2023**, *17* (4), 2200801.

(19) Szymczak, M.; Runowski, M.; Lavín, V.; Marciniak, L. Highly Pressure-Sensitive, Temperature Independent Luminescence Ratiometric Manometer Based on MgO:Cr<sup>3+</sup> Nanoparticles. *Laser Photon. Rev.* **2023**, *17* (4), 2200801.

(20) Szymczak, M.; Woźny, P.; Runowski, M.; Pieprz, M.; Lavín, V.; Marciniak, L. Temperature Invariant Ratiometric Luminescence Manometer Based on Cr<sup>3+</sup> Ions Emission. *Chem. Eng. J.* **2023**, *453*, 139632.

(21) Szymczak, M.; Piotrowski, W.; Woźny, P.; Runowski, M.; Marciniak, L. Highly Sensitive Lifetime-Based Luminescent Manometer and Bi-Functional Pressure-Temperature Sensor Based on a Spectral Shift of the R-Line of Mn<sup>4+</sup> in K<sub>2</sub>Ge<sub>4</sub>O<sub>9</sub>. *J. Mater. Chem. C* **2024**, *12*, 6793.

(22) Tosi, D.; Schena, E.; Molardi, C.; Korganbayev, S. Fiber Optic Sensors for Sub-Centimeter Spatially Resolved Measurements: Review and Biomedical Applications. *Opt. Fiber Technol.* **2018**, *43*, 6–19.

(23) Zheng, T.; Luo, L.; Du, P.; Lis, S.; Rodríguez-Mendoza, U. R.; Lavín, V.; Runowski, M. Highly-Efficient Double Perovskite Mn<sup>4+</sup>-Activated Gd<sub>2</sub>ZnTiO<sub>6</sub> Phosphors: A Bifunctional Optical Sensing Platform for Luminescence Thermometry and Manometry. *Chem. Eng. J.* **2022**, *446*, 136839.

(24) Zhang, L.; Wang, D.; Hao, Z.; Zhang, X.; Pan, G.; Wu, H.; Zhang, J. Cr<sup>3+</sup>-Doped Broadband NIR Garnet Phosphor with Enhanced Luminescence and Its Application in NIR Spectroscopy. *Adv. Opt. Mater.* **2019**, *7* (12), 1900185.

(25) Back, M.; Trave, E.; Ueda, J.; Tanabe, S. Ratiometric Optical Thermometer Based on Dual Near-Infrared Emission in Cr<sup>3+</sup>-Doped Bismuth-Based Gallate Host. *Chem. Mater.* **2016**, *28* (22), 8347–8356.

(26) Grinberg, M.; Suchocki, A. Pressure-Induced Changes in the Energetic Structure of the 3d3 Ions in Solid Matrices. *J. Lumin.* **2007**, *125* (1–2), 97–103.

(27) McClure, D. S. Electronic Structure of Transition-Metal Complex Ions. *Radiat. Res. Suppl.* **1960**, *2*, 218.

(28) Brik, M. G. Crystal Field Analysis, Electron-Phonon Coupling and Spectral Band Shape Modeling in MgO:Cr<sup>3+</sup>. *Z. Naturforsch., A: Phys. Sci.* **2005**, *60* (6), 437–443.

(29) Marciniak, L.; Kniec, K.; Elżbieciak-Piecka, K.; Trejgis, K.; Stefanska, J.; Dramićanin, M. Luminescence Thermometry with Transition Metal Ions. A Review. *Coord. Chem. Rev.* **2022**, *469*, 214671.

(30) Back, M.; Ueda, J.; Xu, J.; Asami, K.; Brik, M. G.; Tanabe, S. Effective Ratiometric Luminescent Thermal Sensor by Cr<sup>3+</sup>-Doped Mullite Bi<sub>2</sub>Al<sub>4</sub>O<sub>9</sub> with Robust and Reliable Performances. *Adv. Opt. Mater.* **2020**, *8* (11), 2000124.

(31) P Beales, T.; H, L.; Goodman, C.; Scarrott, K. A New High Pressure Calibrant: β-Ga<sub>2</sub>O<sub>3</sub>:Cr. *Solid State Commun.* **1990**, *73* (1), 1–3.

(32) Barnett, J. D.; Block, S.; Piermarini, G. J. An Optical Fluorescence System for Quantitative Pressure Measurement in the Diamond-Anvil Cell. *Rev. Sci. Instrum.* **1973**, *44* (1), 1–9.

(33) Lorenz, B.; Shen, Y. R.; Holzapfel, W. B. Characterization of the New Luminescence Pressure Sensor SrFCl: Sm<sup>2+</sup>. *High Pressure Res.* **1994**, *12* (2), 91–99.

(34) Rashchenko, S. V.; Kurnosov, A.; Dubrovinsky, L.; Litasov, K. D. Revised Calibration of the Sm:SrB<sub>4</sub>O<sub>7</sub> Pressure Sensor Using the Sm-Doped Yttrium-Aluminum Garnet Primary Pressure Scale. *J. Appl. Phys.* **2015**, *117* (14), 145902.

(35) Szymczak, M.; Jaśkielewicz, J.; Runowski, M.; Xue, J.; Mahlik, S.; Marciniak, L. Highly-Sensitive, Tri-Modal Luminescent Manometer Utilizing Band-Shift, Ratiometric and Lifetime-Based Sensing Parameters. *Adv. Funct. Mater.* **2024**, *34*, 2314068.

(36) Chang, C.-Y.; Huang, M.-H.; Chen, K.-C.; Huang, W.-T.; Kamiński, M.; Majewska, N.; Klimczuk, T.; Chen, J.-H.; Cherng, D.-H.; Lu, K.-M.; Pang, W. K.; Peterson, V. K.; Mahlik, S.; Leniec, G.; Liu, R.-S. Ultrahigh Quantum Efficiency Near-Infrared-II Emission Achieved by Cr<sup>3+</sup> Clusters to Ni<sup>2+</sup> Energy Transfer. *Chem. Mater.* **2024**, *36* (8), 3941–3948.

(37) Lee, C.; Bao, Z.; Fang, M.-H.; Lesniewski, T.; Mahlik, S.; Grinberg, M.; Leniec, G.; Kaczmarek, S. M.; Brik, M. G.; Tsai, Y.-T.; Tsai, T.-L.; Liu, R.-S. Chromium(III)-Doped Fluoride Phosphors with Broadband Infrared Emission for Light-Emitting Diodes. *Inorg. Chem.* **2020**, *59* (1), 376–385.

(38) Szymczak, M.; Du, P.; Runowski, M.; Woźny, P.; Xue, J.; Zheng, T.; Marciniak, L. Highly Sensitive Optical Manometer Based on the Visible Emissions of Ce<sup>3+</sup>-Doped La<sub>6</sub>Sr<sub>4</sub>(SiO<sub>4</sub>)<sub>6</sub>F<sub>2</sub> Multisite Phosphors. *Adv. Opt. Mater.* **2024**, *12* (7), 2302147.

(39) Geiger, C. A.; Kleppa, O. J.; Mysen, B. O.; Lattimer, J. M.; Grossman, L. Enthalpies of Formation of CaAl<sub>4</sub>O<sub>7</sub> and CaAl<sub>12</sub>O<sub>19</sub> (Hibonite) by High Temperature, Alkali Borate Solution Calorimetry. *Geochim. Cosmochim. Acta* **1988**, *52* (6), 1729–1736.

(40) Vance, E. R.; Gowda, K. A.; Cartz, L.; Karioris, F. G. Irradiation of Pollucite, Spinel and CaAl<sub>12</sub>O<sub>19</sub> by 3 MeV Argon Ions. *Radiat. Eff.* **1983**, *79* (1–4), 245–249.

(41) Brik, M. G.; Pan, Y. X.; Liu, G. K. Spectroscopic and Crystal Field Analysis of Absorption and Photoluminescence Properties of Red Phosphor CaAl<sub>12</sub>O<sub>19</sub>:Mn<sup>4+</sup> Modified by MgO. *J. Alloys Compd.* **2011**, *509* (5), 1452–1456.

(42) Rajendran, V.; Fang, M. H.; Huang, W. T.; Majewska, N.; Lesniewski, T.; Mahlik, S.; Leniec, G.; Kaczmarek, S. M.; Pang, W. K.; Peterson, V. K.; Lu, K. M.; Chang, H.; Liu, R. S. Chromium Ion Pair Luminescence: A Strategy in Broadband near-Infrared Light-Emitting Diode Design. *J. Am. Chem. Soc.* **2021**, *143* (45), 19058–19066.

(43) Kong, L.; Liu, Y.; Dong, L.; Zhang, L.; Qiao, L.; Wang, W.; You, H. Enhanced Red Luminescence in CaAl<sub>12</sub>O<sub>19</sub>:Mn<sup>4+</sup> via Doping Ga<sup>3+</sup> for Plant Growth Lighting. *Dalton Trans.* **2020**, *49* (6), 1947–1954.

(44) Nittler, L. R.; Alexander, C. M. O.; Gallino, R.; Hoppe, P.; Nguyen, A. N.; Stadermann, F. J.; Zinner, E. K. Aluminum-Calcium- and Titanium-Rich Oxide Stardust in Ordinary Chondrite Meteorites. *Astrophys. J.* **2008**, *682* (2), 1450–1478.

(45) Lü, W.; Lv, W.; Zhao, Q.; Jiao, M.; Shao, B.; You, H. A Novel Efficient Mn<sup>4+</sup> Activated Ca<sub>14</sub>Al<sub>10</sub>Zn<sub>6</sub>O<sub>35</sub> Phosphor: Application in Red-Emitting and White LEDs. *Inorg. Chem.* **2014**, *53* (22), 11985–11990.

(46) Murata, T.; Tanoue, T.; Iwasaki, M.; Morinaga, K.; Hase, T. Fluorescence Properties of Mn<sup>4+</sup> in CaAl<sub>12</sub>O<sub>19</sub> Compounds as Red-Emitting Phosphor for White LED. *J. Lumin.* **2005**, *114* (3–4), 207–212.

(47) Rodionovs, P.; Kemere, M.; Antuzevics, A.; Rogulis, U.; Sarakovskis, A.; Fedotovs, A. Multi-Site Incorporation of Cr<sup>3+</sup> in CaAl<sub>12</sub>O<sub>19</sub>. *Materialia* **2023**, *32*, 101927.

(48) Tanabe, Y.; Sugano, S. On the Absorption Spectra of Complex Ions. I. *J. Phys. Soc. Jpn.* **1954**, *9* (5), 753–766.

(49) Adachi, S. Spectroscopy of Cr<sup>3+</sup> Activator: Tanabe–Sugano Diagram and Racah Parameter Analysis. *J. Lumin.* **2021**, *232*, 117844.



- (50) Chen, G.; Jin, Y.; Yuan, L.; Wang, B.; Huo, J.; Suo, H.; Wu, H.; Hu, Y.; Wang, F. Unlocking Cr<sup>3+</sup>-Cr<sup>3+</sup> Coupling in Spinel: Ultrabroadband Near-Infrared Emission beyond 900 nm with High Efficiency and Thermal Stability. *ACS Appl. Mater. Interfaces* **2024**, *16* (23), 30185–30195.
- (51) Rajendran, V.; Fang, M. H.; Huang, W. T.; Majewska, N.; Lesniewski, T.; Mahlik, S.; Leniec, G.; Kaczmarek, S. M.; Pang, W. K.; Peterson, V. K.; Lu, K. M.; Chang, H.; Liu, R. S. Chromium Ion Pair Luminescence: A Strategy in Broadband near-Infrared Light-Emitting Diode Design. *J. Am. Chem. Soc.* **2021**, *143* (45), 19058–19066.
- (52) Liu, S.; Du, J.; Song, Z.; Ma, C.; Liu, Q. Intervalence Charge Transfer of Cr<sup>3+</sup>-Cr<sup>3+</sup> Aggregation for NIR-II Luminescence. *Light Sci. Appl.* **2023**, *12* (1), 181.
- (53) Vink, A. P.; de Bruin, M. A.; Roke, S.; Peijzel, P. S.; Meijerink, A. Luminescence of Exchange Coupled Pairs of Transition Metal Ions. *J. Electrochem. Soc.* **2001**, *148* (7), No. E313.
- (54) Chen, G.; Jin, Y.; Yuan, L.; Wang, B.; Huo, J.; Suo, H.; Wu, H.; Hu, Y.; Wang, F. Unlocking Cr<sup>3+</sup>-Cr<sup>3+</sup> Coupling in Spinel: Ultrabroadband Near-Infrared Emission beyond 900 nm with High Efficiency and Thermal Stability. *ACS Appl. Mater. Interfaces* **2024**, *16* (23), 30185–30195.
- (55) Rajendran, V.; Fang, M. H.; Huang, W. T.; Majewska, N.; Lesniewski, T.; Mahlik, S.; Leniec, G.; Kaczmarek, S. M.; Pang, W. K.; Peterson, V. K.; Lu, K. M.; Chang, H.; Liu, R. S. Chromium Ion Pair Luminescence: A Strategy in Broadband near-Infrared Light-Emitting Diode Design. *J. Am. Chem. Soc.* **2021**, *143* (45), 19058–19066.
- (56) Rajendran, V.; Chang, C. Y.; Huang, M. H.; Chen, K. C.; Huang, W. T.; Kamiński, M.; Lesniewski, T.; Mahlik, S.; Leniec, G.; Lu, K. M.; Wei, D. H.; Chang, H.; Liu, R. S. Chromium Cluster Luminescence: Advancing Near-Infrared Light-Emitting Diode Design for Next-Generation Broadband Compact Light Sources. *Adv. Opt. Mater.* **2024**, *12* (13), 2302645.
- (57) Chang, C. Y.; Huang, M. H.; Chen, K. C.; Huang, W. T.; Kamiński, M.; Majewska, N.; Klimczuk, T.; Chen, J. H.; Cherng, D. H.; Lu, K. M.; Pang, W. K.; Peterson, V. K.; Mahlik, S.; Leniec, G.; Liu, R. S. Ultrahigh Quantum Efficiency Near-Infrared-II Emission Achieved by Cr<sup>3+</sup> Clusters to Ni<sup>2+</sup> Energy Transfer. *Chem. Mater.* **2024**, *36* (8), 3941–3948.
- (58) Awater, R. H. P.; Dorenbos, P. Towards a General Concentration Quenching Model of Bi<sup>3+</sup> Luminescence. *J. Lumin.* **2017**, *188*, 487–489.
- (59) Vink, A. P.; de Bruin, M. A.; Roke, S.; Peijzel, P. S.; Meijerink, A. Luminescence of Exchange Coupled Pairs of Transition Metal Ions. *J. Electrochem. Soc.* **2001**, *148* (7), No. E313.
- (60) Rodionovs, P.; Kemere, M.; Antuzevics, A.; Rogulis, U.; Sarakovskis, A.; Fedotovs, A. Multi-Site Incorporation of Cr<sup>3+</sup> in CaAl<sub>12</sub>O<sub>19</sub>. *Materialia* **2023**, *32*, 101927.
- (61) Low, W. Paramagnetic Resonance and Optical Absorption Spectra of Cr<sup>3+</sup> in MgO. *Phys. Rev.* **1957**, *105* (3), 801–805.
- (62) Viana, B.; Lejus, A. M.; Vivien, D.; Ponçon, V.; Boulon, G. Synthesis, ESR Investigation, and Optical Properties of the Potential Vibronic Laser Material LaMgAl<sub>11-x</sub>Cr<sub>x</sub>O<sub>19</sub>. *J. Solid State Chem.* **1987**, *71* (1), 77–86.
- (63) Chukanov, N. V.; Vorobei, S. S.; Ermolaeva, V. N.; Varlamov, D. A.; Plechov, P. Y.; Jančev, S.; Bovkun, A. V. New Data on Chemical Composition and Vibrational Spectra of Magnetoplumbite-Group Minerals. *Geol. Ore Deposits* **2019**, *61* (7), 637–646.
- (64) Krüger, B.; Galuskin, E. V.; Galuskina, I. O.; Krüger, H.; Vapnik, Y. Kahlenbergite KAl<sub>11</sub>O<sub>17</sub>, a New  $\beta$ -Alumina Mineral and Fe-Rich Hibonite from the Hatrurim Basin, the Negev Desert, Israel. *Eur. J. Mineral.* **2021**, *33* (4), 341–355.
- (65) Piermarini, G. J.; Block, S.; Barnett, J. D.; Forman, R. A. Calibration of the Pressure Dependence of the R<sub>1</sub> Ruby Fluorescence Line to 195 Kbar. *J. Appl. Phys.* **1975**, *46* (6), 2774–2780.
- (66) Chijioke, A. D.; Nellis, W. J.; Soldatov, A.; Silvera, I. F. The Ruby Pressure Standard to 150 GPa. *J. Appl. Phys.* **2005**, *98* (11), 114905.
- (67) Mahlik, S.; Lazarowska, A.; Ueda, J.; Tanabe, S.; Grinberg, M. Spectroscopic Properties and Location of the Ce<sup>3+</sup> Energy Levels in Y<sub>3</sub>Al<sub>2</sub>Ga<sub>3</sub>O<sub>12</sub> and Y<sub>3</sub>Ga<sub>5</sub>O<sub>12</sub> at Ambient and High Hydrostatic Pressure. *Phys. Chem. Chem. Phys.* **2016**, *18* (9), 6683–6690.
- (68) Lesniewski, T.; Barzowska, J.; Mahlik, S.; Behrendt, M.; Padlyak, B. V.; Grinberg, M. Evolution of the Optical Properties of Chromium Doped Calcium Tetraborate Glass under High Pressure. *J. Lumin.* **2016**, *177*, 111–118.
- (69) Suta, M.; Meijerink, A. A Theoretical Framework for Ratiometric Single Ion Luminescent Thermometers—Thermodynamic and Kinetic Guidelines for Optimized Performance. *Adv. Theory Simul.* **2020**, *3* (12), 2000176.
- (70) Szymczak, M.; Runowski, M.; Brik, M. G.; Marciniak, L. Multimodal, Super-Sensitive Luminescent Manometer Based on Giant Pressure-Induced Spectral Shift of Cr<sup>3+</sup> in the NIR Range. *Chem. Eng. J.* **2023**, *466*, 143130.
- (71) Szymczak, M.; Runowski, M.; Lavín, V.; Marciniak, L. Highly Pressure-Sensitive, Temperature Independent Luminescence Ratiometric Manometer Based on MgO:Cr<sup>3+</sup> Nanoparticles. *Laser Photon. Rev.* **2023**, *17* (4), 2200801.
- (72) Szymczak, M.; Runowski, M.; Brik, M. G.; Marciniak, L. Multimodal, Super-Sensitive Luminescent Manometer Based on Giant Pressure-Induced Spectral Shift of Cr<sup>3+</sup> in the NIR Range. *Chem. Eng. J.* **2023**, *466*, 143130.
- (73) Labrador-Páez, L.; Pedroni, M.; Speghini, A.; García-Solé, J.; Haro-González, P.; Jaque, D. Reliability of Rare-Earth-Doped Infrared Luminescent Nanothermometers. *Nanoscale* **2018**, *10* (47), 22319–22328.
- (74) Marciniak, L.; Woźny, P.; Szymczak, M.; Runowski, M. Optical Pressure Sensors for Luminescence Manometry: Classification, Development Status, and Challenges. *Coord. Chem. Rev.* **2024**, *507*, 215770.
- (75) Antoniak, M. A.; Zelewski, S. J.; Oliva, R.; Žak, A.; Kudrawiec, R.; Nyk, M. Combined Temperature and Pressure Sensing Using Luminescent NaBiF<sub>4</sub>:Yb,Er Nanoparticles. *ACS Appl. Nano Mater.* **2020**, *3* (5), 4209–4217.
- (76) Bao, H.; Wang, W.; Li, X.; Liu, X.; Zhang, L.; Yan, X.; Wang, Y.; Wang, C.; Jia, X.; Sun, P.; Kong, X.; Zhang, H.; Lu, G.; Bao, H.; Li, X.; Liu, X.; Zhang, L.; Yan, X.; Wang, C.; Jia, X.; Sun, P.; Lu, G.; Wang, W.; Kong, X.; Wang, Y.; Zhang, H. Interfacial Stress-Modulated Mechanosensitive Upconversion Luminescence of NaErF<sub>4</sub> Based Heteroepitaxial Core–Shell Nanoparticles. *Adv. Opt. Mater.* **2022**, *10* (2), 2101702.
- (77) McLellan, C. A.; Siefe, C.; Casar, J. R.; Peng, C. S.; Fischer, S.; Lay, A.; Parakh, A.; Ke, F.; Gu, X. W.; Mao, W.; Chu, S.; Goodman, M. B.; Dionne, J. A. Engineering Bright and Mechanosensitive Alkaline-Earth Rare-Earth Upconverting Nanoparticles. *J. Phys. Chem. Lett.* **2022**, *13* (6), 1547–1553.
- (78) Zheng, T.; Sójka, M.; Woźny, P.; Woźny, P.; Lavín, V.; Zych, E.; Lavín, V.; Du, P.; Luo, L.; Runowski, M.; Zheng, T.; Woźny, P.; Lis, S.; Runowski, M.; Sójka, M.; Zych, E.; Martin, I. R.; Lavín, V.; Du, P.; Luo, L. Supersensitive Ratiometric Thermometry and Manometry Based on Dual-Emitting Centers in Eu<sup>2+</sup>/Sm<sup>2+</sup>-Doped Strontium Tetraborate Phosphors. *Adv. Opt. Mater.* **2022**, *10* (20), 2201055.
- (79) Szymczak, M.; Woźny, P.; Runowski, M.; Pieprz, M.; Lavín, V.; Marciniak, L. Temperature Invariant Ratiometric Luminescence Manometer Based on Cr<sup>3+</sup> Ions Emission. *Chem. Eng. J.* **2023**, *453*, 139632.
- (80) Szymczak, M.; Jaskielewicz, J.; Runowski, M.; Xue, J.; Mahlik, S.; Marciniak, L. Highly-Sensitive, Tri-Modal Luminescent Manometer Utilizing Band-Shift, Ratiometric and Lifetime-Based Sensing Parameters. *Adv. Funct. Mater.* **2024**, *34* (22), 2314068.
- (81) Runowski, M.; Marciniak, J.; Grzyb, T.; Przybylska, D.; Shyichuk, A.; Barszcz, B.; Katrusiak, A.; Lis, S. Lifetime Nanomanometry-High-Pressure Luminescence of up-Converting Lanthanide Nanocrystals-SrF<sub>2</sub>:Yb<sup>3+</sup>,Er<sup>3+</sup>. *Nanoscale* **2017**, *9* (41), 16030–16037.
- (82) Pieprz, M.; Runowski, M.; Woźny, P.; Xue, J.; Marciniak, L. Temperature Invariant Lifetime Based Luminescent Manometer on Mn<sup>4+</sup> Ions. *J. Mater. Chem. C* **2023**, *11* (33), 11353–11360.



(83) Pieprz, M.; Piotrowski, W.; Woźny, P.; Runowski, M.; Marciniak, L. Highly Sensitive Lifetime-Based Luminescent Manometer on  $\text{Mn}^{4+}$  Luminescence in  $\text{Sr}_4\text{Al}_{14}\text{O}_{25}$   $\text{Mn}^{4+}$ . *Adv. Opt. Mater.* **2023**, *12*, 2301316.

## SUPPORTING INFORMATION

### **Bi-functional luminescent thermometer-manometer based on the Cr<sup>3+</sup> - Cr<sup>3+</sup> pair emission**

**Maja Szymczak<sup>1</sup>, Andris Antuzevics<sup>2</sup>, Pavels Rodionovs<sup>2</sup>, Marcin  
Runowski<sup>3</sup>, Ulises R. Rodríguez-Mendoza<sup>4</sup>, Damian Szymanski<sup>1</sup>, Vasyl  
Kinzhybalo<sup>1</sup>, Lukasz Marciniak<sup>1\*</sup>**

<sup>1</sup> Institute of Low Temperature and Structure Research, Polish Academy of Sciences,

Okólna 2, 50-422 Wrocław, Poland

<sup>2</sup> Institute of Solid State Physics, University of Latvia, Kengaraga 8, Kengaraga 8, LV-1063, Riga, Latvia

<sup>3</sup> Faculty of Chemistry, Adam Mickiewicz University, Uniwersytetu Poznańskiego 8, 61-614 Poznań, Poland

<sup>4</sup> Departamento de Física, Instituto de Materiales y Nanotecnología, IUdEA & MALTA Consolider Team,  
Universidad de La Laguna, Apdo. Correos 456, E-38200 San Cristóbal de La Laguna, Santa Cruz de Tenerife,  
Spain

\*corresponding author: [l.marciniak@intibs.pl](mailto:l.marciniak@intibs.pl)

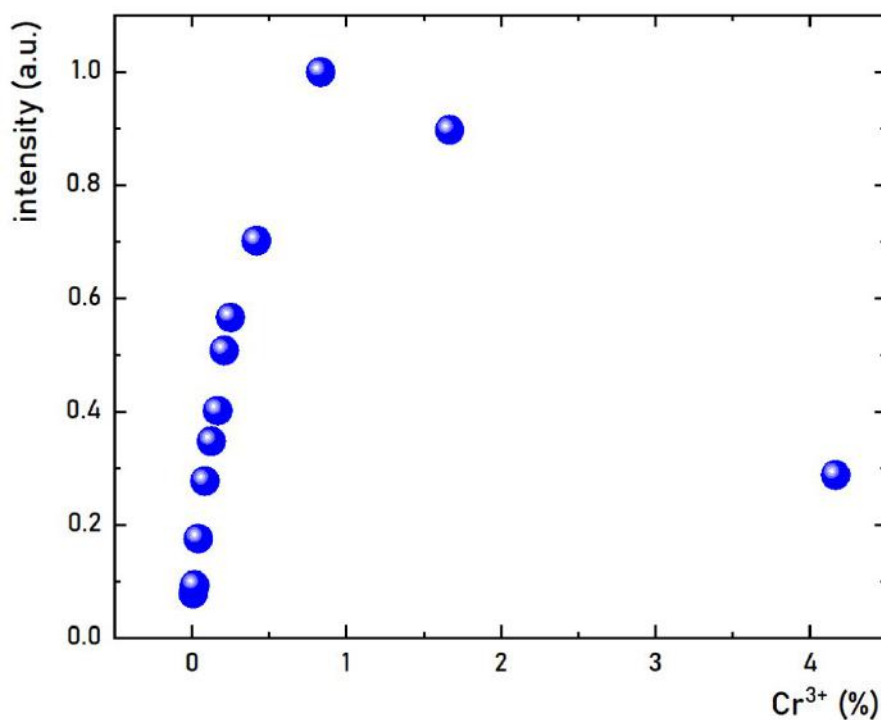


**Figure S1.** Integral room temperature emission intensity of  $\text{CaAl}_{12}\text{O}_{19}:\text{Cr}^{3+}$  as a function of  $\text{Cr}^{3+}$  concentration.

Results of the Rietveld refinement of the XRD pattern of  $\text{CaAl}_{12}\text{O}_{19}:\text{Cr}^{3+}$ :

#### **Global Parameters**

Number of used phases:	1
Number of variables:	27
Number of constraints:	2
Zero shift/ °2Theta:	0.000000
Specimen displacement/ mm :	-0.0800(8)
Profile function:	Pseudo Voigt
Background:	Polynomial
R (expected)/ %:	2.03446
R (profile)/ %:	5.04889
R (weighted profile)/ %:	7.13386
GOF:	12.29565
d-statistic:	0.86388
U standard:	0.000000
V standard:	0.000000
W standard:	0.010000
U Left:	0.000000
V Left:	0.000000
W Left:	0.010000
U Right:	0.000000
V Right:	0.000000
W Right:	0.010000
Asymmetry Type:	No Asymmetry Function
Asymmetry 1:	0.000000
Asymmetry 2:	0.000000
Shape Type:	Shape Individual
Shape 1 Left:	0.600000
Shape 2 Left:	0.000000
Shape 3 Left:	0.000000
Shape 1 Right:	0.600000

Shape 2 Right: 0.000000  
 Shape 3 Right: 0.000000  
 K a1/a2 intensity ratio: 0.500000  
 K alpha/beta intensity ratio: 0.000000  
 Crystal Shape Factor K: 1.0000  
 Instrumental FWHM Curve Type: Caglioti function  
 Instr. Gauss Curve Coefficient A: 0.0045(5)  
 Instr. Gauss Curve Coefficient B: -0.0032(9)  
 Instr. Gauss Curve Coefficient C: 0.0046(3)  
 Instr. Lorentz Curve Coefficient A: 0.0062(7)  
 Instr. Lorentz Curve Coefficient B: -0.004(1)  
 Instr. Lorentz Curve Coefficient C: 0.0064(5)

### **Relevant parameters of Calcium Aluminium Oxide (1/12/19)**

Structure and profile data:  
 Formula sum:  $O_{38.00}Al_{24.00}Ca_{2.00}$   
 Formula mass/ g/mol: 1335.6930  
 Density (calculated)/ g/cm<sup>3</sup>: 3.7805  
 F(000): 656.0000  
 Weight fraction/ %: 100.000000  
 Space group (No.): P 63/m m c (194)  
 Lattice parameters:  
   a/ Å: 5.56079(5)  
   b/ Å: 5.56079(5)  
   c/ Å: 21.9048(3)  
   alpha/ °: 90  
   beta/ °: 90  
   gamma/ °: 120  
 V/ 10<sup>6</sup> pm<sup>3</sup>: 586.60210  
 Overall displacement parameter: 0.000000  
 Extinction: 0.000000  
 Flat Plate Absorption Correction: 0.000000  
 Porosity: 0.000000  
 Roughness: 0.000000  
 Fitting mode: Structure Fit  
   U Left: 0.015(2)  
   V Left: 0.000(2)  
   W Left: 0.0087(5)  
 Preferred orientation direction/ hkl: 0.00 0.00 1.00  
 Preferred orientation parameter: 1.000000  
 Asymmetry parameter 1: 0.000000  
 Asymmetry parameter 2: 0.000000  
 Peak shape:  
   parameter 1 Left: 0.717(9)  
   parameter 2 Left: 0.000000  
   parameter 3 Left: 0.000000  
 R (Bragg)/ %: 4.98400

### **Occupancy, atomic fract. coordinates and Biso for Calcium Aluminium Oxide (1/12/19)**

Atom	Wyck.	s.o.f.	x	y	z	B/ 10 <sup>4</sup> pm <sup>2</sup>
O1	12k	1.000000	0.503250	0.006500	0.149120	0.500000
O2	12k	1.000000	0.155050	0.310100	0.052130	0.500000
O3	6h	1.000000	0.181070	0.362140	0.250000	0.500000
O4	4f	1.000000	0.333333	0.666667	0.554610	0.500000
O5	4e	1.000000	0.000000	0.000000	0.149070	0.500000
Al1	12k	1.000000	0.1694 (2)	0.3388 (4)	0.60950 (6)	0.64 (3)
Al2	4f	1.000000	0.333333	0.666667	0.1905 (1)	0.57 (6)
Al3	4f	1.000000	0.333333	0.666667	0.0288 (1)	0.53 (7)
Al4	2b	1.000000	0.000000	0.000000	0.250000	2.4 (1)
Al5	2a	1.000000	0.000000	0.000000	0.000000	1.1 (1)
Ca1	2d	1.000000	0.333333	0.666667	0.750000	1.73 (7)

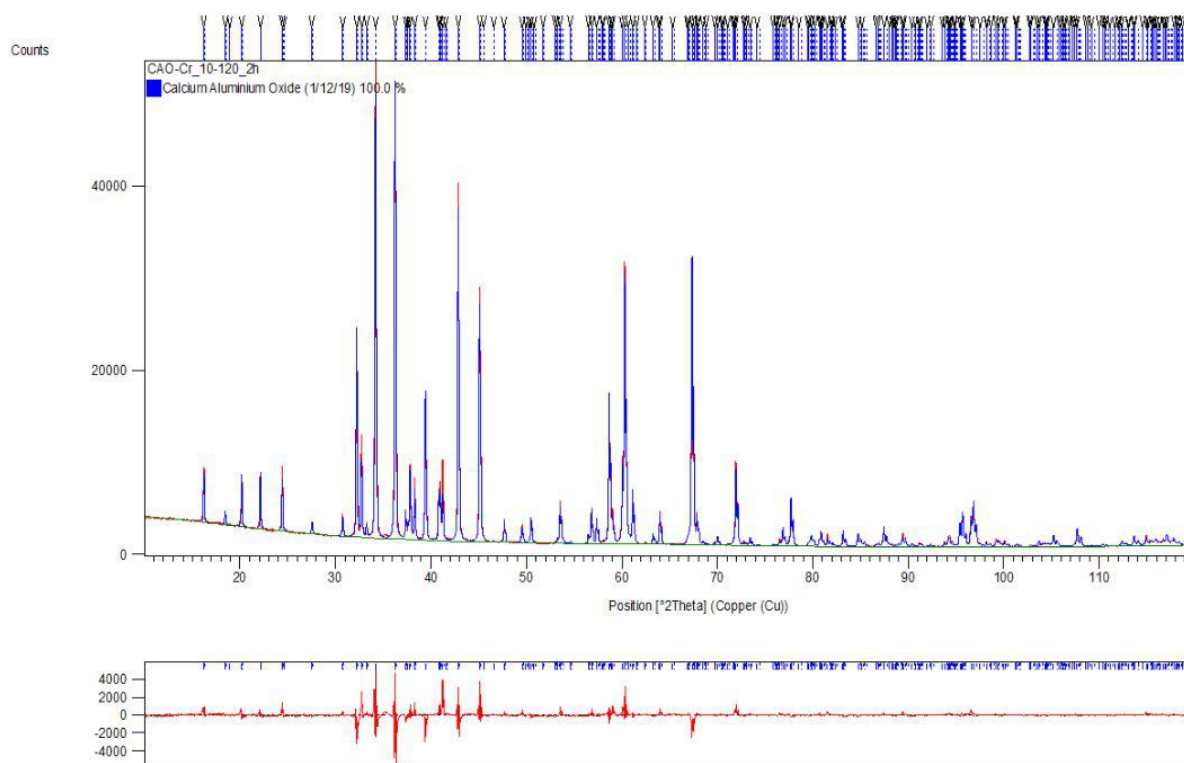


**Figure S2.** Rietveld refinement of the XRD pattern of  $\text{CaAl}_{12}\text{O}_{19}:\text{Cr}^{3+}$ .

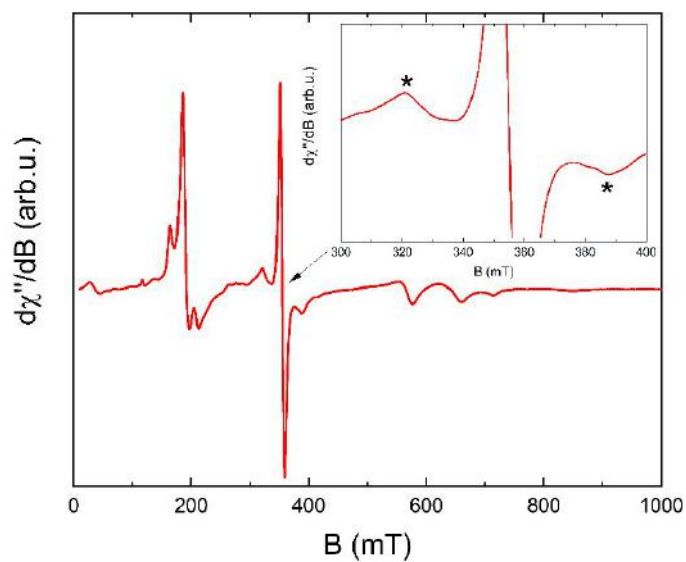


**Figure S3.** EPR spectrum of  $\text{CaAl}_{12}\text{O}_{19}:\text{Cr}^{3+}$ ; inset: a magnified section of the spectrum in the 300-400 mT range.

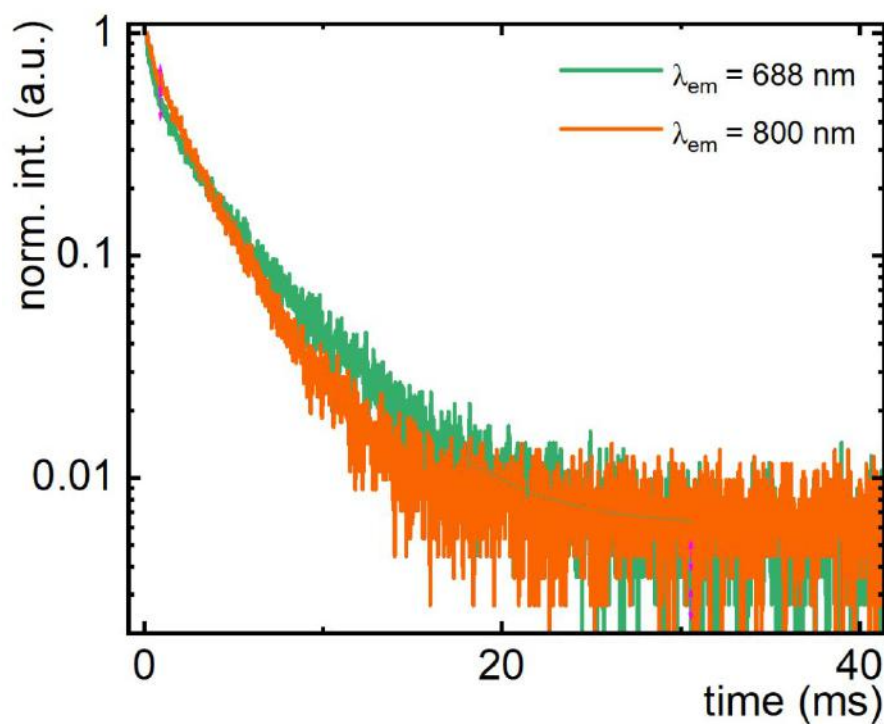


**Figure S4.** The comparison of room temperature luminescence decay profiles measured at  $\lambda_{\text{em}} = 688 \text{ nm}$  and  $\lambda_{\text{em}} = 780 \text{ nm}$  of  $\text{CaAl}_{12}\text{O}_{19}:\text{Cr}^{3+}$ .

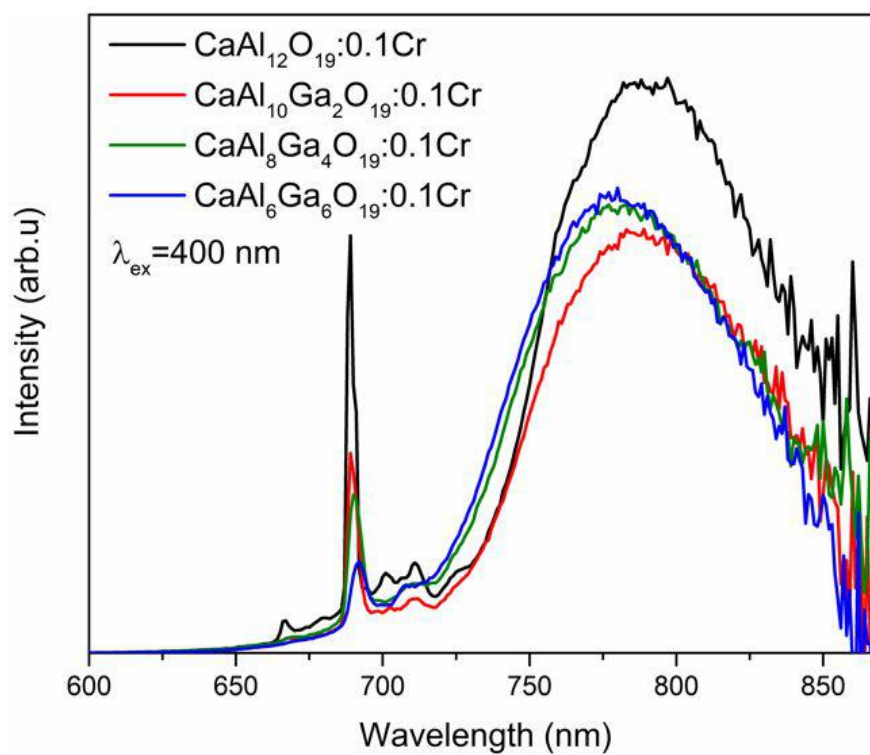


**Figure S5.** The comparison of room temperature emission spectra ( $\lambda_{\text{exc}} = 400 \text{ nm}$ ) of  $\text{CaAl}_{12}\text{O}_{19}:\text{Cr}^{3+}$  for different  $\text{Ga}^{3+}$  amount.

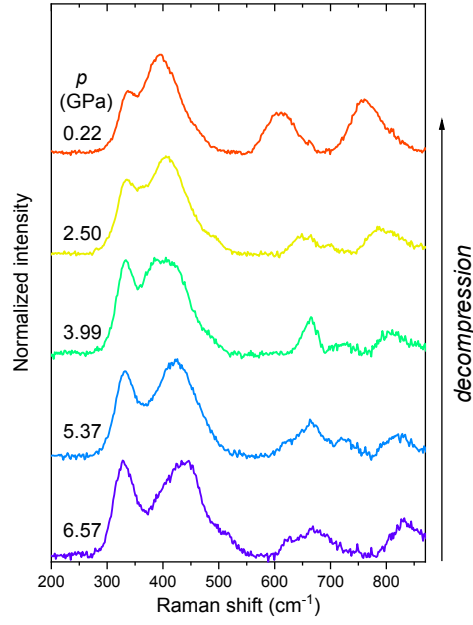


**Figure S6.** Normalized Raman spectra for the  $\text{CaAl}_{11.9}\text{O}_{19}:0.1\text{Cr}^{3+}$  material measured for different pressure values, during the decompression cycle.

**Table S1.** Estimated energies (peak centroids) of the main Raman modes at low pressure, and the corresponding pressure shift rates of the corresponding bands for the CAO material.

Peak centroid at ambient pressure ( $\text{cm}^{-1}$ )	Shift rate ( $\text{cm}^{-1}/\text{GPa}$ )
$\approx 771$	$9.71 \pm 0.57$
$\approx 618$	$9.96 \pm 0.90$
$\approx 395$	$6.21 \pm 0.61$
$\approx 332$	$-0.01 \pm 0.13$



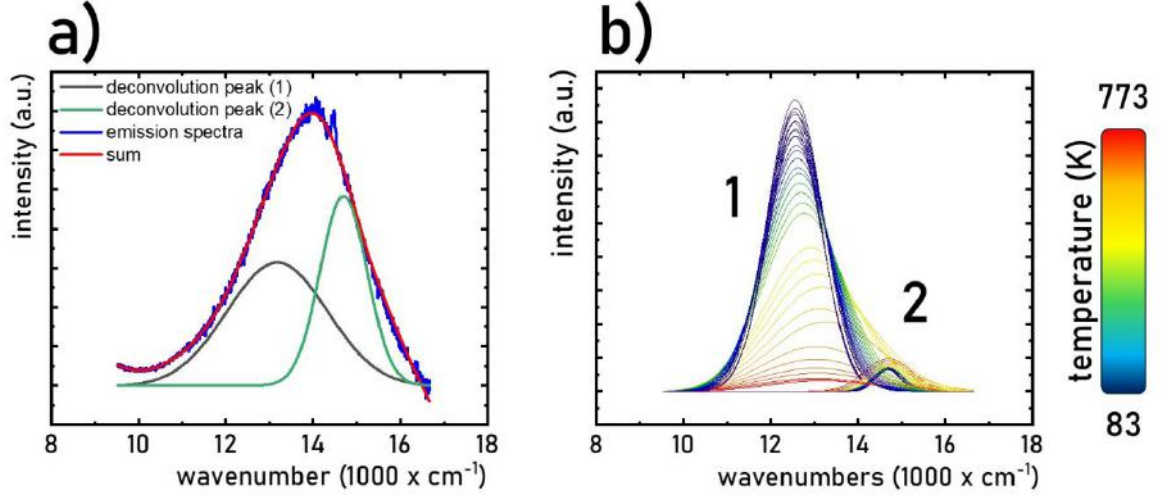


**Figure S7.** The deconvolution of the representative emission spectrum of  $\text{CaAl}_{12}\text{O}_{19}:\text{Cr}^{3+}$  measured at 723 K-a) and the influence of the temperature on the emission intensities of the emission bands obtained from the deconvolution of the emission spectra of  $\text{CaAl}_{12}\text{O}_{19}:\text{Cr}^{3+}$ -b).

Thermal dependence of LIR can be fitted using empirical function, i.e. 5<sup>th</sup>-order polynomial given below:

$$\text{LIR}(T) = A_0 + A_1T + A_2T^2 + A_3T^3 + A_4T^4 + A_5T^5 \quad (\text{S1})$$

where for  $\text{LIR}_1$

$$A_0 = 1.25896; A_1 = -0.02702; A_2 = 2.51136 \cdot 10^{-4}; A_3 = -9.43614 \cdot 10^{-7}; A_4 = 1.76486 \cdot 10^{-9}; A_5 = -1.27904 \cdot 10^{-12}$$

and for  $\text{LIR}_2$

$$A_0 = 0.06659; A_1 = -0.00106; A_2 = 1.87064 \cdot 10^{-5}; A_3 = -6.42395 \cdot 10^{-8}; A_4 = 1.04503 \cdot 10^{-10}; A_5 = -5.78433 \cdot 10^{-14}$$

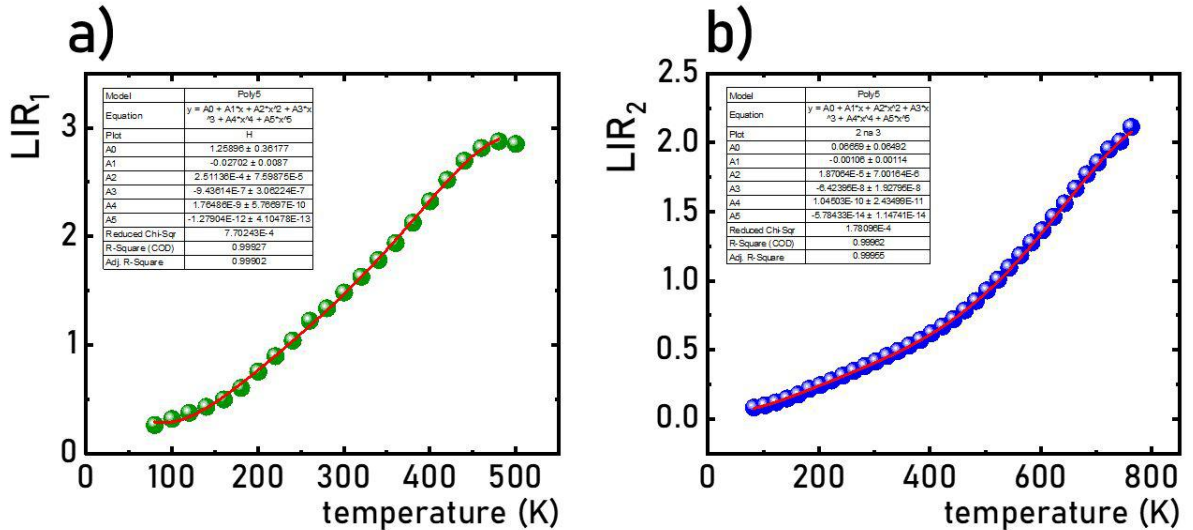


**Figure S8.** Fitting of the thermal dependence of LIR<sub>1</sub>-a) and LIR<sub>2</sub>-b) using the fitting curves presented above.

Based on the results of the deconvolution of the emission spectra of CaAl<sub>12</sub>O<sub>19</sub>:Cr<sup>3+</sup> presented above the LIR<sub>3</sub> was calculated as a ratio of deconvolution peak (1) - <sup>4</sup>A<sub>2</sub>, <sup>4</sup>T<sub>2</sub>→<sup>4</sup>A<sub>2</sub>, <sup>4</sup>A<sub>2</sub> Cr<sup>3+</sup>-Cr<sup>3+</sup>(A) to the deconvolution peak (2) - <sup>4</sup>T<sub>2</sub>→<sup>4</sup>A<sub>2</sub> Cr<sup>3+</sup>(C).

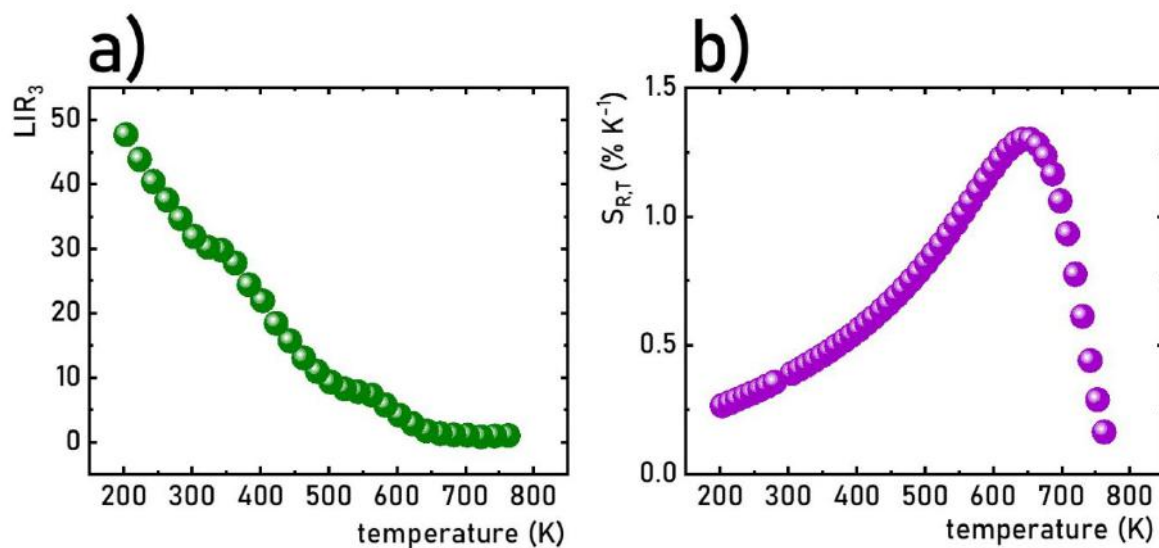


**Figure S9.** The thermal dependence of LIR<sub>3</sub> -a) and the corresponding thermal relative sensitivities-b) of CaAl<sub>12</sub>O<sub>19</sub>:Cr<sup>3+</sup>.

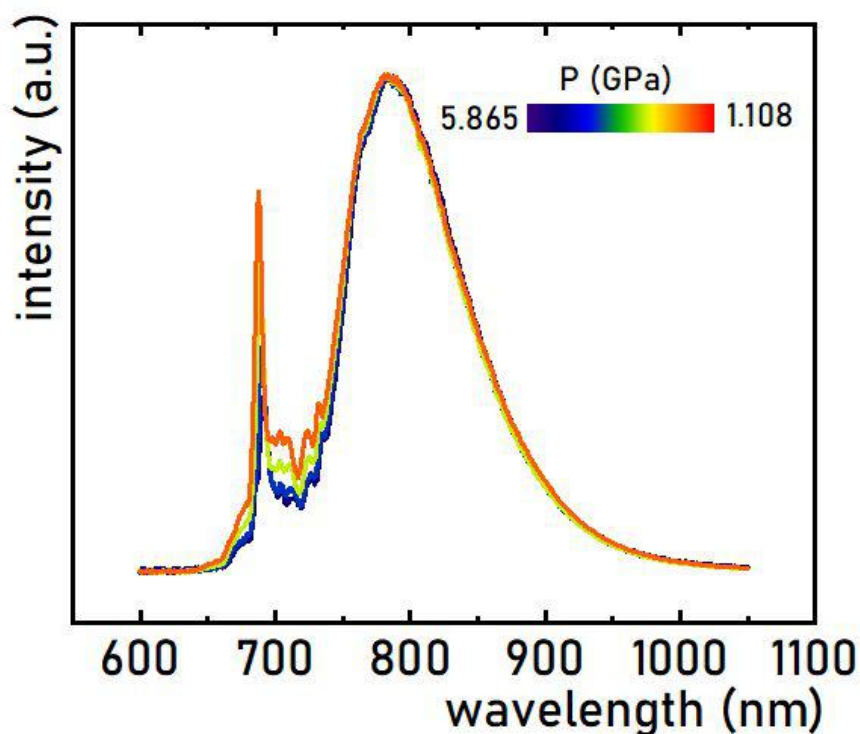


**Figure S10.** Pressure-dependent room temperature emission spectra ( $\lambda_{\text{exc}} = 445$  nm) of CaAl<sub>11.9</sub>O<sub>19</sub>:0.1Cr<sup>3+</sup> measured during decompression.

Pressure dependence of LIR can be fitted using empirical function, i.e. 5<sup>th</sup>-order polynomial given below:

$$LIR(p) = A_0 + A_1p + A_2p^2 + A_3p^3 + A_4p^4 + A_5p^5 \quad (S2)$$

where for LIR<sub>1</sub>

$$A_0=0.87477; A_1= -0.23866; A_2= 0.12035; A_3= -0.03659; A_4= 0.00504; A_5= -2.56502 \cdot 10^{-4}$$

and for LIR<sub>2</sub>

$$A_0=0.47019; A_1= -0.02335; A_2= 0.00636; A_3= -0.00227; A_4= 3.62334 \cdot 10^{-4}; A_5= -2.02296 \cdot 10^{-5}$$

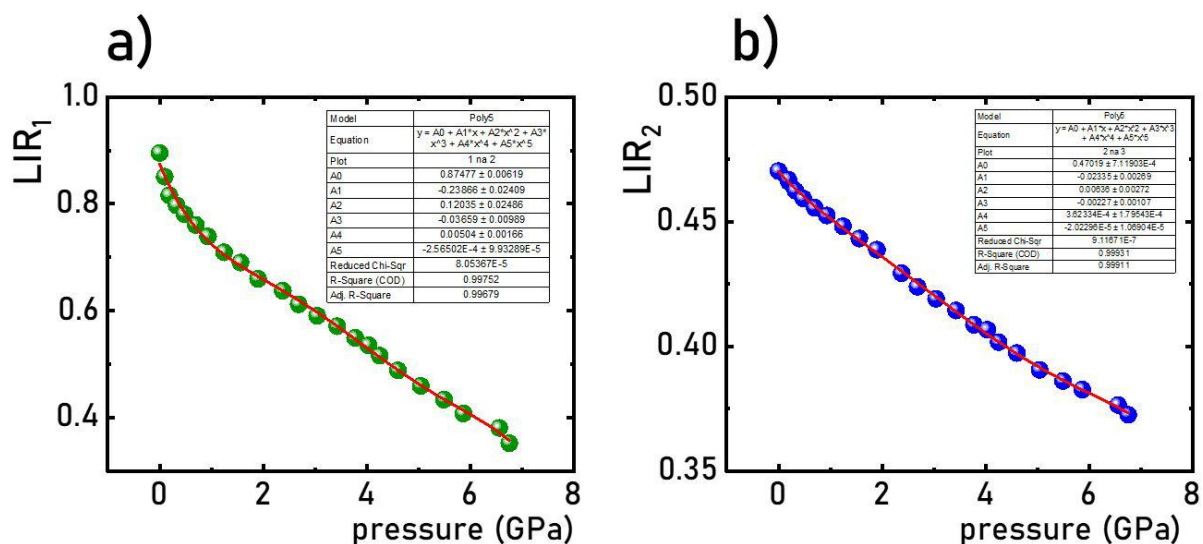


**Figure S11.** Fitting of the pressure dependence of LIR<sub>1</sub>-a) and LIR<sub>2</sub>-b) using the fitting curves presented above.

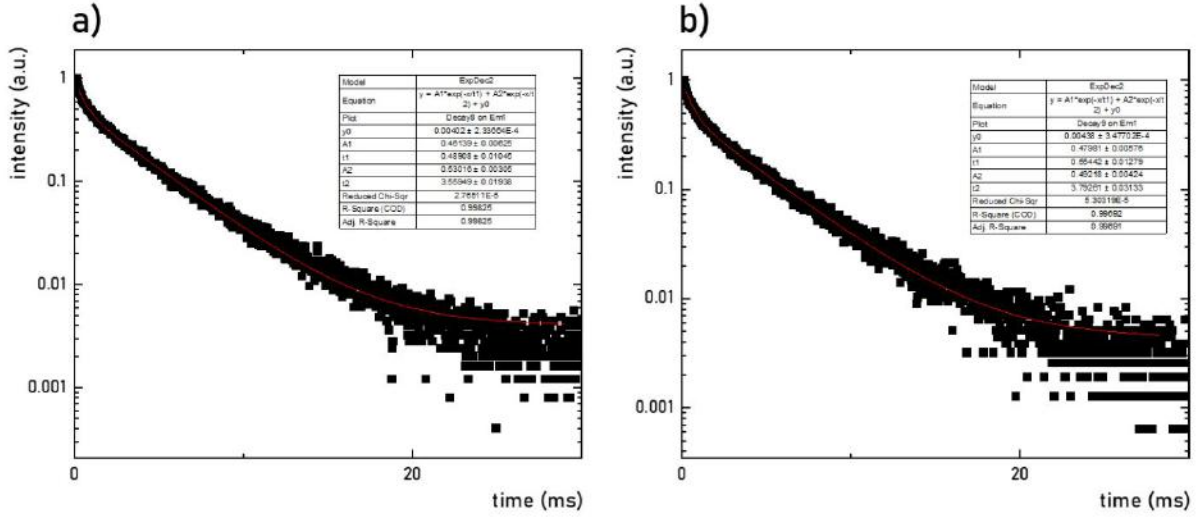


**Figure S12.** Fitting of luminescence decay profile of  $\text{CaAl}_{11.9}\text{O}_{19}:0.1\text{Cr}^{3+}$  ( $\lambda_{\text{exc}} = 445 \text{ nm}$ ) measured at: ambient pressure -a); 0.1856 GPa -b).

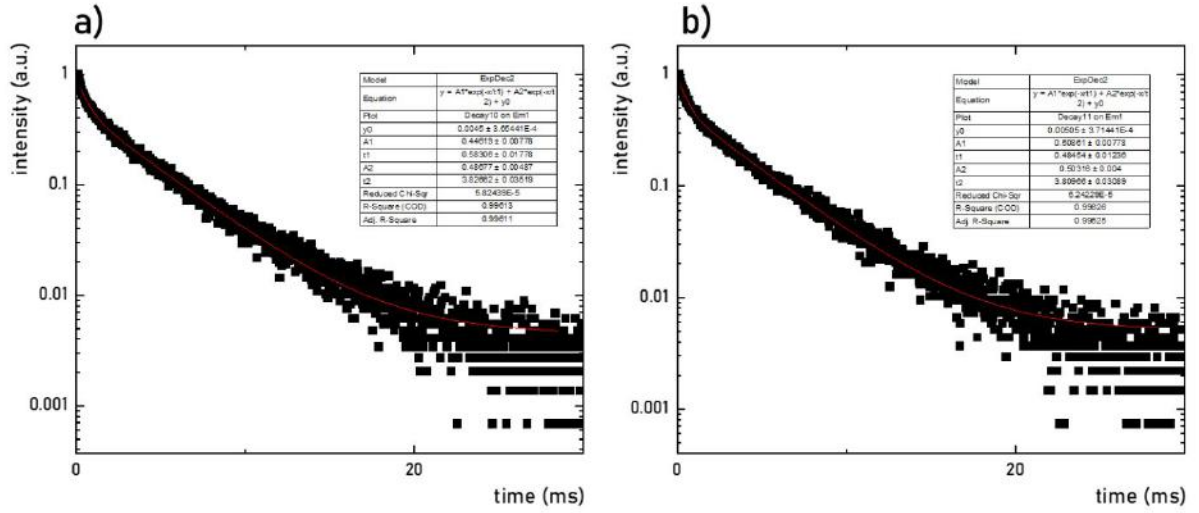


**Figure S13.** Fitting of luminescence decay profile of  $\text{CaAl}_{11.9}\text{O}_{19}:0.1\text{Cr}^{3+}$  ( $\lambda_{\text{exc}} = 445 \text{ nm}$ ) measured at: 0.2035 GPa -a); 0.326 GPa -b).

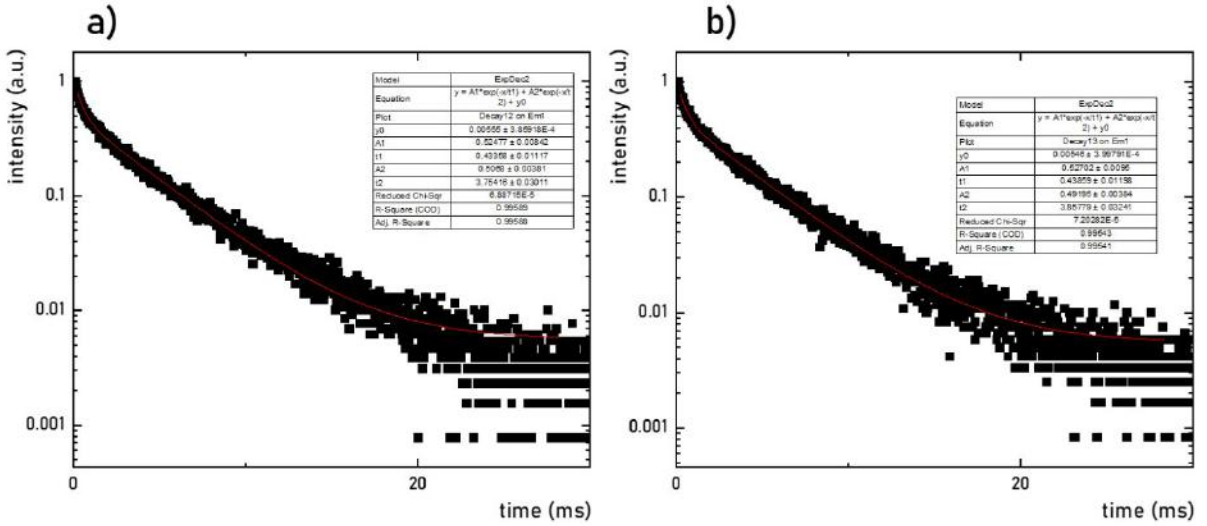


**Figure S14.** Fitting of luminescence decay profile of  $\text{CaAl}_{11.9}\text{O}_{19}:0.1\text{Cr}^{3+}$  ( $\lambda_{\text{exc}} = 445 \text{ nm}$ ) measured at: 0.4788 GPa -a); 0.69982 GPa -b).

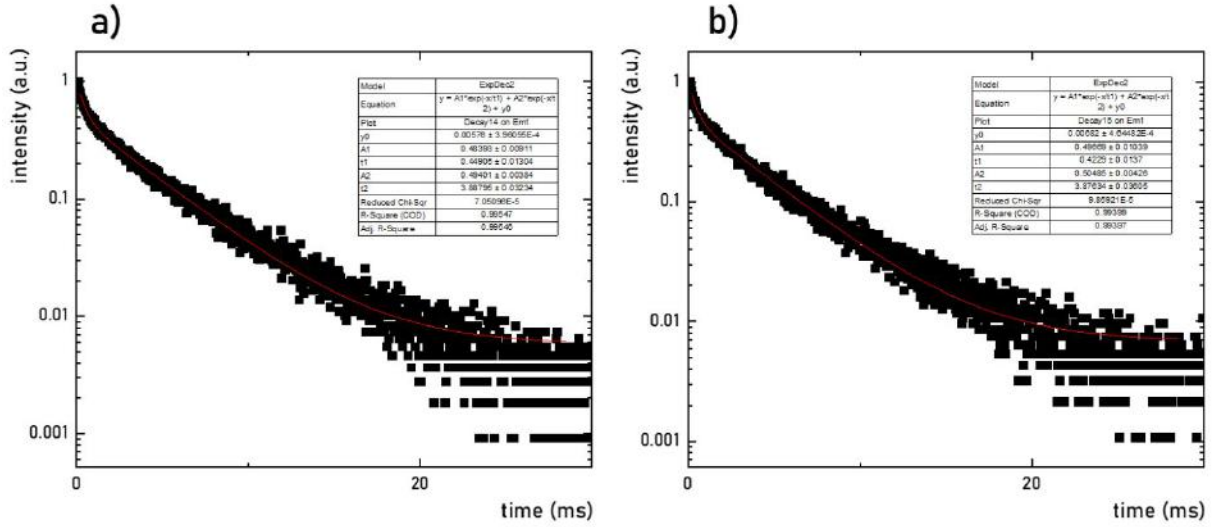


**Figure S15.** Fitting of luminescence decay profile of  $\text{CaAl}_{11.9}\text{O}_{19}:0.1\text{Cr}^{3+}$  ( $\lambda_{\text{exc}} = 445 \text{ nm}$ ) measured at: 0.933 GPa -a); 1.245 GPa -b).

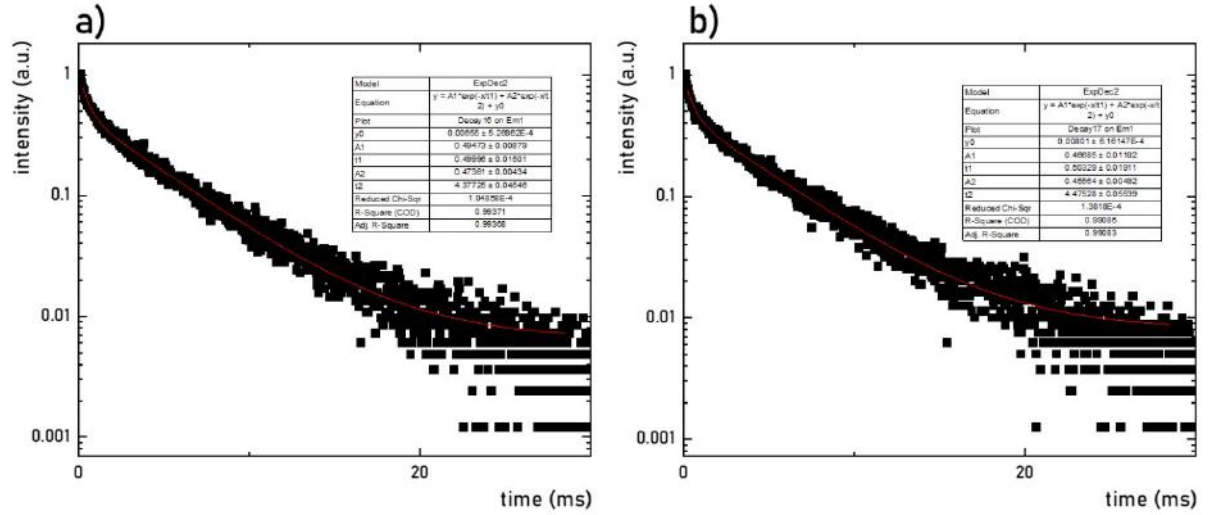


**Figure S16.** Fitting of luminescence decay profile of  $\text{CaAl}_{11.9}\text{O}_{19}:0.1\text{Cr}^{3+}$  ( $\lambda_{\text{exc}} = 445 \text{ nm}$ ) measured at: 1.5635 GPa -a); 1.904 GPa -b).

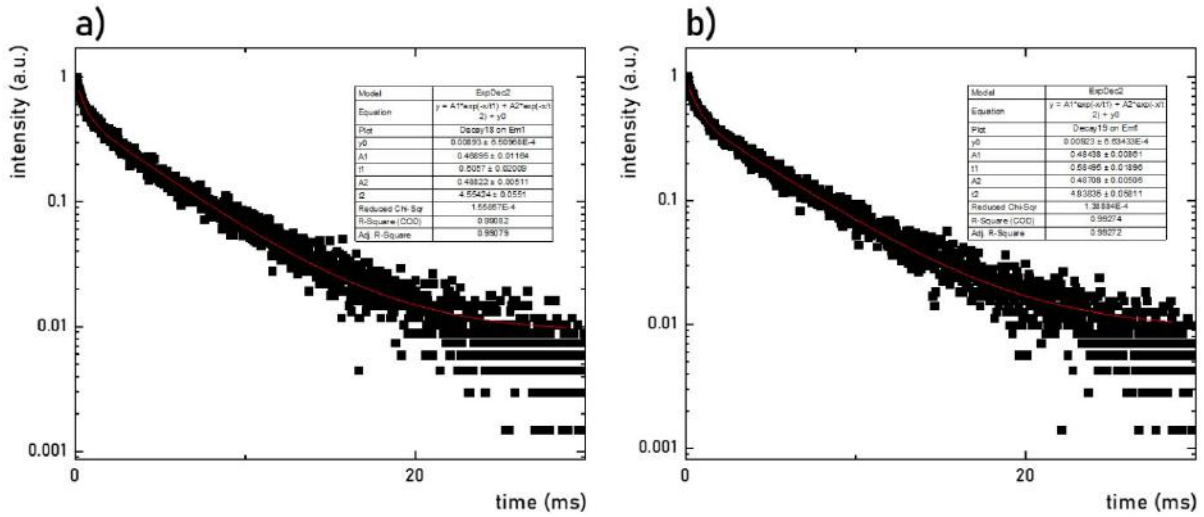


**Figure S17.** Fitting of luminescence decay profile of  $\text{CaAl}_{11.9}\text{O}_{19}:0.1\text{Cr}^{3+}$  ( $\lambda_{\text{exc}} = 445 \text{ nm}$ ) measured at: 2.38 GPa -a); 2.687 GPa -b).



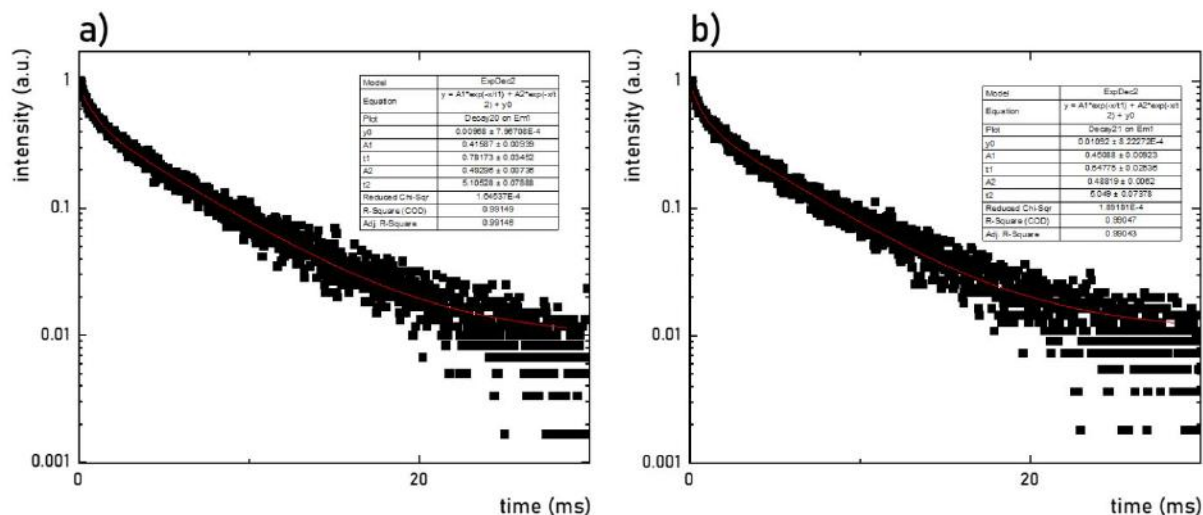


**Figure S18.** Fitting of luminescence decay profile of  $\text{CaAl}_{11.9}\text{O}_{19}:0.1\text{Cr}^{3+}$  ( $\lambda_{\text{exc}} = 445 \text{ nm}$ ) measured at: 3.0465 GPa -a); 3.4317 GPa -b).

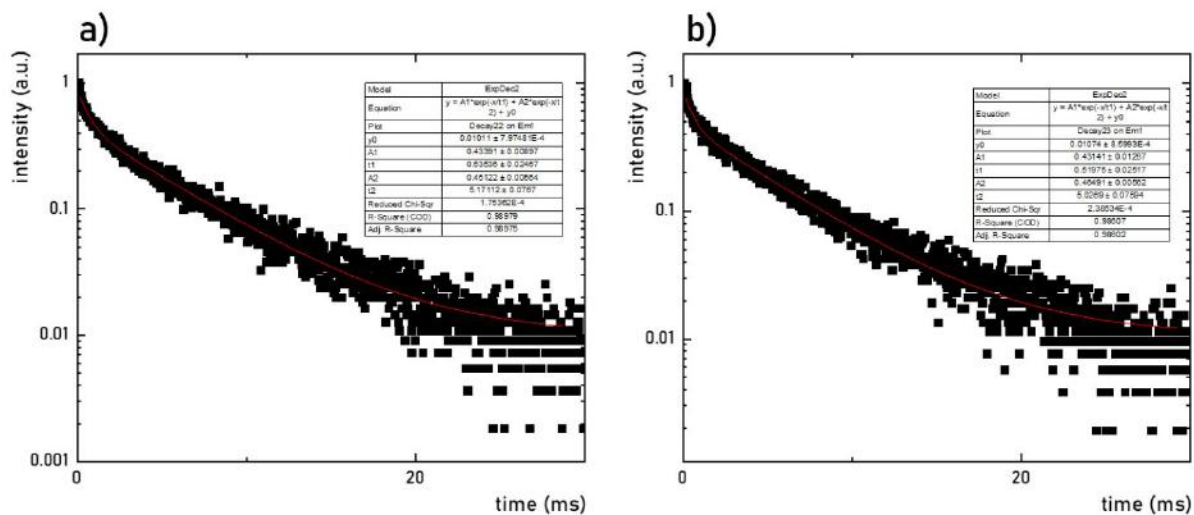


**Figure S19.** Fitting of luminescence decay profile of  $\text{CaAl}_{11.9}\text{O}_{19}:0.1\text{Cr}^{3+}$  ( $\lambda_{\text{exc}} = 445 \text{ nm}$ ) measured at: 3.7786 GPa -a); 4.036 GPa -b).

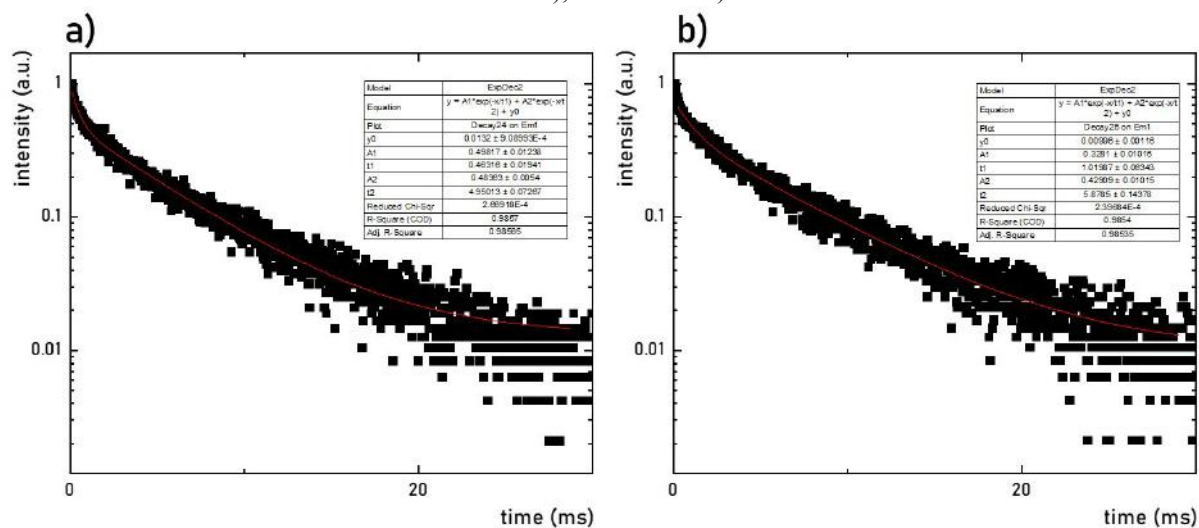


**Figure S20.** Fitting of luminescence decay profile of  $\text{CaAl}_{11.9}\text{O}_{19}:0.1\text{Cr}^{3+}$  ( $\lambda_{\text{exc}} = 445 \text{ nm}$ ) measured at: 4.254 GPa -a); 4.607 GPa -b).

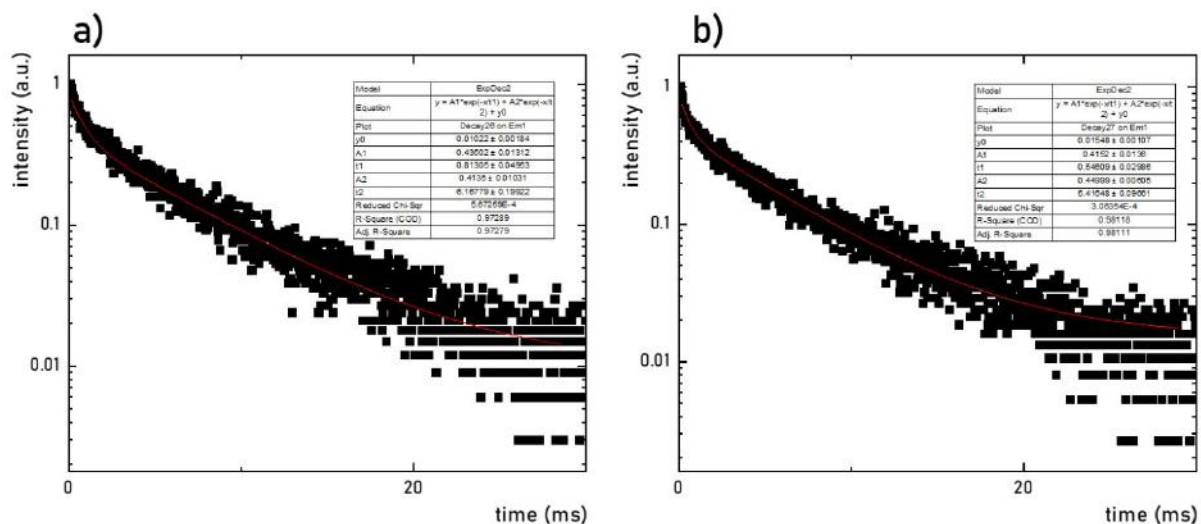


**Figure S21.** Fitting of luminescence decay profile of  $\text{CaAl}_{11.9}\text{O}_{19}:0.1\text{Cr}^{3+}$  ( $\lambda_{\text{exc}} = 445 \text{ nm}$ ) measured at: 5.0465 GPa -a); 5.4967 GPa -b).

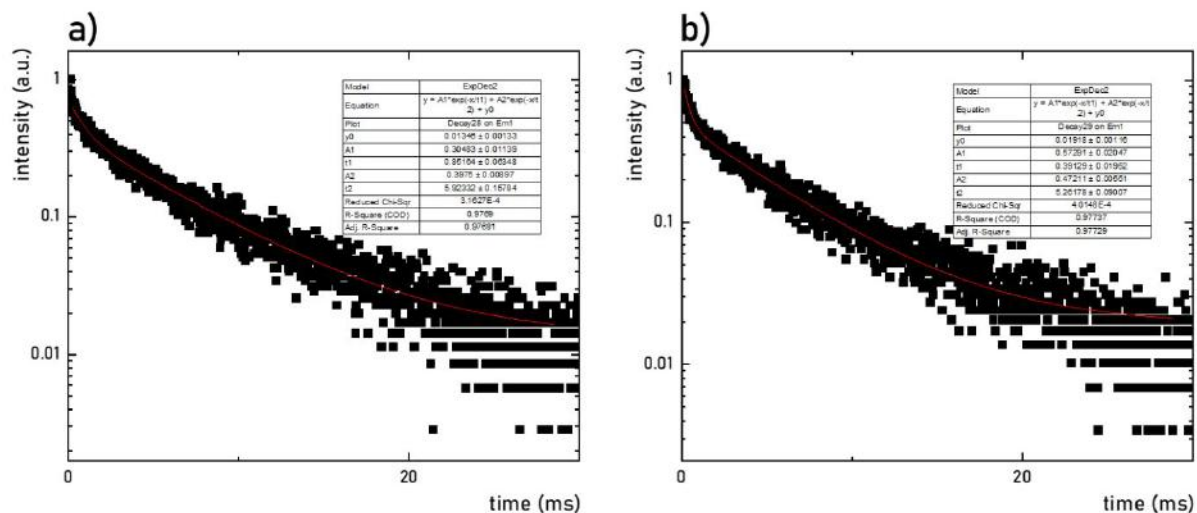


**Figure S22.** Fitting of luminescence decay profile of  $\text{CaAl}_{11.9}\text{O}_{19}:0.1\text{Cr}^{3+}$  ( $\lambda_{\text{exc}} = 445 \text{ nm}$ ) measured at: 5.8699 GPa -a); 6.563 GPa -b).

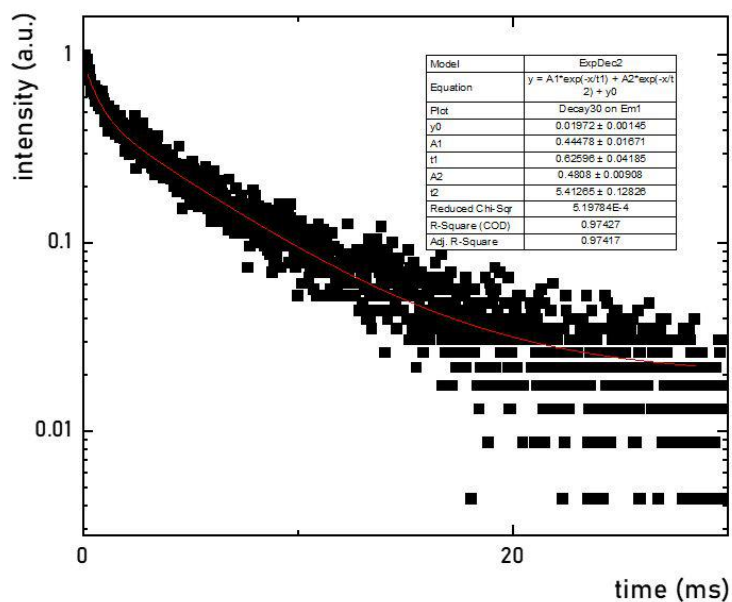




**Figure S23.** Fitting of luminescence decay profile of  $\text{CaAl}_{11.9}\text{O}_{19}:0.1\text{Cr}^{3+}$  ( $\lambda_{\text{exc}} = 445 \text{ nm}$ ) measured at 6.757 GPa.

Pressure dependence of  $\tau_{\text{avr}}$  can be fitted using experimental poly 5 curves as follows:

$$\tau_{\text{avr}}(p) = A_0 + A_1p + A_2p^2 + A_3p^3 + A_4p^4 + A_5p^5 \quad (\text{S3})$$

where

$$A_0=2.61168; A_1=0.3741; A_2=0.21823; A_3=-0.13169; A_4=0.02646; A_5=-0.00173$$

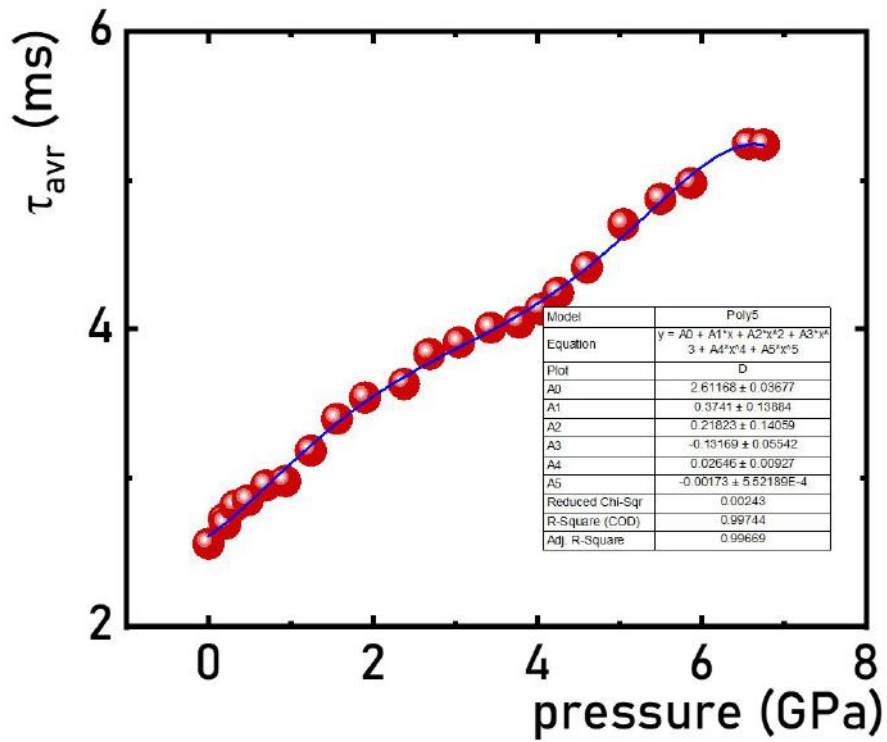


**Figure S24.** Fitting of pressure dependence of  $\tau_{\text{avr}}$  of  $\text{CaAl}_{11.9}\text{O}_{19}:0.1\text{Cr}^{3+}$ .

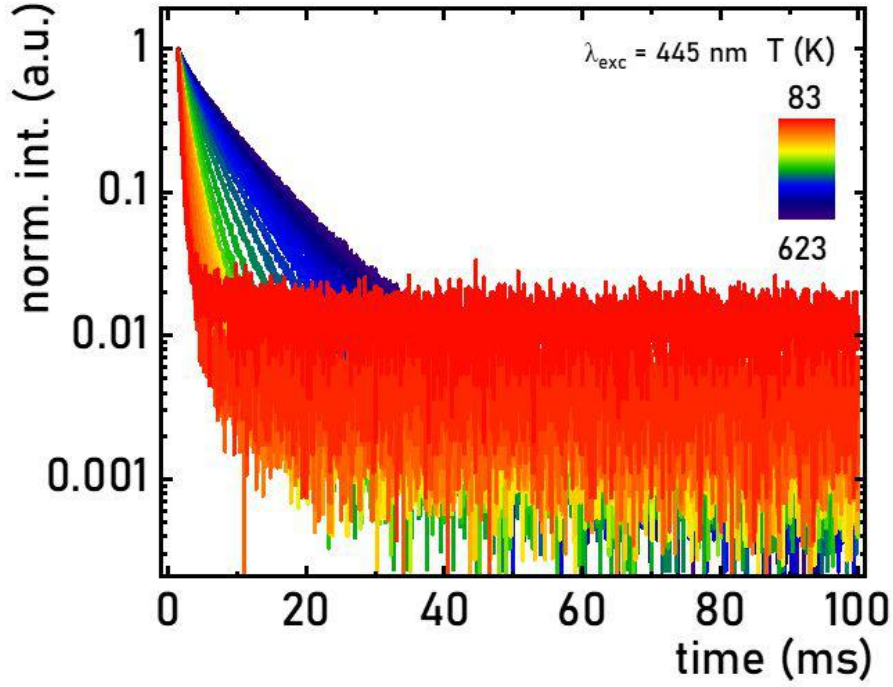


**Figure S25.** Temperature-dependent luminescence decay curves ( $\lambda_{\text{exc}} = 445 \text{ nm}$ ) of  $\text{CaAl}_{11.9}\text{O}_{19}:\text{0.1Cr}^{3+}$ .

Thermal dependence of  $\tau_{\text{avr}}$  can be fitted using experimental poly 5 curves as follows:

$$\tau_{\text{avr}}(T) = A_0 + A_1T + A_2T^2 + A_3T^3 + A_4T^4 + A_5T^5 \quad (\text{S4})$$

$A_0=7.98989$ ;  $A_1=-0.07071$ ;  $A_2=6.03023 \cdot 10^{-4}$ ;  $A_3=-2.55003 \cdot 10^{-6}$ ;  $A_4=4.65578 \cdot 10^{-9}$ ;  $A_5=-3.03189 \cdot 10^{-12}$

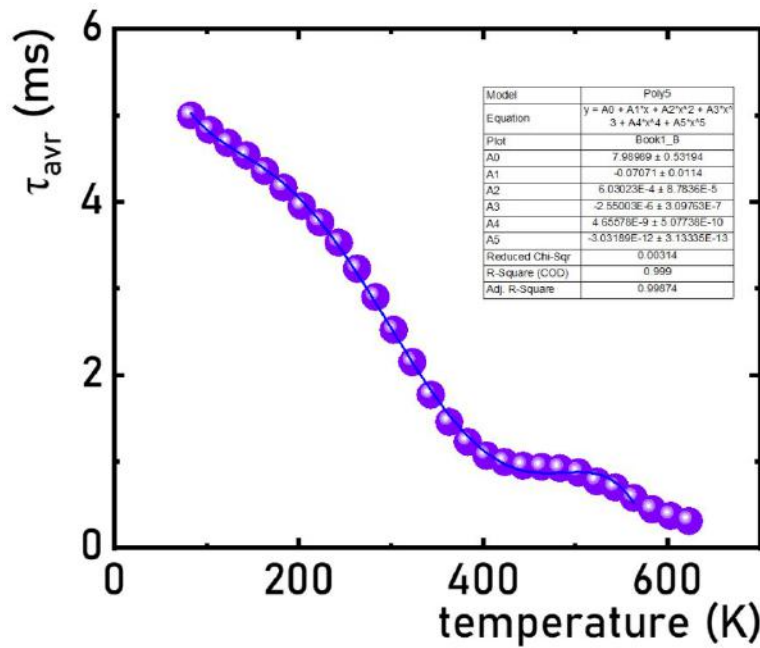


**Figure S26.** Fitting of thermal dependence of  $\tau_{\text{avr}}$  of  $\text{CaAl}_{11.9}\text{O}_{19}:\text{0.1Cr}^{3+}$ .





Cite this: *J. Mater. Chem. C*, 2025, 13, 4224

## Highly sensitive ratiometric luminescence manometers based on the multisite emission of $\text{Cr}^{3+}$

M. Szymczak,<sup>a</sup> W. M. Piotrowski,<sup>a</sup> U. R. Rodríguez-Mendoza,<sup>b</sup> P. Wozny,<sup>c</sup> M. Runowski<sup>c</sup> and L. Marciniak<sup>\*a</sup>

Luminescent materials have been extensively utilized for remote pressure measurement via luminescence manometry for a few decades. However, the drive to enhance the precision of these measurements, while maintaining high sensitivity to pressure changes, necessitates the exploration of new strategies and materials that meet these requirements. A ratiometric pressure readout based on the broadband  $\text{Cr}^{3+}$  emission, associated with the  ${}^4\text{T}_2 \rightarrow {}^4\text{A}_2$  electronic transition, addresses these needs by enabling both the accurate readout and imaging of pressure changes with extremely low thermal susceptibility. This paper demonstrates, for the first time, that employing a material with two crystallographic sites occupied by  $\text{Cr}^{3+}$  ions in  $\text{MgGeO}_3\text{:Cr}^{3+}$  allows for multimodal pressure readings that can be tailored to different measurement conditions. The simultaneous blueshift of both  ${}^4\text{T}_2 \rightarrow {}^4\text{A}_2$  emission bands of  $\text{Cr}^{3+}$  ions with increasing pressure results in changes in the spectral position and shape of the emission band of  $\text{MgGeO}_3\text{:Cr}^{3+}$ . The intensity ratio of these two bands can be employed for ratiometric readout with a relative sensitivity ( $S_{\text{R,p}}$ ) reaching ca. 22%  $\text{GPa}^{-1}$ . Furthermore, as we have shown, utilizing the ratio of emission intensities within the defined spectral ranges not only significantly increases the relative manometric sensitivity to  $S_{\text{R,p}} = 62\% \text{ GPa}^{-1}$ , but also simplifies the measurement methodology. Additionally, by carefully selecting the luminescence intensity ratio, it is possible to achieve high insensitivity to temperature changes, with the thermal invariability manometric factor (TIMF) reaching 600 K  $\text{GPa}^{-1}$ . The conducted studies clearly indicate the high application potential of the  $\text{MgGeO}_3\text{:Cr}^{3+}$  material in luminescence manometry and confirm that the approach based on the ratio of the relevant spectral ranges offers more favorable manometric performance compared to the approach based on deconvolution of the emission spectra.

Received 31st October 2024,  
Accepted 2nd January 2025

DOI: 10.1039/d4tc04639k

rsc.li/materials-c

## 1. Introduction

The ability to exploit luminescence for sensing and imaging physical and chemical quantities offered by luminescence sensors is of significant importance from an application standpoint.<sup>1–7</sup> The sensitivity of the spectroscopic properties of phosphors to changes in physical (e.g., temperature or pressure)<sup>8–17</sup> or chemical (e.g., pH, particle, or ion concentrations)<sup>18–23</sup> stimuli, coupled with the ability to remotely detect these changes,

enables noninvasive and electrically passive sensing (without electromagnetic interference). This is critical for many applications.<sup>24–27</sup> Although a wide range of spectroscopic parameters revealed sensitivity to changes in the analyzed stimuli, many studies have consistently shown that two parameters offer the highest measurement precision, i.e. (I) the luminescence intensity ratio (LIR) of two bands and (II) luminescence kinetics.<sup>8,9,11,28–33</sup> While the ratiometric approach has been extensively explored for temperature measurements in luminescence thermometry, it still remains underexplored in luminescence manometry.

In the case of pressure measurements in diamond anvil cells (DACs), the most common method involves using pressure-induced spectral band shifts.<sup>16,17,34–42</sup> A notable example here is the spectral shift of the  ${}^2\text{E} \rightarrow {}^4\text{A}_2$  band of  $\text{Cr}^{3+}$  in ruby.<sup>16,34–37,43</sup> While this technique is highly effective for pressures up to 150 GPa, it has several limitations.<sup>34</sup> One significant limitation is ruby's low sensitivity to pressure

<sup>a</sup> Institute of Low Temperature and Structure Research, Polish Academy of Sciences, Okólna 2, 50-422 Wrocław, Poland. E-mail: l.marciniak@intibs.pl

<sup>b</sup> Departamento de Física, Instituto de Materiales y Nanotecnología, IUEA & MALTA Consolider Team, Universidad de La Laguna, Apdo. Correos 456, E-38200 San Cristóbal de La Laguna, Santa Cruz de Tenerife, Spain

<sup>c</sup> Faculty of Chemistry, Adam Mickiewicz University, Uniwersytetu Poznańskiego 8, 61-614 Poznań, Poland

† Electronic supplementary information (ESI) available. See DOI: <https://doi.org/10.1039/d4tc04639k>

changes. Additionally, its spectral band position is also sensitive to temperature variations, which can hamper a reliable pressure readout. Moreover, from the perspective of imaging of the pressure changes beyond the DAC chamber, relying on spectral band shifts requires a point-by-point measurement of the emission spectrum across the area of interest. This process is extremely time-consuming and requires a detection system with high spatial resolution. Consequently, the ratiometric approach has gained increasing popularity in recent years, as confirmed by various studies.<sup>17</sup> Although these sensors exhibit high sensitivity to pressure changes, the sensitivity of the LIR to temperature variations limits the temperature-invariant manometry. To address these limitations, a solution based on the ratiometric readout of changes in the emission spectra of broadband phosphors, such as  $^4T_2 \rightarrow ^4A_2$  transition of  $Cr^{3+}$  ions<sup>44–47</sup> or 5d–4f interconfigurational transition of  $Ce^{3+}$  doped<sup>48</sup> inorganic materials, has been recently proposed. In this case, the high sensitivity of the emission bands to environmental changes, leading to their spectral shift, has enabled the development of optical manometers with record relative sensitivities. Furthermore, the implementation of the ratiometric approach, in contrary to band maximum analysis, allows for fast imaging of pressure changes. This approach is particularly well-illustrated in the case of  $Cr^{3+}$  doped phosphors, where material compression leads to a change in the strength of the crystal field acting on  $Cr^{3+}$  ions, resulting in an increase in the energy of the  $^4T_2$  level.<sup>44–47</sup> Importantly, the absence of analogous changes in the crystal field strength due to temperature variations enables the thermally invariant pressure readout. The high application potential of this approach has spurred research into high-pressure gauges. Traditionally, this method has been applied almost exclusively to materials where the  $Cr^{3+}$  ion occupies only one crystallographic position in the host material. In contrast, in the present work, we explore the application potential of a system where  $Cr^{3+}$  ions can occupy two non-equivalent  $Mg^{2+}$  positions in the  $MgGeO_3:Cr^{3+}$  compound. The superposition of changes in the crystallographic environment of  $Cr^{3+}$  ions in both positions can lead to significant changes in the luminescence intensity ratio, thereby achieving high relative sensitivity.

## 2. Experimental section

### Synthesis

The powders of the  $MgGeO_3:x\% Cr^{3+}$  ( $x = 0.1, 0.2, 0.5, 1, 2, 5, 10$ ) microcrystals were synthesized using the solid-state method.  $Mg(CH_3COO)_2 \cdot 4H_2O$  (99.9% purity, Chempur),  $GeO_2$  (99.999% purity, Thermo Scientific Chemicals), and  $Cr(NO_3)_3 \cdot 9H_2O$  (99.99% purity, Alfa Aesar) were used as starting materials without further purification. The stoichiometric amounts of compounds were mixed in *n*-hexane and ground well in an agate mortar three times until the *n*-hexane evaporated. Next, the powders with *x*% molar  $Cr^{3+}$  concentration with respect to  $Mg^{2+}$  ions were annealed in corundum crucibles in air at 1523 K for 10 h (3 K min<sup>−1</sup> heating rate).

### Methods

The X-ray diffraction (XRD) patterns of the synthesized powders were obtained using the X-ray diffractometer (D8 Advance diffractometer, Bruker Corporation, Germany) with Cu K $\alpha$  ( $\lambda = 1.5406$  Å) at 40 kV and 40 mA.

The morphology of the synthesized particles and the distribution of elements were examined by scanning electron microscopy (SEM) and by energy dispersive spectroscopy (EDS). Measurements were carried out with FEI NOVA Nano-SEM 230 equipped with an energy-dispersive spectrometer EDAX Genesis XM4. The powder was dispersed in a few drops of methanol, and then a drop of the obtained suspension was placed on the carbon stub and dried under an infrared lamp.

Scattering Raman spectra were recorded in the pressure range from ambient pressure to 7.18 GPa in a backscattering geometry using a Renishaw InVia confocal micro-Raman system with a 100 mW 532 nm diode laser and an optical system with an Olympus x20 SLMPlan N long working distance objective to focus the laser beam on the material. Raman spectra of the compressed sample were recorded in a Diamond anvil cell (DAC) equipped with the IIas type, low fluorescence diamonds in a methanol : ethanol : water (16 : 3 : 1) solution as the pressure transmitting medium.

The pressure- and temperature-dependent emission spectra, excitation spectra and luminescence decay profiles were measured using an FLS1000 fluorescence spectrometer (Edinburgh Instruments), equipped with the 450 W Xenon lamp and R5509-72 photomultiplier tube from Hamamatsu in nitrogen-flow cooled housing as the detector. A continuous/pulse laser diode with a wavelength of 445 nm was used as the excitation source for measuring emission spectra and luminescence decay profiles, respectively. The luminescence decay profiles were fitted using a biexponential function:

$$y = y_0 + A_1 \cdot \exp\left(-\frac{x}{t_1}\right) + A_2 \cdot \exp\left(-\frac{x}{t_2}\right) \quad (1)$$

and the average lifetime was calculated using eqn (5):

$$\tau_{\text{avr}} = \frac{A_1 \tau_1^2 + A_2 \tau_2^2}{A_1 \tau_1 + A_2 \tau_2} \quad (2)$$

where  $\tau_1$  and  $\tau_2$  represent the luminescence decay time components and  $A_1$  and  $A_2$  are amplitudes obtained based on the parameters of the biexponential function.

A THMS 600 heating-cooling stage from Linkam was used to set and control a temperature during measurements with 0.1 K temperature stability and 0.1 K set point resolution. To stabilize the temperature of the measured sample, it was incubated at the set temperature for 2 min and the results were collected after this time. A Druck PACE 5000 was used to apply pressure, during pressure-dependent luminescence studies. The high-pressure luminescence measurements were carried out in a diamond anvil cell (DAC) purchased from Almax easyLab – Diacell  $\mu$ ScopeDAC-RT(G). The pressure in the DAC was applied through a nitrogen-fed gas membrane. The DAC was equipped with ultra-low fluorescence IIas type diamonds, with 0.4 mm culets.

A 250  $\mu\text{m}$  stainless-steel gasket with a diameter of 10 mm was placed between the diamonds. A hole of 140  $\mu\text{m}$  in diameter was drilled centrally in the gasket, into which an appropriate amount of pressure indicator, a sample and a drop of a pressure transmitting medium (PTM) were placed. The mixture of methanol:ethanol (4:1) was used as PTM and  $\text{SrB}_2\text{O}_4\text{:Sm}^{2+}$  was used as a pressure indicator.<sup>49</sup>

### 3. Results and discussion

$\text{MgGeO}_3$  crystallizes in an orthorhombic crystal system of the *Pbca* (61) space group.<sup>50–54</sup> Its orthopyroxene-type structure ( $a = 18.8099(12)$ ,  $b = 8.9484(8)$ ,  $c = 5.3451(4)$  Å) consists of parallel chains of  $(\text{GeO}_4)^{4-}$  tetrahedra surrounded by  $\text{Mg}^{2+}$  cations (Fig. 1(a)).<sup>55–59</sup> Therefore, the  $\text{Ge}^{4+}$  ions are located in two inequivalent tetrahedral sites, while  $\text{Mg}^{2+}$  ions are surrounded by six  $\text{O}^{2-}$  ions, forming two inequivalent octahedral sites. For  $\text{Ge}^{4+}(1)$ ,  $\text{Ge}^{4+}(2)$ ,  $\text{Mg}^{2+}(1)$  and  $\text{Mg}^{2+}(2)$ , all metal–oxygen distances are inequivalent, but their ranges and average values differ slightly (Table 1). When introducing chromium ions as dopants into  $\text{MgGeO}_3$ , several possibilities for their stabilization should be considered. The most energetically stable oxidation state of Cr ions is  $3^+$ , which is only considered

**Table 1** Comparison of metal–oxygen distances of crystallographic sites in  $\text{MgGeO}_3$

Atom	Coordination number	$\text{Ge}^{4+}\text{--O}^{2-}/\text{Mg}^{2+}\text{--O}^{2-}$ distance range (Å)	Average distance (Å)
$\text{Ge}_1$	4	1.704–1.787	1.744
$\text{Ge}_2$	4	1.707–1.798	1.760
$\text{Mg}_1$	6	2.005–2.160	2.088
$\text{Mg}_2$	6	2.010–2.286	2.129

in octahedral sites. Therefore,  $\text{Cr}^{3+}$  is expected to locate in the crystallographic positions of six-fold coordinated  $\text{Mg}^{2+}$  ions (Fig. 1(b)). This is further justified by the smaller differences between the Shannon effective ionic radii of  $\text{Cr}^{3+}$  (6-fold coordinated,  $R = 61.5$  pm) and  $\text{Mg}^{2+}$  (6-fold coordinated,  $R = 72.0$  pm) in respect to those of  $\text{Cr}^{3+}$  and  $\text{Ge}^{4+}$  ( $R = 39.0$  pm), for which the misfit parameter equals  $(R_{\text{Mg}^{2+}(\text{VI})} - R_{\text{Cr}^{3+}(\text{VI})})/R_{\text{Mg}^{2+}(\text{VI})} = 17.1\%$  and  $(R_{\text{Cr}^{3+}(\text{VI})} - R_{\text{Ge}^{4+}(\text{IV})})/R_{\text{Ge}^{4+}(\text{IV})} = 36.6\%$ , respectively.<sup>60</sup> Consideration should be also given to the stabilization of  $\text{Cr}^{4+}$ , which can be located in both octahedral and tetrahedral positions. Since the effective ionic radius decreases with increasing oxidation state,  $\text{Cr}^{4+}$  is not expected to occupy the  $\text{Mg}^{2+}$  positions, for which the misfit parameter will be even greater than for  $\text{Cr}^{3+}$ . In addition,  $\text{Cr}^{4+}$  ions in the octahedral

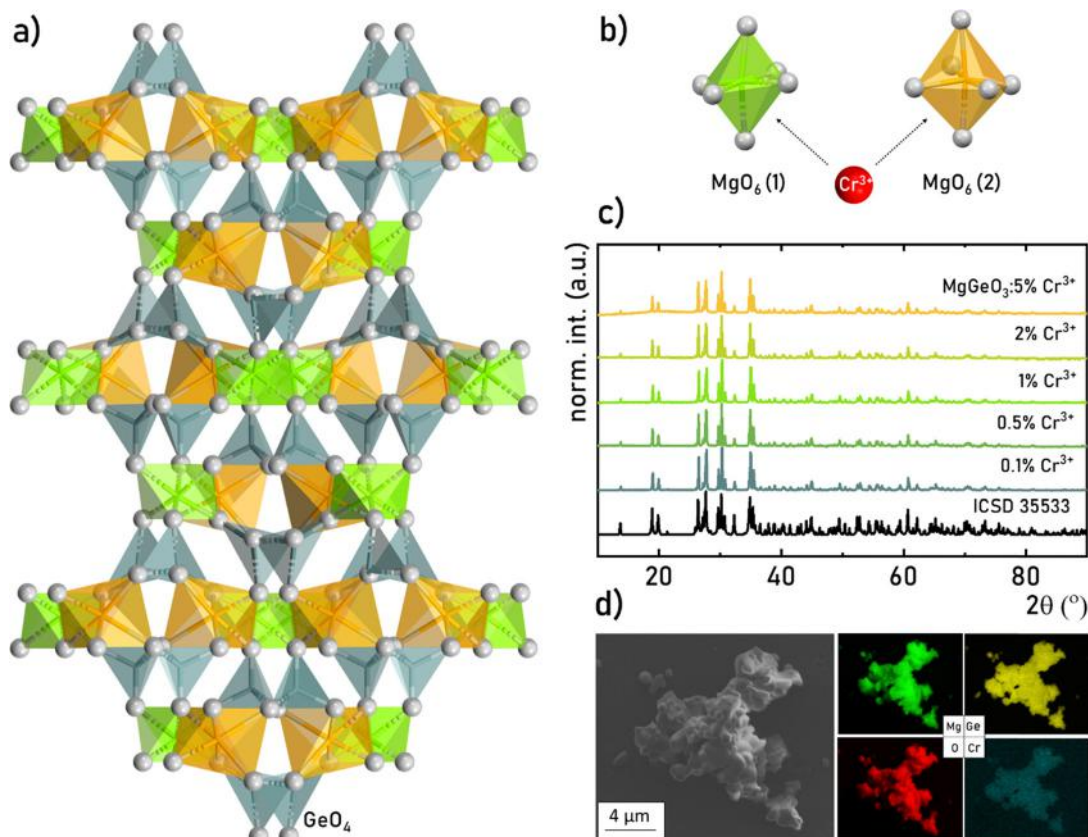


**Fig. 1** 3D-visualization of the  $\text{MgGeO}_3$  crystal structure (a) with schematically shown incorporation of  $\text{Cr}^{3+}$  ions into  $\text{Mg}^{2+}$ -octahedra (b), XRD patterns (c) of the  $\text{MgGeO}_3$  doped with various concentrations of  $\text{Cr}^{3+}$  ions. SEM image and EDS maps for Mg, Ge, O and Cr elements forming the structure of  $\text{MgGeO}_3\text{:}1\%\text{Cr}^{3+}$  material (d).



site do not reveal luminescence either, so they do not affect the spectroscopic properties of the material.<sup>61–63</sup> In contrast,  $\text{Cr}^{4+}$  ions with  $R = 41.0$  pm are well matched to  $(\text{GeO}_4)^{4-}$  tetrahedra, for which the misfit parameter is 4.9%. However, as presented later in this article, the broad emission band of  $\text{Cr}^{4+}$  in the near infrared (NIR) range was not observed, suggesting that their potential effect on the luminescence of  $\text{Cr}^{3+}$  ions is negligible.

The purity of the synthesized  $\text{MgGeO}_3$  powders doped with various concentrations of  $\text{Cr}^{3+}$  was confirmed through XRD analysis, comparing with a reference pattern (no. 35533) from the Inorganic Crystal Structure Database (ICSD), as shown in Fig. 1(c) (see also Fig. S1–S5 (ESI†) for the results of the Rietveld refinement of the XRD patterns). The absence of additional peaks further verifies the successful incorporation of  $\text{Cr}^{3+}$  ions into the crystal structure of  $\text{MgGeO}_3$ . The morphology of the  $\text{MgGeO}_3\cdot 1\%\text{Cr}^{3+}$  sample was examined using SEM. As can be seen in Fig. 1,  $\text{MgGeO}_3$  powders are characterized by micro-sized crystals, forming agglomerates. The elemental maps obtained based on the EDS analysis may indicate a uniform distribution of all elements in the crystals at the resolution offered using the microscope (Fig. 1(d)). However, to definitively confirm the homogeneous distribution of elements at the microscale, higher-resolution imaging is required.

The Raman scattering spectra of  $\text{MgGeO}_3$  were measured to analyze the structural stability of the investigated host material under high-pressure conditions. The recorded Raman spectrum for the  $\text{MgGeO}_3$  material under ambient conditions presents

several intense Raman peaks. For further analysis, we selected six bands initially located around  $\approx 340$ , 360, 570, 710, 860 and  $880\text{ cm}^{-1}$  (Fig. 2(a) and (b)). In the compression process in the system the energies of the phonon modes increase, and the corresponding Raman mode centroids shift linearly toward higher wavenumbers, as shown in Fig. 2(b). The observed tendency is an effect of the bonds shortening, *i.e.*, a decrease of the interatomic distances in the structures under compression. During the high-pressure compression process, when the pressure was around 5 GPa we observed the vanishing and forming new Raman modes in recorded spectra. Disappearing of the Raman modes at 340, 360, 710 and  $800\text{ cm}^{-1}$  and formation of new Raman modes at 400 and  $960\text{ cm}^{-1}$  is a clear evidence of phase transformation of the synthesized  $\text{MgGeO}_3$  material to the new high-pressure phase. The observed phase transition is a result of transforming the orthorhombic  $\text{MgGeO}_3$  (*Pbcn*) crystal structure (isostructural to orthopyroxene  $\text{MgSiO}_3$ ) to the monoclinic  $\text{MgGeO}_3$  phase (*C2/c*).<sup>64</sup> Intense Raman modes at  $860\text{--}880\text{ cm}^{-1}$  result from the antisymmetric ( $A_g$ ) stretching while weak scattering results from symmetric stretching ( $B_g$ ) of the O–Ge–O bonds in the orthorhombic phase. However, the intense vibrational Raman modes around  $600\text{ cm}^{-1}$  correspond to the Ge–O stretching of the bridging oxygen atoms ( $A_g$ ). Finally, the intense Raman modes ( $A_g$ ) at low frequencies around  $400\text{ cm}^{-1}$  originate from the Mg–O bond stretching.<sup>65</sup> After the phase transition to the monoclinic phase, only intense ( $A_g$ ) modes were observed. The Raman modes of the

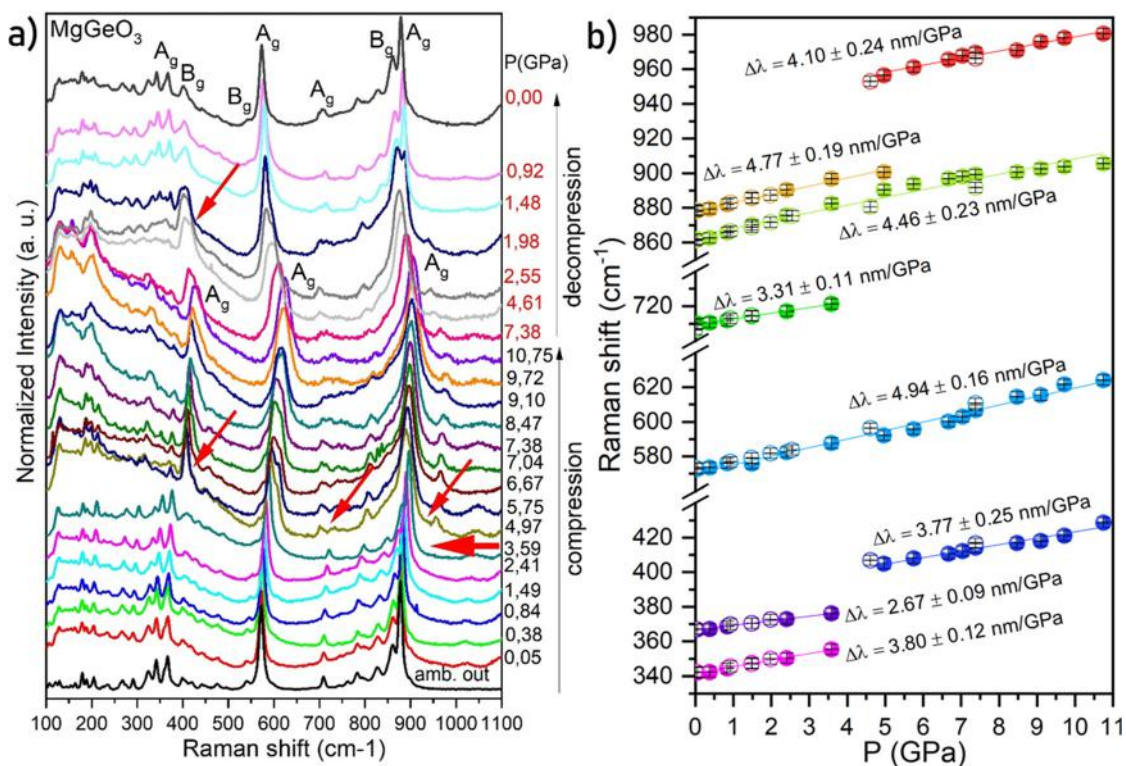


Fig. 2 Normalized Raman spectra for the  $\text{MgGeO}_3$  material in compression and decompression cycles (a). Calculated peak centroids of the most intense Raman modes as a function of pressure (b); full spheres indicate peak centroid in the compression cycle, and empty ones indicate peak centroids in the decompression cycle; the color lines are the linear functions fitted to estimate the pressure shift rates of the Raman modes.



high-pressure phase of the  $\text{MgGeO}_3$  material also exhibit a linear shift towards higher energies with further pressure elevation. The calculated shift rates (in  $\text{cm}^{-1} \text{GPa}^{-1}$ ) for the observed Raman modes are collected in Table S1 in the ESI† data. The observed decreasing signal-to-noise ratio of Raman spectra is related to the increasing strains and formation of crystal defects in the crystal structures under high-pressure compression. In the decompression cycle, the reverse tendency of the Raman modes spectral shift to the initial state was observed (Fig. 2(b)). Hence, the observed formation of the new high-pressure phase of the  $\text{MgGeO}_3$  material was reversible in the decompression cycle (elastic process). The similar position of Raman modes and the same shape of the spectra at ambient conditions after pressure release (compared to the initial spectrum of the uncompressed sample), suggests complete reversibility of the structural changes caused by compression of the material under high-pressure. However, a full reversibility of the high-pressure phase transition of  $\text{MgGeO}_3$  can be observed when pressure is released below  $\approx 2 \text{ GPa}$  in a decompression cycle, indicating some hysteresis in the compression–decompression process, which in fact is typically observed for such kind of experiments.

The spectroscopic properties of  $\text{Cr}^{3+}$  ions are highly sensitive to changes in chemical features (such as variations in the host material composition) and physical parameters (such as temperature or pressure).<sup>66–68</sup> To fully understand this behavior, it is essential to refer to the Tanabe–Sugano diagram<sup>69</sup> for transition metal ions with a  $3d^3$  electronic configuration, as well as the simplified configurational coordination diagram

shown in Fig. 3(a). Given that the luminescence spectrum primarily results from the radiative depopulation of the excited state of the lowest energy, changes in the crystal field strength acting on  $\text{Cr}^{3+}$  ions significantly influence the shape of the emission spectrum. In a host material of weak crystal field,  ${}^4\text{T}_2$  is the excited state of the lowest energy, and the  ${}^4\text{T}_2 \rightarrow {}^4\text{A}_2$  electronic transitions results in a broad emission band. The energy of the  ${}^4\text{T}_2$  level is sensitive to changes in crystal field strength, increasing as the field strength is enhanced. At the values of  $Dq/B$  approximately 2.1 the energy of  ${}^4\text{T}_2$  is comparable with that of the  ${}^2\text{E}$  level.<sup>70</sup> Therefore in the emission spectra of such phosphor co-existence of both broad and narrow (corresponding to the  ${}^2\text{E} \rightarrow {}^4\text{A}_2$  electronic transitions) emission bands can be observed. A further increase in the crystal field strength elevates the energy of the  ${}^4\text{T}_2$  level well above the  ${}^2\text{E}$  level, leading to the observation of only a spectrally narrow band in the  $\text{Cr}^{3+}$  emission spectrum. In the case of the  $\text{MgGeO}_3:\text{Cr}^{3+}$  compound, only broadband emission is observed, and the shape of the emission spectrum exhibits an inhomogeneous broadening, suggesting the presence of more than one emission center (Fig. 3(b)). Deconvolution of the  $\text{MgGeO}_3:\text{Cr}^{3+}$  emission band reveals the presence of two components, consistent with the previously described two positions of  $\text{Mg}^{2+}$  ions that can be occupied by  $\text{Cr}^{3+}$  ions. The shape of these two observed components indicates that a weak crystal field affects both  $\text{Mg}^{2+}$  sites, resulting in  ${}^4\text{T}_2 \rightarrow {}^4\text{A}_2$  bands with maxima at approximately  $11\,271 \text{ cm}^{-1}$  and  $12\,528 \text{ cm}^{-1}$ , which can be attributed to  $\text{Mg}^{2+}(2)$  and  $\text{Mg}^{2+}(1)$ , respectively. Excitation spectra

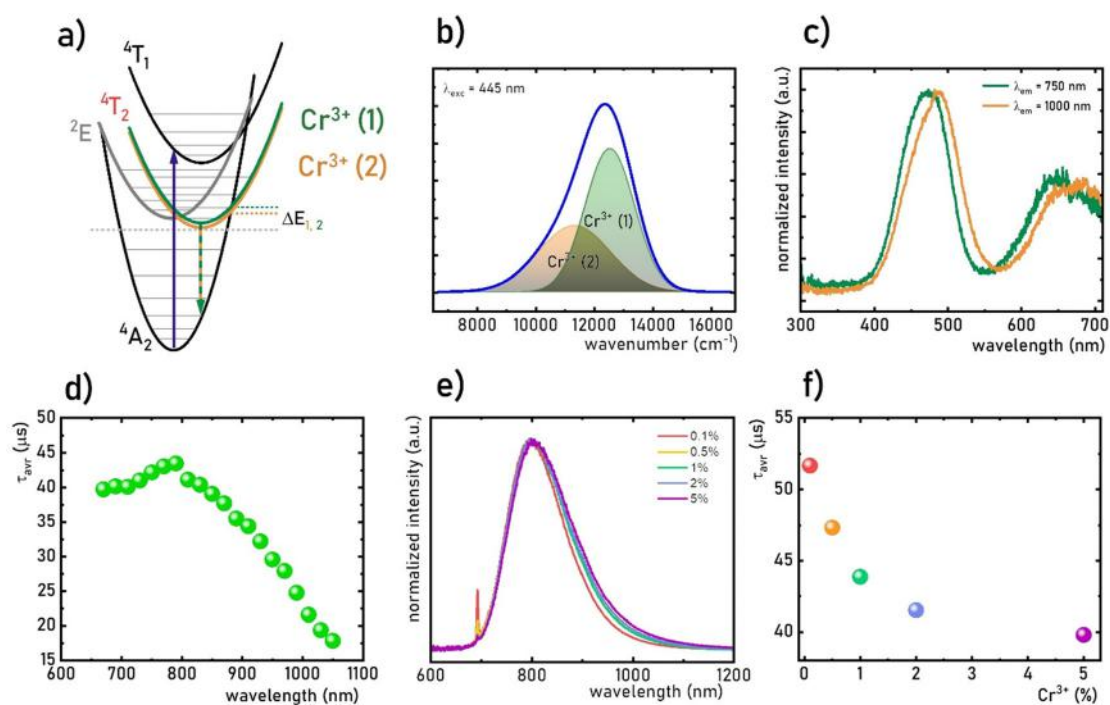


Fig. 3 Simplified configurational coordination diagram for  $\text{Cr}^{3+}$  ions in  $\text{Mg}^{2+}(1)$  and  $\text{Mg}^{2+}(2)$  (a); room temperature emission spectra of  $\text{MgGeO}_3:5\%\text{Cr}^{3+}$  ( $\lambda_{\text{exc}} = 445 \text{ nm}$ ) with the deconvolution of the band (b); excitation spectra of  $\text{Cr}^{3+}$  ions located in the  $\text{Mg}^{2+}(1)$  and  $\text{Mg}^{2+}(2)$  sites of the  $\text{MgGeO}_3:5\%\text{Cr}^{3+}$ , recorded at  $\lambda_{\text{em}} = 750 \text{ nm}$  and  $\lambda_{\text{em}} = 1000 \text{ nm}$ , respectively (c);  $\tau_{\text{avr}}$  of  $\text{Cr}^{3+}$  in  $\text{MgGeO}_3:5\%\text{Cr}^{3+}$  measured as a function of emission wavelength (d); comparison of normalized emission spectra of  $\text{MgGeO}_3:\text{Cr}^{3+}$  (e) and  $\tau_{\text{avr}}$  (f) as a function of  $\text{Cr}^{3+}$  concentration.

measurements for each of these sites reveal bands associated with the  $^4A_2 \rightarrow ^4T_1$  (450 nm) and  $^4A_2 \rightarrow ^4T_2$  ( $\sim 650$  nm) electronic transitions (Fig. 3(c), excitation spectra measured monitoring various  $\lambda_{em}$  are in Fig. S6, ESI†). However, the significant differences in the positions of these band maxima indicate a variation in crystal field strength at each site. Based on the presented spectra, the crystal field strength parameters ( $Dq/B$ ) were determined using the following equations:

$$Dq = \frac{E(^4A_2 \rightarrow ^4T_2)}{10} \quad (3)$$

$$x = \frac{E(^4A_2 \rightarrow ^4T_1) - E(^4A_2 \rightarrow ^4T_2)}{Dq} \quad (4)$$

$$\frac{Dq}{B} = \frac{15(x - 8)}{(x^2 - 10x)} \quad (5)$$

where  $Dq$  is the crystal field splitting energy and  $B$  is the Racah parameter. The values obtained were  $Dq/B = 1.97$  and  $1.9$  for  $Mg^{2+}(1)$  and  $Mg^{2+}(2)$ , respectively. The weak crystal field affecting the  $Cr^{3+}$  ions at these positions results from both the length of the  $Cr^{3+}-O^{2-}$  bonds and the distortion of the  $(MgO_6)^{10-}$  octahedra. Although for an ideal octahedron, the crystal field strength should be inversely proportional to  $R^5$  (where  $R$  represents  $Cr^{3+}-O^{2-}$  distance), in this system, small differences in  $Dq/B$  values would be expected. However, octahedral distortion significantly affects the energies of the  $^4T_2$  levels for individual  $Mg^{2+}$  sites, leading to larger-than-expected (under  $O_h$  symmetry) differences in the  $Dq/B$  values. The larger  $Cr^{3+}-O^{2-}$  distances for  $Mg^{2+}(2)$  result in a lower crystal field strength affecting the  $Cr^{3+}$  ions. It is noteworthy that, the dominant contribution to the emission spectrum of  $MgGeO_3:Cr^{3+}$  comes from luminescence of  $Cr^{3+}$  ions located in the  $Mg^{2+}(1)$  sites, which may be related either to a higher occupancy of the  $Mg^{2+}(1)$  site compared to  $Mg^{2+}(2)$ , or to more effective non-radiative depopulation of the  $^4T_2$  level of  $Cr^{3+}$  at  $Mg^{2+}(2)$  due to the lower activation energy (Fig. 3(a)). However, temperature-dependent emission spectra measurements (Fig. 6(a) and Fig. S7, ESI†) indicate that while luminescence intensity gradually decreases with increasing temperature, the shape of the emission spectrum remains largely unchanged, suggesting similar rates of thermal quenching for both  $Cr^{3+}$  sites. Analyzing luminescence kinetics in the presence of two  $Cr^{3+}$  sites is complex, due to the contribution of the  $^4T_2$  excited state lifetimes of both ions in the luminescence decay profile. Nevertheless, measurements of luminescence decay curves as a function of emission wavelength clearly show that at  $\lambda_{em} \sim 720$  nm, exponential decay is observed, which shortens and deviates from exponentiality as the emission wavelength increases (Fig. 3(d) and Fig. S8, ESI†). On the other hand, for emission wavelengths above  $\lambda_{em} = 930$  nm, exponential decay is again observed but with a shorter decay constant. For comparative analysis, the average lifetime of  $Cr^{3+}$  ions ( $\tau_{avr}$ ) was determined according to the procedure described in the Experimental section. The results show that as the detection wavelength increases from 720 to 930 nm, the average lifetime shortens from approximately 42  $\mu s$  to 17  $\mu s$  (Fig. 3(d)). Since these extreme  $\tau_{avr}$  values correspond to emission wavelengths

dominated by contributions from  $Mg^{2+}(1)$  and  $Mg^{2+}(2)$ , respectively, the obtained values of  $\tau_{avr}$  can be directly attributed to the  $^4T_2$  state of  $Cr^{3+}$  in these sites. Significantly, an increase in the concentration of  $Cr^{3+}$  ions has only a slight effect on the position of the band maximum, which shifts from 796 nm for 0.1%  $Cr^{3+}$  to 803 nm for 5%  $Cr^{3+}$  (Fig. 3(e)). The observed changes result from a slight broadening of the emission band on the longer-wavelength side of the spectrum, which may indicate that an increase in  $Cr^{3+}$  ion concentration leads to a successive increase in occupancy of the  $Mg^{2+}(2)$  site by  $Cr^{3+}$  ions with respect to  $Mg^{2+}(1)$ . However, this difference is marginal. Additionally, an increase in the  $Cr^{3+}$  concentration results in a slight shortening of the  $\tau_{avr}$  from 52  $\mu s$  for the sample with 0.1% of  $Cr^{3+}$  to 42  $\mu s$  for 5% of  $Cr^{3+}$ , which is associated with an increased contribution of the short-lived component of  $Cr^{3+}$  ions in  $Mg^{2+}(2)$  with respect to the  $Cr^{3+}$  in  $Mg^{2+}(1)$  (Fig. 3(f) and Fig. S9, ESI†). The fact that broadband emission of  $Cr^{3+}$  ions is observed for both  $Mg^{2+}$  sites is extremely advantageous from a manometric perspective.

As described above, changes in the strength of the crystal field acting on  $Cr^{3+}$  ions affect the energy of the  $^4T_2$  level. This change can be induced not only by altering the chemical composition of the host material but also by varying the applied pressure. Compression of the material typically leads to a reduction in the  $Cr^{3+}-O^{2-}$  distance, resulting in an increase in the crystal field strength. Consequently, for broadband phosphors based on  $Cr^{3+}$  ion emission, an increase in the  $^4T_2$  level energy is expected with increasing pressure, leading to a blueshift in the emission band. The increase in pressure significantly modifies the shape of the  $Cr^{3+}$  ion emission spectrum of  $MgGeO_3:Cr^{3+}$  (Fig. 4(a)). As clearly shown in Fig. 4(a), a successive shift of the emission band towards higher energies is observed, and the band associated with the  $^4T_2 \rightarrow ^4A_2$  transition of  $Cr^{3+}$  in the  $Mg^{2+}(2)$  site, in respect to the  $Mg^{2+}(1)$  site becomes more prominent, resulting in a distinct distortion of the emission spectrum compared to that measured at ambient pressure. Deconvolution of the obtained emission bands of the  $MgGeO_3:Cr^{3+}$  enables qualitative analysis of pressure-induced changes. Each of the  $^4T_2 \rightarrow ^4A_2$  bands of  $Cr^{3+}$  ions undergoes a shift toward higher energies; however, analysis of the energy corresponding to the band maxima indicates that greater changes occur for  $Cr^{3+}$  in the  $Mg^{2+}(1)$  site (shift from 12 527  $cm^{-1}$  at ambient pressure to 13 887  $cm^{-1}$  at 7.5 GPa) than for the  $Mg^{2+}(2)$  site (shift from 11 320  $cm^{-1}$  to 12 088  $cm^{-1}$  at 7.5 GPa) (Fig. 4(b)). This difference is particularly evident when the change in energy of the band maximum ( $\Delta E$ ) is plotted as a function of the applied pressure (Fig. 4(c)). A monotonic change of nearly 1400  $cm^{-1}$  is observed for  $Mg^{2+}(1)$ , compared to a change of about 600  $cm^{-1}$  for  $Mg^{2+}(2)$  in the analyzed pressure range. This result indicates that compression has a greater effect on the  $Cr^{3+}$  environment in  $Mg^{2+}(1)$  with respect to  $Mg^{2+}(2)$ . However, in the 4–5 GPa pressure range some small deviation can be observed which is most probably related to the described above reversible phase transition. The absence of significant changes in the rate of shift of the emission band maximum with increasing pressure, suggests that compression of  $MgGeO_3:Cr^{3+}$  within the analyzed

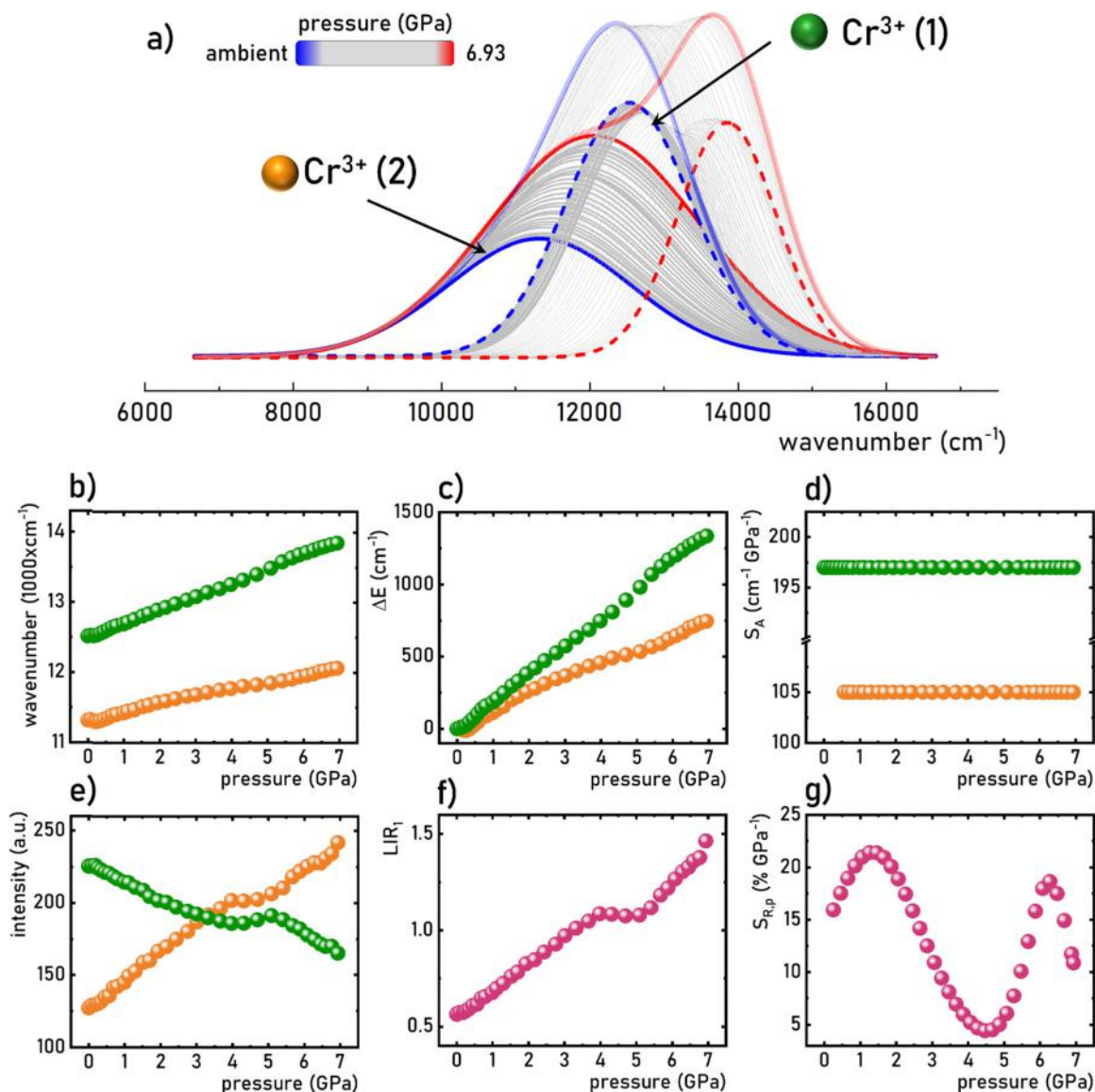


Fig. 4 Normalized emission spectra of  $\text{MgGeO}_3:5\%\text{Cr}^{3+}$  measured at room temperature as a function of pressure with the deconvolution (a); energy of the maxima of the emission bands of  $\text{Cr}^{3+}$  at the  $\text{Mg}^{2+}(1)$  and  $\text{Mg}^{2+}(2)$  sites as a function of pressure (b) and corresponding change in its energy  $\Delta E$  (c);  $S_A$  as a function of pressure (d); change in the emission intensity of  $\text{Cr}^{3+}$  at the  $\text{Mg}^{2+}(1)$  and  $\text{Mg}^{2+}(2)$  sites as a function of pressure (e); pressure dependence of  $\text{LIR}_1$  (f) and the corresponding relative sensitivity  $S_{R,p}$  (g).

pressure range does not induce irreversible structural changes. Importantly, upon decompression, the emission spectra of  $\text{MgGeO}_3:\text{Cr}^{3+}$  return to their original shape. The rate of these band maximum shifts is often quantified by determining the absolute sensitivity ( $S_A$ ), which is calculated as follows:

$$S_{A,p} = \frac{\Delta E}{\Delta p} \quad \text{or} \quad \frac{\Delta \lambda}{\Delta p} \quad (6)$$

For  $\text{MgGeO}_3:\text{Cr}^{3+}$ , the monotonic variation of the  $\text{Cr}^{3+}$  ion band maximum for both sites results in relatively constant  $S_A$  values, changing from  $105 \text{ cm}^{-1} \text{ GPa}^{-1}$  to  $197 \text{ cm}^{-1} \text{ GPa}^{-1}$  from  $\text{Mg}^{2+}(2)$  to  $\text{Mg}^{2+}(1)$ , respectively (Fig. 4(d)). The obtained  $S_A$  values are consistent with expectations and do not significantly differ from

those obtained for other  $\text{Cr}^{3+}$ -doped materials.<sup>17</sup> As previously noted, the compression of the  $\text{MgGeO}_3:\text{Cr}^{3+}$  structure also leads to changes in the relative intensity of the emission bands corresponding to  $\text{Cr}^{3+}$  ions at different sites. Deconvolution of the emission bands of  $\text{MgGeO}_3:\text{Cr}^{3+}$  indicates that as pressure increases, the emission intensity of  $\text{Cr}^{3+}$  ions in  $\text{Mg}^{2+}(2)$  increases across the entire analyzed range of pressures (Fig. 4(e)). However, between 4 and 5 GPa, a slight decrease in the growth rate is observed, with the total increase in intensity nearly doubling. The opposite effect is observed in the case of  $\text{Mg}^{2+}(1)$ , where the emission intensity decreases slightly, and a flattening of the curve is observed between 4 and 5 GPa. The observed effects agree well with Raman data, and they are associated with the discussed reversible phase transition of magnesium germanate, from the

orthorhombic phase to the monoclinic phase. The difference in the monotonicity of the observed changes in the luminescence intensities of  $\text{Cr}^{3+}$  ions at different sites with varying pressure enables the development of a ratiometric luminescence manometer. In this case, the luminescence intensity ratio (LIR) of  $\text{Cr}^{3+}$  in  $\text{Mg}^{2+}(2)$  to  $\text{Mg}^{2+}(1)$  serves as the manometric parameter, defined as:

$$\text{LIR}_1 = \frac{\text{Cr}^{3+}@\text{Mg}^{2+}(2)}{\text{Cr}^{3+}@\text{Mg}^{2+}(1)} \quad (7)$$

In this scenario,  $\text{LIR}_1$  increases from 0.6 at ambient pressure to approximately 1.4 at 6.93 GPa (Fig. 4(f)). The mentioned flattening in intensity changes observed between 4 and 5 GPa for both  $\text{Cr}^{3+}$  sites results in minimal  $\text{LIR}_1$  changes within this pressure range. A quantitative description of the rate of LIR change can be obtained by determining the relative manometric sensitivity ( $S_{\text{R,p}}$ ), defined as:

$$S_{\text{R,p}} = \frac{1}{\text{LIR}} \frac{\Delta \text{LIR}}{\Delta p} \times 100\% \quad (8)$$

The determined  $S_{\text{R,p}}$  values indicate that the maximum relative sensitivity of  $22\% \text{ GPa}^{-1}$  is obtained at around 1.5 GPa (Fig. 4(g)). Significantly, this relative sensitivity does not fall below  $4\% \text{ GPa}^{-1}$  across the entire analyzed pressure range.

As demonstrated, the deconvolution of emission spectra can be effectively employed for ratiometric pressure readout. However, the deconvolution process can complicate the pressure readouts and generate challenges. Moreover, it is based on the entire emission spectrum analysis, which can significantly impede the surface imaging of pressure changes by requiring point-by-point emission spectra measurements across the analyzed region. To overcome these difficulties, a recently proposed ratiometric approach leverages spectral shifts in the emission band by analyzing the ratio of integrated intensities within two spectral regions. This method allows for the development of rapid pressure distribution maps by simply obtaining the quotient of luminescence images collected using appropriate bandpass filters. To evaluate the efficacy of this approach for the  $\text{MgGeO}_3:\text{Cr}^{3+}$  system, we analyzed the pressure-induced changes in emission intensity across four spectral ranges highlighted in Fig. 5(a).

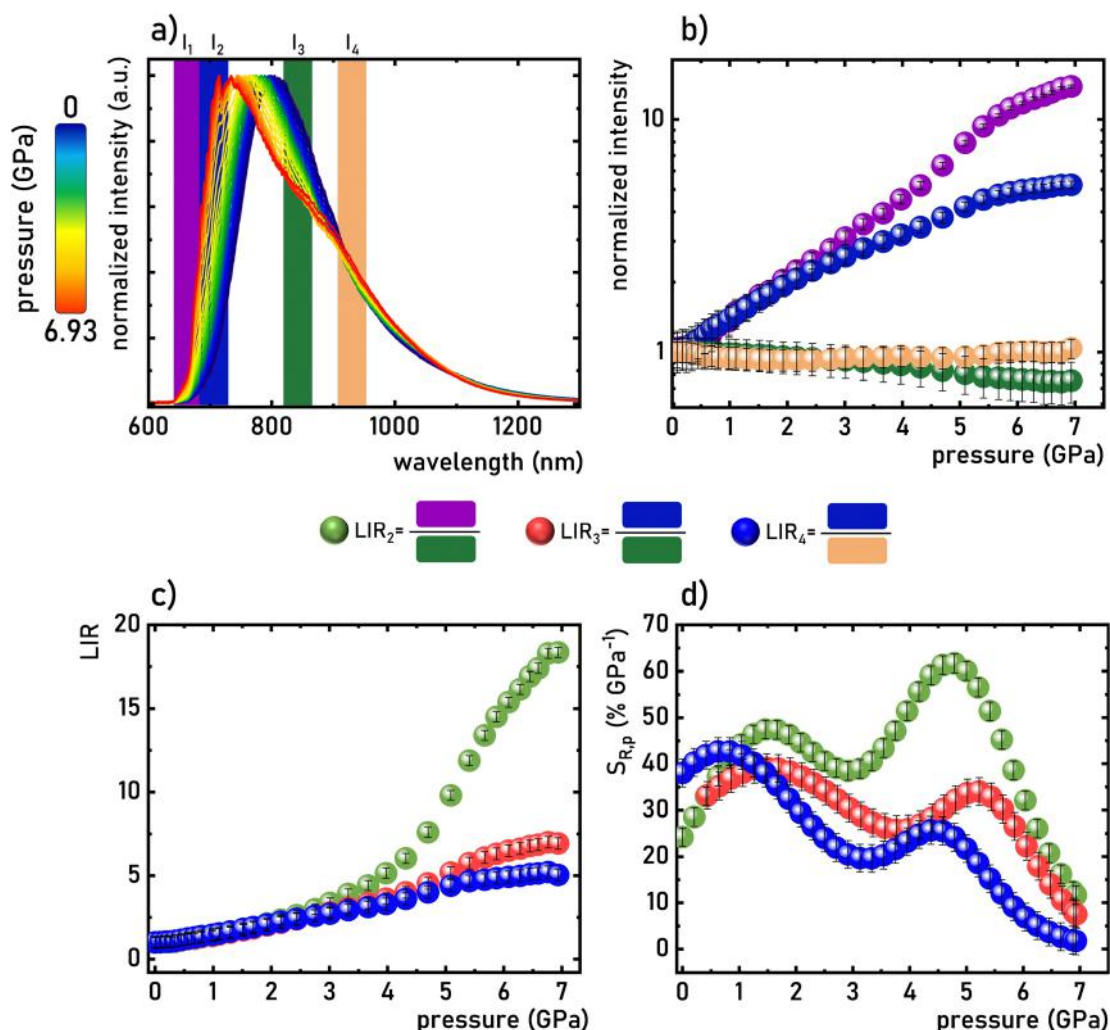


Fig. 5 Normalized emission spectra of  $\text{MgGeO}_3:5\%\text{Cr}^{3+}$  as a function of applied pressure (a), pressure dependence of emission intensities integrated in the spectral regions marked in (a) (b); and pressure dependencies of  $\text{LIR}_2$ ,  $\text{LIR}_3$  and  $\text{LIR}_4$  (c) with corresponding  $S_{\text{R}}$  values as a function of pressure (d).



The spectral width of these ranges, set at 10 nm, was selected to correspond with the typical ranges used for optical bandpass filters. The previously described blueshift of the  $\text{Cr}^{3+}$  emission band with increasing pressure results in an increase in emission intensity in the  $I_1$  and  $I_2$  regions and a decrease in the intensity in the  $I_3$  region. The smallest pressure-induced changes are observed in the  $I_4$  spectral range. A detailed analysis of emission intensities in these ranges revealed that in the  $I_1$  range, the intensity increases monotonically by up to 14 times, in respect to the value recorded at ambient pressure, while the  $I_2$  range exhibits only a 5-fold increase in the corresponding pressure range (see Fig. 5(b)). Conversely, the intensity in the  $I_3$  range decreases to 75% of its ambient pressure value, and the  $I_4$  intensity remains relatively stable across the entire pressure range analyzed. The differences in the monotonicity of emission intensities across these ranges as a function of applied pressure enable ratiometric pressure measurement. Therefore, the following LIRs were proposed:

$$\text{LIR}_2 = \frac{\int_{670\text{nm}}^{680\text{nm}} ({}^4\text{T}_2 \rightarrow {}^4\text{A}_2) d\lambda}{\int_{810\text{nm}}^{820\text{nm}} ({}^4\text{T}_2 \rightarrow {}^4\text{A}_2) d\lambda} \quad (9)$$

$$\text{LIR}_3 = \frac{\int_{710\text{nm}}^{720\text{nm}} ({}^4\text{T}_2 \rightarrow {}^4\text{A}_2) d\lambda}{\int_{810\text{nm}}^{820\text{nm}} ({}^4\text{T}_2 \rightarrow {}^4\text{A}_2) d\lambda} \quad (10)$$

$$\text{LIR}_4 = \frac{\int_{910\text{nm}}^{920\text{nm}} ({}^4\text{T}_2 \rightarrow {}^4\text{A}_2) d\lambda}{\int_{910\text{nm}}^{920\text{nm}} ({}^4\text{T}_2 \rightarrow {}^4\text{A}_2) d\lambda} \quad (11)$$

In the case of all proposed LIRs, an increase in value is observed across the entire range of pressures analyzed (Fig. 5(c)). The largest changes are observed for  $\text{LIR}_2$ , which increases by more than 18 times, compared to a 7-fold increase

for  $\text{LIR}_3$  and a 5-fold increase for  $\text{LIR}_4$ . The monotonic changes of all LIR parameters across the entire pressure range confirm the viability of using each of these parameters for pressure measurement. The difference in the rate of the pressure induced change in LIRs is reflected in their relative manometric sensitivities (Fig. 5(d)). The highest sensitivities across almost the entire pressure range studied are observed for  $\text{LIR}_2$ , with  $S_{R,p,\text{max}} = 62\% \text{ GPa}^{-1}$  at 4.8 GPa. For  $\text{LIR}_3$ , the maximum  $S_{R,p}$  value of  $40\% \text{ GPa}^{-1}$  is obtained at 1.5 GPa, while for  $\text{LIR}_4$ , it reaches  $43\% \text{ GPa}^{-1}$ . Notably, for  $\text{LIR}_2$ , the  $S_{R,p}$  values from ambient pressure to 6.2 GPa exceed the maximum value of  $\text{LIR}_1$  (based on deconvolution). Although only a few luminescent manometers revealed higher sensitivity to pressure changes<sup>71,72</sup> than that observed for  $\text{MgGeO}_3:5\%\text{Cr}^{3+}$ , they emit in the NIR range above 900 nm. Therefore, their usage for pressure readout imposes the requirement for the use of NIR detectors whose cost is significantly higher compared to detectors operating in the Vis. Hence,  $\text{MgGeO}_3:5\%\text{Cr}^{3+}$  with an emission overlapping the detection range of conventional CCDs is an extremely interesting alternative for reducing the cost of temperature readings.

To ensure that pressure can be accurately measured using luminescence manometry, it is crucial to ensure that the manometric parameter is minimally sensitive to changes in other factors, with temperature being the most significant. To assess the effect of temperature on the manometric properties of  $\text{MgGeO}_3:5\%\text{Cr}^{3+}$ , its emission spectra were measured as a function of temperature in the range of 83–673 K (Fig. 6(a), temperature-dependent emission spectra for  $\text{MgGeO}_3$  doped with various  $\text{Cr}^{3+}$  content are shown in Fig. S7, ESI†). As expected, an increase in temperature leads to a progressive decrease in emission intensity, an effect resulting from the thermal crossing of the intersection point between the  ${}^4\text{T}_2$  and  ${}^4\text{A}_2$  parabolas by electrons, the probability of which increases with the thermal

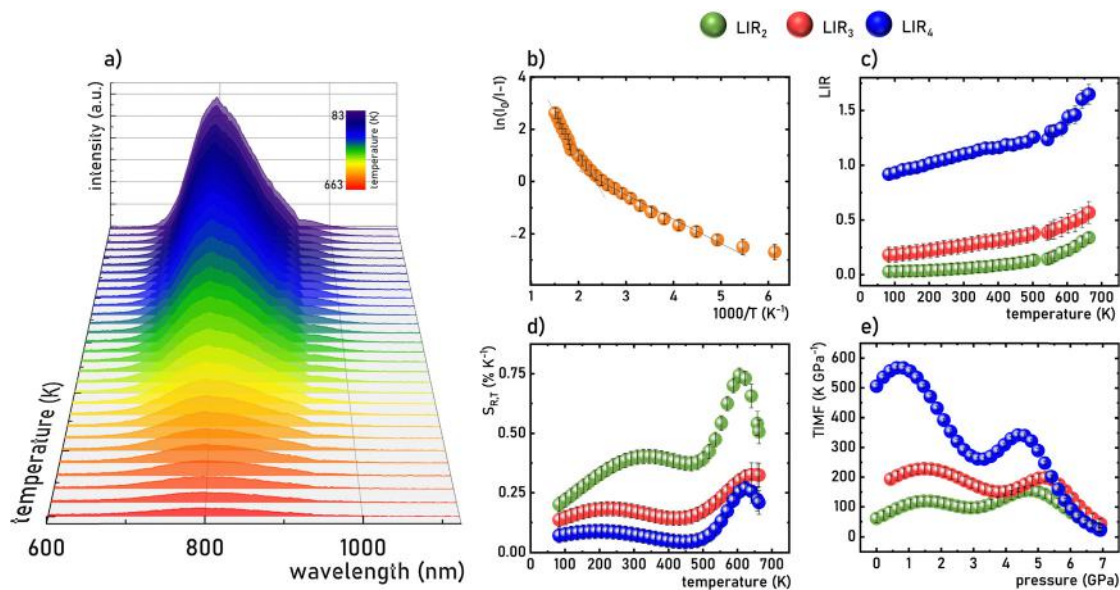


Fig. 6 Emission spectra of  $\text{MgGeO}_3:5\%\text{Cr}^{3+}$  measured as a function of temperature (a); and thermal dependence of integral emission intensity of  $\text{Cr}^{3+}$  in  $\text{MgGeO}_3:5\%\text{Cr}^{3+}$  (b); thermal dependences of  $\text{LIR}_2$ ,  $\text{LIR}_3$  and  $\text{LIR}_4$  (c); and corresponding thermal relative sensitivities  $S_{R,T}$  (d); pressure dependence of TIMF (e).

energy supplied. Importantly, a comparison of the normalized emission spectra measured at 83 K and 653 K clearly shows that the shape of the  $\text{MgGeO}_3\text{:}5\%\text{Cr}^{3+}$  emission spectrum remains unchanged. This is a direct evidence that the rate of thermal depopulation of the  $^4\text{T}_2$  levels of  $\text{Cr}^{3+}$  ions in the  $\text{Mg}^{2+}(1)$  and  $\text{Mg}^{2+}(2)$  sites is very similar. To determine the activation energy, the thermal variation of the integral emission intensity of  $\text{Cr}^{3+}$  ions in  $\text{MgGeO}_3\text{:}\text{Cr}^{3+}$  was analyzed (Fig. 6(b)). The activation energy value ( $E_a$  equals  $594\text{ cm}^{-1}$  below 430 K, and  $1820\text{ cm}^{-1}$  at higher temperatures) is typical for materials doped with  $\text{Cr}^{3+}$  ions in a weak crystal field. Based on the obtained emission spectra, the thermal dependencies of  $\text{LIR}_2$ ,  $\text{LIR}_3$ , and  $\text{LIR}_4$  were determined, all showing a similar trend (Fig. 6(c)). An increase in temperature from 83 K to approximately 513 K results in a slight (about 15%) monotonic increase in  $\text{LIR}_i$  values. However, above this temperature, the  $\text{LIR}_i$  values begin to increase more rapidly. This effect may suggest that at very high temperatures, a difference in the rate of thermal quenching between  $\text{Cr}^{3+}$  ions located at  $\text{Mg}^{2+}(1)$  and  $\text{Mg}^{2+}(2)$  sites becomes apparent or that thermally induced energy transfer occurs between them. Based on the thermal dependence of  $\text{LIR}_i$ , relative thermal sensitivities were determined according to the following equation:

$$S_{R,T} = \frac{1}{\text{LIR}} \frac{\Delta \text{LIR}}{\Delta T} \times 100\% \quad (12)$$

For all  $\text{LIR}_i$ , the relative sensitivities obtained remain below  $0.5\% \text{ K}^{-1}$  in the range of 83 to 513 K (Fig. 6(d)). Above this temperature,  $S_{R,T}$  values increase, reaching a maximum of around 613 K. However, clear differences in  $S_{R,T}$  values are observed among the different  $\text{LIR}_i$ . The highest  $S_{R,T}$  values were observed for  $\text{LIR}_2$ , with  $S_{R,T} = 0.41\% \text{ K}^{-1}$  at 300 K and  $S_{R,T\text{max}} = 0.75\% \text{ K}^{-1}$ . In the case of  $\text{LIR}_3$  and  $\text{LIR}_4$ , thermal sensitivities reached  $0.17\% \text{ K}^{-1}$  and  $0.08\% \text{ K}^{-1}$  at 300 K, with  $S_{R,T\text{max}} = 0.33\% \text{ K}^{-1}$  and  $0.27\% \text{ K}^{-1}$ , respectively. According to standards set for luminescence thermometry, these  $S_{R,T}$  values for the ratiometric approach are relatively low, making it challenging to use such material for remote temperature sensing, which is beneficial for temperature-invariant pressure determination. To quantify this thermal dependence, the thermal invariability manometric factor (TIMF) was determined as follows:<sup>71</sup>

$$\text{TIMF} = \frac{S_{R,p}}{S_{R,T}} \quad (13)$$

The value of this parameter indicates the number of degrees by which the system's temperature must change to produce LIR changes equivalent to a pressure change of 1 GPa. A high TIMF value suggests low thermal sensitivity of the luminescence manometer, which is desirable from an application perspective. Low thermal relative sensitivity values for the  $\text{LIR}_4$  result in the highest TIMF values throughout most of the analyzed pressure range (up to 5.5 GPa), with a maximum of  $577 \text{ K GPa}^{-1}$  at 0.66 GPa (Fig. 6(e)). For the  $\text{LIR}_3$ , the TIMF value reveals a slight variation up to 5.5 GPa, oscillating around  $200 \text{ K GPa}^{-1}$ , while for  $\text{LIR}_2$ , the TIMF oscillates around  $100 \text{ K GPa}^{-1}$ . The comparison of the obtained results with  $\text{TIMF} = 52$  for ruby clearly confirms that  $\text{MgGeO}_3\text{:}5\%\text{Cr}^{3+}$  reveals promising manometric performance.

This comparison indicates that although the highest manometric relative sensitivity was obtained for  $\text{LIR}_2$ , using  $\text{LIR}_4$  as a manometric parameter is more advantageous for achieving high insensitivity to temperature changes. Of course, in applications where the system's temperature is strictly controlled, the thermal variability of  $\text{LIR}_i$  is less critical, and in such cases, using  $\text{LIR}_2$  is most advantageous. However, it is important to consider that in luminescence-based measurements, the optical heating of the phosphor can lead to a local increase in the temperature of the luminescence manometer. For this reason, low optical excitation power densities are recommended for pressure sensing.

## 4. Conclusions

In this study, the spectroscopic properties of  $\text{Cr}^{3+}$  ions in  $\text{MgGeO}_3\text{:}\text{Cr}^{3+}$  were investigated as functions of pressure and temperature to evaluate the performance of a lifetime-based and ratiometric luminescence manometer. In the  $\text{MgGeO}_3$  host material,  $\text{Cr}^{3+}$  ions occupy two non-equivalent crystallographic sites of  $\text{Mg}^{2+}$  ions, each contributing distinct optical responses. As demonstrated, the emission spectrum of  $\text{MgGeO}_3\text{:}\text{Cr}^{3+}$  is a superposition of bands arising from the  $^4\text{T}_2 \rightarrow ^4\text{A}_2$  electronic transitions of  $\text{Cr}^{3+}$  ions located at the  $\text{Mg}^{2+}(1)$  and  $\text{Mg}^{2+}(2)$  sites. The difference in the rates of energy change of the  $^4\text{T}_2$  level of  $\text{Cr}^{3+}$  ions under compression at these crystallographic positions results in notable variations in both the spectral position and shape of the  $\text{MgGeO}_3\text{:}\text{Cr}^{3+}$  emission spectrum. At ambient pressure, the emission spectrum is predominantly influenced by  $\text{Cr}^{3+}$  ions at the  $\text{Mg}^{2+}(1)$  site, which exhibit a greater rate of spectral position change under compression compared to those at the  $\text{Mg}^{2+}(2)$  site ( $105 \text{ cm}^{-1} \text{ GPa}^{-1}$  for  $\text{Mg}^{2+}(2)$  and  $197 \text{ cm}^{-1} \text{ GPa}^{-1}$  for  $\text{Mg}^{2+}(1)$ ). Consequently, the ratio of luminescence intensities of these  $\text{Cr}^{3+}$  ion emission bands, derived from deconvolution, enables the development of a ratiometric luminescence manometer with a maximum sensitivity of  $22\% \text{ GPa}^{-1}$ . However, the requirement for deconvolution in this readout mode can complicate pressure measurements. Therefore, the present work proposes an alternative approach using luminescence intensity ratios (LIRs) in two spectral ranges of the  $\text{MgGeO}_3\text{:}\text{Cr}^{3+}$  emission spectrum. Depending on the spectral range employed, manometric sensitivity values range from  $62\% \text{ GPa}^{-1}$  at 4.8 GPa for  $\text{LIR}_2$  to  $40\% \text{ GPa}^{-1}$  for  $\text{LIR}_4$ . Despite the lower manometric relative sensitivity,  $\text{LIR}_4$  demonstrates reduced thermal variability, yielding TIMF values of  $577 \text{ K GPa}^{-1}$  at 0.66 GPa compared to  $100 \text{ K GPa}^{-1}$  for  $\text{LIR}_2$ . Notably, this study introduces the first ratiometric luminescence manometer exhibiting multisite luminescence of  $\text{Cr}^{3+}$  ions. Unlike previously reported luminescence manometers exploiting this approach, the  $\text{MgGeO}_3\text{:}\text{Cr}^{3+}$  emission range overlaps with the detection range of CCD detectors.

## Data availability

The datasets supporting this article have been uploaded as part of the ESI.†

## Conflicts of interest

There are no conflicts to declare.

## Acknowledgements

This work was supported by the National Science Center (NCN) Poland under project no. DEC-UMO-2020/37/B/ST5/00164. The authors would like to acknowledge Dr Vasyl Kinzhybalov for his invaluable assistance with the structural analysis of the materials investigated.

## References

- 1 Y. Liu, Y. Lu, X. Yang, X. Zheng, S. Wen, F. Wang, X. Vidal, J. Zhao, D. Liu, Z. Zhou, C. Ma, J. Zhou, J. A. Piper, P. Xi and D. Jin, *Nature*, 2017, **543**, 229.
- 2 J. Yao, M. Yang and Y. Duan, *Chem. Rev.*, 2014, **114**, 6130.
- 3 H. Sun, S. Liu, W. Lin, K. Y. Zhang, W. Lv, X. Huang, F. Huo, H. Yang, G. Jenkins, Q. Zhao and W. Huang, *Nat. Commun.*, 2014, **5**, 3601.
- 4 T. Maldiney, A. Bessière, J. Seguin, E. Teston, S. K. Sharma, B. Viana, A. J. J. Bos, P. Dorenbos, M. Bessodes, D. Gourier, D. Scherman and C. Richard, *Nat. Mater.*, 2014, **13**, 418.
- 5 L. Y. Chen, C. W. Wang, Z. Yuan and H. T. Chang, *Anal. Chem.*, 2015, **87**, 216.
- 6 Z. Xia and A. Meijerink, *Chem. Soc. Rev.*, 2017, **46**, 275.
- 7 M. C. Heffern, L. M. Matosziuk and T. J. Meade, *Chem. Rev.*, 2014, **114**, 4496.
- 8 J. Rocha, C. D. S. Brites and L. D. Carlos, *Chem. – Eur. J.*, 2016, **22**, 14782.
- 9 C. D. S. Brites, P. P. Lima, N. J. O. Silva, A. Millán, V. S. Amaral, F. Palacio and L. D. Carlos, *Nanoscale*, 2012, **4**, 4799.
- 10 C. D. S. Brites, R. Marin, M. Suta, A. N. Carneiro Neto, E. Ximendes, D. Jaque and L. D. Carlos, *Adv. Mater.*, 2023, **35**, 2302749.
- 11 J. Zhou, B. del Rosal, D. Jaque, S. Uchiyama and D. Jin, *Nat. Methods*, 2020, **17**, 967.
- 12 D. Jaque and F. Vetrone, *Nanoscale*, 2012, **4**, 4301.
- 13 L. Marciniak, K. Kniec, K. Elżbieciak-Piecka, K. Trejgis, J. Stefanska and M. Dramićanin, *Coord. Chem. Rev.*, 2022, **469**, 214671.
- 14 M. Suta and A. Meijerink, *Adv. Theory Simul.*, 2020, **3**, 2000176.
- 15 K. Syassen, *High Press. Res.*, 2008, **28**, 75.
- 16 R. A. Forman, G. J. Piermarini, J. Dean Barnett and S. Block, *Science*, 1979, **197**(176), 284.
- 17 L. Marciniak, P. Woźny, M. Szymczak and M. Runowski, *Coord. Chem. Rev.*, 2024, **507**, 215770.
- 18 Z. Hu, B. J. Deibert and J. Li, *Chem. Soc. Rev.*, 2014, **43**, 5815.
- 19 Y. Yang, Q. Zhao, W. Feng and F. Li, *Chem. Rev.*, 2013, **113**, 192.
- 20 S. V. Eliseeva, J.-C. G. Bünzli, D. R. Dreyer, S. Park, C. W. Bielawski and R. S. Ruoff, *Chem. Soc. Rev.*, 2009, **39**, 189.
- 21 C. Sanchez, K. J. Shea, S. Kitagawa, J. Rocha, L. Luís, D. Carlos, F. A. Almeida Paz and D. Ananias, *Chem. Soc. Rev.*, 2011, **40**, 926.
- 22 L. Prodi, F. Bolletta, M. Montalti and N. Zaccheroni, *Coord. Chem. Rev.*, 2000, **205**, 59.
- 23 M. Schäferling and M. Schäferling, *Angew. Chem., Int. Ed.*, 2012, **51**, 3532.
- 24 J. C. Zhang, X. Wang, G. Marriott and C. N. Xu, *Prog. Mater. Sci.*, 2019, **103**, 678.
- 25 K. Zheng, K. Y. Loh, Y. Wang, Q. Chen, J. Fan, T. Jung, S. H. Nam, Y. D. Suh and X. Liu, *Nano Today*, 2019, **29**, 100797.
- 26 M. Nikl, A. Yoshikawa, M. Nikl and A. Yoshikawa, *Adv. Opt. Mater.*, 2015, **3**, 463.
- 27 C. N. Xu, T. Watanabe, M. Akiyama and X. G. Zheng, *Appl. Phys. Lett.*, 1999, **74**, 2414.
- 28 C. D. S. Brites, S. Balabhadra and L. D. Carlos, *Adv. Opt. Mater.*, 2019, **7**, 1801239.
- 29 J. C. Martins, C. D. S. Brites, A. N. C. Neto, R. A. S. Ferreira and L. D. Carlos, *Luminescent Thermometry*, 2023, p. 105.
- 30 A. Bednarkiewicz, L. Marciniak, L. D. Carlos and D. Jaque, *Nanoscale*, 2020, **12**, 14405.
- 31 D. Jaque and F. Vetrone, *Nanoscale*, 2012, **4**, 4301.
- 32 M. D. Dramićanin, *J. Appl. Phys.*, 2020, **128**, 40902.
- 33 M. D. Dramićanin, *Methods Appl. Fluoresc.*, 2016, **4**, 042001.
- 34 A. D. Chijioke, W. J. Nellis, A. Soldatov and I. F. Silvera, *J. Appl. Phys.*, 2005, **98**, 114905.
- 35 H. K. Mao, J. Xu and P. M. Bell, *J. Geophys. Res.: Solid Earth*, 1986, **91**, 4673.
- 36 G. J. Piermarini, S. Block, J. D. Barnett and R. A. Forman, *J. Appl. Phys.*, 1975, **46**, 2774.
- 37 G. Shen, J. S. Smith, C. Kenney-Benson and S. Klotz, *High Press. Res.*, 2021, **41**, 175.
- 38 T. Zheng, L. Luo, P. Du, S. Lis, U. R. Rodríguez-Mendoza, V. Lavín and M. Runowski, *Chem. Eng. J.*, 2022, **446**, 136839.
- 39 S. V. Rashchenko, A. Kurnosov, L. Dubrovinsky and K. D. Litasov, *J. Appl. Phys.*, 2015, **117**, 145902.
- 40 J. M. Leger, C. Chateau and A. Lacam, *J. Appl. Phys.*, 1990, **68**, 2351.
- 41 T. Zheng, L. Luo, P. Du, S. Lis, U. R. Rodríguez-Mendoza, V. Lavín, I. R. Martín and M. Runowski, *Chem. Eng. J.*, 2022, **443**, 136414.
- 42 J. D. Barnett, S. Block and G. J. Piermarini, *Rev. Sci. Instrum.*, 1973, **44**, 1.
- 43 H. K. Mao, P. M. Bell, J. W. Shaner and D. J. Steinberg, *J. Appl. Phys.*, 1978, **49**, 3276.
- 44 M. Szymczak, P. Woźny, M. Runowski, M. Pieprz, V. Lavín and L. Marciniak, *Chem. Eng. J.*, 2023, **453**, 139632.
- 45 M. Szymczak, M. Runowski, V. Lavín and L. Marciniak, *Laser Photonics Rev.*, 2023, **17**, 2200801.
- 46 M. Szymczak, M. Runowski, M. G. Brik and L. Marciniak, *Chem. Eng. J.*, 2023, **466**, 143130.
- 47 M. Szymczak, J. Jąskiełewicz, J. J. Jąskiełewicz, M. Runowski, J. Xue, S. Mahlik, L. Marciniak, M. Szymczak, J. J. Jąskiełewicz, L. Marciniak, M. Runowski and S. Mahlik, *Adv. Funct. Mater.*, 2024, **34**, 2314068.



- 48 M. Szymczak, P. Du, M. Runowski, P. Woźny, J. Xue, T. Zheng and L. Marciniak, *Adv. Opt. Mater.*, 2024, **12**, 2302147.
- 49 M. Runowski, P. Woźny, V. Lavín and S. Lis, *Sens. Actuators, B*, 2018, **273**, 585.
- 50 T. Okada, T. Narita, T. Nagai and T. Yamanaka, *Am. Mineral.*, 2008, **93**, 39.
- 51 Q. Mahmood, M. Yaseen, B. Ul Haq, A. Laref and A. Nazir, *Chem. Phys.*, 2019, **524**, 106.
- 52 C. E. Runge, A. Kubo, B. Kiefer, Y. Meng, V. B. Prakapenka, G. Shen, R. J. Cava and T. S. Duffy, *Phys. Chem. Miner.*, 2006, **33**, 699.
- 53 T. Yamanaka, Y. Komatsu, M. Sugahara and T. Nagai, *Am. Mineral.*, 2005, **90**, 1301.
- 54 C. M. Fang and R. Ahuja, *Phys. Earth Planet. Inter.*, 2006, **157**, 1.
- 55 C. D. Martin, W. A. Crichton, H. Liu, V. Prakapenka, J. Chen and J. B. Parise, *Geophys. Res. Lett.*, 2006, **33**, L11305.
- 56 S. Zheng, J. Shi, X. Fu, C. Wang, X. Sun, C. Chen, Y. Zhuang, X. Zou, Y. Li and H. Zhang, *Nanoscale*, 2020, **12**, 14037.
- 57 M. Iwasaki, D. N. Kim, K. Tanaka, T. Murata and K. Morinaga, *Sci. Technol. Adv. Mater.*, 2003, **4**, 137.
- 58 K. Hirose, K. Kawamura, Y. Ohishi, S. Tateno and N. Sata, *Am. Mineral.*, 2005, **90**, 262.
- 59 S. Merkel, A. Kubo, L. Miyagi, S. Speziale, T. S. Duffy, H. K. Mao and H. R. Wenk, *Science*, 2006, (311), 644.
- 60 R. D. Shannon, *Acta Crystallogr., Sect. A*, 1976, **32**, 751.
- 61 D. Reinen, U. Kesper, M. Atanasov and J. Roos, *Inorg. Chem.*, 1995, **34**, 184.
- 62 H. Zhou, H. Cai, J. Zhao, Z. Song and Q. Liu, *Inorg. Chem. Front.*, 2022, **9**, 1912.
- 63 C. Anino, J. Théry and D. Vivien, *Opt. Mater.*, 1997, **8**, 121.
- 64 A. S. Oreshonkov, J. V. Gerasimova, A. A. Ershov, A. S. Krylov, K. A. Shaykhutdinov, A. N. Vtyurin, M. S. Molokeev, K. Y. Terent'Ev and N. V. Mihasheok, *J. Raman Spectrosc.*, 2016, **47**, 531.
- 65 A. Wang, B. L. Jolliff, L. A. Haskin, K. E. Kuebler and K. M. Viskupic, *Am. Mineral.*, 2001, **86**, 790.
- 66 7\_Taylor&Francis\_theoretical Spectroscopy of Transition Mental and Rare Earthions\_from Free State to Crystal Field\_2020, n.d.
- 67 N. M. Avram and M. G. Brik, *J. Lumin.*, 2013, **133**, 69.
- 68 S. Adachi, *J. Lumin.*, 2021, **234**, 117965.
- 69 Y. Tanabe and S. Sugano, *J. Phys. Soc. Jpn.*, 2013, **9**, 766, DOI: [10.1143/JPSJ.9.766](https://doi.org/10.1143/JPSJ.9.766).
- 70 Z. Song, P. A. Tanner and Q. Liu, *J. Phys. Chem. Lett.*, 2024, **15**, 2319.
- 71 M. Szymczak, M. Runowski, M. G. Brik and L. Marciniak, *Chem. Eng. J.*, 2023, **466**, 143130.
- 72 M. Szymczak, J. Jąskiełewicz, J. Xue, S. Mahlik, L. Marciniak, M. Szymczak, J. J. Jąskiełewicz, L. Marciniak, M. Runowski and S. Mahlik, *Adv. Funct. Mater.*, 2024, **34**, 2314068.

## Supporting Information

### Highly sensitive ratiometric luminescence manometer based on the multisite emission of Cr<sup>3+</sup>

M. Szymczak<sup>1</sup>, W.M. Piotrowski<sup>1</sup>, U. R. Rodríguez-Mendoza<sup>2</sup>, P. Wozny<sup>3</sup>,

M. Runowski<sup>3</sup>, L. Marciniak<sup>1\*</sup>

<sup>1</sup> Institute of Low Temperature and Structure Research, Polish Academy of Sciences,

Okólna 2, 50-422 Wrocław, Poland

<sup>2</sup> Departamento de Física, Instituto de Materiales y Nanotecnología, IUdEA & MALTA Consolider Team,

Universidad de La Laguna, Apdo. Correos 456, E-38200 San Cristóbal de La Laguna, Santa Cruz de Tenerife,

Spain

<sup>3</sup> Faculty of Chemistry, Adam Mickiewicz University, Uniwersytetu Poznańskiego 8, 61-614 Poznań, Poland

\*corresponding author: l.marciniak@intibs.pl

**KEYWORDS** *luminescent manometer, luminescence thermometry, optical sensors, ratiometric approach*

**Table S1.** Estimated peak centroids of the main Raman modes at pressure values when start to be visible, and the corresponding pressure shift rates of the Raman modes for the MgGeO<sub>3</sub> material.

Peak centroid (cm <sup>-1</sup> )	Shift rate (cm <sup>-1</sup> /GPa)
≈340	3.80 ± 0.12
≈360	2.67 ± 0.09
≈400	3.77 ± 0.25
≈570	4.94 ± 0.16
≈710	3.31 ± 0.11
≈860	4.46 ± 0.23
≈880	4.77 ± 0.19

# MgGeO<sub>3</sub>:0.1%Cr<sup>3+</sup>

## Global Parameters

Number of used phases:	1
Number of variables:	14
Number of constraints:	0
Zero shift/ °2Theta:	0,000000
Specimen displacement/ mm :	-0,157(1)
Profile function:	Pseudo Voigt
Background:	Polynomial
R (expected)/ %:	0,19313
R (profile)/ %:	1,87123
R (weighted profile)/ %:	3,21522
GOF:	277,16500
d-statistic:	0,65523
U standard:	0,000000
V standard:	0,000000
W standard:	0,010000
U Left:	0,000000
V Left:	0,000000
W Left:	0,010000
U Right:	0,000000
V Right:	0,000000
W Right:	0,010000
Asymmetry Type:	No Asymmetry Function
Asymmetry 1:	0,000000
Asymmetry 2:	0,000000
Shape Type:	Shape Individual
Shape 1 Left:	0,600000
Shape 2 Left:	0,000000
Shape 3 Left:	0,000000
Shape 1 Right:	0,600000
Shape 2 Right:	0,000000
Shape 3 Right:	0,000000
K a1/a2 intensity ratio:	0,500000
K alpha/beta intensity ratio:	0,000000
Crystal Shape Factor K:	1,0000
Instrumental FWHM Curve Type:	Caglioti function
Instr. Gauss Curve Coefficient A:	0,0045(5)
Instr. Gauss Curve Coefficient B:	-0,0032(9)
Instr. Gauss Curve Coefficient C:	0,0046(3)
Instr. Lorentz Curve Coefficient A:	0,0062(7)
Instr. Lorentz Curve Coefficient B:	-0,004(1)
Instr. Lorentz Curve Coefficient C:	0,0064(5)

## Relevant parameters of 35533-ICSD, MgGeO<sub>3</sub>, Pbc<sub>a</sub>

Structure and profile data:	
Formula sum:	Mg <sub>16·00</sub> Ge <sub>16·00</sub> O <sub>48·00</sub>
Formula mass/ g/mol:	2318,2910
Density (calculated)/ g/cm <sup>3</sup>	4,2745
F(000):	1088,0000
Weight fraction/ %:	100,000000
Space group (No.):	P b c a (61)
Lattice parameters:	
a/ Å:	18,8091(5)
b/ Å:	8,9588(2)
c/ Å:	5,3438(1)
alpha/ °:	90
beta/ °:	90
gamma/ °:	90
V/ 10 <sup>6</sup> pm <sup>3</sup>	900,47090
Overall displacement parameter:	0,000000
Extinction:	0,000000
Flat Plate Absorption Correction:	0,000000
Porosity:	0,000000

Roughness: 0,000000  
 Fitting mode: Structure Fit  
 U Left: 0,034(7)  
 V Left: -0,010(6)  
 W Left: 0,014(1)  
 Preferred orientation direction/ hkl: 0,00 0,00 1,00  
 Preferred orientation parameter: 1,000000  
 Asymmetry parameter 1: 0,000000  
 Asymmetry parameter 2: 0,000000  
 Peak shape:  
   parameter 1 Left: 0,65(1)  
   parameter 2 Left: 0,000000  
   parameter 3 Left: 0,000000  
 R (Bragg)/ %: 2,27669

**Occupancy, atomic fract. coordinates and Biso for 35533-ICSD, MgGeO<sub>3</sub>, Pbcn**

Atom	Wyck.	s.o.f.	x	y	z	B/ 10 <sup>4</sup> pm <sup>2</sup>	
Mg1	8c	1,000000	0,123360	0,656530	0,851890	0,000000	
Mg2	8c	1,000000	0,122190	0,488820	0,343520	0,000000	
Ge1	8c	1,000000	0,027800	0,339590	0,805350	0,000000	
Ge2	8c	1,000000	0,229070	0,345090	0,041410	0,000000	
O1	8c	1,000000	0,935450	0,338430	0,814780	0,000000	
O2	8c	1,000000	0,069360	0,488810	0,670450	0,000000	
O3	8c	1,000000	0,055450	0,319810	0,125190	0,000000	
O4	8c	1,000000	0,320480	0,340070	0,021910	0,000000	
O5	8c	1,000000	0,187680	0,514400	0,033320	0,000000	
O6	8c	1,000000	0,193260	0,289580	0,336850	0,000000	

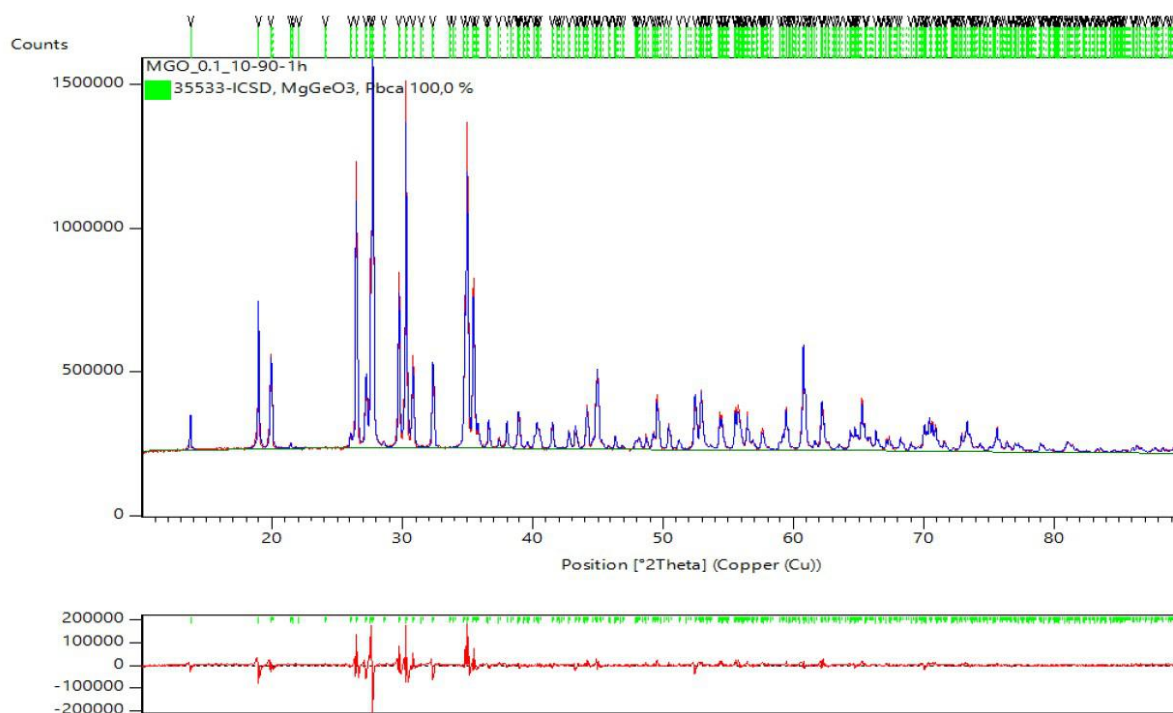


**Figure S1.** Rietveld refinement of XRD pattern of MgGeO<sub>3</sub>:0.1%Cr<sup>3+</sup>.

MgGeO<sub>3</sub>:0.5%Cr<sup>3+</sup>

## **Global Parameters**

Number of used phases:	1
Number of variables:	14
Number of constraints:	0
Zero shift/ °2Theta:	0,000000
Specimen displacement/ mm :	-0,098(1)
Profile function:	Pseudo Voigt
Background:	Polynomial
R (expected)/ %:	0,19064
R (profile)/ %:	1,96927
R (weighted profile)/ %:	3,36953
GOF:	312,39200
d-statistic:	0,66770
U standard:	0,000000
V standard:	0,000000
W standard:	0,010000
U Left:	0,000000
V Left:	0,000000
W Left:	0,010000
U Right:	0,000000
V Right:	0,000000
W Right:	0,010000
Asymmetry Type:	No Asymmetry Function
Asymmetry 1:	0,000000
Asymmetry 2:	0,000000
Shape Type:	Shape Individual
Shape 1 Left:	0,600000
Shape 2 Left:	0,000000
Shape 3 Left:	0,000000
Shape 1 Right:	0,600000
Shape 2 Right:	0,000000
Shape 3 Right:	0,000000
K a1/a2 intensity ratio:	0,500000
K alpha/beta intensity ratio:	0,000000
Crystal Shape Factor K:	1,0000
Instrumental FWHM Curve Type:	Caglioti function
Instr. Gauss Curve Coefficient A:	0,0045(5)
Instr. Gauss Curve Coefficient B:	-0,0032(9)
Instr. Gauss Curve Coefficient C:	0,0046(3)
Instr. Lorentz Curve Coefficient A:	0,0062(7)
Instr. Lorentz Curve Coefficient B:	-0,004(1)
Instr. Lorentz Curve Coefficient C:	0,0064(5)

## **Relevant parameters of 35533-ICSD, MgGeO<sub>3</sub>, Pbc<sub>a</sub>**

Structure and profile data:	
Formula sum:	Mg <sub>16·00</sub> Ge <sub>16·00</sub> O <sub>48·00</sub>
Formula mass/ g/mol:	2318,2910
Density (calculated)/ g/cm <sup>3</sup>	4,2746
F(000):	1088,0000
Weight fraction/ %:	100,000000
Space group (No.):	P b c a (61)
Lattice parameters:	
a/ Å:	18,8114(5)
b/ Å:	8,9575(2)
c/ Å:	5,3439(1)
alpha/ °:	90
beta/ °:	90
gamma/ °:	90
V/ 10 <sup>6</sup> pm <sup>3</sup>	900,45860
Overall displacement parameter:	0,000000
Extinction:	0,000000
Flat Plate Absorption Correction:	0,000000
Porosity:	0,000000
Roughness:	0,000000
Fitting mode:	Structure Fit
U Left:	0,034(8)
V Left:	-0,010(6)
W Left:	0,014(1)
Preferred orientation direction/ hkl:	0,00 0,00 1,00
Preferred orientation parameter:	1,000000
Asymmetry parameter 1:	0,000000

Asymmetry parameter 2: 0,000000  
Peak shape:  
parameter 1 Left: 0,66(1)  
parameter 2 Left: 0,000000  
parameter 3 Left: 0,000000  
R (Bragg)/ %: 2,53705

### Occupancy, atomic fract. coordinates and Biso for 35533-ICSD, MgGeO<sub>3</sub>, Pbcn

Atom	Wyck.	s.o.f.	x	y	z	B/ 10 <sup>4</sup> pm <sup>2</sup>
Mg1	8c	1,000000	0,123360	0,656530	0,851890	0,000000
Mg2	8c	1,000000	0,122190	0,488820	0,343520	0,000000
Ge1	8c	1,000000	0,027800	0,339590	0,805350	0,000000
Ge2	8c	1,000000	0,229070	0,345090	0,041410	0,000000
O1	8c	1,000000	0,935450	0,338430	0,814780	0,000000
O2	8c	1,000000	0,069360	0,488810	0,670450	0,000000
O3	8c	1,000000	0,055450	0,319810	0,125190	0,000000
O4	8c	1,000000	0,320480	0,340070	0,021910	0,000000
O5	8c	1,000000	0,187680	0,514400	0,033320	0,000000
O6	8c	1,000000	0,193260	0,289580	0,336850	0,000000

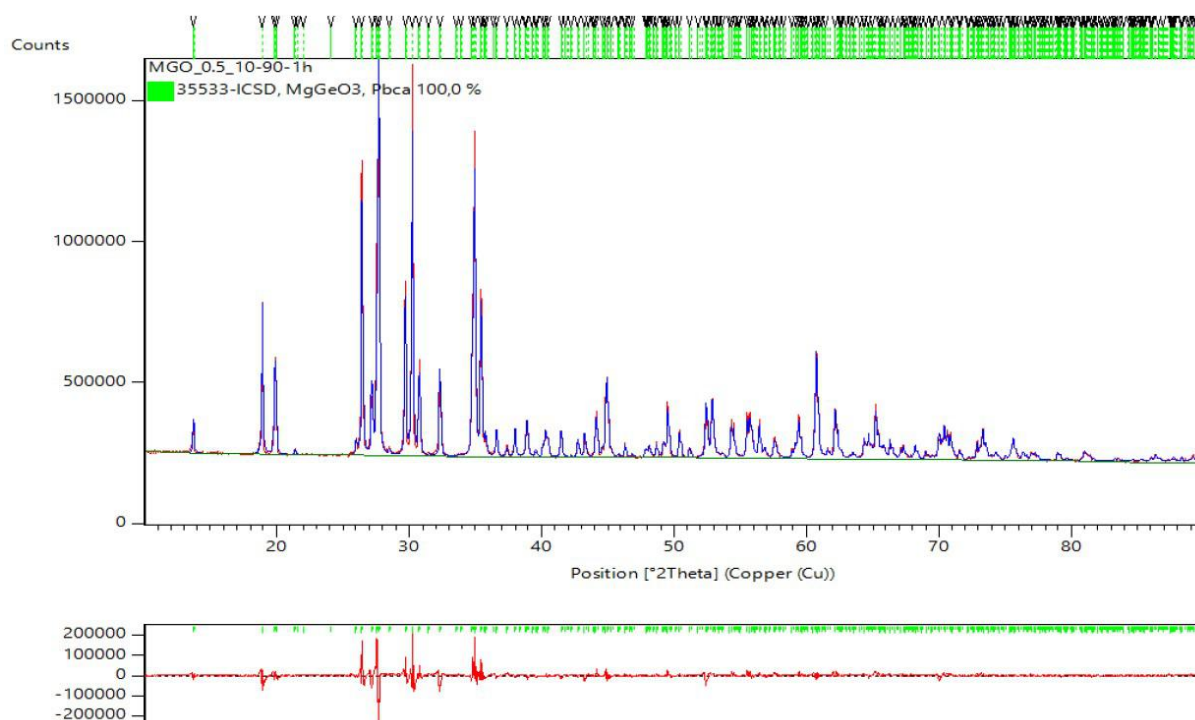


Figure S2. Rietveld refinement of XRD pattern of MgGeO<sub>3</sub>:0.5%Cr<sup>3+</sup>.

MgGeO<sub>3</sub>:1%Cr<sup>3+</sup>

### Global Parameters

Number of used phases: 1  
Number of variables: 14  
Number of constraints: 0  
Zero shift/ °2Theta: 0,000000

Specimen displacement/ mm :	-0,184(1)
Profile function:	Pseudo Voigt
Background:	Polynomial
R (expected)/ %:	0,19091
R (profile)/ %:	2,04571
R (weighted profile)/ %:	3,50891
GOF:	337,80620
d-statistic:	0,57519
U standard:	0,000000
V standard:	0,000000
W standard:	0,010000
U Left:	0,000000
V Left:	0,000000
W Left:	0,010000
U Right:	0,000000
V Right:	0,000000
W Right:	0,010000
Asymmetry Type:	No Asymmetry Function
Asymmetry 1:	0,000000
Asymmetry 2:	0,000000
Shape Type:	Shape Individual
Shape 1 Left:	0,600000
Shape 2 Left:	0,000000
Shape 3 Left:	0,000000
Shape 1 Right:	0,600000
Shape 2 Right:	0,000000
Shape 3 Right:	0,000000
K a1/a2 intensity ratio:	0,500000
K alpha/beta intensity ratio:	0,000000
Crystal Shape Factor K:	1,0000
Instrumental FWHM Curve Type:	Caglioti function
Instr. Gauss Curve Coefficient A:	0,0045(5)
Instr. Gauss Curve Coefficient B:	-0,0032(9)
Instr. Gauss Curve Coefficient C:	0,0046(3)
Instr. Lorentz Curve Coefficient A:	0,0062(7)
Instr. Lorentz Curve Coefficient B:	-0,004(1)
Instr. Lorentz Curve Coefficient C:	0,0064(5)

### **Relevant parameters of 35533-ICSD, MgGeO<sub>3</sub>, Pbca**

Structure and profile data:	
Formula sum:	Mg <sub>16*00</sub> Ge <sub>16*00</sub> O <sub>48*00</sub>
Formula mass/ g/mol:	2318,2910
Density (calculated)/ g/cm <sup>3</sup>	4,2744
F(000):	1088,0000
Weight fraction/ %:	100,000000
Space group (No.):	P b c a (61)
Lattice parameters:	
a/ Å:	18,8111(5)
b/ Å:	8,9575(2)
c/ Å:	5,3441(1)
alpha/ °:	90
beta/ °:	90
gamma/ °:	90
V/ 10 <sup>6</sup> pm <sup>3</sup>	900,49250
Overall displacement parameter:	0,000000
Extinction:	0,000000
Flat Plate Absorption Correction:	0,000000
Porosity:	0,000000
Roughness:	0,000000
Fitting mode:	Structure Fit
U Left:	0,033(8)
V Left:	-0,010(7)
W Left:	0,014(1)
Preferred orientation direction/ hkl:	0,00 0,00 1,00
Preferred orientation parameter:	1,000000
Asymmetry parameter 1:	0,000000
Asymmetry parameter 2:	0,000000
Peak shape:	
parameter 1 Left:	0,63(1)
parameter 2 Left:	0,000000
parameter 3 Left:	0,000000
R (Bragg)/ %:	2,71266



# **Occupancy, atomic fract. coordinates and Biso for 35533-ICSD, MgGeO<sub>3</sub>, Pbca**

Atom	Wyck.	s.o.f.	x	y	z	B/ 10 <sup>4</sup> pm <sup>2</sup>
Mg1	8c	1,000000	0,123360	0,656530	0,851890	0,000000
Mg2	8c	1,000000	0,122190	0,488820	0,343520	0,000000
Ge1	8c	1,000000	0,027800	0,339590	0,805350	0,000000
Ge2	8c	1,000000	0,229070	0,345090	0,041410	0,000000
O1	8c	1,000000	0,935450	0,338430	0,814780	0,000000
O2	8c	1,000000	0,069360	0,488810	0,670450	0,000000
O3	8c	1,000000	0,055450	0,319810	0,125190	0,000000
O4	8c	1,000000	0,320480	0,340070	0,021910	0,000000
O5	8c	1,000000	0,187680	0,514400	0,033320	0,000000
O6	8c	1,000000	0,193260	0,289580	0,336850	0,000000

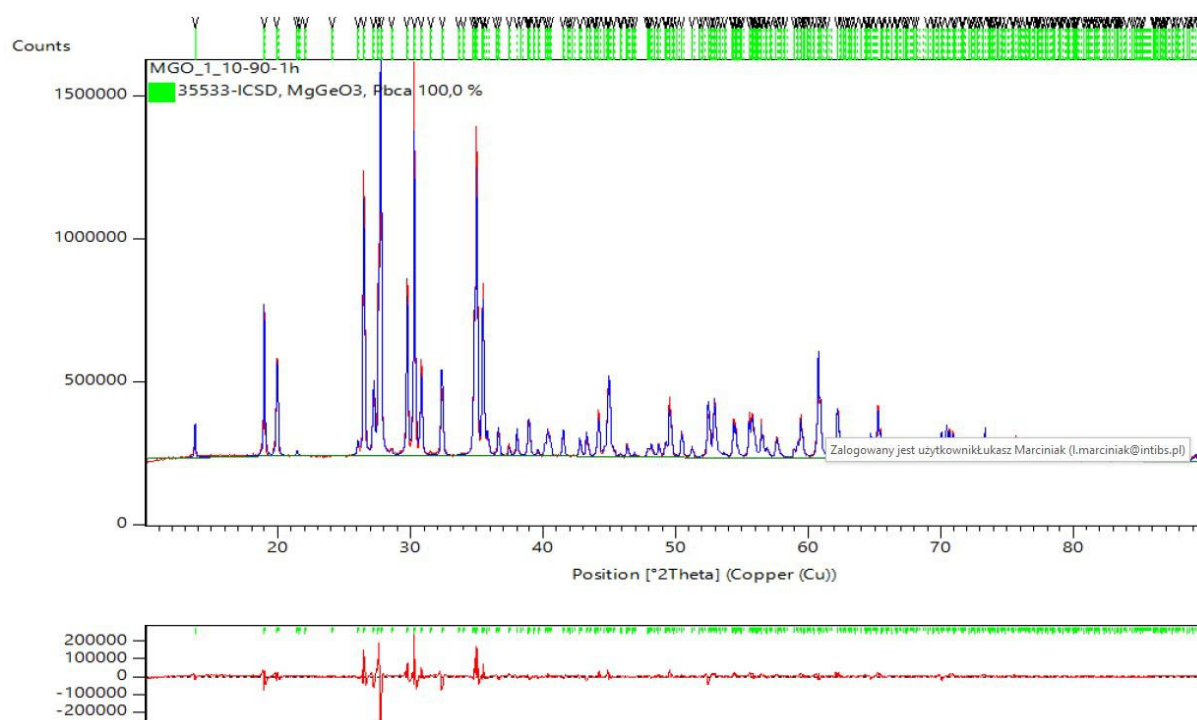


**Figure S3.** Rietveld refinement of XRD pattern of MgGeO<sub>3</sub>:1%Cr<sup>3+</sup>.

MgGeO<sub>3</sub>:2%Cr<sup>3+</sup>

## **Global Parameters**

Number of used phases:	1
Number of variables:	14
Number of constraints:	0
Zero shift/ °2Theta:	0,000000
Specimen displacement/ mm :	-0,076(1)
Profile function:	Pseudo Voigt
Background:	Polynomial
R (expected)/ %:	0,19556

R (profile)/ %:	2,05567
R (weighted profile)/ %:	3,66397
GOF:	351,04610
d-statistic:	0,56927
U standard:	0,000000
V standard:	0,000000
W standard:	0,010000
U Left:	0,000000
V Left:	0,000000
W Left:	0,010000
U Right:	0,000000
V Right:	0,000000
W Right:	0,010000
Asymmetry Type:	No Asymmetry Function
Asymmetry 1:	0,000000
Asymmetry 2:	0,000000
Shape Type:	Shape Individual
Shape 1 Left:	0,600000
Shape 2 Left:	0,000000
Shape 3 Left:	0,000000
Shape 1 Right:	0,600000
Shape 2 Right:	0,000000
Shape 3 Right:	0,000000
K a1/a2 intensity ratio:	0,500000
K alpha/beta intensity ratio:	0,000000
Crystal Shape Factor K:	1,0000
Instrumental FWHM Curve Type:	Caglioti function
Instr. Gauss Curve Coefficient A:	0,0045(5)
Instr. Gauss Curve Coefficient B:	-0,0032(9)
Instr. Gauss Curve Coefficient C:	0,0046(3)
Instr. Lorentz Curve Coefficient A:	0,0062(7)
Instr. Lorentz Curve Coefficient B:	-0,004(1)
Instr. Lorentz Curve Coefficient C:	0,0064(5)

### **Relevant parameters of 35533-ICSD, MgGeO<sub>3</sub>, Pbc<sub>a</sub>**

Structure and profile data:	
Formula sum:	Mg <sub>16·00</sub> Ge <sub>16·00</sub> O <sub>48·00</sub>
Formula mass/ g/mol:	2318,2910
Density (calculated)/ g/cm <sup>3</sup>	4,2742
F(000):	1088,0000
Weight fraction/ %:	100,000000
Space group (No.):	P b c a (61)
Lattice parameters:	
a/ Å:	18,8114(5)
b/ Å:	8,9576(3)
c/ Å:	5,3442(2)
alpha/ °:	90
beta/ °:	90
gamma/ °:	90
V/ 10 <sup>6</sup> pm <sup>3</sup>	900,52460
Overall displacement parameter:	0,000000
Extinction:	0,000000
Flat Plate Absorption Correction:	0,000000
Porosity:	0,000000
Roughness:	0,000000
Fitting mode:	Structure Fit
U Left:	0,035(9)
V Left:	-0,010(7)
W Left:	0,014(1)
Preferred orientation direction/ hkl:	0,00 0,00 1,00
Preferred orientation parameter:	1,000000
Asymmetry parameter 1:	0,000000
Asymmetry parameter 2:	0,000000
Peak shape:	
parameter 1 Left:	0,64(1)
parameter 2 Left:	0,000000
parameter 3 Left:	0,000000
R (Bragg)/ %:	2,90631

### **Occupancy, atomic fract. coordinates and Biso for 35533-ICSD, MgGeO<sub>3</sub>, Pbc<sub>a</sub>**

Atom	Wyck.	s.o.f.	x	y	z	B/ 10 <sup>4</sup> pm <sup>2</sup>
Mg1	8c	1,000000	0,123360	0,656530	0,851890	0,000000

Mg2	8c	1,000000	0,122190	0,488820	0,343520	0,000000
Ge1	8c	1,000000	0,027800	0,339590	0,805350	0,000000
Ge2	8c	1,000000	0,229070	0,345090	0,041410	0,000000
O1	8c	1,000000	0,935450	0,338430	0,814780	0,000000
O2	8c	1,000000	0,069360	0,488810	0,670450	0,000000
O3	8c	1,000000	0,055450	0,319810	0,125190	0,000000
O4	8c	1,000000	0,320480	0,340070	0,021910	0,000000
O5	8c	1,000000	0,187680	0,514400	0,033320	0,000000
O6	8c	1,000000	0,193260	0,289580	0,336850	0,000000

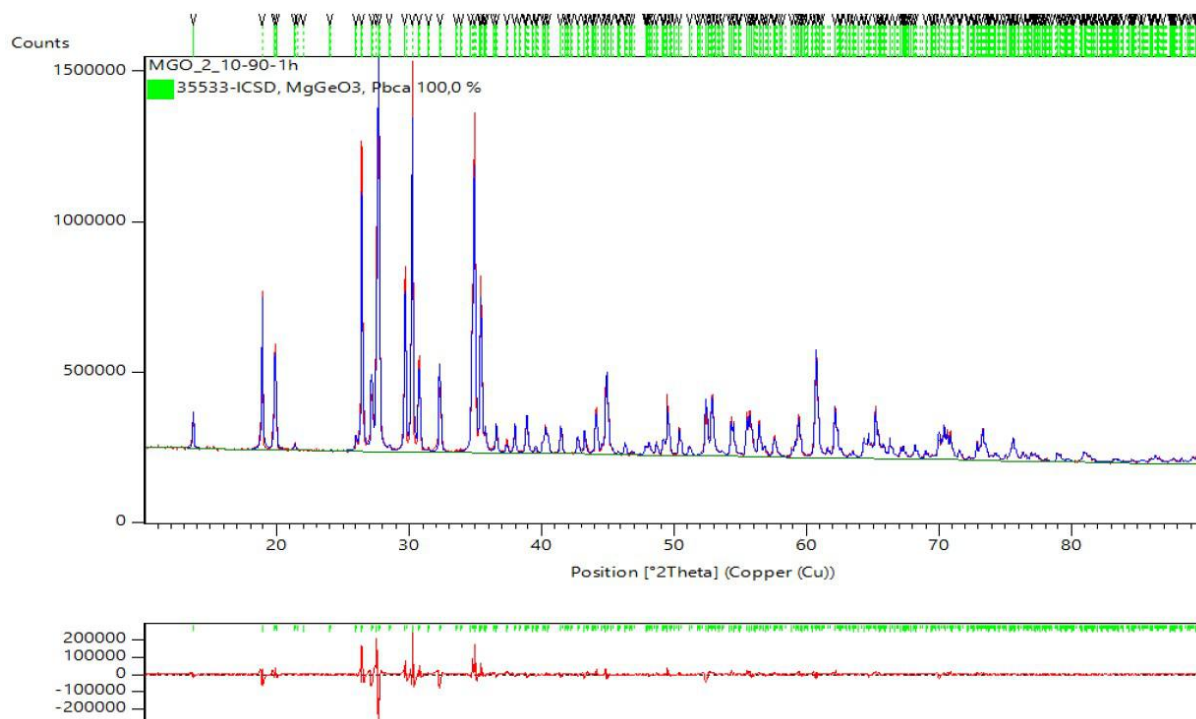


**Figure S4.** Rietveld refinement of XRD pattern of  $\text{MgGeO}_3\text{:}2\%\text{Cr}^{3+}$ .

$\text{MgGeO}_3\text{:}5\%\text{Cr}^{3+}$

### **Global Parameters**

Number of used phases:	1
Number of variables:	14
Number of constraints:	0
Zero shift/ °2Theta:	0,000000
Specimen displacement/ mm :	-0,051(2)
Profile function:	Pseudo Voigt
Background:	Polynomial
R (expected)/ %:	0,20980
R (profile)/ %:	2,56354
R (weighted profile)/ %:	3,93195
GOF:	351,25220
d-statistic:	0,45203
U standard:	0,000000
V standard:	0,000000
W standard:	0,010000

U Left:	0,000000
V Left:	0,000000
W Left:	0,010000
U Right:	0,000000
V Right:	0,000000
W Right:	0,010000
Asymmetry Type:	No Asymmetry Function
Asymmetry 1:	0,000000
Asymmetry 2:	0,000000
Shape Type:	Shape Individual
Shape 1 Left:	0,600000
Shape 2 Left:	0,000000
Shape 3 Left:	0,000000
Shape 1 Right:	0,600000
Shape 2 Right:	0,000000
Shape 3 Right:	0,000000
K a1/a2 intensity ratio:	0,500000
K alpha/beta intensity ratio:	0,000000
Crystal Shape Factor K:	1,0000
Instrumental FWHM Curve Type:	Caglioti function
Instr. Gauss Curve Coefficient A:	0,0045(5)
Instr. Gauss Curve Coefficient B:	-0,0032(9)
Instr. Gauss Curve Coefficient C:	0,0046(3)
Instr. Lorentz Curve Coefficient A:	0,0062(7)
Instr. Lorentz Curve Coefficient B:	-0,004(1)
Instr. Lorentz Curve Coefficient C:	0,0064(5)

### **Relevant parameters of 35533-ICSD, MgGeO3, Pbca**

Structure and profile data:	
Formula sum:	Mg <sub>16·00</sub> Ge <sub>16·00</sub> O <sub>48·00</sub>
Formula mass/ g/mol:	2318,2910
Density (calculated)/ g/cm <sup>3</sup>	4,2735
F(000):	1088,0000
Weight fraction/ %:	100,000000
Space group (No.):	P b c a (61)
Lattice parameters:	
a/ Å:	18,8102(6)
b/ Å:	8,9594(3)
c/ Å:	5,3444(2)
alpha/ °:	90
beta/ °:	90
gamma/ °:	90
V/ 10 <sup>6</sup> pm <sup>3</sup>	900,68280
Overall displacement parameter:	0,000000
Extinction:	0,000000
Flat Plate Absorption Correction:	0,000000
Porosity:	0,000000
Roughness:	0,000000
Fitting mode:	Structure Fit
U Left:	0,04(1)
V Left:	-0,012(9)
W Left:	0,014(2)
Preferred orientation direction/ hkl:	0,00 0,00 1,00
Preferred orientation parameter:	1,000000
Asymmetry parameter 1:	0,000000
Asymmetry parameter 2:	0,000000
Peak shape:	
parameter 1 Left:	0,63(2)
parameter 2 Left:	0,000000
parameter 3 Left:	0,000000
R (Bragg)/ %:	2,83244

### **Occupancy, atomic fract. coordinates and Biso for 35533-ICSD, MgGeO3, Pbca**

Atom	Wyck.	s.o.f.	x	y	z	B/ 10 <sup>4</sup> pm <sup>2</sup>
Mg1	8c	1,000000	0,123360	0,656530	0,851890	0,000000
Mg2	8c	1,000000	0,122190	0,488820	0,343520	0,000000
Ge1	8c	1,000000	0,027800	0,339590	0,805350	0,000000
Ge2	8c	1,000000	0,229070	0,345090	0,041410	0,000000
O1	8c	1,000000	0,935450	0,338430	0,814780	0,000000
O2	8c	1,000000	0,069360	0,488810	0,670450	0,000000

O3	8c	1,000000	0,055450	0,319810	0,125190	0,000000
O4	8c	1,000000	0,320480	0,340070	0,021910	0,000000
O5	8c	1,000000	0,187680	0,514400	0,033320	0,000000
O6	8c	1,000000	0,193260	0,289580	0,336850	0,000000

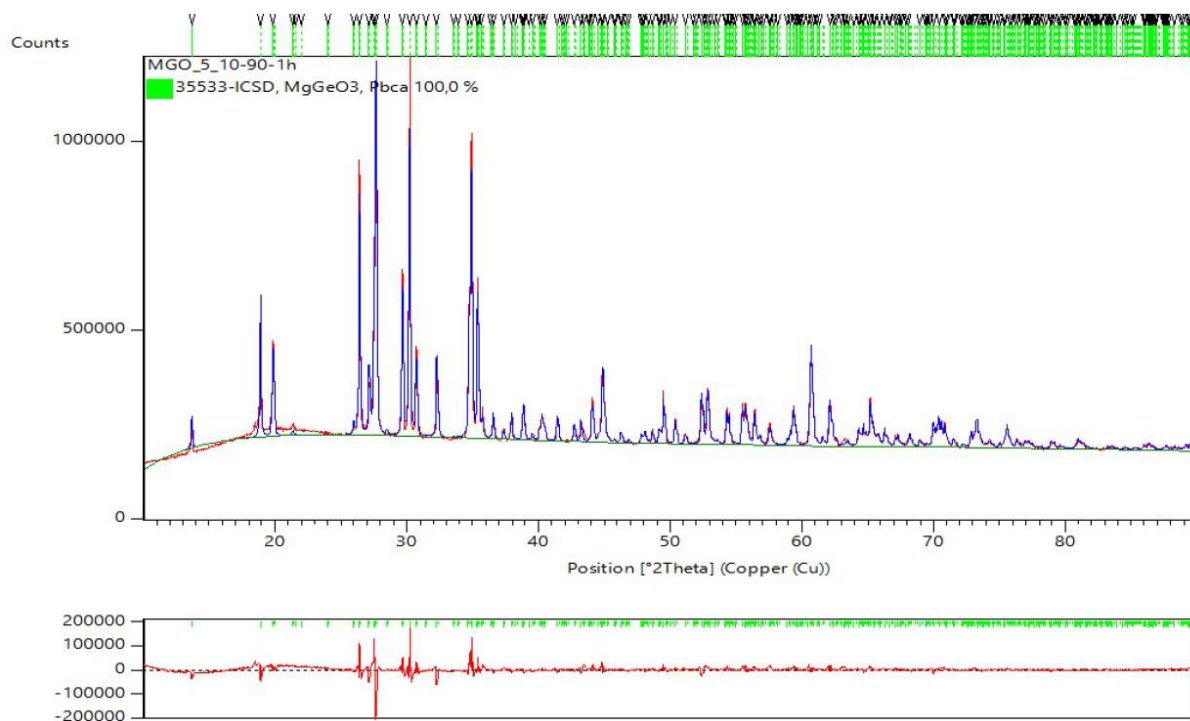


**Figure S5.** Rietveld refinement of XRD pattern of  $\text{MgGeO}_3:5\%\text{Cr}^{3+}$ .

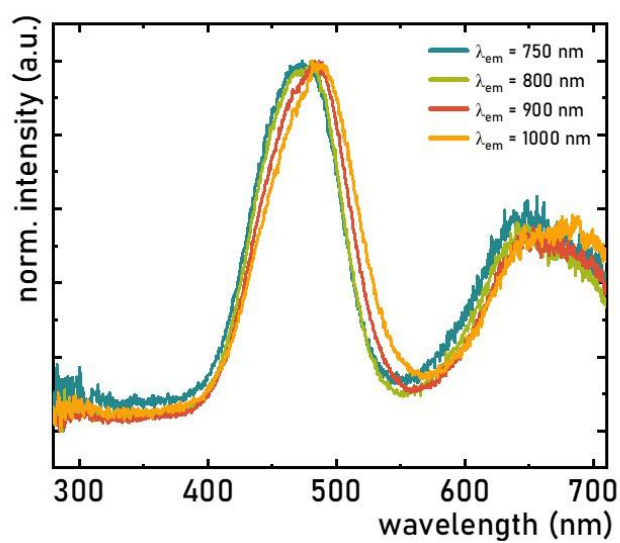


**Figure S6.** Room-temperature excitation spectra as a function of  $\lambda_{\text{em}}$  for the  $\text{MgGeO}_3:5\%\text{Cr}^{3+}$  ( $\lambda_{\text{exc}} = 445 \text{ nm}$ ).

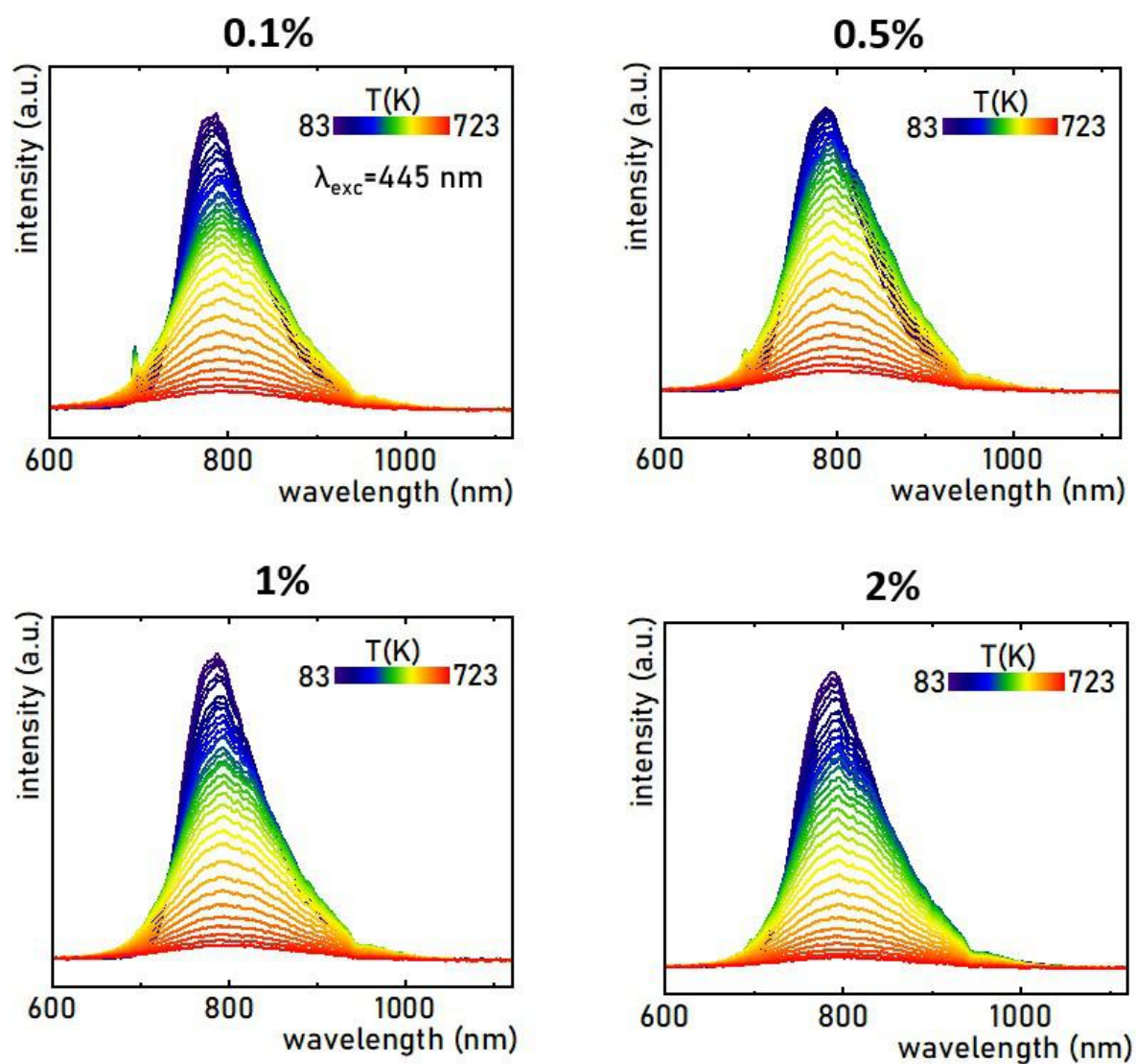


**Figure S7.** Temperature-dependent emission spectra for the MgGeO<sub>3</sub> doped with various Cr<sup>3+</sup> concentration (0,1, 0.5, 1, 2%) upon  $\lambda_{\text{exc}} = 445 \text{ nm}$ .

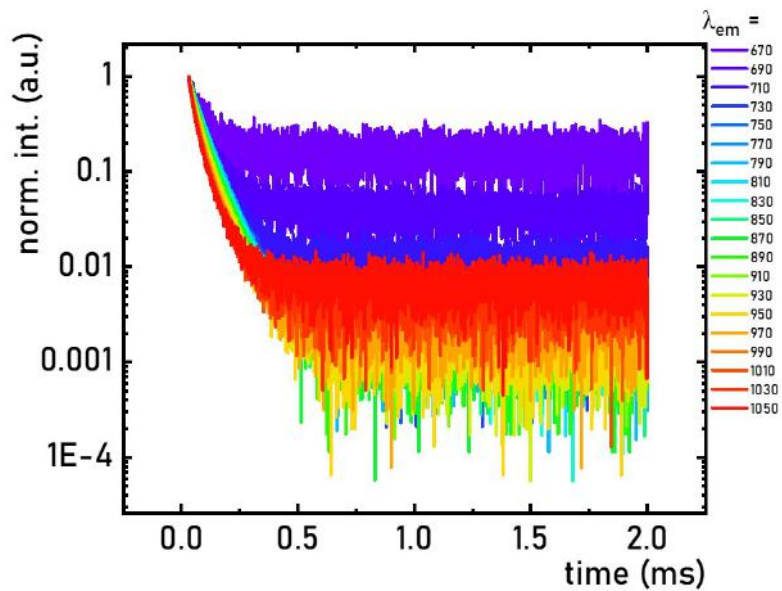


**Figure S8.** Room-temperature decay curves as a function of  $\lambda_{em}$  for the  $MgGeO_3:1\%Cr^{3+}$ .

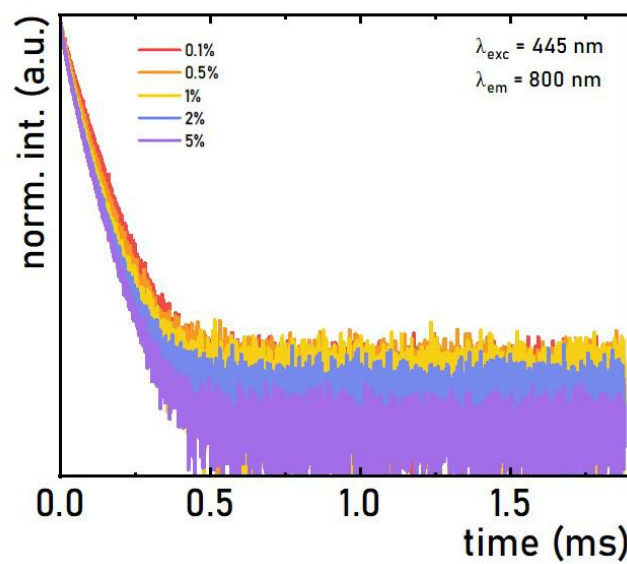


**Figure S9.** Room-temperature decay curves as a function of  $Cr^{3+}$  concentration in doped  $MgGeO_3$  ( $\lambda_{exc} = 445$  nm).





---

## COPIES OF THE CO-AUTHORS' STATEMENTS

---

### LIST OF CO-AUTHORS:

M.Sc. Eng. Mateusz Pieprz (**P1**)

Dr Su Ke (**P3**)

Prof. Lefu Mei (**P3**)

Prof. Quingfeng Guo (**P3**)

Prof. Libing Liao (**P3**)

Prof. Mikhail G. Brik (**P4**)

M.Sc. Eng. Julia Jaśkielewicz (**P5**)

Prof. Junpeng Xue (**P5**)

Dr hab. Sebastian Mahlik, prof. UG (**P5**)

Dr Andris Antuzevics (**P6**)

M. Sc. Pavels Rodionovs (**P6**)

Dr Damian Szymański (**P6**)

Dr Vasyl Kinzhybalo (**P6**)

Dr Eng. Wojciech Piotrowski (**P7**)

Prof. Ulises R. Rodriguez-Mendoza (**P6, P7**)

Prof. Victor Lavin (**P1, P2**)

Dr Przemysław Woźny (**P1, P3, P7**)

Dr hab. Marcin Runowski, prof. UAM (**P1-P7**)

Prof. dr hab. Łukasz Marciniak (**P1-P7**)

mgr inż. Mateusz Pieprz  
15.05.2025

Wrocław,

### **Declaration of the co-authorship of the publications**

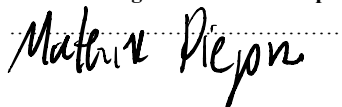
I confirm my participation in the following publication:

M. Szymczak, P. Wozny, M. Runowski, M. Pieprz, V. Lavin, L. Marciniak, *Temperature invariant ratiometric luminescence manometer based on  $Cr^{3+}$  ions emission*, Chemical Engineering Journal, 2023, 453, 139632

My contribution to this publication consisted of participation in synthesis of selected samples.

**I confirm that M. Sc. Maja Szymczak was the lead co-author of this publication.**

mgr inż. Mateusz Pieprz

A handwritten signature in black ink, reading "Mateusz Pieprz", written over a horizontal dotted line.

China University of Geosciences, Beijing

**Declaration of the co-authorship of the publication**

I confirm my participation in the following publication:

M. Szymczak, **K. Su**, L. Mei, M. Runowski, P. Woźny, Q. Guo, L. Liao, L. Marciniak, *Investigating the Potential of Cr<sup>3+</sup>-Doped Pyroxene for Highly Sensitive Optical Pressure Sensing*, ACS Applied Materials & Interfaces 2024, 16, 44, 60491-60500.

My contribution to this publication consisted of sample synthesis and initial spectroscopic characterization at room temperature.

**I confirm that M. Sc. Maja Szymczak had significant contribution in mentioned publication.**

**Dr Su Ke**

Su ke.

**Declaration of the co-authorship of the publication**

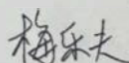
I confirm my participation in the following publication:

M. Szymczak, K. Su, L. Mei, M. Runowski, P. Woźny, Q. Guo, L. Liao, L. Marciniak, *Investigating the Potential of Cr<sup>3+</sup>-Doped Pyroxene for Highly Sensitive Optical Pressure Sensing*, ACS Applied Materials & Interfaces 2024, 16, 44, 60491-60500.

My contribution to this publication consisted of reviewing and editing the manuscript.

**I confirm that M. Sc. Maja Szymczak had significant contribution in mentioned publication.**

Prof Lefu Mei



.....

Prof Qingfeng Guo

Beijing, 15.05.2025

China University of Geosciences, Beijing

**Declaration of the co-authorship of the publication**

I confirm my participation in the following publication:

M. Szymczak, K. Su, L. Mei, M. Runowski, P. Woźny, **Q. Guo**, L. Liao, L. Marciniak, *Investigating the Potential of Cr<sup>3+</sup>-Doped Pyroxene for Highly Sensitive Optical Pressure Sensing*, ACS Applied Materials & Interfaces 2024, 16, 44, 60491-60500.

My contribution to this publication consisted of reviewing and editing the manuscript.

**I confirm that M. Sc. Maja Szymczak had significant contribution in mentioned publication.**

Prof Qingfeng Guo

郭庆丰

**Prof Libing Liao**

Beijing, 15.05.2025

**China University of Geosciences, Beijing**

**Declaration of the co-authorship of the publication**

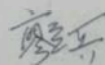
I confirm my participation in the following publication:

M. Szymczak, K. Su, L. Mei, M. Runowski, P. Woźny, Q. Guo, **L. Liao**, L. Marciniak, *Investigating the Potential of Cr<sup>3+</sup>-Doped Pyroxene for Highly Sensitive Optical Pressure Sensing*, ACS Applied Materials & Interfaces 2024, 16, 44, 60491-60500.

My contribution to this publication consisted of reviewing and editing the manuscript.

**I confirm that M. Sc. Maja Szymczak had significant contribution in mentioned publication.**

**Prof Libing Liao**



.....



**Prof. Mikhail G. Brik**

Tartu, 15.05.2025

**Institute of Physics**

**University of Tartu**

**Declaration of the co-authorship of the publications**

I confirm my participation in the following publication:

M. Szymczak, M. Runowski, **M.G. Brik**, L. Marciniak, *Multimodal, super-sensitive luminescent manometer based on giant pressure-induced spectral shift of  $\text{Cr}^{3+}$  in the NIR range*, Chemical Engineering Journal, 2023, 466, 143130,

My contribution to this publication consisted of performing crystal field calculations and comparing them with the experimental spectra.

**I confirm that M. Sc. Maja Szymczak was the lead co-author of this publication.**

**Prof. Mikhail G. Brik**



.....

**Declaration of the co-authorship of the publications**

I confirm my participation in the following publication:

M. Szymczak, **J. Jaśkielewicz**, M. Runowski, J. Xue, S. Mahlik, L. Marciniak, *Highly-Sensitive, Tri-Modal Luminescent Manometer Utilizing Band-Shift, Ratiometric and Lifetime-Based Sensing Parameters*, Advanced Functional Materials, 2024, 34(22), 2314068.

My contribution to this publication consisted of participating in the temperature-dependent emission measurements of selected samples.

**I confirm that M. Sc. Maja Szymczak was the lead co-author of this publication.**

mgr inż. Julia Jaśkielewicz

.....*Jaśkielewicz*.....

Prof. Junpeng Xue

Zhenjiang, 12.05.2025

School of Science

Jiangsu University of Science and Technology

**Declaration of the co-authorship of the publications**

I confirm my participation in the following publication:

M. Szymczak, J. Jaśkielewicz, M. Runowski, **J. Xue**, S. Mahlik, L. Marciniak, Highly-Sensitive, Tri-Modal Luminescent Manometer Utilizing Band-Shift, Ratiometric and Lifetime-Based Sensing Parameters, *Advanced Functional Materials*, 2024, 34(22), 2314068.

My contribution to this publication consisted of measuring the Raman spectra as a function of pressure.

**I confirm that M. Sc. Maja Szymczak was the lead co-author of this publication.**

**Prof. Junpeng Xue**

*Junpeng Xue*

.....

dr hab. Sebastian Mahlik, prof. UG

Gdańsk, 15.05.2025

Institute of Experimental Physics

Faculty of Mathematics, Physics and Informatics

University of Gdansk

**Declaration of the co-authorship of the publications**

I confirm my participation in the following publication:

M. Szymczak, J. Jaśkielewicz, M. Runowski, J. Xue, **S. Mahlik**, L. Marciniak, *Highly-Sensitive, Tri-Modal Luminescent Manometer Utilizing Band-Shift, Ratiometric and Lifetime-Based Sensing Parameters*, Advanced Functional Materials, 2024, 34(22), 2314068.

My contribution to this publication consisted of reviewing and editing the manuscript.

**I confirm that M. Sc. Maja Szymczak was the lead co-author of this publication.**

dr hab. Sebastian Mahlik, prof. UG



Dr Andris Antuzevics

Riga, 15.05.2025

Institute of Solid State Physics

University of Latvia

**Declaration of the co-authorship of the publications**

I confirm my participation in the following publication:

M. Szymczak, A. Antuzevics, P. Rodionovs, M. Runowski, U.R. Rodríguez-Mendoza, D. Szymanski, V. Kinzhybalo, L. Marciniak, *Bifunctional Luminescent Thermometer-Manometer Based on  $Cr^{3+}$ - $Cr^{3+}$  Pair Emission*, ACS Applied Materials & Interfaces, 2024, 16, 47, 64976–64987.

My contribution to this publication consisted of reviewing and editing the manuscript.

I confirm that M. Sc. Maja Szymczak was the lead co-author of mentioned publication.

Dr Andris Antuzevics

**Declaration of the co-authorship of the publications**

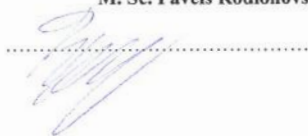
I confirm my participation in the following publication:

M. Szymczak, A. Antuzevics, **P. Rodionovs**, M. Runowski, U.R. Rodriguez-Mendoza, D. Szymanski, V. Kinzhybalo, L. Marciniak, *Bifunctional Luminescent Thermometer-Manometer Based on  $Cr^{3+}$ - $Cr^{3+}$  Pair Emission*, ACS Applied Materials & Interfaces, 2024, 16, 47, 64976–64987,

My contribution to this publication consisted of the synthesis of samples.

**I confirm that M. Sc. Maja Szymczak was the lead co-author of mentioned publication.**

**M. Sc. Pavels Rodionovs**



Wojciech Piotrowski PhD Eng.  
Faculty of Chemistry  
Wrocław University of Science and Technology

Wrocław, 15.05.2025

### Declaration of the co-authorship of the publications

I confirm my participation in the following publication:

M. Szymczak, W.M. Piotrowski, U. R. Rodríguez-Mendoza, P. Wozny, M. Runowski, L. Marciniak, *Highly sensitive ratiometric luminescence manometer based on the multisite emission of Cr<sup>3+</sup>*, Journal of Materials Chemistry C, 2025, 13, 4224-4235.

My contribution to this publication consisted of the synthesis of samples.

I confirm that M. Sc. Maja Szymczak was the lead co-author of mentioned publication.

Wojciech Piotrowski

A handwritten signature in black ink, reading "Wojciech Piotrowski", is written over a horizontal dotted line.



dr Damian Szymański

Wrocław, 14.05.2025

Institute of Low Temperature and Structure Research

Polish Academy of Sciences

### Declaration of the co-authorship of the publication

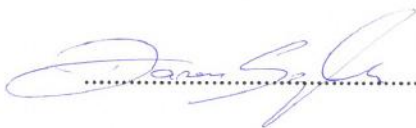
I confirm my participation in the following publication:

M. Szymczak, A. Antuzevics, P. Rodionovs, M. Runowski, U.R. Rodríguez-Mendoza, **D. Szymanski**, V. Kinzhybalo, L. Marciniak, *Bifunctional Luminescent Thermometer-Manometer Based on  $Cr^{3+}$ - $Cr^{3+}$  Pair Emission*, ACS Applied Materials & Interfaces, 2024, 16, 47, 64976–64987.

My contribution to this publication consisted of measuring SEM images and EDS maps.

**I confirm that M. Sc. Maja Szymczak was the lead co-author of mentioned publication.**

dr Damian Szymański



dr Vasyl Kinzhybalo

Wrocław, 15.05.2025

Institute of Low Temperature and Structure Research

Polish Academy of Sciences

### Declaration of the co-authorship of the publication

I confirm my participation in the following publication:

M. Szymczak, A. Antuzevics, P. Rodionovs, M. Runowski, U.R. Rodríguez-Mendoza, D. Szymanski, **V. Kinzhybalo**, L. Marciniak, *Bifunctional Luminescent Thermometer-Manometer Based on  $Cr^{3+}$ - $Cr^{3+}$  Pair Emission*, ACS Applied Materials & Interfaces, 2024, 16, 47, 64976–64987.

My contribution to this publication consisted of performing XRD measurement and Rietveld analysis.

**I confirm that M. Sc. Maja Szymczak was the lead co-author of mentioned publication.**

dr Vasyl Kinzhybalo

A handwritten signature in blue ink that reads "Vasyl Kinzhybalo". The signature is written over a horizontal dotted line.

**Prof. Dr. Ulises R. Rodríguez-Mendoza** San Cristóbal de La Laguna, 12.05.2025  
Department of Physics.  
Faculty of Sciences  
Universidad de La Laguna.  
E-38200. San Cristóbal de La Laguna.  
Canary Islands. Spain.  
Phone: +34922318321.  
E-mail: [urguez@ull.edu.es](mailto:urguez@ull.edu.es)

### **Declaration of the co-authorship of the publications**

I confirm my participation in the following publications:

M. Szymczak, A. Antuzevics, P. Rodionovs, M. Runowski, U.R. Rodríguez-Mendoza, D. Szymanski, V. Kinzhybalo, L. Marciniak, *Bifunctional Luminescent Thermometer-Manometer Based on  $Cr^{3+}$ - $Cr^{3+}$  Pair Emission*, ACS Applied Materials & Interfaces, 2024, 16, 47, 64976–64987,

M. Szymczak, W.M. Piotrowski, U.R. Rodríguez-Mendoza, P. Wozny, M. Runowski, L. Marciniak, *Highly sensitive ratiometric luminescence manometer based on the multisite emission of  $Cr^{3+}$* , Journal of Materials Chemistry C, 2025, 13, 4224–4235.

My contribution to this publication consisted of measuring the Raman spectra as a function of pressure.

**I confirm that M. Sc. Maja Szymczak was the lead co-author of mentioned publications.**

**Prof. Dr. U. R. Rodríguez-Mendoza**



San Cristóbal de La Laguna, 14.05.2025

Prof. Víctor Lavín.  
Departamento de Física.  
Universidad de La Laguna.  
E-38200 San Cristóbal de La Laguna.  
Santa Cruz de Tenerife.  
España (Spain).  
vlavin@ull.edu.es

### DECLARATION OF THE CO-AUTHORSHIP OF PUBLICATIONS

**1.-** I confirm my participation in the following publication:

*M. Szymczak, P. Wozny, M. Runowski, M. Pieprz, V. Lavín, L. Marciniak, Temperature invariant ratiometric luminescence manometer based on Cr<sup>3+</sup> ions emission, Chemical Engineering Journal, 2023, 453, 139632.*

My contribution to this publication consisted of measuring the Raman spectra as a function of pressure.

**2.-** I also confirm my participation in the following publication:

*M. Szymczak, M. Runowski, V. Lavín, L. Marciniak, Highly Pressure-Sensitive, Temperature Independent Luminescence Ratiometric Manometer Based on MgO:Cr<sup>3+</sup> Nanoparticles, Laser & Photonics Reviews, 2023, 17, 2200801.*

My contribution to this publication consisted of reviewing and editing the manuscript.

Finally, I confirm that **M. Sc. Maja Szymczak** was the lead co-author of mentioned publications.

**Dr. Víctor Lavín**

A handwritten signature in blue ink, appearing to read 'Victor Lavín', with a horizontal line drawn through the middle of the signature.

dr Przemysław Woźny

Poznań, 14.05.2025

Faculty of Chemistry

Adam Mickiewicz University

### Declaration of the co-authorship of the publications

I confirm my participation in the following publications:

M. Szymczak, **P. Woźny**, M. Runowski, M. Pieprz, V. Lavín, L. Marciniak, *Temperature invariant ratiometric luminescence manometer based on  $Cr^{3+}$  ions emission*, Chemical Engineering Journal, 2023, 453, 139632

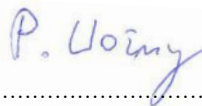
M. Szymczak, K. Su, L. Mei, M. Runowski, **P. Woźny**, Q. Guo, L. Liao, L. Marciniak, *Investigating the Potential of  $Cr^{3+}$ -Doped Pyroxene for Highly Sensitive Optical Pressure Sensing*, 2024, 16, 44, 60491–60500,

M. Szymczak, W.M. Piotrowski, U. R. Rodríguez-Mendoza, **P. Woźny**, M. Runowski, L. Marciniak, *Highly sensitive ratiometric luminescence manometer based on the multisite emission of  $Cr^{3+}$* , Journal of Materials Chemistry C, 2025, 13, 4224–4235.

My contribution to this publication consisted of measuring the Raman spectra as a function of pressure.

**I confirm that M. Sc. Maja Szymczak was the lead co-author and had significant contribution in mentioned publication.**

dr Przemysław Woźny



.....

### Declaration of the co-authorship of the publications

I confirm my participation in the following publications:

- M. Szymczak, P. Wozny, **M. Runowski**, M. Pieprz, V. Lavín, L. Marciniak, *Temperature invariant ratiometric luminescence manometer based on  $Cr^{3+}$  ions emission*, Chemical Engineering Journal, 2023, 453, 139632
- M. Szymczak, K. Su, L. Mei, **M. Runowski**, P. Woźny, Q. Guo, L. Liao, L. Marciniak, *Investigating the Potential of  $Cr^{3+}$ -Doped Pyroxene for Highly Sensitive Optical Pressure Sensing*, 2024, 16, 44, 60491–60500,
- M. Szymczak, **M. Runowski**, M.G. Brik, L. Marciniak, *Multimodal, super-sensitive luminescent manometer based on giant pressure-induced spectral shift of  $Cr^{3+}$  in the NIR range*, Chemical Engineering Journal, 2023, 466, 143130,
- M. Szymczak, J. Jaśkielewicz, **M. Runowski**, J. Xue, S. Mahlik, L. Marciniak, *Highly-Sensitive, Tri-Modal Luminescent Manometer Utilizing Band-Shift, Ratiometric and Lifetime-Based Sensing Parameters*, Advanced Functional Materials, 2024, 34(22), 2314068,
- M. Szymczak, A. Antuzevics, P. Rodionovs, **M. Runowski**, U.R. Rodríguez-Mendoza, D. Szymanski, V. Kinzhybalo, L. Marciniak, *Bifunctional Luminescent Thermometer-Manometer Based on  $Cr^{3+}$ - $Cr^{3+}$  Pair Emission*, ACS Applied Materials & Interfaces, 2024, 16, 47, 64976–64987,
- M. Szymczak, W.M. Piotrowski, U. R. Rodríguez-Mendoza, P. Wozny, **M. Runowski**, L. Marciniak, *Highly sensitive ratiometric luminescence manometer based on the multisite emission of  $Cr^{3+}$* , Journal of Materials Chemistry C, 2025, 13, 4224-4235.

My contribution to this publication consisted of interpreting the Raman spectra as a function of pressure and of reviewing and editing the manuscript..

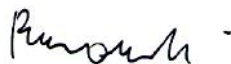
I also confirm my participation in the following publication:

- M. Szymczak, **M. Runowski**, V. Lavín, L. Marciniak, *Highly Pressure-Sensitive, Temperature Independent Luminescence Ratiometric Manometer Based on  $MgO:Cr^{3+}$  Nanoparticles*, Laser & Photonics Reviews, 2023, 17, 2200801

My contribution to this publication consisted of reviewing and editing the manuscript.

**I confirm that M. Sc. Maja Szymczak was the lead co-author or had significant contribution in mentioned publications.**

dr hab. Marcin Runowski, prof. UAM



.....

Prof. dr hab. Łukasz Marciniak

Wrocław, 13.05.2025

Institute of Low Temperature and Structure Research

Polish Academy of Sciences

### Declaration of the co-authorship of the publications


I confirm my participation in the following publications:

- M. Szymczak, P. Wozny, M. Runowski, M. Pieprz, V. Lavín, **L. Marciniak**, *Temperature invariant ratiometric luminescence manometer based on  $Cr^{3+}$  ions emission*, Chemical Engineering Journal, 2023, 453, 139632
- M. Szymczak, M. Runowski, V. Lavín, **L. Marciniak**, *Highly Pressure-Sensitive, Temperature Independent Luminescence Ratiometric Manometer Based on  $MgO:Cr^{3+}$  Nanoparticles*, Laser & Photonics Reviews, 2023, 17, 2200801
- M. Szymczak, K. Su, L. Mei, M. Runowski, P. Woźny, Q. Guo, L. Liao, **L. Marciniak**, *Investigating the Potential of  $Cr^{3+}$ -Doped Pyroxene for Highly Sensitive Optical Pressure Sensing*, 2024, 16, 44, 60491–60500,
- M. Szymczak, M. Runowski, M.G. Brik, **L. Marciniak**, *Multimodal, super-sensitive luminescent manometer based on giant pressure-induced spectral shift of  $Cr^{3+}$  in the NIR range*, Chemical Engineering Journal, 2023, 466, 143130,
- M. Szymczak, J. Jaśkielewicz, M. Runowski, J. Xue, S. Mahlik, **L. Marciniak**, *Highly-Sensitive, Tri-Modal Luminescent Manometer Utilizing Band-Shift, Ratiometric and Lifetime-Based Sensing Parameters*, Advanced Functional Materials, 2024, 34(22), 2314068,
- M. Szymczak, A. Antuzevics, P. Rodionovs, M. Runowski, U.R. Rodríguez-Mendoza, D. Szymanski, V. Kinzhybalo, **L. Marciniak**, *Bifunctional Luminescent Thermometer-Manometer Based on  $Cr^{3+}$ - $Cr^{3+}$  Pair Emission*, ACS Applied Materials & Interfaces, 2024, 16, 47, 64976–64987,
- M. Szymczak, W.M. Piotrowski, U. R. Rodríguez-Mendoza, P. Wozny, M. Runowski, **L. Marciniak**, *Highly sensitive ratiometric luminescence manometer based on the multisite emission of  $Cr^{3+}$* , Journal of Materials Chemistry C, 2025 13, 4224-4235.

As the Supervisor of M. Sc. Maja Szymczak, I was responsible for the conceptualization, as well as the review, editing and preparing the final versions of the manuscripts.

I confirm that M. Sc. Maja Szymczak was the lead co-author or had significant contribution in mentioned publications.

Prof. dr hab. Łukasz Marciniak





---

## REFERENCES

---

- (1) Mao, H. K.; Xu, J.; Bell, P. M. Calibration of the Ruby Pressure Gauge to 800 Kbar under Quasi-Hydrostatic Conditions. *J. Geophys. Res. Solid Earth* **1986**, *91* (B5), 4673–4676. <https://doi.org/10.1029/JB091iB05p04673>.
- (2) Piermarini, G. J.; Block, S.; Barnett, J. D.; Forman, R. A. Calibration of the Pressure Dependence of the R1 Ruby Fluorescence Line to 195 Kbar. *J. Appl. Phys.* **1975**, *46* (6), 2774–2780. <https://doi.org/10.1063/1.321957>.
- (3) Chijioke, A. D.; Nellis, W. J.; Soldatov, A.; Silvera, I. F. The Ruby Pressure Standard to 150 GPa. *J. Appl. Phys.* **2005**, *98* (11), 114905. <https://doi.org/10.1063/1.2135877>.
- (4) Yen, J.; Nicol, M. Temperature Dependence of the Ruby Luminescence Method for Measuring High Pressures. *J. Appl. Phys.* **1992**, *72* (12), 5535–5538. <https://doi.org/10.1063/1.351950>.
- (5) Marek, Ł.; Sobczyk, M. Highly Sensitive Luminescent Pressure Sensor for Vacuum Measurement Based on Pr<sup>3+</sup>:TeO<sub>2</sub>-ZnO-Na<sub>2</sub>O-La<sub>2</sub>O<sub>3</sub> Glasses. *Mater. Lett.* **2021**, *290*, 129492. <https://doi.org/10.1016/j.matlet.2021.129492>.
- (6) Runowski, M.; Woźny, P.; Lavín, V.; Lis, S. Optical Pressure Nano-Sensor Based on Lanthanide Doped SrB<sub>2</sub>O<sub>4</sub>:Sm<sup>2+</sup> Luminescence – Novel High-Pressure Nanomanometer. *Sens. Actuators B Chem.* **2018**, *273*, 585–591. <https://doi.org/10.1016/j.snb.2018.06.089>.
- (7) Runowski, M.; Zheng, T.; Woźny, P.; Du, P. NIR Emission of Lanthanides for Ultrasensitive Luminescence Manometry—Er<sup>3+</sup>-Activated Optical Sensor of High Pressure. *Dalton Trans.* **2021**, *50* (41), 14864–14871. <https://doi.org/10.1039/D1DT02681J>.
- (8) Sójka, M.; Runowski, M.; Woźny, P.; Carlos, L. D.; Zych, E.; Lis, S. Y<sub>2</sub>(Ge,Si)O<sub>5</sub>:Pr Phosphors: Multimodal Temperature and Pressure Sensors Shaped by Bandgap Management. *J. Mater. Chem. C* **2021**, *9* (39), 13818–13831. <https://doi.org/10.1039/D1TC03202J>.
- (9) Runowski, M.; Shyichuk, A.; Tymiąski, A.; Grzyb, T.; Lavín, V.; Lis, S. Multifunctional Optical Sensors for Nanomanometry and Nanothermometry: High-Pressure and High-Temperature Upconversion Luminescence of Lanthanide-Doped Phosphates—LaPO<sub>4</sub>/YPO<sub>4</sub>:Yb<sup>3+</sup>–Tm<sup>3+</sup>. *ACS Appl. Mater. Interfaces* **2018**, *10* (20), 17269–17279. <https://doi.org/10.1021/acsami.8b02853>.
- (10) Goderski, S.; Runowski, M.; Woźny, P.; Lavín, V.; Lis, S. Lanthanide Upconverted Luminescence for Simultaneous Contactless Optical Thermometry and Manometry—Sensing under Extreme Conditions of Pressure and Temperature. *ACS Appl. Mater. Interfaces* **2020**, *12* (36), 40475–40485. <https://doi.org/10.1021/acsami.0c09882>.

- (11) Rodríguez-Mendoza, U. R.; León-Luis, S. F.; Muñoz-Santiuste, J. E.; Jaque, D.; Lavín, V. Nd<sup>3+</sup>-Doped Ca<sub>3</sub>Ga<sub>2</sub>Ge<sub>3</sub>O<sub>12</sub> Garnet: A New Optical Pressure Sensor. *J. Appl. Phys.* **2013**, *113* (21), 213517. <https://doi.org/10.1063/1.4809217>.
- (12) Kobayakov, S.; Kamińska, A.; Suchocki, A.; Galanciak, D.; Malinowski, M. Nd<sup>3+</sup>-Doped Yttrium Aluminum Garnet Crystal as a near-Infrared Pressure Sensor for Diamond Anvil Cells. *Appl. Phys. Lett.* **2006**, *88* (23), 234102. <https://doi.org/10.1063/1.2210084>.
- (13) Antoniuk, M. A.; Zelewski, S. J.; Oliva, R.; Żak, A.; Kudrawiec, R.; Nyk, M. Combined Temperature and Pressure Sensing Using Luminescent NaBiF<sub>4</sub>:Yb,Er Nanoparticles. *ACS Appl. Nano Mater.* **2020**, *3* (5), 4209–4217. <https://doi.org/10.1021/acsanm.0c00403>.
- (14) León-Luis, S. F.; Muñoz-Santiuste, J. E.; Lavín, V.; Rodríguez-Mendoza, U. R. Optical Pressure and Temperature Sensor Based on the Luminescence Properties of Nd<sup>3+</sup> Ion in a Gadolinium Scandium Gallium Garnet Crystal. *Opt. Express* **2012**, *20* (9), 10393–10398. <https://doi.org/10.1364/OE.20.010393>.
- (15) Gupta, S. K.; Mao, Y. High Pressure Induced Disappearing <sup>5</sup>D<sub>0</sub> → <sup>7</sup>F<sub>2</sub> and Broadening <sup>5</sup>D<sub>0</sub> → <sup>7</sup>F<sub>1</sub> Transitions from Y<sub>2</sub>Hf<sub>2</sub>O<sub>7</sub>:Eu<sup>3+</sup> Nanoparticles. *Mater. Lett.* **2021**, *303*, 130560. <https://doi.org/10.1016/j.matlet.2021.130560>.
- (16) Runowski, M.; Shyichuk, A.; Tyminiński, A.; Grzyb, T.; Lavín, V.; Lis, S. Multifunctional Optical Sensors for Nanomanometry and Nanothermometry: High-Pressure and High-Temperature Upconversion Luminescence of Lanthanide-Doped Phosphates—LaPO<sub>4</sub>/YPO<sub>4</sub>:Yb<sup>3+</sup>–Tm<sup>3+</sup>. *ACS Appl. Mater. Interfaces* **2018**, *10* (20), 17269–17279. <https://doi.org/10.1021/acsami.8b02853>.
- (17) Runowski, M.; Woźny, P.; Stopikowska, N.; Guo, Q.; Lis, S. Optical Pressure Sensor Based on the Emission and Excitation Band Width (Fwhm) and Luminescence Shift of Ce<sup>3+</sup>-Doped Fluorapatite—High-Pressure Sensing. *ACS Appl. Mater. Interfaces* **2019**, *11* (4), 4131–4138. <https://doi.org/10.1021/acsami.8b19500>.
- (18) Zheng, B.; Zhang, X.; Zhang, D.; Wang, F.; Zheng, Z.; Yang, X.; Yang, Q.; Song, Y.; Zou, B.; Zou, H. Ultra-Wideband Phosphor Mg<sub>2</sub>Gd<sub>8</sub>(SiO<sub>4</sub>)<sub>6</sub>O<sub>2</sub>:Ce<sup>3+</sup>,Mn<sup>2+</sup>: Energy Transfer and Pressure-Driven Color Tuning for Potential Applications in LEDs and Pressure Sensors. *Chem. Eng. J.* **2022**, *427*, 131897. <https://doi.org/10.1016/j.cej.2021.131897>.
- (19) Masubuchi, Y.; Nishitani, S.; Miyazaki, S.; Hua, H.; Ueda, J.; Higuchi, M.; Tanabe, S. Large Red-Shift of Luminescence from BaCN<sub>2</sub>:Eu<sup>2+</sup> Red Phosphor under High Pressure. *Appl. Phys. Express* **2020**, *13* (4), 042009. <https://doi.org/10.35848/1882-0786/ab8055>.
- (20) Zheng, T.; Runowski, M.; Xue, J.; Luo, L.; Rodríguez-Mendoza, U. R.; Lavín, V.; Martín, I. R.; Rodríguez-Hernández, P.; Muñoz, A.; Du, P. Giant Pressure-Induced Spectral Shift in Cyan-Emitting Eu<sup>2+</sup>-Activated Sr<sub>8</sub>Si<sub>4</sub>O<sub>12</sub>C<sub>18</sub> Microspheres for Ultrasensitive Visual Manometry. *Adv. Funct. Mater.* **2023**, *33* (26), 2214663. <https://doi.org/10.1002/adfm.202214663>.

- (21) Zhang, D.; Zheng, B.; Zheng, Z.; Li, L.; Yang, Q.; Song, Y.; Zou, B.; Zou, H. Multifunctional  $\text{Ca}_9\text{NaZn}_{1-y}\text{Mg}_y(\text{PO}_4)_7\text{:Eu}^{2+}$  Phosphor for Full-Spectrum Lighting, Optical Thermometry and Pressure Sensor Applications. *Chem. Eng. J.* **2022**, *431*, 133805. <https://doi.org/10.1016/j.cej.2021.133805>.
- (22) Su, K.; Mei, L.; Guo, Q.; Shuai, P.; Wang, Y.; Liu, Y.; Jin, Y.; Peng, Z.; Zou, B.; Liao, L. Multi-Mode Optical Manometry Based on  $\text{Li}_4\text{SrCa}(\text{SiO}_4)_2\text{:Eu}^{2+}$  Phosphors. *Adv. Funct. Mater.* **2023**, *33* (49), 2305359. <https://doi.org/10.1002/adfm.202305359>.
- (23) Lv, Q.; Wang, C.; Chen, S.; Zheng, H.; Dong, E.; Zhu, G. Ultrasensitive Pressure-Induced Optical Materials: Europium-Doped Hafnium Silicates with a Khibinskite Structure for Optical Pressure Sensors and WLEDs. *Inorg. Chem.* **2022**, *61* (7), 3212–3222. <https://doi.org/10.1021/acs.inorgchem.1c03674>.
- (24) Chen, H.; Seto, T.; Wang, Y. An Efficient Blue Phosphor with High Thermal Stability for Lighting and Optical Pressure Sensor Applications. *Inorg. Chem. Front.* **2022**, *9* (8), 1644–1654. <https://doi.org/10.1039/D2QI00025C>.
- (25) Su, C.; Xu, D.; Li, K.; Xie, X.; Ren, Y.; Liu, Y.; Jin, Y.; Du, M.; Shen, P.  $\text{Mn}^{4+}$ -Activated Inorganic Phosphor  $\text{Zn}_3\text{Ga}_2\text{GeO}_8$ : A High-Sensitivity and Broad-Range Pressure Sensor Material for Optical Manometry. *J. Phys. Chem. C* **2024**, *128* (39), 16791–16796. <https://doi.org/10.1021/acs.jpcc.4c05162>.
- (26) Pieprz, M.; Runowski, M.; Woźny, P.; Xue, J.; Marciniak, L. Temperature Invariant Lifetime Based Luminescent Manometer on  $\text{Mn}^{4+}$  Ions. *J. Mater. Chem. C* **2023**, *11* (33), 11353–11360. <https://doi.org/10.1039/D3TC00911D>.
- (27) Chen, Z.; Du, S.; Li, F.; Zhang, S.; Zhao, S.; Tian, Z.; Zhang, J.; Yuan, X.; Liu, G.; Chen, K. Bifunctional Optical Probe Based on  $\text{La}_3\text{Mg}_2\text{SbO}_9\text{:Mn}^{4+}$  Phosphors for Temperature and Pressure Sensing. *J. Mater. Sci. Technol.* **2024**, *194*, 98–109. <https://doi.org/10.1016/j.jmst.2023.12.074>.
- (28) Pieprz, M.; Piotrowski, W.; Woźny, P.; Runowski, M.; Marciniak, L. Highly Sensitive Lifetime-Based Luminescent Manometer on  $\text{Mn}^{4+}$  Luminescence in  $\text{Sr}_4\text{Al}_{14}\text{O}_{25}\text{Mn}^{4+}$ . *Adv. Opt. Mater.* **2024**, *12* (1), 2301316. <https://doi.org/10.1002/adom.202301316>.
- (29) Szymczak, M.; Piotrowski, W. M.; Woźny, P.; Runowski, M.; Marciniak, L. A Highly Sensitive Lifetime-Based Luminescent Manometer and Bi-Functional Pressure–Temperature Sensor Based on a Spectral Shift of the R-Line of  $\text{Mn}^{4+}$  in  $\text{K}_2\text{Ge}_4\text{O}_9$ . *J. Mater. Chem. C* **2024**, *12* (19), 6793–6804. <https://doi.org/10.1039/D3TC04812H>.
- (30) Zheng, T.; Luo, L.; Du, P.; Lis, S.; Rodriguez-Mendoza, U. R.; Lavin, V.; Runowski, M. Highly-Efficient Double Perovskite  $\text{Mn}^{4+}$ -Activated  $\text{Gd}_2\text{ZnTiO}_6$  Phosphors: A Bifunctional Optical Sensing Platform for Luminescence Thermometry and Manometry. *Chem. Eng. J.* **2022**, *446*, 136839. <https://doi.org/10.1016/j.cej.2022.136839>.

- (31) Zeng, Q.; Runowski, M.; Xue, J.; Luo, L.; Marciniak, L.; Lavín, V.; Du, P. Pressure-Induced Remarkable Spectral Red-Shift in  $\text{Mn}^{2+}$ -Activated  $\text{NaY}_9(\text{SiO}_4)_6\text{O}_2$  Red-Emitting Phosphors for High-Sensitive Optical Manometry. *Adv. Sci.* **2024**, *11* (9), 2308221. <https://doi.org/10.1002/advs.202308221>.
- (32) Du, P.; Xue, J.; González, A. M.; Luo, L.; Woźny, P.; Rodríguez-Mendoza, U. R.; Lavín, V.; Runowski, M. Highly Pressure-Responsive Dual-Mode Optical Manometer Based on  $\text{Mn}^{2+}$ -Activated  $\text{Ca}_2\text{Gd}_8(\text{SiO}_4)_6\text{O}_2$  Phosphors. *Chem. Eng. J.* **2025**, *505*, 159652. <https://doi.org/10.1016/j.cej.2025.159652>.
- (33) Zheng, Z.; Song, Y.; Zheng, B.; Zhao, Y.; Wang, Q.; Zhang, X.; Zou, B.; Zou, H.  $\text{Eu}^{2+}$  and  $\text{Mn}^{2+}$  Co-Doped  $\text{Lu}_2\text{Mg}_2\text{Al}_2\text{Si}_2\text{O}_{12}$  Phosphors for High Sensitivity and Multi-Mode Optical Pressure Sensing. *Inorg. Chem. Front.* **2023**, *10* (9), 2788–2798. <https://doi.org/10.1039/D3QI00198A>.
- (34) Nataf, L.; Rodríguez, F.; Valiente, R.; Gonzalez, J. Spectroscopic and Luminescence Properties of  $(\text{CH}_3)_4\text{NMnCl}_3$ : A Sensitive  $\text{Mn}^{2+}$ -Based Pressure Gauge. *High Press. Res.* **2009**, *29*, 653–659. <https://doi.org/10.1080/08957950903414979>.
- (35) Zheng, T.; Runowski, M.; Martín, I. R.; Soler-Carracedo, K.; Peng, L.; Skwierczyńska, M.; Sójka, M.; Barzowska, J.; Mahlik, S.; Hemmerich, H.; Rivera-López, F.; Kulpiński, P.; Lavín, V.; Alonso, D.; Peng, D. Mechanoluminescence and Photoluminescence Heterojunction for Superior Multimode Sensing Platform of Friction, Force, Pressure, and Temperature in Fibers and 3D-Printed Polymers. *Adv. Mater.* **2023**, *35* (40), 2304140. <https://doi.org/10.1002/adma.202304140>.
- (36) Díaz, M.; Lahoz, F.; Villacampa, B.; Cases, R.; Sobolev, B.; Alcalá, R. Optical Properties of  $\text{Mn}^{2+}$  Ions in Solid Solutions of Fluorite-Type Crystals. *J. Lumin.* **1999**, *81* (1), 53–60. [https://doi.org/10.1016/S0022-2313\(98\)00053-2](https://doi.org/10.1016/S0022-2313(98)00053-2).
- (37) Wiśniewski, K.; Zorenko, Y. U.; Gorbenko, V.; Zorenko, T.; Kukliński, B.; Grinberg, M. High Pressure Spectroscopy Study of SCF  $\text{Tb}_3\text{Al}_5\text{O}_{12}:\text{Mn}$ . *J. Phys. Conf. Ser.* **2010**, *249* (1), 012015. <https://doi.org/10.1088/1742-6596/249/1/012015>.
- (38) Grinberg, M.; Barzowska, J.; Shen, Y. R.; Bray, K. L.; Padlyak, B. V.; Buchynskii, P. P. High-Pressure Luminescence of  $\text{Cr}^{3+}$ -Doped  $(3\text{CaO}-\text{Ga}_2\text{O}_3-3\text{GeO}_2)$  Glasses. *Phys. Rev. B* **2002**, *65* (6), 064203. <https://doi.org/10.1103/PhysRevB.65.064203>.
- (39) Lee, C.; Bao, Z.; Fang, M.-H.; Lesniewski, T.; Mahlik, S.; Grinberg, M.; Leniec, G.; Kaczmarek, S. M.; Brik, M. G.; Tsai, Y.-T.; Tsai, T.-L.; Liu, R.-S. Chromium(III)-Doped Fluoride Phosphors with Broadband Infrared Emission for Light-Emitting Diodes. *Inorg. Chem.* **2020**, *59* (1), 376–385. <https://doi.org/10.1021/acs.inorgchem.9b02630>.
- (40) Majewska, N.; Tsai, Y.-T.; Zeng, X.-Y.; Fang, M.-H.; Mahlik, S. Advancing Near-Infrared Light Sources: Enhancing Chromium Emission through Cation Substitution in Ultra-

- Broadband Near-Infrared Phosphors. *Chem. Mater.* **2023**, *35* (23), 10228–10237. <https://doi.org/10.1021/acs.chemmater.3c02466>.
- (41) Liu, X.; Niu, G.; Jiang, J.; Che, L.; Sui, L.; Wang, X.; Zeng, X.; Wu, G.; Yuan, K.; Yang, X. High-Pressure Modulation of NIR Luminescence in Cr<sup>3+</sup>-Doped Cs<sub>2</sub>AgInCl<sub>6</sub> Double Perovskites: The Role of Ultrafast Energy Transfer. *Laser Photonics Rev.* **2025**, *19* (4), 2401000. <https://doi.org/10.1002/lpor.202401000>.
  - (42) Wang, J.; Liang, Y.; Zhang, H.; Li, H.; Zhu, X.; Wang, Z.; Cheng, X. Temperature- and Pressure-Dependent Luminescence Properties of K<sub>3</sub>AlF<sub>6</sub>: Cr<sup>3+</sup> Phosphor. *Ceram. Int.* **2024**, *50* (13, Part A), 22704–22710. <https://doi.org/10.1016/j.ceramint.2024.03.372>.
  - (43) Galanciak, D.; Perlin, P.; Grinberg, M.; Suchocki, A. High Pressure Spectroscopy of LLGG Doped with Cr<sup>3+</sup>. *J. Lumin.* **1994**, *60–61*, 223–226. [https://doi.org/10.1016/0022-2313\(94\)90135-X](https://doi.org/10.1016/0022-2313(94)90135-X).
  - (44) Pilch, M.; Ortyl, J.; Chachaj-Brekiesz, A.; Galek, M.; Popielarz, R. Europium-Based Luminescent Sensors for Mapping Pressure Distribution on Surfaces. *Sens. Actuators B Chem.* **2020**, *305*, 127409. <https://doi.org/10.1016/j.snb.2019.127409>.
  - (45) Zheng, T.; Luo, L.; Du, P.; Lis, S.; Rodríguez-Mendoza, U. R.; Lavín, V.; Martín, I. R.; Runowski, M. Pressure-Triggered Enormous Redshift and Enhanced Emission in Ca<sub>2</sub>Gd<sub>8</sub>Si<sub>6</sub>O<sub>26</sub>:Ce<sup>3+</sup> Phosphors: Ultrasensitive, Thermally-Stable and Ultrafast Response Pressure Monitoring. *Chem. Eng. J.* **2022**, *443*, 136414. <https://doi.org/10.1016/j.cej.2022.136414>.
  - (46) Zhang, K.; Gao, C.; Jiang, Z.; Wei, Y.; Pan, Y.; Wei, C.; Li, H.; Wang, K.; Zou, B.; Huang, L. Design of Layer-Structured KAlF<sub>4</sub>:Yb/Er for Pressure-Enhanced Upconversion Luminescence. *Adv. Opt. Mater.* **2020**, *8* (2), 1901031. <https://doi.org/10.1002/adom.201901031>.
  - (47) Lorenz, B.; Shen, Y. R.; and Holzapfel, W. B. Characterization of the New Luminescence Pressure Sensor SrFCl:Sm<sup>2+</sup>. *High Press. Res.* **1994**, *12* (2), 91–99. <https://doi.org/10.1080/08957959408203170>.
  - (48) Runowski, M.; Marciniak, J.; Grzyb, T.; Przybylska, D.; Shyichuk, A.; Barszcz, B.; Katrusiak, A.; Lis, S. Lifetime Nanomanometry – High-Pressure Luminescence of up-Converting Lanthanide Nanocrystals – SrF<sub>2</sub>:Yb<sup>3+</sup>,Er<sup>3+</sup>. *Nanoscale* **2017**, *9* (41), 16030–16037. <https://doi.org/10.1039/C7NR04353H>.
  - (49) Zhou, P.; Zhang, Q.; Peng, F.; Sun, B.; Dou, X.; Liu, B.; Han, D.; Xue, Y.; Ding, K. Optical Properties of Nd<sup>3+</sup> Ions Doped GdTaO<sub>4</sub> for Pressure and Temperature Sensing. *J. Rare Earths* **2022**, *40* (6), 870–877. <https://doi.org/10.1016/j.jre.2021.04.003>.
  - (50) Tian, M.; Gao, Y.; Zhou, P.; Chi, K.; Zhang, Y.; Liu, B. Improving Persistent Luminescence in Pressure-Tuned CsPbBr<sub>3</sub> Nanocrystals by Ce<sup>3+</sup> Doping. *Phys. Chem. Chem. Phys.* **2021**, *23* (36), 20567–20573. <https://doi.org/10.1039/D1CP02864B>.

- (51) McLellan, C. A.; Siefe, C.; Casar, J. R.; Peng, C. S.; Fischer, S.; Lay, A.; Parakh, A.; Ke, F.; Gu, X. W.; Mao, W.; Chu, S.; Goodman, M. B.; Dionne, J. A. Engineering Bright and Mechanosensitive Alkaline-Earth Rare-Earth Upconverting Nanoparticles. *J. Phys. Chem. Lett.* **2022**, *13* (6), 1547–1553. <https://doi.org/10.1021/acs.jpclett.1c03841>.
- (52) Antoniak, M. A.; Zelewski, S. J.; Oliva, R.; Żak, A.; Kudrawiec, R.; Nyk, M. Combined Temperature and Pressure Sensing Using Luminescent NaBiF<sub>4</sub>:Yb,Er Nanoparticles. *ACS Appl. Nano Mater.* **2020**, *3* (5), 4209–4217. <https://doi.org/10.1021/acsanm.0c00403>.
- (53) Bao, H.; Wang, W.; Li, X.; Liu, X.; Zhang, L.; Yan, X.; Wang, Y.; Wang, C.; Jia, X.; Sun, P.; Kong, X.; Zhang, H.; Lu, G. Interfacial Stress-Modulated Mechanosensitive Upconversion Luminescence of NaErF<sub>4</sub> Based Heteroepitaxial Core–Shell Nanoparticles. *Adv. Opt. Mater.* **2022**, *10* (2), 2101702. <https://doi.org/10.1002/adom.202101702>.
- (54) Zheng, T.; Sójka, M.; Woźny, P.; Martín, I. R.; Lavín, V.; Zych, E.; Lis, S.; Du, P.; Luo, L.; Runowski, M. Supersensitive Ratiometric Thermometry and Manometry Based on Dual-Emitting Centers in Eu<sup>2+</sup>/Sm<sup>2+</sup>-Doped Strontium Tetraborate Phosphors. *Adv. Opt. Mater.* **2022**, *10* (20), 2201055. <https://doi.org/10.1002/adom.202201055>.
- (55) Su, K.; Mei, L.; Guo, Q.; Shuai, P.; Wang, Y.; Liu, Y.; Jin, Y.; Peng, Z.; Zou, B.; Liao, L. Multi-Mode Optical Manometry Based on Li<sub>4</sub>SrCa(SiO<sub>4</sub>)<sub>2</sub>:Eu<sup>2+</sup> Phosphors. *Adv. Funct. Mater.* **2023**, *33* (49), 2305359. <https://doi.org/10.1002/adfm.202305359>.
- (56) Szymczak, M.; Du, P.; Runowski, M.; Woźny, P.; Xue, J.; Zheng, T.; Marciniak, L. Highly Sensitive Optical Manometer Based on the Visible Emissions of Ce<sup>3+</sup>-Doped La<sub>6</sub>Sr<sub>4</sub>(SiO<sub>4</sub>)<sub>6</sub>F<sub>2</sub> Multisite Phosphors. *Adv. Opt. Mater.* **2024**, *12* (7), 2302147. <https://doi.org/10.1002/adom.202302147>.
- (57) Umezawa, M.; Haraguchi, H.; Sugawara, G.; Sato, K.; Kurahashi, H.; Oda, T.; Okubo, K.; Soga, K. Temperature Imaging inside Fluid Devices Using a Ratiometric near Infrared (NIR-II/III) Fluorescent Y<sub>2</sub>O<sub>3</sub>: Nd<sup>3+</sup>, Yb<sup>3+</sup>, Er<sup>3+</sup> Nanothermometer. *Anal. Sci.* **2024**, *40* (7), 1323–1330. <https://doi.org/10.1007/s44211-024-00564-0>.
- (58) Piotrowski, W. M.; Kniec-Stec, K.; Suta, M.; Bogielski, B.; Pozniak, B.; Marciniak, L. Positive Luminescence Thermal Coefficient of Mn<sup>2+</sup> Ions for Highly Sensitive Luminescence Thermometry. *Chem. Eng. J.* **2023**, *464*, 142492. <https://doi.org/10.1016/j.cej.2023.142492>.
- (59) Xu, M.; Zou, X.; Su, Q.; Yuan, W.; Cao, C.; Wang, Q.; Zhu, X.; Feng, W.; Li, F. Ratiometric Nanothermometer in Vivo Based on Triplet Sensitized Upconversion. *Nat. Commun.* **2018**, *9* (1), 2698. <https://doi.org/10.1038/s41467-018-05160-1>.
- (60) Cai, P.; Qin, L.; Chen, C.; Wang, J.; Bi, S.; Kim, S.; Yanlin, H.; Seo, H. Optical Thermometry Based on Vibration Sidebands in Y<sub>2</sub>MgTiO<sub>6</sub>:Mn<sup>4+</sup> Double Perovskite. *Inorg. Chem.* **2018**, *57*, 6, 3073–3081. <https://doi.org/10.1021/acs.inorgchem.7b02938>.

- (61) Li, G.; Li, G.; Mao, Q.; Pei, L.; Yu, H.; Liu, M.; Chu, L.; Zhong, J. Efficient Luminescence Lifetime Thermometry with Enhanced  $\text{Mn}^{4+}$ -Activated  $\text{BaLaCa}_{1-x}\text{Mg}_x\text{SbO}_6$  Red Phosphors. *Chem. Eng. J.* **2022**, *430*, 132923. <https://doi.org/10.1016/j.cej.2021.132923>.
- (62) Ueda, J.; Back, M.; Brik, M. G.; Zhuang, Y.; Grinberg, M.; Tanabe, S. Ratiometric Optical Thermometry Using Deep Red Luminescence from  $^4\text{T}_2$  and  $^2\text{E}$  States of  $\text{Cr}^{3+}$  in  $\text{ZnGa}_2\text{O}_4$  Host. *Opt. Mater.* **2018**, *85*, 510–516. <https://doi.org/10.1016/j.optmat.2018.09.013>.
- (63) Back, M.; Ueda, J.; Xu, J.; Asami, K.; Brik, M. G.; Tanabe, S. Effective Ratiometric Luminescent Thermal Sensor by  $\text{Cr}^{3+}$ -Doped Mullite  $\text{Bi}_2\text{Al}_4\text{O}_9$  with Robust and Reliable Performances. *Adv. Opt. Mater.* **2020**, *8* (11), 2000124. <https://doi.org/10.1002/adom.202000124>.
- (64) Marciniak, L.; Szalkowski, M.; Bednarkiewicz, A.; Elzbieciak-Piecka, K. A  $\text{Cr}^{3+}$  Luminescence Based Ratiometric Optical Laser Power Meter. *J. Mater. Chem. C* **2022**, *10* (30), 11040–11047. <https://doi.org/10.1039/D2TC02348B>.
- (65) Wang, Q.; Liao, M.; Mu, Z.; Zhang, X.; Dong, H.; Liang, Z.; Luo, J.; Yang, Y.; Wu, F. Ratiometric Optical Thermometer with High Sensitivity Based on Site-Selective Occupancy of  $\text{Mn}^{2+}$  Ions in  $\text{Li}_5\text{Zn}_8\text{Al}_5\text{Ge}_9\text{O}_{36}$  under Controllable Synthesis Atmosphere. *J. Phys. Chem. C* **2020**, *124* (1), 886–895. <https://doi.org/10.1021/acs.jpcc.9b09379>.
- (66) Matuszewska, C.; Marciniak, L. The Influence of Host Material on NIR II and NIR III Emitting  $\text{Ni}^{2+}$ -Based Luminescent Thermometers in  $\text{ATiO}_3\text{:Ni}^{2+}$  ( $\text{A} = \text{Sr}, \text{Ca}, \text{Mg}, \text{Ba}$ ) Nanocrystals. *J. Lumin.* **2020**, *223*, 117221. <https://doi.org/10.1016/j.jlumin.2020.117221>.
- (67) Gaft, M.; Reisfeld, R.; Panczer, G. *Modern Luminescence Spectroscopy of Minerals and Materials*; Springer Mineralogy; Springer International Publishing: Cham, 2015. <https://doi.org/10.1007/978-3-319-24765-6>.
- (68) Bünzli, J.-C. G.; Piguet, C. Taking Advantage of Luminescent Lanthanide Ions. *Chem. Soc. Rev.* **2005**, *34* (12), 1048–1077. <https://doi.org/10.1039/B406082M>.
- (69) Sarkar, S.; Biswas, A.; Jana, Y.; Piwowarska, D.; Gnutek, P.; Rudowicz, C. Analysis of Crystal-Field Effects on the Energy Levels of  $\text{Mn}^{4+}$  Ions Doped in Different Photoluminescent Host Lattices, Exhibiting Lowering of Site Symmetry: Exchange Charge and Superposition Model Calculations, for Potential Applications. *J. Lumin.* **2023**, *253*, 119458. <https://doi.org/10.1016/j.jlumin.2022.119458>.
- (70) Elzbieciak, K.; Bednarkiewicz, A.; Marciniak, L. Temperature Sensitivity Modulation through Crystal Field Engineering in  $\text{Ga}^{3+}$  Co-Doped  $\text{Gd}_3\text{Al}_{5-x}\text{Ga}_x\text{O}_{12}\text{:Cr}^{3+}, \text{Nd}^{3+}$  Nanothermometers. *Sens. Actuators B Chem.* **2018**, *269*, 96–102. <https://doi.org/10.1016/j.snb.2018.04.157>.
- (71) Yu, S.; Wei, Z.; Wu, J.; Wang, T.; Zhang, J.; Luo, X.; Li, Y.; Wang, C.; Zhao, L. Design and Tuning  $\text{Cr}^{3+}$ -Doped near-Infrared Phosphors for Multifunctional Applications: Via Crystal Field Engineering. *Dalton Trans.* **2022**, *51*. <https://doi.org/10.1039/D1DT03461H>.



- (72) Li, G.; Shi, X.; Lu, X.; Mao, Q.; Pei, L.; Zhu, Y.; Liu, M.; Chu, L.; Zhong, J. Local Structure Modulation-Induced Highly Efficient Red-Emitting  $\text{Ba}_2\text{Gd}_{1-x}\text{Y}_x\text{NbO}_6\text{:Mn}^{4+}$  Phosphors for Warm WLEDs. *Inorg. Chem.* **2021**, *60*, 22, 17398–17406. <https://doi.org/10.1021/acs.inorgchem.1c02969>
- (73) Zhu, M.; Pan, Y.; Huang, Y.; Lian, H.; Lin, J. Designed Synthesis, Morphology Evolution and Enhanced Photoluminescence of a Highly Efficient Red Dodec-Fluoride Phosphor,  $\text{Li}_3\text{Na}_3\text{Ga}_2\text{F}_{12}\text{:Mn}^{4+}$ , for Warm WLEDs. *J. Mater. Chem. C* **2018**, *6* (3), 491–499. <https://doi.org/10.1039/C7TC04878E>.
- (74) Hong, F.; Yang, L.; Xu, H.; Chen, Z.; Liu, Q.; Liu, G.; Dong, X.; Yu, W. A Red-Emitting  $\text{Mn}^{4+}$  Activated Phosphor with Controlled Morphology and Two-Dimensional Luminescence Nanofiber Film: Synthesis and Application for High-Performance Warm White Light-Emitting Diodes (WLEDs). *J. Alloys Compd.* **2019**, *808*, 151551. <https://doi.org/10.1016/j.jallcom.2019.07.263>.
- (75) Gao, X.; Song, Y.; Liu, G.; Dong, X.; Wang, J.; Yu, W.  $\text{BaTiF}_6\text{:Mn}^{4+}$  Bifunctional Microstructures with Photoluminescence and Photocatalysis: Hydrothermal Synthesis and Controlled Morphology. *CrystEngComm* **2016**, *18* (31), 5842–5851. <https://doi.org/10.1039/C6CE01046F>.
- (76) Figgis, B. N.; Hitchman, M. A. *Ligand Field Theory and Its Applications*; Wiley, **2000**.
- (77) Lever, A. B. P.; Alfred B. P. *Inorganic Electronic Spectroscopy*; Elsevier: Amsterdam, **1968**.
- (78) Li, L.; Cao, Q.; Xie, J.; Wang, W.; Wang, Y.; Chen, H.; Li, Z.; Pan, Y.; Wei, X.; Li, Y. Enhancing the Luminescence Performance of an LED-Pumped  $\text{Mn}^{4+}$ -Activated Highly Efficient Double Perovskite Phosphor with A-Site Defects via Local Lattice Tuning. *Dalton Trans.* **2022**, *51* (45), 17180–17191. <https://doi.org/10.1039/D2DT02806A>.
- (79) Chen, K.; Jia, S.; Shao, Z.; Han, X.; Yuan, J.; Zhou, Y.; Deng, T. Exploring Dual-Emission Properties in  $\text{Mn}^{4+}$  Distinctively Activated  $\text{BaTaF}_7$  Red Emitting Phosphor. *J. Mater. Chem. C* **2023**, *11* (23), 7603–7610. <https://doi.org/10.1039/D3TC01294H>.
- (80) Du, M. H.  $\text{Mn}^{4+}$  Emission in Pyrochlore Oxides. *J. Lumin.* **2015**, *157*, 69–73. <https://doi.org/10.1016/j.jlumin.2014.08.038>.
- (81) Yao, L.; He, S.; Nie, W.; Fu, L.; Liao, Z.; Cai, W.; Wang, R.; Peng, J.; Ye, X. Enhanced Red Emission from  $\text{Mn}^{4+}$  Activated Phosphor Induced by Fluoride to Oxyfluoride Phase Transformation. *J. Lumin.* **2021**, *238*, 118315. <https://doi.org/10.1016/j.jlumin.2021.118315>.
- (82) Chen, X. H.; Song, E. H.; Zhou, Y. Y.; He, F. Q.; Yang, J. Q.; Zhang, Q. Y. Distorted Octahedral Site Occupation-Induced High-Efficiency Broadband near-Infrared Emission in  $\text{LiScGe}_2\text{O}_6\text{:Cr}^{3+}$  Phosphor. *J. Mater. Chem. C* **2021**, *9* (39), 13640–13646. <https://doi.org/10.1039/D1TC03057D>.

- (83) Babu, B. C.; Wang, G.-G.; Yan, B.; Yang, Q.; Baker, A. P. Effects of Cr<sup>3+</sup> Addition on the Structure and Optical Properties of  $\alpha$ -Zn<sub>2</sub>SiO<sub>4</sub> Synthesized by Sol-Gel Method. *Ceram. Int.* **2018**, *44* (1), 938–946. <https://doi.org/10.1016/j.ceramint.2017.10.026>.
- (84) Zheng, W.-C. Local Tetragonal Distortions of the Octahedral Environment for Substituting Cr<sup>3+</sup>, Mn<sup>2+</sup> and Fe<sup>3+</sup> Ions in Rb<sub>2</sub>ZnF<sub>4</sub> Crystals. *Phys. B Condens. Matter* **1997**, *233* (2), 125–129. [https://doi.org/10.1016/S0921-4526\(96\)01149-0](https://doi.org/10.1016/S0921-4526(96)01149-0).
- (85) Kumarbekov, K. K.; Zhilgildinov, Z. S.; Karipbayev, Z. T.; Zhunusbekov, A. M.; Nurmoldin, E. E.; Brik, M. G.; Suchikova, Y.; Kemere, M.; Popov, A. I.; Kassymzhanov, M. T. A Novel Method of Preparation of Y<sub>3</sub>Al<sub>5</sub>O<sub>12</sub>:Cr<sup>3+</sup> Ceramics and Its Structural and Optical Characterization. *Opt. Mater.* **2025**, *159*, 116535. <https://doi.org/10.1016/j.optmat.2024.116535>.
- (86) Pan, Z.; Lu, Y.-Y.; Liu, F. Sunlight-Activated Long-Persistent Luminescence in the near-Infrared from Cr<sup>3+</sup>-Doped Zinc Gallogermanates. *Nat. Mater.* **2012**, *11* (1), 58–63. <https://doi.org/10.1038/nmat3173>.
- (87) Liu, F.; Yan, W.; Chuang, Y.-J.; Zhen, Z.; Xie, J.; Pan, Z. Photostimulated Near-Infrared Persistent Luminescence as a New Optical Read-out from Cr<sup>3+</sup>-Doped LiGa<sub>5</sub>O<sub>8</sub>. *Sci. Rep.* **2013**, *3* (1), 1554. <https://doi.org/10.1038/srep01554>.
- (88) Miao, S.; Liang, Y.; Zhang, Y.; Chen, D.; Wang, X.-J. Broadband Short-Wave Infrared Light-Emitting Diodes Based on Cr<sup>3+</sup>-Doped LiScGeO<sub>4</sub> Phosphor. *ACS Appl. Mater. Interfaces* **2021**, *13* (30), 36011–36019. <https://doi.org/10.1021/acsami.1c10490>.
- (89) Zhao, S.; Lou, L.; Yuan, S.; Zhu, D.; Wu, F.; Mu, Z. Ultra-Broadband near-Infrared Phosphor Li<sub>3</sub>Sc<sub>2</sub>(PO<sub>4</sub>)<sub>3</sub>:Cr<sup>3+</sup> Realized by Two-Sites Occupation. *J. Lumin.* **2022**, *251*, 119188. <https://doi.org/10.1016/j.jlumin.2022.119188>.
- (90) Jiang, L.; Jiang, X.; Zhang, L.; Liu, Q.; Mi, X.; Yu, Z.; Lv, G.; Su, Y. Broadband Near-Infrared Luminescence in Garnet Y<sub>3</sub>Ga<sub>3</sub>MgSiO<sub>12</sub>:Cr<sup>3+</sup> Phosphors. *Inorg. Chem.* **2023**, *62* (10), 4220–4226. <https://doi.org/10.1021/acs.inorgchem.2c04319>.
- (91) Song, E.; Ming, H.; Zhou, Y.; He, F.; Wu, J.; Xia, Z.; Zhang, Q. Cr<sup>3+</sup>-Doped Sc-Based Fluoride Enabling Highly Efficient Near Infrared Luminescence: A Case Study of K<sub>2</sub>NaScF<sub>6</sub>:Cr<sup>3+</sup>. *Laser Photonics Rev.* **2021**, *15* (2), 2000410. <https://doi.org/10.1002/lpor.202000410>.
- (92) Zhong, J.; Zhuo, Y.; Du, F.; Zhang, H.; Zhao, W.; Brgoch, J. Efficient and Tunable Luminescence in Ga<sub>2-x</sub>In<sub>x</sub>O<sub>3</sub>:Cr<sup>3+</sup> for Near-Infrared Imaging. *ACS Appl. Mater. Interfaces* **2021**, *13* (27), 31835–31842. <https://doi.org/10.1021/acsami.1c05949>.
- (93) Zeng, H.; Zhou, T.; Wang, L.; Xie, R.-J. Two-Site Occupation for Exploring Ultra-Broadband Near-Infrared Phosphor—Double-Perovskite La<sub>2</sub>MgZrO<sub>6</sub>:Cr<sup>3+</sup>. *Chem. Mater.* **2019**, *31* (14), 5245–5253. <https://doi.org/10.1021/acs.chemmater.9b01587>.

- (94) Adachi, S. Spectroscopy of Cr<sup>3+</sup> Activator: Tanabe–Sugano Diagram and Racah Parameter Analysis. *J. Lumin.* **2021**, *232*, 117844. <https://doi.org/10.1016/j.jlumin.2020.117844>.
- (95) *Theoretical Spectroscopy of Transition Metal and Rare Earth Ions: From Free State to Crystal Field*; Brik, M. G., Chong-Geng, M., Eds.; Jenny Stanford Publishing: New York, 2019. <https://doi.org/10.1201/9780429278754>.
- (96) Casalboni, M.; Luci, A.; Grassano, U. M.; Mill, B. V.; Kaminskii, A. A. Optical Spectroscopy of La<sub>3</sub>Ga<sub>5</sub>SiO<sub>14</sub>:Cr<sup>3+</sup> Crystals. *Phys. Rev. B* **1994**, *49* (6), 3781–3790. <https://doi.org/10.1103/PhysRevB.49.3781>.
- (97) Katayama, Y.; Kobayashi, H.; Tanabe, S. Deep-Red Persistent Luminescence in Cr<sup>3+</sup>-Doped LaAlO<sub>3</sub> Perovskite Phosphor for in Vivo Imaging. *Appl. Phys. Express* **2014**, *8* (1), 012102. <https://doi.org/10.7567/APEX.8.012102>.
- (98) Liao, Z.; Sójka, M.; Zhong, J.; Brgoch, J. Developing the Na<sub>2</sub>CaZr<sub>2</sub>Ge<sub>3</sub>O<sub>12</sub>:Cr<sup>3+</sup> Garnet Phosphor for Advanced NIR Pc-LEDs in Night Vision and Bioimaging. *Chem. Mater.* **2024**, *36* (9), 4654–4663. <https://doi.org/10.1021/acs.chemmater.4c00426>.
- (99) Ou, J.; Fang, S.; Zhu, Q.; Zhai, Y.; Zhang, H.; Wang, L. Extending the Optical Temperature Sensing Range of Cr<sup>3+</sup> by Synchronously Tuning <sup>2</sup>E and <sup>4</sup>T<sub>2</sub> Emission. *Phys. Chem. Chem. Phys.* **2023**, *25* (25), 16866–16871. <https://doi.org/10.1039/D3CP02111D>.
- (100) Zhang, Q.; Wei, X.; Zhou, J.; Milićević, B.; Lin, L.; Huo, J.; Li, J.; Ni, H.; Xia, Z. Thermal Stability Improvement of Cr<sup>3+</sup>-Activated Broadband Near-Infrared Phosphors via State Population Optimization. *Adv. Opt. Mater.* **2023**, *11* (14), 2300310. <https://doi.org/10.1002/adom.202300310>.
- (101) Zhang, H.; Zhong, J.; Li, C.; Wang, L.; Zhao, W. Broadband Near-Infrared Luminescence in the NaAlP<sub>2</sub>O<sub>7</sub>:Cr<sup>3+</sup> Phosphor for Spectroscopy Applications. *J. Lumin.* **2022**, *251*, 119211. <https://doi.org/10.1016/j.jlumin.2022.119211>.
- (102) Bai, B.; Dang, P.; Huang, D.; Lian, H.; Lin, J. Broadband Near-Infrared Emitting Ca<sub>2</sub>LuScGa<sub>2</sub>Ge<sub>2</sub>O<sub>12</sub>:Cr<sup>3+</sup> Phosphors: Luminescence Properties and Application in Light-Emitting Diodes. *Inorg. Chem.* **2020**, *59*, 18, 13481–13488. <https://doi.org/10.1021/acs.inorgchem.0c01890>
- (103) Zhong, J.; Zhuo, Y.; Du, F.; Zhang, H.; Zhao, W.; Brgoch, J. Efficient and Tunable Luminescence in Ga<sub>2–x</sub>In<sub>x</sub>O<sub>3</sub>:Cr<sup>3+</sup> for Near-Infrared Imaging. *ACS Appl. Mater. Interfaces* **2021**, *13* (27), 31835–31842. <https://doi.org/10.1021/acsami.1c05949>.
- (104) Marciniak, L.; Kniec, K.; Elżbieciak-Piecka, K.; Trejgis, K.; Stefanska, J.; Dramićanin, M. Luminescence Thermometry with Transition Metal Ions. A Review. *Coord. Chem. Rev.* **2022**, *469*, 214671. <https://doi.org/10.1016/j.ccr.2022.214671>.
- (105) Taikar, D. R.; Sonkusare, K.; Dhoble, S. J.; Yadav, R. S. Recent Progress in Cr<sup>3+</sup> Doped Phosphors for Indoor Plant Cultivation LEDs: A Review. *J. Mol. Struct.* **2025**, *1331*, 141564. <https://doi.org/10.1016/j.molstruc.2025.141564>.

- (106) Wamsley, P. R.; Bray, K. L. The Effect of Pressure on the Luminescence of  $\text{Cr}^{3+}$ : YAG. *J. Lumin.* **1994**, *59* (1–2), 11–17. [https://doi.org/10.1016/0022-2313\(94\)90016-7](https://doi.org/10.1016/0022-2313(94)90016-7).
- (107) Grinberg, M.; Barzowska, J.; Shen, Y. R.; Bray, K. L.; Hanuza, J.; Dereń, P. J. The Effect of Pressure on Luminescence Properties of  $\text{Cr}^{3+}$  Ions in  $\text{LiSc}(\text{WO}_4)_2$  Crystals—Part II: Pressure- and Temperature-Dependent Luminescence Kinetics. *J. Lumin.* **2006**, *116* (1), 15–27. <https://doi.org/10.1016/j.jlumin.2005.02.011>.
- (108) Elzbieciak-Piecka, K.; Drabik, J.; Jaque, D.; Marciniak, L.  $\text{Cr}^{3+}$  Based Nanocrystalline Luminescent Thermometers Operating in a Temporal Domain. *Phys. Chem. Chem. Phys.* **2020**, *22* (44), 25949–25962. <https://doi.org/10.1039/D0CP03453C>.
- (109) Yamaga\*, M.; Henderson, B.; O'Donnell, K. P.; Yue, G. Temperature Dependence of the Lifetime of  $\text{Cr}^{3+}$  Luminescence in Garnet Crystals. *Appl. Phys. B* **1990**, *51* (2), 132–136. <https://doi.org/10.1007/BF00326013>.
- (110) Ślawska-Waniewska, A. Crystal Field of  $\text{Cr}^{3+}$  Ion in Spinel Lattice: The Effect of High Hydrostatic Pressure. *Phys. Status Solidi B* **1981**, *104* (2), 679–684. <https://doi.org/10.1002/pssb.2221040235>.
- (111) Kudoh, Y.; Takéuchi, Y. The crystal structure of forsterite  $\text{Mg}_2\text{SiO}_4$  under high pressure up to 149 kb. *Z. Für Krist. - Cryst. Mater.* **1985**, *171* (1–4), 291–302. <https://doi.org/10.1524/zkri.1985.171.14.291>.
- (112) Johannsen, P. G.; Holzapfel, W. B. EFFECT OF PRESSURE ON INTERMOLECULAR BONDS IN SOLID HALOGENS. *J. Phys. Colloq.* **1984**, *45* (C8), C8–194. <https://doi.org/10.1051/jphyscol:1984834>.
- (113) Majewska, N.; Muñoz, A.; Liu, R.-S.; Mahlik, S. Influence of Chemical and Mechanical Pressure on the Luminescence Properties of Near-Infrared Phosphors. *Chem. Mater.* **2023**, *35* (12), 4680–4690. <https://doi.org/10.1021/acs.chemmater.3c00203>.
- (114) Stedman, G. E. Crystal Field of Ruby and Stressed  $\text{MgO}:\text{Cr}^{3+}$ . *J. Chem. Phys.* **1969**, *50* (3), 1461–1466. <https://doi.org/10.1063/1.1671211>.
- (115) Back, M.; Ueda, J.; Hua, H.; Tanabe, S. Predicting the Optical Pressure Sensitivity of  ${}^2\text{E} \rightarrow {}^4\text{A}_2$  Spin-Flip Transition in  $\text{Cr}^{3+}$ -Doped Crystals. *Chem. Mater.* **2021**, *33* (9), 3379–3385. <https://doi.org/10.1021/acs.chemmater.1c00678>.
- (116) Adachi, S. Full Understanding of  $\text{K}_3\text{GaF}_6:\text{Cr}^{3+}$  Properties under Hydrostatic Pressure Based on the Tanabe–Sugano Energy-Level Diagram. *J. Lumin.* **2022**, *248*, 118999. <https://doi.org/10.1016/j.jlumin.2022.118999>.
- (117) Martín-Rodríguez, R.; Valiente, R.; Rodríguez, F.; Bettinelli, M. Temperature and Pressure Dependence of the Optical Properties of  $\text{Cr}^{3+}$ -Doped  $\text{Gd}_3\text{Ga}_5\text{O}_{12}$  Nanoparticles. *Nanotechnology* **2011**, *22* (26), 265707. <https://doi.org/10.1088/0957-4484/22/26/265707>.

- (118) Sanz-Ortiz, M. N.; Rodríguez, F.; Hernández, I.; Valiente, R.; Kück, S. Origin of the  $^2E \rightarrow ^4T_2$  Fano Resonance in  $\text{Cr}^{3+}$ -Doped  $\text{LiCaAlF}_6$ : Pressure-Induced Excited-State Crossover. *Phys. Rev. B* **2010**, *81* (4), 045114. <https://doi.org/10.1103/PhysRevB.81.045114>.
- (119) Dolan, J. F.; Rinzler, A. G.; Kappers, L. A.; Bartram, R. H. Pressure and Temperature Dependence of Chromium Photoluminescence Spectra in Fluoride Elpasolites. *J. Phys. Chem. Solids* **1992**, *53* (7), 905–912. [https://doi.org/10.1016/0022-3697\(92\)90117-V](https://doi.org/10.1016/0022-3697(92)90117-V).
- (120) Grinberg, M.; Barzowska, J.; Shen, Y.; Bray, K. L. Inhomogeneous Broadening of  $\text{Cr}^{3+}$  Luminescence in Doped  $\text{LiTaO}_3$ . *Phys. Rev. B* **2001**, *63* (21), 214104. <https://doi.org/10.1103/PhysRevB.63.214104>.
- (121) Hernández, I.; Rodríguez, F.; Tressaud, A. Optical Properties of the  $(\text{CrF}_6)_3^-$  Complex in  $\text{A}_2\text{BMF}_6:\text{Cr}^{3+}$  Elpasolite Crystals: Variation with M–F Bond Distance and Hydrostatic Pressure. *Inorg. Chem.* **2008**, *47* (22), 10288–10298. <https://doi.org/10.1021/ic800606h>.
- (122) Wu, W.-L.; Fang, M.-H.; Zhou, W.; Lesniewski, T.; Mahlik, S.; Grinberg, M.; Brik, M.; Sheu, H.-S.; Cheng, B.-M.; Wang, J.; Liu, R.-S. High Color Rendering Index of  $\text{Rb}_2\text{GeF}_6:\text{Mn}^{4+}$  for Light-Emitting Diodes. *Chem. Mater.* **2017**, *29*. <https://doi.org/10.1021/acs.chemmater.6b05244>.
- (123) Wen-Chen, Z. Determination of the Local Compressibilities for  $\text{Cr}^{3+}$  Ions in Some Garnet Crystals from High-Pressure Spectroscopy. *J. Phys. Condens. Matter* **1995**, *7* (43), 8351. <https://doi.org/10.1088/0953-8984/7/43/013>.
- (124) Wen-Chen, Z. Explanation of the Pressure-Induced Red Shifts of  $^2E \rightarrow ^4A_2$  Transition Line for  $\text{Cr}^{3+}$  Ions in the Two Sites of Chrysoberyl. *Solid State Commun.* **1996**, *98* (2), 167–169. [https://doi.org/10.1016/0038-1098\(95\)00783-0](https://doi.org/10.1016/0038-1098(95)00783-0).
- (125) Zheng, W.-C. Estimation of the Local Compressibilities for  $\text{Gd}_3\text{Ga}_5\text{O}_{12}:\text{Cr}^{3+}$  and  $\text{Gd}_3\text{Sc}_2\text{Ga}_3\text{O}_{12}:\text{Cr}^{3+}$  Crystals from Their High Pressure Spectroscopies. *Phys. Status Solidi B* **1996**, *196* (2), 297–302. <https://doi.org/10.1002/pssb.2221960203>.
- (126) Sadao, A. Racah Parameter Ratio C/B for the  $3d^3$ -Configuration Ions Like  $\text{Mn}^{4+}$  and  $\text{Cr}^{3+}$  in the Tanabe-Sugano Diagram. *ECS J. Solid State Sci. Technol.* **2020**, *9*, 066003. <https://doi.org/10.1149/2162-8777/aba679>
- (127) Sánchez-Alejo, M. A.; Rodríguez, F.; Barreda-Argüeso, J. A.; Camarillo, I.; Flores J., C.; Murrieta S., H.; Hernández A., J. M.; Jaque, F.; Camarillo, E. Photoluminescence Study of  $\text{LiNbO}_3:\text{Cr}^{3+}; \text{W}^{4+}$  at High Pressure. Pressure Dependence of Spectroscopic Parameters and Local Structure of  $\text{Cr}^{3+}$ . *Opt. Mater.* **2016**, *60*, 94–100. <https://doi.org/10.1016/j.optmat.2016.07.013>.
- (128) Zheng-Jie, Z.; Dong-Ping, M. Pressure-Induced Shifts of  $R_1$  and  $R_2$  Lines of  $\text{YAG}:\text{Cr}^{3+}$ . *Commun. Theor. Phys.* **2006**, *45* (4), 754. <https://doi.org/10.1088/0253-6102/45/4/036>.
- (129) Jara, E.; Valiente, R.; González, J.; Espeso, J. I.; Khaidukov, N.; Rodríguez, F. Optical Spectroscopy of the  $\text{Sr}_4\text{Al}_{14}\text{O}_{25}:\text{Mn}^{4+}, \text{Cr}^{3+}$  Phosphor: Pressure and Temperature

- Dependences. *J. Mater. Chem. C* **2022**, *10* (16), 6380–6391. <https://doi.org/10.1039/D2TC00485B>.
- (130) Szymczak, M.; M. Runowski; Brik, M. G.; Marciniak, L. Multimodal, Super-Sensitive Luminescent Manometer Based on Giant Pressure-Induced Spectral Shift of  $\text{Cr}^{3+}$  in the NIR Range. *Chem. Eng. J.* **2023**, *466*, 143130. <https://doi.org/10.1016/j.cej.2023.143130>.
- (131) Grinberg, M.; Barzowska, J.; Shen, Y.; Bray, K.; Hanuza, J.; Derén, P. The Effect of Pressure on Luminescence Properties of  $\text{Cr}^{3+}$  Ions in  $\text{LiSc}(\text{WO}_4)_2$  Crystals-Part II: Pressure- and Temperature-Dependent Luminescence Kinetics. *J. Lumin.* **2006**, *116*, 15–27. <https://doi.org/10.1016/J.JLUMIN.2005.02.011>.
- (132) Szymczak, M.; Su, K.; Mei, L.; Runowski, M.; Woźny, P.; Guo, Q.; Liao, L.; Marciniak, L. Investigating the Potential of  $\text{Cr}^{3+}$ -Doped Pyroxene for Highly Sensitive Optical Pressure Sensing. *ACS Appl. Mater. Interfaces* **2024**. <https://doi.org/10.1021/acsami.4c12145>.
- (133) Szymczak, M.; Jaśkielewicz, J.; Runowski, M.; Xue, J.; Mahlik, S.; Marciniak, L. Highly-Sensitive, Tri-Modal Luminescent Manometer Utilizing Band-Shift, Ratiometric and Lifetime-Based Sensing Parameters. *Adv. Funct. Mater.* **2024**, *34* (22), 2314068. <https://doi.org/10.1002/adfm.202314068>.
- (134) Shen, Y. R.; Bray, K. L. Effect of Pressure and Temperature on the Lifetime of  $\text{Cr}^{3+}$  in Yttrium Aluminum Garnet. *Phys. Rev. B* **1997**, *56* (17), 10882–10891. <https://doi.org/10.1103/PhysRevB.56.10882>.
- (135) Galanciak, D.; Grinberg, M.; Gryk, W.; Kobayakov, S.; Suchocki, A.; Boulon, G.; Brenier, A. Influence of High Pressure on the Luminescence Transitions of  $\text{Mn}^{4+}$ -Doped Gadolinium Gallium Garnet. *J. Phys. Condens. Matter* **2005**, *17* (46), 7185. <https://doi.org/10.1088/0953-8984/17/46/003>.
- (136) Grinberg, M.; Suchocki, A. Pressure-Induced Changes in the Energetic Structure of the  $3d^3$  Ions in Solid Matrices. *J. Lumin.* **2007**, *125* (1), 97–103. <https://doi.org/10.1016/j.jlumin.2006.08.018>.
- (137) Zhang, L.; Lang, Z.; Lu, Y.; Zhao, X.; Jiang, B.; Yan, X.; Sun, P.; Liu, F.; Zhou, G.; Zhou, M.; Wang, Y.; Liu, X.; Lu, G. Excitation Wavelength-Dependent Upconversion Luminescence Enhancement in  $\text{Tm}^{3+}$ -Doped  $\text{LiErF}_4@ \text{LiYF}_4$  System Under High Pressure. *Adv. Opt. Mater.* **2023**, *11* (10), 2202884. <https://doi.org/10.1002/adom.202202884>.
- (138) Cascales, C.; de Andrés, A.; Sánchez-Benitez, J. Effects of High Pressure on the Luminescence Spectra of  $\text{Eu}(\text{SO}_4)_2 \cdot \text{NH}_4$  Microcrystals: Anisotropically Induced Structural Distortions. *J. Phys. Chem. A* **2008**, *112* (7), 1464–1472. <https://doi.org/10.1021/jp710044p>.
- (139) Wang, F.; Ravel, B.; Yacoby, Y.; Stern, E.; Ingalls, R. The Effect of Hydrostatic Pressure on the Local Structure of  $\text{K}_{1-x}\text{Na}_x\text{TaO}_3$  and  $\text{KTa}_{1-x}\text{Nb}_x\text{O}_3$ . *J. Phys. Iv* **1997**, *7*. <https://doi.org/10.1051/JP4:19972205>.

- (140) Aguado, F.; Rodríguez, F.; Valiente, R.; Itié, J.; Munsch, P. Pressure-Induced Closure of the Jahn-Teller Distortion in  $\text{Rb}_2\text{CuC}_{14}(\text{H}_2\text{O})_2$ . *High Press. Res.* **2003**, *23*, 181–186. <https://doi.org/10.1080/0895795031000147731>.
- (141) Angel, R. J.; Zhao, J.; Ross, N. L.; Jakeways, C. V.; Redfern, S. A. T.; Berkowski, M. High-Pressure Structural Evolution of a Perovskite Solid Solution  $(\text{La}_{1-x}\text{Nd}_x)\text{GaO}_3$ . *J. Solid State Chem.* **2007**, *180* (12), 3408–3424. <https://doi.org/10.1016/j.jssc.2007.09.019>.
- (142) Knight, K. S. Parameterization of the Crystal Structure of Garnet in Terms of Symmetry-Adapted Basis-Vectors of the Ideal Tetrahedron and Octahedron: Application to the Pressure-Dependence of the Crystal Structure of  $\text{Y}_3\text{Al}_5\text{O}_{12}$  between 0 and 126 GPa. *Mater. Chem. Phys.* **2019**, *227*, 72–82. <https://doi.org/10.1016/j.matchemphys.2019.01.067>.
- (143) Adachi, S. Review—Photoluminescence Properties of  $\text{Cr}^{3+}$ -Activated Oxide Phosphors. *ECS J. Solid State Sci. Technol.* **2021**, *10* (2), 026001. <https://doi.org/10.1149/2162-8777/abdc01>.
- (144) Jin, Y.; Hu, Y.; Yuan, L.; Chen, L.; Wu, H.; Ju, G.; Duan, H.; Mu, Z. Multifunctional Near-Infrared Emitting  $\text{Cr}^{3+}$ -Doped  $\text{Mg}_4\text{Ga}_8\text{Ge}_2\text{O}_{20}$  Particles with Long Persistent and Photostimulated Persistent Luminescence, and Photochromic Properties. *J. Mater. Chem. C* **2016**, *4*, 6614–6625. <https://doi.org/10.1039/C6TC01640E>.
- (145) Zhou, J.-F.; Chen, P.; Li, J.; Yang, M.; Jiang, W.; Zhang, Q.; Ni, H.; Huo, J. Crystal-Field Induced Tuning of Luminescence Properties of  $\text{Na}_3\text{Ga}_x\text{Al}_{11-x}\text{F}_6:\text{Cr}^{3+}$  Phosphors with Good Thermal Stability for NIR LEDs. *Dalton Trans.* **2022**. <https://doi.org/10.1039/d2dt01559e>.
- (146) Jiang, L.; Zhang, L.; Jiang, X.; Wang, J.; Zhang, J.; Jiang, W.; Li, G.; Yu, H.; Si, W.; Shi, Z.; Zhang, Z.; Su, Y.  $\text{MTiTaO}_6:\text{Cr}^{3+}$  ( $\text{M} = \text{Al}^{3+}, \text{Ga}^{3+}, \text{Sc}^{3+}$ ) Phosphors with Ultra-Broadband Excitation Spectra and Enhanced Near-Infrared Emission for Solar Cells. *Laser Photonics Rev.* **2025**, *19* (9), 2401854. <https://doi.org/10.1002/lpor.202401854>.
- (147) Mi, H.; Huang, Y.; Lin, Z.; Zhang, L.; Wang, G.  $\text{Cr}^{3+}$ -Doped  $\text{CaMgSi}_2\text{O}_6$  Crystal: A Promising Tunable Laser and Ultrashort Laser Crystal. *CrystEngComm* **2013**, *16* (5), 763–765. <https://doi.org/10.1039/C3CE41799A>.
- (148) Tan, T.; Wang, S.; Su, J.; Yuan, W.; Wu, H.; Pang, R.; Wang, J.; Li, C.; Zhang, H. Design of a Novel Near-Infrared Luminescence Material  $\text{Li}_2\text{Mg}_3\text{TiO}_6:\text{Cr}^{3+}$  with an Ultrawide Tuning Range Applied to Near-Infrared Light-Emitting Diodes. *ACS Sustain. Chem. Eng.* **2022**, *10* (12), 3839–3850. <https://doi.org/10.1021/acssuschemeng.1c07054>.
- (149) Shiu, W.-T.; Li, X.; Chang, L.-Y.; Chen, J.-L.; Lin, Y.-Y.; Lin, B.-H.; Sterbinsky, G. E.; Wu, T.; McLeod, J. A.; Liu, L. The Influence of Hydrothermal Synthesis Temperature on the Electronic Structure and Luminescence Property of Cr-Doped  $\text{ZnGa}_2\text{O}_4$  Nanoparticles. *J. Lumin.* **2023**, *263*, 120113. <https://doi.org/10.1016/j.jlumin.2023.120113>.



- (150) Liu, D. Effects of Cr Content and Morphology on the Luminescence Properties of the Cr-Doped Alpha-Al<sub>2</sub>O<sub>3</sub> Powders. *Ceram. Int.* **2013**, *39* (5), 4765–4769. <https://doi.org/10.1016/j.ceramint.2012.11.063>.
- (151) Mondal, A.; Das, S.; Manam, J. Hydrothermal Synthesis, Structural and Luminescent Properties of a Cr<sup>3+</sup> Doped MgGa<sub>2</sub>O<sub>4</sub> near-Infrared Long Lasting Nanophosphor. *RSC Adv.* **2016**, *6* (86), 82484–82495. <https://doi.org/10.1039/C6RA15119A>.
- (152) Szymczak, M.; Piotrowski, W. M.; Rodríguez-Mendoza, U. R.; Wozny, P.; Runowski, M.; Marciniak, L. Highly Sensitive Ratiometric Luminescence Manometers Based on the Multisite Emission of Cr<sup>3+</sup>. *J. Mater. Chem. C* **2025**, *13* (8), 4224–4235. <https://doi.org/10.1039/D4TC04639K>.
- (153) Maciejewska, K.; Paściak, A.; Szymczak, M.; Ledwa, K.; Bednarkiewicz, A.; Marciniak, L. Bimodal Role of Cr<sup>3+</sup> Ions: The Nanoscaled Photothermal Agent and Luminescence Thermometry. *Mater. Today Chem.* **2023**, *30*, 101579. <https://doi.org/10.1016/j.mtchem.2023.101579>.
- (154) Szymczak, M.; Woźny, P.; Runowski, M.; Pieprz, M.; Lavín, V.; Marciniak, L. Temperature Invariant Ratiometric Luminescence Manometer Based on Cr<sup>3+</sup> Ions Emission. *Chem. Eng. J.* **2023**, *453*, 139632. <https://doi.org/10.1016/j.cej.2022.139632>.
- (155) Back, M.; Ueda, J.; Nambu, H.; Fujita, M.; Yamamoto, A.; Yoshida, H.; Tanaka, H.; Brik, M. G.; Tanabe, S. Boltzmann Thermometry in Cr<sup>3+</sup>-Doped Ga<sub>2</sub>O<sub>3</sub> Polymorphs: The Structure Matters! *Adv. Opt. Mater.* **2021**, *9* (9), 2100033. <https://doi.org/10.1002/adom.202100033>.
- (156) Ristić, Z.; Đorđević, V.; Medić, M.; Kuzman, S.; Sekulić, M.; Antić, Ž.; Dramićanin, M. D. Triple-Temperature Readout in Luminescence Thermometry with Cr<sup>3+</sup>-Doped Mg<sub>2</sub>SiO<sub>4</sub> Operating from Cryogenic to Physiologically Relevant Temperatures. *Meas. Sci. Technol.* **2021**, *32* (5), 054004. <https://doi.org/10.1088/1361-6501/abdc9a>.
- (157) Shi, M.; Yao, L.; Yu, S.; Dong, Y.; Shao, Q. Enhancing the Temperature Sensitivity of Cr<sup>3+</sup> Emissions by Modification of the Host's Composition for Fluorescence Thermometry Applications. *Dalton Trans.* **2022**, *51* (2), 587–593. <https://doi.org/10.1039/D1DT03480D>.
- (158) Back, M.; Ueda, J.; Brik, M. G.; Lesniewski, T.; Grinberg, M.; Tanabe, S. Revisiting Cr<sup>3+</sup>-Doped Bi<sub>2</sub>Ga<sub>4</sub>O<sub>9</sub> Spectroscopy: Crystal Field Effect and Optical Thermometric Behavior of Near-Infrared-Emitting Singly-Activated Phosphors. *ACS Appl. Mater. Interfaces* **2018**, *10* (48), 41512–41524. <https://doi.org/10.1021/acsami.8b15607>.
- (159) Jiang, R.; Yang, J.; Meng, Y.; Yan, D.; Liu, C.; Xu, C.; Liu, Y. The Effects of the Amount of Ge<sup>4+</sup> Doped in Zn<sub>2</sub>Ga<sub>3.98-4x/3</sub>Ge<sub>x</sub>O<sub>8</sub>:Cr<sub>0.02</sub> Nanoparticles on Size Distribution, NIR Afterglow Imaging and Temperature Sensing. *J. Alloys Compd.* **2020**, *822*, 153626. <https://doi.org/10.1016/j.jallcom.2019.153626>.

- (160) Back, M.; Ueda, J.; Brik, M. G.; Tanabe, S. Pushing the Limit of Boltzmann Distribution in  $\text{Cr}^{3+}$ -Doped  $\text{CaHfO}_3$  for Cryogenic Thermometry. *ACS Appl. Mater. Interfaces* **2020**, *12* (34), 38325–38332. <https://doi.org/10.1021/acsami.0c08965>.
- (161) Marciniak, L.; Bednarkiewicz, A. Nanocrystalline NIR-to-NIR Luminescent Thermometer Based on  $\text{Cr}^{3+}$ ,  $\text{Yb}^{3+}$  Emission. *Sens. Actuators B Chem.* **2017**, *243*, 388–393. <https://doi.org/10.1016/j.snb.2016.12.006>.
- (162) Marciniak, L.; Bednarkiewicz, A.; Drabik, J.; Trejgis, K.; Strek, W. Optimization of Highly Sensitive  $\text{YAG:Cr}^{3+}$ ,  $\text{Nd}^{3+}$  Nanocrystal-Based Luminescent Thermometer Operating in an Optical Window of Biological Tissues. *Phys. Chem. Chem. Phys.* **2017**, *19* (10), 7343–7351. <https://doi.org/10.1039/C6CP07213E>.
- (163) Chen, D.; Liu, S.; Xu, W.; Li, X.  $\text{Yb}^{3+}/\text{Ln}^{3+}/\text{Cr}^{3+}$  ( $\text{Ln} = \text{Er}, \text{Ho}$ ) Doped Transparent Glass Ceramics: Crystallization,  $\text{Ln}^{3+}$  Sensitized  $\text{Cr}^{3+}$  Upconversion Emission and Multi-Modal Temperature Sensing. *J. Mater. Chem. C* **2017**, *5* (45), 11769–11780. <https://doi.org/10.1039/C7TC04410K>.
- (164) Elzbieciak, K.; Bednarkiewicz, A.; Marciniak, L. Temperature Sensitivity Modulation through Crystal Field Engineering in  $\text{Ga}^{3+}$  Co-Doped  $\text{Gd}_3\text{Al}_{5-x}\text{Ga}_x\text{O}_{12}:\text{Cr}^{3+}$ ,  $\text{Nd}^{3+}$  Nanothermometers. *Sens. Actuators B Chem.* **2018**, *269*, 96–102. <https://doi.org/10.1016/j.snb.2018.04.157>.
- (165) Periša, J.; Ristić, Z.; Đorđević, V.; Sekulić, M.; Dramićanin, T.; Antić, Ž.; Dramićanin, M. D. Multiparametric Luminescence Thermometry from  $\text{Dy}^{3+}$ ,  $\text{Cr}^{3+}$  Double Activated YAG. *J. Lumin.* **2021**, *238*, 118306. <https://doi.org/10.1016/j.jlumin.2021.118306>.
- (166) Mondal, A.; Manam, J. Structural, Optical and Temperature Dependent Photoluminescence Properties of  $\text{Cr}^{3+}$ -Activated  $\text{LaGaO}_3$  Persistent Phosphor for Optical Thermometry. *Ceram. Int.* **2020**, *46* (15), 23972–23984. <https://doi.org/10.1016/j.ceramint.2020.06.174>.
- (167) Shen, Y.; Tong, L.; Wang, Y.; Ye, L. Sapphire-Fiber Thermometer Ranging from 20 to 1800 °C. *Appl. Opt.* **1999**, *38* (7), 1139–1143. <https://doi.org/10.1364/AO.38.001139>.
- (168) Eldridge, J. I.; Chambers, M. D. Fiber Optic Thermometer Using Cr-Doped  $\text{GdAlO}_3$  Broadband Emission Decay. *Meas. Sci. Technol.* **2015**, *26* (9), 095202. <https://doi.org/10.1088/0957-0233/26/9/095202>.
- (169) Szymczak, M.; Runowski, M.; Lavín, V.; Marciniak, L. Highly Pressure-Sensitive, Temperature Independent Luminescence Ratiometric Manometer Based on  $\text{MgO:Cr}^{3+}$  Nanoparticles. *Laser Photonics Rev.* **2023**, *17* (4), 2200801. <https://doi.org/10.1002/lpor.202200801>.
- (170) Szymczak, M.; Antuzevics, A.; Rodionovs, P.; Runowski, M.; Rodríguez-Mendoza, U. R.; Szymanski, D.; Kinzhybalo, V.; Marciniak, L. Bifunctional Luminescent Thermometer-Manometer Based on  $\text{Cr}^{3+}$ - $\text{Cr}^{3+}$  Pair Emission. *ACS Appl. Mater. Interfaces* **2024**, *16* (47), 64976–64987. <https://doi.org/10.1021/acsami.4c11806>.

- (171) P Beales, T.; H L Goodman, C.; Scarrott, K. A New High Pressure Calibrant:  $\beta$ -Ga<sub>2</sub>O<sub>3</sub>:Cr. *Solid State Commun.* **1990**, 73 (1), 1–3. [https://doi.org/10.1016/0038-1098\(90\)90002-S](https://doi.org/10.1016/0038-1098(90)90002-S).
- (172) Barnett, J. D.; Block, S.; Piermarini, G. J. An Optical Fluorescence System for Quantitative Pressure Measurement in the Diamond-Anvil Cell. *Rev. Sci. Instrum.* **1973**, 44 (1), 1–9. <https://doi.org/10.1063/1.1685943>.
- (173) Rodríguez-Mendoza, U. R.; León-Luis, S. F.; Muñoz-Santiuste, J. E.; Jaque, D.; Lavín, V. Nd<sup>3+</sup>-Doped Ca<sub>3</sub>Ga<sub>2</sub>Ge<sub>3</sub>O<sub>12</sub> Garnet: A New Optical Pressure Sensor. *J. Appl. Phys.* **2013**, 113 (21), 213517. <https://doi.org/10.1063/1.4809217>.
- (174) Kobayakov, S.; Kamińska, A.; Suchocki, A.; Galanciak, D.; Malinowski, M. Nd<sup>3+</sup>-Doped Yttrium Aluminum Garnet Crystal as a near-Infrared Pressure Sensor for Diamond Anvil Cells. *Appl. Phys. Lett.* **2006**, 88 (23), 234102. <https://doi.org/10.1063/1.2210084>.
- (175) Marciniak, L.; Woźny, P.; Szymczak, M.; Runowski, M. Optical Pressure Sensors for Luminescence Manometry: Classification, Development Status, and Challenges. *Coord. Chem. Rev.* **2024**, 507, 215770. <https://doi.org/10.1016/j.ccr.2024.215770>.
- (176) Nataf, L.; Rodríguez ,F.; Valiente ,R.; and González, J. Spectroscopic and Luminescence Properties of (CH<sub>3</sub>)<sub>4</sub>NMnCl<sub>3</sub>: A Sensitive Mn<sup>2+</sup>-Based Pressure Gauge. *High Press. Res.* **2009**, 29 (4), 653–659. <https://doi.org/10.1080/08957950903414979>.
- (177) Shapira, O.; Levy, R.; Okun, Z.; Shpigelman, A. The Effect of Pressure on Degradation Kinetics of Polyphenols: Impact of Polyphenol Structure at Hyperbaric Storage Conditions. *Innov. Food Sci. Emerg. Technol.* **2024**, 93, 103631. <https://doi.org/10.1016/j.ifset.2024.103631>.
- (178) Katrusiak, A. Lab in a DAC – High-Pressure Crystal Chemistry in a Diamond-Anvil Cell. *Acta Crystallogr. Sect. B Struct. Sci. Cryst. Eng. Mater.* **2019**, 75 (6), 918–926. <https://doi.org/10.1107/S2052520619013246>.
- (179) Bassett, W. A. Diamond Anvil Cell, 50th Birthday. *High Press. Res.* **2009**, 29 (2), 163–186. <https://doi.org/10.1080/08957950802597239>.
- (180) Mahlik, S. High-Pressure Study of Phosphors Emission. In *Phosphor Handbook*; CRC Press, 2022.
- (181) Boehler, R. Diamond Cells and New Materials. *Mater. Today* **2005**, 8 (11), 34–42. [https://doi.org/10.1016/S1369-7021\(05\)71158-5](https://doi.org/10.1016/S1369-7021(05)71158-5).
- (182) Vohra, Y. K.; Vagarali, S. S. Isotopically Pure Diamond Anvil for Ultrahigh Pressure Research. *Appl. Phys. Lett.* **1992**, 61 (24), 2860–2862. <https://doi.org/10.1063/1.108057>.
- (183) Ruoff, A. L.; and Vohra, Y. K. Synthetic Diamonds for Multimegabar Pressures in the Diamond Anvil Cell. *High Press. Res.* **1990**, 5 (1–6), 791–793. <https://doi.org/10.1080/08957959008246260>.
- (184) Dunstan, D. J. Theory of the Gasket in Diamond Anvil High-pressure Cells. *Rev. Sci. Instrum.* **1989**, 60 (12), 3789–3795. <https://doi.org/10.1063/1.1140442>.

- (185) Barzowska, J.; Leśniewski, T.; Mahlik, S.; Seo, H. J.; Grinberg, M.  $\text{KMgF}_3\text{:Eu}^{2+}$  as a New Fluorescence-Based Pressure Sensor for Diamond Anvil Cell Experiments. *Opt. Mater.* **2018**, *84*. <https://doi.org/10.1016/j.optmat.2018.06.057>.
- (186) Tateiwa, N.; Haga, Y. Evaluations of Pressure-Transmitting Media for Cryogenic Experiments with Diamond Anvil Cell. *Rev. Sci. Instrum.* **2009**, *80* 12. <https://doi.org/10.1063/1.3265992>.
- (187) Shen, Y.; Kumar, R. S.; Pravica, M.; Nicol, M. Characteristics of Silicone Fluid as a Pressure Transmitting Medium in Diamond Anvil Cells. *Rev. Sci. Instrum.* **2004**, *75*, 4450–4454. <https://doi.org/10.1063/1.1786355>.
- (188) Pechini, M. P. Method of Preparing Lead and Alkaline Earth Titanates and Niobates and Coating Method Using the Same to Form a Capacitor. US3330697A, July 11, 1967. <https://patents.google.com/patent/US3330697A/en> (accessed 2025-05-19).
- (189) Shannon, R. D. Revised Effective Ionic Radii and Systematic Studies of Interatomic Distances in Halides and Chalcogenides. *Acta Crystallogr. A* **1976**, *32* (5), 751–767. <https://doi.org/10.1107/S0567739476001551>.
- (190) Bednarkiewicz, A.; Marciniak, L.; D. Carlos, L.; Jaque, D. Standardizing Luminescence Nanothermometry for Biomedical Applications. *Nanoscale* **2020**, *12* (27), 14405–14421. <https://doi.org/10.1039/D0NR03568H>.
- (191) Minomura, S.; Drickamer, H. G. Effect of Pressure on the Spectra of Transition Metal Ions in  $\text{MgO}$  and  $\text{Al}_2\text{O}_3$ . *J. Chem. Phys.* **1961**, *35* (3), 903–907. <https://doi.org/10.1063/1.1701235>.
- (192) Jovanic, B. R. High Pressure and Fluorescence Lifetime of the  $^2\text{E}$  Level in  $\text{MgO:Cr}^{3+}$ . *Phys. Scr.* **1997**, *56* (5), 477. <https://doi.org/10.1088/0031-8949/56/5/014>.
- (193) Ma, D.; Zheng, X.; Zhang, Z.; Xu, Y. Theoretical Calculations of the Pressure-Induced Blue and Red Shifts of Spectra of  $\text{MgO:Cr}^{3+}$ . *Phys. Lett. A* **1987**, *121* (2), 97–100. [https://doi.org/10.1016/0375-9601\(87\)90273-8](https://doi.org/10.1016/0375-9601(87)90273-8).
- (194) Wu, Z.; Wentzcovitch, R. M.; Umemoto, K.; Li, B.; Hirose, K.; Zheng, J.-C. Pressure-Volume-Temperature Relations in  $\text{MgO}$ : An Ultrahigh Pressure-Temperature Scale for Planetary Sciences Applications. *J. Geophys. Res. Solid Earth* **2008**, *113* (B6). <https://doi.org/10.1029/2007JB005275>.
- (195) Rajendran, V.; Fang, M.-H.; Huang, W.-T.; Majewska, N.; Lesniewski, T.; Mahlik, S.; Leniec, G.; Kaczmarek, S. M.; Pang, W. K.; Peterson, V. K.; Lu, K.-M.; Chang, H.; Liu, R.-S. Chromium Ion Pair Luminescence: A Strategy in Broadband Near-Infrared Light-Emitting Diode Design. *J. Am. Chem. Soc.* **2021**, *143* (45), 19058–19066. <https://doi.org/10.1021/jacs.1c08334>.
- (196) Saidi, K.; Hernández-Álvarez, C.; Runowski, M.; Dammak, M.; Martín, I. R. Ultralow Pressure Sensing and Luminescence Thermometry Based on the Emissions of  $\text{Er}^{3+}/\text{Yb}^{3+}$

- Codoped  $\text{Y}_2\text{Mo}_4\text{O}_{15}$  Phosphors. *Dalton Trans.* **2023**, 52 (41), 14904–14916. <https://doi.org/10.1039/D3DT02613B>.
- (197) Saidi, K.; Hernández-Álvarez, C.; Runowski, M.; Dammak, M.; Rafael Martín Benenzuela, I. Temperature and Pressure Sensing Using an Optical Platform Based on Upconversion Luminescence in  $\text{NaSrY}(\text{MoO}_4)_3$  Codoped with  $\text{Er}^{3+}$  and  $\text{Yb}^{3+}$  Nanophosphors. *ACS Appl. Nano Mater.* **2023**, 6 (20), 19431–19442. <https://doi.org/10.1021/acsanm.3c04031>.